Klimash, Anastasiia (2019) *Novel thermally activated delayed fluorescence materials for optoelectronic applications.* PhD thesis.

https://theses.gla.ac.uk/75087/

Novel thermally activated delayed fluorescence materials for optoelectronic applications

Anastasiia Klimash

Submitted in fulfilment of the requirements for the degree of

Doctor of Philosophy in Chemistry

School of Chemistry

College of Science and Engineering

University of Glasgow

May 2019

Abstract

Organic light-emitting diode (OLED) technology is steadily gaining more and more popularity, and, as of 2019, is the most commercially successful application of organic electronics. Compared to light-emitting diodes (LEDs), OLEDs possess several advantages such as colour tunability, quick switching times, higher brightness, better contrast, larger fields of view, the possibility to use lighter substrates instead of commonly used glass, and, potentially, cheaper production costs.

Improving the performance of OLED devices could open new opportunities for the development of the technology and might be crucial for it to strengthen its position in the market. Upon electrical excitation singlets and triplets are formed in 1:3 ratio, and one of the challenges is to design materials that can efficiently utilise triplet excited states to generate electroluminescence. In purely organic fluorescent compounds normally only singlets are emissive at room temperature, so in fluorescent devices only 25% of the excited states are used. Phosphorescent OLEDs are known for their high efficiency compared to their fluorescent predecessors, however the structure of these materials is limited to heavy metal-containing organic compounds. Thus, creation of purely organic light emitting materials is of a great interest for the field. One of the solutions is to use thermally activated delayed fluorescence (TADF) emitters where dark triplets can be converted into singlet excited states and thus 100% internal quantum efficiency could be achieved. The design and synthesis of new TADF emitters is the main scope of this thesis.

Chapter 1 gives a brief overview of the history of lighting technology with an emphasis on solid-state lighting. The milestones in the development of organic semiconductors are also described. The main concepts of organic electronics and the working principles of OLED devices are briefly approached. Furthermore, the existing ways of enhancing the efficiency of luminescent organic materials in light-emitting devices is discussed. A substantial part of the chapter is dedicated to the description of the main principles used for the design of materials exhibiting thermally-activated delayed fluorescence (TADF), recent advances in their development and future perspectives.

Chapter 2 describes the photophysical properties of new helicene-based TADF emitters, in particular their behaviour in the solid state. This includes the presentation of time resolved measurements of helical compounds in crystals and films. The performance of the materials in OLEDs was also investigated.

In Chapter 3 the synthesis and physical properties of novel-star-shaped donor-acceptor structures based on a truxene-benzothiadiazole-truxene core are discussed. The application of these materials in fluorescent OLEDs and as colour-converters in hybrid LEDs is described.

Chapter 4 demonstrates a new way of preparing materials exhibiting delayed fluorescence (DF) from non-DF quinoline-based starting materials by simple methylation. These methylated compounds exhibit either TADF or triplet-triplet annihilation (TTA) depending on the relative position of donor and acceptor moieties in the molecule. They also show aggregation-induced emission and mechanochromic properties. The photophysical behaviour of these compounds was investigated mainly in the solid state.

The experimental procedures for chapters 2–4 are presented in Chapter 5.

Table of contents

List of figures

List of schemes

List of tables

Acknowledgments

First, I would like to thank Prof. Peter Skabara for giving me the opportunity to work in his research group and for his guidance, advice and encouragement throughout my studies. I thank the European Union's Horizon 2020 research and innovation programme for funding my PhD under the Marie Skłodowska-Curie grant agreement H2020-MSCA-ITN-2015/674990 project "EXCILIGHT".

I thank postdoctoral researchers of the group Dr Neil Findlay, Dr Joseph Cameron and Dr Alexander Kanibolotsky for their day-to-day assistance and support throughout my PhD and for the help I received from them while writing my thesis. I extend my thanks to all past and present members of the Skabara group for providing a welcoming working environment. I am grateful to the technical staff at the University of Strathclyde, Ms Patricia Keating and Mr Craig Irving, and at the University of Glasgow, Dr Holly Yu, Mr Michael Beglan, Dr David Adam and Mr James Tweedie for their assistance.

I thank our collaborators from the Organic Electroactive Materials group at Durham University, working under the supervision of Prof. Andy Monkman and Dr Fernando Dias, for their invaluable contribution. My special thanks go to Piotr Pander for his help in characterisation of the materials presented in Chapter 2, and to Dr Marc Etherington for sharing with me his ideas that inspired the work described in Chapter 4 and for the photophysical characterisation of the materials presented in the same chapter.

I would like to thank Prof. Juozas Grazulevicius and the members of his research group for hosting me during my visit to Kaunas University of Technology (Lithuania).

I thank Dr Dmytro Volyniuk for the time-resolved measurements presented in Chapter 3. I am grateful to Dr Jochen Bruckbauer for the fabrication and study of hybrid LEDs presented in the same chapter. I thank Benjamin Breig for his help in preparation of OLEDs and Manon Bousquet for testing an alternative synthetic procedure discussed in Chapter 3.

I am grateful to all members of the EXCILIGHT team for the time we have spent together discussing exciton up-conversion, the universe and everything. I would especially like to thank Dr Przemyslaw Data for his work as a coordinator of this project.

Finally, I would like to thank my parents Tanya and Igor for all their love and support. I also thank my friends who never left me feeling alone.

Declaration

I declare that, except where explicit reference is made to the contribution of others, that this dissertation is the result of my own work and has not been submitted for any other degree at the University of Glasgow or any other institution.

Printed Name: Anastasiia Klimash

Signature:

Abbreviations and symbols

°C	degree Celsius
1/2/3D	one/two/three-dimensional
^{1}CT	singlet charge-transfer excited state
^{1}LE	singlet locally excited state
2-MeTHF	2-methyltetrahydrofuran
^{3}CT	triplet charge-transfer excited state
^{3}LE	triplet locally excited state
A	absorption/acceptor
Å	angstrom
a.u.	arbitrary units
Ac	acetate
AIE	aggregation-induced emission
BT	2,1,3-benzothiadiazole
C_{60}	fullerene
CB	conduction band
CBZ	carbazole
CCT	correlated colour temperature
cd	candela
CE	current efficiency
CES	Consumers Electronic Show
CHDV	1,4-cyclohexanedimethanol divinyl ether
CIE	Commission Internationale d’Eclairage
cm	centimetre
CPL	circularly polarised light
CRI	colour rendering index
CSA	camphosulfonic acid
CT	charge transfer
D	donor/debye
d	deuterated/doublet

dba	dibenzylideneacetone
DCM	dichloromethane
DF	delayed fluorescence
DMAC	9,9-dimethyl-9,10-dihydroacridine
DMF	dimethyl formamide
DSC	differential scanning calorimetry
e	electron charge
$E_{1/2}$	half-wave potential
EBL	electron blocking layer
E_g	HOMO-LUMO energy gap
$E_{g(opt)}$	optical HOMO-LUMO gap
EI	electron ionisation
EIL	electron injection layer
EL	electroluminescence
em	emission
EML	emissive layer
E_{orb}	orbital energy
E_{ox}	oxidation potential
EQE	external quantum efficiency
E_{red}	reduction potential
E_{S_1}	energy of the lowest singlet excited state
ESI	electrospray ionisation
ESIPT	excited-state intramolecular proton transfer
E_{T_1}	energy of the lowest triplet excited state
ETL	electron transport layer
eV	electronvolt
exc	excitation
exp	experimental
F	fluorescence
f	oscillator strength
Fc	ferrocene

f_{Hex}	hexane fraction
FRET	Förster energy transfer
FWHM	full width at half maximum
GCMS	gas chromatography-mass spectrometry
GPC	gel permeation chromatography
h	Planck’s constant/hours
H	HOMO
HBL	hole blocking layer
HID	high-intensity discharge
HIL	hole injection layer
HOMO	highest occupied molecular orbital
HPLC	high-performance liquid chromatography
HTL	hole transport layer
Hz	hertz
I	illuminance
IC	internal conversion
iCCD	intensified charge coupled device
ICT	internal charge transfer
IQE	internal quantum efficiency
irr	irreversible
ISC	intersystem crossing
ITO	Indium-doped tin-oxide
J	exchange energy of two unpaired electrons in the excited state
J	coupling constant
K	Kelvin/electron repulsion energy
k_B	Boltzmann constant
k_r	radiative rate constant
k_{rISC}	reverse intersystem crossing rate
L	luminance/LUMO
LE	locally excited
LED	light-emitting diode
lm	lumen

LUMO	lowest unoccupied molecular orbital
M	spin multiplicity/molar (mol/litre)/molecule
m	multiplet
MALDI	matrix-assisted laser desorption/ionisation
MC	mechanochromism
MCH	methylcyclohexane
MO	molecular orbital
MS	mass spectrometry
MUE	mean unsigned error
n	non-bonding orbital/number of units
NBS	N-bromosuccinimide
Nd:YAG	neodymium-doped yttrium aluminium garnet
NMR	nuclear magnetic resonance
O.D.	optical density
OFET	organic field-effect transistor
O_{ia}	orbital overlap
OLED	organic light-emitting diode
OPV	organic photovoltaic
OSC	organic solar cell
P	phosphorescence
PAH	polyaromatic hydrocarbon
PE	power efficiency
PF	prompt fluorescence
PGM	platinum group metals
PHOLED	phosphorescent organic light-emitting diode
PL	photoluminescence
PLQY	photoluminescence quantum yield
PMMA	Poly(methyl methacrylate)
ppm	parts per million
PPV	poly(p-phenylene vinylene)
PXZ	phenoxazine
q	quadruplet

q-r	quasi-reversible
R	substituent group
Ref.	reference
RGB	red, green and blue
rIC	reverse internal conversion
rISC	reverse intersystem crossing
rpm	rotations per minute
RT	room temperature
RTP	room-temperature phosphorescence
S	spin quantum number/singlet electronic state
s	second/singlet
SiC	silicon carbide
S_n	upper singlet state
SOC	spin-orbit coupling
sr	steradian
T	triplet electronic state/temperature
t	triplet/*tert*-
TADF	thermally activated delayed fluorescence
tBu-CBZ	*3,6*-di-*tert*-butyl carbazole
TCSPC	time-correlated single-photon counting
TDDFT	time-dependent density functional theory
Tf	triflate
T_g	glass transition temperature
TGA	thermal gravimetric analysis
THF	tetrahydrofuran
TLC	thin layer chromatography
TMS	trimethylsilyl group
TOF	time of flight
Tol	toluene
T_{st}	solid-solid phase transition temperature
TTA	triplet-triplet annihilation
UV	ultraviolet

V	volt
VB	valence band
VC	vibronic coupling
vis	visible
VR	vibrational relaxation
W	watt
w/w	weight percent
XPhos	2-dicyclohexylphosphino-2′,4′,6′-triisopropylbiphenyl
Z	atomic number
z	charge number of ions

Greek

γ	charge balance factor
δ	chemical shift
$\Delta E_{a(TADF)}$	thermal activation energy of TADF
ΔE_{ST}	singlet-triplet energy gap
ε	molar extinction coefficient
η_{int}	internal quantum efficiency
η_{out}	light out-coupling efficiency
η_{ST}	exciton production efficiency
κ_{ia}	electronic transition contribution
λ	wavelength
Λ	spatial overlap
μ	micro/dipole moment
π	pi-bonding orbital
π^*	pi-anti-bonding orbital
ρ_{FC}	Franck-Condon-weighted density of states
σ	sigma bonding orbital
σ^*	sigma anti-bonding orbital
$\boldsymbol{\tau}$	lifetime
υ	frequency

ϕ	wavefunction of HOMO
φ_a	unoccupied orbital
φ_i	occupied orbital
Φ_{PL}	Photoluminescence quantum yield
ψ	wavefunction of LUMO/wavefunction of exciplex

Chapter 1. Introduction

For centuries human life revolved around the natural cycle of day and night. The invention of the electric light source has completely changed how people manage their time, extending the notion of daily activity into night. Artificial light not only let people perform various tasks outside of daylight time, but also improved public safety and in general became a symbol of technological progress. Despite all the positive changes artificial light brings, its ever-increasing use results in light pollution that can negatively impact individual biological species as well as whole ecosystems.[1,2] It can also lead to the disruption of circadian rhythms in humans, and give rise to undesired metabolic changes.[3] In 2006 illumination was responsible for 17.5% of the total global energy consumption.[4] According to the report of the International Energy Agency 1.2 billion people have gained access to electricity worldwide since 2000.[5] With the amount of population using artificial illumination only growing in the future, making lighting more energy efficient, safe and environmentally friendly is of a great importance.

The development of modern lighting technology began with the invention of the incandescent light bulb in the 19th century. Since then more efficient high-intensity discharge (HID) lamps have widely replaced their predecessors. Mercury-vapour, metal-halide and sodium-vapour lamps are among the most commercially successful (HID) lamps.[6] In recent years solid-state lighting has emerged as an alternative to conventional light sources. Light emitting diodes (LEDs) and their organic-based counterparts, organic light-emitting diodes (OLEDs), are semiconductor devices that emit light due to electron-hole recombination process when current is applied (this effect will be further discussed in Section 1.3). This process, later termed electroluminescence, was first observed by Henry Round in 1907 by applying voltage to a crystal of silicon carbide (SiC).[7] In 1927 Losev has filed a patent for the use of the light-emitting SiC detectors for information transfer and recording, which was well ahead of the commercial development of optical storage and communication.[6] The modern definition of electroluminescence was developed by Lehovec in 1951[8] after the discovery of the transistor by Bardeen and Brattain in 1948[9]. The first visible light (red) LED based on a GaAsP alloy was reported by Holonyak and Bevacqua in 1962.[10] In the 1970s, the first commercial products such as calculators and wristwatches containing GaAsP red LEDs were introduced.[6] The work on blue LEDs began in the early 1970s and culminated in the development of high brightness GaN/InGaN LEDs by Nakamura *et al*. in 1993.[11] This was a starting point for the development of white LEDs, which in turn has made solid-state lighting technology as popular as it is nowadays. In 2014 Nakamura, Amano and Akasaki were awarded the Nobel Prize in Physics for the invention of efficient blue LEDs.[12] The advantages of LEDs over traditional light sources include higher efficiencies, better brightness modulation, higher reliability, durability and longer lifetime. More recently developed OLEDs can be considered the youngest lighting technology and are the focus of this thesis.

Organic electronics is a field of materials science concerning the development of organic small molecules and polymers with semiconducting properties. Apart from OLEDs these compounds find application in devices such as organic field-effect transistors (OFETs), and organic solar cells (OSCs).

The semiconductor industry is still predominantly based on inorganic materials. Yet organic compounds have advantages that can extend the range of possible applications and meet the needs that cannot be addressed with silicon-based semiconductors. Flexible and stretchable organic materials can be used in biomedical devices and health monitoring systems.[13,14] Biodegradable materials might not only make the technology more environmentally friendly, but also open new opportunities for the use of disposable electronic devices.[15,16] Lightweight transparent materials can also provide new design solutions. For example, it is possible to cover with organic solar cells a variety of surfaces including windows[17] or use transparent OLED screens[18] for augmented reality applications and heads-up displays. Due to their expected low production costs, organic electronic devices can be considered more suitable for large area applications. Also, organic semiconductors have the potential to be more sustainable.[19] Finally, there is nearly unlimited structural diversity of applied materials that can be achieved by means of organic synthesis.

The electrical activity of carbon-based materials has been investigated since the beginning of the twentieth century. The electrical conductivity of graphite has long been studied and was attributed to the specific arrangement of carbon atoms that form a π-conjugated system within the layers of the material.[20] More than fifty years later the individual layers of graphite (graphene) were isolated, and the history of two-dimensional materials began.[21] In the 1950s, electrical conductivity was observed and investigated in many more polycyclic aromatic hydrocarbons such as violanthrone and pyranthrone.[22] In 1954 Akamatu *et al.* reported the observation of electrical conductivity in a phenanthrene complex with bromine.[23] In 1964

William Little discussed the possibility of synthesising organic superconductors,[24] and during the next decade the emphasis was on the development of conductive organic materials.

The investigation of conductivity in conjugated structures was not confined to carbon-based compounds. In 1973 Labes and co-workers reported the study of electrical conductivity of polymeric sulphur nitride $(SN)_x$.[25] This work inspired MacDiarmad and Heeger to take a closer look at the structure of this material,[26] later leading to a collaborative project with Shirakawa, who was working on polyacetylenes that had an unusual (for polymers at least) silvery colour. It turned out that both *cis*- and *trans*-polyacetylenes when doped with halogens demonstrate metallic conductivity.[27,28] For this discovery Shirakawa, MacDiarmad, and Heeger were awarded the Nobel Prize in Chemistry in 2000.[29]

Nowadays, of all organic electroactive materials, semiconductors attract the most attention. The photovoltaic effect was first reported in organic compounds in 1958,[30] although the efficiencies were limited to about 1% for a few decades.[31] In recent years significant improvements were made in the field. Thus, in 2018 the record for organic solar cells efficiencies was surpassed twice in tandem OPV devices with 15% and 17.3% reported by Che *et al.*[32] and Meng *et al.*,[33] respectively. Electroluminescence in organic materials has been known since the 1960s when it was first observed by applying alternating current to brilliant acridine orange E, and direct current to anthracene.[34,35] However, because the minimum thickness of the materials was in the range of few thousands of nanometres, efficient charge injection was only possible when a very high voltage is applied, making the concept not suitable for technological applications. In 1987 Tang *et al.* reported the first stable electroluminescent diode based on thin films of small organic molecules[36] followed by the work of Burroughes *et al.* on first polymer-based OLEDs,[37] and interest in organic semiconductors was reignited. Around the same time the first organic field-effect transistor with polythiophene as a semiconducting material was reported by Koezuka *et al.*[38] Since then more organic-based devices were developed including lasers,[39] photodiodes[40] and all-polymer integrated circuits.[41] Many of these technologies have yet to pass the product development phase.

Clearly, the field is relatively young, but it has already achieved a stage of maturity with numerous examples of commercially successful applications, including xerography[42] being the earliest. The first OLED TV was launched by SONY in October 2007.[43] Samsung

Display remains the leading manufacturer of active-matrix OLED panels with almost 90% share of the market as for 2017,[44] and some of Samsung's flagship devices such as the Galaxy S9 and Note 9 smartphones, and Galaxy Tab S4 tablet can be cited among the most famous products present at the market in 2018.[45] Finally, at the Consumer Electronic Show (CES) 2019 LG has presented its first rollable TV that is expected to be commercially available within 12 months.[46]

Organic electronics is a highly interdisciplinary field where knowledge of photophysics, device architecture and organic synthesis is required for the development of materials for semiconducting devices. In the following sections, the basic electronic processes in organic semiconductors as well as the main principles for the design of highly efficient organic light emitting materials are described.

1.1 Band theory

The properties of materials are determined by their atomic scale structure and, more precisely, by interactions between atoms or molecules in the solid state. Electrical conductivity can be explained in terms of electronic band theory. In isolated atoms electrons are found in discrete energy states. When more atoms are joined together in the solid state, atoms' outer shell atomic orbitals are overlapped at the greatest extent with the difference between energy states of the atoms becoming so low that they form continuous energy bands.[47]

According to the Aufbau principle valence electrons fill the lowest available energy levels first with higher levels being occupied subsequently. In metals, the electrons in the outer shells are delocalised and can easily move into neighbouring empty energy levels. At absolute zero these electrons fill the valence band (VB) up to the Fermi level, making it the highest level occupied at 0 K. At higher temperature electrons can move into neighbouring empty energy levels in the conduction band (CB) leaving behind positively charged "holes" in the valence band.

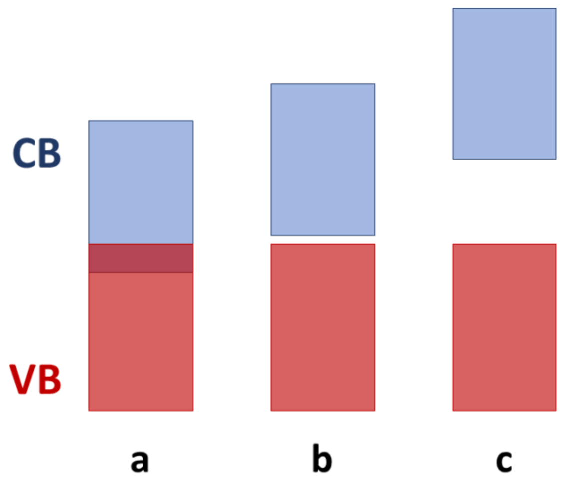

Figure 1.1. Schematic representation of energy bands for metal (a), semiconductor (b) and insulator (c)

For semiconductors and insulators, the conduction and the valence band are separated by an energy gap (also called the bandgap). Its magnitude defines the properties of the material (Figure 1.1). In semiconductors the bandgap is relatively small, and electrons can gain enough energy from heating or an applied electric field to move from the valence to the conduction band. In insulators the energy difference between the valence and conduction band is too large for electrons to overcome and thus no electric current can flow through such solids.[48]

In molecular organic semiconductors instead of the terms valence and conduction band the concept of highest occupied molecular orbital (HOMO) and lowest unoccupied molecular orbital (LUMO) is used. According to the linear combination of atomic orbitals theory, n atoms in the molecule form n/2 bonding and n/2 antibonding molecular orbitals (MOs). Normally electrons are situated at bonding orbitals that are lower in energy than antibonding. The highest orbital filled with electrons is considered the HOMO and the unoccupied orbital with the lowest energy is called the LUMO.[4]

All organic semiconducting materials possess conjugated motifs consisting of alternating double and single bonds. The sp^2 hybridisation of carbon gives three planar hybrid orbitals separated by an angle of 120° and one $2p_z$ orbital perpendicular to them. The overlap of two sp^2 hybridised orbitals leads to the formation of a σ bond, and the two remaining $2p_z$ orbitals can overlap to form a π bond. The energy difference between π bonding (HOMO) and π^* antibonding (LUMO) orbitals is relatively small and when the molecule has an extended conjugated system the overlap between MOs is increased to the point where they form continuous energy bands similar to the valence and the conduction bands in inorganic semiconductors (Figure 1.2).[49]

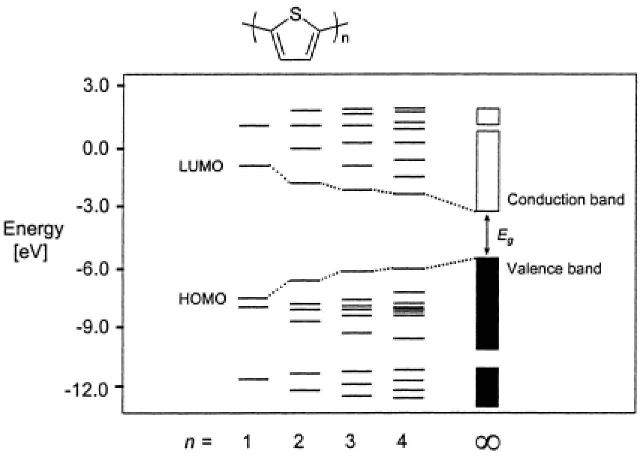

Figure 1.2. Energy levels calculated for oligothiophenes with n = 1-4 and polythiophene. Reproduced from Ref.[49]

1.2 Excited states and electronic transitions in organic molecules

Upon optical or electrical excitation an electron is promoted from an orbital of a molecule in the ground state (HOMO) to an unoccupied orbital (LUMO), creating an excited state. There are three types of molecular orbitals where electronic transitions can occur: σ and π orbitals, that were discussed in the previous section, and n-orbitals where non-bonding electrons of heteroatoms such as oxygen or nitrogen are located. Figure 1.3 shows possible electronic transitions for σ, π and n-orbitals taking as example a molecule of formaldehyde. The transition $\sigma \rightarrow \sigma^*$ requires a lot of energy with the absorption maxima located in the far UV, hence they are not typically observed in a standard UV-Visible absorption spectrum. Mainly absorption spectroscopy is based on $n \rightarrow \pi^*$ and $\pi \rightarrow \pi^*$ transitions that occur at lower energies and fall in a convenient region of the spectra between 200 and 700 nm.[50]

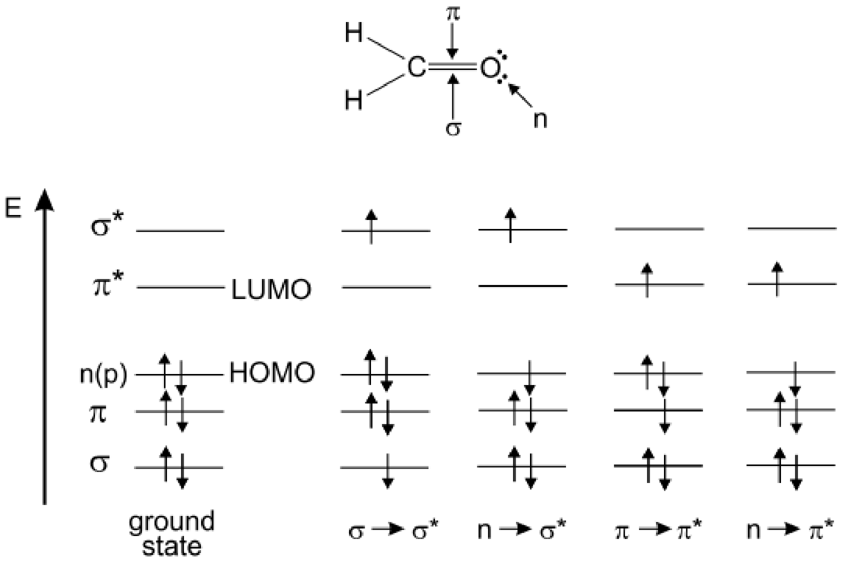

Figure 1.3. Possible electronic transitions in formaldehyde. Reproduced from Ref.[50]

The type of excited state created upon energy absorption depends on the total spin quantum number S ($S = \sum s_i$, where $s_i = +\frac{1}{2}$ or $-\frac{1}{2}$), which in turn determines the spin multiplicity M. The multiplicity is defined as 2S+1, and it is the number of possible orientations of the spin angular momentum relative to a given S. A singlet excited state is formed if the spin of the electron promoted to the LUMO is anti-parallel to that of the electron left at the HOMO (spin multiplicity is equal to 1). If the spins of the electrons are parallel, a triplet state is created with the multiplicity of 3 (Figure 1.4).[51] According to Hund's rule the term with the highest spin multiplicity is the lowest in energy, so a triplet excited state is normally lower in energy than a singlet.[50]

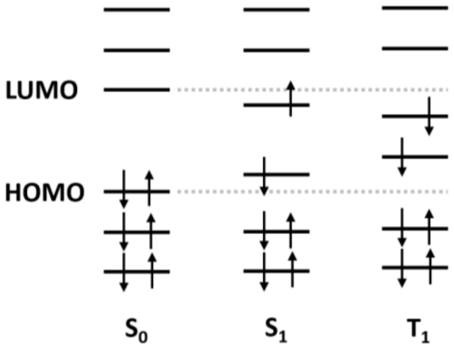

Figure 1.4. Schematic representation of singlet and triplet excited states.

In general, the physical processes that occur after a molecule absorbs light can be illustrated by a Jabłoński diagram (Figure 1.5). Electronic states are shown in the diagram in bold lines and denoted by S_0, S_1– S_n for singlet states and T_1 – T_n for triplet states. Each electronic state also consists of many vibrational energy levels (depicted as black horizontal lines). Normally at room temperature only the lowest vibrational level of the ground state (S_0) is populated.

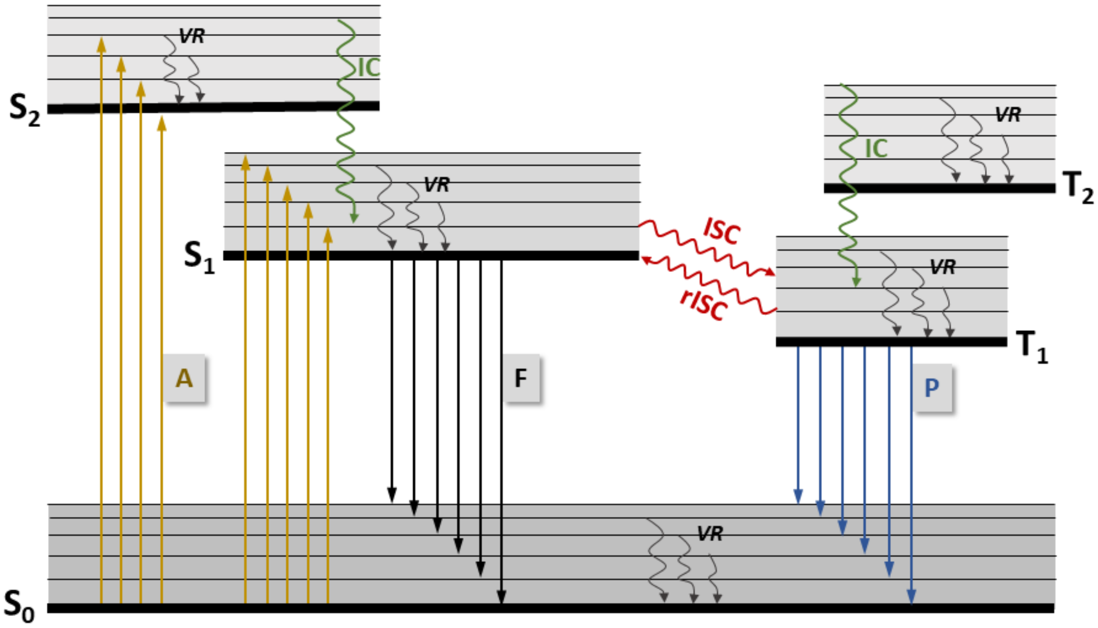

Figure 1.5. Jabłoński diagram.

When a molecule absorbs a photon (yellow arrows, A), an electron is excited to one of the vibrational levels of the upper singlet state (S_n). Several processes can occur afterwards that can be either radiationless or luminescent. Among the main non-radiative processes are internal conversion, vibrational relaxation, intersystem crossing and reverse intersystem crossing. Vibrational relaxation (VR) occurs from vibrational excited states to the lowest vibrational level within one electronic state (wavy black arrows). Internal conversion (IC) is a de-excitation process between a higher and a lower electronic excited state of the same spin multiplicity (wavy green arrows). IC is more likely to occur between upper states, as the energy gap between S_1 and S_0 is usually too high. Intersystem crossing (ISC) is a transition between two isoenergetic vibrational levels of two electronic levels with different multiplicities (wavy red arrow). Thus, ISC can occur between the lowest vibrational level of the singlet excited state (S_1) and the closest in energy vibrational level of the triplet state (T_1), then vibrational relaxation can occur. Transition between electronic states of different multiplicity is a forbidden process, but it can take place if the spin-orbit coupling (SOC) is large enough.[50] If the energy of S_1 is close to that of T_1, and the lifetime of T_1 is long enough, reverse intersystem crossing (rISC) can occur (wavy red arrow). The latter process will be discussed in more detail in Sections1.3.3 and 1.4.

A molecule can relax to the ground state (S_0) from S_1 or T_1 by losing the energy via photon emission. These luminescent processes are called fluorescence (F) for $S_1 \rightarrow S_0$ transition and phosphorescence (P) for $T_1 \rightarrow S_0$ transition.[52] However, in organic compounds at room temperature non-radiative decay is usually predominant for the triplet excited state, especially in solutions. Phosphorescence is more favoured in a rigid medium, but even in this case it is usually observed only at low temperatures. Still, it is possible to induce phosphorescence at room temperature in organic molecules.[53]

Clearly, there are many de-excitation pathways, and the probability of each depends on both external factors (such as temperature, the type of medium containing the molecule or the presence of impurities), and the molecular structure of a compound itself.

1.3 General principles of OLED devices

The simplest OLED device is composed of a thin organic luminescent layer placed between two electrodes. When a voltage is applied, holes and electrons are injected from the anode and cathode respectively into the organic semiconductor layer (emissive layer (EML)). After charge carriers migrate through the organic layer to meet, they recombine and form excitons. During the radiative decay of the excitons to the ground state, light is emitted. One of the first reported OLEDs contained poly(p-phenylene vinylene) (PPV) as an emissive layer, and its performance was quite low by modern standards, as PPV is mainly a hole-transporting material, so the charge mobility was not properly balanced.[37] In general, electrons are less mobile than holes, so excitons formed in a single-layer device will be most likely located closer to the cathode and can be easily quenched through non-radiative processes. In the early days of the development of OLEDs Tang *et al.*[36] reported a multi-layer device structure (Figure 1.6-a) containing 4,4′-cyclohexylidenebis[N,N-bis(4-methylphenyl)benzenamine] (TAPC) as a hole-transporting layer (HTL), and tris(8-hydroxyquinoline)aluminium (Alq_3) as an emissive layer (EML), which, due to its good electron mobility, also acted as an electron-transporting layer (ETL) (Figure 1.6-b). In such a device excitons are predominantly formed away from the cathode and closer to the interface between the two organic layers.

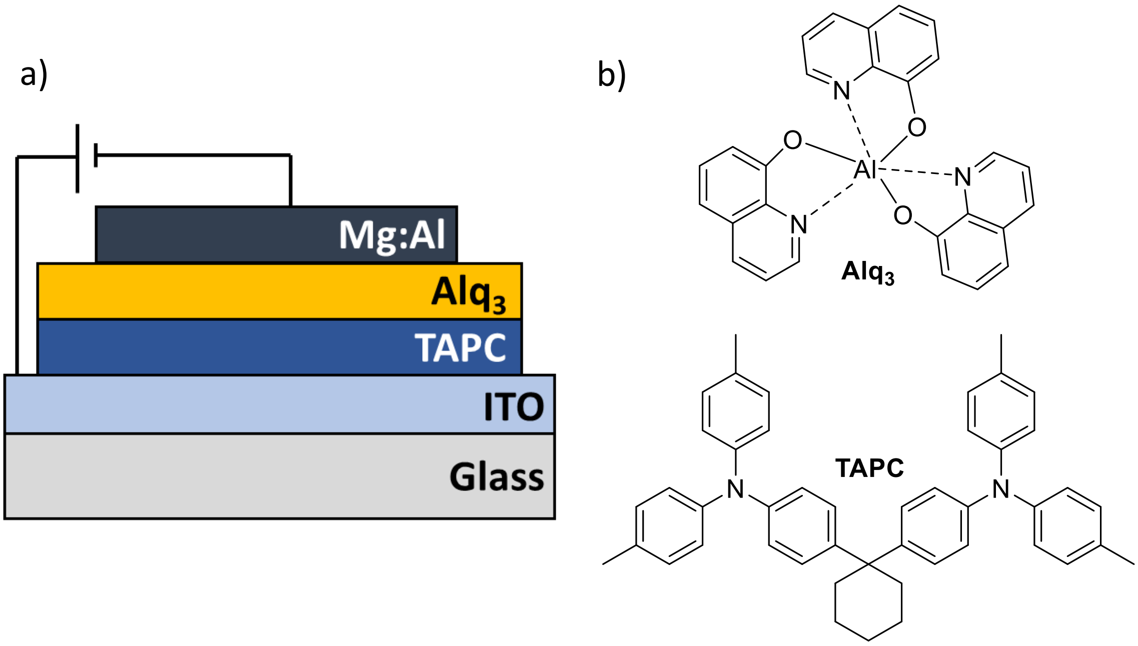

Figure 1.6. The architecture of the first double-layer OLED (a) and the molecular structure of the materials used (b).

Modern OLED devices can have even more complicated structures with a few additional organic layers including a hole injection layer (HIL), a hole transport layer (HTL) (often also used as an electron blocking layer (EBL)), an electron transport layer (ETL) (that can also act as a hole blocking layer (HBL)), and an electron injection layer (EIL) (Figure 1.7).[54] Additionally, the device can contain separate HBL and EBL that prevent charge carriers from migrating further in the bulk and force them to recombine in the emissive layer.

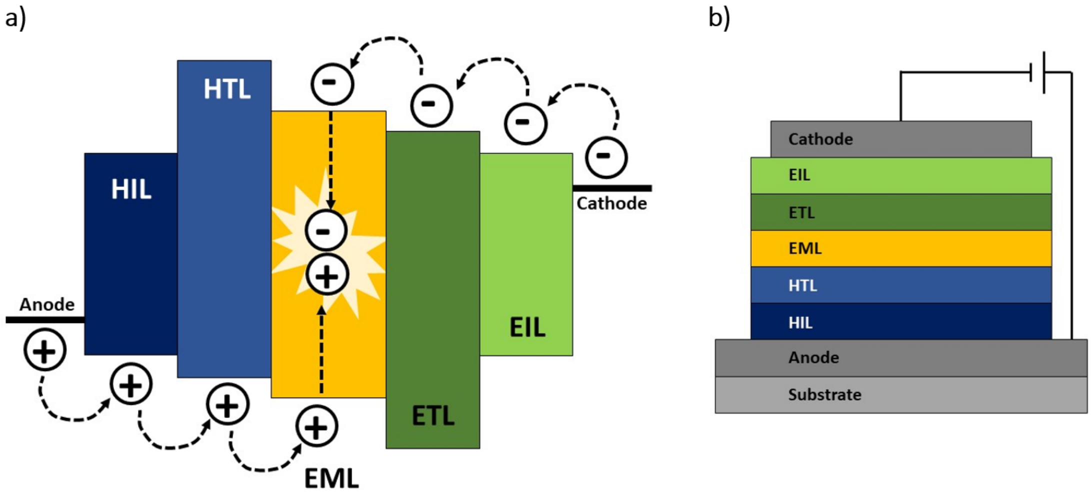

Figure 1.7. General structure of a multiple layer OLED device.

1.3.1 Materials for OLEDs

Indium-doped tin oxide (ITO) is the most commonly used anode material due to its high transparency and electrical conductivity. An HIL is usually inserted between the ITO and HTL to lower the operating voltage by minimising the energy barrier for the injection of holes. The conductive polymer blend PEDOT:PSS (poly(3,4-ethylenedioxythiophene) polystyrene sulfonate) is often used as an organic HIL[55] (Figure 1.8). It is a water-soluble material that can be deposited by solution processing.

As previously discussed, HTLs are very often used to improve the migration of holes into the EML, and to do so an HTL should have a HOMO level close to that of the EML. Due to its inherently poor electron transport properties, the HTL can also be used as an EBL, providing the confinement of excitons in the EML. Thus it is preferable for the HTL to also have a shallow LUMO level and a large band gap to provide a sufficient energy barrier for electrons and avoid exciton diffusion.[56] Triaryl amines such as tris(4-carbazoyl-9-ylphenyl)amine (TCTA) or 4,4',4''-tris[(3-methylphenyl)phenylamino]triphenylamine (m-MTDATA) are typical materials used as HTLs (Figure 1.8).[57]

Similarly to HTLs, ETL materials act in two ways. Apart from providing a high electron mobility they should also serve as an HBL, so the HOMO of the material needs to be deep enough to prevent holes from migrating past the EML and the LUMO level needs to be comparable to the work function of the cathode. Among common materials for ETLs are phenanthroline derivatives such as 4,7-diphenyl-1,10-phenanthroline (BPhen) and its methylated analogue 2,9-dimethyl-4,7-diphenyl-1,10-phenanthroline (BCP),[58] oxadiazole-based compounds such as 2-(4-tert-butylphenyl)-5-(4-biphenylyl)-1,3,4-oxadiazole (PBD),[59] and pyridine derivatives (1,3,5-tri(m-pyridin-3-ylphenyl)benzene (Tm_3PyPB)) (Figure 1.8).[60]

Cathodes are normally made of materials with a low work function that favours electron injection into the LUMO of the organic layer. Low work function metals such as Li, Mg and Ca are highly sensitive to moisture and oxygen. Using them in combination with less reactive Ag or Al can improve the stability of the device.[56] Alkaline metal compounds such as LiF, CsF, Cs_2CO_3, and Li_2O are widely used as EIL materials.[61] A LiF/Al bilayer is often used to lower the injection barrier. Usually only a thin layer (≈ 1 nm) of LiF is used. Some studies explain the enhancement of the electron injection by electron tunnelling between a cathode and an ETL through the thin metal complex layer,[62] whereas others suggest that the LiF reacts with thermally activated aluminium resulting in the doping of the ETL material by Li.[63] Lithium quinolate complexes such as 8-hydroxyquinolinolatolithium (Liq) or 2-methyl-8-hydroxyquinolinolatolithium (LiMeq) are sometimes used instead of LiF to improve the processability (Figure 1.8).[64]

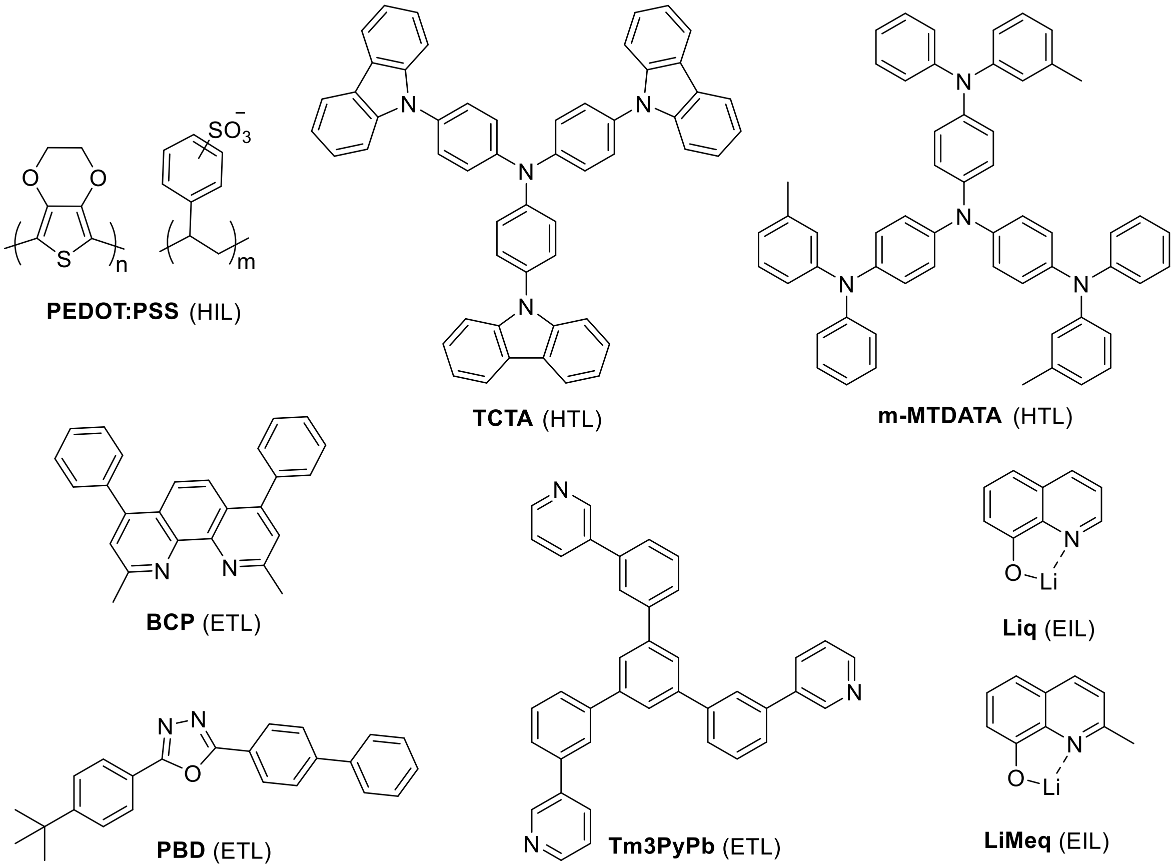

Figure 1.8. Examples of some HIL, HTL, ETL and EIL materials.

1.3.2 Characterisation of OLEDs

Luminescence produced by electrical rather than optical excitation is called electroluminescence (EL). Unlike for optical excitation which preserves spin, so that only singlet excitons are created, electrical excitation results in the formation of both singlets and triplets in a 1:3 ratio (according to the spin statistics). This distribution for organic electroluminescent devices was also experimentally proven by Baldo and co-workers.[65]

Fluorescent OLEDs can utilise only 25% of excitons, as the remaining 75% of formed triplet excitons are usually non-emissive at room temperature. External quantum efficiency (EQE) is one of the main parameters used to evaluate the performance of OLED devices which can be calculated with the formula:

$$\mathrm{EQE} = \eta_{int} \times \eta_{out} = \gamma \times \eta_{ST} \times \Phi_{PL} \times \eta_{out} \qquad (1.1)$$

Where γ is the charge balance factor, which is the ratio of the number of exciton-forming events to the electrons flowing in the external circuit, η_{ST} is exciton production efficiency, η_{int} is internal quantum efficiency (IQE), η_{out} is light out-coupling efficiency, which is a function of the refractive index of the emitter layer usually considered to be 20-30% because of optical reflection and loss in layers, and Φ_{PL} is the photoluminescence quantum efficiency (PLQY) defined by the ratio of photons emitted to photons absorbed by the material.[56,66] It is worth noting that for most devices only an approximate value of η_{out} is known, so the comparison of EQEs for different devices should be done with caution. For fluorescence-based OLEDs the maximum EQE is limited to 5-7.5%. All parameters can be optimised to attain best performances of the devices. Photoluminescence quantum efficiency of up to 100% can be achieved for organic materials, and there is a substantial amount of work dedicated to improving a charge balance in OLEDs with some of the methods described above. In recent years several methods to increase the light out-coupling efficiency in OLEDs were also developed, including the use of low-refracting index materials for the ETL,[67] using a crystallised organic scattering layer formed on the outside of the OLED,[68] or employing embedded microlens arrays as light extraction structures.[69] Still the efficiency of devices is particularly limited by exciton production efficiency, and for high performance devices both triplets and singlets should be used. The ways of overcoming spin statistics limitations for the increase of EQE will be discussed in Section 1.3.3.

Apart from EQE expressed in radiometric units there is a variety of metrics used to evaluate and compare different light sources considering the human eye sensitivity. These units are called photometric. One of the photometric quantities is luminous flux which is the light power of a source perceived by the human eye. It is measured in lumens (lm). The radiometric analogue for the luminous flux is the optical power (also called radiant flux) which is the radiant energy emitted or received per unit of time. Optical power is measured in watts (W). A monochromatic source that emits an optical power of 1/683 W at 555 nm (the wavelength at which the human eye has the highest sensitivity) has a luminous flux of

1 lm[7]. The luminous intensity is the luminous flux emitted at a certain angle. It is measured in candelas (cd) with 1 cd being the luminous flux emitted into the solid angle of 1 steradian (sr). Thus, 1 candela equals 1 lumen per steradian (cd = lm/sr). The illuminance (I) and the luminance (L) are the luminous flux and the luminous intensity incident per unit area respectively. Illuminance is measured in units of lux (lux = lm/m^2) and luminance in cd/m^2. Typical luminance of displays is around 50-400 cd/m^2, while a luminance of above 1000 cd/m^2 is required for lighting applications.[7]

The electrical performance of light-emitting devices can be defined by three main characterisations: external quantum efficiency (EQE), current efficiency (CE) and luminous efficacy, also referred here as power efficiency (PE).[70–72] Current efficiency is defined as the luminance produced by the current flowing through the unit area of the light-emitting device and is measured in cd/A. Power efficiency is the amount of luminous flux generated per Watt of electrical input power (lm/W).[70]

The colour quality of the light source can be defined by the Commission Internationale d'Eclairage (CIE) chromaticity diagram (x,y), the correlated colour temperature (CCT) and the colour rendering index (CRI). In order to establish a link between the wavelengths in the electromagnetic visible spectrum and human colour vision the International Commission for Illumination has developed the CIE (x,y) chromaticity diagram (Figure 1.9-a)[7]. Pure colours are situated on the perimeter of the diagram and white light is located at the centre with coordinates (0.33, 0.33). The colour temperature of a white source is defined as the temperature of an ideal black body radiator (also called a Planckian radiator) that radiates light of the same colour as a given light source. The colour of many light sources does not fall on the Planckian locus, and thus the correlated colour temperature (CCT) is used to quantify the colour. The CCT is the temperature at which the colour of the Planckian black body is the closest to that of the given light source. The CCT can be determined by using isothermal lines crossing the locus (Figure 1.9-b).[7] Achieving daylight spectra (with CCT between 5000 K and 7000 K[7]) in white LEDs seems to be a preferable option as it is the most natural type of light for human eye perception. However, the requirements for the CCT of the white light vary over the world. Thus, warm white light (2800 K to 3000 K) is preferred in the US and UK households while Japan, for example, uses mainly 5000 K white lighting.[73] Also, in some places, indoor lighting with a CCT of up to 7500 K is acceptable.

Another important parameter characterising the white light source is the colour rendering index (CRI). The CRI defines the ability of the white light source to accurately render the colours of objects illuminated by this source. The Planckian black body source is considered to provide a perfect colour rendering and has the highest CRI value (100).

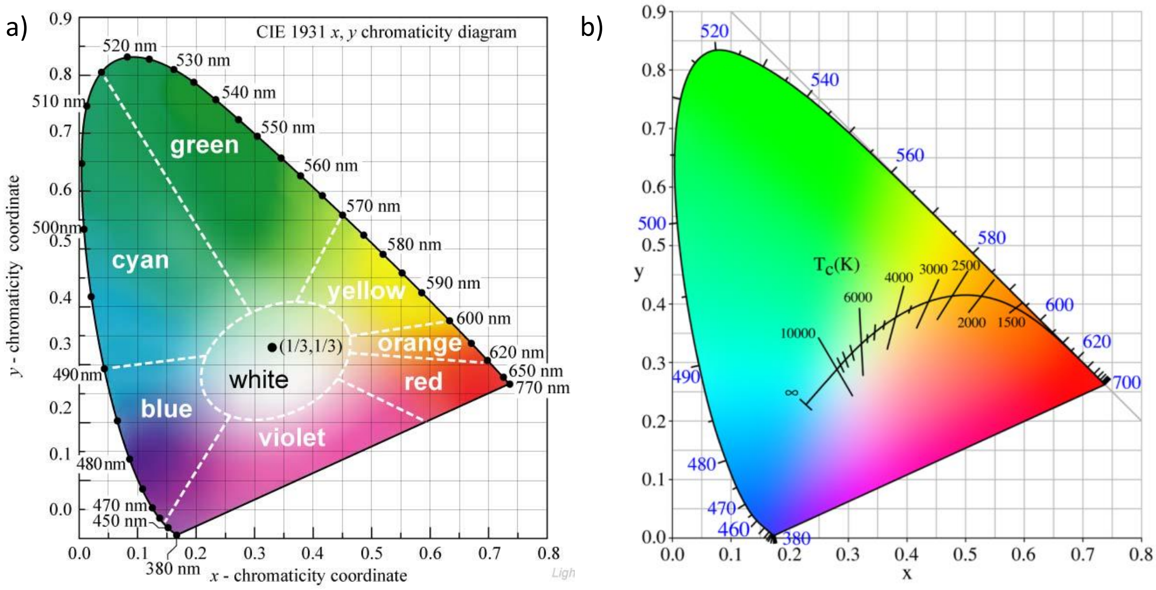

Figure 1.9. (a) CIE 1931 (x,y) chromaticity diagram with pure white light located in the middle and monochromatic light at the boundaries, reproduced from Ref.[7]; (b) Planckian locus and isothermal lines of constant correlated colour temperature in the CIE 1931 chromaticity diagram, reproduced from Ref.[74]

1.3.3 The main mechanisms of triplet harvesting in OLEDs

There are a few different mechanisms of triplet harvesting that can be used in materials for OLEDs. The most widespread approach is to use organometallic complexes containing heavy metals that enhance spin-orbit coupling (SOC). This increases the rate of ISC and allows the radiative decay of the triplet excited state.[75] In such a way, IQEs of phosphorescent OLEDs (PHOLEDs) can achieve 100% (Figure 1.10-a). However there are still problems with achieving stable blue emission for organic phosphorescent materials.[76] Also, commercially used emitter materials for PHOLEDs are mostly iridium and platinum-based. Platinum group metals (PGM) are required for a large variety of industrial applications other than optoelectronics, and the demand most likely will only increase in future. Consequently, the replacement of scarce elements with more abundant alternatives is of a great interest for the field.[19]

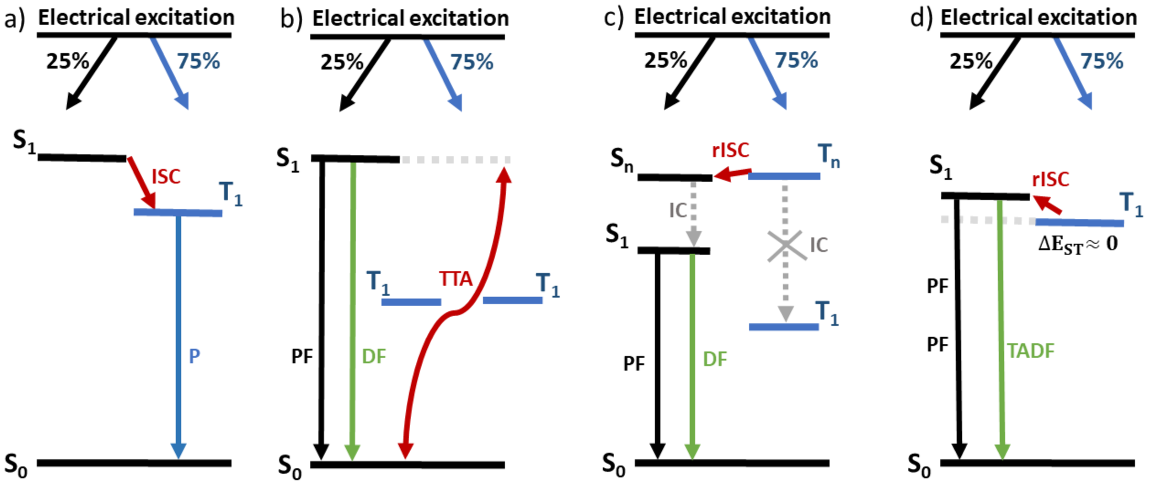

Figure 1.10. Main ways of triplet harvesting. Introduction of heavy metals into organic structure (a); Triplet-triplet annihilation (b); Reverse intersystem crossing in hot excitons (c); Thermally activated delayed fluorescence (d).

Another way to harvest triplet states in OLEDs is triplet fusion through the triplet-triplet annihilation (TTA) process (Figure 1.10-b). In this case two molecules in the T_1 state collide and form one singlet excited state that can decay radiatively. The process can be described by the following reaction:

$$T_1 + T_1 \rightarrow S_1 + S_0 \rightarrow 2S_0 + h\nu \qquad (1.2)$$

Since the process involves an additional transition of the molecules from T_1 to S_1, the resulting fluorescence has a much longer radiative decay. It was first observed in perylene and is also called P-type delayed fluorescence.[50] It is however difficult to control the behaviour of materials with TTA in devices due to the bimolecular nature of the process.

More importantly, an IQE of 100% cannot be achieved in this case, as the maximum yield of singlet excited states from the TTA process is 0.5. This makes the possible maximum for the IQE to be 25%+0.5×75% = 62.5%.[77,78]

Reverse intersystem crossing (rISC) from upper excited states (sometimes referred to as hot excitons) has also been investigated as a way of triplet harvesting. In this case higher lying singlet and triplet excited states, S_n and T_n, have strong charge transfer character (CT) and are close enough in energy so that the rISC rate constant between T_n and S_n states can compete with the rate of internal conversion (IC) within the triplet manifold. The IC can also be suppressed if the energy gap between T_2 and T_1 is sufficiently large (Figure 1.10-c). The upper triplet states T_n are converted to upper singlet excited states S_n and are then internally converted to the first singlet excited state (S_1) that can decay radiatively.[79,80] The rISC from upper triplet states was reported in a variety of materials such as quinoline isomers, anthracene derivatives, organic dyes and some excited-state intramolecular proton transfer (ESIPT) molecules, however the PLQY of such materials was usually low.[81] Ma and co-workers have investigated the potential application of such materials in OLEDs. The reported compounds contain donor and acceptor moieties. To explain the theoretical behaviour of such materials compounds **TPA-QAP** and **TPA-AC** can be used as an example[81] (Figure 1.11). **TPA-QAP** demonstrates a large energy gap between the lowest excited singlet and triplet states (ΔE_{ST}) of around 0.75 eV. At the same time, a relatively small T_2-T_1 gap favours the IC to the lowest excited state, and further non-radiative decay of triplets, which makes **TPA-QAP** a simple fluorescent compound. For **TPA-AC** not only is the ΔE_{ST} higher (1.27 eV), but so is the $T_2 - T_1$ gap (1.12 eV), thus IC is suppressed. At the same time, the $S_1 - T_2$ gap is sufficiently small (0.14 eV) for rISC to occur. Clearly, other upper excited states can be involved, and the general process can be described as a $T_m \rightarrow S_n \rightarrow S_1$ transition.

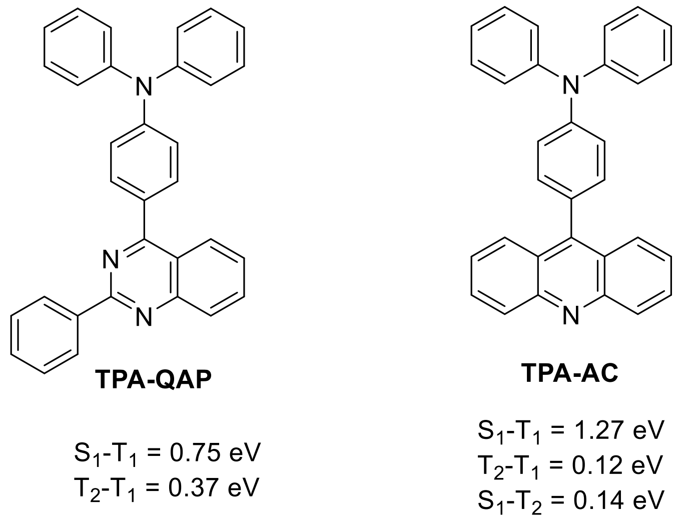

Figure 1.11. Molecular structures of **TPA-QAP** and **TPA-AC** and the energy gaps between first singlet and two first triplet excited states.

Yet, the design of molecules where hot-exciton rISC can compete with IC between T_n and T_1 remains very challenging. The explanation of the process relies mainly on theoretical calculations, and thus in some cases it can be suggested that it is actually TADF (described below).

Compared to hot-exciton rISC, there are no parasitic IC processes for reverse intersystem crossing between the lowest singlet S_1 and triplet T_1 excited states, as in most cases the energy gap between T_1 and S_0 is too large for non-radiative decay. Thus, the materials exhibiting rISC between the lowest excited states are better candidates for the application in OLEDs.

Normally T_1 is lower in energy than S_1, so some thermal activation is required for rISC to occur.[50] Radiative decay of singlet excited states S_1 after rISC can be distinguished from simple fluorescence by the much longer transient lifetime τ. As such, this is called delayed fluorescence (DF), in the same way as TTA (Table 1.1).[54] Delayed fluorescence originating from rISC can be distinguished from that of TTA due to the monomolecular nature of the first process. It is worth noting that ISC can occur along with rISC, but it has to compete with often more favourable radiative decay from S_1 to S_0.

Table 1.1. Transition times for absorption and excited-state decay processes.

Process	**Transition time**
Absorption	10^{-15} s
Internal conversion	10^{-15} s – 10^{-10} s
Fluorescence	10^{-9} s – 10^{-5} s
Intersystem crossing	10^{-8} s – 10^{-5} s
Phosphorescence	10^{-6} s – 10^{2} s
TADF	10^{-6} s – 10^{-2} s

This type of DF was first reported in eosin in 1961 and was called E-type delayed fluorescence.[82] It has been investigated in some other structures such as fullerenes[83] over the few past decades, and its application in temperature and oxygen sensors was reported,[84] but only recently Adachi and co-workers have proved it to be a viable method for triplet harvesting in OLEDs.[85] It is now more often called thermally activated delayed fluorescence (TADF) in the ever-growing amount of publications related to the subject, and some of the reported devices containing TADF materials reach an EQE of about 30%.[86]

1.3.4 Thermally-activated delayed fluorescence materials and their use in OLEDs

The main advantage of TADF is that 100% IQE can be achieved in purely organic materials. However, there are still some limitations that should be considered.

1.3.5 Design of TADF materials

The main goal in the design of TADF materials is to achieve simultaneously a relatively large radiative rate constant (k_r) and a small energy gap between the lowest singlet and triplet excited states (ΔE_{ST}). Non-radiative decay from the T_1 state should be minimised so that rISC becomes the dominant process. The reverse intersystem crossing rate constant (k_{rISC}) can be determined according to the equation:[87]

$$\mathrm{k_{rISC}} = A \exp\left(-\frac{\Delta \mathrm{E_{ST}}}{\mathrm{k_B T}}\right) \tag{1.3}$$

Here k_B is the Boltzmann constant and T is the temperature, and it is clear that minimising ΔE_{ST} is crucial for efficient rISC. When the energy of the lowest singlet (E_{S_1}) and triplet (E_{T_1}) excited states is calculated there are several parameters to consider including orbital energy (E_{orb}), the electron repulsion energy (K), and the exchange energy of two unpaired electrons in the excited state (J) (Equation (1.4) and (1.5)). Thus, ΔE_{ST} depends on the value of the exchange energy (Equation (1.6)), which can be approximated as an overlap between the ground and excited state wave functions.[88]

$$\mathrm{E_{S_1}} = \mathrm{E_{orb}} + \mathrm{K} + \mathrm{J} \tag{1.4}$$

$$\mathrm{E_{T_1}} = \mathrm{E_{orb}} + \mathrm{K} - \mathrm{J} \tag{1.5}$$

$$\Delta \mathrm{E_{ST}} = \mathrm{E_{S_1}} - \mathrm{E_{T_1}} = 2\mathrm{J} \tag{1.6}$$

Assuming that for S_1 and T_1 the unpaired electrons are situated on the HOMO and LUMO which then have the same value of *J*, the exchange energy of two electrons can be calculated by Equation (1.7):[87]

$$\mathrm{J} = \iint \phi(r_1)\psi(r_2)\left(\frac{e^2}{r_1 - r_2}\right)\phi(r_2)\psi(r_1)\mathrm{d}r_1\mathrm{d}r_2 \tag{1.7}$$

Here, ϕ and ψ correspond to the wavefunctions of the HOMO and LUMO, respectively, and e is the electron charge. Consequently, the value of ΔE_{ST} can be minimised if the overlap between HOMO and LUMO is reduced.[89] It can be achieved in donor-acceptor (D-A) structures, where singlet and triplet excited states have strong CT character. There are several ways to achieve good separation of HOMO and LUMO: create a twist between donor and acceptor by introducing bulky substituents[90] (Figure 1.12-a), break conjugation between donor and acceptor by spiro-linking[91] or another kind of physical separation[92] (Figure 1.12-b,c), or introduce π-bridge between donor and acceptor[93] (Figure 1.12-d).

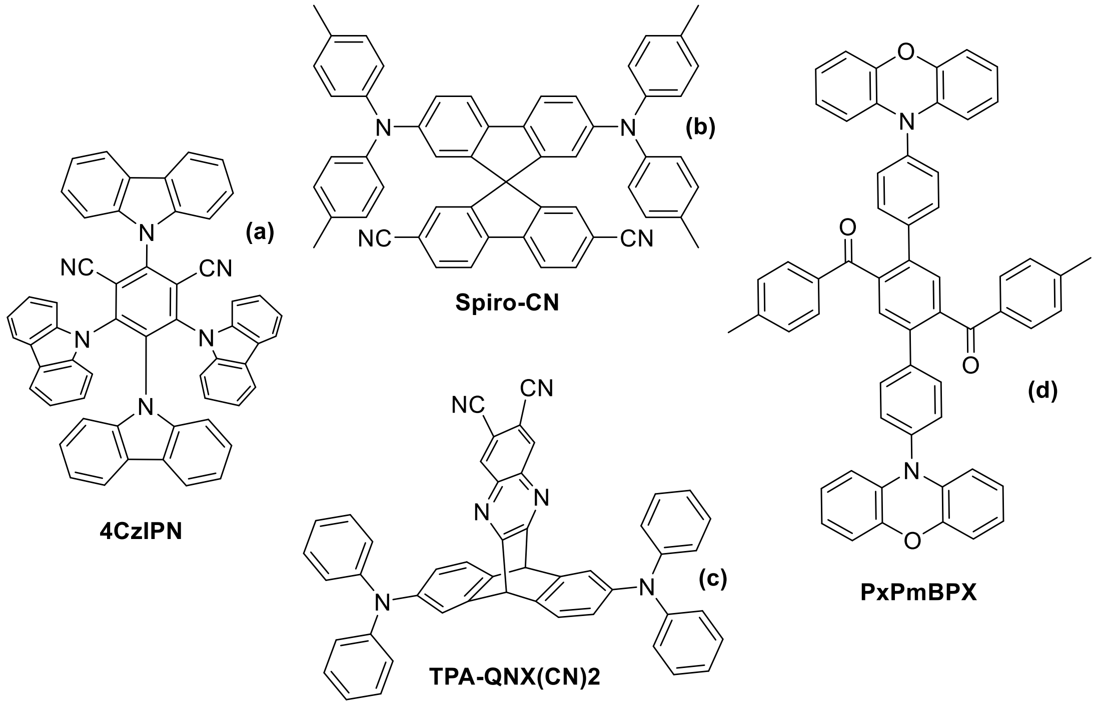

Figure 1.12. Examples of TADF molecules with separated HOMO and LUMO

Although the use of approaches described above has given a lot of efficient TADF materials, there are some exceptions to these rules. For example, while TADF is normally observed in highly twisted D-A structures, more sterically hindered analogues might show higher pronounced room-temperature phosphorescence (RTP) instead (Figure 1.13-a).[94] The position of substituents, as well as their conformation, also plays an important role in achieving TADF (Figure 1.13-a,b).[95]

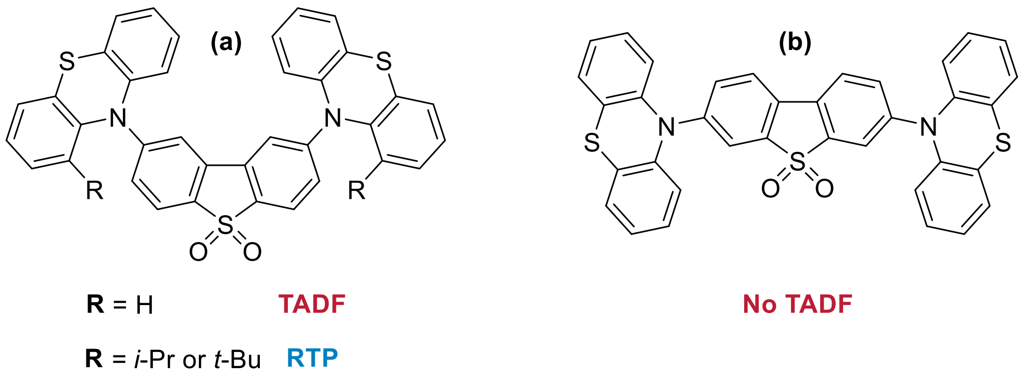

Figure 1.13. Interplay between TADF and RTP.

Increasing the efficiency of rISC by strong localisation of HOMO and LUMO often leads to decreased electronic coupling between the ground and excited singlet states, low radiative rate and, consequently, low Φ_{PL}.[96] Also, the spatial separation of HOMO and LUMO is not enough to reduce ΔE_{ST}, and other criteria should be taken into consideration to optimise rISC. According to the El-Sayed rule, ISC (as well as rISC) is most efficient if the transition happens with a change of orbital type. For example, in the case of transition between S_1 and T_1 the $^1(\pi, \pi^*) \rightarrow {}^3(n, \pi^*)$ ISC is expected to be faster than $^1(\pi, \pi^*) \rightarrow {}^3(\pi, \pi^*)$, and ISC for $^1(n, \pi^*) \rightarrow {}^3(\pi, \pi^*)$ should be faster than $^1(n, \pi^*) \rightarrow {}^3(n, \pi^*)$.[97] Consequently, ISC can be enhanced in conjugated organic molecules containing heteroatoms with unpaired electrons or empty orbitals. Indeed, to date, most TADF materials have this kind of structure.

The non-radiative transitions between states of a different multiplicity (both ISC and rISC) are also highly dependent on the strength of the SOC, which is approximately proportional to Z^4, where Z is the atomic number.[50] It certainly plays an important role for the compounds containing heavy atoms and was widely exploited to enhance both radiative and non-radiative spin-forbidden transitions in phosphorescent organometallic complexes. SOC can also affect the behaviour of purely organic molecules. It is particularly prominent when two electronic states of different multiplicity are close enough in energy.[97] There are still relatively few studies discussing the influence of the SOC on the rISC rate. However, the first TADF materials used in OLEDs were Sn^{4+}–porphyrin complexes, where, just as in phosphors, the SOC was enhanced by an internal heavy atom effect.[85] For the same reason the use of Cu(I)-complexes as TADF emitters has been receiving increasing attention.[98] Another study has shown that the halogenation of the acceptor moiety in a TADF emitter can affect the rISC rates resulting in shorter emission lifetimes and enhanced PLQY of materials.[99] The external heavy atom effect can influence the rISC rate in a similar way. It was demonstrated that the incorporation of a thin (~ 0.5nm) layer of the blue phosphorescent iridium complex into TADF-based device increases the EQE by the factor of ~1.4.[100]

According to theoretical calculations, the strength of SOC and the magnitude of ΔE_{ST} can be equally important for achieving high rISC rates in purely organic TADF materials. For example, Samanta *et al.* have demonstrated that fast rISC occurs when the molecule shows simultaneously small ΔE_{ST} and strong SOC, as the rISC rate k_{rISC} is proportional to the square of SOC matrix element $\langle S_1|\hat{H}_{SO}|T_1\rangle$ (Equation 1.8).[101]

$$k_{rISC} = \frac{2\pi}{\hbar}\rho_{FC}\left|\langle S_1|\hat{H}_{SO}|T_1\rangle\right|^2 \qquad (1.8)$$

Here, ρ_{FC} is the Franck-Condon-weighted density of states. In the same study the importance of the excited state character for TADF processes was discussed. When S_1 has predominantly CT character and T_1 is mainly locally excited (LE) state, the SOC is the strongest, while when both first singlet and triplet excited states have CT character SOC is negligible. This is consistent with the previous findings stating that ISC is forbidden between singlet and triplet CT excited states due to unfavourable SOC.[102] At the same time SOC can be strong between T_2 and S_1 states when T_2 is a LE state, and the ΔE_{ST} can be reduced when the T_1 and T_2 are close in energy. Some studies demonstrate that the two excited states involved in rISC can be tuned independently, and therefore they are most likely of different character,[103,104] which is well in agreement with the theoretical findings.

It was also proposed to qualitatively estimate the SOC strength by investigating the changes in π-conjugation of hole or electron wave functions between singlet and triplet excited states. This is well in correlation with the El-Sayed rule. For example, in the cases of **4CzPN** and **4CzIPN** (Figure 1.14), the CT contribution is strong for S_1 as well as for T_1 for both molecules, which makes the difference in SOC matrix elements seem surprising. However, although S_1 and T_1 have similar electron wave functions, the difference can be observed in the hole wave functions. For **4CzPN** the different carbazole moieties are participating in electronic transitions to the S_1 and T_1 states. Carbazole substituents that are in *ortho*-positions relative to the cyano groups are involved in the transition to the S_1 state, while *meta*-substituted carbazoles contribute to a T_1 state. This causes the difference in π-conjugation for the hole wave functions of the S_1 and T_1 similar to that for LE triplet and CT singlet states. At the same time, for **4CzIPN** the difference between hole wave functions of S_1 and T_1 is less noticeable.[101]

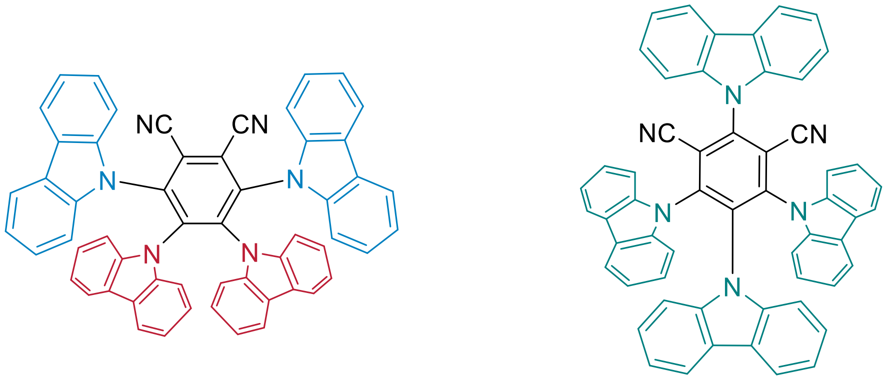

ΔE_{STcalc} = 0.00 eV
SOCME = 0.61 cm^{-1}
4CzPN

ΔE_{STcalc} = 0.01 eV
SOCME = 0.27 cm^{-1}
4CzIPN

Figure 1.14. Molecular structures of 4CzPN and 4CzIPN, and the relative values of their ΔE_{ST} and spin-orbit coupling matrix elements (SOCME).

It is important to modulate properly the HOMO-LUMO energy gap ($\Delta E_{H\text{-}L}$) to decrease the value of ΔE_{ST}. For the excited states with CT character the $\Delta E_{H\text{-}L}$ for the whole molecule should be considered where the HOMO is situated at the donor and the LUMO at the acceptor moiety (ΔE_{H-L}^{CT} , Figure 1.15). For the LE states it is more relevant to consider the energy gap (ΔE_{H-L}^{LE}) between HOMO and LUMO of either donor or acceptor moiety, where the excited state is localised. In donor-acceptor molecules S_1 states are normally of a CT character while the nature of T_1 state can be modulated. For example, in the above discussed compound **4CzPN** (Figure 1.14) T_1 has predominantly CT character, but when the number of carbazole units is decreased from four to one, the T_1 has dominant LE feature, and the ΔE_{ST} gap is increased.[105] The excited states of a CT character are more sensitive to the overall change of the molecule's HOMO-LUMO energy gap, so they can be modulated to decrease the ΔE_{ST} by lowering the HOMO and LUMO energy levels of acceptor moieties or increasing them for donor units (Figure 1.15).[101]

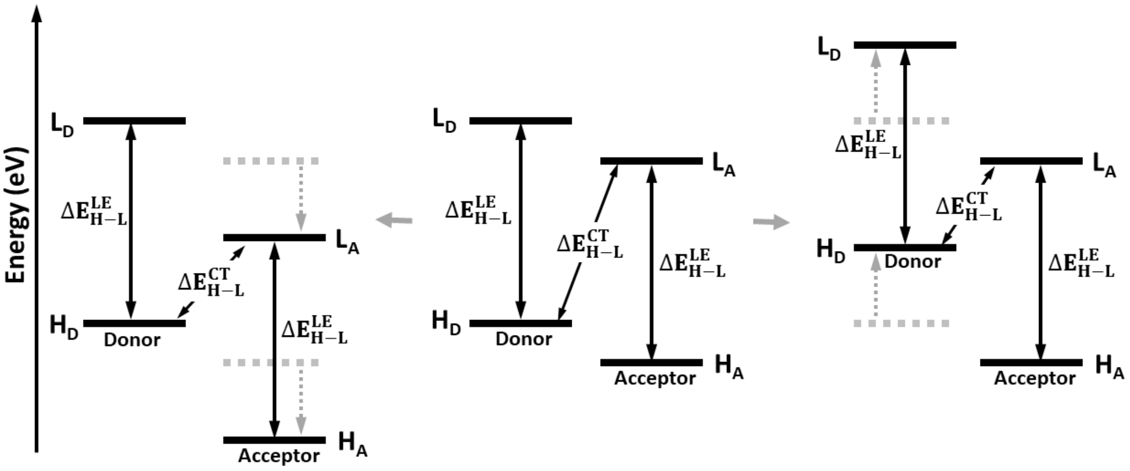

Figure 1.15. The ways of modulation of the HOMO-LUMO energy gap for the CT triplet state in a donor-acceptor molecule. Here ΔE^{CT}_{H-L} and ΔE^{LE}_{H-L} are HOMO-LUMO gaps for the CT and LE triplet state respectively, H_D (H_A) and L_D (L_A) are the HOMO and LUMO of the donor (acceptor) moieties, respectively. HOMO and LUMO of the whole molecule are H_D and L_A respectively. The scheme is adapted from the Ref.[101]

As shown, optimisation of rISC can be performed in a different manner, and as more research has been done in this field, it is clear that there is no strict set of rules as to how approach the design of the materials. For example, some ways of achieving an efficient SOC (involving singlet and triplet states of a different character, notably CT and LE) can seemingly contradict the requirement for T_1 and S_1 excited states to be predominantly of a CT nature to have a small ΔE_{ST}. There are several theoretical studies that might resolve this contradiction. It is worth mentioning though, that they were performed for a limited set of compounds, and it is possible that the mechanisms differ for other types of structures. Marian has demonstrated that the efficient coupling between the singlet CT (^{1}CT) and triplet CT (^{3}CT) states is possible when mediated by mixing with an energetically close triplet LE state (^{3}LE).[106] The influence of nonadiabatic (vibronic) coupling on ISC and rISC rates was investigated in the works of Chen *et al.*[107] and Gibson *et al.*[108] Initially a two-step mechanism for rISC was suggested by Adachi and co-workers in their study of blue TADF emitters.[109] Later the concept was supported by theoretical and experimental studies and was described in more detail.[110,111] First, the vibronic coupling between ^{3}LE and ^{3}CT results in an equilibrium between two states *via* reverse IC, then ^{3}CT is coupled to ^{1}CT with ^{3}LE acting as an intermediate. This coupling is most efficient when ^{3}CT and ^{1}CT are nearly isoenergetic thus providing good vibrational overlap. In summary, both vibronic and spin-orbit coupling elements are important to achieve an efficient rISC. This is consistent with the experimental results showing that in sterically hindered D-A compounds (*i.e.*, where the vibronic coupling is reduced) TADF is suppressed and RTP is observed instead (Figure 1.13).[94] This type of mixed mechanism that goes beyond simple spin-orbit interaction and takes into account the contribution of the vibrational motion is also called a second order spin-vibronic coupling.[112]

It was experimentally proven that the environment can strongly influence the energy levels of the excited states. For example, Santos *et al.* have demonstrated that in TADF molecules the relative energy levels of ^{1}CT and ^{3}LE states can be tuned by changing the polarity of the media.[113] Etherington *et al.* have performed another study on the influence of the host's polarity and rigidity on the relative position of the excited states and rISC.[110] Both singlet and triplet CT states are stabilised in a more polar environment as well as with decreased host rigidity. The relative energy ordering of the three lowest excited states that are involved in spin-vibronic coupling can be categorised in three distinct groups (Figure 1.16): (a) CT states are above the LE state, (b) CT states are nearly isoenergetic with LE state, (c) CT states are below the LE state.[108] Case (b) represents the best scenario for the efficient TADF. Also, if in the case (c) the ^{1}CT is isoenergetic with ^{3}LE ($E_{S_1} \cong E_{T_2}$), an efficient TADF can be possible even when the energy gap between ^{1}CT and ^{3}CT is relatively large ($E_{S_1} \gg E_{T_1}$), which would allow their use as TADF emitters the molecules with higher overlap between HOMO and LUMO. Although molecular design strategies for achieving this are yet to be defined.[111]

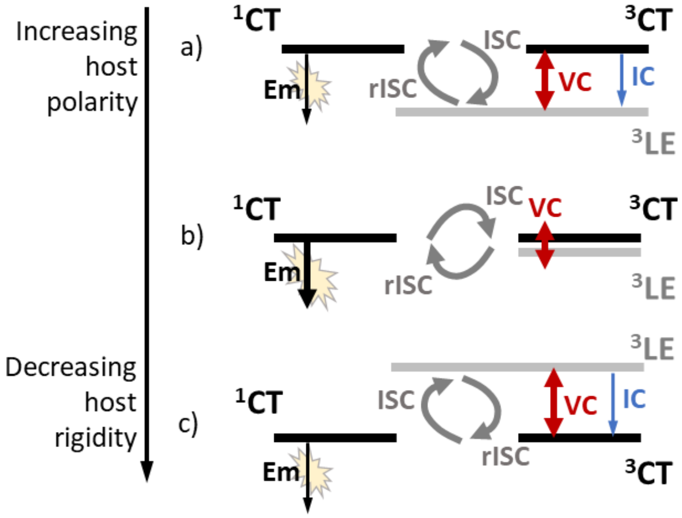

Figure 1.16. Three possible TADF mechanisms according to the relative order of three lowest involved excited states. Here VC is vibronic coupling and Em corresponds to the emission. The scheme is adapted from Ref.[110]

Clearly, molecular structure is crucial for efficient TADF, but the host environment is equally important as it can influence the excited states involved in the TADF process. The role of the host materials in efficient TADF devices will be discussed in more detail in Section 1.4.3.

To conclude, both spin-orbit and vibronic coupling contribute to the efficiency of rISC, and for TADF to occur it is important for materials to have proper alignment of the excited states involved in the transition. However, achieving high rISC rates alone is not enough for the design of efficient TADF materials. Additionally, the PLQY of the compound should be high enough for it to be used in OLED devices.

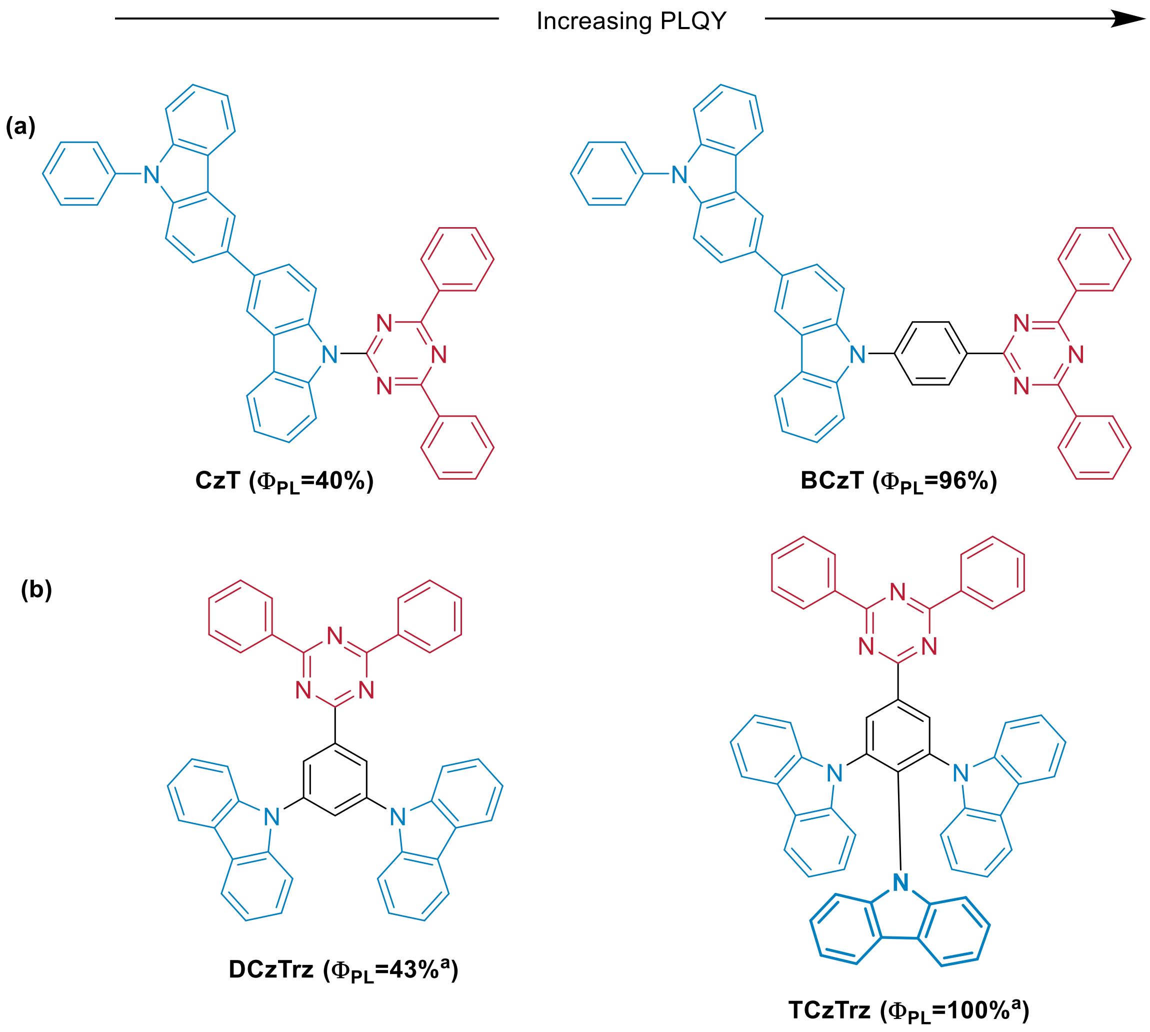

CzT (Φ_{PL}=40%)

BCzT (Φ_{PL}=96%)

DCzTrz (Φ_{PL}=43%^{a})

TCzTrz (Φ_{PL}=100%^{a})

Figure 1.17. The widespread methods of increasing PLQY of TADF materials. (a) Introduction of a phenyl linker between donor and acceptor moieties. (b) Delocalisation of the HOMO.

There are several approaches to increase the PLQY of a material. One is to introduce a phenyl linker between the donor and acceptor moiety in order to extend both the HOMO and LUMO and reduce their isolation, which can lead to an increase of the oscillator strength.[114] As an example, **BCzT** containing such a linker exhibits a much higher PLQY compared to the simple donor-acceptor compound **CzT** (Figure 1.17-a).[115] However, the presence of a phenyl linker can also lead to a weaker CT character of the S_1 excited state and, consequently, an increase of ΔE_{ST}.[114] The strength of CT character can be maintained in such structures by using stronger donor and acceptor groups. Another method to achieve higher PLQY is to increase the delocalisation of the HOMO by increasing the conjugation of the donor moiety or by introducing additional donor units which would lead to an increase of the transition dipole moment.[116] For example, compound **DCzTrz** demonstrates a PLQY of 43% (Figure 1.17-b), but this increases to nearly 100% for **TCzTrz** when the third carbazole substituent is introduced.[117] As it can be seen, even though all the compounds from the examples described above consist of carbazole-based donor and triazine-based acceptor moieties, their PLQYs differ dramatically depending on the arrangement of these units in the molecule.

Interestingly, compounds **CPT3** and **CPT4** reported by Hirata *et al.* demonstrate that the stronger delocalisation of the HOMO leads not only to an increase of PLQY, but also to a decrease of ΔE_{ST} (Figure 1.18).[116] Theoretical calculations demonstrate that while the delocalisation of HOMO decreases the energy of the S_1 state it has no effect on the T_1 state. The T_1 wavefunction for both compounds is confined to the central carbazole-phenylene-triazine moiety due to the strong electronic coupling between carbazole and phenylene triazine fragments and thus provides low triplet energy.[118]

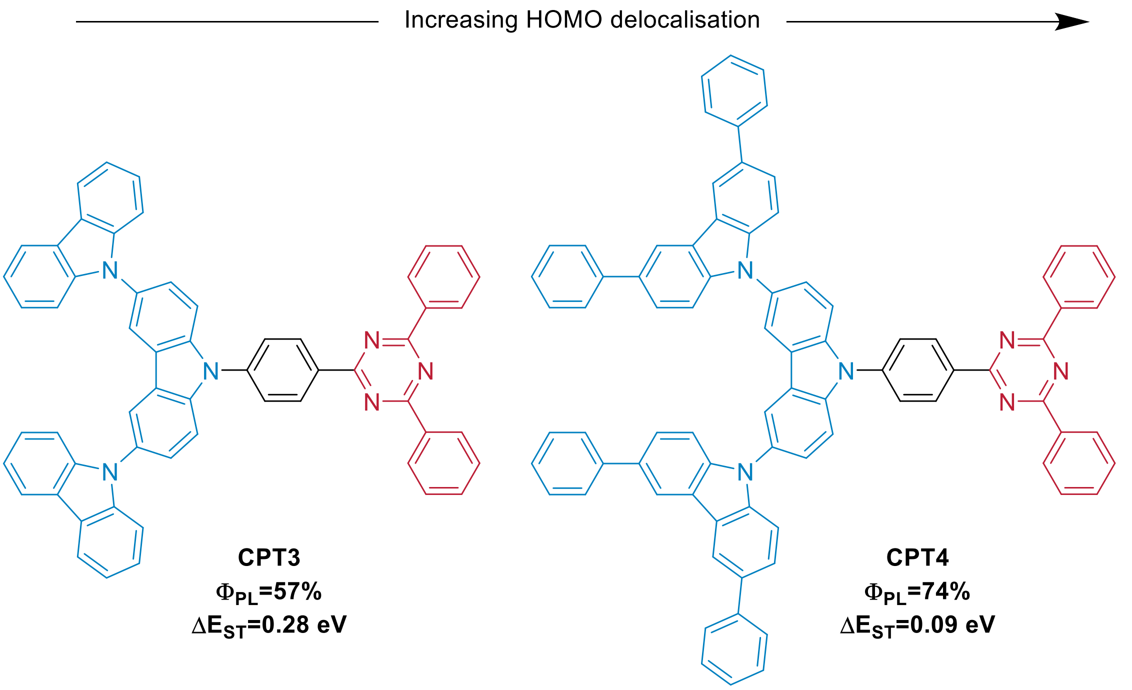

Figure 1.18. Molecular structures of the compounds **CPT3** and **CPT4**.

Although in some cases PLQY and ΔE_{ST} in donor-acceptor TADF systems can be tuned nearly independently, more often there is a clear trade-off between the efficiency of the rISC and the radiative rates. Also, when the above described method of separating HOMO and LUMO is used, the emission originating from the CT excited states is too broad.[119] Normally, full width at half maximum (FWHM) of EL peaks for such materials is around 70 –100 nm,[120] for comparison FWHM of below 20 nm can be achieved for LEDs.[121] FWHM of above 50 nm impairs the colour purity and reduces EQE since commercial displays require the use of colour filters.[120] This makes TADF compounds less suitable for display applications.[114] Hence, it is desirable to create an efficient TADF material without using a donor-acceptor strategy.

Li *et al.* have reported the acceptor-only compound **HAP-3MF** (Figure 1.19-a) with the rISC occurring between $^{3}(n, \pi^{*})$ and $^{1}(n, \pi^{*})$ excited states.[122] Although it demonstrated a moderate PLQY of 26%, the 6% EQE indicates that TADF is most likely involved. However, the mechanism of the TADF process in **HAP-3MP** was not explained. Hatakeyama *et al.* have demonstrated that the separation of HOMO and LUMO could be achieved by a multiple-resonance effect (Figure 1.19-b).[120] In both **DABNA-1** and **DABNA-2** the LUMO is localised on the boron atom and at *ortho*- and *para*-positions relative to it, while the HOMO is localised on the nitrogen atoms and at *meta*-positions relative to the boron atom (Figure 1.19-c). In the theoretical study Northey and Penfold found that in **DABNA-1** the rISC to S_1 occurs *via* an upper triplet excited state T_2.[123] **DABNA-2** has demonstrated a PLQY of around 85–90% and an EQE of more than 20%. More importantly, due to the non-CT character of the excited states in the compound, a FWHM of only 28 nm was observed.

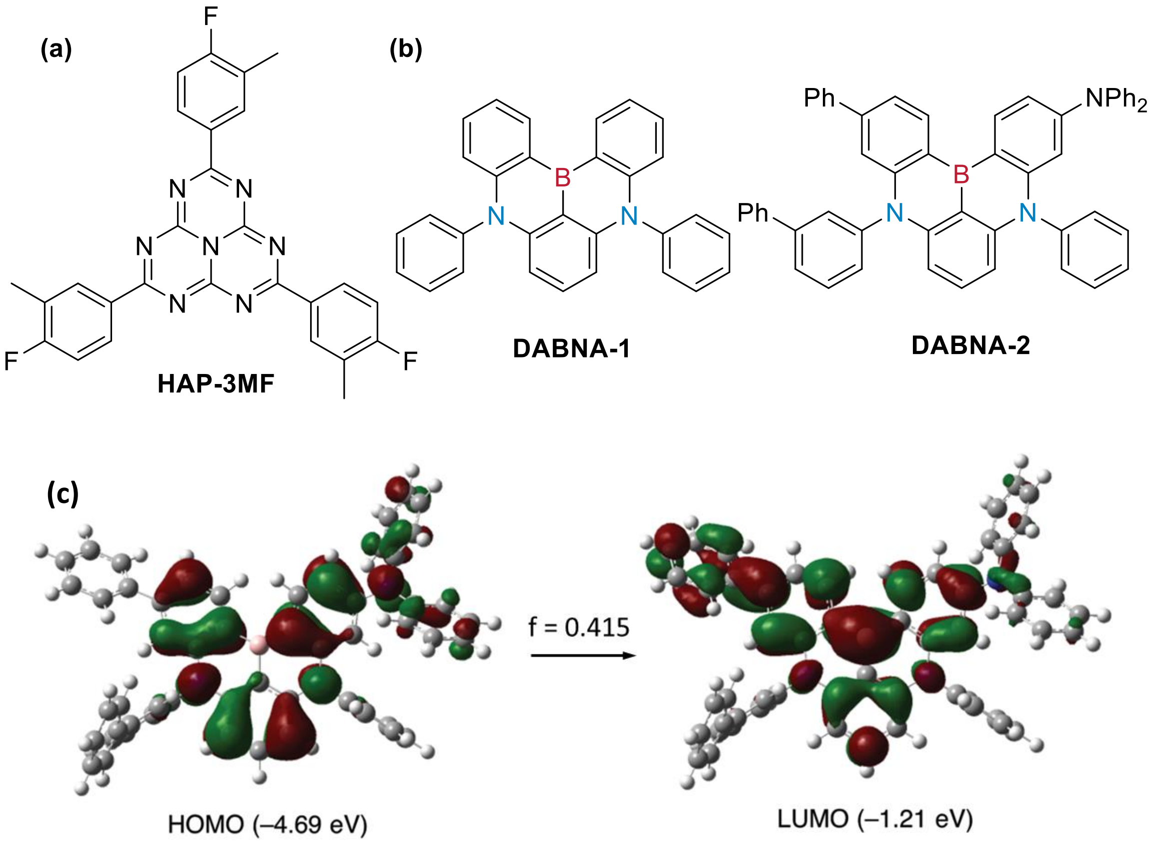

Figure 1.19. Molecular structures of non-CT TADF emitters. (a) Acceptor-only structure. (b) Compounds with a multiple-resonance effect HOMO-LUMO separation. (c) Orbital localisation and energies for DABNA-2 (reproduced from Ref.[120]).

Mamada *et al.* have shown that HOMO-LUMO separation in triquinolonobenzene (**TQB**) occurs due to excited state intramolecular proton transfer (ESIPT) (Figure 1.20-a).[124] The ESIPT requires the presence of proton donor and proton acceptor groups (R_2NH and $R_2C{=}O$ respectively for **TQB**) situated close to each other in a molecule. The excitation $M \rightarrow M^*$ (Figure 1.20-b) causes the redistribution of electronic charge which leads to an increased acidity of the proton donor and basicity of the proton acceptor.[125] This results in a proton transfer between the proton donor and the proton acceptor leading to formation of a tautomer A^* (in the example described above, M and M^* correspond to **TQB,** and A and A^* to **TQB-A**). After radiative decay, $A^* \rightarrow A$ reverse proton transfer occurs to the initial form $A \rightarrow M$ (**TQB**). Although TADF was observed previously in imidazole-based ESIPT materials,[126] Mamada *et al.* were first to report the use of such emitters in OLEDs,[124] Compound **TQB** demonstrates PLQY of up to 62% in the solid state, and the EQE of their devices reached 14%.

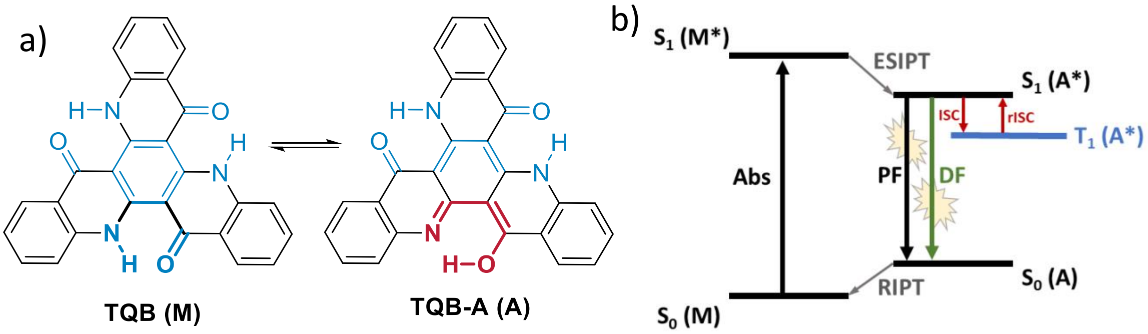

Figure 1.20. TADF from an excited state intramolecular proton transfer. (a) Molecular structures of **TQB** and its tautomer **TQB-A**. (b) Jablonski diagram for the ESIPT-assisted TADF process. Abs and RIPT denote absorption and reverse intramolecular proton transfer respectively.

Recently, Pander *et al.* have reported TADF in pure donor systems (Figure 1.21).[127] Interestingly, all compounds demonstrate moderate ΔE_{ST} gaps of around 0.21–0.28 eV. This could be attributed to the fact that the molecules have sufficient conjugation for the delocalisation of the S_1 state (thus lowering it), but at the same time a propeller-like slightly distorted structure increases the energy of the triplet state to observe the reduced ΔE_{ST}. It was suggested that rISC in these materials originates from the upper triplet states T_2 and T_3 populated *via* the reverse internal conversion (rIC) from the T_1 excited state, and the whole mechanism was called reverse internal conversion delayed fluorescence. The molecules also demonstrate high PLQY of up to 89%, which was explained by the mixed nπ*-ππ* character of the excited states that enhances their coupling to the ground state. All compounds demonstrate a strong contribution of DF, however when **TCA-C4** was used in OLEDs, the maximum EQE of devices was 4.1%. This could be explained by the strong electron-blocking properties of the material that hinders the injection of electrons into the emissive layer. Nevertheless, the devices demonstrate a very narrow EL peak with a FWHM of 38 nm.

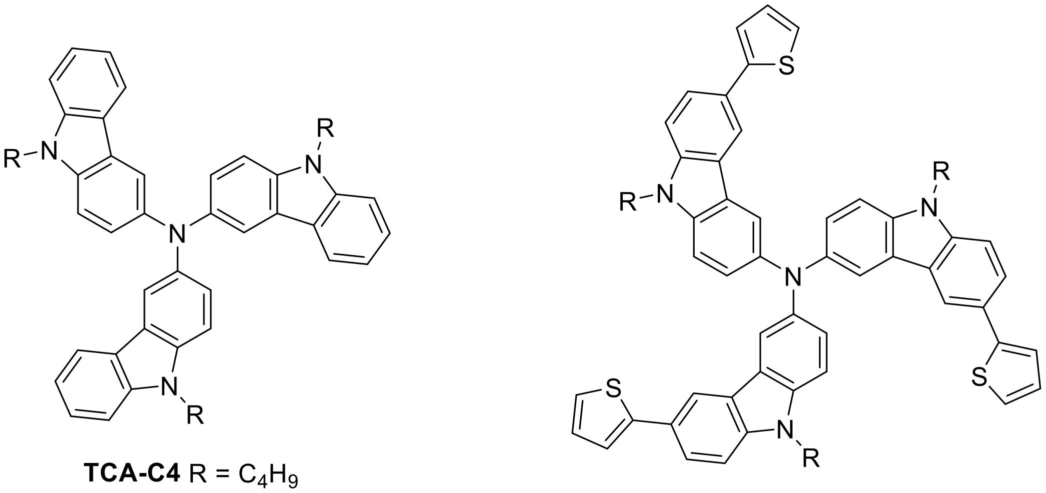

TCA-C4 R = C_4H_9
TCA-C8 R = C_8H_{17}

ThTCA-C12 R = $C_{12}H_{25}$

Figure 1.21. Chemical structures of donor-only TADF systems.

While the above described examples are still perceived rather as an exception to the rule, they prove that TADF can be observed in a wide variety of organic materials and is often mediated by the additional photophysical processes.

1.3.6 Colour tuning in TADF emitters

The colour of the emission is another important parameter in the design of any luminescent compound. Just as in case of fluorescent and phosphorescent emitters, the creation of efficient green and yellow TADF materials is relatively easy compared to blue and red. Blue emission is difficult to achieve in TADF compounds because it requires maintenance of a small ΔE_{ST} while keeping the HOMO-LUMO gap large enough to emit in the blue region. In red TADF emitters the excited states are particularly susceptible to non-radiative decay, which is consistent with the energy gap law.[128] Yet, there are already quite a few blue and red TADF emitters reported up to date. Blue TADF emission could be achieved when weak donors and acceptors are used, while it can also be beneficial to reduce π-conjugation in the molecule. Diphenylamine, carbazole, and 9,9-dimethyl-9,10-dihydroacridine (DMAC) are among the popular donors for blue emitters, while diphenyl sulfone and triazine derivatives are often used as acceptors.[129] Some TADF materials were described above: **BCzT** (Figure 1.17-a) is an efficient blue emitter with an EL peak (λ_{EL}) at 492 nm, commission internationale de l'éclairage (CIE) chromaticity coordinates of (0.18, 0.34) and an EQE of nearly 22%,[115] while **CPT4** (Figure 1.18) has demonstrated λ_{EL} = 487 nm, CIE (0.19, 0.35) and an EQE of around 20%.[129] Another example of a blue TADF material is **DDMA-TXO2** where 9.9-dimethylthioxanthene-S,S-dioxide (which can be perceived as a rigidified modification of a diphenyl sulfone) is used as an acceptor and DMAC as a donor (Figure 1.22). It demonstrated an λ_{EL} of 465 nm, CIE (0.16, 0.25) and a maximum EQE of around 22%.[130] However, reports of deep blue TADF emitters (with CIE y $<$ 0.1) remain scarce. One example is **DS-Cbz** (Figure 1.22) with CIE (0.15, 0.07) and an EQE of 9.9%.[109]

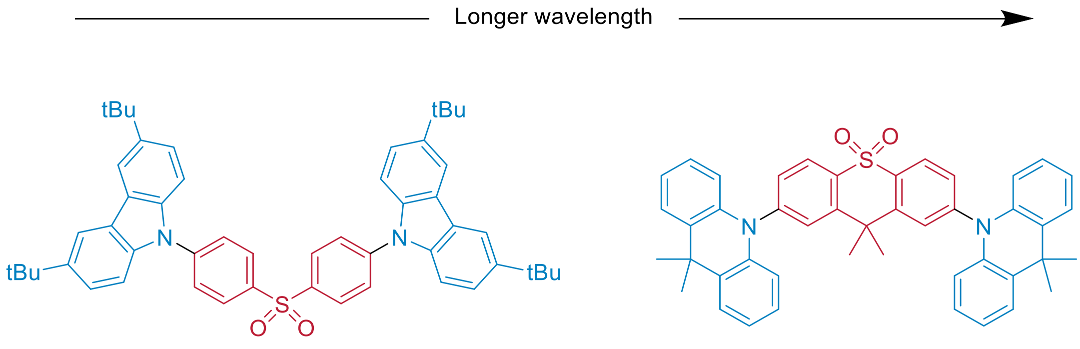

DS-Cbz

DDMA-TXO2

Figure 1.22. Examples of blue TADF emitters.

For green and yellow emitters stronger donors such as phenoxazine and phenothiazine are often used along with carbazole and DMAC derivatives. Triazine-based moieties as well as cyano-substituted aromatic compounds are often the acceptors of choice.[131] **4CzIPN** (Figure 1.23) described at the beginning of this chapter is one of the most popular green TADF emitters that was used in a variety of OLED structures, and some of the devices have achieved nearly 30% EQE with λ_{EL}=499 nm and CIE (0.20, 0.49).[90,132] Green compound **Px-VPN** and yellow **Ac-CNP** are good examples of successful colour tuning by changing the strength of donor and acceptor moieties (Figure 1.23).[133] **Px-VPN** demonstrates an EQE of around 14% and CIE (0.35, 0.57), and **Ac-CNP** shows an EQE of 13% with CIE (0.47, 0.51).

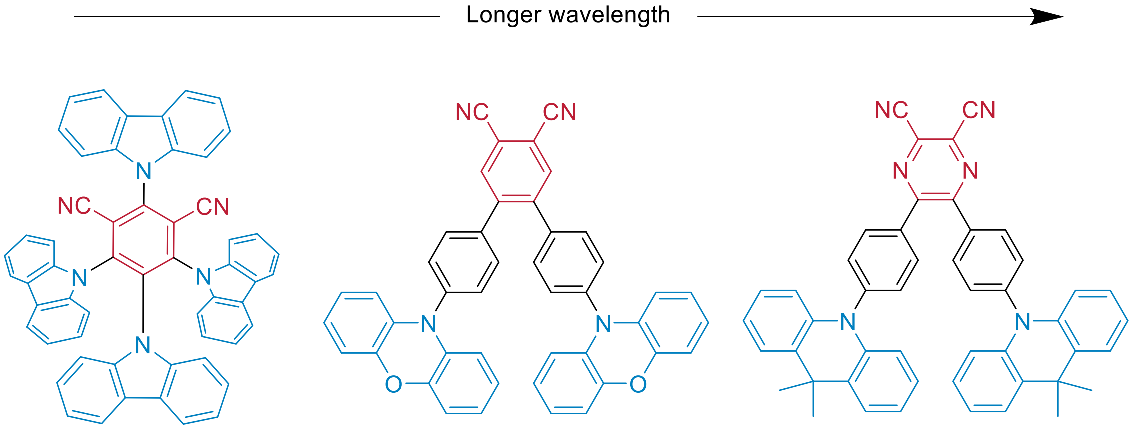

4CzIPN

Px-VPN

Ac-CNP

Figure 1.23. Examples of green and yellow TADF emitters.

Red TADF emitters are often based on strong polycyclic heteroaromatic acceptors such as dicyanodiazatriphenylene or dibenzo[*a*,*j*]phenazine.[134] For example **POZ-DBPHZ** demonstrated a good efficiency in devices with an EQE of 16% and λ_{EL}= 610 nm (Figure 1.24).[135] Recently, two new red emitters **Da-CNBQx** (λ_{EL}=617 nm) and **Da-CNBPz** (λ_{EL}=670 nm) were reported (Figure 1.24). Devices for both compounds demonstrate particularly impressive performance for red emitters with EQEs of 20% and 15%, respectively.[136]

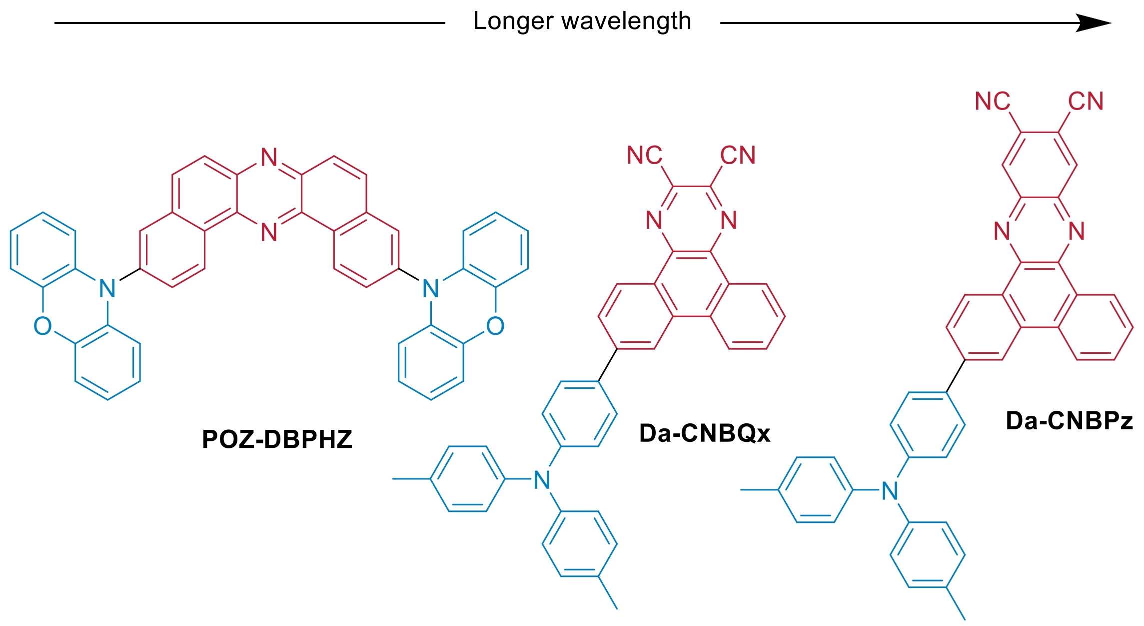

Figure 1.24. Examples of red TADF emitters.

1.3.7 Host materials for TADF emitters

For phosphorescent and TADF emitters their luminescence involves long lived triplets, which gives a much higher probability of non-radiative relaxation of the excited states. When neat films of such emitters are used in devices, performance is often compromised by concentration quenching, triplet-triplet annihilation, excimer formation, exciton migration and other unwanted processes.[137] Some neat films of TADF emitters can give an EQE of up to 20% in OLEDs,[138] but this is an exception. More often TADF compounds should be dispersed in a host matrix to suppress side de-excitation processes and achieve high efficiencies. Some of the requirements for TADF hosts are similar to those for phosphorescent emitters. First, the triplet energy of the host should be significantly higher than that of the emissive material to avoid quenching the triplet states of the emitter and to confine the excitons in the emissive layer.[87] It is particularly difficult to find an appropriate host for blue emitters, as the triplet level should preferably be above 3 eV. The HOMO and LUMO of the host should match those of the adjacent layers to provide efficient injection of charge carriers, and the host should also have balanced charge transport properties to ensure efficient recombination of charge carriers, thus bipolar hosts are normally performing better than unipolar.[139] Many of the hosts applied in PhOLEDs such as 1,3-bis(N-carbazolyl)benzene (mCP), 4,4′-bis(N-carbazolyl)-1,1′-biphenyl (CBP) or bis[2-(diphenylphosphino)phenyl]ether oxide (DPEPO) are used as well for TADF OLEDs (Figure 1.25).[87] Due to a high triplet level ($T_1 \approx 3$ eV) DPEPO is often used as a host for blue TADF emitters,[130,140] mCP ($T_1 \approx 2.9$ eV)[90] is a common host for green materials, and CBP ($T_1 \approx 2.6$ eV) can be used in red OLEDs.[135] It is also important for a good host material to provide an efficient transfer of excitons to the emitter (guest). To achieve this, HOMO and LUMO levels of the guest should ideally be within the HOMO-LUMO gap of the host, and the absorption spectra of the TADF guest should overlap the emission spectra of the host.[87] In addition, the thermal and morphological stability of the host plays a crucial role in increasing the lifetime of the device.[139]

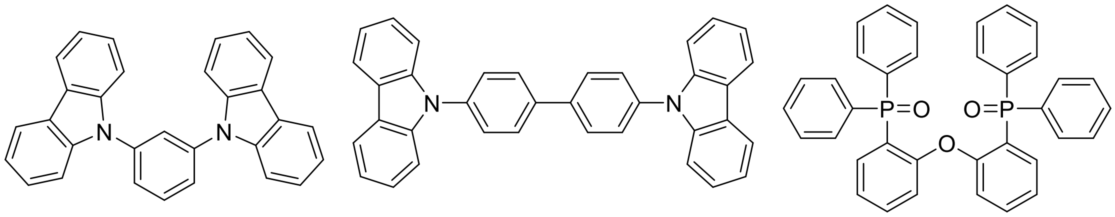

mCP **CBP** **DPEPO**

Figure 1.25. Examples of the commercially available host materials for TADF OLEDs.

As discussed in Section 1.4.1, excited states in TADF compounds have strong CT character, and rISC involves a complex spin-vibronic coupling mechanism between ^{3}CT and ^{3}LE triplet states mediating the following up-conversion to the ^{1}CT singlet excited state.[110] Since the excited states with CT character are more sensitive to the polarity of the environment than LE states,[119] the polarity of the host material can affect significantly the ΔE_{ST}. For example, the CT states of a blue emitter **DDMA-TXO2** described in Section 1.4.2. (Figure 1.22) are stabilised in a polar DPEPO host.[130] This leads to a reduced ΔE_{ST} gap, higher rISC rates and, consequently, a higher PLQY of the material with the EQE of the devices containing this blend being above 22%.

Traditional host materials cannot always satisfy all the requirements for achieving high efficiencies of TADF OLEDs. Currently the design of new TADF hosts might be of even higher interest than that of TADF emitters themselves. It is also particularly interesting to find cost-efficient methods for the preparation of the host materials, as sometimes they constitute the bulk of the emissive layer with doping concentrations of TADF emitter being as low as 1 wt.%.

Cho *et al.* reported a new bipolar host material **DCzDCN** (Figure 1.26) that was used in green OLEDs based on the **4CzIPN** emitter.[141] They showed a maximum EQE of 26.7%, which is much higher compared to the devices using **CBP** as a host (EQE = 17.1%). The authors have also highlighted the importance of balance between achieving high triplet energy levels and keeping the bandgap of the material sufficiently low to avoid the increase in driving voltage caused by a high energy barrier for charge injection. The turn-on voltage of the **DCzDCN:4CzIPN** device is 3.0 eV. Remarkably, the lifetime of the devices with **DCzDPN** as host was almost 20 times higher (200 h) than of those containing **CBP** (10.2 h), which is due to a higher morphological stability of **DCzDPN** films. Gaj *et al.* have reported another bipolar TADF host **mCPSOB** (Figure 1.26) that also demonstrated high performance in devices (EQE = 26.5%).[142] Another interesting example is a pure hydrocarbon host **SF34** based on a spirobifluorene unit (Figure 1.26).[143] The authors claim it to have a higher chemical stability than comparable heteroatom-containing compounds. The strongly twisted skeleton of **SF34** provides a higher ambipolar charge transfer and a good thermal stability. The **SF34:4CzIPN** devices demonstrated an EQE of 22.3%, very low efficiency roll-off (EQE = 20.8% at 5000 cd/m^2), and a device lifetime of above 250 h.

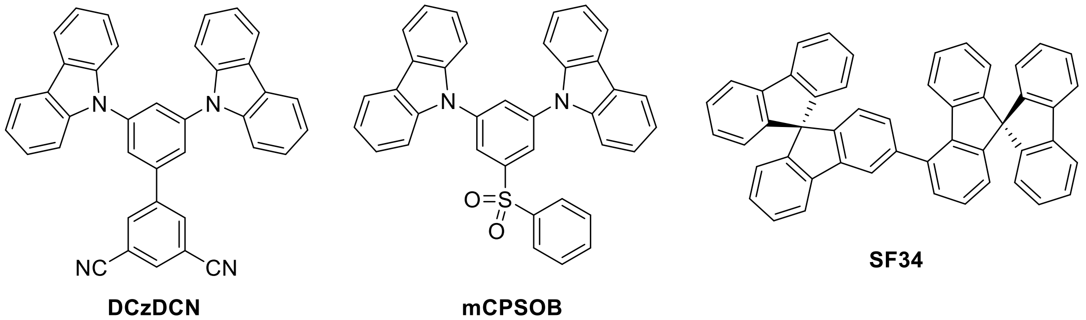

Figure 1.26. Molecular structures of some bespoke TADF hosts.

Lee *et al.* have investigated the influence of the relative position of the donor and acceptor on the properties of the bipolar host in the series of compounds ***p*CzB-2CN**, ***m*CzB-2CN** and ***o*CzB-2CN** (Figure 1.27).[144] Triplet energies for the materials were 2.58, 2.73 and 2.99 eV, respectively. The increase of triplet energy is due to the shortening of the conjugation between carbazole and isophthalonitrile. The current density and luminance of the devices with the **4CzIPN** emitter increased from ***o*CzB-2CN** to ***p*CzB-2CN**. The highest EQE of 26% was achieved in the device based on ***m*CzB-2CN:4CzIPN**, as the film of this blend also had the highest PLQY (≈100%). The lower PLQY of the ***p*CzB-2CN:4CzIPN** film could be explained by the low triplet level of the host, while in the case of ***o*CzB-2CN** it is caused by poor energy transfer.

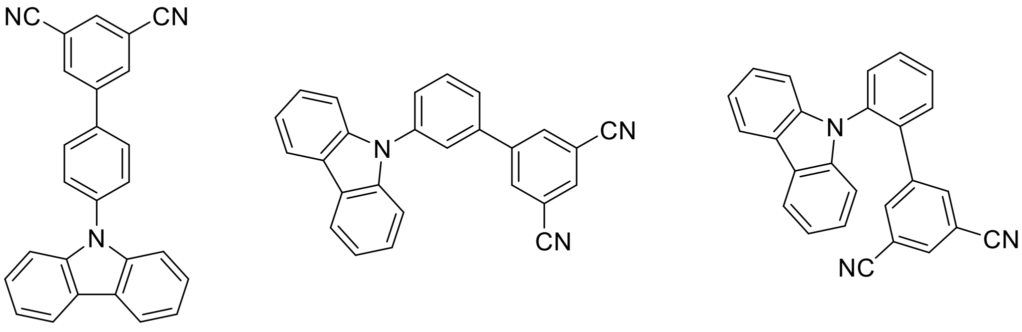

***p*CzB-2CN** ***m*CzB-2CN** ***o*CzB-2CN**

Figure 1.27. Donor-acceptor host materials with different interconnection positions of donor and acceptor moieties.

Another way to achieve a balanced charge mobility is to use a blend of hole- and electron-transporting materials instead of bipolar hosts. Kim and Lee have studied the behaviour of mixed hosts and **4CzIPN** in devices where the **mCP:BmPyPb** blend gave the highest EQE of 28.6%.[145] The high efficiency of the devices is due to the strong overlap of the emission spectrum of the host blend with the absorption of the TADF emitter. It is also important that the employed hole transporting material has a deeper HOMO than that of the emitter to avoid exciton quenching.

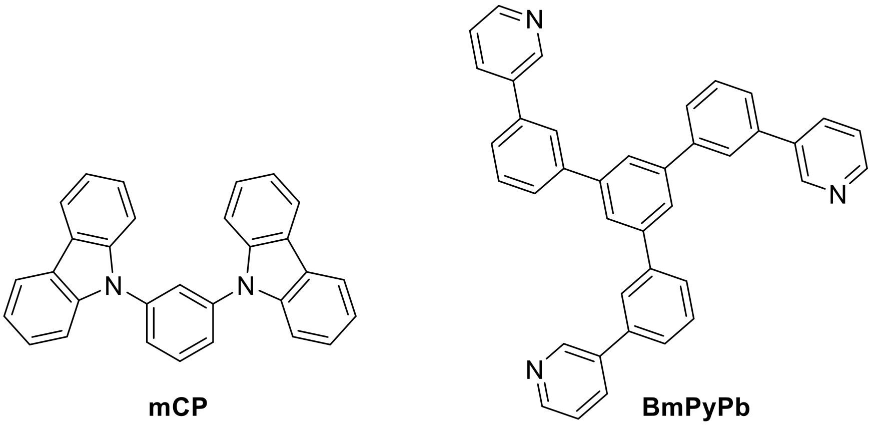

mCP **BmPyPb**

Figure 1.28. Materials used as mixed hosts by Kim and Lee.

Other studies have also pointed out the importance of molecular orientation of the host as well as the compatibility of molecular structure and polarity of host and guest materials for increased efficiency of devices.[146] With a constantly growing amount of efficient TADF emitters reported each year, the development of TADF host materials becomes an increasingly appealing direction of research in the field with more exciting findings to make.

1.3.8 TADF in dendrimers and polymers

Polymers and dendrimers possess many advantages such as the possibility to use solution-processing methods for device fabrication (which can be cheaper and more suitable for large area deposition), better film-forming properties and increased thermal stability. However, there are still relatively few examples of TADF macromolecules reported to date. Most macromolecular materials demonstrating TADF show rather moderate EQEs in OLEDs compared to devices containing small molecules. This is probably due to the methods used in the device fabrication which are rarely optimised, so the development of materials convenient for more versatile device optimisation is of the high interest in the area, and some of the approaches seem to be very promising.

As discussed in the previous section, for enhanced performance of devices small TADF molecules are usually dispersed in a host matrix. However, hosts can negatively affect the photophysical behaviour of the emitter, reduce the PLQY and change the fluorescence and photoluminescence spectra profiles. These changes can be caused by the formation of exciplexes between a guest and a host molecule, which can make the non-radiative decay more favourable for the excited states of the guest molecule.[137] The emission of exciplexes is also usually red-shifted and more broad compared to that of the isolated molecule.[147] Efficiency losses in host-guest blends can also result from phase separation caused by differences in the molecular structures of two materials.[87] One solution would be to use a self-host TADF material instead of the heterogeneous system. In recent years several dendrimer and polymer TADF materials containing an intramolecular host moiety were reported. There are three main ways to incorporate host units into the polymer or dendrimer backbone.[148] The TADF core of the dendrimer can be surrounded by dendrons serving as a host (Figure 1.29-a), the TADF unit can be copolymerised with the host monomer (Figure 1.29-b) or pending TADF and host groups can be grafted onto the main polymer chain (Figure 1.29-c). Currently, most self-host materials are dendrimers.

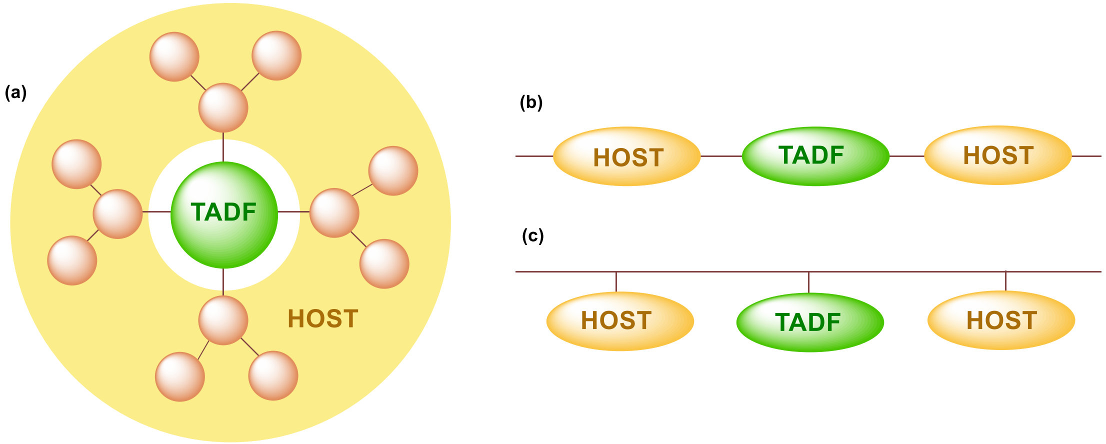

Figure 1.29. Schematic structures of polymer (a,b) and dendrimer (c) self-host materials.

Dendrimers are peculiar macromolecules that combine the advantages of both small molecules and polymers. In a similar way to small molecules they have a precise chemical structure that allows increased tuneability of HOMO and LUMO levels, which in turn can lead to better device efficiencies.[149] At the same time, much like polymers, they demonstrate good film morphology and are more suitable for solution deposition. Albrecht *et al.* were first to report the **G*n*TAZ** series of TADF dendrimers with a triazine core and carbazole dendrons (Figure 1.30-a).[150] The bulky dendrimer structure inhibited the intermolecular interactions and reduced concentration quenching. The luminescence spectra are very similar for dendrimers of different generations proving that the emission originates from the central triazine-carbazole core. **G3TAZ** has demonstrated the best efficiency, although the EQE of the devices was only 3.4%. Later, the same group reported a modified version of **G3TAZ** with *tert*-butyl groups introduced on the terminal carbazoles.[151] The maximum EQE of the optimised devices was 9.4%. The same idea of the encapsulation of the TADF core with carbazole dendrons later led to the preparation of dendrimers based on diphenyl sulfone-DMAC TADF unit (maximum EQE of the device is 12.2%),[152] and benzophenone-carbazole TADF core (EQE = 17.0%).[153]

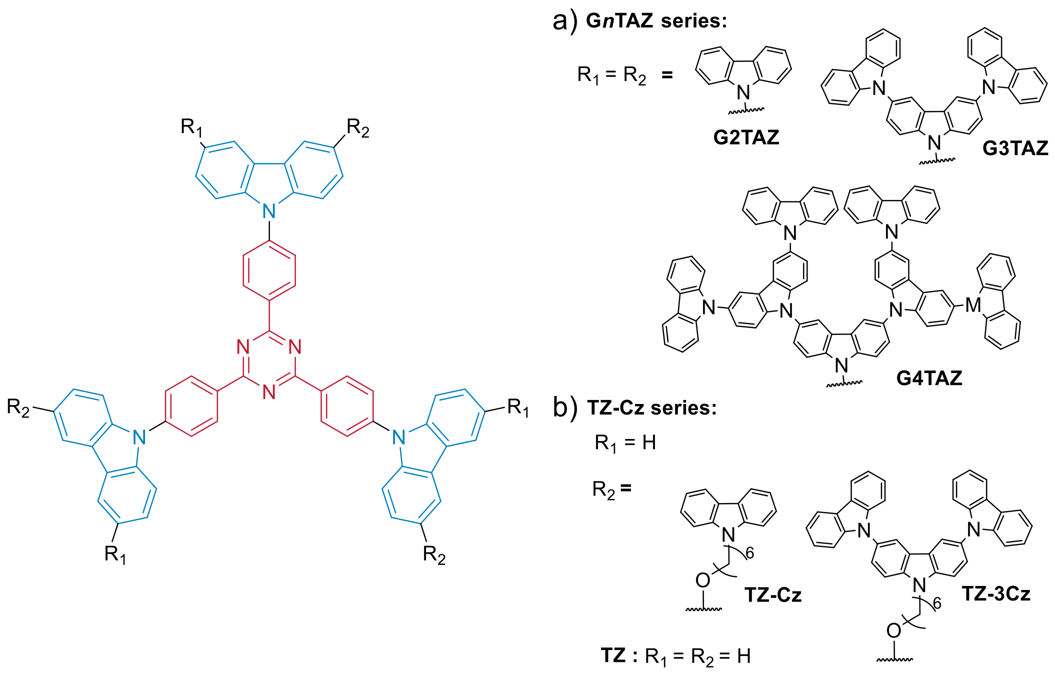

Figure 1.30. Molecular structures of the triazine-based TADF dendrimers series.

In the examples described above carbazole dendrons are conjugated with the TADF core, and in some cases the photophysical properties of the emissive core can be influenced by the peripheric dendrons, which is not always desirable.[154] To avoid this, the dendrons can be grafted to the central TADF unit by non-conjugated linkages. Ban *et al.* have developed two new dendrimers **TZ-Cz** and **TZ-3Cz** (first and second generation, respectively) based on the same triazine-carbazole core as the **GnTAZ** series (Figure 1.30-b).[155] Here the carbazole dendrons are connected to the central unit *via* alkyl chains. A device based on **TZ-3Cz** has demonstrated a maximum EQE of 10.1% which is higher than that for **TZ-Cz** (6.5%) and for the unsubstituted TADF unit **TZ** (1.09%). The turn-on voltage of the devices decreased for higher generations being 4.7 V for **TZ**, 4.0 V for **TZ-Cz** and 3.6 V for **TZ-3Cz**. Current density is also higher for **TZ-3Cz**, demonstrating that the bulky dendrone enhances charge injection and charge transporting properties of the compound. The same group has prepared several bipolar self-host TADF demdrimers such as **poCz-SO**[156] and **POCz-DPS**[157] based on the diphenyl sulfone-carbazole blue TADF emitter (**DMOC-DPS**) (Figure 1.31). The attached dendrons were based on a bipolar phosphine oxide carbazole moiety, which is particularly interesting considering that most of the previously used dendrons are carbazole-only based. The highest EQE was achieved for the **POCz-DPS** (7.3%).

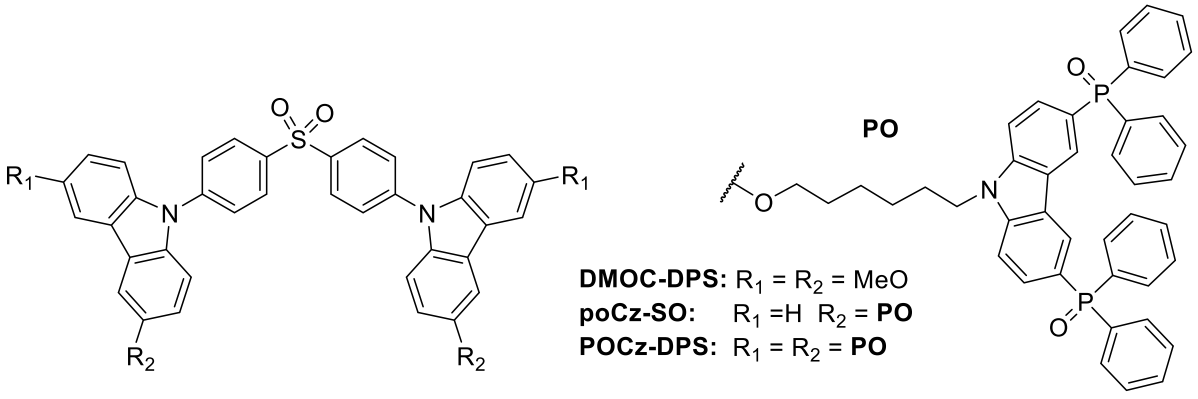

Figure 1.31. Molecular structures of bipolar self-host dendrons.

Polymer **PAPTC** is another example of a self-hosting TADF material (Figure 1.32-a).[158] Here the acceptor is connected *via* the side chain to the donor part of the TADF unit situated in the backbone and alternated with carbazole which plays the role of the intramolecular host. **PAPTC** has demonstrated a maximum EQE of 12.6%, which is the highest efficiency reported to date for polymeric non-doped solution-processed TADF emitters. Most of the time, to achieve high device performance, TADF polymers are dispersed in a host matrix. Xie *et al.* have reported a series of side chain type TADF polymers **PCzDP** prepared with various feed molar ratios of the TADF monomer (Figure 1.32-b).[159] The highest EQEs of 5.0% (non-doped) and 16.1% (doped with the small molecule TADF emitter in the mCP host) were observed for devices based on the **PCzDP-20** material. Wang *et al.* have prepared another series of TADF polymers **PSFOTT** with a different content of TADF units, where a pending acceptor is attached to a donor in the backbone (Figure 1.32-c).[160] A TADF monomer was copolymerised with fluorene and dibenzothiophene-S,S-dioxide derivatives. Films of polymers with a low TADF unit content (0.5-1 mol%) exhibit dual blue and orange emission originating from the backbone and TADF moiety, respectively, which results in an overall white photoluminescence. The emissions of polymers containing 2-10 mol% of TADF unit is predominantly orange due to a more efficient energy transfer from the backbone to a TADF unit. The best performance was demonstrated for **PFSOTT2** with 4.8% EQE in non-doped devices, and an EQE of 19.4% in the mCP host. Ren *et al.* have reported a series of copolymers **Copo1**, **Copo2**, **Copo3** and **Homopo** containing different ratios of dibenzothiophene-S,S-dioxide-phenothiazine TADF moiety and styrene unit used as a spacer suppressing TTA processes (Figure 1.32-d).[161] It was demonstrated that the presence of styrene reduces the interactions between TADF units and provides a higher colour purity of the material. The best performance was achieved for the **Copo1**-based device with a maximum EQE of 20.1%, although at a higher brightness of 100 cd/m^2 the EQE was 5.3%. The emitter was used in an mCP host.

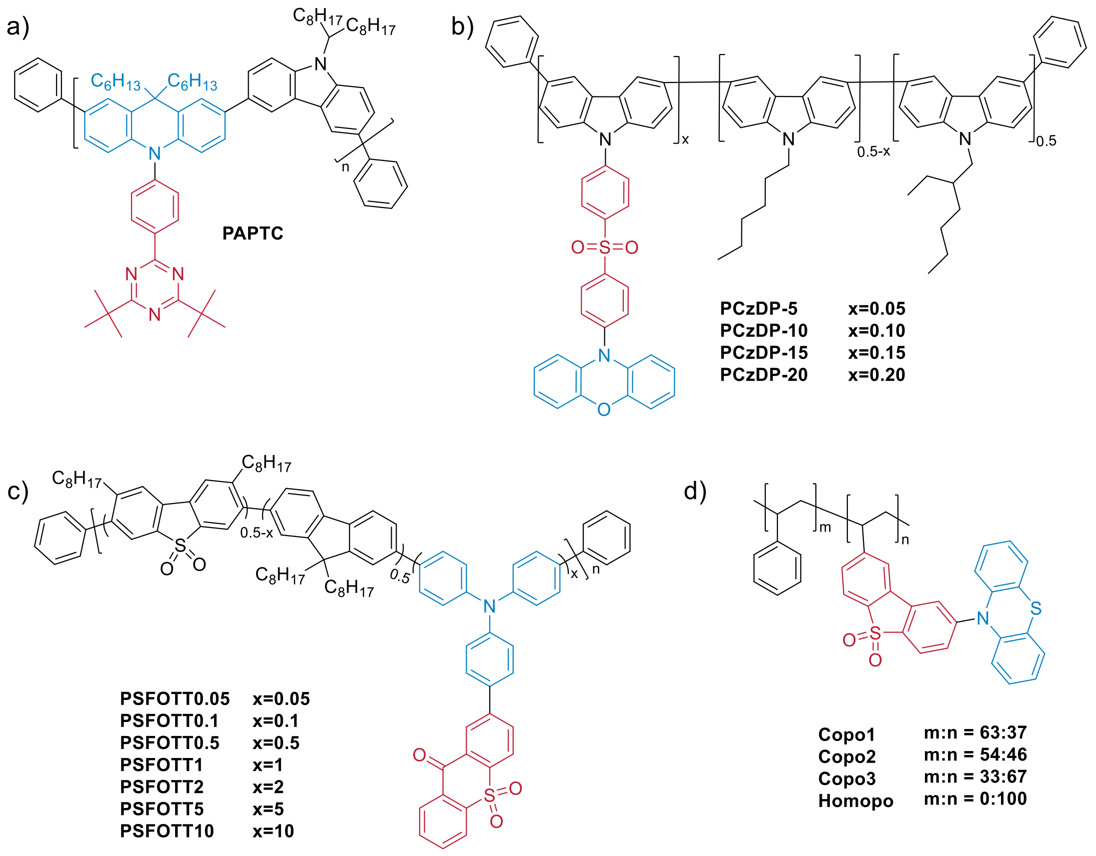

Figure 1.32. Molecular structures of some TADF polymers.

It is also possible to achieve TADF in polymers with a non-conjugated backbone *via* a through-space charge transfer effect between pendant donor and acceptor moieties.[162] TADF can also be observed in oligomers prepared from non-TADF monomers.[163]

1.3.9 TADF in exciplexes

An alternative way to achieve TADF is to use two different molecules that can form an intermolecular excited state complex, which is also called an exciplex.[164]

Exciplexes and excimers are bimolecular complexes formed upon excitation of one of the participating molecules. The interaction between the excited molecule A* and ground state molecule A can result in formation of the excited state dimer (AA)* also called an excimer. When two different molecules participate in a process, one being a donor (D) and another an acceptor (A), the newly formed complex (DA)* is an exciplex (Figure 1.33).[147,165]

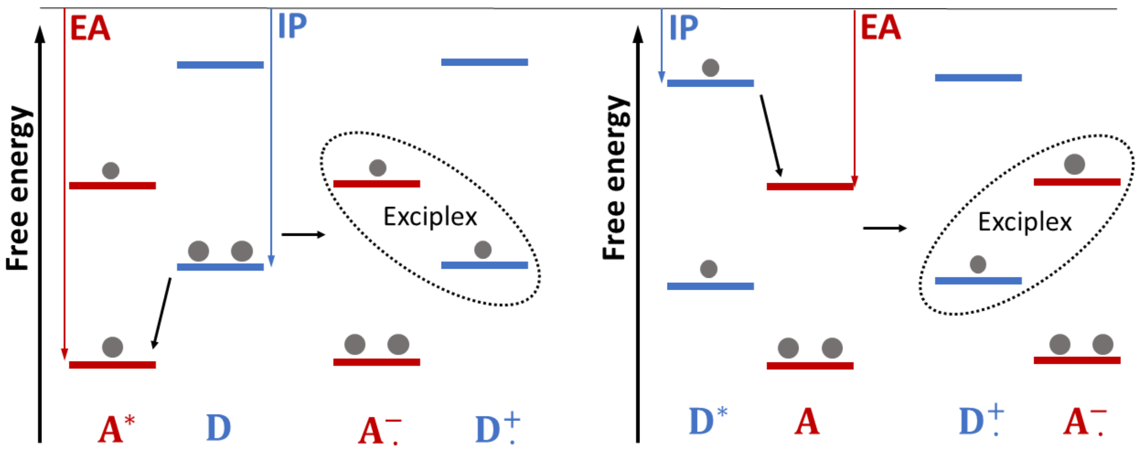

Figure 1.33. Schematic representation of the exciplex formation when either acceptor (left) or donor (right) are excited. Adapted from Ref.[165]

The wave function of the exciplex can be expressed as a linear combination of LE and CT states, and the influence of ground states can be neglected (Equation 1.9).[165]

$$\psi([DA]^*) \approx c_3\phi(\mathrm{D}^*\mathrm{A}) + c_2\phi(\mathrm{DA}^*) + c_1\phi(D^+A^-) \qquad (1.9)$$

Here the coefficients indicate the relative contribution of each state. The first two terms represent local excited states of a donor ($\mathrm{LE_D}$) and an acceptor ($\mathrm{LE_A}$), and the last term corresponds to an intermolecular CT state.[166]

The formation of exciplexes is a common process in organic electronic devices. First reports of exciplex emission in OLEDs date back to 1998 when it was observed by Itano *et al.*[167] The exciplex was formed on the interface between the emitter and a hole-transporting material. The first exciplex-based TADF OLED was reported by Goushi *et al.*[168] The emissive layer comprised the mixture of either 50mol% ***m*-MTDATA:*t*-Bu-PBD** or ***m*-MTDATA:3TPYMB** (Figure 1.34). OLEDs consisting of ITO (110nm)/m-MTDATA (20 nm)/50 mol% *m*-MTDATA:3TPYMB (60 nm)/3-TPYMB (20 nm)/LiF (0.8 nm)/Al (50 nm) have demonstrated a maximum EQE of 5.4%. Nowadays efficiencies of above 10% can be achieved for exciplex-based devices.[169]

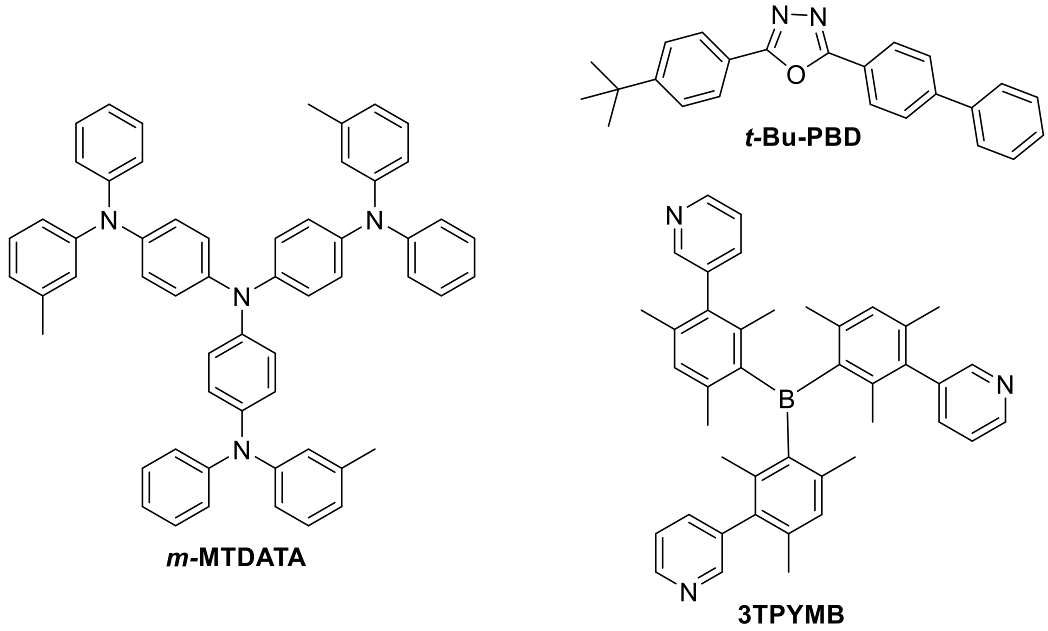

Figure 1.34. Molecular structure of donor (**m-MTDATA**) and acceptors (***t*-Bu-PBD** and **3TPYMB**) forming exciplexes.

The main advantage of exciplex-based devices is the simplicity of the structure, as two materials are used in three layers. The donor component of the exciplex can be used simultaneously as an HTL, while the acceptor is applied as an ETL. This can reduce the voltage drops normally caused by charge injection and transport through additional layers, and that is why many exciplex devices demonstrate low turn-on voltages of around 2.5 V.[87] However, for efficient formation of exciplexes the materials should be used as neat films, which makes it impossible to improve the efficiency of devices by dispersing the emissive compound in a host matrix.

1.3.10 Other uses and future perspectives for TADF emitters

TADF molecules can also be used as assistant dopants in fluorescent OLEDs. In this case the emissive layer comprises of a host material, a TADF assistant dopant and a fluorescent emissive dopant. Nakanotani *et al.* have reported a series of blue, green, yellow and red OLEDs based on such a system.[170] In these devices triplet excitons formed upon electrical excitation of the TADF dopant are converted to singlet excitons and transferred to the S_1 state of the fluorescent emissive dopant *via* Förster energy transfer (FRET) followed by radiative decay. The concentrations of the TADF dopants in the reported devices varied from 15 to 50 wt% to ensure that they act as main charge recombination centres, and the concentrations of the emissive dopant were as low as 1 wt% to avoid charge carrier trapping on fluorescent molecules. To provide an efficient FRET there should be a significant overlap between the absorption spectra of the emitter and photoluminescence spectra of the TADF dopant. The maximum EQE of the devices was 18%. Recently, this approach was used to prepare near-infrared OLEDs for biosensing applications.[171] Such three-component systems might be difficult to technically realise on an industrial scale,[172] but it is also possible to create a two-component system consisting of a TADF compound, used as a host, and a fluorescent dopant.[173] TADF materials were also used as hosts in phosphorescent OLEDs.[174] This approach however does not possess the advantage of metal-free TADF systems. Apart from being applied in OLEDs, TADF emitters encapsulated in a polymer matrix were applied in fluorescence imaging in living cells.[175]

Since the beginning of 2019, the amount of reports on current or planned releases of OLED-based devices is on the rise. That includes the promise of Apple to switch from LCDs to OLEDs in all its iPhones by 2020,[176] the release of laptops from Dell, HP and Lenovo with OLED screens,[177] and a spectacular presentation of rollable OLED TVs from LG during CES 2019.[46] This means that OLEDs are here to stay at least for the near future. Using TADF materials could be the way to make technology more viable and attractive for mass market applications. Until now most of the commercial OLED displays use phosphorescent organic materials for red and green pixels while blue pixels are based on fluorescent compounds which impairs the overall efficiency of the device.[172] One of the first steps for the commercial application of TADF materials would be to use them as blue emitters in OLED displays. At the moment CYNORA in collaboration with LG Display is developing deep-blue TADF emitters, and expects to get blue TADF materials in mass production by 2020.[178] This could possibly lead to further exploration of TADF phenomena in commercial products. It is also interesting to explore further the TADF mechanism in materials designed without the use of a common donor-acceptor scheme, such as compounds with ESIPT-mediated TADF or molecules with non-CT excited states. Other challenges can be found in the design of efficient host materials and macromolecular TADF compounds. Thus, while dozens of reports on new TADF emitters appear each week with many of them demonstrating performance in OLED devices that might appear hard to surpass, there are still numerous problems related to the topic that do not receive enough attention and are waiting to be solved.

Chapter 2. Helicene-Based TADF emitters

In this chapter the behaviour of two new helicene-based TADF emitters is examined with an emphasis on the photophysical properties of the materials in the solid state. The influence of the molecular packing within crystal lattice on TADF emission is also discussed in this study. When solvent is present in the crystal lattice of the diaza[5]helicene-based compound, aggregation is suppressed and the material demonstrates higher PLQY and stronger TADF emission. Solution processed OLED devices show maximum EQE of 7.1% for the materials.

The work presented in this chapter was published in Journal of Materials Chemistry C (Klimash, A.; Pander, P.; Klooster, W. T.; Coles, S. J.; Data, P.; Dias, F. B.; Skabara, P. J. Intermolecular Interactions in Molecular Crystals and Their Effect on Thermally Activated Delayed Fluorescence of Helicene-Based Emitters. J. Mater. Chem. C 2018, 6 (39), 10557–10568.). This was a collaborative project between the group of Professor Peter Skabara from the School of Chemistry (University of Glasgow), Organic Electroactive Materials (OEM) group at Durham University and the National Crystallography Service at the University of Southampton. A. Klimash has worked on the design, synthesis, purification, structure characterisation, and electrochemical and thermal analysis of new materials. P. Pander has performed steady state and time-resolved photophysical measurements, device fabrication and device testing. W. Klooster has performed X-ray crystallographic analysis.

2.1 Introduction

Despite the increasing amount of TADF materials reported to date, very few studies have focused on investigating TADF behaviour of compounds in a pure solid state, without dispersing the emitter in a host. Recently, several TADF emitters with mechanochromism were reported. Okazaki *et al*. have presented new TADF dibenzo[*a*,*j*]phenazine-based materials with a detailed analysis of their tricolour-changeable mechanochromic luminescence.[179] Pashazadeh *et al.* have presented a similar study of quinoxaline-based TADF emitters,[180] The influence of the solid state solvation on the behaviour of TADF compounds was also discussed in several works.[181,182] It is also important to understand prompt and delayed fluorescence processes in the solid state for materials demonstrating aggregation-induced emission.[183] Also, the study of TADF in crystals would be beneficial for extending the application of TADF phenomena to organic light-emitting transistors[184] as crystalline materials can provide a rare combination of high charge carrier mobility and high luminescence.[185]

The photophysical properties of two helicene-based TADF materials are discussed in this chapter, and their behaviour in the crystalline phase is described.

2.1.1 Structure and properties of helicenes

Helicenes belong to a family of polycyclic aromatic hydrocarbons (PAHs) (Figure 2.1). While most PAHs have a planar backbone, helicenes that consist of several *ortho*-fused aromatic rings have a twisted structure due to an intramolecular steric repulsion.

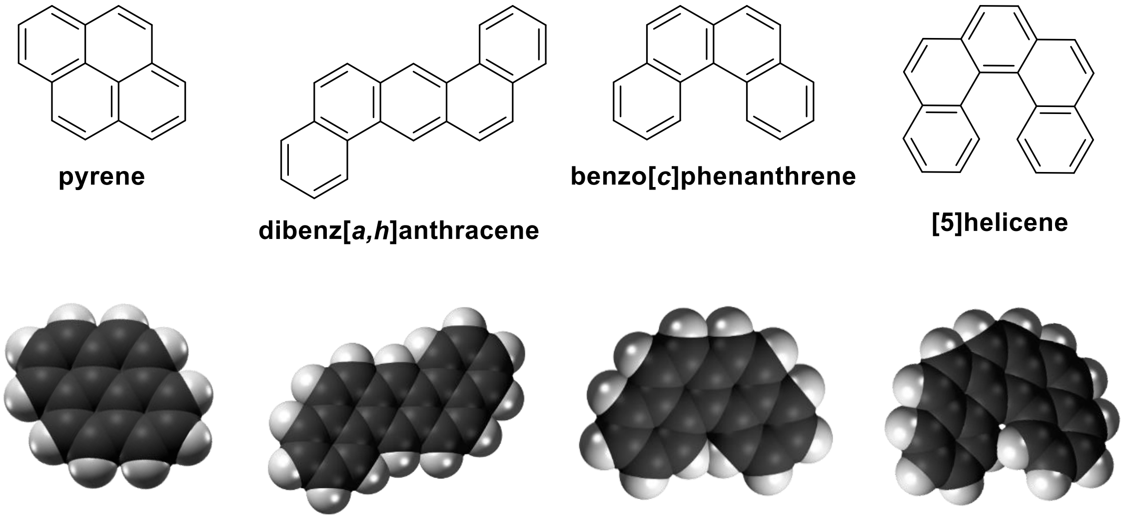

Figure 2.1. Chemical structures of various polycyclic aromatic hydrocarbons and their space-filling models (reproduced from Ref.[186]).

Despite the absence of chiral centres, helicenes are chiral compounds (Figure 2.2). Due to a nonplanarity, the benzene rings in helicenes are not regular hexagons, as the length of the bonds in the inner helix of helicenes are bigger than of those in the outer helix.[187] Yet, π-electrons can still be efficiently delocalised through the distorted backbone.[188] Enantiopure helicenes have high specific optical rotation,[189] and their less rigid skeleton makes them more soluble compared to planar PAHs.[190] Such particularity has encouraged the application of helicenes in fields ranging from asymmetric catalysis[191,192] to chemical sensors,[193–195] nonlinear optics,[196,197] and circularly polarised luminescent materials.[198,199]

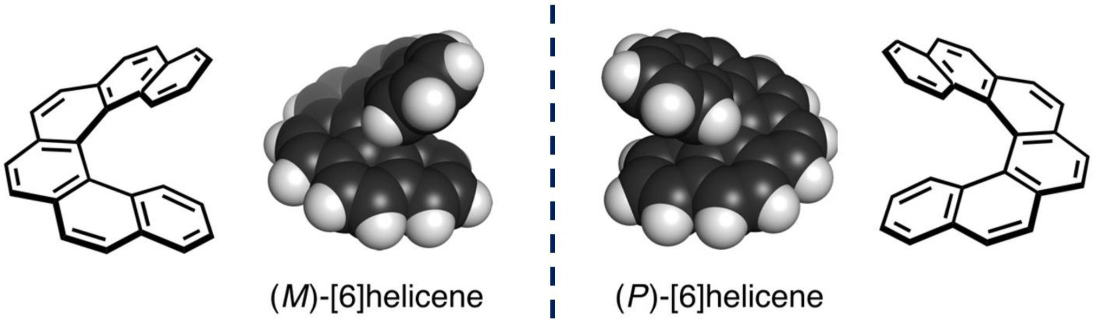

Figure 2.2. Chirality of [6]helicene. Space-filling models reproduced from Ref.[186]

Photoluminescence quantum yields of unsubstituted helicenes are low due to a fast intersystem crossing rate.[200] This is likely to be the reason why they were not considered for use in OLEDs until recently.[201] However, as in many other organic compounds, the emissive properties of helicenes can be tuned by further functionalisation.[202] The reduced π-conjugation, caused by a distorted molecular structure, results in a relatively large HOMO-LUMO gap even in higher helicenes, which makes them interesting candidates for blue OLEDs.[203–205] Schmidt *et al.* have demonstrated that the deviation from planarity in monoaza[5]helicenes directly influences the strength of the spin-orbit coupling and, consequently, the intersystem crossing rates in materials.[206,207] Another theoretical study by Yang *et al.* has demonstrated that the chirality of the compounds can significantly influence the behaviour of material in the bulk.[208] It was shown that crystalline 1-aza[6]helicene can demonstrate up to 80 times higher hole mobility in a racemic mixture compared to an enantiopure one. All these findings prove that helicenes are an exciting and promising class of materials to be used in organic electronics, and more in-depth understanding of the photophysical behaviour of these compounds is required.

2.2 Results and Discussion

The key materials in this work are **H1-PXZ** and **H2-PXZ** (Scheme 2.1). Mono- and diaza[5]helicene were used as acceptors that provide particular steric hindrance with their distorted skeleton thus reducing the ΔE_{ST} gap. Phenoxazine is used as a donor. Its morpholine-like central ring fused to two benzene rings contributes to a higher twist within the structure, better separation of HOMO and LUMO, and induced CT transition.[209] The final materials were prepared from helical cores **2.6** and **2.10** (Scheme 2.1).

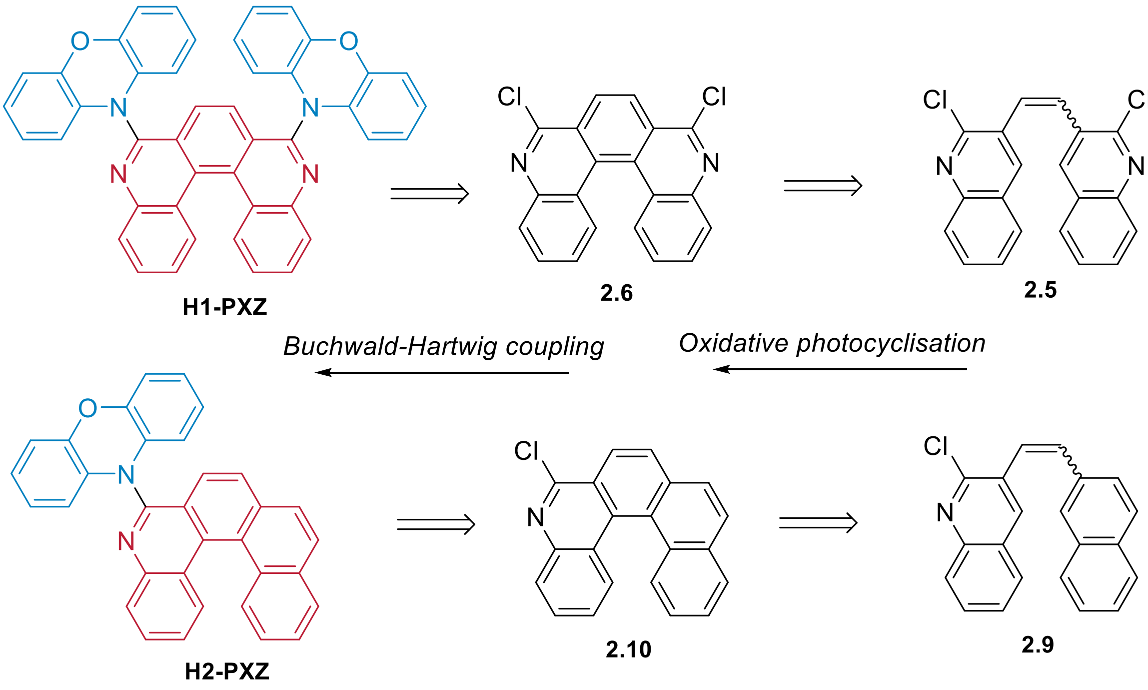

Scheme 2.1. Retrosynthetic strategy for the preparation of compounds **H1-PXZ** and **H2-PXZ**

2.2.1 Synthesis and characterisation of the materials

A modified literature procedure was used for the preparation of the helical core **2.6**[210] and its synthesis is summarised in Scheme 2.2.

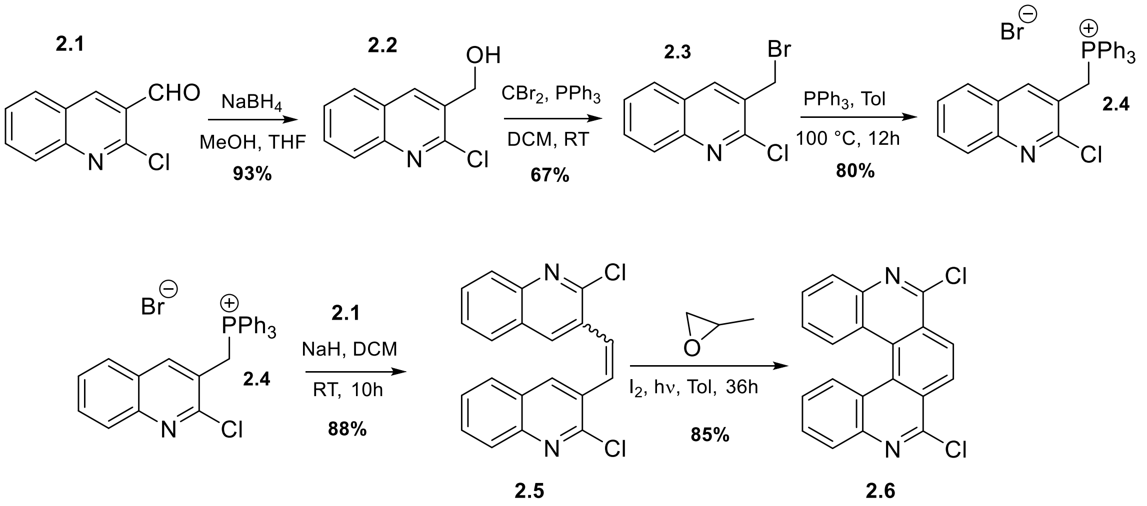

Scheme 2.2. Synthesis of the helical core **2.6**.

First, 2-chloroquinoline-3-carboxaldehyde **2.1** was reduced to alcohol **2.2** which was next converted into bromide **2.3** *via* an Appel reaction. The phosphonium salt **2.4** was then prepared from **2.3** and used next for the preparation of alkene **2.5** *via* Wittig olefination with aldehyde **2.1**. Helicene **2.6** was prepared from **2.5** by oxidative photocyclization under UV irradiation. The preparation of helical acceptor core **2.6** was the limiting step for the scale-up of the material as the reaction was performed in highly diluted solution to avoid side products of [2+2] cycloaddition. The final compound **H1-PXZ** was prepared *via* Buchwald-Hartwig coupling between phenoxazine and the core **2.6** (Scheme 2.3).

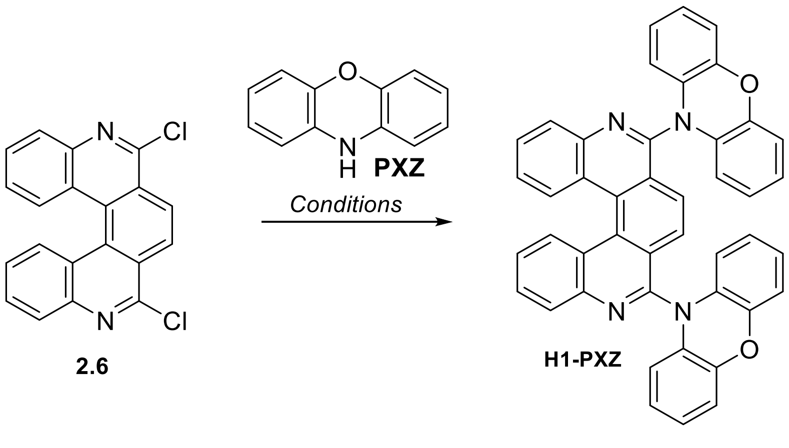

Scheme 2.3. Synthesis of the target molecule **H1-PXZ**.

Several different procedures were investigated for the preparation of **H1-PXZ** (Table 2.1). The reaction was found to be the most efficient when carried out in a microwave synthesiser. When $Pd_2(dba)_3$ was used as a catalyst, the final product could not be fully separated from the dibenzylideneacetone ligand by column chromatography, so $Pd(OAc)_2$ was used as an alternative.

Table 2.1. Attempted syntheses of **H1-PXZ**.

Entry	Conditions	Yield, %
1	$Pd_2(dba)_3$, tBu_3P, Cs_2CO_3, Tol, 110°C, 19 h	-
2	$Pd_2(dba)_3$, tBu_3P, Cs_2CO_3, Tol, 100°C, microwave, 2 h	34%
3	$Pd(OAc)_2$, tBu_3P, Cs_2CO_3, Tol, 100°C, microwave, 2 h	45%

The synthesis of helicene **H2-PXZ** is shown in Scheme 2.4. The procedure is similar to that used for the preparation of **H1-PXZ**. 2-(bromomethyl)naphthalene **2.7** was converted into a phosphonium salt **2.8**, which was next used for the preparation of the alkene **2.9**. The helical acceptor core **2.10** was prepared next *via* oxidative photocyclisation. The yield of the reaction was lower than that for the helicene **2.6**, as in this case planar side products also formed. Finally, **H2-PXZ** was prepared following the Buchwald-Hartwig procedure described above.

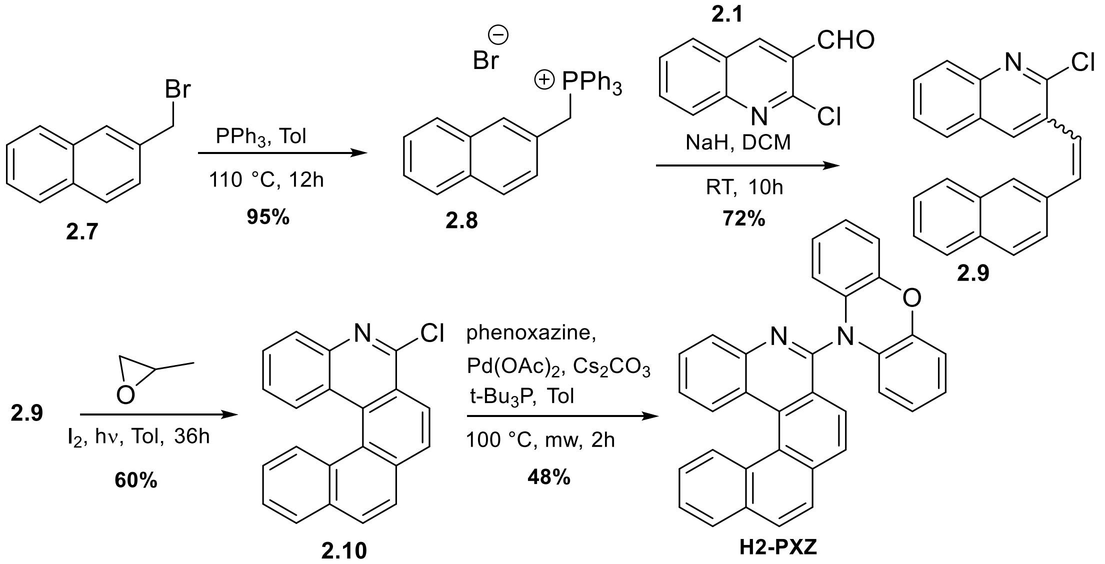

Scheme 2.4. Synthesis of the compound **H2-PXZ**.

The molecular structure of **H1-PXZ** and **H2-PXZ** was confirmed by ^{1}H NMR, ^{13}C NMR (see Appendix) and high-resolution mass spectrometry. The ^{1}H NMR spectra of both compounds at room temperature display broad peaks corresponding to protons of phenoxazine units.

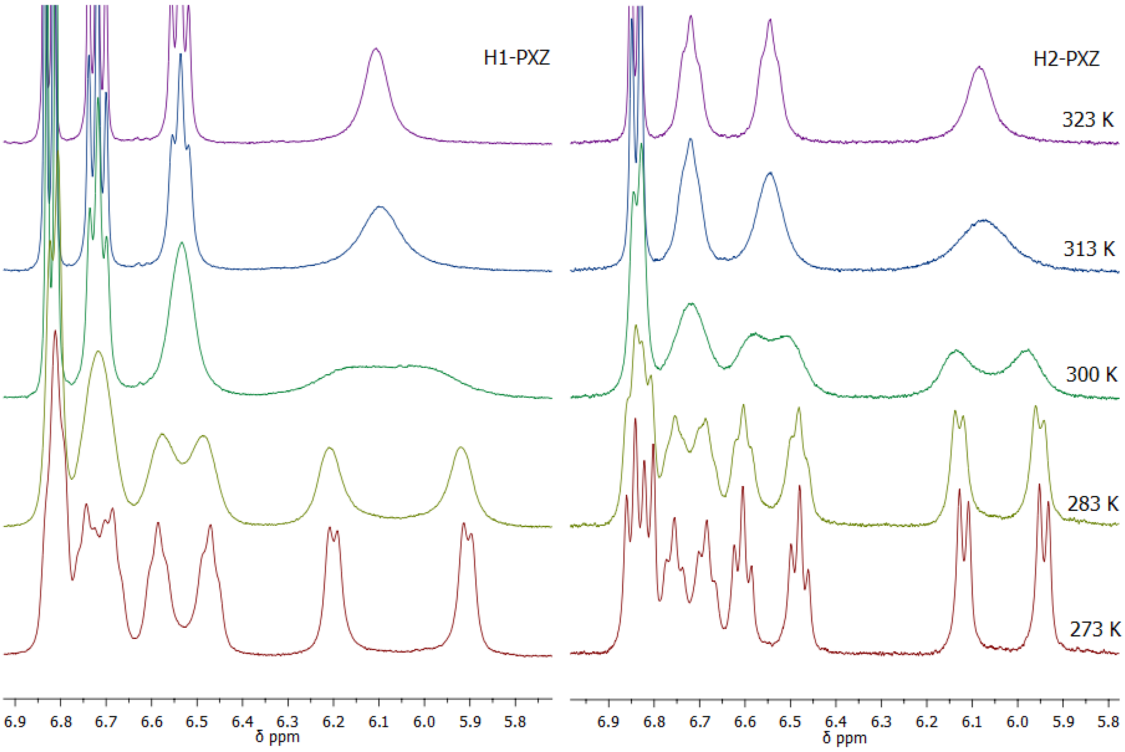

Figure 2.3. Variable temperature ^{1}H NMR experiments for **H1-** and **H2-PXZ** at 273–323 K in chloroform-d, showing the aromatic peaks in the range 5.8 to 6.9 ppm.

Variable temperature NMR experiments (Figure 2.3) demonstrate that at lower temperature these peaks are separated and sharp, which most likely indicates the presence of two conformers existing due to a restricted rotation between donor and acceptor. This is also consistent with the results of temperature-dependent photophysical studies described below. At higher temperatures the peaks coalesce.

2.2.2 X-ray crystallography

The structures of both compounds were further confirmed by single crystal X-ray diffraction studies. Crystals of both **H1-PXZ** and **H2-PXZ** were obtained by slow evaporation from a mixture of ethyl acetate : hexane (1 : 7). For **H1-PXZ** two types of crystals were formed simultaneously: luminescent orange blocks (**H1-PXZ-o**) and non-luminescent red needles (**H1-PXZ-r**). In each case, the compounds are present as a racemic mixture of two enantiomers. The torsion angles between the donor and acceptor moieties in **H1-PXZ-o** are reduced compared to **H1-PXZ-r** (Figure 2.4), being 73.14°, and 87.98°, respectively.

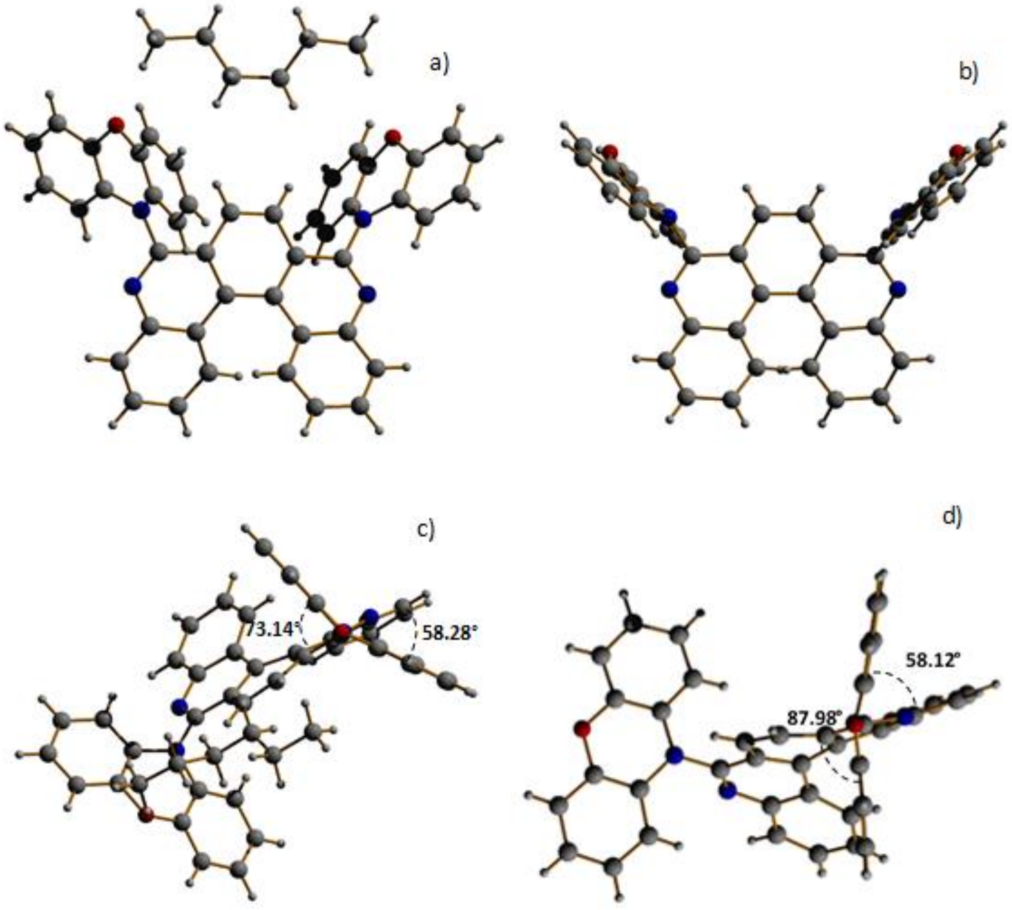

Figure 2.4. Molecular structures of **H1-PXZ-o** (a, c) and **H1-PXZ-r** (b, d).

The structure of **H2-PXZ** is shown in Figure 2.5 and the molecule has a torsion angle of 82.92°.

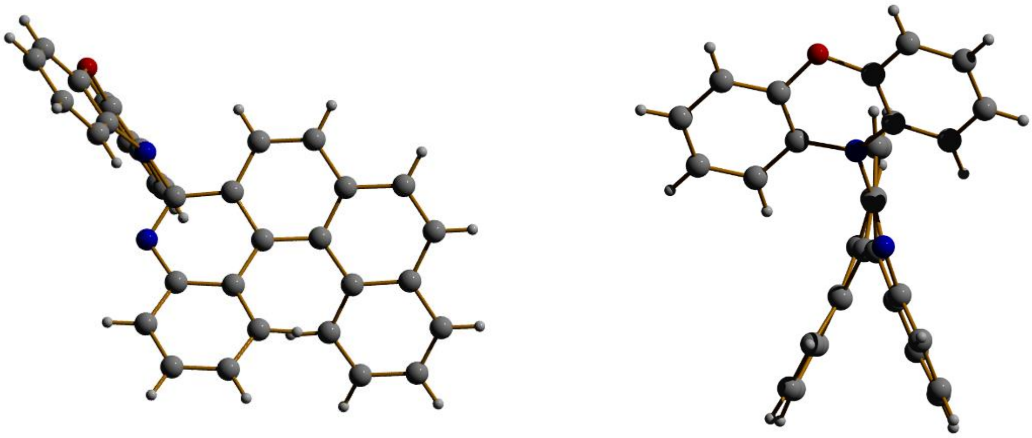

Figure 2.5. Molecular structure of H2-PXZ.

Unlike the other two crystals, **H1-PXZ-o** contains hexane in the crystal lattice which significantly influences the packing within the crystal (Figure 2.6-a) and its photophysical behaviour. In **H1-PXZ-r** (Figure 2.6-b) intermolecular π-π close contacts (ca. 3.2-3.5 Å) can be observed between the benzene rings of the phenoxazine units, whilst for **H1-PXZ-o** there are no close contacts due to the presence of the occluded hexane molecules. Since there are two phenoxazines per **H1-PXZ** molecule, this produces infinite chains of close contacts, which can result in the formation of low-emissive excimers.[147] In **H2-PXZ** there is only one phenoxazine moiety, and this unit has a close intermolecular π-π interaction with an adjacent molecule to form aggregated pairs of molecules (Figure 2.7).

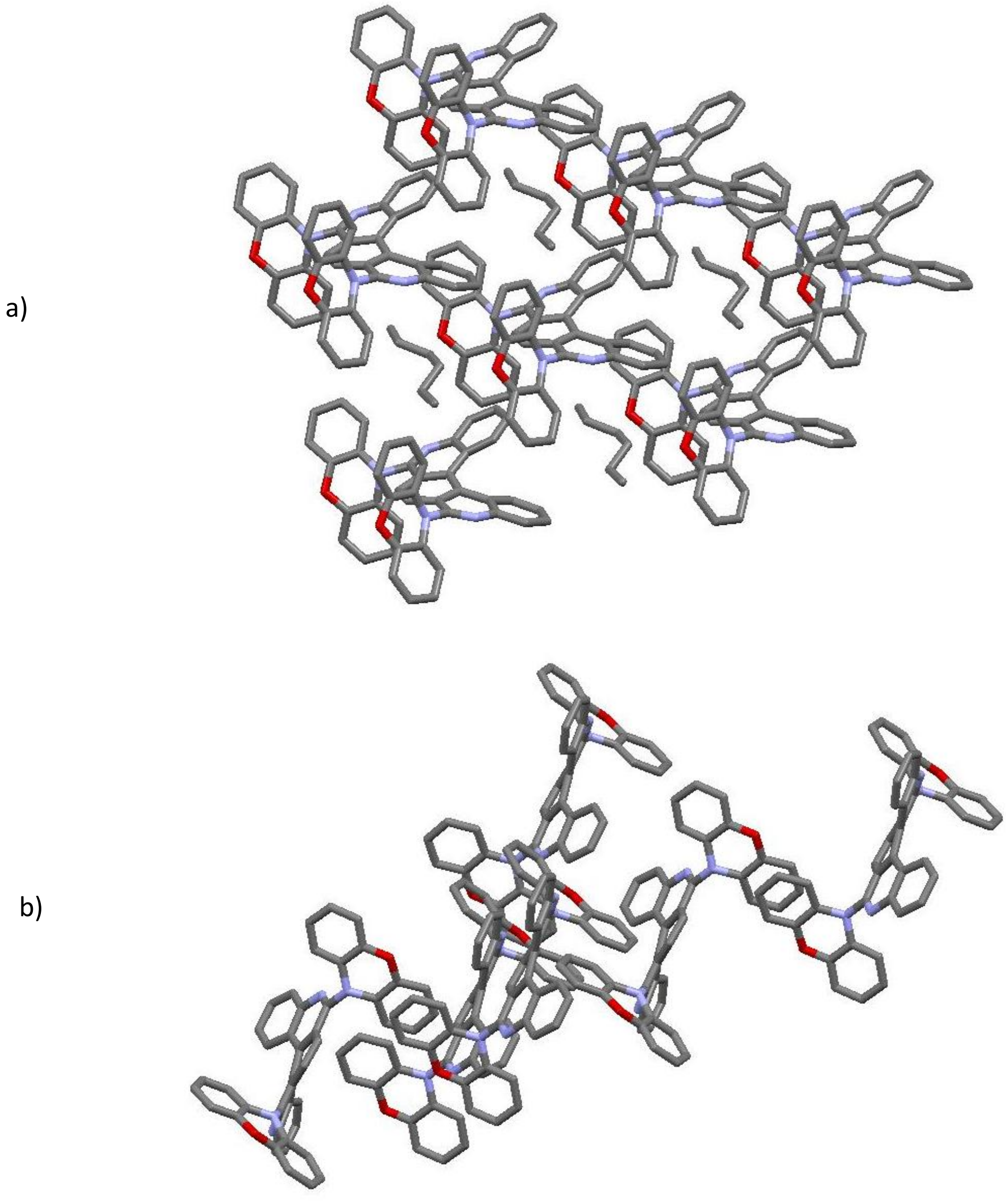

Figure 2.6. Crystal packing structure of **H1-PXZ-o** (a) and **H1-PXZ-r** (b). H atoms omitted for clarity.

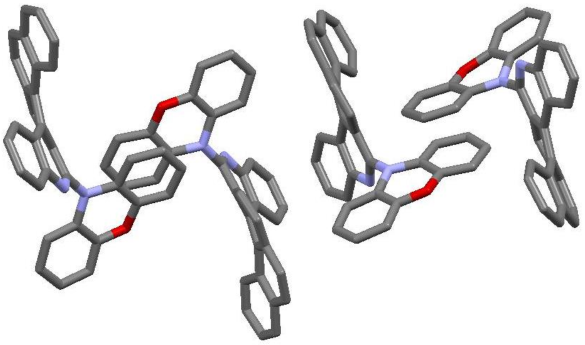

Figure 2.7. Dimers of **H2-PXZ** with H atoms omitted for clarity.

2.2.3 Electrochemical and thermal analysis

The electrochemistry data are presented in Table 2.2. The cathodic and anodic peaks are shown for reversible and irreversible (irr) processes and determined from the onset potentials.

Table 2.2. HOMO-LUMO levels and E_g for **H1-** and **H2-PXZ**.

	HOMO, eV	**LUMO, eV**	**E_g, eV**	**E_{ox}, eV**	**E_{red}, eV**
H1-PXZ	-5.35	-2.96	2.39	0.55	-1.84; -2.20(irr)[a]
H2-PXZ	-5.25	-2.57	2.68	0.45	-2.23(irr)

[a] (irr) denotes irreversible; [b] HOMO(LUMO) calculated from the peak of the corresponding redox wave and referenced to ferrocene.

Both compounds demonstrate one reversible peak around 0.5 eV. **H1-PXZ** presents first reversible and second irreversible reduction peaks (Figure 2.8) while for **H2-PXZ** there is only an irreversible reduction peak (Figure 2.9).

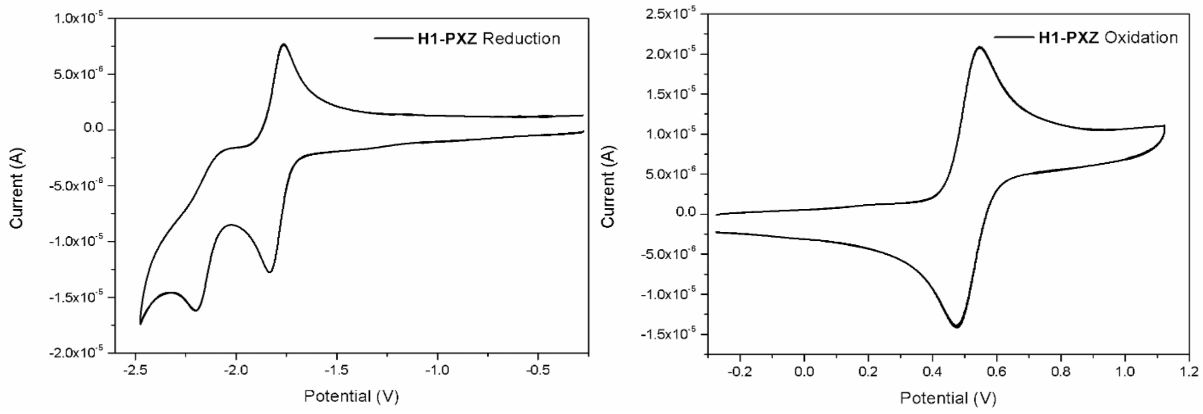

Figure 2.8. Reduction (left) and oxidation (right) curves from cyclic voltammetry of **H1-PXZ** referenced against the $E_{1/2}$ of the Fc/Fc$^+$ redox couple; $5\cdot10^{-4}$ M solutions in 0.1 M *n*-Bu_4NPF_6 (CH_2Cl_2).

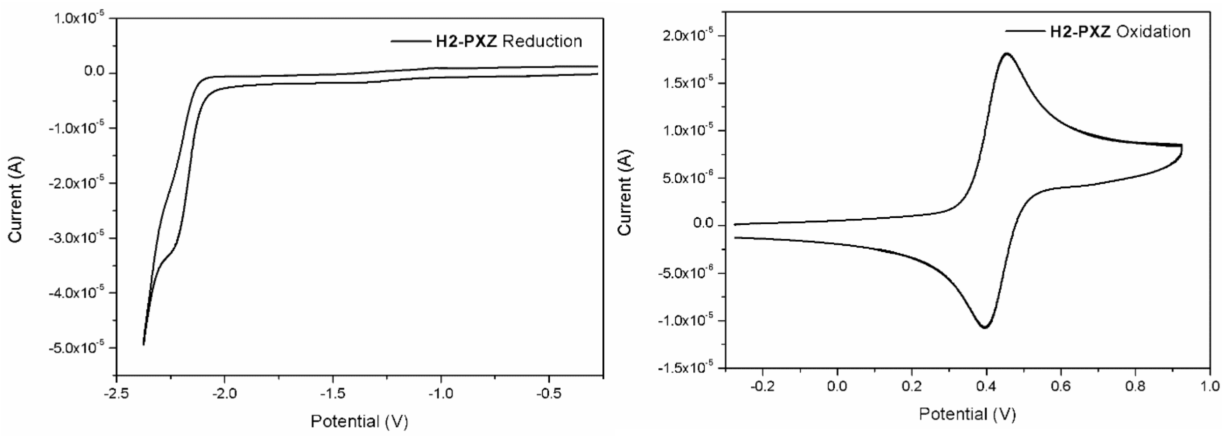

Figure 2.9. Reduction (left) and oxidation (right) curves from cyclic voltammetry of **H2-PXZ** referenced against the $E_{1/2}$ of the Fc/Fc$^+$ redox couple; $5 \cdot 10^{-4}$ M solutions in 0.1 M *n*-Bu_4NPF_6 (CH_2Cl_2).

Thermal properties for both compounds were investigated in powder by differential scanning calorimetry (DSC) and thermal gravimetric analysis (TGA). The DSC curves do not reveal any thermal events for **H1-PXZ** and **H2-PXZ**. Both compounds have high thermal stability and demonstrate 5% weight loss only at 356.5 °C and 334.4 °C for **H1-PXZ** and **H2-PXZ** respectively.

2.2.4 Photophysics of helicene-based emitters

The photophysical properties of both **H1-PXZ** and **H2-PXZ** were investigated in solution and in the solid state in Zeonex matrix and in crystals. The measurements were performed by Piotr Pander from the OEM group in Durham University. Both molecules demonstrate the typical behaviour of TADF materials with D-A and D-A-D structure.[87,89]

2.2.4.1 Photophysical studies in solution

The absorption spectra of both compounds demonstrate the presence of a charge transfer (CT) band (Figure 2.8). The materials exhibit mixed local (LE) and CT emission in solution. Remarkably, the contribution of the LE photoluminescence in solution is much stronger for **H1-PXZ** and **H2-PXZ** compared to other TADF materials with a small S-T gap. This could be possibly explained by a steric hindrance between donor and acceptor moieties that restricts the rotation of the substituents around the C-N axis, as described in previous studies.[94] The dihedral angle between donor and acceptor is nearly orthogonal due to the limited rotation of the donor moiety around the C-N bond. In this case the radiative decay rate from the LE state can compete with the formation of the CT states, as the population of the CT state is slowed down. However, other TADF compounds with similar arrangements of donor and acceptor units often show strong TADF in solution. Thus, the orientation of D and A moieties itself cannot explain the quenching of the CT emission. Therefore, the internal conversion (IC) is the most plausible cause of the suppressed CT photoluminescence. Long-lived emission of the CT state is more strongly affected by the IC compared to that of the short-lived LE state. Due to the strong electron-accepting properties of the helical core of **H1-PXZ**, the compound exhibits CT emission only in non-polar methylcyclohexane (Figure 2.8). In more polar toluene and dichloromethane (DCM) the CT emission is quenched. On the other hand, **H2-PXZ** demonstrates a clear solvatochromic shift of the CT luminescence in more polar solvents. This suggests that **H1-PXZ** has a much stronger CT character compared to **H2-PXZ**. Due to this, the HOMO-LUMO of **H1-PXZ** situated at D and A moieties respectively are nearly orthogonal in the solvent.

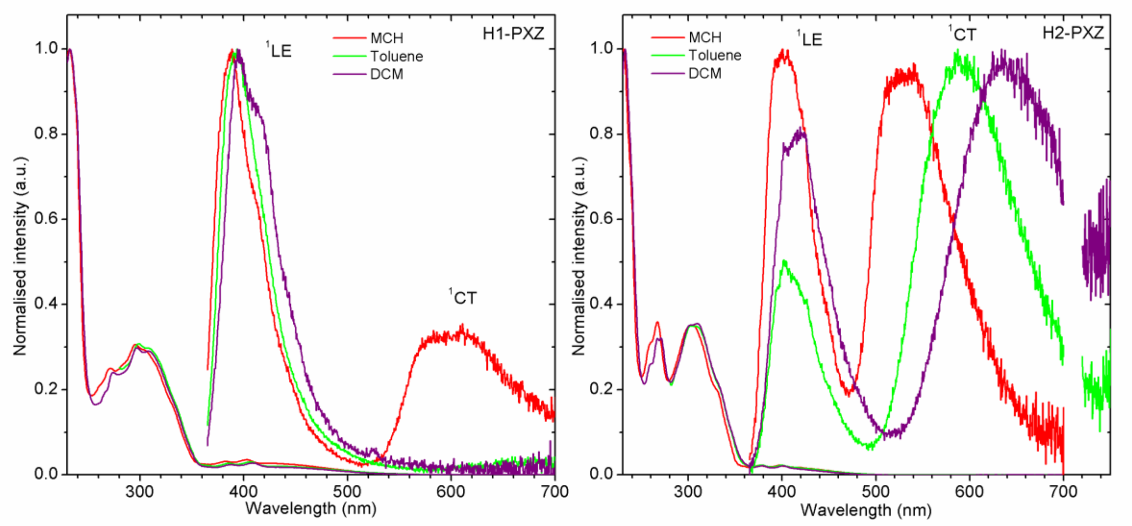

Figure 2.10. Photoluminescence spectra of **H1-PXZ** and **H2-PXZ** in solutions of various polarity, λ_{ex} = 355 nm.

One of the simplest ways to determine whether there is a contribution of triplet excited states to the photoluminescence process is to compare the intensity of the emission in the presence of oxygen and in degassed solution. Molecular oxygen is a quencher of luminescence. Its ground state is a triplet $^3O_2$, and the excited triplet or singlet states of the molecule (M*) can be quenched *via* energy transfer resulting in the non-radiative decay of M* to the ground state (M) and the formation of the singlet excited state oxygen (Equation 2.1).[50]

$$A^* + {}^3O_2 \rightarrow A + {}^1O_2 \qquad (2.1)$$

The longer the lifetime of the excited state the stronger its sensitivity to the presence of oxygen. Consequently, triplets are more strongly affected than singlet excited states. Indeed, the emission is suppressed for both **H1-PXZ** and **H2-PXZ** in the presence of oxygen (Figure 2.11).

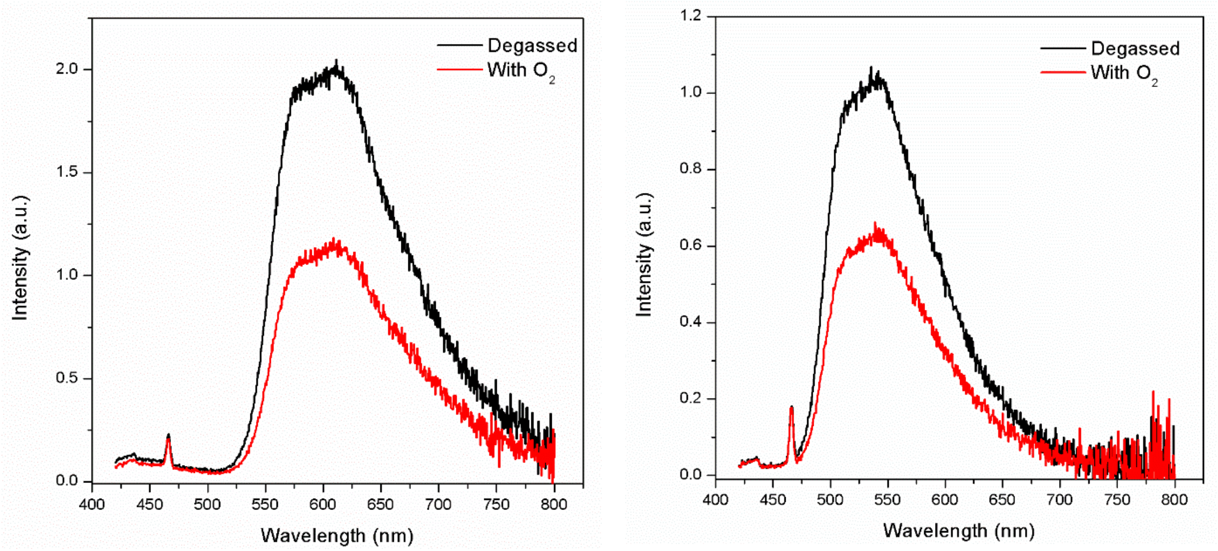

Figure 2.11. Emission of H1-PXZ (left) and H2-PXZ (right) in the presence of oxygen and in degassed solution; λ_{ex} = 355 nm.

To understand complex photophysical processes involved in TADF the luminescence should be investigated using time-resolved measurements. In this study phosphorescence, prompt fluorescence (PF) and delayed fluorescence (DF) spectra as well as fluorescence decay (from 400 ps to 1 s) were measured using nanosecond gated luminescence and lifetime measurements. Here, a pulsed Nd:YAG laser emitting at 355 nm or a N_2 laser emitting at 337 nm was used as the excitation source. The resulting emission was focused onto a spectrograph and detected on a sensitive gated intensified charge coupled device (iCCD) camera with sub-nanosecond resolution. Time resolved measurements can be performed by varying the gating delay, also called time delay, that determines the time when the collection of emitted by the sample photons begins, and integration times (the duration of collection). The photoluminescence decay curves can be obtained by recording multiple spectra while logarithmically increasing the gating delay and integration times.

Photoluminescence decay of **H1-PXZ** and **H2-PXZ** in MCH solution at room temperature shows the usual behaviour of a TADF emitter with two exponential regimes corresponding to prompt and delayed fluorescence (Figure 2.12). It is worth noting that the presented decays reflect only CT emission, as ^{1}LE states decay within the first nanosecond.

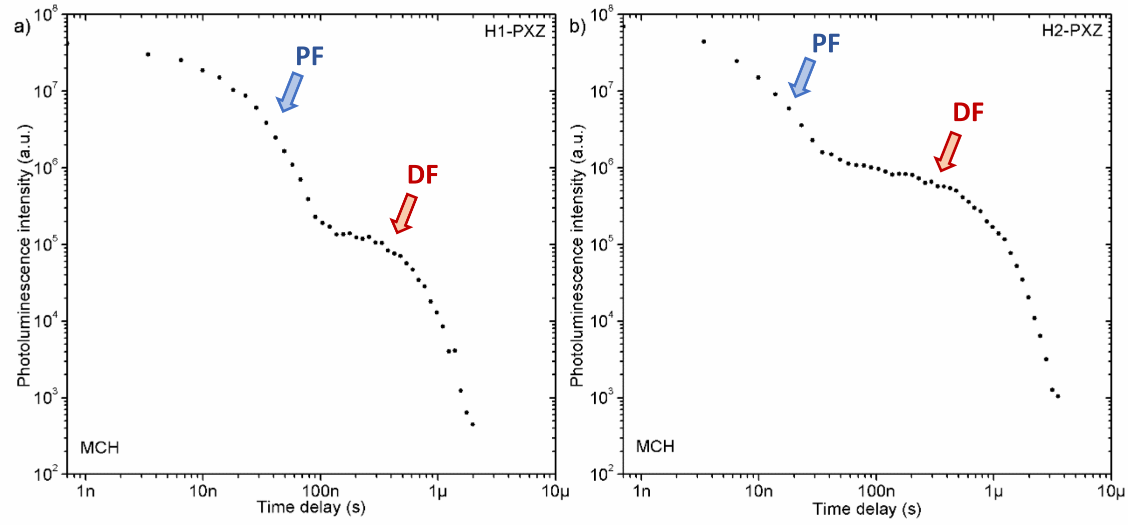

Figure 2.12. Photoluminescence decay of **H1-PXZ** and **H2-PXZ** in methylcyclohexane (MCH) solutions.

The photophysical properties of **H1-** and **H2-PXZ** are summarised in Table 2.3. The PLQY of degassed solutions is 7% and 4% respectively, which is caused by the strong contribution of the non-radiative decay for the materials.

Table 2.3. Photophysical properties of materials in methylcyclohexane

Compound	**λ_{max}, nm**[a]	**Φ_{PL}**[b]	**τ_{PF}, ns**[c]	**τ_{DF}, μs**[d]
H1-PXZ	611	0.07	15.0 ± 0.2	0.40 ± 0.02
H2-PXZ	536	0.04	6.1 ± 0.2	0.47 ± 0.02

[a] Charge transfer photoluminescence maximum λ_{exc} = 410 nm; [b] photoluminescence quantum yield in degassed solution, λ_{exc} = 410 nm ; [c] prompt fluorescence lifetime in a degassed solution; [d] delayed fluorescence lifetime in a degassed solution.

2.2.4.2 Photophysical properties in polymer matrix

Both compounds show TADF emission when doped in non-polar polymer Zeonex, 1 wt.% (Figure 2.13-a,b; Figure 2.14). The lifetime of both prompt and delayed fluorescence is longer in the solid state than in solution (Figure 2.14 and Figure 2.12). This suggests that the non-radiative decay is suppressed in the solid state. In solution **H2-PXZ** appears to be a more efficient CT emitter than **H1-PXZ** (Figure 2.10) most likely due to a faster radiative decay of the CT state which can compete effectively with internal conversion. At the same time the CT emission is observed for both molecules in Zeonex matrix (Figure 2.13-a), and TADF is more prominent. Thus, the investigation of the photophysical properties of the systems are focused on materials in the solid state, i.e. in films and crystals.

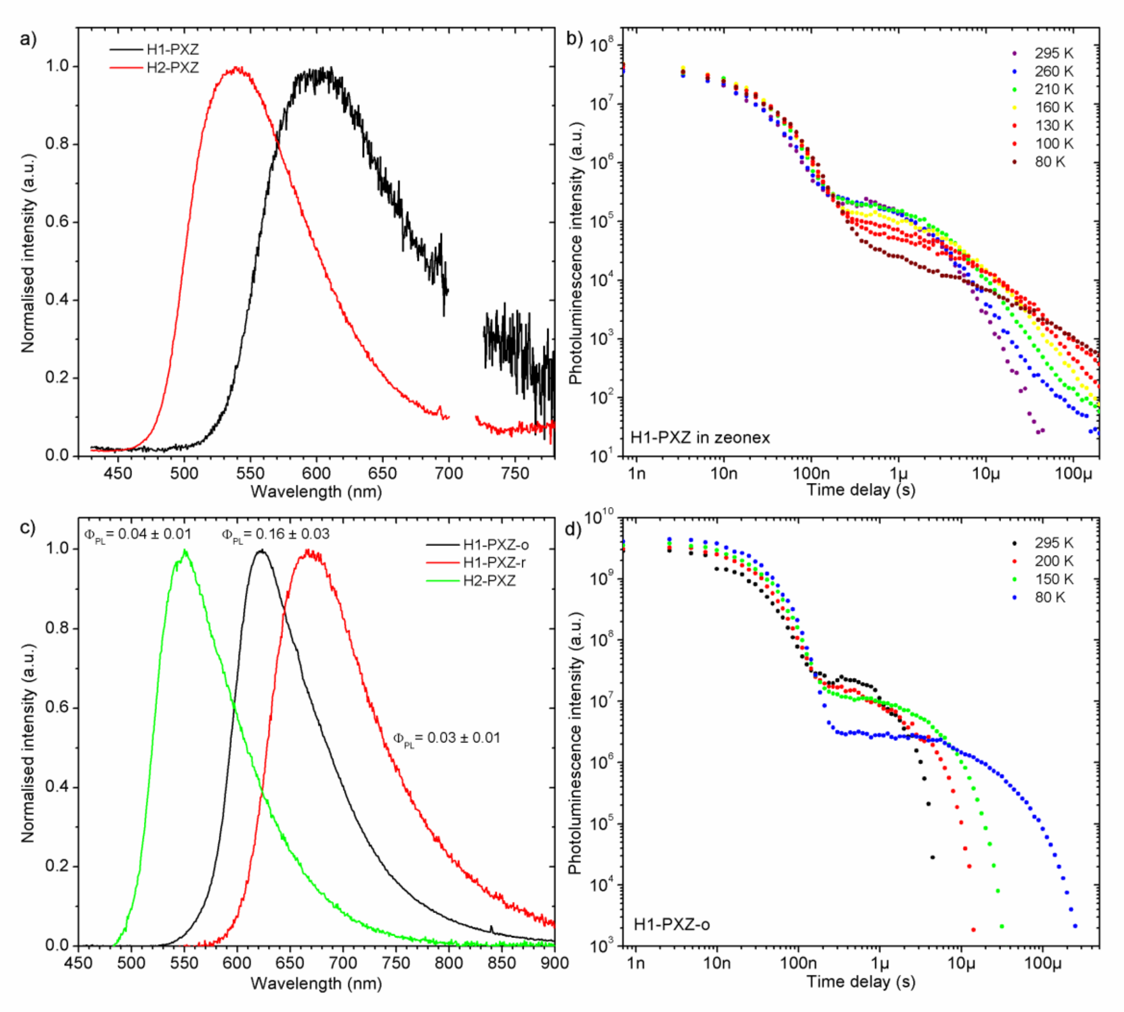

Figure 2.13. Photophysical characteristics of the materials in the solid state: a) steady-state emission spectra in Zeonex; b) photoluminescence decay of **H1-PXZ** in Zeonex; c) steady-state photoluminescence spectra of molecular crystals; d) photoluminescence decay of **H1-PXZ-o** crystals.

Temperature is one of the crucial parameters that influences k_{rISC} and resulting TADF emission, as it follows from Equation 1.3 discussed in Section 1.4.1 of Chapter 1. Thus, the temperature dependence is an important proof of TADF character of the delayed fluorescence as the integral of the DF increases with the increase of temperature for TADF materials.[87]

However, the fluorescence decay of **H1-PXZ** and **H2-PXZ** demonstrates a slightly different situation due to a strong contribution of non-radiative decay for the triplet state of the molecules. Instead of decreasing, the TADF intensity increases as the temperature decreases to 160 K (Figure 2.14) for both **H1-PXZ and H2-PXZ**. This is caused by the suppression of the non-radiative decay at lower temperature. Below 160 K the DF intensity decreases as is expected for TADF materials.

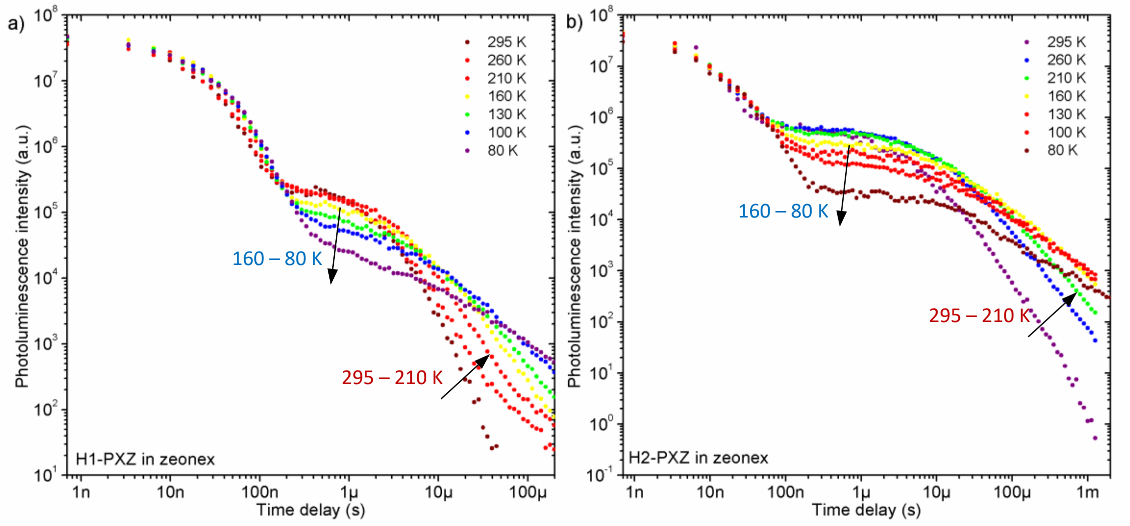

Figure 2.14. Photoluminescence decay of **H1-PXZ** and **H2-PXZ** in Zeonex film (1% *w/w*) at various temperatures.

There are two different ways to experimentally determine ΔE_{ST}. The first is to calculate the difference between the onset of the fluorescence and phosphorescence peaks, and it is an optical gap.[211] The second is calculated by fitting the integrated DF emission as a function of temperature giving the thermal activation energy ($\Delta E_{a(TADF)}$) derived from the Arrhenius equation. Similarly to the HOMO-LUMO gap calculations, different approaches in this case can give very different values, and the variation is usually greater for higher performing compounds. It was suggested that the difference is caused by the presence of an intermediate state,[211] which is in agreement with the spin-vibronic mechanism of TADF described in Section 1.4.1 of Chapter 1. Conformational changes occurring after the generation of a relatively long lived triplet excited state could also explain such a discrepancy.[116]

The design of both **H1-PXZ** and **H2-PXZ** allows a perfect alignment of singlet and triplet states even in non-polar media, leading to a nearly zero S-T gap. Remarkably, in these systems phosphorescence is hardly observable even at 80 K making the determination of the triplet state energy difficult (Figure 2.15 and Figure 2.16). Yet, phosphorescence can be distinguished in **H2-PXZ**, indicating an S-T gap of 0.01 eV. In **H1-PXZ** the phosphorescence is not easily observed, and therefore the triplet energy cannot be determined directly from the phosphorescence.

The temperature dependence of TADF intensity according to Arrhenius equation (Figure 2.15-c and Figure 2.16-c) shows that the $E_{a(TADF)}$ is below 0.02 eV (12 ± 3 meV and 15 ± 3 meV in **H1-PXZ** and **H2-PXZ**, respectively). This demonstrates that the S-T gap in **H1-PXZ** is the same order of magnitude as it is in **H2-PXZ**. As discussed above, the increase in the DF intensity between 295 and 220 K indicates the suppression of the non-radiative decay (Figure 2.15 c and Figure 2.16 c).

For the delayed fluorescence it is important to track the changes in the emission spectrum with time. For that, time resolved spectra were recorded. The spectra of PF and DF should be identical for TADF, as the emission results from the relaxation of the same singlet excited state.[212]

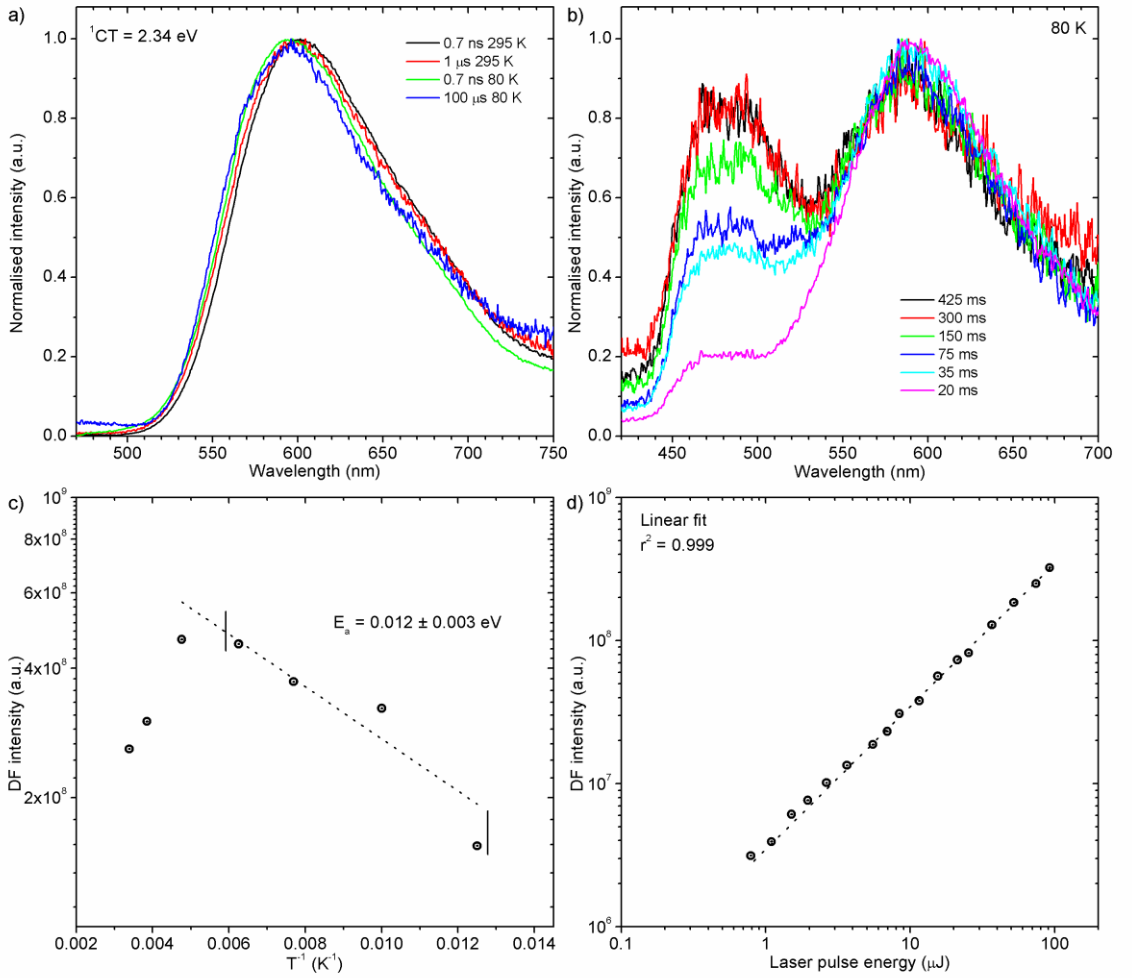

Figure 2.15. Time-resolved photoluminescence analysis of **H1-PXZ** in Zeonex film (1% w/w): a) time-resolved spectra at 295 and 80 K; b) time-resolved spectra recorded at late delay times at 80 K; c) temperature dependence of delayed fluorescence; d) power dependence of delayed fluorescence at 295 K.

In **H1-PXZ** prompt and delayed fluorescence spectra are nearly identical. They are slightly blue-shifted at 80 K (Figure 2.15-a). As mentioned previously, the observation of phosphorescence in **H1-PXZ** is impossible even at low temperatures due to a nearly zero S-T gap. At long delays above 100 ms, two emission components that have comparative photoluminescence lifetimes can be observed at low temperatures (Figure 2.15-b). The one at 2.34 eV is identical to the CT emission of the molecule and thus can be attributed to the delayed fluorescence. The other component with approximatively 0.5 eV higher energy resembles the typical behaviour of phosphorescence in TADF materials; it however most likely originates from a different population of **H1-PXZ** molecules. In this case there is no communication between the emissive states at 2.34 eV and 2.84 eV as they are located in different molecules. This can happen if, in a rigid polymer matrix at 80 K, some of the molecules cannot adapt a conformation suitable for the fast formation of a CT state due to the lack of freedom possible at higher temperatures. These molecules thus emit phosphorescence from the LE state (emission at 2.84 eV). At the same time normal TADF CT emission can be observed for the rest of the molecules (emission at 2.34 eV).

As there are two types of delayed fluorescence, it is important to distinguish TADF from the delayed fluorescence originating from TTA. While the former is an intramolecular process, TTA involves the interaction of two molecules in the triplet state. Measuring the power dependence of the delayed fluorescence intensity can differentiate between the two mechanisms. The TTA process is controlled by diffusion and it competes with the monomolecular decay of triplet excited states.[87] When triplet deactivation occurs more quickly than triplet-triplet annihilation, the DF resulting from TTA shows a quadratic power dependence.[213] The following increase of the excitation dose produces higher triplet concentrations, and the TTA becomes a dominant process. At this stage the dependence becomes linear. Unlike TTA, TADF intensity always demonstrates linear power dependence. Indeed, in the case of **H1-PXZ** the intensity of DF varies linearly with increasing excitation power (Figure 2.15-d).

H2-PXZ shows more complicated photophysical behaviour compared to **H1-PXZ**. For this material the spectrum of prompt fluorescence changes over time (Figure 2.16-a). The spectra at 0.7 ns delay and 35 ns delay are different, and the latter is more similar to the DF spectrum recorded at longer delay. This indicates the relaxation of the excited state molecule geometry with time. It takes molecules several nanoseconds to relax, thus DF originates from the molecules with relaxed geometry. For **H2-PXZ** at 80 K it is possible to observe the phosphorescence at longer delays (Figure 2.16-b). The phosphorescence spectrum is well resolved and can be distinguished from the CT emission. The TADF is however still present even at 80 K. Interestingly, the phosphorescence onset (2.57 eV) and relaxed CT emission onset (2.58 eV) are nearly isoenergetic. The lowest triplet state of the molecule (^{3}LE) is most likely located at the acceptor, as the phosphorescence of the donor is expected at a higher energy of around 2.8 eV.[113] Just as in the case of **H1-PXZ**, the power dependence of DF for **H2-PXZ** is linear (Figure 2.16-d), which confirms the unimolecular origin of the process and indicates TADF.

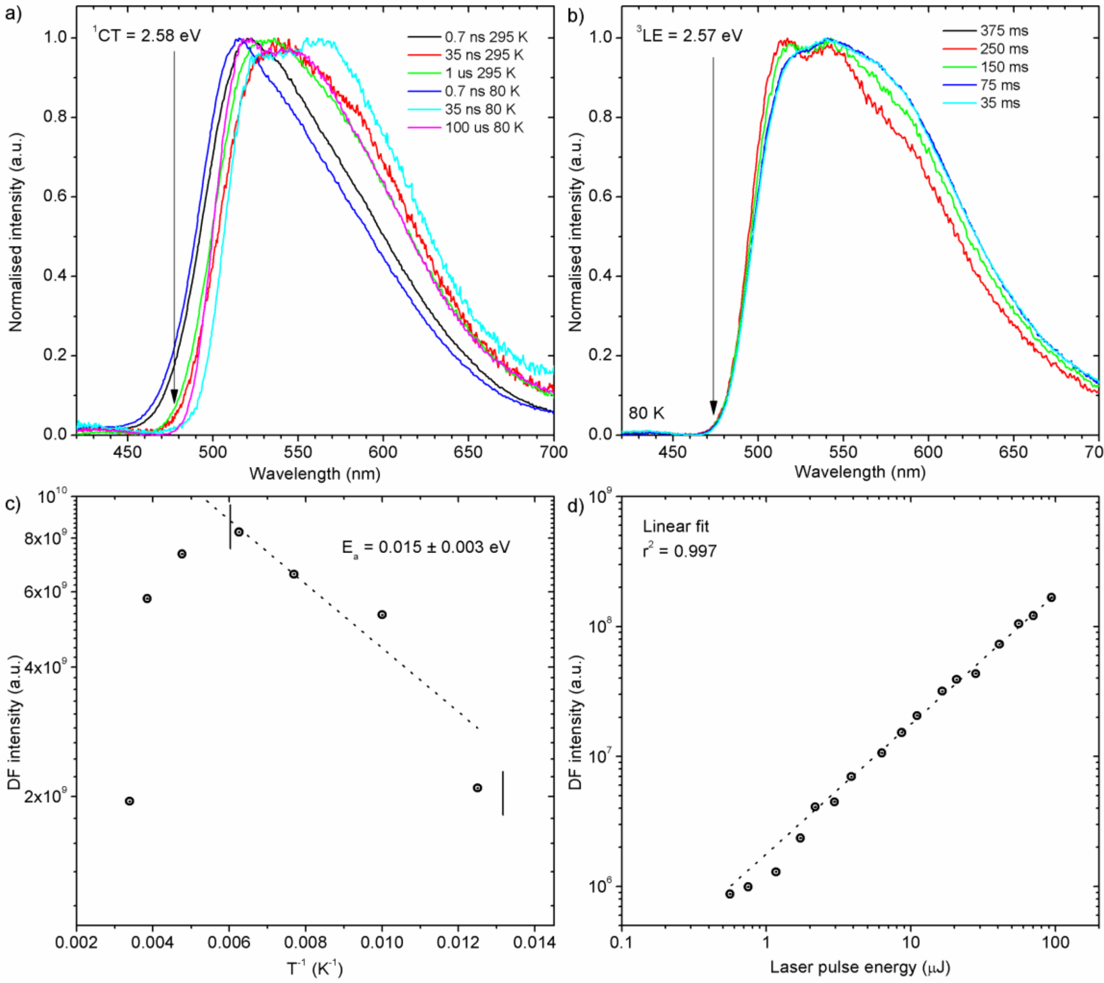

Figure 2.16. Time-resolved photoluminescence analysis of **H2-PXZ** in Zeonex film (1% w/w): a) time-resolved spectra at 295 and 80 K; b) time-resolved spectra recorded at late delay times at 80 K; c) temperature dependence of delayed fluorescence; d) power dependence of delayed fluorescence at 295 K.

2.2.4.3 Photophysics in crystals

Solutions and Zeonex films are isotropic environments. The formation of aggregates is very unlikely during the film fabrication, as both compounds are well soluble in toluene. In addition, both emitters are used in very low concentrations, so the bimolecular interactions between emitter molecules are suppressed. At the same time, the intermolecular interactions play an important role in crystals of **H1-PXZ** and **H2-PXZ**. They can suppress the non-radiative decay and control the CT state energy. Normally the intermolecular interactions cause the aggregation induced quenching of the emission.[214] That is why **H1-PXZ-r** and **H2-PXZ** crystals exhibit a low PLQY (3-4%). Not only is the PLQY low for these two types of crystals, but also the TADF emission arising from the crystals is very weak at room temperature (Figure 2.15). On the contrary, **H1-PXZ-o** crystals containing a molecule of hexane per each molecule of emitter (Figure 2.4-a, -c and Figure 2.6-a), demonstrate an increased PLQY (0.16 ± 0.03) and a prominent TADF (Figure 2.13-d). Thus, the influence of the hexane molecule is significant for the observation of TADF when comparing crystals of **H1-PXZ-r** and **H1-PXZ-o**. It is worth noting that the D-A dihedral angles in both crystals are very close (Figure 2.4-c, -d). Consequently, the difference in the TADF behaviour observed for two types of **H1-PXZ** crystals can be attributed to the presence of the solvent molecules in the crystal lattice. As was discussed in Section 2.2.2, in **H1-PXZ-r** crystals the radiative decay is suppressed due to the intermolecular π-π close contacts. On the other hand, the presence of the hexane molecules in the lattice perturbs the molecular packing in the **H1-PXZ-o** crystals and reduces the luminescence quenching caused by the aggregation. Remarkably, the **H1-PXZ-o** crystal shows a higher CT state energy compared to **H1-PXZ-r**. As there is no significant difference in the relative position of D-A units in both crystals, this can be explained by the change in the dielectric constant of each crystal type. As a D-A-D molecule, **H1-PXZ** shows a significant dipole moment even in the ground state, giving rise to a larger dielectric constant in the solid state. Contrary to that, the presence of hexane might lead to a decrease in the dielectric constant resulting in the difference of CT energy between the crystals. The variation of CT energy affects not only the colour of emission but also TADF. In **H1-PXZ-o** the TADF emission is observable even at 80 K (Figure 2.13-d). This indicates that for **H1-PXZ-o** the S-T gap is close to zero. As the CT state is lower in **H1-PXZ-r** crystals, the non-radiative decay increases according to the energy gap law. This affects both the lowest singlet (S_1) and triplet (T_1) states. This can explain the lower PLQY of **H1-PXZ-r** (resulting from both S$_1$ and T$_1$ being affected by a non-radiative decay), and much weaker, hardly observable TADF (suggesting that the T$_1$ state is being affected).

Compared to **H1-PXZ-o**, **H1-PXZ-r** crystals demonstrate a much lower photoluminescence quantum yield (0.03-0.04), and thus the TADF is also much weaker (Figure 2.17 a). However, the TADF intensity is decreased at lower temperature. At the same time, **H2-PXZ** crystals show a negative temperature dependence of delayed fluorescence intensity, so the TADF increases significantly at low temperature (Figure 2.17 b). This indicates a significant contribution of the non-radiative decay and a small S-T gap in the crystal.

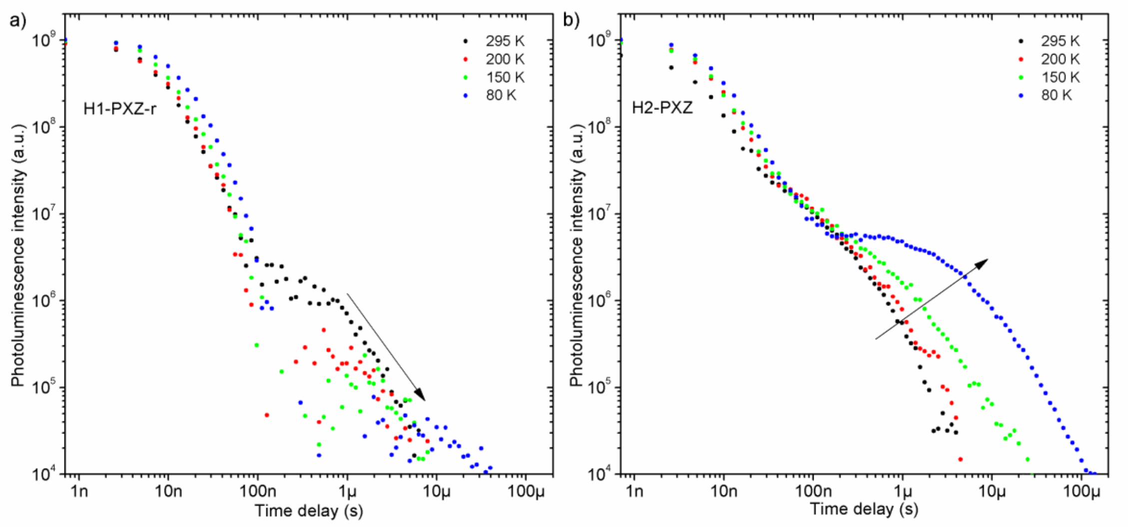

Figure 2.17. Photoluminescence decay of **H1-PXZ-r** (a) and **H2-PXZ** (b) crystals at various temperatures.

H1-PXZ-o crystals show typical TADF behaviour at 295 K. The spectra of prompt and delayed fluorescence are nearly identical, and there is no evidence of the presence of any meta-stable conformers (Figure 2.18-a). At lower temperature (Figure 2.18-b) the presence of at least two conformers, existing on short (PF) and long (DF) timescale, can be observed. This is due to a significant restriction of molecular motion at 80 K. The signal appearing in the microsecond timescale is unlikely to be phosphorescence, as otherwise the third exponential component would be present in the photoluminescence decay (with the first component corresponding to a prompt fluorescence, the second being delayed fluorescence, and the third being phosphorescence).[94,215] The TADF mechanism involves a competition between delayed fluorescence and phosphorescence, thus there should be an additional exponential regime in the intermediate temperatures between 295 and 80 K if phosphorescence is observed. In the case of **H1-PXZ-o**, however, the decay consists of only two exponential components at all temperatures up to 80 K. It is also unlikely that the phosphorescence is that short-lived (around 10-100 μs) in the absence of any heavy atoms.

Prompt fluorescence spectra are clearly different at 295 K and 80 K (Figure 2.18-c). This indicates a substantial change in the geometry of the excited state at lower temperature. It means that molecular motion is restricted at low temperature, and the singlet state cannot rapidly relax its geometry. The linear power dependence (Figure 2.18-d) confirms that the delayed fluorescence recorded for **H1-PXZ-o** is an intramolecular process and thus it is TADF.

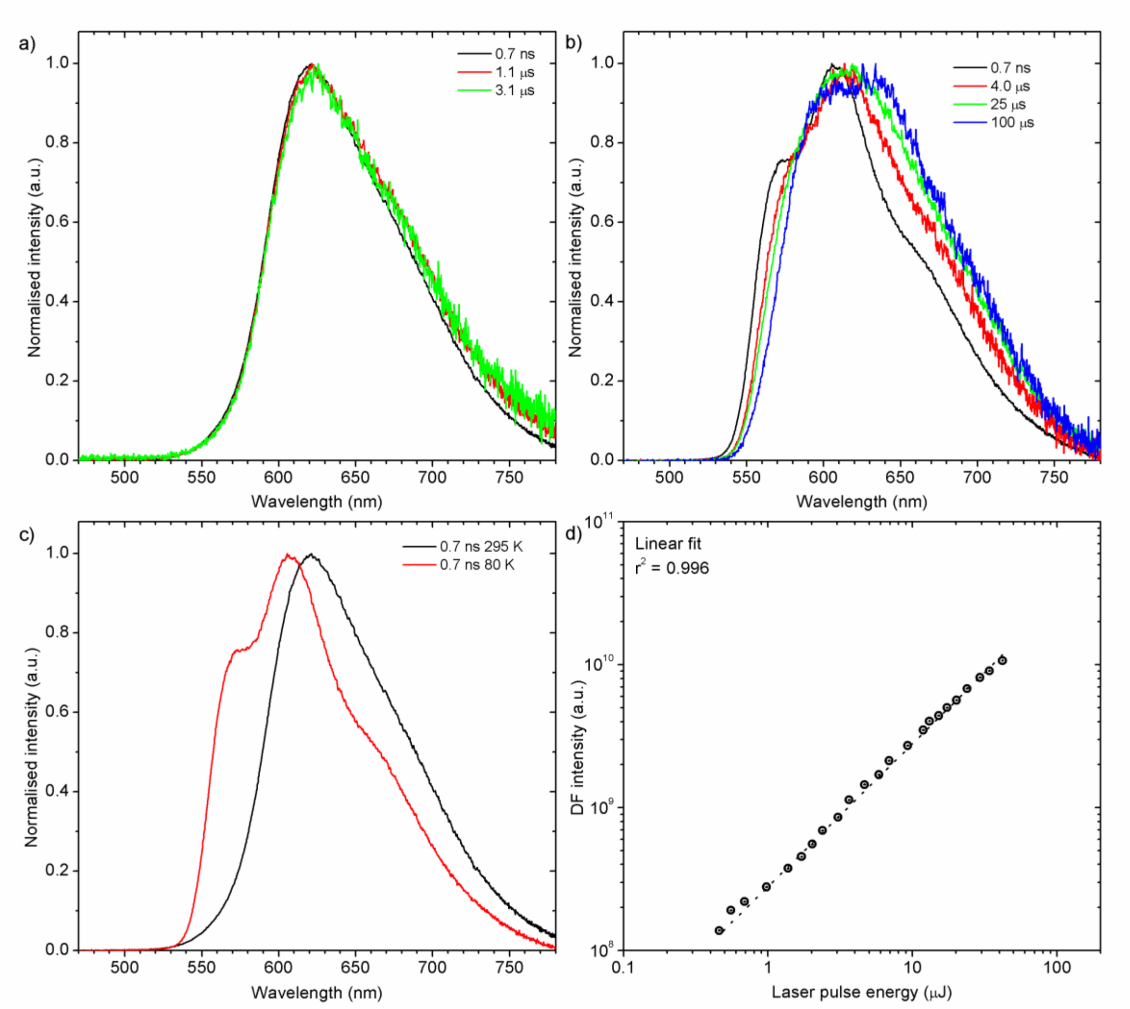

Figure 2.18. Photoluminescence properties of **H1-PXZ-o** crystals: a) Time-resolved spectra at 295 K; b) Time-resolved spectra at 80 K; c) Comparison of prompt fluorescence spectra at 295 K and 80 K; d) Power dependence of delayed fluorescence at 295 K.

H1-PXZ-r also demonstrated TADF emission properties at 295 K, but the delayed fluorescence is very weak (Figure 2.19-a). The prompt and delayed fluorescence have the same emission spectrum, and no conformers are present (Figure 2.19-a). The molecular motion is restricted in **H1-PXZ-r** similarly to **H1-PXZ-o** (Figure 2.19-b). Due to that the late prompt (35 ns) and delayed fluorescence (microsecond region) differ from early prompt fluorescence (0.7 ns). This can be caused by a restricted molecular motion. As a consequence the emission arises from two different populations of conformers. For similar reasons described for **H1-PXZ-o**, the emission observed at the microsecond timescale is unlikely to be phosphorescence.

Prompt fluorescence spectra at 295 K and 80 K are visibly different (Figure 2.19-c), which again indicates a significant geometrical change in the singlet excited state at low temperatures, resulting in the singlet state not being able rapidly relax its geometry because of the obstructed molecular motion at low temperature. The linear power dependence (Figure 2.19-d) proves that the delayed fluorescence of **H1-PXZ-r** is a monomolecular process, thus it is TADF.

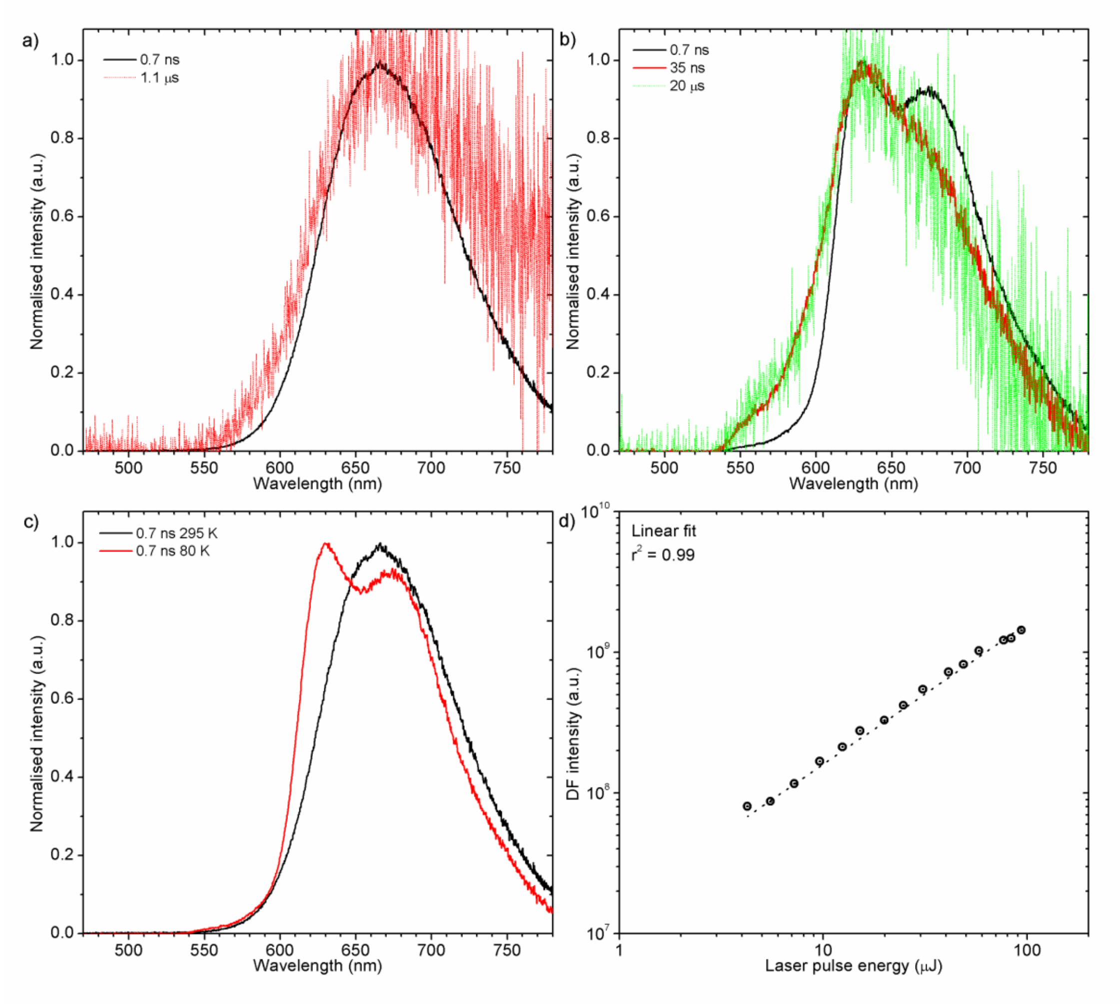

Figure 2.19. Photoluminescence properties of **H1-PXZ-r** crystals: a) Time-resolved spectra at 295 K; b) Time-resolved spectra at 80 K; c) Comparison of prompt fluorescence spectra at 295 K and 80 K; d) Power dependence of delayed fluorescence at 295 K.

H2-PXZ crystals demonstrate typical behaviour of TADF emitters at 295 K with prompt and delayed fluorescence having the same emission spectrum (Figure 2.20-a). The delayed fluorescence is weak, but it is stronger than that in **H1-PXZ-r** crystals (Figure 2.20-b). The restricted molecular motion can be observed in **H1-PXZ** crystals at low temperatures (Figure 2.20-b). Similarly to **H1-PXZ-o,** prompt fluorescence (0.7 ns) and delayed fluorescence (at 1µs – 1 ms) spectra differ for **H2-PXZ** due to a restricted molecular motion. This is due to the reasons described above for other molecular crystals.

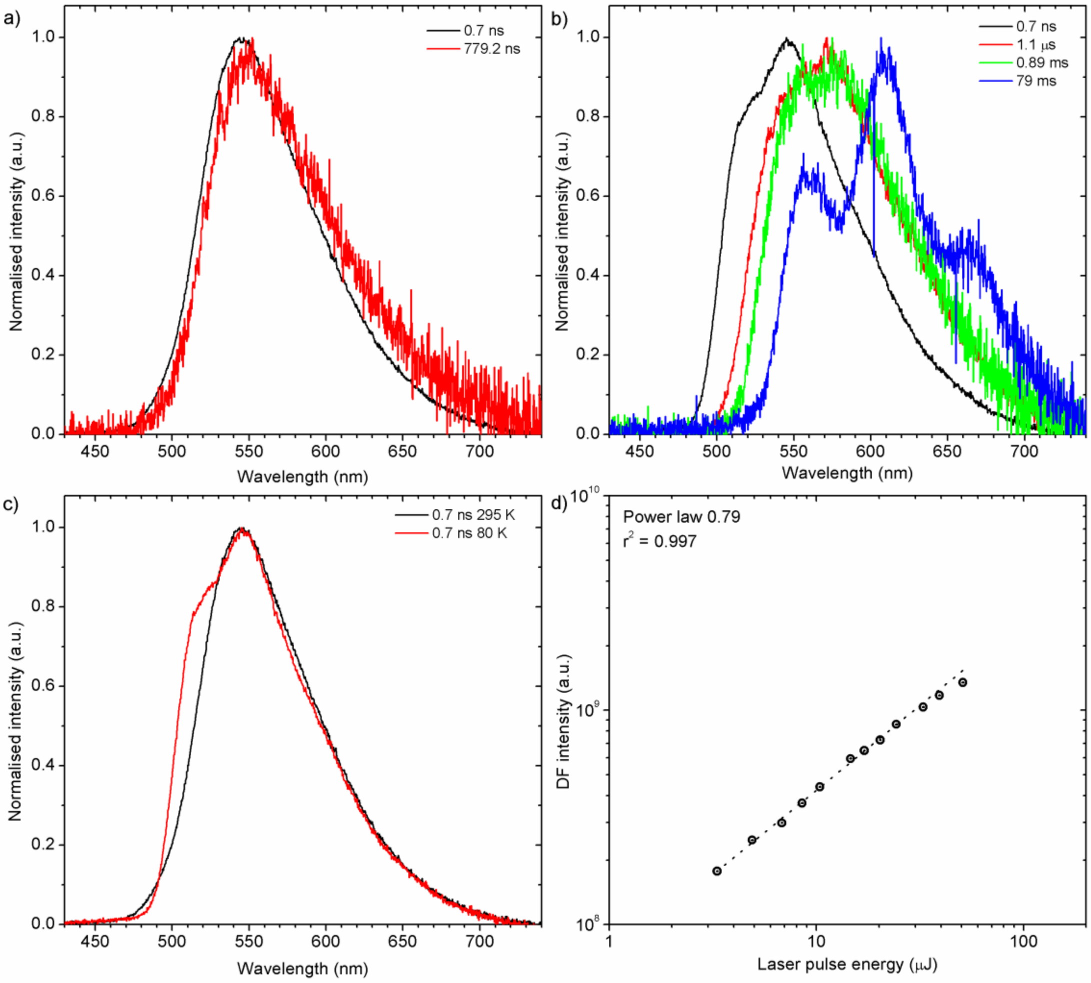

Figure 2.20. Photoluminescence properties of **H2-PXZ** crystals: a) Time-resolved spectra at 295 K; b) Time-resolved spectra at 80 K; c) Comparison of prompt fluorescence spectra at 295 K and 80 K; d) Power dependence of delayed fluorescence at 295 K.

However, **H2-PXZ** crystals are different from those described before. For **H2-PXZ** phosphorescence can be observed at very late delay times (79 ms) (Figure 2.20-b). The emission spectrum at 79 ms has a clearly vibronic shape. Also, the photoluminescence decay apparently reveals a third exponential component (>50 ms) which is different from the delayed fluorescence region (200 ns – 1 ms) (Figure 2.21). At low temperatures there is a significant geometrical change in the singlet excited state, which results in the clear difference between prompt fluorescence spectra at 295 K and 80 K, which is similar to the cases described above. For **H2-PXZ** crystals power dependence is sublinear (Figure 2.20-d). This most likely indicates the monomolecular origin of the delayed fluorescence. However, there should be the influence of an additional exciton quenching process. It is not quite clear what causes this effect, but it can possibly be explained by the singlet-singlet annihilation.

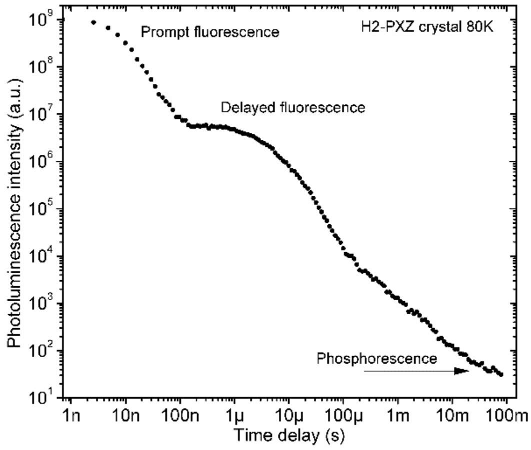

Figure 2.21. Photoluminescence decay of **H2-PXZ** crystals at 80 K in broad timescale.

Because of the difference in PLQY of the crystals, the best parameter describing the amount of TADF produced in each type of crystal would be the delayed to prompt fluorescence ratio (Figure 2.22). The variation in DF/PF with temperature is insignificant for **H1-PXZ-o** and **H1-PXZ-r**. At all temperatures **H1-PXZ-o** shows more TADF than the **H1-PXZ-r** crystals. This implies that in **H1-PXZ-o** the coupling between the CT state and ^{3}LE state is much stronger than it is in **H1-PXZ-r**, which results in a higher triplet formation yield. On the contrary, **H2-PXZ** demonstrates a large variation of the DF/PF ratio with temperature. At 80 K the delayed fluorescence to prompt fluorescence ratio is much higher than at all other temperatures. This indicates that **H2-PXZ** is actually a better TADF emitter compared to both **H1-PXZ** crystals, but a strong non-radiative decay more effectively quenches triplet states, so the contribution of DF at room temperature is very low.

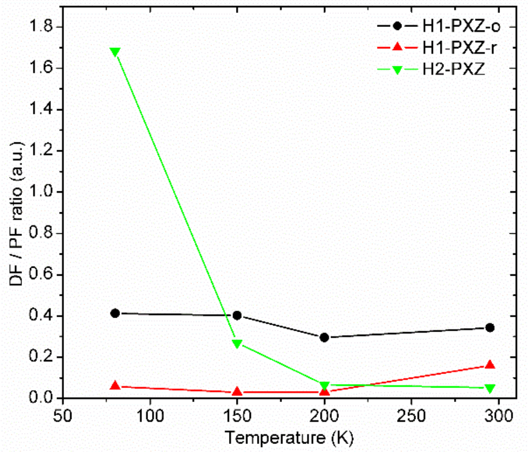

Figure 2.22. Delayed (DF) to prompt fluorescence (PF) ratio in the organic crystals as a function of temperature.

2.2.5 Device fabrication and characterisation

The electroluminescence performance of the new materials was evaluated in solution-processed devices. **H1-PXZ** (Dev 1) and **H2-PXZ** (Dev 2) were used as dopants (5%) in a mixed host poly(N-vinylcarbazole):2-t-butylphenyl-5-biphenyl-1,3,4-oxadiazole (PVK:PBD, 60:40 w/w).

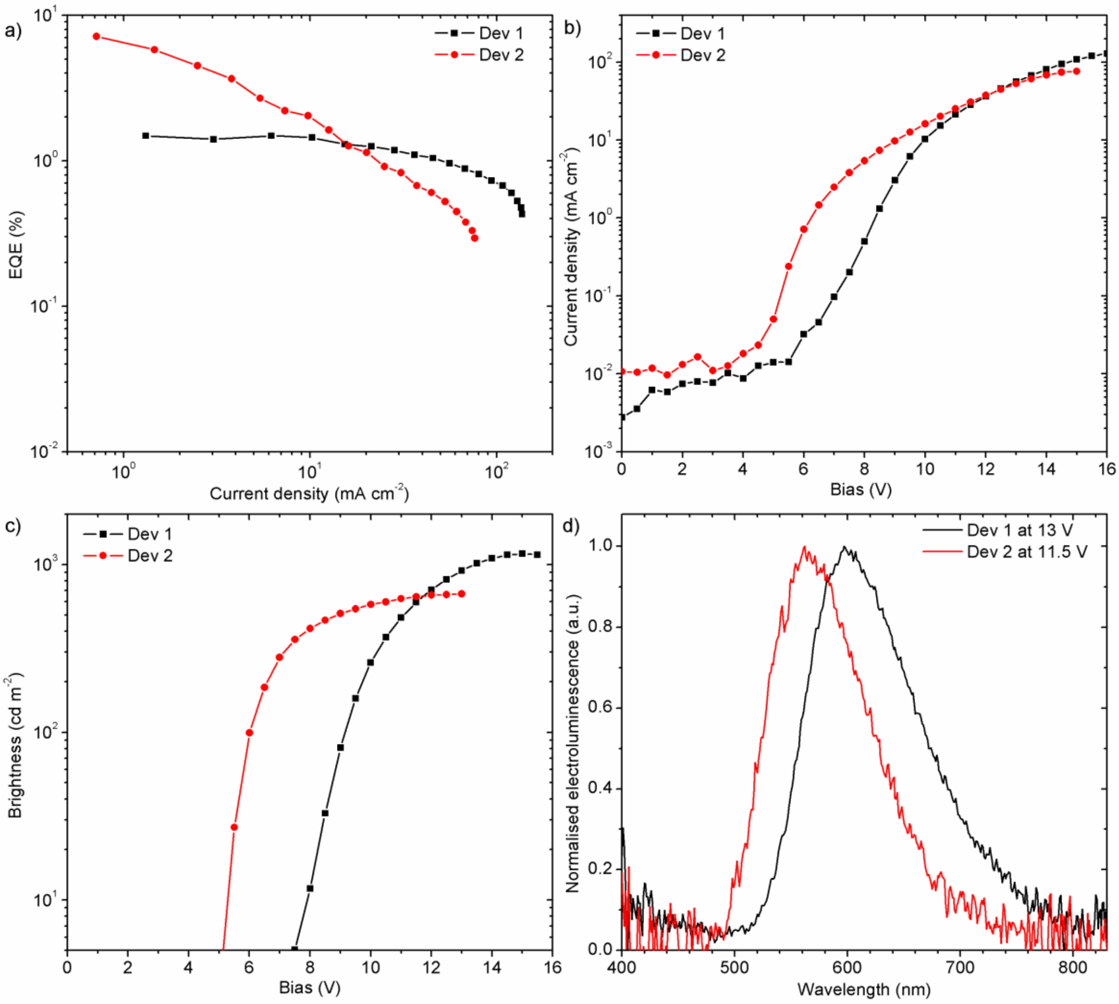

Figure 2.23. Electroluminescence characteristics of OLED devices fabricated using **H1-PXZ** and **H2-PXZ** as emitters: a) EQE vs. current density; b) Current density vs. applied bias; c) Brightness vs applied bias; d) Electroluminescence spectra. Device structure: ITO | HIL 1.3N (45 nm) | PVKH (10 nm) | PVK:PBD (60:40) co 5% X (32 nm) | TPBi (50 nm) | LiF (0.8 nm) | Al (100 nm). Where X = **H1-PXZ** (Dev 1), X = **H2-PXZ** (Dev 2).

OLEDs were fabricated by a hybrid spin-coating / evaporation method. PEDOT:PSS (Heraeus Clevios 1.3N) was used as a hole injection layer. High molecular weight poly(9-vinylcarbazole) (PVKH) was used as an electron blocking/hole transporting layer. TPBi was used as an electron transporting/hole blocking layer. The devices had the following structure: ITO/PEDOT:PSS/PVKH/EML/TPBi/LiF/Al.

H1-PXZ in Dev 1 exhibited orange electroluminescence, CIE (0.52, 0.41). Dev 2 containing **H2-PXZ** demonstrated yellow emission, CIE (0.44, 0.50). Dev 1 and Dev 2 achieved an EQE of 1.5% and 7.1%, and current efficiency of 2.7 cd A^{-1} and 13.9 cd A^{-1}, respectively (Figure 2.23 and Figure 2.24). The maximum brightness is 1160 cd m^{-2} and 670 cd m^{-2} for Dev 1 and Dev 2 respectively. At 5 cd m^{-2} the turn on voltage is lower for Dev 2 (5.1 V) than for Dev 1 (7.5 V). The efficiency roll-off is much higher for Dev 2 than for Dev 1. This is probably due to an unknown degradation process in Dev 2.

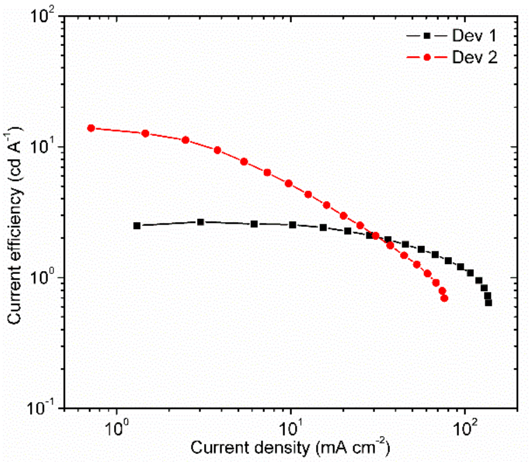

Figure 2.24. Current efficiency vs. current density characteristics of OLED devices.

2.2.6 Theoretical calculations

In addition to experimental measurements theoretical calculations using density functional theory (DFT) and time-dependent density functional theory (TDDFT) were performed by Dr Joseph Cameron (University of Glasgow) for the helicene-based compounds. Firstly, the geometries of **H1-** and **H2-PXZ** were optimised using coulomb-attenuated CAM-B3LYP functional and 6-31+G(d) basis set. The calculated structures are in good correlation with the determined crystal structures of compounds (Figure 2.25, Table 2.4).

Table 2.4. Correlation between calculated structures and crystal structures.

Compound	**MUE (Å)**[a]	**Calculated helicene twist (exp) (°)**
H1-PXZ	0.004	38.71 (38.75)
H2-PXZ	0.008	39.74 (42.39)

[a] Mean unsigned error (MUE) is calculated from non-hydrogen containing bonds, toluene as polarisable-continuum model solvent

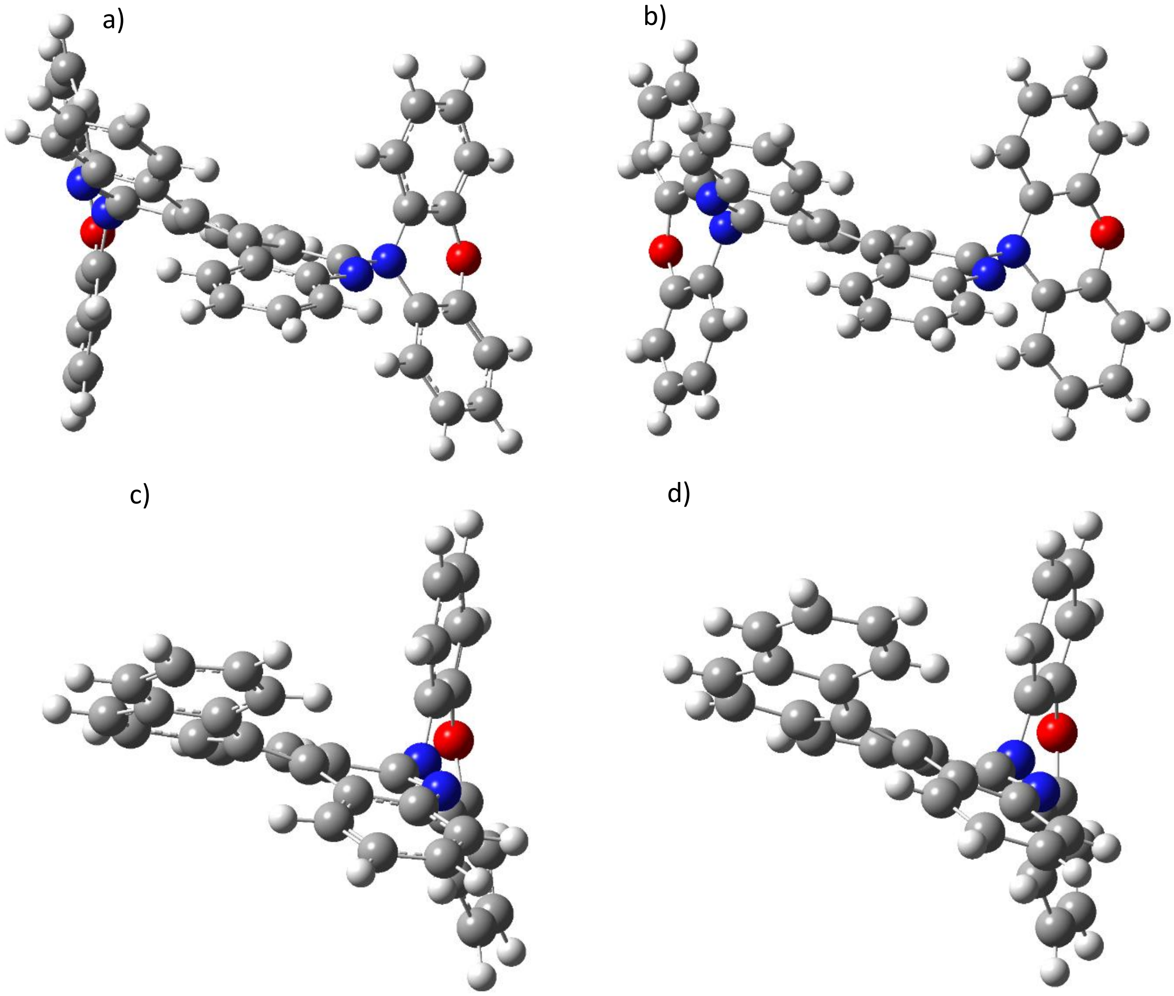

Figure 2.25. Crystal structures (left) and calculated structures (right) for H1-PXZ (a, b) and H2-PXZ (c, d).

Calculations were also performed to investigate the influence of the donor moiety on the magnitude of the oscillator strength and spatial overlap between HOMO and LUMO. This can help to estimate a relative PLQY and ΔE_{ST} for a given set of compounds. For this, vertical transitions from the optimised ground state geometries were calculated using TDDFT. The calculations were carried out for the compounds with **H2** core as an acceptor and phenoxazine (**H2-PXZ**), phenothiazine (**H2-PTHZ**) and acridine (**H2-ACR**) as donor groups to determine how suitable each donor group would be for achieving high PLQYs and rISC rates (Figure 2.26).

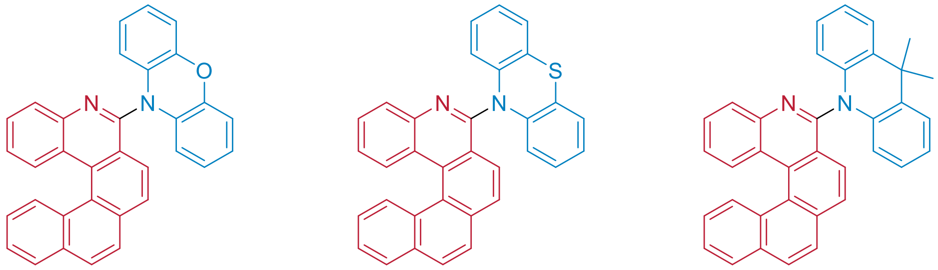

H2-PXZ **H2-PTHZ** **H2-ACR**

Figure 2.26. Molecular structures of the compounds **H2-PXZ**, **H2-PTHZ** and **H2-ACR**

For a transition between a given couple of occupied (φ_i) and unoccupied (φ_a) orbitals the orbital overlap (O_{ia}) can be calculated as the inner product of the moduli of two orbitals (Equation 2.2).[216]

$$O_{ia} = \langle|\varphi_i|||\varphi_a|\rangle = \int |\varphi_i(\mathbf{r})|\,|\varphi_a(\mathbf{r})|d\mathbf{r} \qquad (2.2)$$

Normally in TDDFT, multiple transitions between occupied and unoccupied pairs of orbitals contribute to a given excitation, so the contribution of each transition (κ_{ia}) should be considered. Thus, the spatial overlap (Λ) for linear excitations was calculated using the method described by Peach *et al.*[216] (Equation 2.3). As was discussed in Chapter 1, a smaller spatial overlap provides a smaller ΔE_{ST} gap, so it is a useful parameter in determining good TADF candidates.

$$\Lambda = \frac{\sum_{i,a} \kappa_{ia}^2 O_{ia}}{\sum_{i,a} \kappa_{ia}^2} \qquad (2.3)$$

CAM-B3LYP functional[217] was used in these calculations. Compared to B3LYP, it has a greater Hartree-Fock exchange at long range which provides a higher accuracy in calculation of CT excitations where the orbital overlap is low. This can be useful for measuring the separation between HOMO and LUMO in donor-acceptor molecules with a strong CT character. The data from TDDFT calculations for **H2-PXZ**, **H2-PTHZ** and **H2-ACR** are shown in the Table 2.5. Here, **H2-PXZ** demonstrates an optimal combination between a small spatial overlap and relatively big oscillator strength (f) compared to compounds with phenothiazine and acridine donor moieties. Scheme 2.5 shows the orbital transitions associated with LE and CT excitations for **H2-PXZ**. While **H2-PTHZ** can potentially demonstrate higher PLQY due to a higher oscillator strength, the spatial overlap of 0.44 indicates that it is most likely will not exhibit TADF due to a larger S-T gap and so would lead to a reduced efficiency of the material in devices compared to **H2-PXZ**. **H2-ACR** has the lowest spatial overlap, but at the same time demonstrates a very low oscillator strength, which suggests it will not be suitable for OLED applications.

Table 2.5. Vertical transitions, oscillator strength, excitation energies and spatial overlap calculated for helical compounds with **H2** core.

Compound	MO transitions	f	Excitation energy (eV)	Λ
H2-PXZ	H→L (0.644) H→L+1 (-0.101) H→L+2 (0.175)	0.073	3.35	0.24
H2-PTHZ	H-2→L+1 (0.219) H-1→L (-0.316) H→L (0.532) H→L+2 (-0.137)	0.145	3.66	0.44
H2-ACR	H→L+1 (0.658) H→L+2 (0.168)	0.003	3.40	0.17

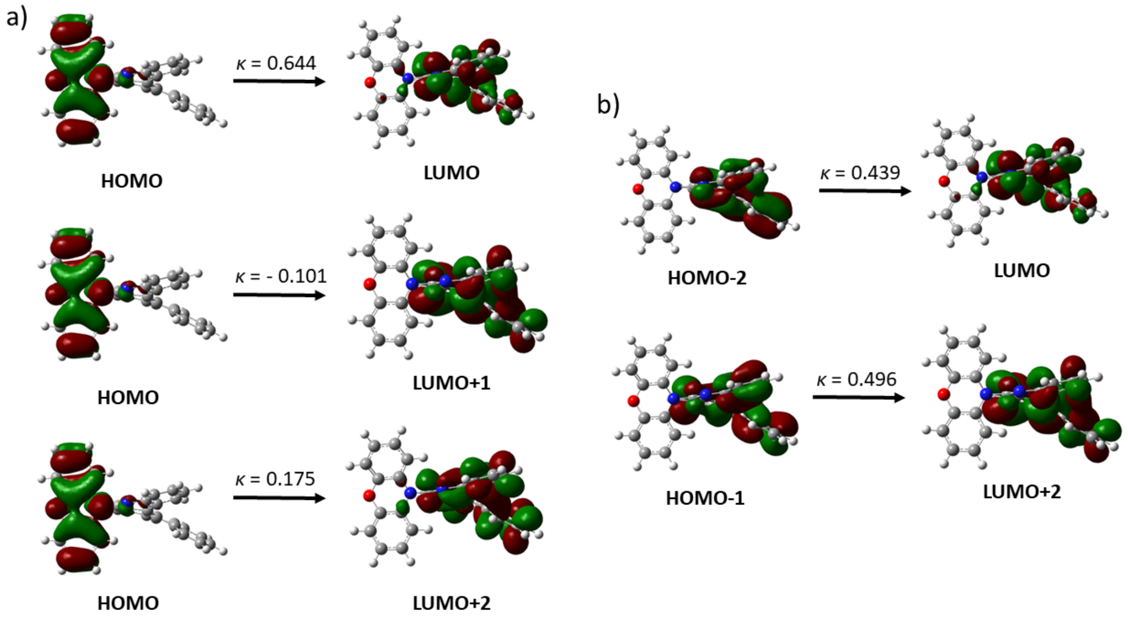

Scheme 2.5. LE (a) and CT (b) excitations for H2-PXZ.

Excited state optimisation was performed as well for **H2-PXZ** to investigate the structural changes upon excitation. The optimisation was carried out using CAM-B3LYP functional and 6-31+G(d) basis set. As expected for a compound with a strong solvatochromism and a large Stokes shift, **H2-PXZ** undergoes noticeable excited state structural relaxation. Thus, planarisation of the phenoxazine unit is observed in the excited state, and the twist of the helical moiety decreases (Table 2.6, Figure 2.27). Similarly, dipole moment increases upon excitation, which is a sign of the substantial changes in the charge distribution characteristic for CT excitations. At the same time, the direction of the dipole moment does not change significantly.

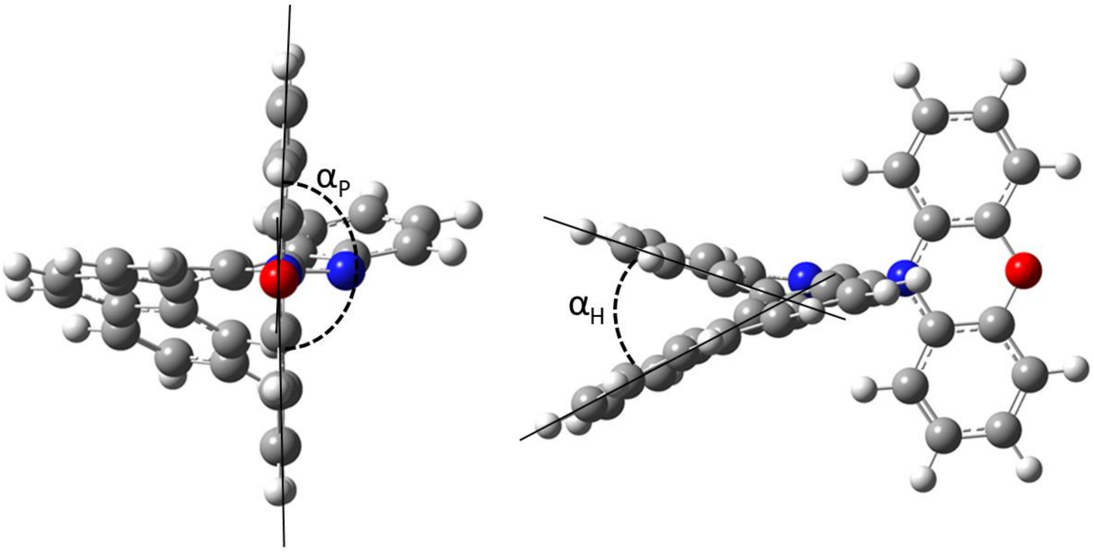

Figure 2.27. Optimised excited state geometry for **H2-PXZ**.

Table 2.6 Structural and dipole moment changes upon excitation.

Structure	**Helicene twist, α_H (°)**	**Phenoxazine twist, α_P (°)**	**Dipole moment, μ (D)**
H2-PXZ (ground state)	39.74	176.25	4.64
H2-PXZ (excited state)	37.26	179.76	5.84

In summary, when compared to compounds with acridine (**H2-ACR**) and phenothiazine (**H2-PHTZ**) donors, **H2-PXZ** demonstrates a better balance of small orbital overlap and moderately high oscillator strength to be the best TADF candidate. **H2-PXZ** also shows significant changes in the geometry and dipole moment upon excitation, which confirms a CT character of the compound.

2.3 Conclusions and perspectives

Two new helicene-based D-A-D and D-A compounds demonstrating TADF in the solid state and in solution were prepared. The photophysical study of crystals has demonstrated that for **H1-PXZ** the presence of hexane in a crystal lattice increases the PLQY as well as the intensity of TADF emission. This signifies that both parameters are influenced by packing of the molecules in the lattice rather than by relative position of donor and acceptor moieties in the molecule. Basic theoretical calculations were also performed for **H2-PXZ** and they were in good correlation with the experimental results. As discussed in the introduction to this chapter, the curved structure of helicene can induce spin-orbit coupling (SOC) in these materials. It would be interesting to perform additional theoretical calculations on **H1-** and **H2-PXZ** and their planar analogues such as **P1-PXZ** and **P2-PXZ** (Figure 2.28) to investigate whether the contribution of spin-orbit and spin-vibronic coupling to the rISC process in helicenes is higher compared to planar compounds.

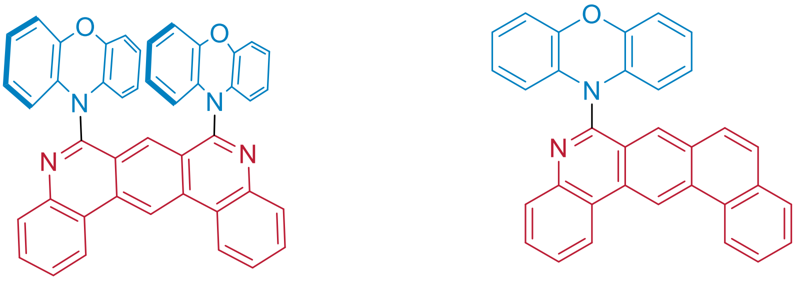

P1-PXZ **P2-PXZ**

Figure 2.28. Molecular structures of some planar analogues of **H1-PXZ** (**P1-PXZ**) and **H2-PXZ** (**P2-PXZ**).

For both **H1-** and **H2-PXZ** there is a strong contribution of the non-radiative processes resulting in a low PLQY of the materials. To avoid this problem, it is possible to design TADF emitters based on higher helicenes, such as hexa- or-heptahelicenes, that have a more rigid structure compared to pentahelicenes (Figure 2.29).

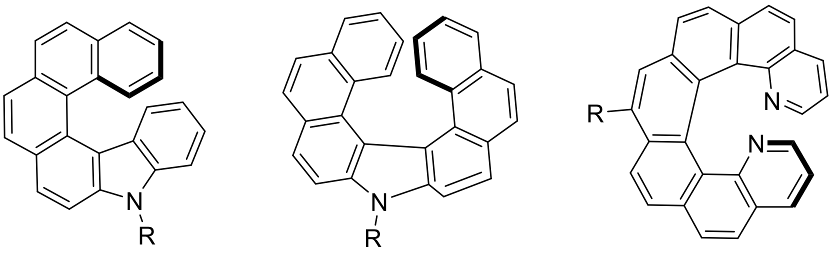

Figure 2.29. Possible molecular structures of higher helicenes than can be used as TADF emitters or chiral dopants for TADF emissive layers in OLEDs.

It was demonstrated in the previous studies that helicene can be used as a chiral dopant for the achiral light-emitting polymer to induce CPL.[218] Thus, the preparation of the enantiopure helicene-based compounds would also be of significant interest for TADF OLEDs with circularly polarised electroluminescence. This is another reason to use higher helicenes in future work instead of pentahelicenes that have a very low racemisation barrier.[210] To prepare helical compounds on a larger scale it is also preferable to modify procedures for use in flow reactors. For the same reasons it would be advantageous to use chiral resolution techniques rather than chiral HPLC to obtain enantiopure compounds. This may include resolution by recrystallisation or the use of chiral resolving agents.

Chapter 3. Multifunctional materials with truxene-benzothiadiazole-truxene core

*Truxene, with its C_3 symmetry, is recognised as a building block for star-shaped structures. Such compounds combine advantages of both polymers and conjugated small molecules making these materials interesting candidates for optoelectronic applications. This chapter describes the synthesis and properties of two novel donor-acceptor compounds **A1** and **A2** containing a benzothiadiazole acceptor moiety connected through two truxene linkers to four donor moieties. Triphenylamine and phenoxazine are donors of choice for **A1** and **A2,** respectively. The electroluminescent properties of the compound **A1** were investigated in OLED devices whilst this compound was also used as a down-converter in hybrid LEDs.*

Part of the bibliographic review presented in the introduction to this chapter was published in the Display and Imaging journal (Orofino, C.; Klimash, A.; Kanibolotsky, A. L.; Skabara, P. J. Synthesis and Analysis of Hyperbranched Oligofluorenes for Optoelectronic Applications. *Display and Imaging* **2017**, *2*, 175–196.)

3.1 Introduction

Conjugated polymers are widely used as semiconductor materials in OPVs, OLEDs and OFETs.[219] They demonstrate good film forming properties and solubility, allowing such materials to be processed using low-cost deposition methods, such as spin-coating,[220] roll-to-roll processing and ink-jet printing[221] for the fabrication of polymer-based devices. In the case of small molecules, more expensive vapour deposition methods are often used. Moreover, the tendency of small molecules to spontaneously crystallise can impair their efficiency in OLED devices, thus materials forming amorphous films, such as polymers, are preferred.[222] However, contrary to small molecules polymers suffer from poor batch-to-batch reproducibility and can be difficult to purify. This can affect the performance of polymer-based devices. To combine advantages of both polymers and small molecules well-defined monodisperse oligomers can be used. Like small molecules, oligomers possess precise HOMO and LUMO energy levels due to high purity, but have desirable characteristics of polymers such as good solubility, high thermal stability and superior film-forming properties.[149] In the simplest case oligomers used in organic electronics are linear (*i.e.* one-dimensional, 1D) π-conjugated systems. The charge mobility in such structures is limited to one dimension which can lead to an anisotropy of electronic properties of materials in the bulk.[223] This problem can be solved by increasing the dimensionality of oligomers into second (2D) and third (3D) dimensions.[149,223] In this case oligomeric arms are attached to the central core. The resulting macromolecules can be called star-shaped oligomers or dendrimers. Among the popular cores used in the design of star-shaped materials for optoelectronic applications are benzene (Figure 3.1-a,b,c),[224] triphenylamine (Figure 3.1-d),[225] sp^3-carbon (Figure 3.1-e),[226] pyrene (Figure 3.1-f)[227] and triazine (Figure 3.1-g).[225]

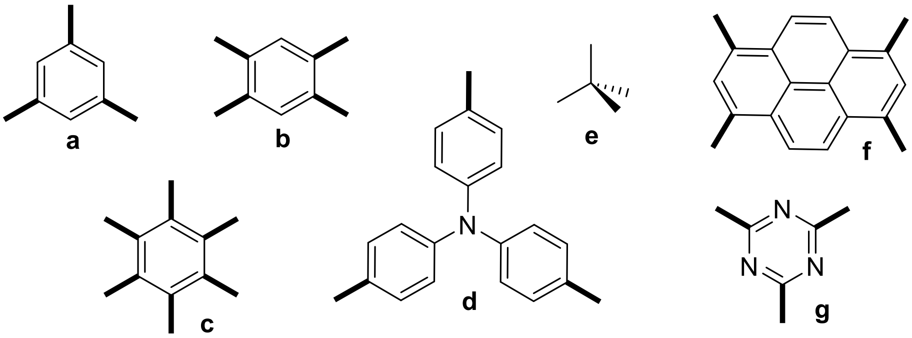

Figure 3.1. Examples of some central units for star-shaped materials.

3.1.1 Star-shaped materials with a truxene core

Truxene (10,15-dihydro-5H-diindeno[1,2-a:1',2'-c]fluorene; Figure 3.2) is another recognised building block for star-shaped systems. It is possible to functionalise the truxene unit at the C-2, C-7 and C-12 positions, as well as at the C-5, C-10 and C-15 positions. These latter three positions, however, are usually derivatised with alkyl chains to provide better solubility of the material by reducing π- π stacking.[149]

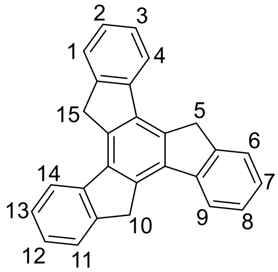

Figure 3.2. Truxene core with the carbon skeleton labelled.

One of the interesting examples of truxene-based dendrimers was presented in the work of Cao *et al.* (Figure 3.3). The dendrimers contained up to nine truxene moieties and were spaced by benzene linkers. The same group later reported star-shaped compounds with a truxene core and hexa-*peri*-hexabenzocoronene arms,[228] as well as giant dendrimers containing up to 22 truxene moieties with no additional spacers.[229]

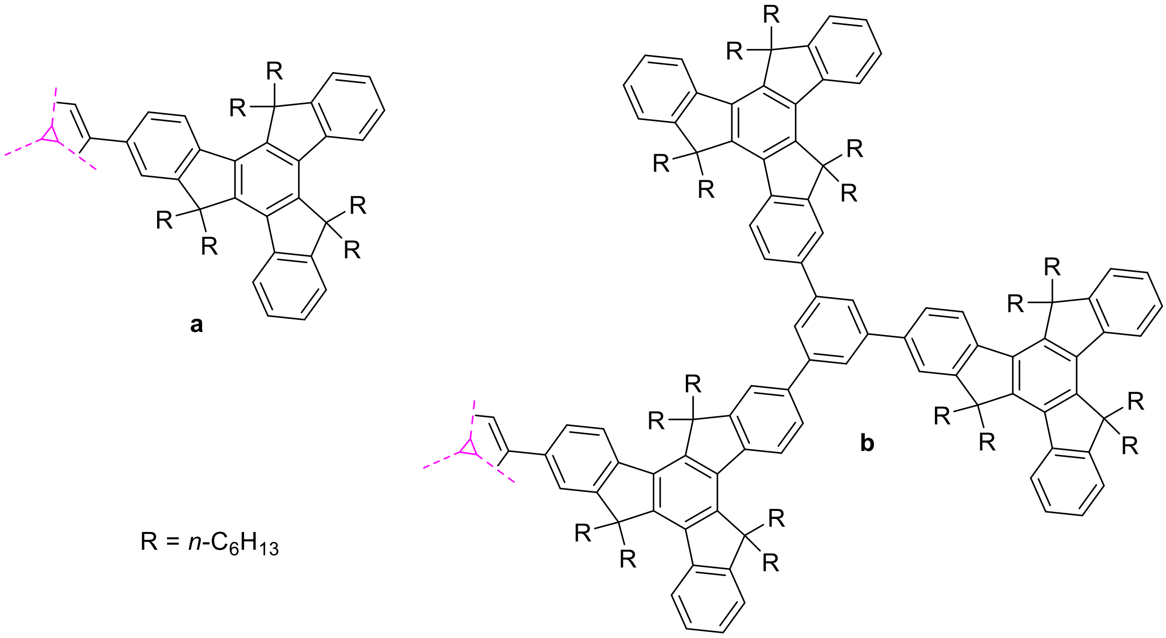

Figure 3.3. Truxene-based dendrimers with phenyl spacers.

Among other reported star-shaped materials with a truxene core are a series with oligothiophene branches (Figure 3.4-a)[230] that were used in OFETs.[231] It was demonstrated that the materials with longer oligothiophene arms had decreased hole mobility due to the lower degree of crystallinity. Other examples include a series of materials with thiophene derivatives arms end-capped with C_{60} groups (Figure 3.4-b) reported by Wang *et al.*[232] The same group has developed star-shaped materials with thiophen-2-yl and 5-(2-(thiophen-2-yl)vinyl)thiophene-2-yl arms ending with a 4-(diphenylamino)styryl donor or 2-(4-cyano-5-(dicyanomethylene)-2,2-dimethyl-2,5-dihydrofuran-3-yl)vinyl acceptor groups (Figure 3.4-c). Both symmetrical donor- or acceptor-only (Figure 3.4-c,d) as well as asymmetrical donor-acceptor (Figure 3.4-e,f) molecules were synthesised.[233] These materials can potentially be applied in OPVs. Recently Wu *et al.* have reported the series of wide bandgap star-shaped acceptors (Figure 3.4-d) where electron-accepting 4-(3-ethylhexyl-4-oxothiazolidine-2-yl)dimalononitrile-benzothiadiazole moiety was attached to truxene core in meta- or para- position.[234] When combined with low-bandgap 3,9-bis(2-methylene-(3-(1,1-dicyanomethylene)-indanone)-5,5,11,11-tetrakis(4-hexylthienyl)-dithieno[2,3-d:2′,3′-d′]-s-indaceno[1,2-b:5,6-b′]-dithiophene (ITIC-Th) acceptor and poly[4,8-bis(5-(2-ethylhexyl)thiophen-2-yl)benzo[1,2-b;4,5-b']dithiophene-2,6-diyl-alt-(4-(2-ethylhexyl)-3-fluorothieno[3,4-b]thiophene-)-2-carboxylate-2-6-diyl)] (PTB7-Th) donor materials in a ternary blend film, both compounds showed high power conversion efficiencies of 10.15% for meta- and 8.28% for para-substituted truxenes in solar cells. A better performance of the meta-substituted compound was attributed to a more compact intermolecular packing and shorter π–π stacking distances in this material. Recently Sharma *et al.* have also reported new AIE materials with tetraphenylethene arms (Figure 3.4-e) that were used for the preparation of fluorescent OLED devices.[235]

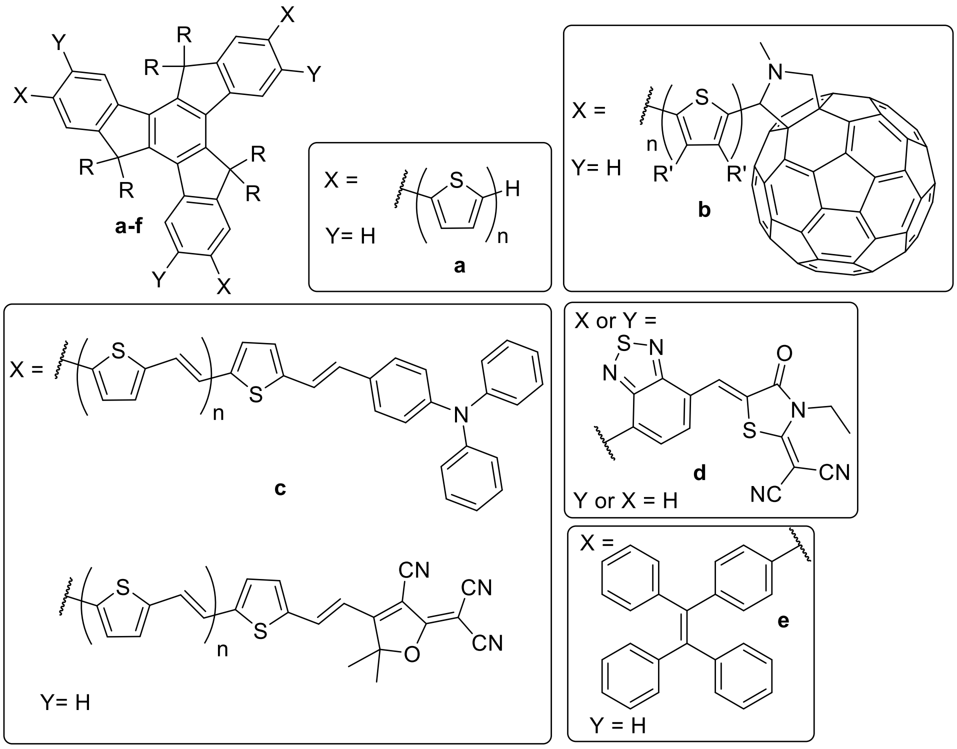

Figure 3.4. Some examples of star-shaped materials with a truxene core.

Truxene can be regarded as three overlapping fluorene moieties, thus it is a natural branching point for oligofluorene systems creating star-shaped oligomers with a virtually no-core moiety. Star-shaped oligomers based on a truxene core functionalised at C-2, C-7 and C-12 positions with oligofluorenes were synthesised by the Skabara group (Figure 3.5).[236,237] All the molecules are blue emitters (λ_{PL} = 400–420 nm). When the length of oligofluorene arms increases from 3 to 6, molecules exhibit increasing two-photon absorption due to the elongated π-conjugation. The oligomer **T6** shows a threshold for two-photon absorption pumped amplified spontaneous emission of 2.43 mJ cm^{-2}, which is the lowest for organic semiconductors. It makes these radial oligofluorene truxenes amongst the most suitable candidates for non-linearly pumped light-emitting materials.[236,237]

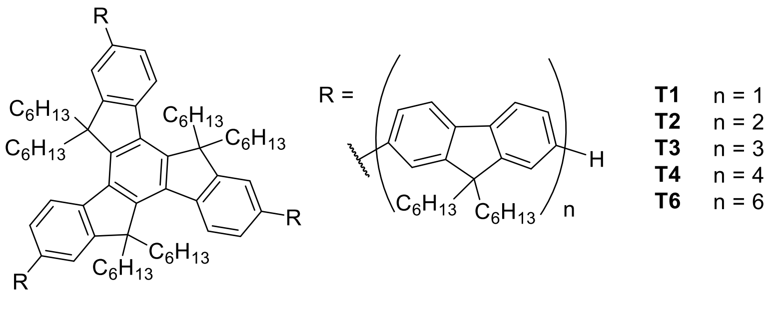

Figure 3.5. Oligofluorene truxene with the arm length rising from one fluorene unit (T1) to six (T6).

Following the study of the aforementioned oligofluorene truxene structures (**T1-T6**), new **T4**-based compounds with the fused bicyclic 2,1,3-benzothiazole molecule inserted sequentially at each of five possible positions were reported (Figure 3.6).[238] The electron-deficient character of the 2,1,3-benzothiadiazole (BT) heterocycle can be used for stabilisation and spatial localisation of the LUMO in conjugated structures and it is widely applied in the design of organic semiconductors.[239]

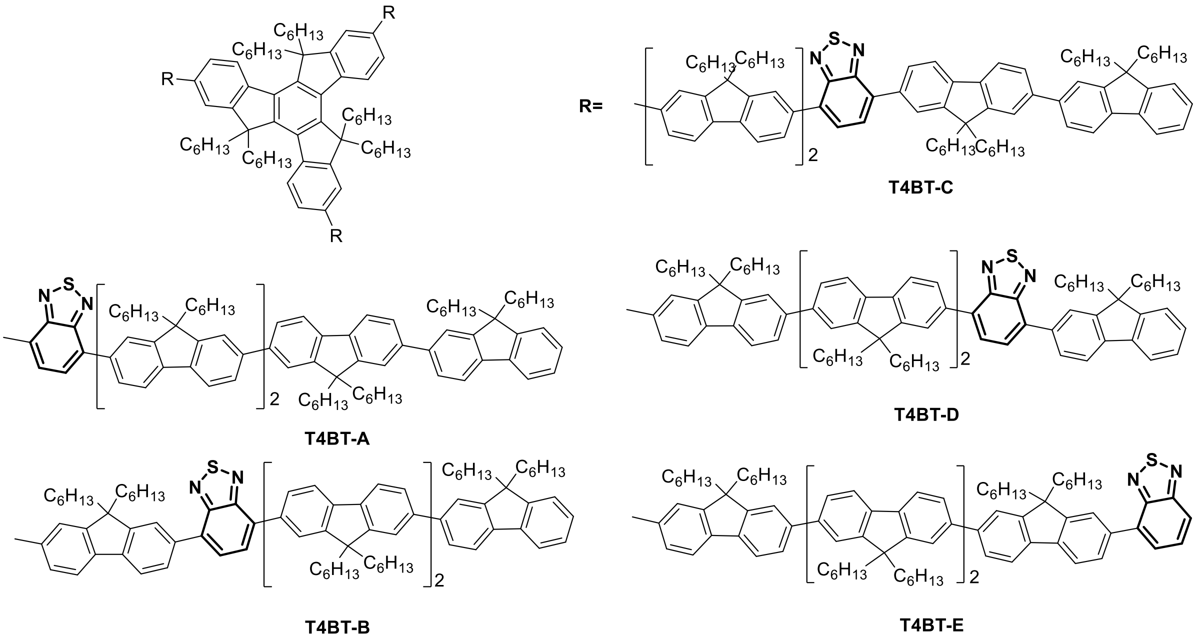

Figure 3.6. Structure of oligofluorene-truxene star-shaped systems containing the 2,1,3-benzothiadiazole unit.

Absorption spectra of **T4BT-A, -B, -C, -D** and **–E** in the solid state show three bands. The first high energy peaks around 220 nm correspond to a localised-localised π-π* transition. For **T4BT-A** and **T4BT-D** second peaks corresponding to a delocalised-delocalised π-π* transition at 362 nm and 370 nm, respectively, are the most intense with a well-defined shoulder at 320 nm. This signifies that the transitions between HOMO and upper delocalised unoccupied orbitals are split into two components. Similarly, transitions for **T4BT-B** and **T4BT-C** show a high intensity peak around 356 nm with an unresolved shoulder around 320 nm. The position of the BT unit in the chain between peripheral 9,9-dihexylfluorene units and 9,9-dihexylfluorene units attached to the core influences the characteristics of the spectra. The absorption spectra of **T4BT-E** where all five 9,9-dihexylfluorene units are involved in transitions show the most red-shifted delocalised-delocalised π-π* transition. All compounds in the **T4BT** series, excluding **T4BT-E**, demonstrate a delocalised-localised transition (from the HOMO delocalised across the oligofluorene arms to the LUMO localised on the BT units), with peaks at 445 nm for **T4BT-A** and **T4BT-D** and 440 nm for **T4BT-B** and **T4BT-C**. This transition with an intramolecular charge transfer (CT) character is not present in the spectrum of **T4BT-E**. TD-DFT calculations for this compound reveal the low oscillator strength for the ICT transition due to a small overlap between the HOMO and LUMO of **T4BT-E**. Photoluminescence spectra show the same kind of correlation. **T4BT-B** and **T4BT-C** exhibit the most red-shifted PL (562 nm), **T4BT-A** and **T4BT-D** show slightly blue-shifted emission (553 nm) and **T4BT-E** has a strongly blue-shifted PL (507 nm). All the compounds of the series are green emitters with good thermal stability, solubility and film-forming properties. The **T4BT-B** molecule has demonstrated efficient electrogenerated chemiluminescence (ECL), which makes the compounds of the series promising candidates for use in highly sensitive ECL sensors.[240,241]

Lai *et al.* have reported a series of starburst oligofluorene truxenes **Tr1-Tr4** with six arms of varied length (Figure 3.7-a).[242] The compounds demonstrate deep-blue emission in solution and solid state (λ_{PL} = 398–441 nm), which is blue-shifted compared to **T1-T4** analogues. This is due to the result of the decreased degree of conjugation caused by steric hindrance between fluorene arms in **Tr1-Tr4**. The PLQY of the materials is in the range of 64–100% in solution and 50–90% in the solid (film) state. **Tr3** was also used in an organic laser device as the gain media demonstrating a low lasing threshold ($E_{th} \approx 0.4$ nJ pulse^{-1}, 1.3 μJ cm^{-2}). Recently Zhang *et al.* reported analogues of compounds **Tr1-Tr4** in which oligofluorene arms are end-capped with a diphenylamine moiety in order to improve charge carrier mobility (Figure 3.7-b).[243] The emission of **Tr1F-Tr3F** is red-shifted compared to the **T** and **Tr** series (λ_{PL} = 435–450 nm), with PLQYs in the range of 56–89% in films and 63–93% in solutions. Compound **Tr3F** demonstrated the best lasing properties out of the series with the lowest amplified spontaneous emission threshold of 1.5 μJ cm^{-2} (27.4 nJ pulse^{-1}).

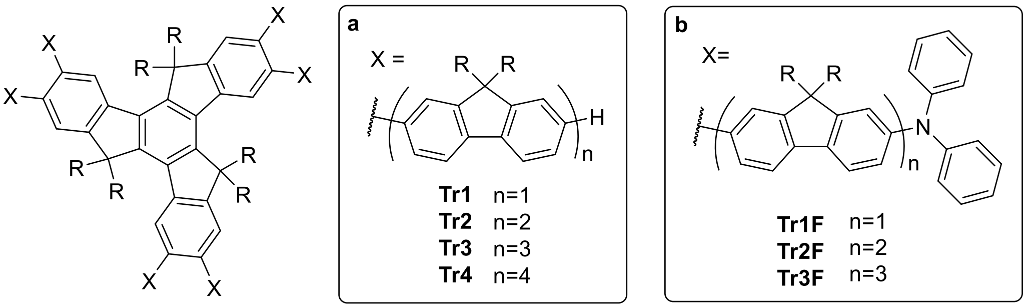

Figure 3.7. Structures of radial truxene-based oligofluorenes with six arms.

Another example of truxene-based dendrimers is represented by dumbbell-shaped molecules where two truxene moieties are used as π-linkers between the central core and four arms.[244,245] The Pei group presented a series of D-π-A dendrimers with benzothiadiazole as an acceptor core and triphenylamine donor end-groups connected to truxene through various conjugated thiophene-based linkers (Figure 3.8). The emission of **SB** and **DB** (614 nm and 628 nm in hexane) is more red-shifted compared to **TB** (592 nm). Also, compound **DB** with a vinylene-containing linker had the highest molar extinction coefficient in the series indicating the longest effective conjugation length.

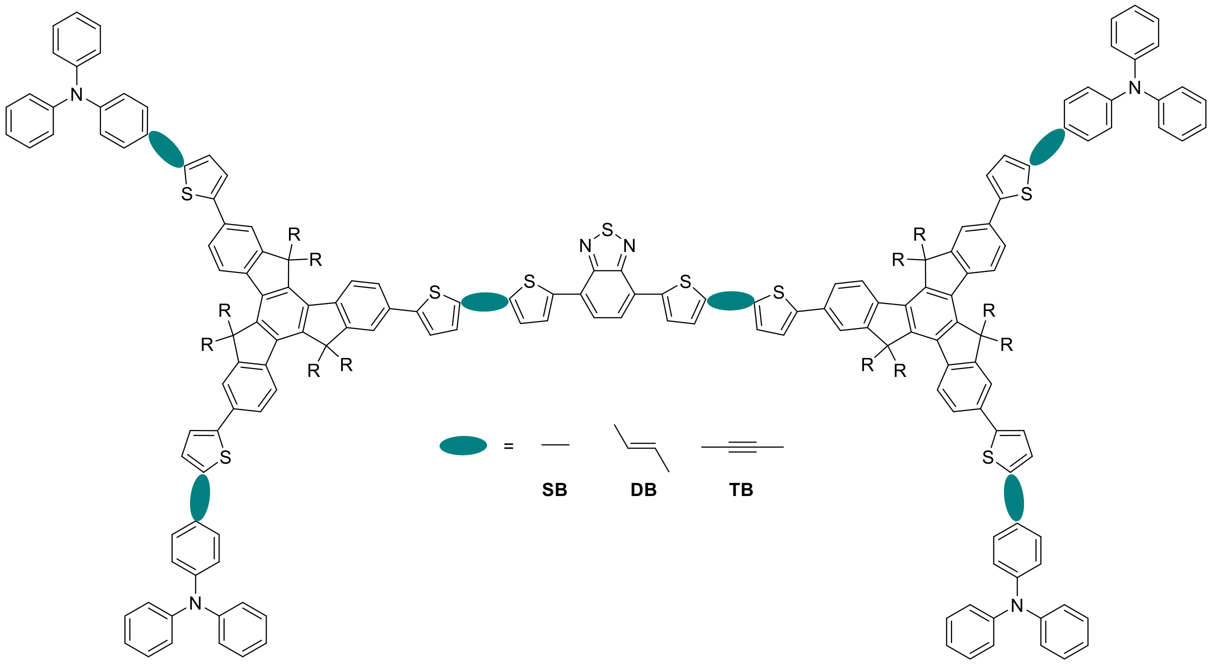

Figure 3.8. Structures of truxene-based dendrimers **SB**, **DB** and **TB**.

The same group reported a series of conjugated molecules **BTTyn** and **BTDyn** with a benzothiadiazole core and truxene arms end-capped with thiophene moieties (Figure 3.9).[246]

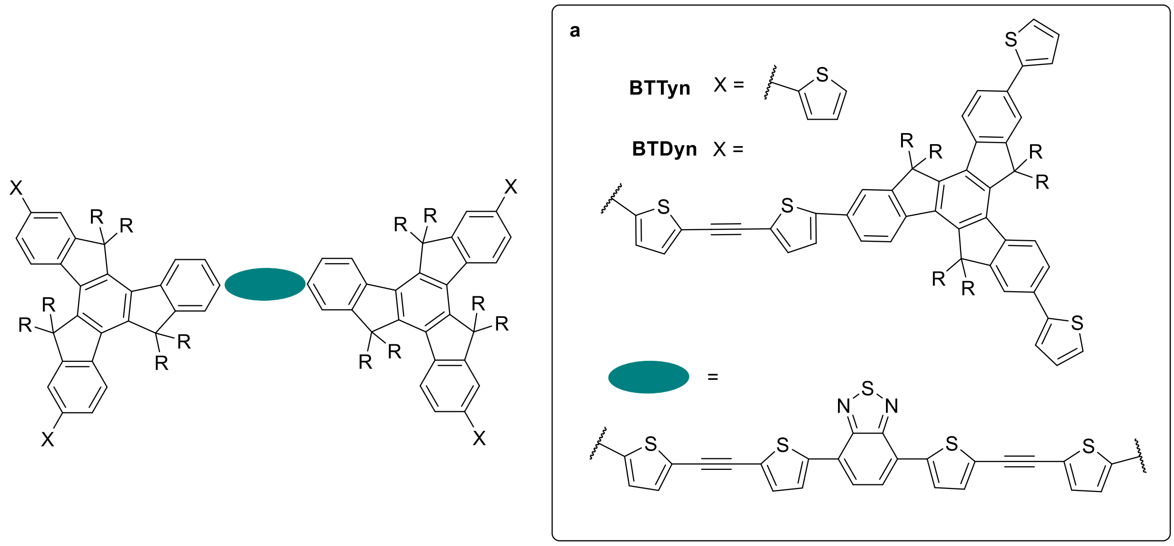

Figure 3.9. Molecular structures of dumbbell-shaped molecules with truxene π-linkers.

Emission spectra of **BTTyn** and **BTDyn** are very similar with the PL maxima around 630 nm in solution, 640 nm in films, and a PLQY of 25% in solution for both compounds. While both dendrimers demonstrate very similar photophysical behaviour their performance in OLED devices differ significantly. The larger molecule **BTDyn** demonstrates one order of magnitude higher maximum luminescence efficiency (1.07 cd/A) compared to **BTTyn** (0.11 cd/A).

In summary, truxene can be used as a central unit for a variety of electroactive materials, and the properties of these materials can be easily tuned depending on the nature of the introduced substituent. The applications of truxene-based materials include, but are not limited to, OLEDs, OPVs and lasers. For example, truxene-based materials were also used as down-converters in hybrid LEDs.

3.1.2 White hybrid LEDs containing down-converting materials

Solid state lighting is a well-established technology with LEDs being used virtually everywhere nowadays from street lighting to displays. There are a few approaches to achieve white LED light. One method is to use a set of three inorganic LEDs emitting red, green and blue (RGB) light.[247] Another way to use additive RGB colour systems is to coat an UV LED chip with red, green and blue phosphors that absorb high energy UV light and re-emit it at longer wavelengths, producing white light.[248] It is also possible to generate white light by combining a blue LED with a yellow phosphor.[249] This last method is advantageous due to its relative simplicity and the high efficiency of the used blue LEDs, and it is widely employed for the fabrication of commercial white LEDs. There are several requirements for the phosphor materials to be efficient in down-converters. The absorption spectrum of a phosphor should have a significant overlap with the emission of the blue LED (around 440-470 nm) in order to achieve an optimised energy transfer; the material needs to demonstrate a high PLQY for the efficient energy conversion, and have good chemical and thermal stability.[250] The same principle can be applied for the fabrication of hybrid organic/inorganic LEDs where an organic fluorescent material is used as a down-converter instead of a phosphor.[251] Employing organic compounds can reduce the use of materials containing rare-earth elements and provide a better tunability of the emitted light. Furthermore, because the excited states in fluorescent materials have a much shorter lifetime compared to those in phosphors, hybrid LEDs can be applied in visible light communication providing much higher data transmission speeds compared to conventional white LEDs.[252]

While the first hybrid LEDs used polymers for colour conversion,[253] the use of well-defined small molecules would be advantageous in this case for the reasons explained above. For example, Findlay *et al.* reported the down-converting small molecule material **(BODFluTh)$_2$FB** (Figure 3.10).[254] The photophysical properties of the compound were investigated in solution and in solid state (encapsulated in a 1,4-cyclohexanedimethanol divinyl ether (CHDV) matrix). Absorption spectra are very similar in both solution and solid state with two peaks around 403 nm and 526 nm. The emission is slightly red-shifted in CHDV (565 nm compared to 550 nm in solution). The material also demonstrates a high PLQY of 60% in solution and 63% when encapsulated. Its colour converting properties were investigated by depositing the material in a CHDV matrix on a blue LED. The encapsulation of materials provides a better film morphology, reduces the amount of the material used in the device and helps to suppress the aggregation of the molecules in the solid state. The resulting hybrid device demonstrated two emission peaks: one in a blue region characteristic of the inorganic blue LED and an additional yellow emission originating from the organic layer. The chromaticity coordinates for the bare blue LED were (0.16, 0.02) while for the hybrid device, the coordinates were (0.34, 0.31) which is closer to the Planckian locus. The correlated colour temperature (CCT) was calculated to be 5137 K, which is perceived as a cool white light. In the next study the influence of **(BODFluTh)$_2$FB** concentration on the colour and the conversion efficiency of the resulting white LED was investigated.[255] The material was used in various concentrations ranging from 0.25% to 4% (w/v) in the CHDV matrix. With increased concentration more blue light is absorbed and thus the intensity of the blue emission peak decreases. At the same time the intensity of yellow emission from the organic colour converter decreases at higher concentrations, which can be due to the aggregation of the molecules that in turn causes emission quenching. The parameters of the optimum LED (1%(w/v) of down-converter in 1 μL of the matrix), were remeasured after 15 months in order to study the stability of the device. The decreased intensity of the yellow peak indicates the degradation of the organic material.

The presence of the absorption band in a green region for **(BODFluTh)$_2$FB** caused self-absorption in the molecule, thus reducing the luminous efficacy. To tackle this problem another series of organic down-converting materials with benzothiadiazole (**(TPA-Flu)$_2$BT**) or bisbenzothiadiazole (**(TPA-Flu)$_2$BTBT**) core and fluorene arms end-capped with triphenylamine moieties was synthesised (Figure 3.10).[256] Both compounds demonstrate two absorption peaks that are blue-shifted compared to **(BODFluTh)$_2$FB** (345 nm and 430 nm for **(TPA-Flu)$_2$BT**, and 343 nm and 443 nm for **(TPA-Flu)$_2$BTBT**). This shift provides a better overlap of the absorption peak of the organic material with the emission from the blue LED. Both materials also exhibit larger Stokes shifts with emission at 570 nm for **(TPA-Flu)$_2$BT** (PLQY = 61%) and 584 nm for **(TPA-Flu)$_2$BTBT** (PLQY = 17%). Both materials have higher intensity emission in the green region when compared to **(BODFluTh)$_2$FB** and therefore demonstrate good colour rendering index (CRI) values (60 < CRI < 70).

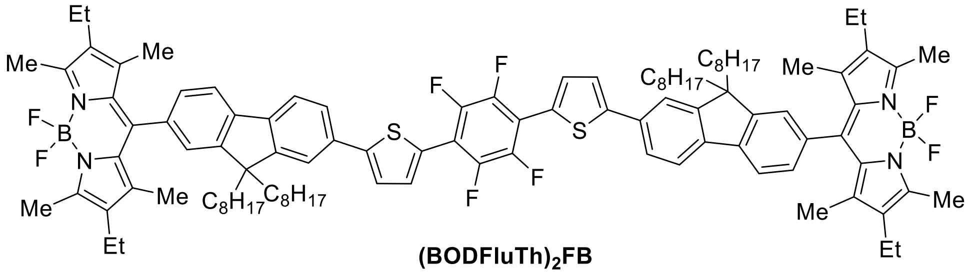

(BODFluTh)$_2$FB

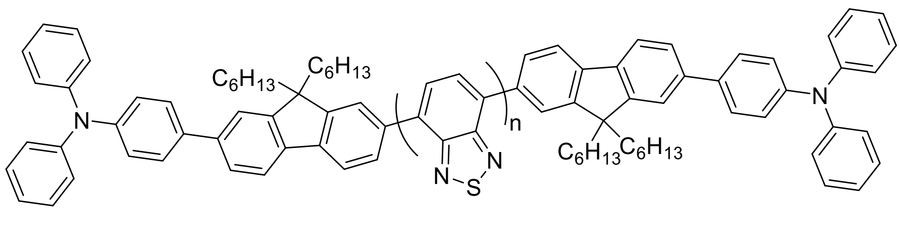

(TPAFlu)$_2$BT n=1
(TPAFlu)$_2$BTBT n=2

Figure 3.10. Examples of molecular structures for small molecule organic down-converters.[254,256]

3.2 Results and discussion

As was previously discussed in Chapter 1, one of the ways of achieving a small S_1-T_1 gap and, thus, TADF properties in molecules, is to spatially separate the HOMO and LUMO. It can be done by creating D-A structures with a π-linker between donor and acceptor units and the use of sterically encumbered substituents. The truxene core presents an opportunity for such separation due to the absence of conjugation between its three arms. In structure **A-n,** the benzothiadiazole core is linked *via* two truxene units to four donor moieties (Scheme 3.1). Compounds **A-n** can be prepared from compound **A** *via* Suzuki C-C or Buchwald-Hartwig C-N coupling. Compound **A** was prepared by Suzuki coupling of compound **4** with 4,7-bis(4,4,5,5-tetramethyl-1,3,2-dioxaborolan-2-yl)benzo[c][1,2,5]thiadiazole.

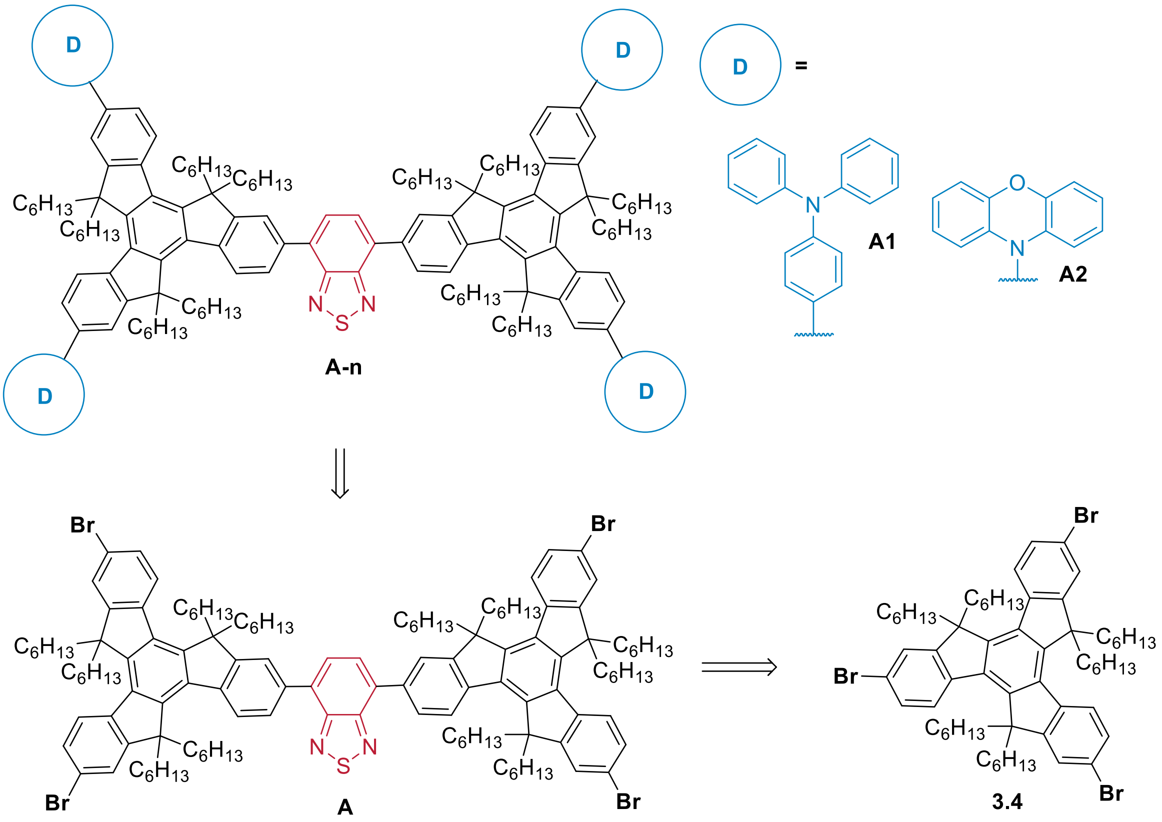

Scheme 3.1. Retrosynthetic strategy for the preparation of the **A-n** series of molecules.

3.2.1 Synthesis and properties of new truxene-based materials

Tribromo-hexahexyltruxene **3.4** was prepared according to the well-established procedure (Scheme 3.2).[236] Truxene **3.2** was synthesised from indanone **3.1** and then alkylated to form hexahexyltruxene **3.3.** Compound **3.4** was prepared *via* halogenation with Br_2.

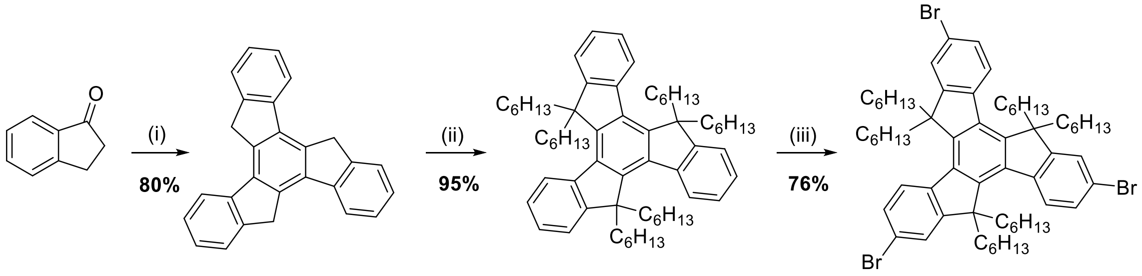

3.1 **3.2** **3.3** **3.4**

Scheme 3.2. Synthesis of tribromo-hexahexyltruxene. Reagents and conditions: (i) CH_3COOH, HCl, 100 °C, 16 h; (ii) (1) *n*-BuLi, THF, 5°C, (2) *n*-$C_6H_{13}Br$, 5°C, 8h; (iii) Br_2, CH_2Cl_2, RT, 14 h.

Compound **A** was synthesised *via* Suzuki-Miyaura coupling between bromide **3.4** and 2,1,3-benzothiadiazole-4,7-bis(boronic acid pinacol ester) **3.5** (Scheme 3.3).[238] Truxene derivative **3.4** was used in large excess (7:1 ratio of **3.4** to **3.5** was found to be an optimal, Table 2) in order to minimise side polymerisation reactions and achieve higher selectivity. For the same reasons, the base used for coupling is the relatively weak K_2CO_3. Use of a stronger base, such as $Ba(OH)_2·8H_2O$, resulted in a lower yield (Table 2, entry 4). However, the best yield for the reaction is still as low as 18 %.

3.5

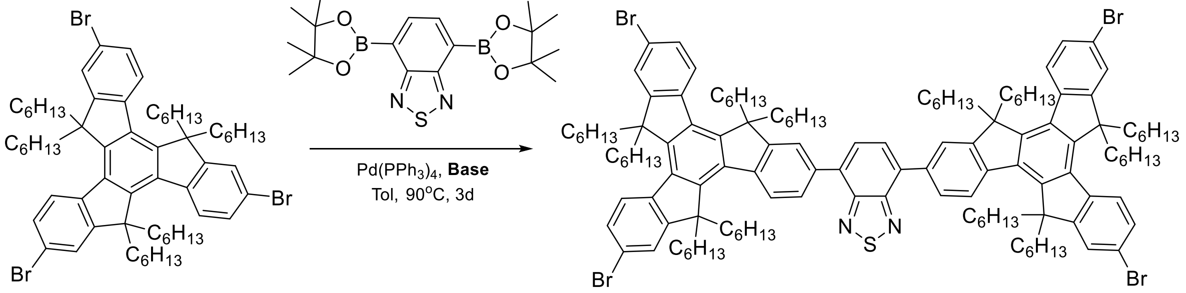

3.4 **A**

Scheme 3.3. Synthesis of molecule **A.**

Table 3.1 Attempted syntheses of **A.**

Entry	**Base**	**(3.4):(3.5) ratio**	**Yield,%**	**Comments**
1	K_2CO_3	7:1	9	Product easily separated by column chromatography, but a lot of additional side products are formed, starting material can be separated and recycled.
2		12:1	7	
3		3:1	6	
4	$Ba(OH)_2\cdot 8H_2O$	7:1	5	The lowest yield
5	K_2CO_3	7:1	18	Reaction performed on a large scale. The highest yield.

In order to avoid selectivity problems during the coupling, the synthetic route was modified, firstly by preparing monohalogenated hexahexyl truxene **3.6** from **3.4** and preparing compound **A0** *via* Suzuki coupling. This could possibly then be brominated to form compound **A** (Scheme 3.4).

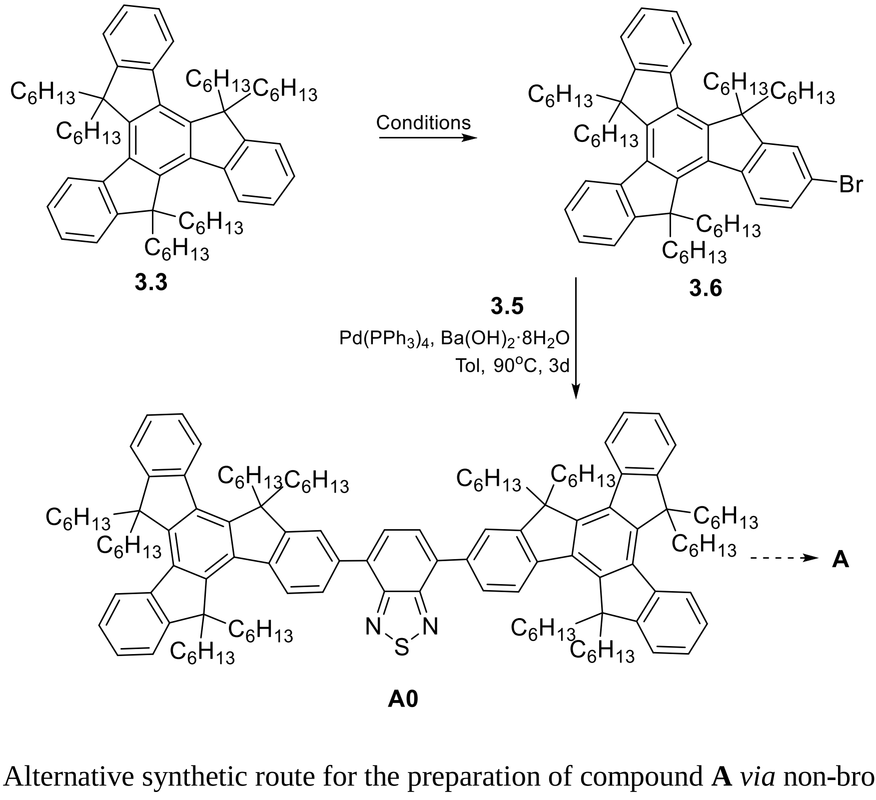

Scheme 3.4. Alternative synthetic route for the preparation of compound **A** *via* non-brominated intermediate **A0.**

N-Bromosuccinimide was used as the halogenating agent for the preparation of compound **3.6.** Different solvents were screened for the reaction including 1,2-propanediol carbonate, dichloromethane and dimethyl formamide (DMF) (Table 3.2). Only reaction in acetic acid, with heating, gave monobrominated product (Table 3.2, entry 5) which is probably due to a more efficient heterolysis of NBS in a polar acidic environment.[257]

Table 3.2. Attempted syntheses of monobrominated compound **3.6**.

Entry	Conditions	Yield (%)	Comments
1	NBS , 1,2-propanediol carbonate, 60°C, 2 h	-	No product
2	NBS, CH_2Cl_2, RT, 18 h	-	No product
3	NBS, CH_2Cl_2/CH_3COOH(1:1), RT, 18 h	-	No product
4	NBS, DMF, RT, 72 h	-	No product
5	NBS; CH_3COOH, 80°C, 72 h	57	Mixture of starting material with monobrominated product and traces of dibrominated truxene

Separation of product **3.6** from the starting material and dibrominated hexahexyltruxene turned out to be a challenging procedure, as compound **3.6** was inseparable from the by-products on silica gel. Recrystallisation in ethanol and methanol also failed to provide sufficiently pure compound. Additionally, preparative gel permeation chromatography (GPC) was unsuccessful in separating mono- and dibrominated products; ^{1}H NMR analysis of all collected fractions did not show any significant change in the ratio of compounds in the mixture. As MALDI and ^{1}H NMR (for entry 6, Table 3.2) analysis confirmed that monohalogenated product (**3.6**) was the major compound (ratio of mono- to dibrominated compound was 9:1), the mixture was used without additional purification for the preparation of compound **A0**.

As selectivity in the reaction of monobrominated truxene **3.6** is not the main concern anymore, the procedure for Suzuki coupling to form compound **A0** was slightly modified; $Ba(OH)_2{\cdot}8H_2O$ was used as a base and the relative amount of truxene derivative **3.6** to boronic ester **3.5** was decreased (Table 3.3). On a small scale the compound **A0** was synthesised with significantly higher yield (Table 3.3, entry 1), but on a large scale (Table 3.3, entry 2) the yield is similar to that of **A** (Table 3.3, entry 2). The necessity of the additional step makes this synthetic route (Scheme 3.4) even less efficient than the initial one (Scheme 3.3).

Table 3.3 Attempted syntheses of compound **A0**.

Entry	(3.6):(3.5) ratio	Yield (%)	Comments
1	4:1	42	Small scale synthesis. Side products formed. Formation of **A0** is confirmed by MALDI-MS
2	4:1	10	Large scale synthesis. Standard separation procedure, low yield

In order to improve the efficiency of the reaction, another strategy to increase the yield of the core **A** was attempted. Two main problems when synthesising the core **A** from the tribrominated truxene derivatives are a side polymerisation reaction and the low reactivity of the boronic ester in the Suzuki-Miyaura coupling when it is situated on the electron accepting unit. One way to increase the reactivity is to prepare the boronic acid derivative of truxene and use 4,7-dibromobenzo[c][1,2,5]thiadiazole **3.8** for the coupling (Scheme 3.5). In order to avoid a side polymerisation reaction the number of the reactive sites on truxene can be reduced to one with two others being protected by trimethylsilyl (TMS) groups (Scheme 3.5, compound **3.7**). Compound **3.9** can then be prepared *via* Suzuki-Miyaura coupling, and then converted into the desired product **A**. The synthesis of compound **3.7** was attempted by a visiting Masters student, Manon Bousquet. The synthesis was performed in two steps following the procedure for the preparation of 9,9-dihexyl-7-trimethylsilylfluoren-2-ylboronic acid described by Belton *et al.*[238] Firstly, two out of three bromine atoms were substituted with lithium by adding 2 equivalents of *n*-BuLi, with subsequent introduction of TMS groups by adding trimethylsilyl chloride to the reaction mixture. Next, lithium-halogen exchange was performed on the remaining bromine atom, followed by the addition of the triisopropyl borate. After the work-up the NMR of the crude mixture indicated that the majority product formed was the trisilylated side product.

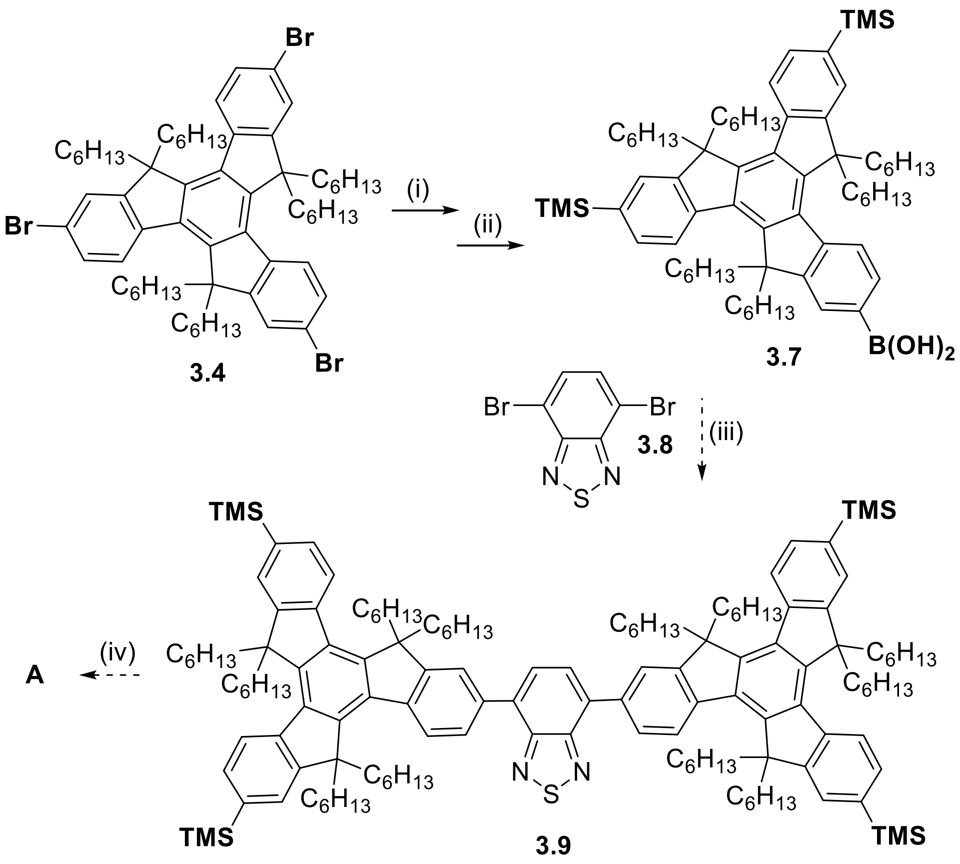

Scheme 3.5. Alternative synthetic route for the preparation of **A** via the boronic acid derivative **3.7**. Reagents and conditions: (i) (1) *n*-BuLi (2 eq.), -85°C, THF; (2) TMSCl (2 eq.), -100°C, RT, 1 h; (ii) (1) *n*-BuLi (1.2 eq.), -85°C, THF (2) (i-PrO)$_3$B (3 eq.), -100°C, RT, 12 h; (iii) Pd(PPh$_3$)$_4$, Ba(OH)$_2$·8H$_2$O, THF, 85°C, 12 h; (iv) Br$_2$, CH$_3$COONa, THF, 0 °C, 30 min.

Due to the low yields of the intermediate in the first attempted alternative synthesis (Scheme 3.4) and unsuccessful second attempt (Scheme 3.5), the initial synthetic route (Scheme 3.3) was used for the preparation of compound **A**.

The first target **A1** was synthesised *via* Suzuki coupling of **A** with (4-(diphenylamino)phenyl)boronic acid **3.10**. The first attempt (Table 3.4, entry 3) was unsuccessful. Side products, where cross-coupling had occurred at fewer than four sites, were isolated by column chromatography whilst the target compound **A1** was obtained with a 3% yield. After increasing amounts of boronic acid **3.10** and Ba(OH)$_2$·8H$_2$O and scaling up the reaction, product **A1** was prepared with a much higher yield of 61%.

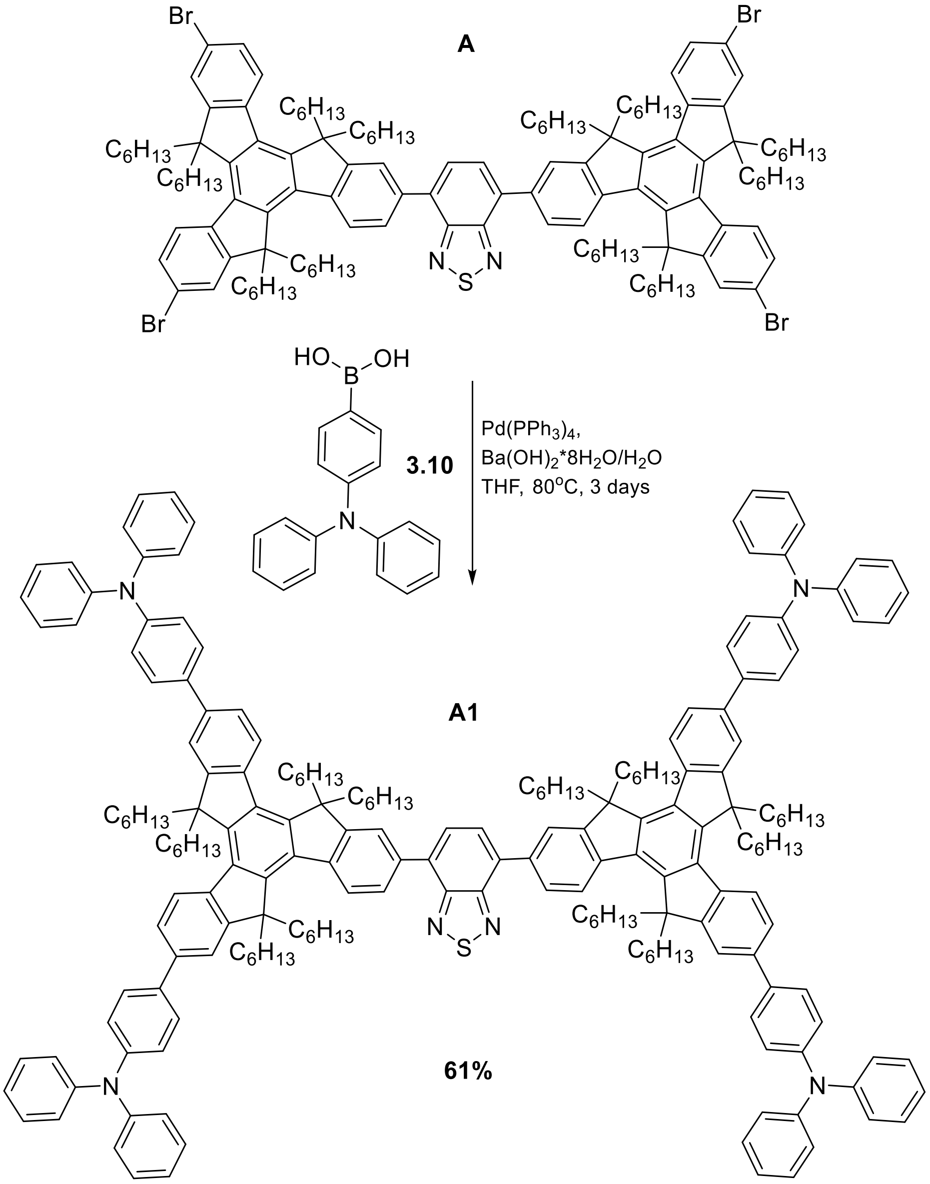

Scheme 3.6. Synthesis of the molecule **A1.**

Table 3.4. Attempted syntheses of **A1**.

Entry	A:(3.7):Base ratio	Yield (%)	Comments
1	1:10:5	3	8 different fractions were collected. MALDI shows the presence of mono- di- and tris- coupled intermediate products. The last fraction contains product **A1**
2	1:15:25	51	Small scale reaction. Reduction in quantity of side products. Product easily purified by chromatography. Molecular mass confirmed by MALDI analysis.
3	1:15:25	61	Large scale reaction

Target **A2** can be prepared *via* C-N coupling. Buchwald-Hartwig methodology was considered as the strategy of choice. A standard procedure employing palladium (II) acetate with tri-*tert*-butylphosphine as a ligand and potassium *tert*-butoxide as a base was used for the coupling between phenoxazine (PXZ) and compound **A,** giving the product **A2** with a yield of 76% (Scheme 3.7).

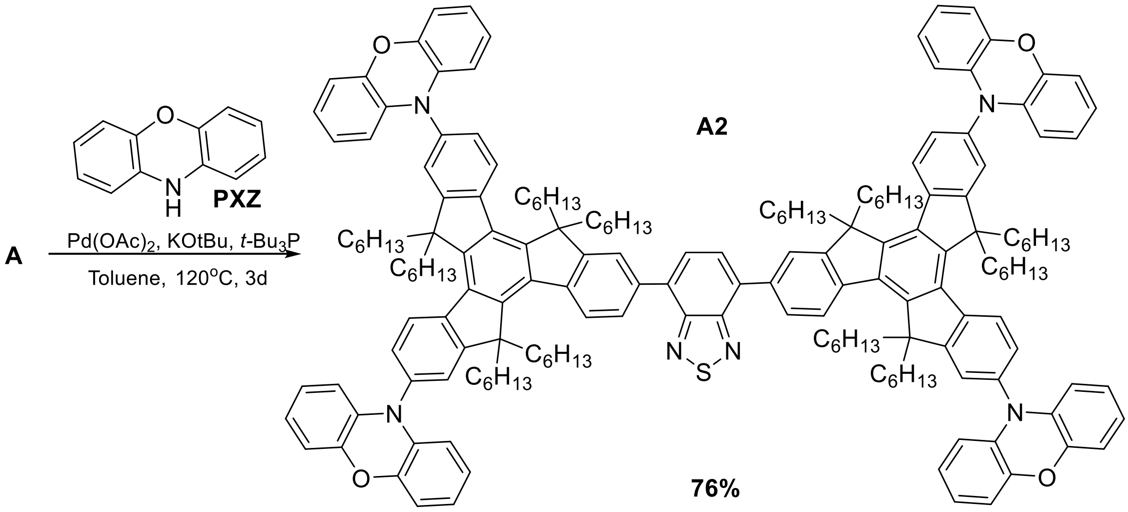

Scheme 3.7. Synthesis of compound **A2**.

3.2.2 Physical properties of **A**, **A0**, **A1** and **A2**

Electrochemical and photophysical measurements were performed for compounds **A0, A**, **A1** and **A2** (Figure 3.11).

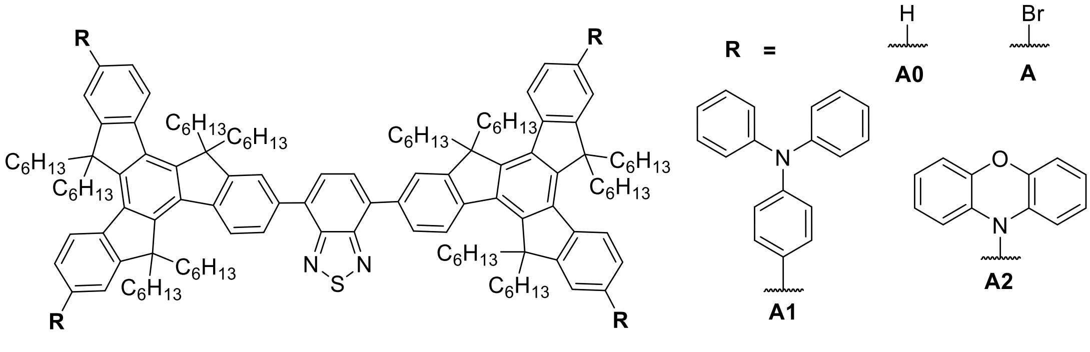

Figure 3.11. Molecular structures of the materials from the **A-n** series.

Absorption and emission spectra were measured in both solution (toluene and tetrahydrofuran (THF)) and solid state, including neat film and in a CHDV matrix (Figure 3.12). Additionally, the emission and photoluminescence quantum yield (PLQY) were measured in powder samples (Table 3.6 and Table 3.8, respectively). All materials demonstrate two main absorption bands, the most intense peak corresponding to a local π–π* transition at a shorter wavelength, and a weaker band associated with intramolecular charge transfer at a longer wavelength. Compounds **A** and **A2** demonstrate very similar absorption spectra in toluene with an intense band around 315 nm and a weaker band around 425 nm. The latter band is slightly red-shifted in THF and film and corresponds to a charge transfer process. Absorption spectra of **A0** and **A1** also reveal two bands. For **A0** the more intense band is blue-shifted compared to other compounds and is at 308 nm with the second band situated around 330 nm. **A1** differs from the other three compounds by a widened and significantly red-shifted first absorption band at around 355 nm with the CT band at around 426 nm. This difference can be explained by the extension of π-conjugation to the phenyl ring of the triphenyl amine moiety in **A1**. The similarity of the absorption spectra for all compounds except **A1** indicates that the absorption is mainly influenced by the truxene-benzothiadiazole-truxene core, and that the ICT transition occurs between occupied orbitals of truxene moieties and unoccupied orbitals of the BT unit. In the CHDV matrix all compounds demonstrated a red shift (≈20 nm) of the absorption band corresponding to a local π–π* transition with no significant changes of the CT band.

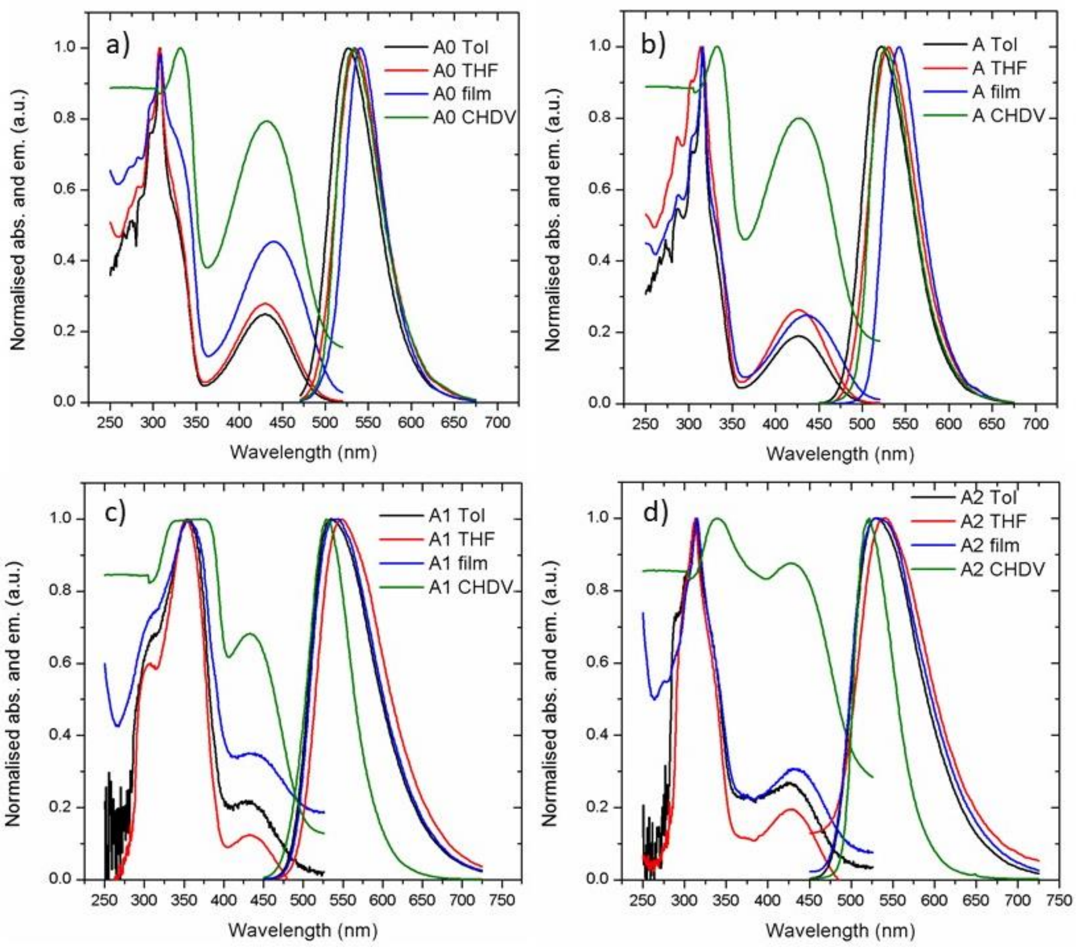

Figure 3.12. UV-vis absorption (left axis) and emission (right axis) spectra of **A0** (a)**, A** (b)**, A1** (c) and **A2** (d) in toluene, THF, neat film and CHDV matrix.

Table 3.5. Absorption maxima for **A0, A, A1** and **A2** in solution, neat film and CHDV matrix.

	λ_{abs} (Toluene) nm	**λ_{abs} (THF) nm**	**λ_{abs} (film) nm**	**λ_{abs} (CHDV) nm**
A0	308, 430	307, 430	308, 440	332, 432
A	315, 426	313, 426	316, 435	332, 427
A1	355, 427	351, 431	356, 427	374, 432
A2	315, 423	312, 430	315, 435	339, 428

Photoluminescence spectra were recorded with excitation of the molecules at the wavelength of the most intense absorption band. All compounds are green emitters with emission peaks at around 530 nm (Table 3.6). Compounds **A** and **A0** show a small red shift in polar solvent and in film state. For **A1** and **A2** the red-shift of the emission is larger in THF solution than in films when both are compared to toluene solution. In the CHDV matrix all compounds demonstrate blue-shifted emission when compared to neat films. Also, for **A1** and **A2** the narrowing of the emission peak is observed in the CHDV matrix, which is probably due to a partial suppression of the molecular vibrations in the matrix. The emission in powder form is red-shifted (≈10 nm) compared to films of **A0**, **A1** and **A2,** whilst it is almost identical for **A**.

Table 3.6. Emission maxima for **A0, A, A1** and **A2** in solution, neat film, CHDV matrix and powder.

	λ_{PL} (Toluene) nm	**λ_{PL} (THF) nm**	**λ_{PL} (film) nm**	**λ_{PL} (CHDV) nm**	**λ_{PL} (powder) nm**
A0	527	535	541	533	550
A	523	530	543	526	540
A1	535	549	544	529	557
A2	529	541	531	522	552

Table 3.7. PLQY (%) of **A, A0, A1** and **A2** in solution and solid state. Measured when excited at a longer absorption wavelength of the materials.

	Toluene	**THF**	**Neat Film**	**CHDV matrix**	**Powder**
A0	22	34	58	62	87
A	22	31	58	68	82
A1	38	27	39	70	65
A2	38	<1	10	48	20

Despite the similarity of absorption and emission spectra for all four molecules, there is a significant difference in the PLQY between **A2** and the rest of the compounds (Table 3.7). While **A0, A** and **A1** show moderate PLQY in the range of 22-38% in both toluene and THF, for **A2** fluorescence is practically quenched in more polar THF. Compounds **A0** and **A** exhibit high PLQY values of 58% in neat films and even higher PLQY of 62% and 68% in a CHDV matrix. Interestingly, the highest PLQY for these materials is observed in powder form (87% for **A1** and 82% for **A2**). Material **A1** has demonstrated the highest PLQY of 70% when encapsulated in a CHDV matrix, and the emission is partially quenched in a neat film (39%). For **A2** the PLQY is almost five times lower in a neat film compared to the CHDV matrix (10% and 48% respectively). The quenching of **A2** emission in a more polar THF can indicate a stronger CT character in a molecule compared to the other three compounds. Luminescence quenching observed in a neat film of **A2** material signifies that intermolecular interactions arising in the solid suppress the radiative decay. The emission of **A2** in powder form (20%) is also much lower compared to **A1** (65%) as well as **A0** and **A**. To conclude, for the materials **A0**, **A** and **A1** the non-radiative decay is suppressed in the solid state, thus they exhibit aggregation-enhanced emission. Contrary to this **A2** exhibits a prominent quenching of the emission in the neat film and powder even though the extinction coefficient is the highest for this material (Table 3.8). This is probably due to a formation of non-emissive aggregates possibly arising from the π-π interactions between phenoxazine units for **A2** in the solid state.

Table 3.8. Molar extinction coefficient **ε** for **A**, **A0**, **A1** and **A2** in toluene, calculated for the two absorption maxima.

	A0	**A**	**A1**	**A2**
ε_1 (λ, nm)	118 804 (308)	151 370 (315)	155 736 (355)	159 546 (315)
ε_2 (λ, nm)	29 838 (430)	28 884 (426)	28 366 (427)	36 504 (423)

The lifetimes of the excited states of the materials **A1** and **A2** were evaluated using the time-correlated single-photon counting method (TCSPC). The measurements were performed by Dr Dmytro Volyniuk at Kaunas University of Technology.

In TCSPC the sample is excited with a pulse of light and the detection of the emitted light occurs at a very low rate so that less than one photon is detected per pulse. A large number of excitation-relaxation events is recorded together with the time between the excitation pulse and the detection of the photon emitted by the material. The measurements can be represented as a histogram with the *x*-axis corresponding to a time difference and the *y*-axis representing the number of detected photons with a given time interval.[52]

Figures 3.13 and 3.14 show the photoluminescence decay curves recorded for **A1** and **A2**. There are three curves in each graph including measured decay, instrument response and fit. The fitted function is a result of a convolution of the instrument response with the measured decay data. In solution, fluorescence decay profiles are mono-exponential for both **A1** (Figure 3.13-a) and **A2** (Figure 3.14-a), and the materials demonstrate short fluorescence lifetimes of around 3.6 ns. Thus, no delayed fluorescence is observed for the solutions. In films, both **A1** and **A2** demonstrate multi-exponential decay. The lifetimes of the excited states are longer in films, but they still remain within the range of prompt fluorescence. Short-lived fluorescence is predominant for **A1** with average decay times being 0.89 ns (15%), 4.18 ns (65%) and 12.5 ns (20%). The behaviour of **A2** is more complex in films with four decay times having almost identical rate: 0.27 ns (20%), 1.69 ns (29%), 7.97 ns (26%) and 28.8 ns (25%). This is most likely the result of intermolecular interactions arising in the film state that are leading to a formation of different excited species, such as excimers. This is in good agreement with the results of the PLQY measurements discussed above.

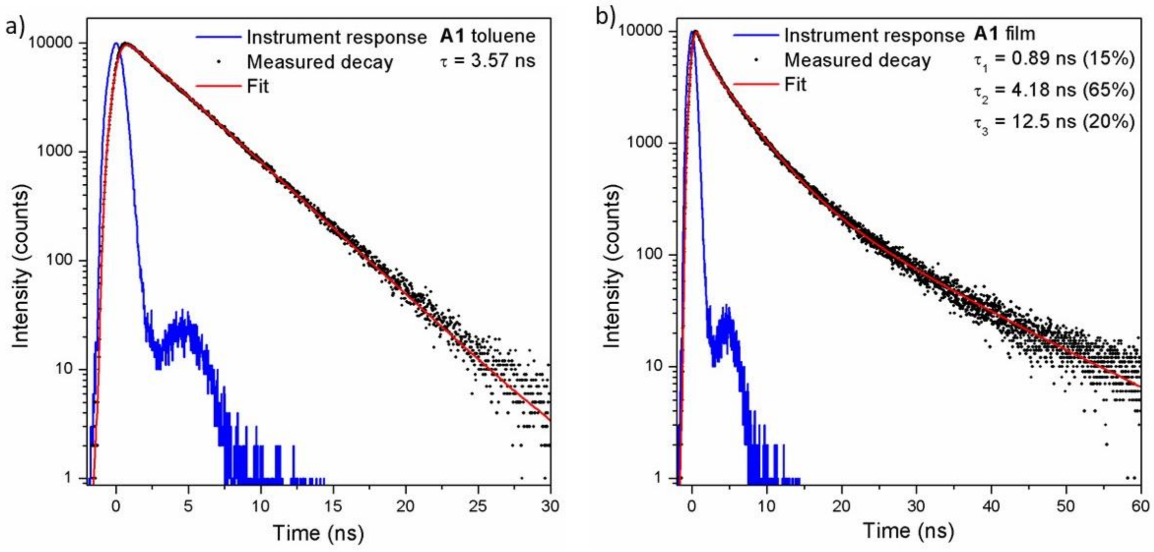

Figure 3.13. Time-correlated single-photon counting fluorescence decay profiles and fitted functions for **A1** in $2\cdot10^{-4}$ M toluene solution (a) and film (b). Excitation wavelength $\lambda_{exc} = 350$ nm.

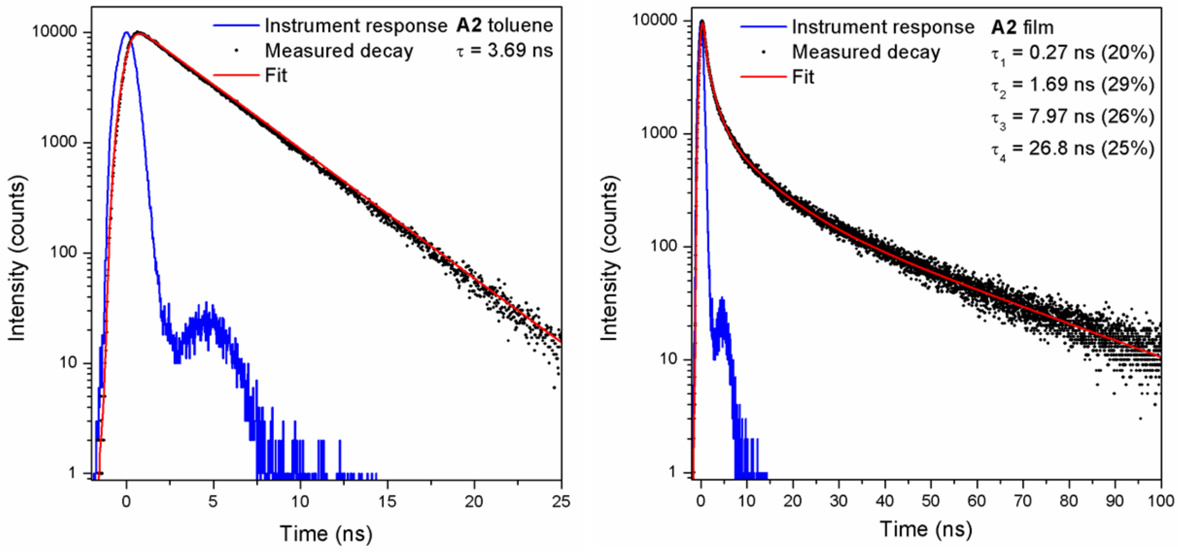

Figure 3.14. Time-correlated single-photon counting fluorescence decay profiles and fitted functions for **A2** in $2\cdot10^{-4}$ M toluene solution (a) and film (b). Excitation wavelength $\lambda_{exc} = 315$ nm.

The electrochemical properties of **A1** and **A2** were studied by cyclic voltammetry. The experiments were performed using $\approx5\cdot10^{-4}$ M concentrations of both compounds in a 0.1 M solution of tetrabutylammonium hexafluorophosphate in the 1 : 2 acetonitrile : toluene mixture. Acetonitrile has a relatively low reduction potential, and toluene enhances the solubility of molecules. The oxidation of compound **A0** shows two irreversible waves (Figure 3.15). The reduction demonstrates two sets of quasi-reversible waves, each followed by one irreversible wave; it also shows an additional quasi-reversible wave at a higher negative potential. The HOMO and LUMO energies were calculated for material **A0** and were found to be -5.67 and -2.87 eV respectively.

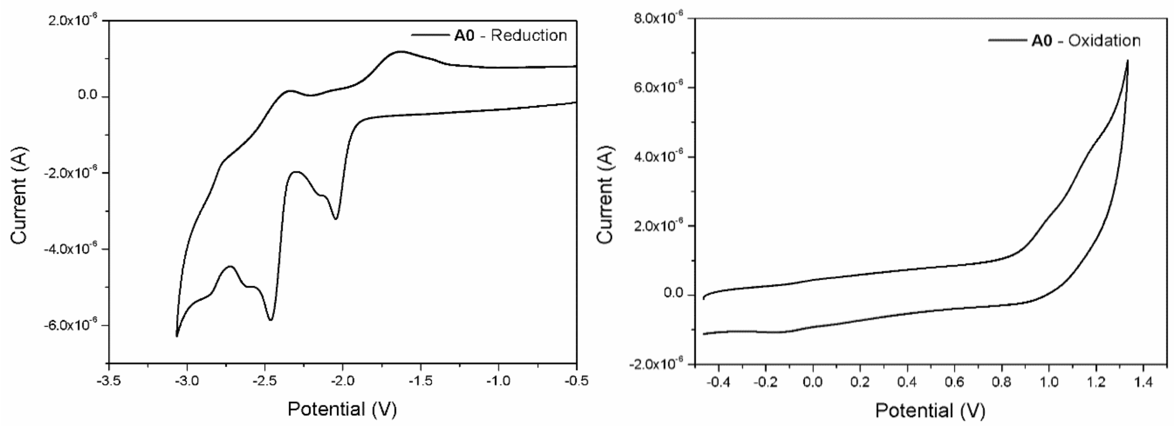

Figure 3.15. Reduction (left) and oxidation (right) curves from cyclic voltammetry of **A0** referenced against the $E_{1/2}$ of the Fc/Fc^+ redox couple; $5 \cdot 10^{-4}$ M solutions in 0.1 M *n*-Bu_4NPF_6 (1:2 acetonitrile:toluene mixture).

Compound **A** demonstrates two quasi-reversible oxidation peaks, whilst for the reduction two quasi-reversible peaks are followed by one irreversible wave (Figure 3.16). The calculated HOMO and LUMO energies for **A** are -5.68 and -2.95 eV, respectively.

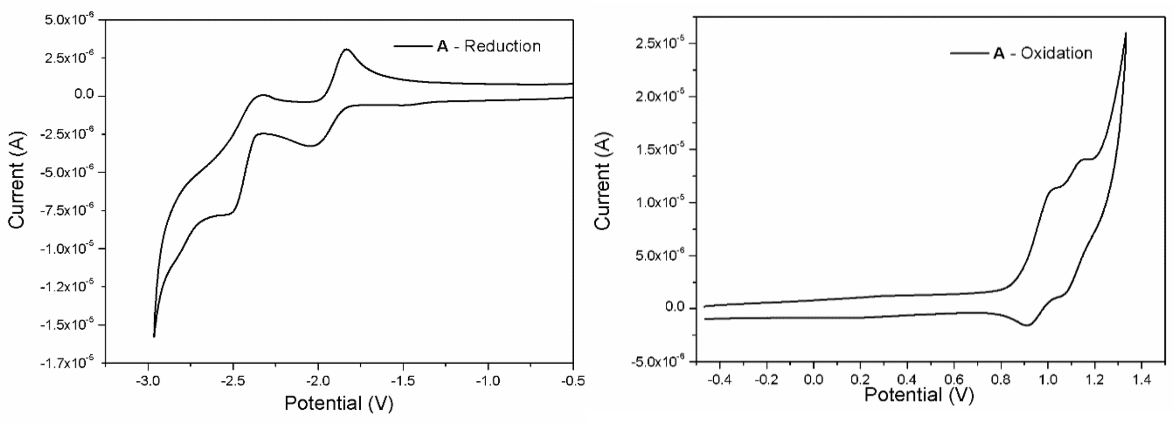

Figure 3.16. Reduction (left) and oxidation (right) curves from cyclic voltammetry of **A** referenced against the $E_{1/2}$ of the Fc/Fc^+ redox couple; $5 \cdot 10^{-4}$ M solutions in 0.1 M *n*-Bu_4NPF_6 (1:2 acetonitrile:toluene mixture).

The oxidation and reduction curves of compounds **A1** and **A2** are shown in Figures 3.17 and 3.18, respectively. The oxidation of **A1** demonstrates one reversible and two quasi-reversible peaks. The reduction shows three quasi-reversible waves and one irreversible process. The calculated HOMO and LUMO energy levels for **A1** are -5.20 eV and -2.94 eV, respectively. The HOMO level is almost 0.5 eV higher compared to **A0** and **A,** and the electrochemical band gap is narrowed, due to the introduction of four electron-donating triphenylamine groups.

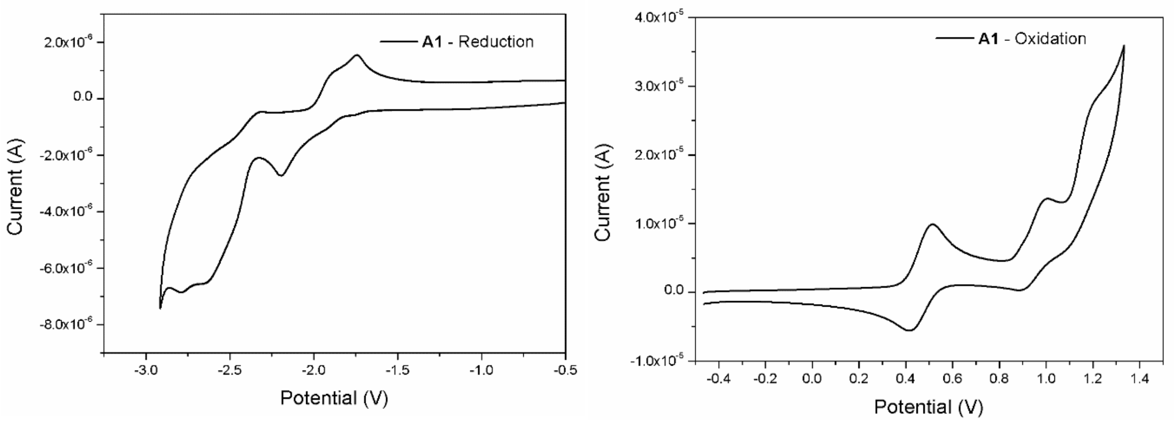

Figure 3.17. Reduction (left) and oxidation (right) curves from cyclic voltammetry of **A1** referenced against the $E_{1/2}$ of the Fc/Fc^{+} redox couple; $5 \cdot 10^{-4}$ M solutions in 0.1 M *n*-Bu_4NPF_6 (1:2 acetonitrile:toluene mixture).

For compound **A2** the first reversible oxidation peak appears at the lowest potential compared to the other three compounds, and it is followed by a second irreversible peak (Figure 3.18). The reduction processes involve three quasi-reversible waves. The calculated HOMO and LUMO energies are -5.04 eV and -2.93 eV. In this case phenoxazine is introduced into the backbone as a stronger electron-donating moiety, and the $E_{g(CV)}$ is even lower than that for **A1**. The LUMO energy levels are nearly identical for all four compounds due to the presence of the same 2,1,3-benzothiadiazole acceptor moiety.

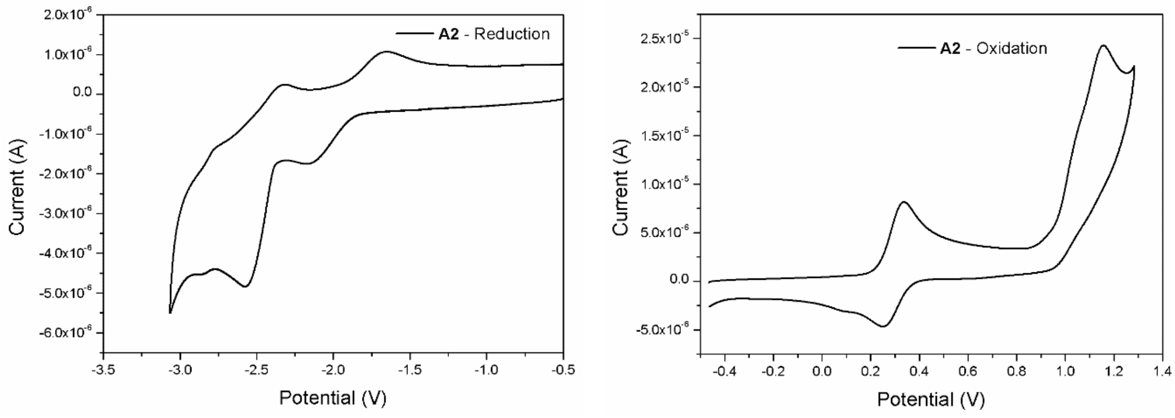

Figure 3.18. Reduction (left) and oxidation (right) curves from cyclic voltammetry of **A2** referenced against the $E_{1/2}$ of the Fc/Fc^{+} redox couple; $5 \cdot 10^{-4}$ M solutions in 0.1 M *n*-Bu_4NPF_6 (1:2 acetonitrile:toluene mixture).

A comparison of the optical and electrochemical band gaps for compounds **A0, A, A1** and **A2** is shown in Table 3.9. The difference between $E_{g(opt)}$ and $E_{g(CV)}$ is more significant for compounds **A0** and **A** than it is for **A1** and **A2**. Normally, the optical band gap is lower than the electrochemical band gap.[258] This difference corresponds to the exciton binding energy, i.e. the energy needed for the transformation of the electrostatically bound excited state into the ionised state.[259] In this case it can be concluded that for **A0** and **A** the exciton binding energy is much higher than it is for **A1** and **A2**, which is in agrement with the previous studies where the dependence of the exciton binding energy on the molecule length is observed with smaller molecules, demonstrating higher energies.[260]

Thermal properties of materials were studied by differential scanning calorimetry (DSC) and thermal analysis (TGA). All compounds demonstrate high thermal stability with 5% weight loss at 380°C (**A**), 402°C (**A0**) and 415°C (**A1** and **A2**). When measured by DSC compound **A1** demonstrates a transition peak at 161°C which is most likely a glass transition (see Appendix).

Table 3.9. Correlation of optical and electrochemical HOMO-LUMO gaps for **A0, A, A1** and **A2**.

	E_{ox}	**E_{red}**	**HOMO**[c] **(eV)**	**LUMO**[c] **(eV)**	**$E_{g(CV)}$ (eV)**	**$E_{g(opt)}$**[d] **(eV) d**
A0	0.97(irr) 1.16(irr)	-2.05 (q-r)[a] -2.15 (irr)[b] -2.47 (q-r) -2.61 (irr) -2.85 (irr)	-5.77	-2.75	3.02	2.55
A	1.01(q-r) 1.14(q-r)	-2.02 (q-r) -2.51 (q-r) -2.81 (irr)	-5.81	-2.78	3.03	2.55
A1	0.51 1.00(q-r) 1.19(q-r)	-1.94 (q-r) -2.19 (q-r) -2.63 (q-r) -2.79 (irr)	-5.31	-2.86	2.45	2.52
A2	0.34 1.16(irr)	-2.15 (irr) -2.58 (irr) -2.86 (irr)	-5.14	-2.65	2.49	2.52

[a] (q-r) denotes quasi-reversible; [b] (irr) denotes irreversible; [c] HOMO (LUMO) calculated from the peak of the corresponding redox wave and referenced to ferrocene. [d] The optical HOMO-LUMO gap ($E_{g(opt)}$) is calculated from the onset of the long wavelength-edge of the absorption band.

3.2.3 Fabrication and characterisation of fluorescent OLEDs

The final material **A1** had the highest PLQY in the solid state and was therefore chosen to be used as an emissive layer in OLED devices. Table 3.10 presents the summary of all the device structures used in this study. In all cases ITO was used as an anode. PEDOT:PSS or MoO_3 were used as the HIL, and LiF | Al or Ca | Al as the cathode layers. PEDOT:PSS was spin-coated at 3000 rpm for 60 s. MoO_3, LiF | Al and Ca | Al were thermally evaporated. **A1** was spin-coated at 1000 rpm for 60 s from a toluene or chloroform solution at the stated concentration. The EQE of the devices was calculated using the method proposed by Okamoto *et al.*[261] All the devices demonstrate green emission with $\lambda_{EL} \approx 540$ nm, CIE (0.40, 0.60) (Figure 3.19-b). The wavelength of the emission is slightly red-shifted at higher concentrations of **A1** (Figure 3.19-a).

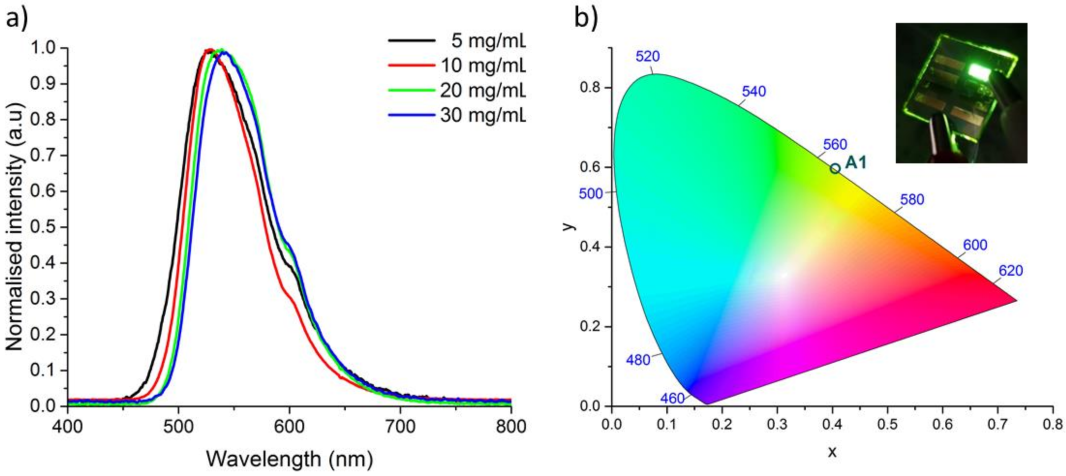

Figure 3.19. Example of the electroluminescence spectra (a) and CIE coordinates (b) for the devices using **A1** as the emitter. Device structure: ITO | PEDOT:PSS | **A1** | Ca (40 nm) | Al (60 nm). **A1** spin-coated from toluene.

Table 3.10. Summary of the device structures used for the investigation of the EL properties of **A1**.

Series	**Device structure**	**Conditions**
Dev A	ITO | PEDOT:PSS | **A1** | Ca (40 nm) | Al (60 nm)	**A1** spin-coated from chloroform solution. Concentration: 5–30 mg/mL
Dev B	ITO | PEDOT:PSS | **A1** | Ca (40 nm) | Al (60 nm)	**A1** spin-coated from toluene solution; Concentration: 5–30 mg/mL
Dev C	ITO | MoO_3 | **A1** | Ca (40 nm) | Al (60 nm)	**A1** spin-coated from toluene solution. Concentration: 20 mg/mL. Annealing temperature: 25–150°C.
Dev D	ITO | PEDOT:PSS | **A1** | LiF (1 nm) | Al (100 nm)	**A1** spin-coated from toluene solution. Concentration: 10–25 mg/mL.
Dev E	ITO | PEDOT:PSS | **A1** | TPBi | LiF (1 nm) | Al (100 nm)	**A1** spin-coated from toluene solution. Concentration: 5–10 mg/mL.

In the first series of OLED devices, a Ca (40 nm) | Al (60 nm) bilayer was used as a cathode. To investigate the influence of the solvent used for the spin-coating of the emissive layer on the performance of devices, solutions of **A1** were prepared in chloroform (Dev A) or toluene (Dev B) with concentrations varying from 5 mg/mL to 30 mg/mL. Table 3.11 presents the main characteristics of OLED devices from Dev A and Dev B series.

Table 3.11. Performance of Dev A and Dev B OLED devices fabricated using **A1** as emitter. Device structure: ITO | PEDOT:PSS | **A1** | Ca (40 nm) | Al (60 nm).

Concentration of the EML (mg/mL)	**Solvent**	**Turn on voltage at 10 cd m^{-2} (V)**	**Luminance (cd m^{-2})** [a]	**Current efficiency (cd A^{-1})** [a]	**Power efficiency (lm W)** [a]	**EQE (%)** [a]
5	Chloroform	3.3	4962 (8.5 V)	0.73 (4.7 V)	0.43 (4.7 V)	0.14
	Toluene	2.92	1422 (10.9 V)	0.05 (3.2 V)	0.05 (3.1 V)	0.01
10	Chloroform	4.2	4077 (10.2 V)	0.95 (6.2 V)	0.41 (5.25 V)	0.18
	Toluene	2.97	4674 (8.47 V)	0.52 (3.3 V)	0.47 (2.8 V)	0.12
20	Chloroform	5.76	1281 (17.8 V)	1.71 (8.1 V)	0.82 (5.0 V)	0.28
	Toluene	4.05	5393 (12.9V)	1.17 (3.9 V)	0.83 (3.9 V)	0.28
30	Chloroform	7.79	372 (18.8 V)	2.55 (12.4 V)	0.81 (6.8 V)	0.60
	Toluene	4.68	6292 (15.8 V)	2.17 (5.22 V)	1.26 (4.1 V)	0.52

[a] Maximum performance is shown

All devices demonstrate an increase in the turn-on voltage with an increase in concentration (Table 3.11, Figure 3.20 and Figure 3.21). Maximum EQE and current efficiency of the devices also increases at higher concentrations (Table 3.11, Figure 3.22 and Figure 3.23). The Dev B series has demonstrated a higher maximum luminance (6292 cd/m^2) compared to the Dev A series (4964 cd/m^2). Also, the luminance increases with increased concentration of the material for the Dev B series, whilst it decreases for Dev A (Figure 3.21). The maximum EQE of the devices increases at higher concentrations; whilst at 30 mg/mL it is slightly higher for Dev A compared to Dev B (0.60% and 0.51%, respectively), Dev B device demonstrates more than 15 times higher luminance. Additionally, the Dev B series demonstrated lower turn-on voltages which is most likely due to the slower evaporation rates of toluene compared to chloroform used for the deposition of the EML in Dev A.[262,263] As the Dev B series has demonstrated better performance compared to Dev A, toluene was used for spin-coating of the EML for all the following series of devices.

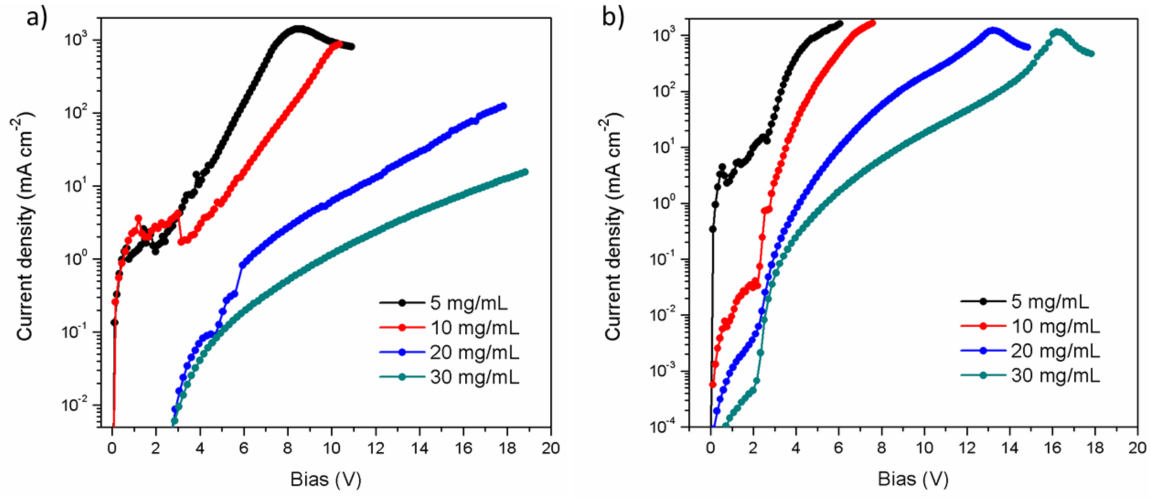

Figure 3.20. Current density vs applied bias for Dev A (a) and Dev B (b) series. Device structure: ITO | PEDOT:PSS | A1 | Ca (40 nm) | Al (60 nm).

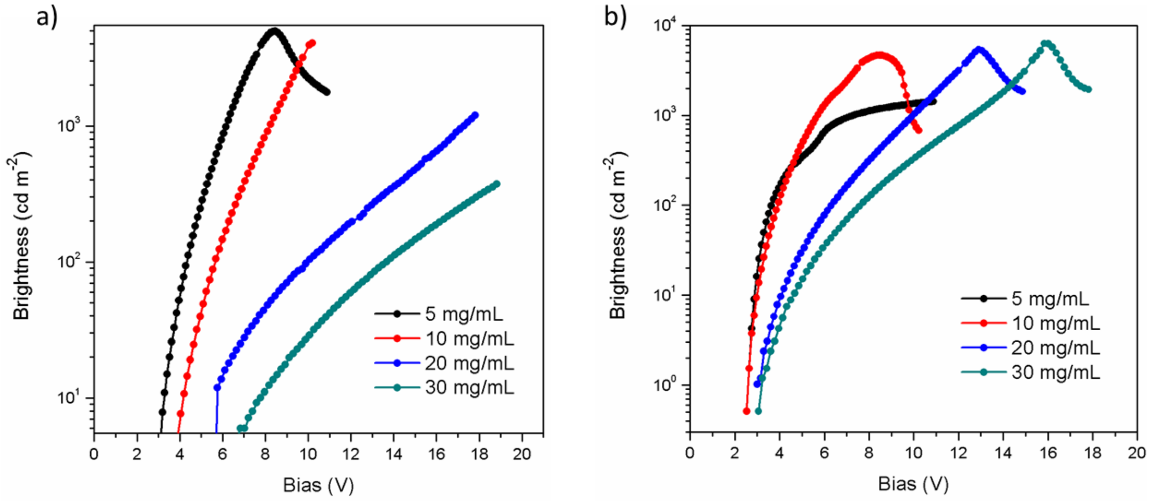

Figure 3.21. Brightness vs applied bias for Dev A (a) and Dev B (b) series. Device structure: ITO | PEDOT:PSS | A1 | Ca (40 nm) | Al (60 nm).

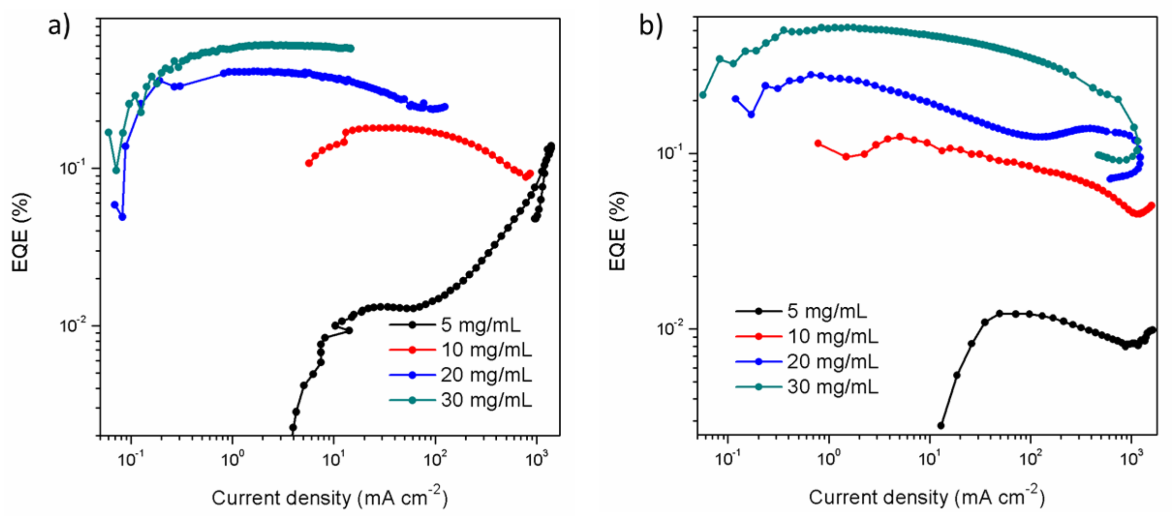

Figure 3.22. EQE *vs.* current density for Dev A (a) and Dev B (b) series. Device structure: ITO | PEDOT:PSS | **A1** | Ca (40 nm) | Al (60 nm).

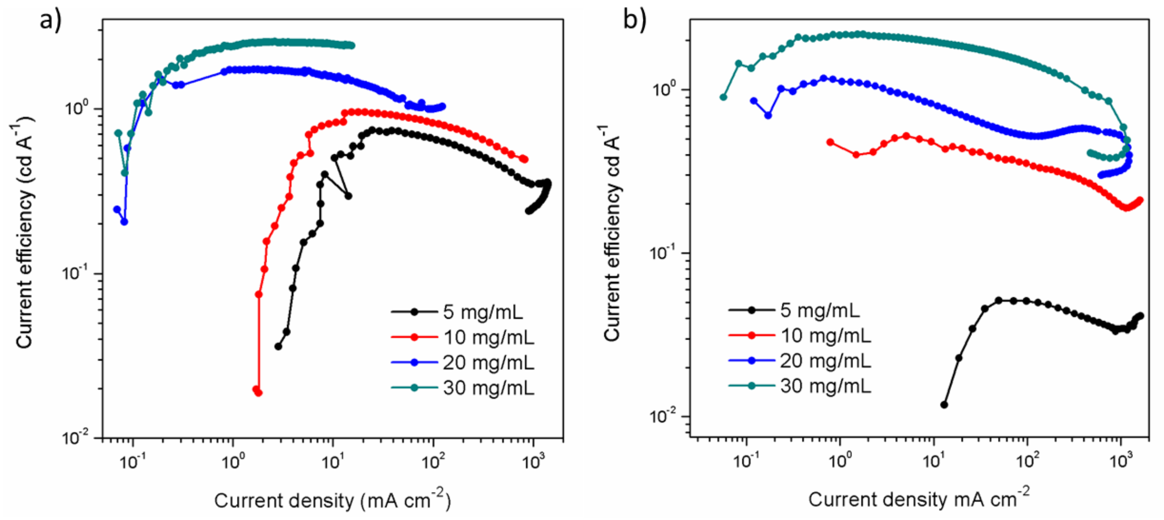

Figure 3.23. Current efficiency *vs* current density for Dev A (a) and Dev B (b) series. Device structure: ITO | PEDOT:PSS | **A1** | Ca (40 nm) | Al (60 nm).

In the next series (Dev C), MoO_3 was used as the HIL. The concentration of the **A1** material in the toluene solution for spin-coating was 20 mg/mL (Table 3.12). Annealing temperatures varied from 50°C to 150°C. Unannealed devices demonstrate the highest brightness (7990 cd/m^2), the lowest turn on voltage (5.7 V) and EQE comparable to the devices annealed at 50°C and 100°C (0.30%, 0.29% and 0.34%, respectively). Devices annealed at 150°C have shown the lowest efficiencies. The performance of Dev C is similar to that of Dev B at 20 mg/mL concentration of **A1** in toluene. The driving voltage is, however, lower for Dev B. Thus, PEDOT:PSS was used as the HIL in the following series of devices.

Table 3.12. Performance of Dev C OLED devices fabricated using **A1** as the emitter. Device structure: ITO | MoO_3 (10 nm) | **A1** | Ca (40 nm) | Al (60 nm). **A1** spin-coated from toluene and annealed at various temperatures.

Annealing temperature (°)	**Turn on voltage at 10 cd m^{-2} (V)**	**Luminance (cd m^{-2})** [a]	**Current efficiency (cd A^{-1})** [a]	**Max power efficiency (lm W)** [a]	**EQE (%)**[a]
no annealing	5.7	7990 (13.1 V)	1.11 (11.5 V)	0.31 (11.2 V)	0.30
50	6.45	6775 (14.9 V)	1.08 (13.5 V)	0.26 (13.2 V)	0.29
100	7.31	7142 (15.8 V)	1.25 (11.9 V)	0.36 (9.52 V)	0.34
150	6.24	6333 (15.1 V)	0.76 (14.9 V)	0.16 (14.2 V)	0.20

[a] Maximum performance is shown

In the Dev D series LiF (1 nm) | Al (100 nm) bilayer was used as a cathode instead of Ca | Al, and the concentration of the emissive layer varied from 10 mg/mL to 25 mg/mL. The devices show very low EQEs (<0.01%) and brightness below 200 cd/m^2 as well as very high driving voltages of around 8 V (Table 3.13).

Table 3.13. Performance of Dev D OLED devices fabricated using **A1** as emitter. Device structure: ITO | PEDOT:PSS | **A1** | LiF (1 nm) | Al (100 nm). **A1** spin-coated from toluene.

Concentration of the EML (mg/mL)	**Turn on voltage at 10 cd m^{-2} (V)**	**Luminance (cd m^{-2})** [a]	**Current efficiency (cd A^{-1})** [a]	**Max power efficiency (lm W)** [a]	**EQE (%)**[a]
10	7.95	17 (9.2 V)	0.01 (9.2 V)	0.0003 (9.2 V)	0.0003
15	7.35	143 (12.6 V)	0.02 (9.0 V)	0.006 (8.7 V)	0.005
20	7.95	157 (13.8 V)	0.02 (10.1 V)	0.006 (9.6 V)	0.005
25	9.20	113 (14.4 V)	0.04 (10.2 V)	0.01 (9.8 V)	0.009

[a] Maximum performance is shown

The introduction of TPBi as an ETL (spin-coated at 2000 rpm for 30 s from a 6 mg/mL solution of methanol),[264] has led to a higher brightness of the devices (400–500 cd/m^2) and lower turn on voltages (≈5V), but the EQE of the devices still did not surpass 0.01 % (Table 3.14).

Table 3.14. Performance of Dev E OLED devices fabricated using A1 as the emitter and TPBi as an ETL. Device structure: ITO | PEDOT:PSS | **A1** | TPBi | LiF (1 nm) | Al (100 nm).
A1 spin-coated from toluene, and TPBi spin-coated from methanol at 2000 rpm for 60 s.

Concentration of the EML (mg/mL)	**Turn on voltage at 10 cd m^{-2} (V)**	**Luminance (cd m^{-2})** [a]	**Current efficiency (cd A^{-1})** [a]	**Max power efficiency (lm W)** [a]	**EQE (%)**[a]
5	4.5	523 (7.8 V)	0.03 (7.8 V)	0.013 (7.7 V)	0.009
10	5.4	410 (8.55 V)	0.04 (8.55 V)	0.013 (8.4 V)	0.01

[a] Maximum performance is shown

Out of the five series, Dev B has shown the best all-round performance with the maximum EQE of 0.52 %, luminance of 6292 cd/m^2 and a turn on voltage of about 4.7 V. The Ca | Al cathode is thus the best choice for the fabrication of devices with **A1** as an emissive layer. This is probably due to a better matching work function of the Ca | Al cathode to the LUMO of **A1**, compared to the LiF | Al cathode (Figure 3.24).[265] The performance of the OLEDs can possibly be further improved by introducing an ETL.

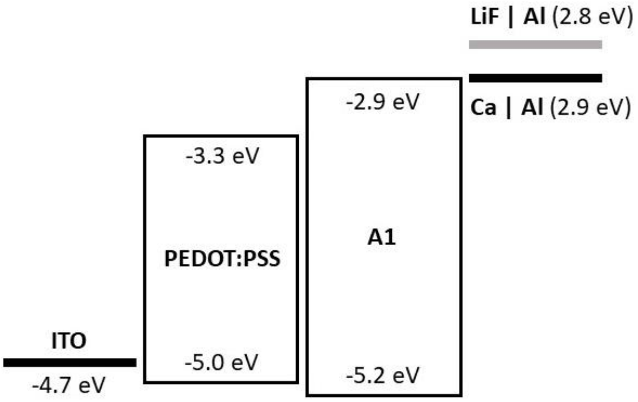

Figure 3.24. Energy diagram for the series Dev A and Dev B of the OLED devices.

3.2.4 Use of materials as down-converters in hybrid LEDs

In addition to studying **A1** as an emissive layer for OLEDs, the material **A1** was also used as a down-converter in hybrid LEDs. The preparation of devices and all related measurements were performed at the University of Strathclyde by Dr Jochen Bruckbauer. To prepare the devices, compound **A1** was incorporated into a transparent CHDV matrix, deposited onto an LED chip, and the organic layer was next cured with UV light.[254] In order to investigate the colour converting properties of the material, different amounts of **A1** (0.6

– 4.6 mg) per 1 mL of CHDV matrix were used. The EL spectra for hybrid LEDs show two peaks: one around 455 nm corresponding to the emission of the blue LED and another around 530 nm originating from the **A1** material (Figure 3.25). When the concentration of **A1** increases, the intensity of the blue emission decreases as more of the blue light is absorbed by the organic material. The intensity of the emission from **A1** increases until the concentration of the organic material raises to 1.8 mg/mL and decreases afterwards. This behaviour can be attributed to aggregation induced quenching at higher concentrations of the organic material.[255] The calculated chromaticity coordinates in the CIE 1931 (x, y) chromaticity diagram for the light emitted by hybrid LEDs, together with the emission from the bare blue LED are shown in the Figure 3.26. The colour of the light emitted by the LEDs with **A1** concentration of 0.9 and 1.3 mg/mL is the closest to the Planckian locus. When the concentration of the material increases, the colour shifts to the green region, and at 4.6 mg/mL the emission originates almost completely from the organic material. The colour shift occurs on a straight line between the coordinates from the blue LED and the green region, which makes it pass above the Planckian locus. An additional red-shifted component in the emission of the organic material in this case could have made the line to pass through the Planckian locus and thus produce a better-quality white light. The difference in the chromaticity of the devices using the same concentrations of the colour-converter are most likely due to the inaccuracies in the volume measurements for the deposited organic layer.

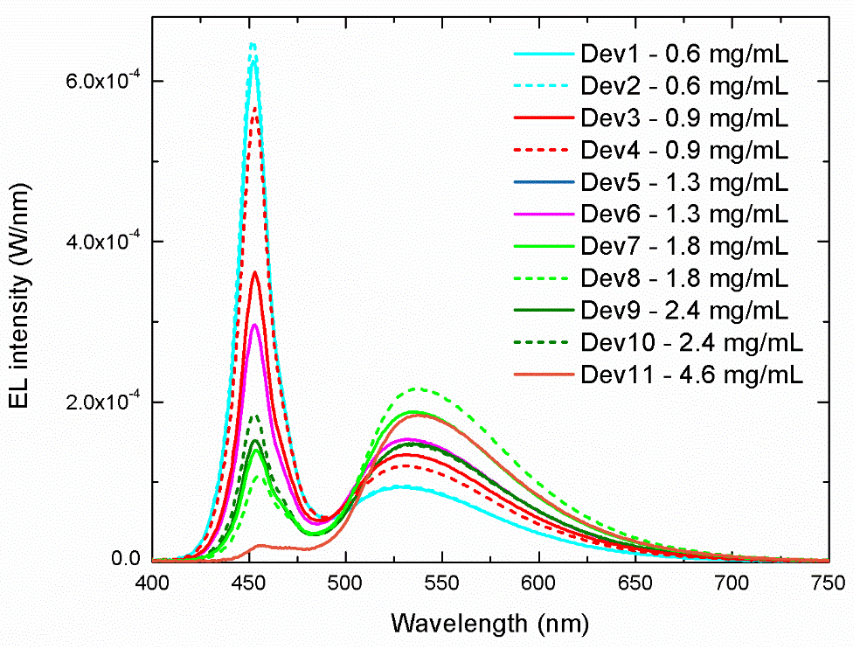

Figure 3.25. EL spectra of the blue LED after encapsulation with different amounts of the organic wavelength converter.

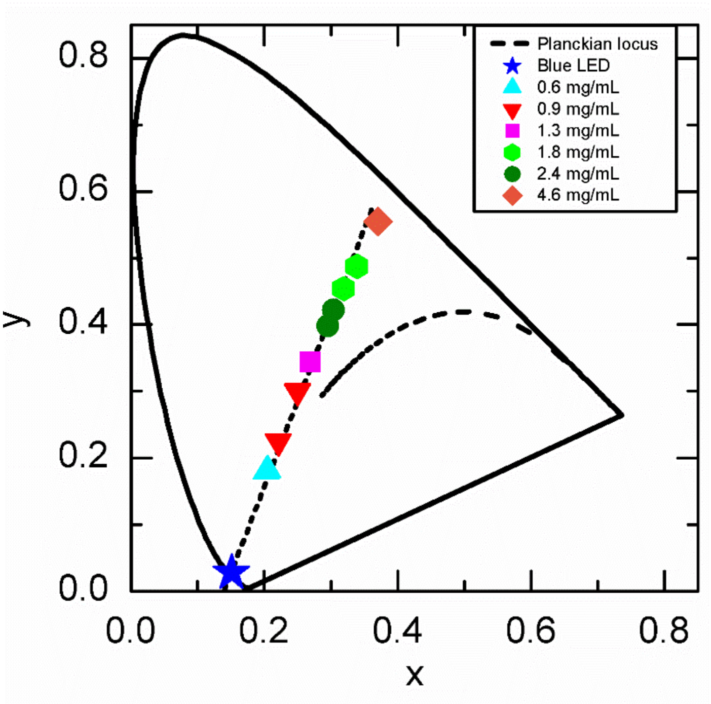

Figure 3.26. Chromaticity diagram (CIE 1931) showing coordinates of LEDs encapsulated with different concentrations of organic down-converter.

The quality of the hybrid LED light was evaluated by determining CRI and CCT colorimetry values discussed in Section 1.3.2 of Chapter 1 (Figure 3.27). The CRI varies from around 40 to 70 for different concentrations of **A1**. At 0.9 mg/mL the CRI value is the highest (67), and it decreases at higher concentrations.

According to the CCT of the prepared hybrid LEDs, the light varies from cool to warm white with increased concentration. The lowest CCT is around 4870 K (4.6 mg/mL). At 0.9 mg/mL the CCT is the highest (around 12730 K). Only concentrations of **A1** between 1.8 mg/mL and 4.6 mg/mL provide CCT values within a 3000 – 7000 K range, which is acceptable for indoor lighting.

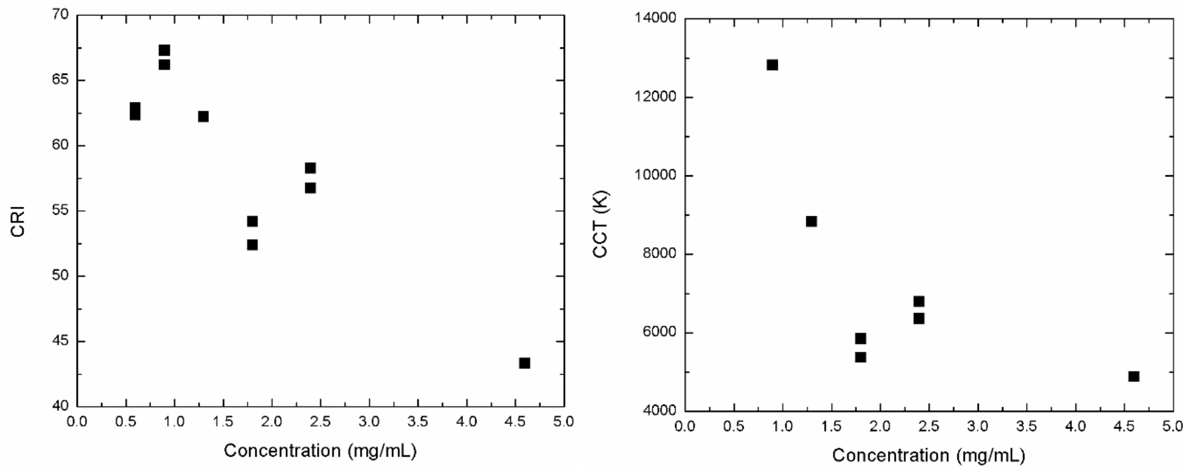

Figure 3.27. CRI (left) and CCT (right) values for hybrid LEDs encapsulated with different concentrations of organic down-converter.

While the radiant flux is higher at lower concentrations of the down-converter, the luminous flux (characterising the light power perceived by the human eye), increases with concentration up until 1.8 mg/mL and slightly decreases afterwards (Figure 3.28). Luminous efficacy (Figure 3.29) follows the same trend, as the electrical power is roughly the same for all LEDs. This trend demonstrates that the use of the colour converter enhances the perception of the light by the human eye.

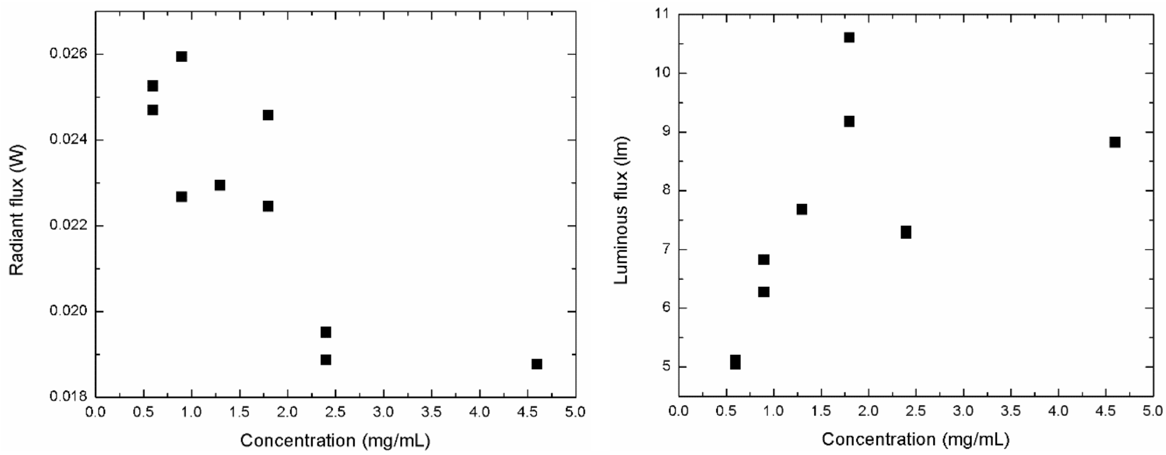

Figure 3.28. Radiant flux (left) and luminous flux (right) values for hybrid LEDs encapsulated with different concentrations of organic down-converter.

Another parameter which can evaluate the efficiency of the hybrid LED containing a colour converter is the blue-to-white efficacy, which is the ratio of the luminous flux of the hybrid LED to the radiant flux of the bare blue LED, and has values above 200 lm/W for phosphor-based commercial white LEDs.[256] The highest blue-to-white efficacy of 320 lm/W is achieved for devices with a concentration of 1.8 mg/mL for **A1**.

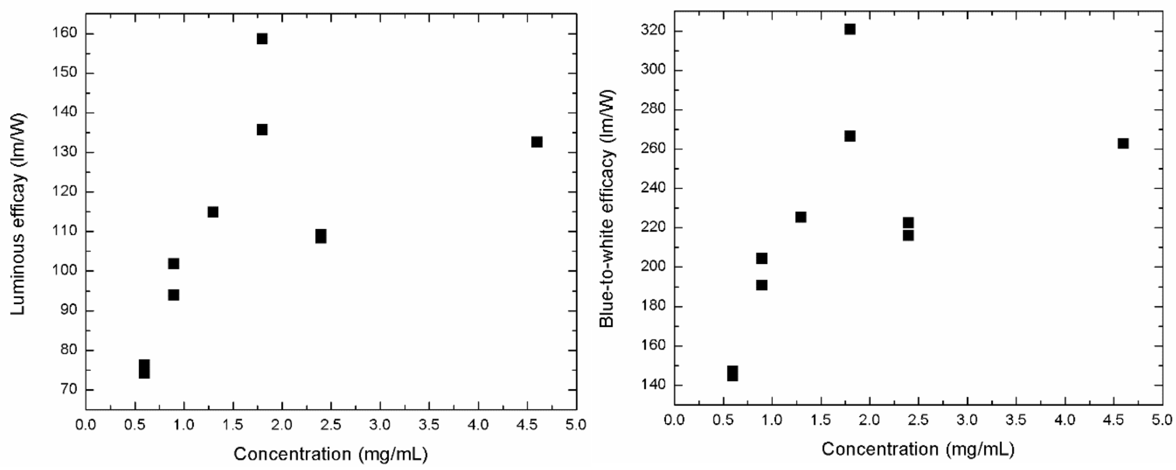

Figure 3.29. Luminous efficacy (left) and blue-to-white efficacy (right) values for hybrid LEDs encapsulated with different concentrations of organic down-converter.

In summary, concentrations of 0.9 mg/mL of down-converter provide the best colour quality. whilst the efficiency of the device is highest at 1.8 mg/mL for **A1**. The chromaticity coordinates are, however, quite far away from the Planckian locus for all devices, and CCT and CRI values considered acceptable for industrial applications could not be achieved simultaneously. In order to achieve a better colour quality, the emission of the material should be broader and extend further into the longer wavelength. This could be achieved by using a stronger electron-donating group and extending the conjugation in the system by, for example, introducing additional π-linkers, such as fluorene moieties between the truxene-based core and the donor.

3.3 Conclusions

In summary, two new donor-acceptor compounds **A1** and **A2** based on a truxene-BT-truxene core were synthesised. The absorption and emission profiles of the materials do not differ significantly from their precursor (**A**) and the unsubstituted core **A0**, which signifies that it is mainly influenced by the core unit. Material **A1** has demonstrated a higher PLQY in solution and in solid state compared to **A2**. The electroluminescent properties of **A1** were investigated in OLEDs. The highest EQE for the devices is 0.60%, and the maximum achieved brightness is 7990 cd/m^2. The performance of the devices could possibly be further improved by introducing an ETL, such as BCP, with the LUMO energy level matching the work function of the cathode and the LUMO level of **A1**. The material **A1** was also used as a colour-converter in hybrid LED devices. Whilst the material efficiently absorbs blue light and re-emits it at a longer wavelength, the quality of light is not satisfactory for lighting applications and a pure white light could not be achieved using the material. For a better colour quality, the colour-converter should emit light at a longer wavelength compared to **A1**. The increase of conjugation between the core and the donor unit can red-shift the emission of the material as well as increase the absorptivity, thus providing a better colour-conversion.

While the materials **A1** and **A2** do not demonstrate TADF properties, the delayed fluorescence can potentially be achieved in isotruxene-based materials, as in isotruxenes the conjugation is interrupted only partially (Figure 3.30-a), and when the combination of two donor (acceptor) and one acceptor (donor) substituents is used this can lead to a reduced ΔE_{ST} gap whilst simultaneously keeping the conjugation strong enough to achieve high PLQY. Triazatruxene, an heterocyclic analogue of truxene (Figure 3.30-b), was recently successfully used as a donor core in a TADF compound with dibenzothiophene-S,S-dioxide as an acceptor.[266] The material has demonstrated exceptionally high PLQY (≈1) and fast rISC rates. This was explained by the presence of three quasi-equivalent acceptors in the system that give rise to multiple excited triplet and singlet states that are close in energy and vibronically coupled to each other. The strategy employing multiple acceptor systems can be further extended to the preparation of TADF materials based on a cyclic tetraindole core (Figure 3.30-c), which can often be separated as a side product during the synthesis of triazatruxene.[267]

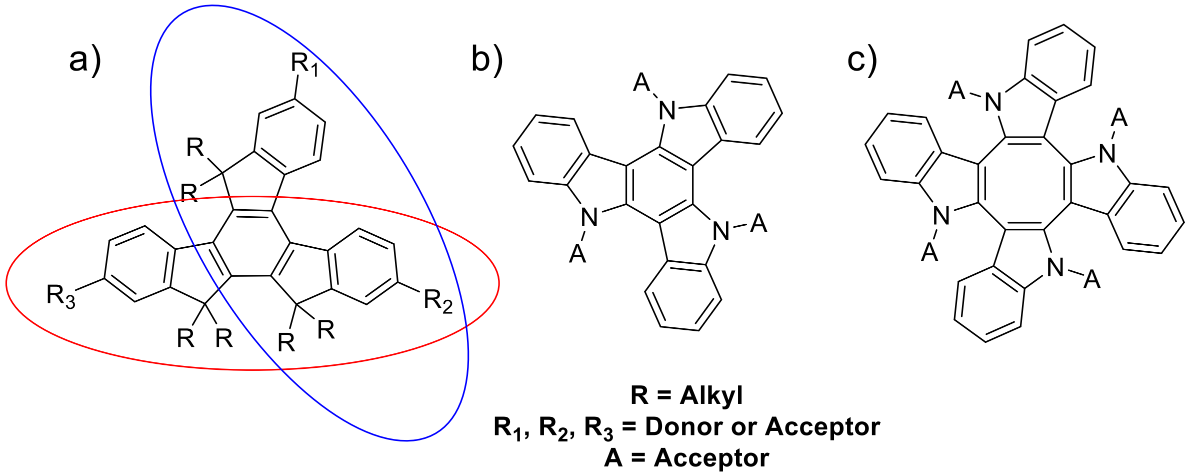

Figure 3.30. Suggested molecular structures for TADF emitters with isotruxene (a), triazatruxene (b) and tetraindole (c) cores. Conjugated arms of isotruxene are circled in blue and red.

Moreover, the core **A** can be employed as a building block for the preparation of dendrimers with oligofluorene arms (Figure 3.31). These materials can be used in lasing applications as well as for visible light communications. In fact, two new compounds **A-Fl$_1$** and **A-Fl$_2$** were already prepared in the group by a visiting Masters student Manon Bousquet, and their properties should be investigated further. The yield of material **A** can be increased by further optimisation of the coupling procedure. For example, the influence of the concentration of the starting material in the reaction mixture was not investigated in this study. Lower concentrations could minimise the unwanted side polymerisation processes in this case.

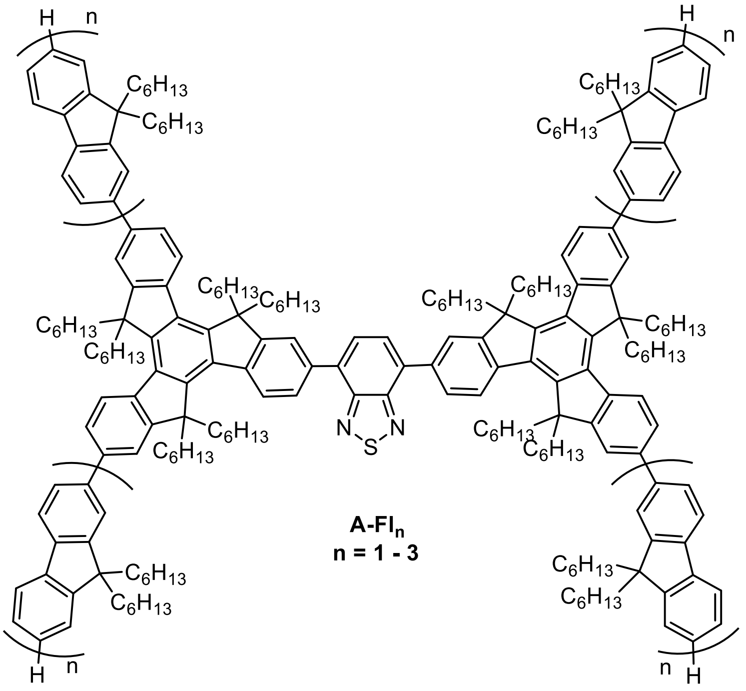

Figure 3.31. Molecular structure of the materials with **A** core and oligofluorene arms.

Chapter 4. “Chemeleon” quinolines: Compounds exhibiting mechanochromic aggregation-induced delayed emission

Here the properties of new charge-transfer (CT) compounds with quinoline used as an acceptor and di-tert-butyl carbazole as a donor are discussed. When the nitrogen atom of the quinoline moiety in ***Q1*** *and* ***Q2*** *is methylated, formed salts show mechanochromism and aggregation-induced emission (AIE). Moreover, depending on the relative position of the donor and acceptor the materials demonstrate either TTA or TADF. Due to the AIE character of the methylated compounds the properties of materials were mainly investigated in the solid state. The influence of the counter-ion on the properties of quinoline derivatives is also discussed in this chapter. In addition, the material* ***Q2-S1*** *was tested in organic light-emitting diode (OLED) devices.*

4.1 Introduction

Even though organic electronics is a relatively young field of materials science, thousands of novel semiconducting organic materials have already been reported. For many of these compounds the preparation involves complex multi-step syntheses using time-consuming procedures and tedious purification methods. This can limit the scale-up of the materials and their use in commercial products. Thus, using easily available starting materials and simple synthetic routes for the preparation of highly efficient compounds would be beneficial for the field.

Finding good candidates for use in organic semiconducting devices among already existing fluorescent materials is particularly tempting. One such compound is quinine, an alkaloid naturally occurring in cinchona trees. It is widely used as an antimalarial drug[268], and is fluorescent in acidic environments, such as tonic water. The compound was known since the beginning of the 19th century, and the first observation of fluorescence, originally termed 'epipolic dispersion', was first reported by John Hershel[269] using a solution of quinine sulphate in 1845. Moreover the solution of quinine sulphate was used for the first description of the change in refrangibility between absorbed and emitted light later termed the Stokes' shift[270], after its discoverer George Stokes, who also coined the term fluorescence. Despite the fact that quinine helped give birth to the field of fluorescence spectroscopy and is still widely used as a fluorescence standard,[271] its photophysical properties have not been fully investigated to date.

Dr Marc Etherington from the OEM group in Durham University in his study of quinine has observed several new properties. For example, in polar solvents an additional emission band emerges for quinine. It is red-shifted with the increase of the solvent polarity indicating the CT character of the band (Figure 4.1).

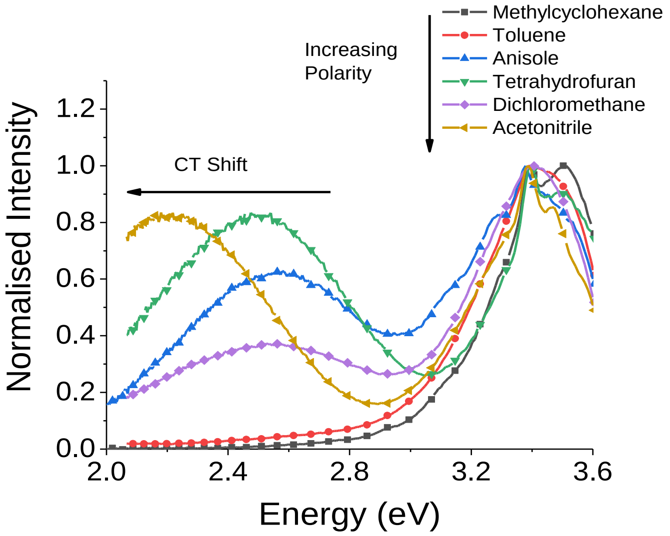

Figure 4.1. Solvatochromism of quinine (unpublished work).

Moreover, it is possible to achieve similar fluorescent properties to the acidified quinine in neutral solutions when the nitrogen atoms of quinine are methylated. Indeed, Dr Marc Etherington has discovered that the methylation of one or both nitrogen atoms of quinine leads to significant changes in its emission profile (Figure 4.2). The methylation of the tertiary amine leads to the suppression of the CT emission discussed above, and only a high energy band can be observed (Figure 4.2-b). When both nitrogen atoms are methylated the emission shifts to around 450 nm and is similar to the emission profile of quinine sulphate in acidic solution (Figure 4.2-c).[272] Thus, the most significant changes are observed when the sp^2 nitrogen of quinine is methylated.

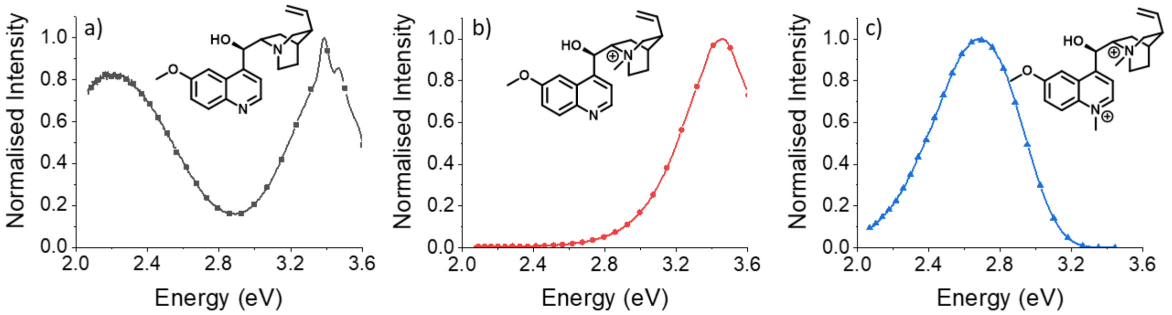

Figure 4.2. Influence of the methylation of nitrogen atoms of quinine on the emission profile (unpublished work).

Numerous readily available natural compounds containing heteroaromatic rings could be modified by this simple procedure and can potentially demonstrate a drastic change in their photophysical properties. Moreover, it is probably possible to induce thermally activated delayed fluorescence (TADF) in such compounds. Initially TADF was observed in eosin Y (hence also being known as E-type delayed fluorescence), a material that similarly to quinine exhibits proton transfer. Also, as it was discussed in Section 1.4.1 of Chapter 1, HOMO-LUMO separation sufficient for inducing reverse intersystem crossing (rISC) and, thus, TADF can be achieved in molecules with excited-state intramolecular proton transfer (ESIPT)[124,126]. Thus, quinine and similar compounds, such as quinoline, are good candidates for further investigations in the area of proton transfer TADF materials.

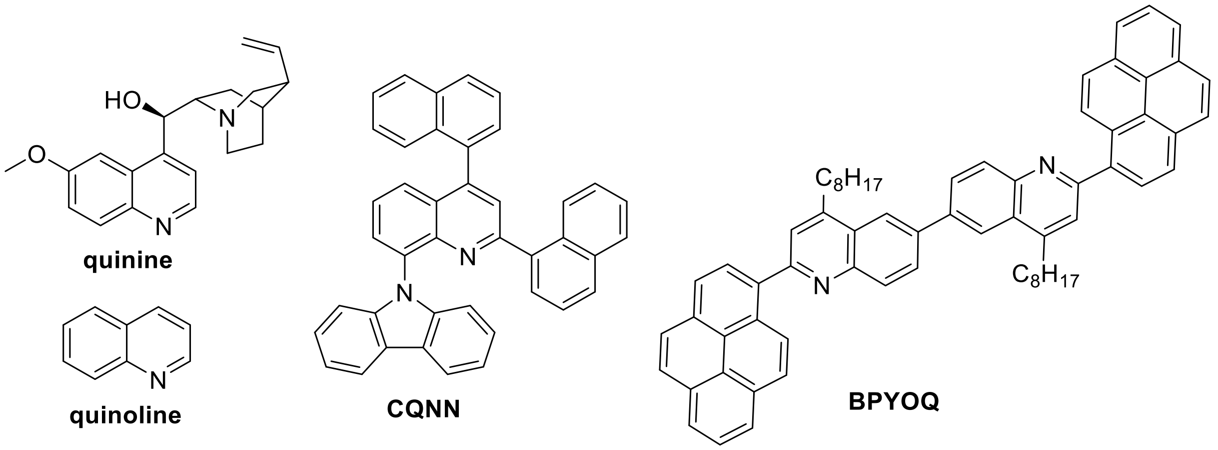

Figure 4.3. Molecular structures of quinine, quinoline and its derivatives used for optoelectronic applications.

It was also previously observed that in molecules with CT character the ΔE_{ST} gap can be modulated by changing the polarity of the media, which in turn can enhance TADF (Section 1.4.1, Chapter 1)[110,113]. Thus, it would be interesting to investigate whether the CT state can be tuned and TADF can be induced by methylation of the sp^2 nitrogen atom in donor-acceptor compounds containing heterocyclic aromatic moieties, such as quinoline (Figure 4.3).

Quinoline is already used as an acceptor in a TADF emitter. In the compound **CQNN** carbazole is introduced in the 8-position of quinoline, and naphthyl moieties are situated in 2- and 4-positions (Figure 4.3)[273]. This material exhibits mechanoluminescent properties. In its **α-CQNN** form with non-centric $Pna2_1$ symmetry the material exhibits prompt fluorescence together with phosphorescence. After mechanical grinding it turns into **β-CQNN** with centric $P2_1/n$ symmetry which demonstrates TADF *via* rISC from T_2 to S_1 and RTP from T_1 relaxation. According to theoretical calculations the conformational change results into a significant reduction of S_1-T_2 gap from 0.732 eV for **α-CQNN** to 0.016 eV for **β-CQNN**.

Protonation of the quinoline moiety was previously used for tuning the optoelectronic properties of fluorescent materials. Hancock *et al.* have reported a quinoline-based fluorescent emitter **BPYOQ** (Figure 4.3) where the luminescence was modulated by protonation of one or both of its nitrogen atoms by camphorsulfonic acid (CSA)[274]. The colour of the emission could be changed by mixing **BPYOQ** and CSA in different molar ratios. In chloroform solution the pure **BPYOQ** demonstrates one emission peak at 434 nm, and upon the addition of CSA a second band emerges at 523–530 nm. And the overall colour of the emission shifts from blue to green. However, the addition of CSA also quenches the emission, reducing the photoluminescence quantum yield (PLQY) from 87% to 37%. Contrary to the solution, in solid state the material demonstrates only one emission band which shifts gradually from green to red with increasing amounts of CSA. Authors suggest that this is due to the fusion of two PL bands at lower concentrations of CSA when protonated and non-protonated forms of **BPYOQ** are in equilibrium. At higher concentrations emission originates exclusively from the doubly protonated compound. The electroluminescent properties of **BPYOQ**:*n*CSA mix ($n = 0, 0.2, 0.5, 1$ and 2, and is a molar ratio of CSA) were investigated in OLED devices. Increasing amounts of CSA decreases the turn-on voltage of the devices (from 5.1 to 4.2 V), and the current efficiency is also decreased (from 1.44 cd/A to 0.1 cd/A).

The materials containing the methylated quinoline moiety have already been used for optoelectronic applications. Recently reported compounds **HM6FQ** and **HM7FQ** demonstrate second-order nonlinear optical response with good characteristics for terahertz wave generation (Figure 4.4)[275]. In this case the introduction of a fluorine atom into the quinoline backbone results into a higher thermal stability of the material compared to non-fluorinated **HMQ-T** due to the formation of additional hydrogen bonds. Quinolinium salts can also demonstrate luminescent properties. For example, the star-shaped liquid-crystalline molecule **QN3** (Figure 4.4) exhibited AIE, which is most likely caused by the electrostatic repulsion between the molecules and steric hindrance that inhibits the π–π stacking.[276]

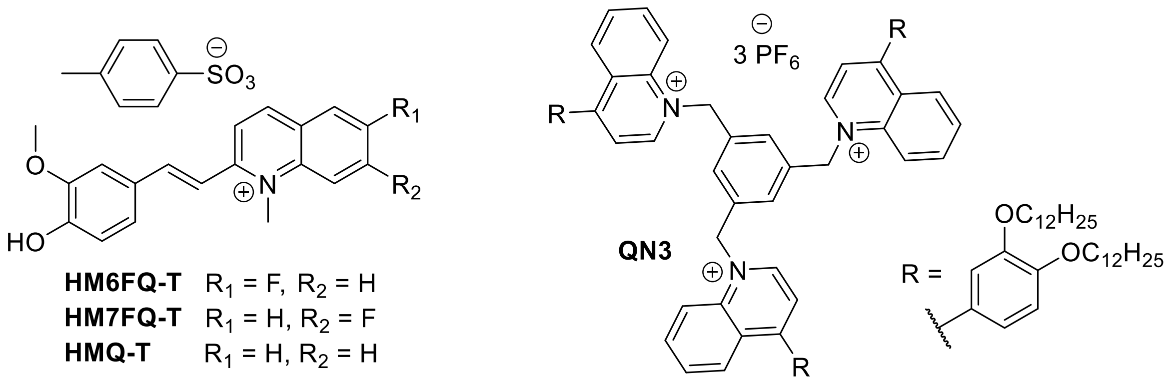

Figure 4.4. Examples of molecular structures of quinolinium salts.

Pyridine is another heterocyclic aromatic moiety that can be modified by methylation of its nitrogen atom. Pyridinium salts can exhibit aggregation-induced emission and are soluble in water, which makes them good candidates for the applications in optical and biological research. For example, Λ-shaped pyridinium salt **DMDPS** based on Tröger's Base (Figure 4.2) have demonstrated AIE, which is most likely due to the conformational twist of the molecule in the solid state that leads to loose stacking.[277] Another example of pyridinium salts demonstrating AIE is the **CPN** series where the colour of the emission can be tuned by the introduction of the various aromatic substituents into the central benzene ring (Figure 4.5). AIE in these materials is most likely caused by their highly twisted structure[278]. The materials demonstrated a good biocompatibility and could be used for mitochondrial and bacterial imaging. Moreover, they can potentially be used in anticancer and antibacterial treatment.

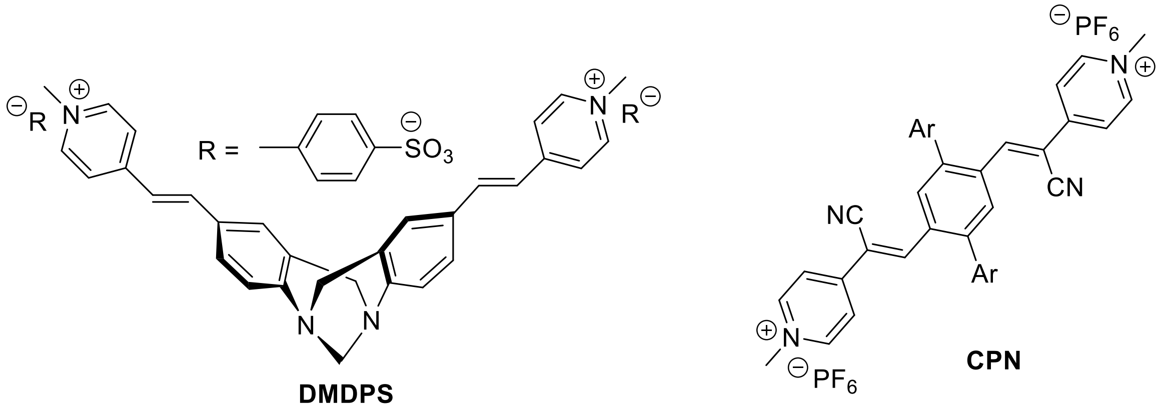

Figure 4.5. Examples of molecular structures of pyridinium salts demonstrating AIE.

Methylated quinoline-based donor-acceptor compounds exhibiting delayed fluorescence have not yet been reported and are the scope of this chapter. Furthermore, the materials presented in this work demonstrate aggregation-induced emission (AIE) and mechanochromism (MC). In the last few years several series of materials simultaneously exhibiting TADF, AIE and MC have been reported.[179,279] However, to our knowledge this is the first time they have been observed in organic salts prepared from non-TADF materials.

4.2 Results and discussion

To investigate the influence of the methylation on the photophysical properties of quinoline-based donor-acceptor materials two new compounds **Q1** and **Q2** were synthesised (Scheme 4.1). Here, 3,6-di-tert-butylcarbazole (tBu-CBZ) was introduced as a donor in the 3- or 4-position of quinoline. The compounds were then methylated to prepare a series of quinoline salts **Q1-Sn** and **Q2-Sn** with different counter-ions including triflate, iodide and tetrafluoroborate (Scheme 4.1).

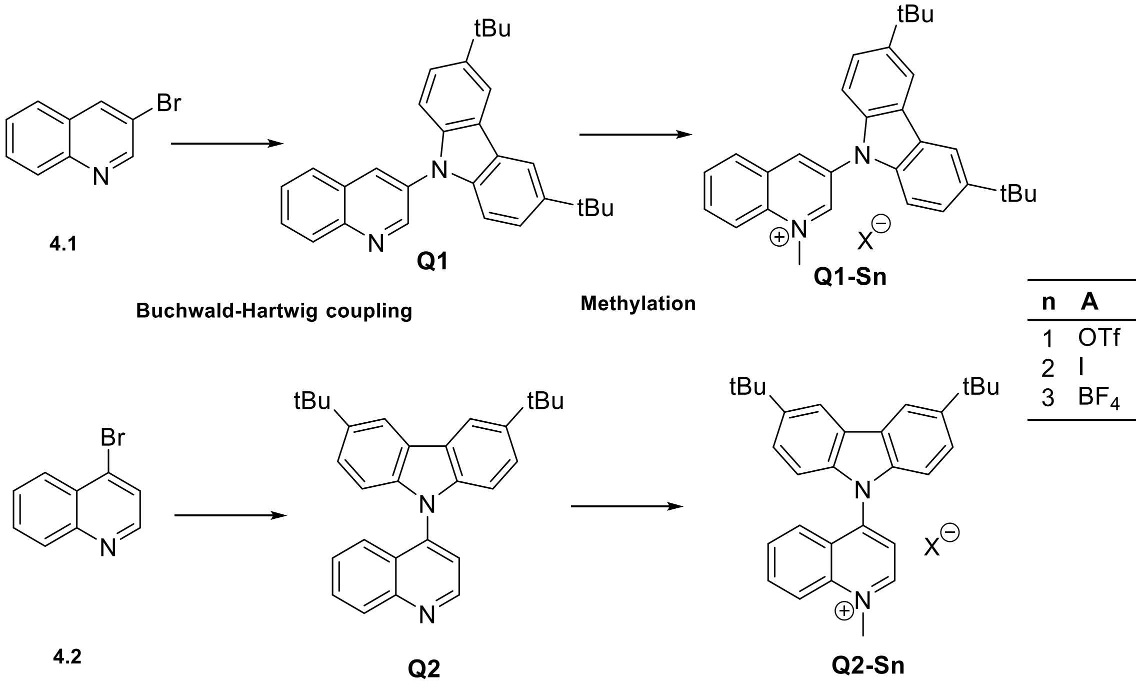

Scheme 4.1. General strategy for the preparation of the series of methylated quinoline-based compounds **Q1-Sn** and **Q2-Sn.**

4.2.1 Synthesis of quinoline-based charge-transfer compounds

Both **Q1** and **Q2** were prepared *via* Buchwald-Hartwig coupling between 3,6-Di-tert-butylcarbazole (**tBu-CBZ**) and 3-bromoquinoline (**4.1**) or 4-bromoquinoline (**4.2**), respectively (Scheme 4.2). Tris(dibenzylideneacetone)dipalladium(0) ($Pd_2(dba)_3$) was used as a catalyst, 2-dicyclohexylphosphino-2′,4′,6′-triisopropylbiphenyl (XPhos) as a ligand and sodium *tert*-butoxide was a base of choice. Compound **Q1** was prepared with 60% yield while the reaction for the preparation of **Q2** demonstrated a much lower yield of 12%.

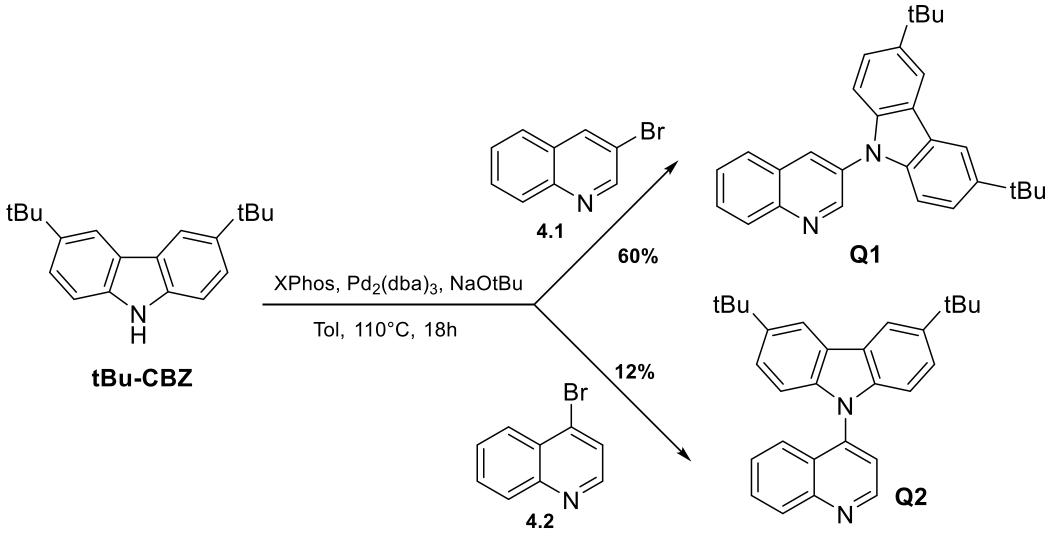

Scheme 4.2. Synthesis of compounds **Q1** and **Q2**.

Compounds **Q1-S1** and **Q2-S1** were prepared by the methylation of **Q1** and **Q2**, respectively, with methyl trifluoromethanesulfonate (Scheme 4.3). Products could be easily separated by filtration. Both compounds exhibit aggregation-induced emission and mechanochromism.

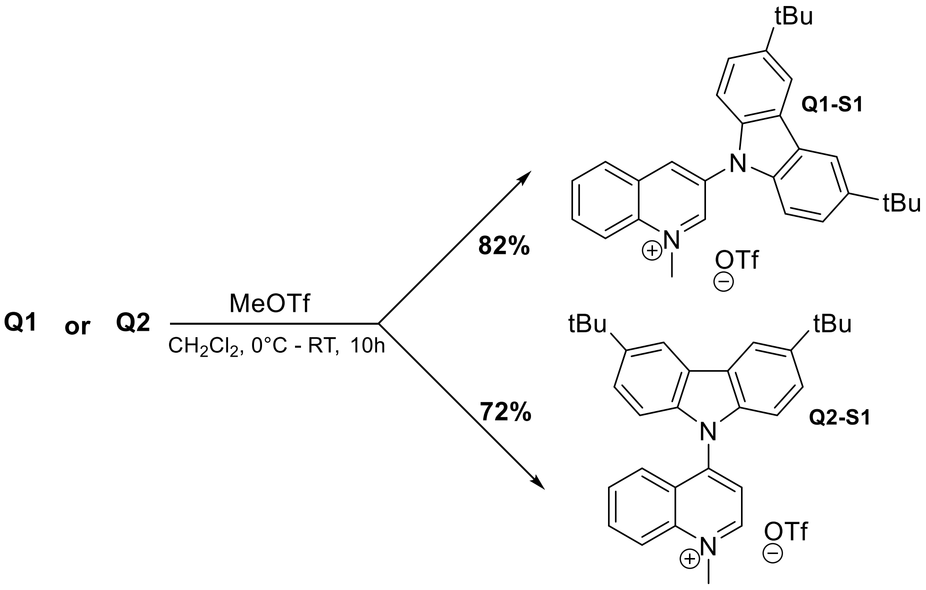

Scheme 4.3. Synthesis of compounds **Q1-S1** and **Q2-S1.**

Materials **Q1-S2** and **Q2-S2** were prepared following the modified synthetic procedure described in the literature[280] by the reaction between methyl iodide and **Q1** or **Q2**, respectively, in the microwave reactor (Scheme 4.4). Unlike the methylated compounds with triflate counter-ion (**Q1-S1** and **Q2-S1**), **Q1-S2** and **Q2-S2** do not exhibit AIE, but still demonstrate mechanochromism. The synthesis of **Q1-S3** and **Q2-S3** was attempted in the ion exchange reaction between $AgBF_4$ and **Q1-S2** or **Q2-S2**, respectively (Scheme 4.4). The product could not be purified from the silver halide contamination, and an alternative method was used (Scheme 4.5)[281].

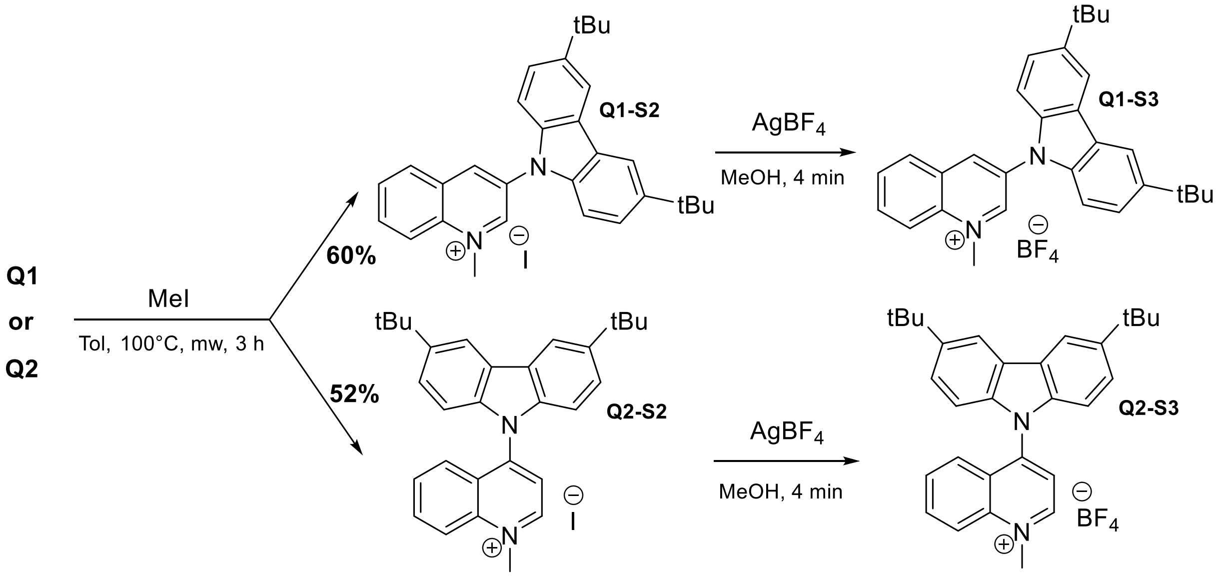

Scheme 4.4. Synthesis of **Q1-** and **Q2-S2**, and **Q1-** and **Q2-S3** materials.

Here the desired products **Q1-S3** and **Q2-S3** were prepared from **Q1** and **Q2**, respectively, using a one-step reaction with trimethyl orthoformate and ammonium tetrafluoroborate. The reaction was performed in the microwave reactor.

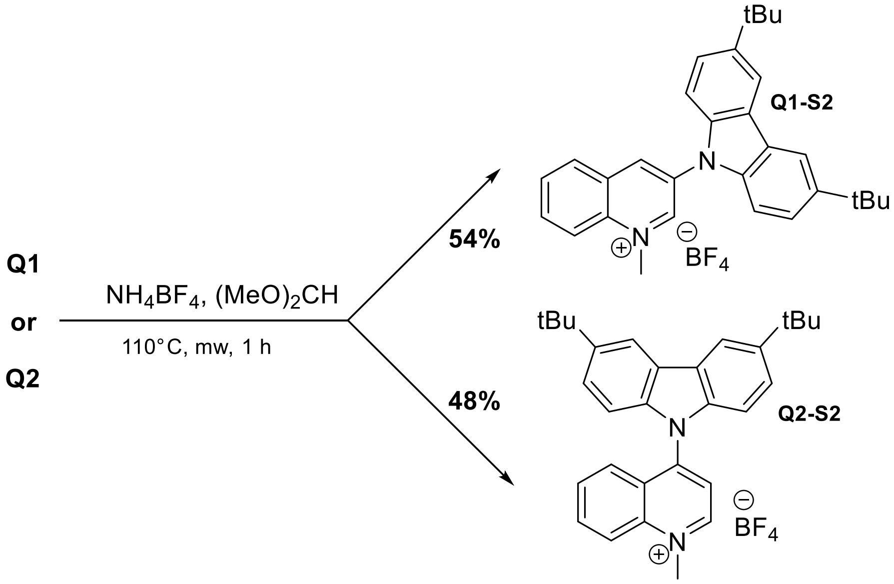

Scheme 4.5. Alternative synthetic route for the preparation of compounds **Q1-S3** and **Q2-S3**.

4.2.2 Electrochemical characterisation and thermal properties

The electrochemistry data are presented in Table 4.1. The cathodic and anodic peaks are shown for reversible, quasi-reversible (q-r) and irreversible (irr) processes.

Table 4.1. HOMO-LUMO levels and electrochemical bandgap $E_{g(CV)}$ for the **Q** series.

	E_{ox}	E_{red}	HOMO[c] (eV)	LUMO[c] (eV)	$E_{g(CV)}$ (eV)
Q1	0.87 1.06 (q-r)[a]	-1.80 (irr)[b]	-5.67	-3.00	2.67
Q2	0.89 1.14 (q-r)	-1.63 (irr)	-5.69	-3.17	2.52
Q1-S1	0.95	-1.31 (irr) -1.74 (irr)	-5.75	-3.49	2.26
Q2-S1	0.95	-1.27 (irr) -1.67 (irr)	-5.75	-3.53	2.22
Q1-S2	0.81 (irr) 0.96 (irr) 1.49	-0.75 (irr)	-5.61	-4.05	1.56
Q2-S2	0.55 (irr) 0.73 (irr) 1.57	-0.83 (irr)	-5.35	-3.97	1.38
Q1-S3	1.16	-1.09 (irr)	-5.96	-3.71	2.25
Q2-S3	1.19	-1.23 (irr)	-5.99	-3.57	2.42

[a] (q-r) denotes quasi-reversible; [b] (irr) denotes irreversible; [c] HOMO(LUMO) calculated from the peak of the corresponding redox wave and referenced to ferrocene.

The pairs of **Q1** and **Q2** derivatives demonstrate very similar electrochemical behaviour for all four sets of compounds. Materials **Q1** and **Q2** both show one reversible and one quasi-reversible oxidation peak (Figure 4.6, Table 4.1). The reduction demonstrates one irreversible peak. HOMO energies of materials are almost identical (-5.67 eV for **Q1** and -5.69 eV for **Q2**) while the LUMO energy is 0.17 eV higher for **Q1** material compared to **Q2** (-3.00 eV and -3.17 eV, respectively) which is probably due to a less efficient conjugation between carbazole and quinoline moiety for **Q1**.

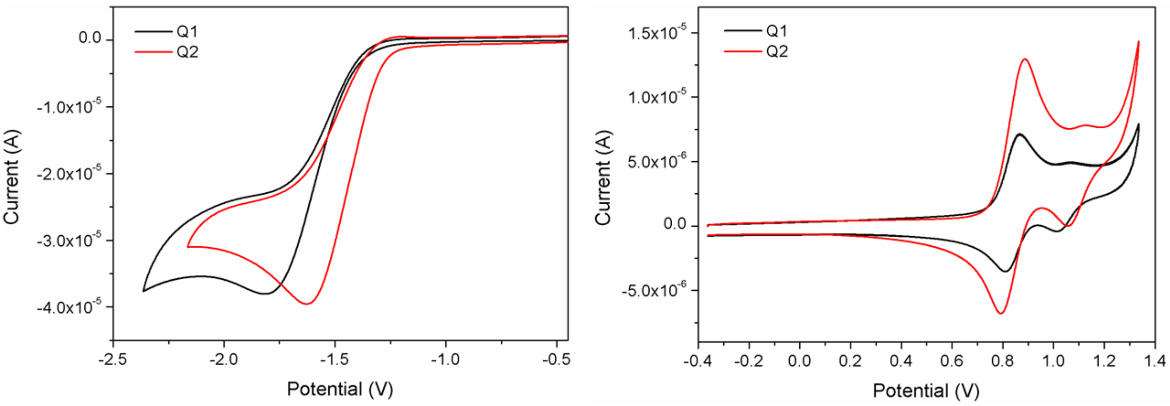

Figure 4.6. Reduction (left) and oxidation (right) curves from cyclic voltammetry of **Q1** and **Q2** referenced against the $E_{1/2}$ of the Fc/Fc$^+$ redox couple; 5·10^{-4} M solutions in 0.1 M *n*-Bu_4NPF_6 (CH_2Cl_2).

The oxidation of materials **Q1-S1** and **Q2-S1** demonstrates one reversible wave and the reduction shows two irreversible waves (Figure 4.7, Table 4.1). The methylated materials have lower $E_{g(CV)}$ (2.26 eV for **Q1-S1** and 2.22 eV for **Q2-S1**) compared to **Q1** (2.67 eV) and **Q2** (2.52 eV).

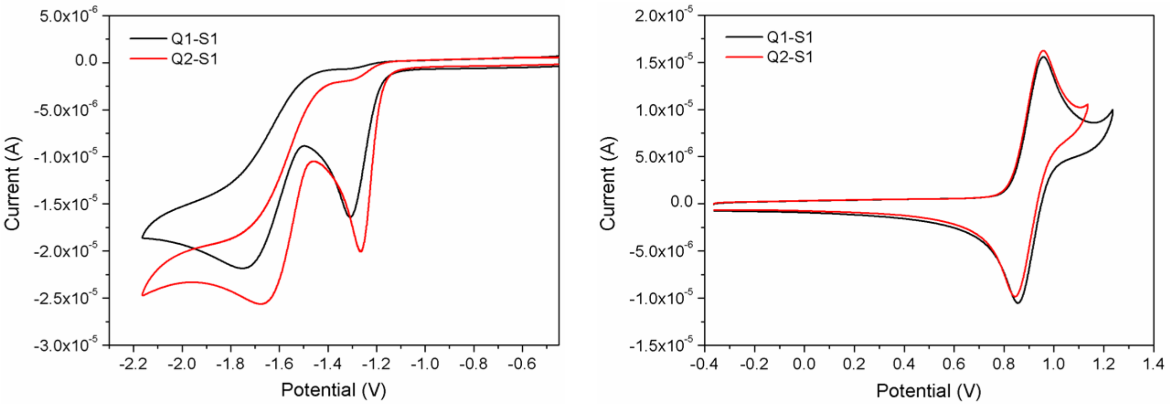

Figure 4.7. Reduction (left) and oxidation (right) curves from cyclic voltammetry of Q1-S1 and Q2-S2 referenced against the E1/2 of the Fc/Fc+ redox couple; 5·10-4 M solutions in 0.1 M n-Bu4NPF6 (CH2Cl2).

The materials **Q1-S2** and **Q2-S2** show one reversible and two irreversible oxidation peaks, and one irreversible reduction peak (Figure 4.8, Table 4.1). These compounds demonstrate the smallest $E_{g(CV)}$ (1.56 eV for **Q1-S2** and 1.38 eV for **Q2-S2**) out of the whole series.

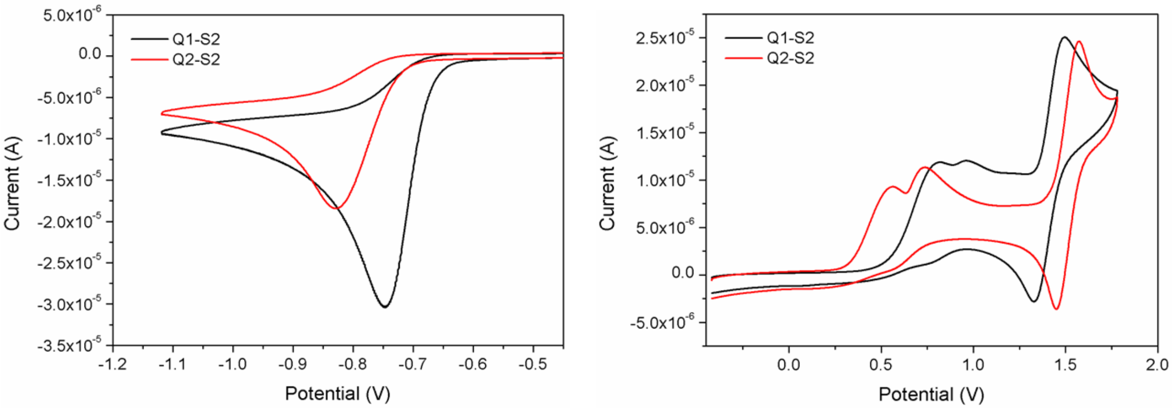

Figure 4.8. Reduction (left) and oxidation (right) curves from cyclic voltammetry of **Q1-S2** and **Q2-S2** referenced against the $E_{1/2}$ of the Fc/Fc$^+$ redox couple; $5\cdot10^{-4}$ M solutions in 0.1 M *n*-Bu_4NPF_6 (CH_2Cl_2).

For the compounds **Q1-S3** and **Q2-S3** there is one reversible oxidation peak and one irreversible reduction peak (Figure 4.9, Table 4.1). These compounds demonstrate the lowest HOMO energy levels in the series (≈ 6 eV).

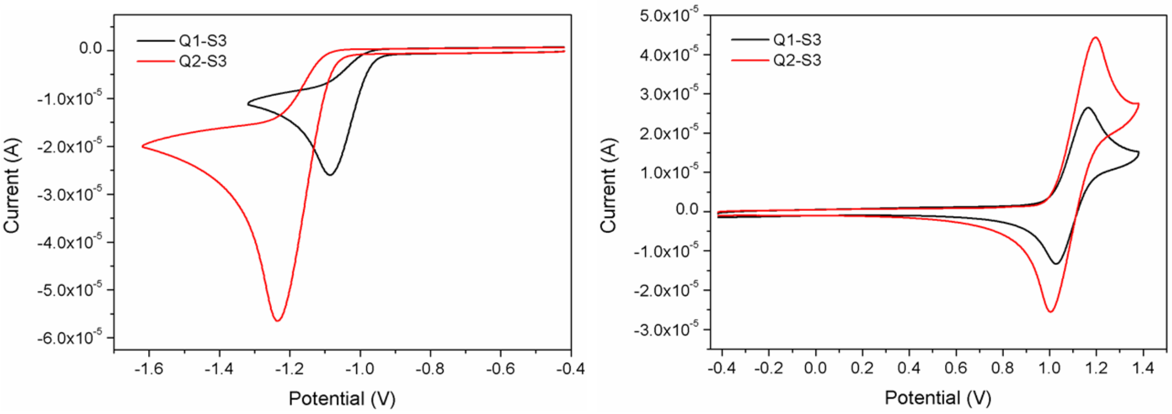

Figure 4.9. Reduction (left) and oxidation (right) curves from cyclic voltammetry of **Q1-S3** and **Q2-S3** referenced against the $E_{1/2}$ of the Fc/Fc$^+$ redox couple; $5\cdot10^{-4}$ M solutions in 0.1 M *n*-Bu_4NPF_6 (CH_2Cl_2).

Thermal properties of the materials were investigated using TGA and DSC (Table 4.2). All compounds demonstrate high thermal stability with 5% weight loss above 290 °C for **Q1**, **Q2,** and **Q1-** and **Q2-** derivatives with triflate and tetrafluoroborate counter-ions. The materials with iodine counter ions exhibited a slightly lower thermal stability with 5% weight loss at 211 °C for **Q1-S2** and 251 °C for **Q2-S2**. Some of the materials demonstrate thermal transitions when measured by differential scanning colorimetry (Table 4.2). Lower temperature transitions are most likely glass transitions (T_g). All salts exhibit mechanochromic properties which suggests that the conformational changes can occur in the solid state for these compounds. Thus, some of the higher temperature transitions (T_{st}) can be attributed to the solid-solid phase transformations.

Table 4.2. Thermal properties of the quinoline-based materials.

	Q1	**Q2**	**Q1-S1**	**Q2-S1**	**Q1-S2**	**Q2-S2**	**Q1-S3**	**Q2-S3**
5% weight loss (°C)	290	310	330	315	211	251	328	319
DSC transitions (°C)	-	92 (T_g)	91 (T_g)	110 (T_g) 251 (T_{st})	-	95 (T_g)	129 (T_g) 222 (T_{st}) 273 (T_{st})	-

4.2.3 Photophysics of quinoline derivatives

The photophysical properties of the compounds were investigated in solution and solid state. The measurements were performed by Dr Marc Etherington from the OEM group in Durham University. All **Q1-** and **Q2-**based salts demonstrate very similar absorption and emission profiles, so most of the measurements were performed only for **Q1-S1** and **Q2-S1** compounds.

4.2.3.1 Photophysical properties in solution

The emission and absorption for **Q1** and **Q2** were investigated in solutions of Methylcyclohexane (MCH), chloroform, 2-methyltetrahydrofuran (2-MeTHF) and dichloromethane (DCM). Due to the quenching of the emission for the salts, only the absorption spectra could be recorded for **Q1-S1** and **Q2-S1**.

The absorption spectra for **Q1** in most solvents demonstrates two strong and several weaker bands corresponding to π-π* transitions (Figure 4.10, Table 4.3). **Q1** is a blue emitter with the photoluminescence exhibiting bathochromic shifts of up to 100 nm in more polar solvents that indicates the charge-transfer character of the emission (Figure 4.10, Table 4.4).

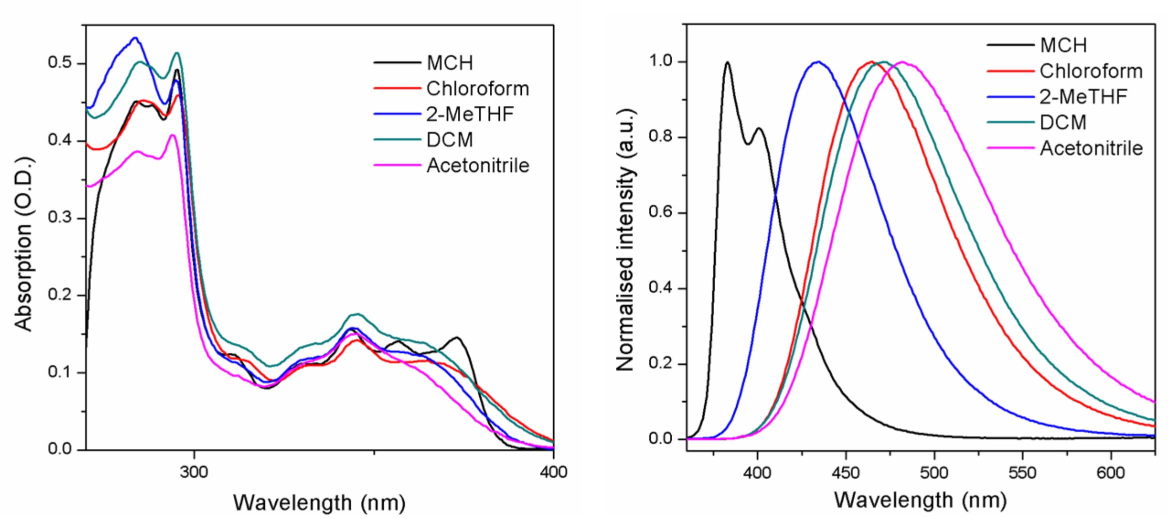

Figure 4.10. UV-vis absorption (left) and emission (right) spectra for **Q1** in solution.

The absorption spectra of **Q2** exhibits strong absorption band corresponding to π-π* transition and four weaker ones (Figure 4.11, Table 4.3). The emission is slightly red-shifted compared to **Q1**, but it also demonstrates similar bathochromic shifts in more polar solvents (Table 4.4).

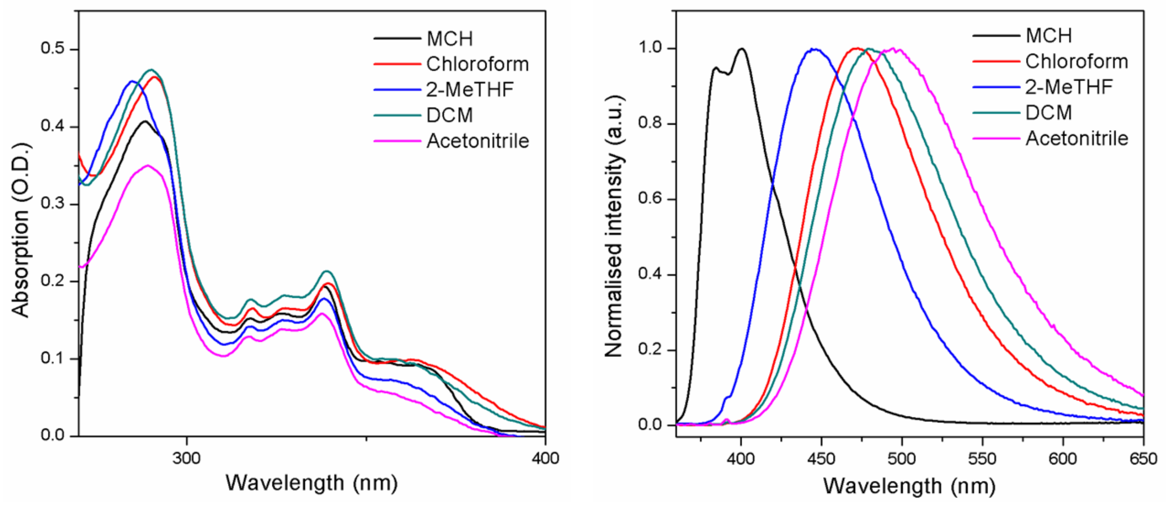

Figure 4.11. UV-vis absorption (left) and emission spectra (right) for **Q2** in solution.

Table 4.3. Absorption peaks (nm) for **Q1**, **Q2**, **Q1-S1** and **Q2-S1** in MCH, 2-MeTHF, dichloromethane and chloroform.

	Q1	**Q2**	**Q1-S1**[a]	**Q2-S1**[a]
MCH	284, *287*, 295, 310, 329, 343, 356, *373*	289, 316, 326, 337, 358	-	-
2-MeTHF	283, 295, 313, 329, 344, 363	285, 317, 327, 338, 360	294, 320, 334, 452	286, 322, 345, 450
Dichloromethane	284, 294, 314, 330, 344,364	289, 317, 327, 339, 359	290, 306, 319, 333, 493	284, 312, 324, 480
Chloroform	286, 295, 315, 330, 344, 368	291, 317, 327, 339, 365	292, 306, 321, 334, 493	285, 313, 325, 473
Acetonitrile	284, 294, 329, 344, 361	288, 317, 326, 338, 364	293,322, 333, 450	283, 318, 448

[a] compound insoluble in MCH

Table 4.4. Emission peaks (nm) for **Q1** and **Q2** in solutions of MCH, 2-MeTHF, dichloromethane and chloroform

	MCH	**2-MeTHF**	**Dichloromethane**	**Chloroform**	**Acetonitrile**
Q1	383	434	471	465	482
Q2	401	444	479	472	494

Compounds **Q1-S1** and **Q2-S1** are non-emissive in solution due to AIE, so only absorption spectra could be recorded for these materials. The compounds are insoluble in MCH, so the spectra were recorded in 2-MeTHF, dichloromethane and chloroform. Similarly to **Q1** the absorption spectra of **Q1-S1** exhibits several absorption bands between 290 nm and 334 nm. A new CT band emerges at a longer wavelength (around 450 nm in 2-MeTHF and acetonitrile, Figure 4.12-a, Table 4.3). The last band demonstrates almost 40 nm red-shift in dichloromethane and chloroform.

Q2-S1 demonstrates a very similar behaviour exhibiting a new CT band around 450 nm in 2-MeTHF and acetonitrile that is red-shifted in dichloromethane (30 nm) and chloroform (23 nm) (Figure 4.12-b, Table 4.3).

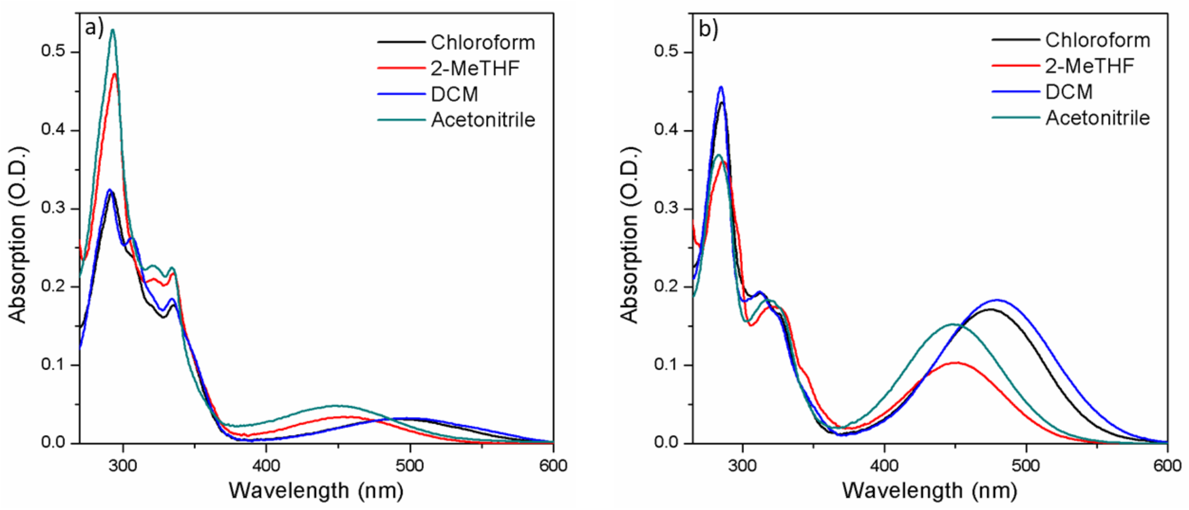

Figure 4.12. UV-vis absorption spectra for **Q1-S1** (a) and **Q2-S1** (b) in solution.

While in solution the luminescence is fully quenched for **Q1-S1** and **Q2-S1**, both materials emit strongly in solid state. The salts are insoluble in hexane, so it is possible to form nanoaggregates by adding hexane in THF solutions of materials. The intensity of the emission is increased for both **Q1-S1** and **Q2-S1** with the increase of the volume fraction of hexane (Figure 4.13). This confirms the AIE properties of the materials.

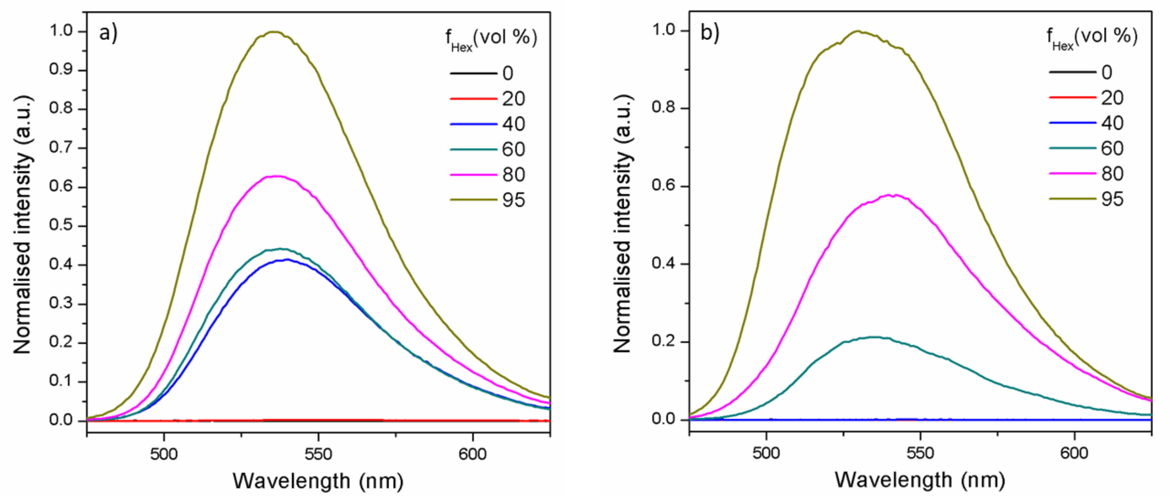

Figure 4.13. Photoluminescence spectra of **Q1-S1** (a) and **Q2-S1**(b) in THF/hexane mixtures with different hexane fractions (f_{Hex}). The excitation wavelength is 450 nm.

4.2.3.2 Photophysical studies in solid state

The emission and absorption spectra were recorded for all eight materials in PMMA film with 1 % w/w of compounds in the matrix.

Absorption spectra of materials **Q1** and **Q2** in PMMA films are very similar to those recorded in solution (Figure 4.14, Table 4.5). **Q1** shows two strong absorption π–π* transition bands at 286 nm and 296 nm, and three weaker bands between 330 nm and 366 nm. Compound **Q2** exhibits one strong absorption peak at 291 nm and four lower intensity bands between 318 nm and 361 nm. Both **Q1** and **Q2** emit light in a blue region with peaks at 407 nm and 412 nm, respectively (Figure 4.14, Table 4.5). The PLQY of materials in PMMA films is around 20% for both compounds.

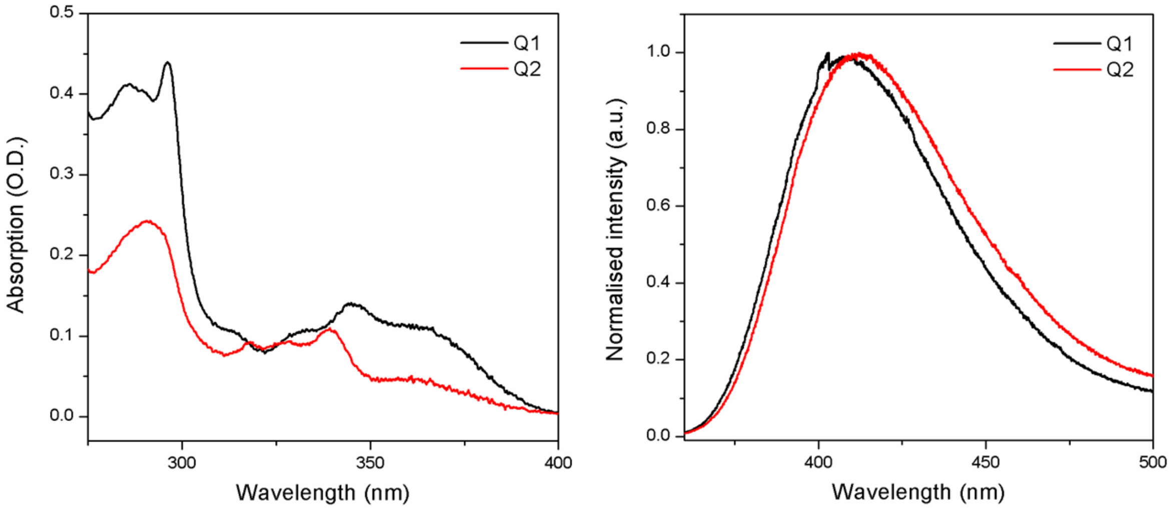

Figure 4.14. UV-vis absorption (left) and emission spectra (right) for **Q1** and **Q2** in PMMA film.

The absorption spectra for the methylated derivatives of **Q1** are nearly identical independently of the nature of the counter-ion (Figure 4.15-a, Table 4.5). **Q2** derivatives demonstrate similar behaviour (Figure 4.15-b, Table 4.5). All six salts are yellow emitters with photoluminescence peaks between 578 nm and 590 nm (Figure 4.16, Table 4.5).

Due to the similarity of the photophysical properties of the salts with different counter-ions, the more in-depth study was performed only on **Q1-S1** and **Q2-S1** compounds. These materials were also prepared in the highest yields, so they can be considered the best candidates for OLED applications.

For compounds **Q1-S1** and **Q2-S1** PLQY was recorded in both PMMA and neat film. The emission is quenched in PMMA matrix for both **Q1-S1** (13% in neat film and 4% in PMMA) and **Q2-S1** (34% in neat film and 13% in PMMA). This is due to the aggregation-induced nature of the emission of the materials.

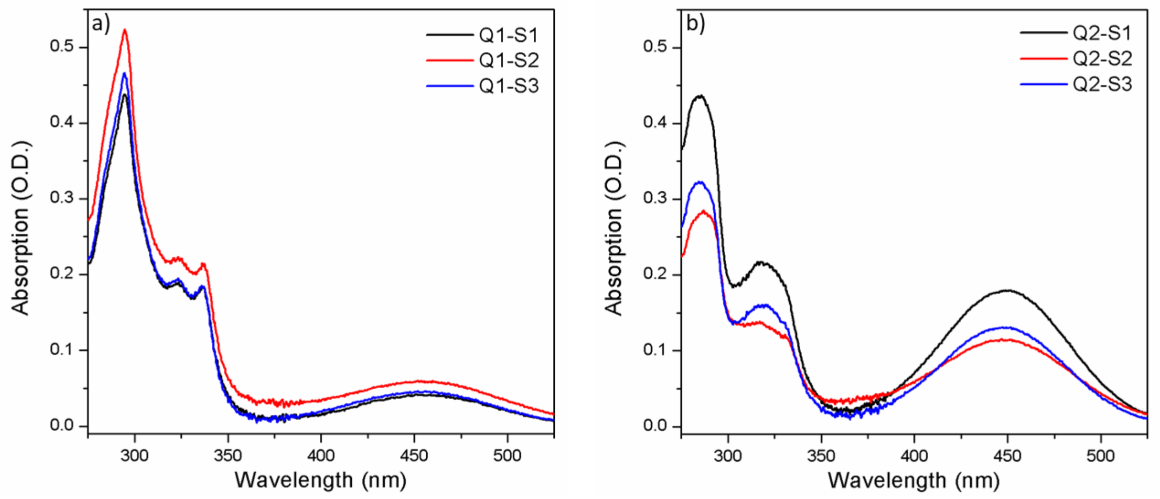

Figure 4.15. UV-vis absorption spectra for **Q1-**based (a) and **Q2-**based (b) salts in PMMA film.

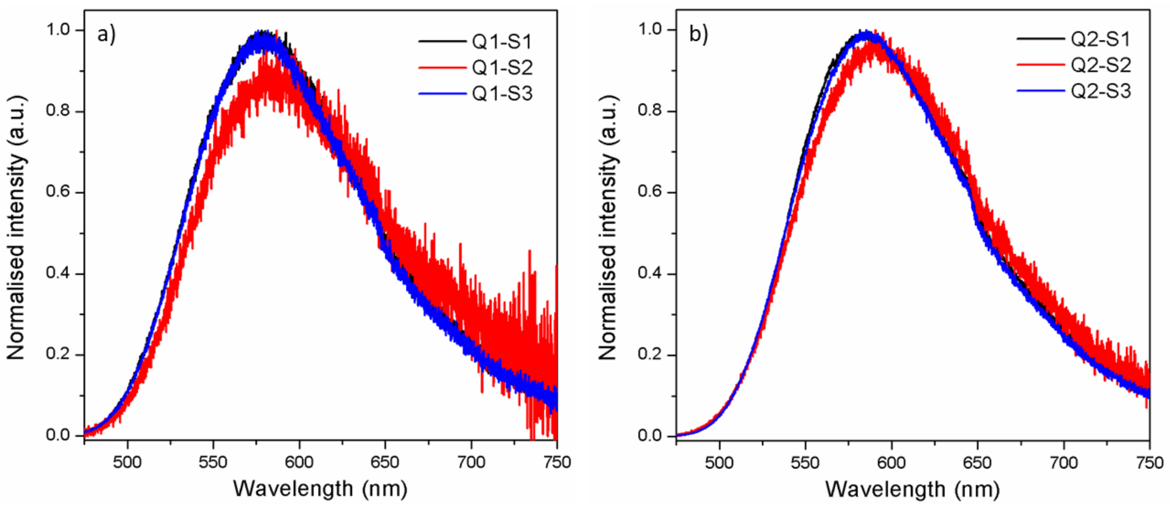

Figure 4.16. Photoluminescence spectra for **Q1-**based (a) and **Q2-**based (b) salts in PMMA film.

Table 4.5. Absorption and emission maxima for Q-series in PMMA matrix film.

	Q1	**Q2**	**Q1-S1**	**Q1-S2**	**Q1-S3**	**Q2-S1**	**Q2-S2**	**Q2-S3**
Absorption nm	286 296 330 344 366	291 318 329 339 361	295 323 337 451	295 323 336 452	294 325 336 455	285 321 449	287 317 446	286 318 449
Emission nm	407	412	578	586	581	581	590	585

Apart from PMMA the absorption and emission spectra of **Q1-S1** and **Q2-S1** were also recorded in neat films with acetonitrile and chloroform used as solvents for deposition, and in Zeonex and DPEPO matrix. Absorption spectra are very similar for different films of both **Q1-S1** (Figure 4.17) and **Q2-S1** (Figure 4.18).

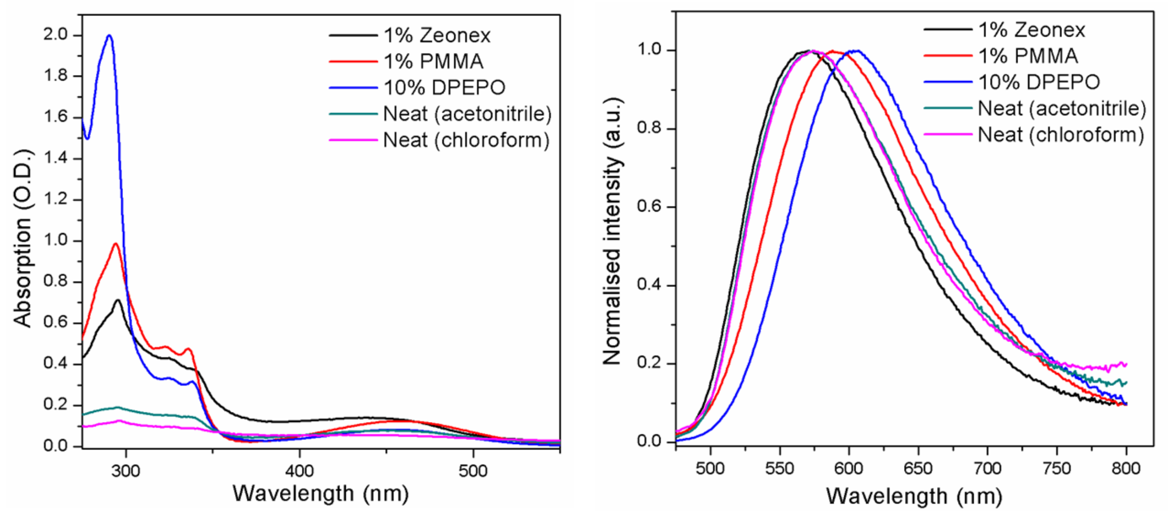

Figure 4.17. UV-vis absorption and emission spectra for **Q1-S1** in film.

For **Q1-S1** the photoluminescence spectra in a more polar, compared to Zeonex and PMMA, DPEPO matrix demonstrates red shift (Figure 4.17, Table 4.6), which confirms the CT character of the emission. Neat films have very similar emission profiles.

In the similar way, for **Q2-S1** the emission in DPEPO is more red-shifted than in Zeonex and PMMA (Figure 4.18, Table 4.6). However, unlike for **Q1-S1**, there is a drastic difference in the colour of the emission between neat films deposited from different solvents. The photoluminescence of the neat film deposited from acetonitrile is red-shifted for almost 70 nm compared to chloroform films. It is possible that due to a slightly slower evaporation rates of acetonitrile compared to chloroform there is the difference between the films morphology or even the conformation of the molecules of **Q2-S1** in film.

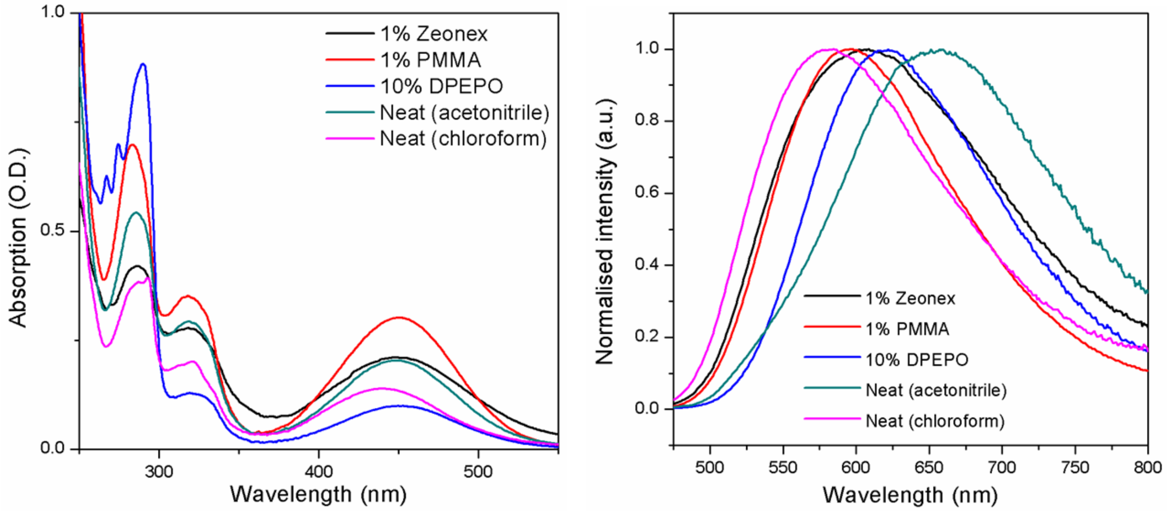

Figure 4.18. UV-vis absorption and emission spectra for **Q2-S1** in film.

Table 4.6. Emission peaks (nm) for **Q1-S1** and **Q2-S1** in films.

	1% Zeonex	**1% PMMA**	**10% DPEPO**	**Neat (acetonitrile)**	**Neat (chloroform)**
Q1-S1	571	588	607	574	575
Q2-S1	606	596	622	651	582

All salts exhibit mechanochromism, *i.e.* their colour changes after the mechanical force is applied. Due to the quenching of the luminescence for **Q1-S2** and **Q2-S2**, the emission spectra before and after grinding were recorded only for **Q1-S1**, **Q2-S1** (Figure 4.19-a,b), **Q1-S3** and **Q2-S3** (Figure 4.19-c,d). Initially all four materials are yellow emitters that after grinding exhibit the shift of the photoluminescence into the red region (Figure 4.19, Table 4.7). Both **Q1-S1** and **Q1-S3** demonstrate much smaller PL shift of 28 nm and 15 nm, respectively, compared to **Q2-S1** (43 nm) and **Q2-S3** (54 nm). This indicates that when tBu-CBZ is in the para-position in the molecule, the material exhibits more significant change in the packing after grinding than when tBu-CBZ is in the meta- position. This can also signify that the initial molecular structure of **Q2**-based compounds is more twisted than in **Q1**-based materials. This in its turn can lead to a reduced ST gap observed in **Q2-S1** (described below). However, more in-depths study of the materials' structures in powders is needed to confirm these hypotheses.

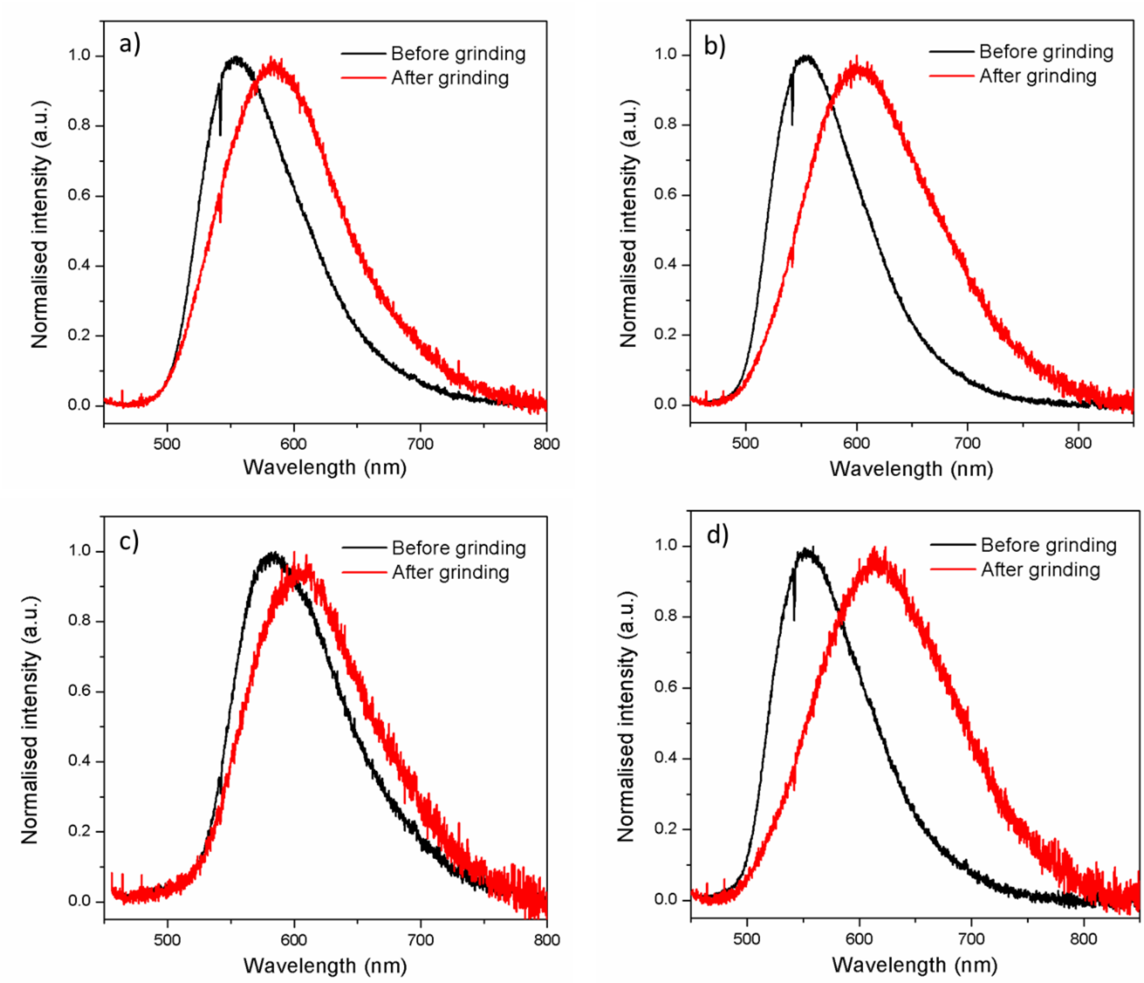

Figure 4.19. Emission spectra for powders of **Q1-S1** (a), **Q2-S1** (b), **Q1-S3** (c) and **Q2-S3** (c) before and after grinding.

Table 4.7. Emission maxima for powders of **Q1-S1**, **Q2-S1**, **Q1-S3** and **Q2-S3** before and after grinding.

	Q1-S1	**Q2-S1**	**Q1-S3**	**Q2-S3**
Before grinding nm	554	557	585	559
After grinding nm	582	600	600	613

4.2.3.3 Time-resolved measurements

Due to the AIE nature of **Q1-S1** and **Q2-S1** time-resolved measurements were first performed in neat films.

Both compounds show delayed emission at room temperature (RT) (Figure 4.20 for **Q1-S1** and Figure 4.21 for **Q2-S1**). For **Q1-S1** the lifetime of prompt fluorescence (~28 ns) and delayed fluorescence (~9 μs) are longer than those for **Q2-S1** (around 15 ns and 7 μs, respectively).

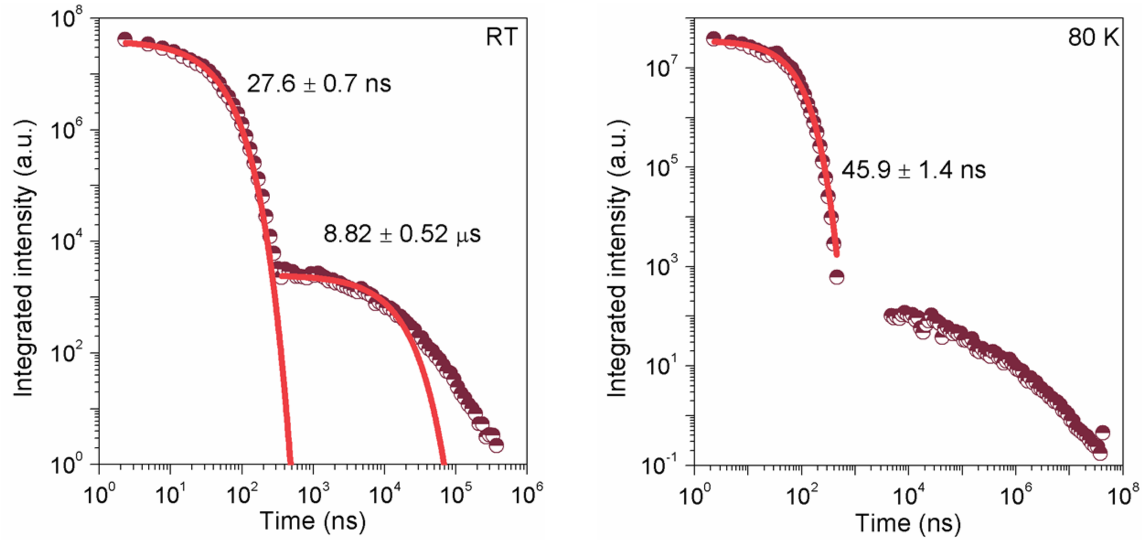

Figure 4.20. Photoluminescence decay for Q1-S1 at RT (left) and 80 K (right).

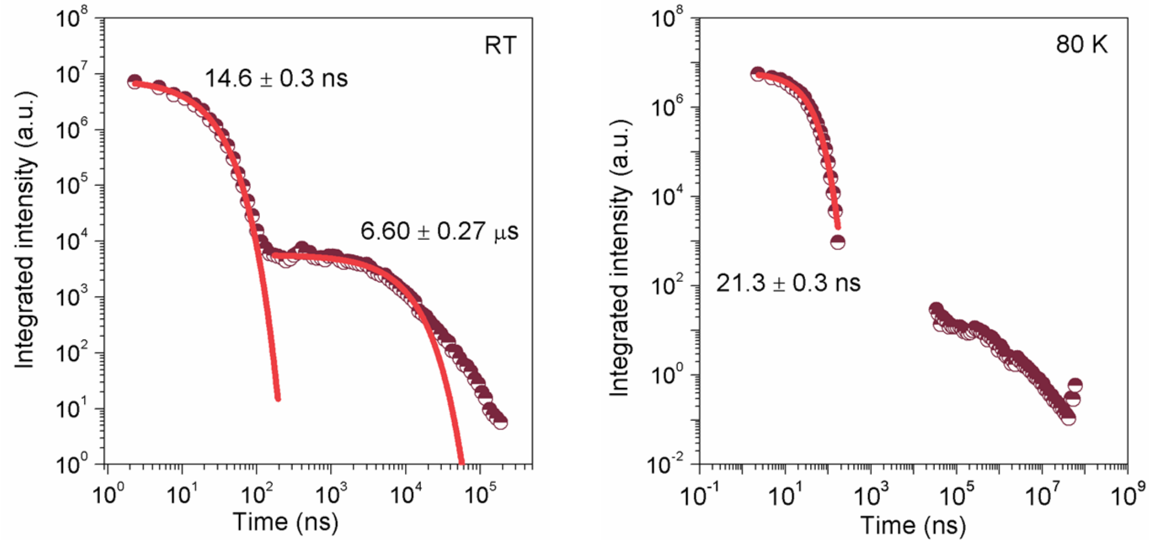

Figure 4.21. Photoluminescence decay for **Q2-S1** at RT (left) and 80 K (right).

As it was discussed in Chapter 2, it is possible to distinguish TADF from TTA by measuring the dependence of fluorescence intensity (I_F) on laser fluence (E_{ex}). The TTA process demonstrates quadratic power dependence at lower excitation dose with the slope n being 2 for $I_F \sim E_{ex}^n$ that turns into 1 at high triplet densities.[51,282] For TADF materials the dependence is always linear. The estimated slope for the **Q1-S1** is 1.29, which indicates that the emission results from TTA (Figure 4.22-a). For **Q2-S1** the power dependence is linear, thus fluorescence originates from TADF (Figure 4.22-b). This correlates well with the values of ΔE_{S-T} gaps for **Q1-S1** and **Q2-S1**.

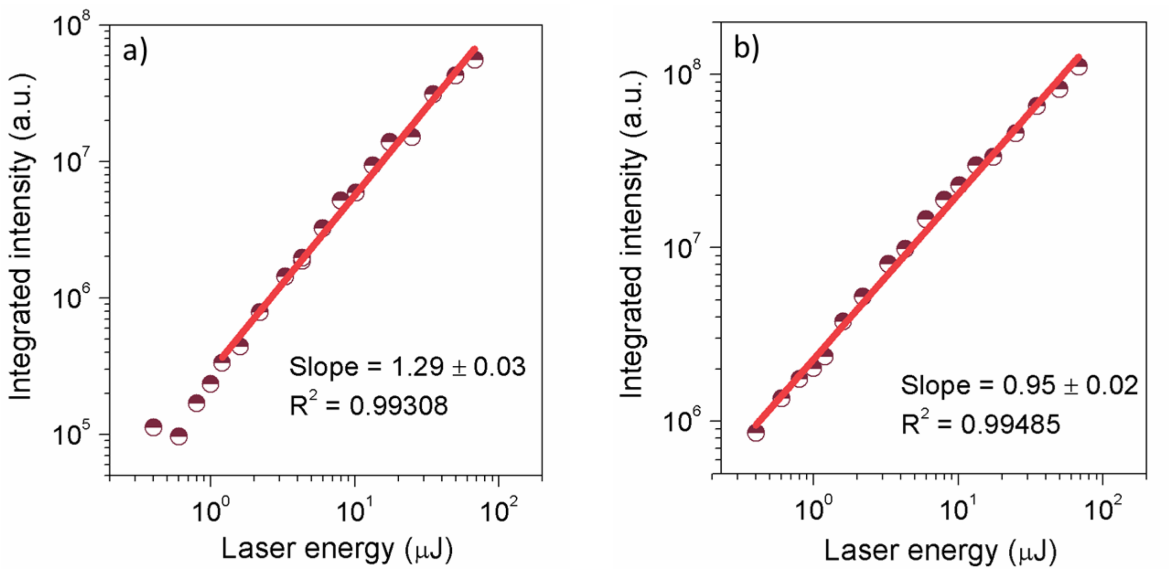

Figure 4.22. Power dependence of delayed fluorescence for **Q1-S1** (a) and **Q2-S1** (b) at 295 K.

Photoluminescence decay was also recorded at 80 K for both materials (Figure 4.20 for **Q1-S1** and Figure 4.21 for **Q2-S1**). In this case mainly prompt fluorescence and phosphorescence are observed for both compounds, the presence of the TTA component is however also possible in this case for **Q1-S1**.

For **Q1-S1** the spectra of prompt and delayed fluorescence are nearly identical at room temperature (Figure 4.23-a), and the prompt fluorescence spectra is slightly blue shifted at 80 K. At long delay around 40 ms phosphorescence spectra demonstrates a presence of a lower intensity high energy shoulder. It is most likely singlet emission, as its onset is very close to that of a PF at 80 K, and it most likely originates from TTA. This correlates well with the laser fluence measurements discussed above.

Likewise, for **Q2-S1** prompt and delayed fluorescence spectra are very similar at RT, and prompt fluorescence is slightly blue-shifted at 80 K (Figure 4.23-b). No additional peaks are however observed at longer delay at low temperature.

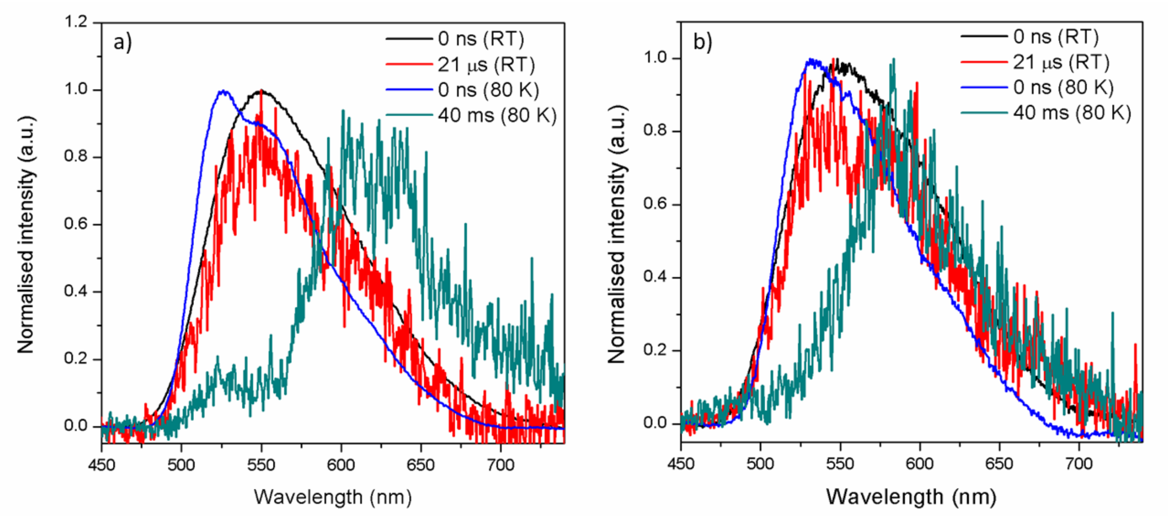

Figure 4.23. Time resolved spectra at RT and 80 K for **Q1-S1** (a) and **Q2-S1** (b).

The ^{1}CT and ^{3}LE energies for both samples were measured from the onset of the short wavelength-edge of the maximum fluorescence and phosphorescence peaks, respectively (Table 4.8). While the first singlet excited states ^{1}CT are nearly isoenergetic for **Q1-S1** and **Q2-S2** (2.51 eV), the energy of ^{1}LE triplet state is 0.17 eV lower for the **Q1-S1** (2.23 eV) compared to **Q2-S1** (2.40 eV). The ΔE_{S-T} is consequently is much smaller for **Q2-S1** (0.11 eV) compared to **Q1-S1** (0.28 eV). This in itself is a quite surprising outcome as one would expect **Q2-S1** with tBu-CBZ in para- position to have a better conjugation between donor and acceptor moieties and thus a larger overlap between HOMO and LUMO levels compared to **Q1-S1** where the communication between quinoline and tBu-CBZ situated in meta-position should be interrupted. This might indicate that other factors can influence the magnitude of the ΔE_{S-T} gap. It is also possible that in the solid state the twist between donor and acceptor moieties is stronger for **Q2-S1** than it is **Q1-S1**, which leads to a better separation of HOMO and LUMO for the former. This however still needs to be further confirmed by X-ray crystallography studies.

Table 4.8. The measured energies of ^{1}CT and ^{3}LE, respective ΔE_{S-T} and reverse intersystem crossing rates of **Q1-S1** and **Q2-S1** samples in neat film. Determined from the spectra recorded at 80 K.

Sample	**^{1}CT^a / eV**	**^{3}LE^a / eV**	**ΔE_{S-T} / eV**	**k_{rISC} ($\times 10^5$ s^{-1})**
Q1-S1	2.51 (2.25)	2.23 (1.98)	0.28	3.8
Q2-S1	2.51 (2.33)	2.40 (2.13)	0.11	1.2

^{a}Peak energies are in brackets.

4.2.4 Device fabrication

Electroluminescent properties of the material **Q2-S1** were also evaluated in OLED devices. All layers were thermally evaporated. For all devices ITO was used as a anode, N,N′-di(1-naphthyl)-N,N′-diphenyl-(1,1′-biphenyl)-4,4′- diamine (NPB) as an HIL, 4,4'-(Diphenylsilanediyl)bis(N,Ndiphenylaniline) (TSBPA) as an HTL, TPBi as an ETL, lithium fluoride (LiF) as an EIL, and aluminium (Al) as a cathode. An additional layer of Bis[2-(diphenylphosphino)phenyl]ether oxide (DPEPO) was used in half of the devices as HBL. Thus, two series of devices were fabricated, Dev 4.1 and Dev 4.2 with and without DPEPO layer, respectively. The structures of devices are presented in the Table 4.9.

Table 4.9. Device structure for Dev 4.1 and Dev 4.2 series.

Device series	Structure
Dev 4.1	2 ITO | NPB (40 nm) | TSBPA (10 nm) | **Q2-S1** (20 nm) | DPEPO (10 nm) | TPBi (40 nm) | LiF (1 nm) | Al (100 nm).
Dev 4.2	2 ITO | NPB (40 nm) | TSBPA (10 nm) | **Q2-S1** (20 nm) | TPBi (40 nm) | LiF (1 nm) | Al (100 nm).

Dev 4.2 demonstrates the best all round performance with a turn-on voltage of around 5.6 V and the maximum brightness of 519 cd m^{-2} (Figure 4.24, Table 4.10). The efficiency is however very low for both Dev 4.1 and Dev 4.2 (Figure 4.25) with a maximum EQE of 0.16% and 0.25%, and current efficiency of 0.21 cd A^{-1} and 0.20 cd A^{-1}, respectively. The NMR of the evaporated films suggests that some chemical modification occurs, so the emissive layer most likely consists of the products of a partial degradation of material **Q2-S1**. The evaporation occurs at around 250 °C, which is well below the temperature of thermal decomposition for **Q2-S1,** thus the reasons for the modifications occurring in the emissive layer upon thermal deposition should be further investigated.

Table 4.10. Performance of Dev 4.1 and Dev 4.2 OLED devices fabricated using **Q2-S1** as emitter.

Device series	Turn on voltage at 10 cd m^{-2} (V)	Brightness (cd m^{-2}) [a]	Current efficiency (cd A^{-1}) [a]	EQE (%)[a]
Dev 4.1	8.5	227 (15.0 V)	0.21 (10.0 V)	0.16
Dev 4.2	5.6	519 (10.5 V)	0.20 (8.0 V)	0.25

[a] Maximum performance

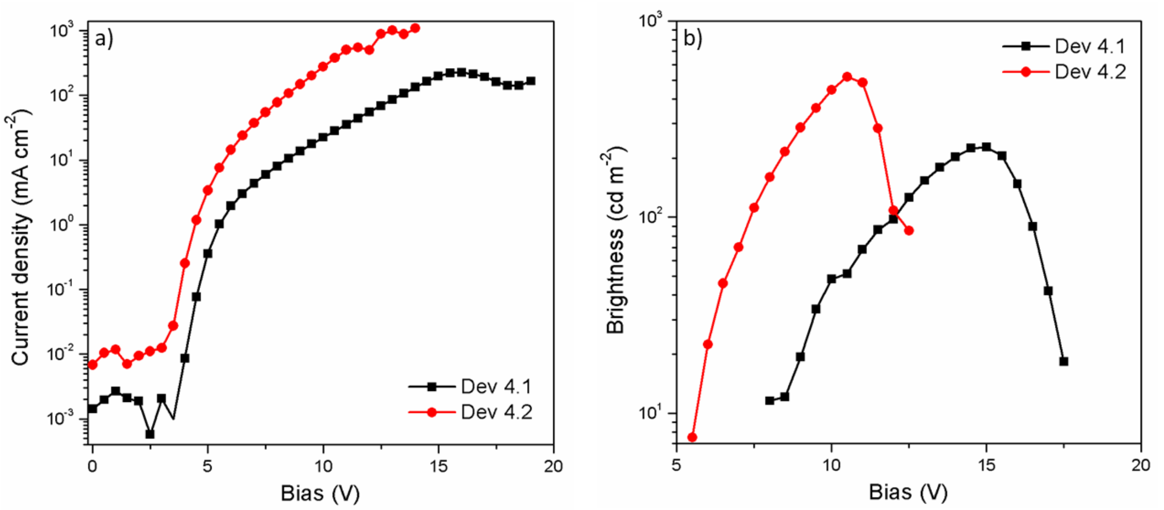

Figure 4.24. Current density vs. applied bias (a) and brightness vs. bias for Dev 4.1 and Dev 4.2.

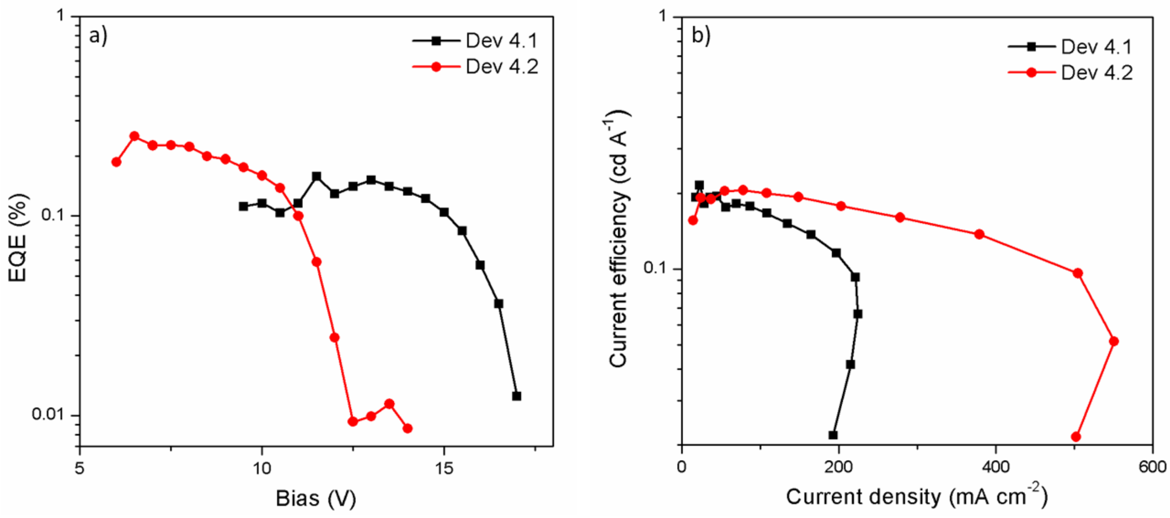

Figure 4.25. EQE vs. applied bias (a) and current efficiency vs. current density (b) for Dev 4.1 and Dev 4.2.

Both devices exhibit pink electroluminescence (Figure 4.26) with CIE (0.60, 0.40) for Dev 4.1 (EL peak at 632 nm) and CIE (0.52, 0.35) for Dev 4.2 (646 nm).

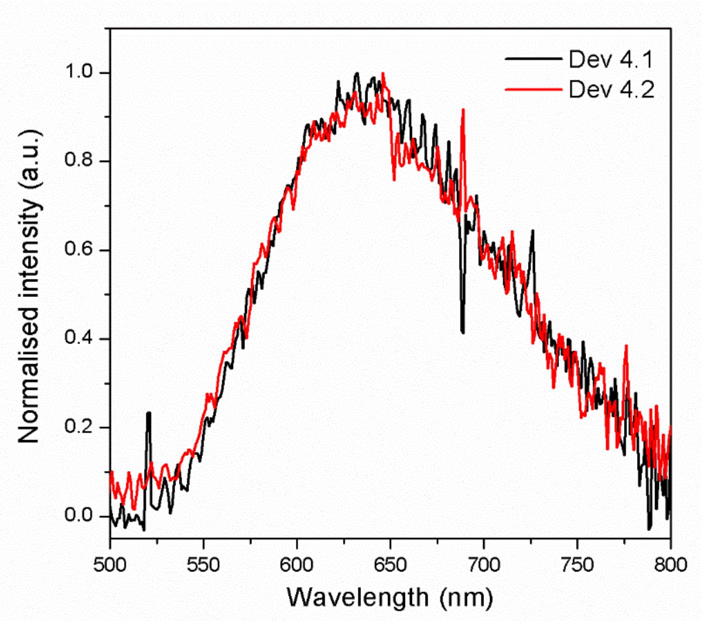

Figure 4.26. Electroluminescence spectra for Dev 4.1 and Dev 4.2.

4.3 Conclusions and future work

The materials presented in this chapter could be prepared *via* a simple two-step synthesis involving a relatively quick purification process. In total six new quinoline-based salts were synthesised. Initially only salts **Q1-S1** and **Q2-S1** with triflate counter-ion were prepared from **Q1** and **Q2** materials. Both have demonstrated mechanochromism and aggregation-induced emission. In order to investigate the influence of the counter-ion on the properties of the materials in the solid state four more compounds were prepared, **Q1-S2** and **Q2-S2** with iodide, and **Q1-S3** and **Q2-S3** with tetrafluoroborate counter-ions. **Q1-** and **Q2-** derivatives with different counter-ions demonstrate very similar absorption profiles. All compounds exhibit mechanochromism, the emission is however quenched for **Q1-S2** and **Q2-S2** most likely because of the heavy atom effect. Thus, excluding the materials containing heavy atom in the structure, the AIE and mechanochromism are observed in quinoline-based salts independently of the type of the counter-ion.

Time-resolved measurements were performed for the compounds **Q1-S1** and **Q2-S1**. Both materials exhibit delayed fluorescence, but despite of a very similar structure, **Q1-S1** shows TTA while **Q2-S1** is a TADF emitter. For **Q1-S1** the ΔE_{ST} gap is around 0.28 eV while it is 0.11 eV for **Q2-S1**. This implies that either in solid state the twist between donor and acceptor units is stronger for **Q2-S1** than it is for **Q1-S1** leading to a better HOMO-LUMO separation in **Q2-S1**, or apart from the orbital overlap there are other factors influencing the magnitude of the ΔE_{ST} gap that should be further investigated. To get a more in-depth understanding of the processes happening in materials in solid state the X-ray crystallography study will be carried out on the quinoline-based compounds in the future.

OLED devices containing material **Q2-S1** were prepared by thermal deposition. The performance of the devices was low with the maximum EQE of only 0.25%. Apparently during the thermal deposition in the vacuum chamber, the degradation of the material occurs. In the first instance the electroluminescent properties of materials should be tested in solution processed devices, and the conditions for the thermal evaporation should be further optimised. It would be also beneficial to carry out theoretical calculations for materials **Q1-S1** and **Q2-S1** that could possibly explain the reasons behind the difference in behaviour of materials.

Chapter 5. General conclusions and outlook

The main theme of this thesis was the synthesis and experimental investigation of organic luminescent materials. The principal goal was to apply these compounds in organic light-emitting diodes. Different methods of harvesting 100% of excitons via reverse intersystem crossing were explored in order to achieve high external quantum efficiencies in devices. In all cases the aim was to synthesise materials exhibiting thermally-activated delayed fluorescence (TADF). This was achieved for the compounds described in Chapters 2 and 4. While the materials in Chapter 3 did not demonstrate delayed fluorescence, the modification of the molecular structures could probably induce TADF in their analogues.

Chapter 2 describes the properties of two new TADF emitters H1-PXZ and H2-PXZ where di- or monoaza[5]helicene is used as an acceptor moiety. The helical structure of the materials induces a twist between the donor and acceptor and in both cases the ΔEST gap of the materials is close to zero, increasing the rISC rate. Additionally, the crystals of compound H1-PXZ have demonstrated an increase in PLQY when hexane is present in the crystal lattice. This also leads to an increased intensity of TADF emission. Both materials were also tested in OLED devices demonstrating EQEs of 1.5 % for H1-PXZ and 7.1 % for H2-PXZ. The relatively low performance of the devices can be explained by a low PLQY of the materials caused by the strong contribution of non-radiative processes in pentahelicenes. The use of higher helicenes can probably solve this problem. In the future, enantiopure helicenes could also be employed as dopants for TADF materials to induce circularly-polarised light. In total this is one of the first investigations of TADF materials in the crystalline state, and a better understanding of TADF processes in crystals could contribute to the development of organic light-emitting transistors in the future.

In Chapter 3 the synthesis and photophysical properties of four new materials A0, A, A1 and A2 with truxene-BT-truxene cores are presented. All four materials are fluorescent emitters with photoluminescence mainly influenced by the core unit. Material A2 demonstrates a significant luminescence quenching in the solid state compared to the three other compounds which is most likely caused by intermolecular interactions giving rise to the formation of non-emissive excited species, such as excimers, in the solid state. Compound A1 was used for the preparation of fluorescent OLEDs. The highest EQE for the devices was 0.6 %. It is possible to improve the performance of the devices by introducing an appropriate ETL. The material A1 was also used as a colour converter for inorganic blue LEDs. The organic layer successfully absorbs blue light and re-emits green light which results in a shift of the emission colour closer to the Planckian locus. However, pure white light could not be achieved in this case, and to improve the colour quality the emission of the material should have an additional longer wavelength component. This could probably be accomplished by extension of the π-conjugation in the materials. The truxene-BT-truxene unit can also be used as a core building block for the preparation of a variety of dendrimers. Thus, by introducing oligofluorene arms it is possible to prepare materials suitable for lasing or visible-light communication applications.

A new approach to the design of materials with delayed fluorescence was investigated in Chapter 4. First, two donor-acceptor materials Q1 and Q2 were prepared. Here quinoline was used as an acceptor and 3,6-di-tert-butylcarbazole (tBu-CBZ) as a donor. The methylation of the sp2 nitrogen atom of the quinoline acceptor moiety can induce either TTA or TADF in donor-acceptor systems depending on the position of the donor substituent in the molecule. Thus, when the 3,6-di-tert-butylcarbazole donor unit is in the meta- position the material exhibits TTA (Q1-S1), and in the para- position it shows TADF (Q2-S1). The methylated salts were prepared with different counter-ions such as triflate (Q1-S1 and Q2-S1), iodide (Q1-S2 and Q2-S2) and tetrafluoroborate (Q1-S3 and Q2-S3). All six materials show very similar photophysical properties and exhibit mechanochromism with the colour of the powders shifting from yellow to orange after grinding. However, for compounds containing an iodide counter-ion, fluorescence is quenched due to a heavy atom effect. Q1-S1, Q2-S1, Q1-S3 and Q2-S3 all demonstrate aggregation-induced emission. Due to that, the properties of the materials were mainly investigated in the solid state. In total, the methylation of non-DF materials is an interesting new method for the preparation of materials exhibiting delayed fluorescence. The compound Q2-S1 was also used for the preparation of OLED devices. The performance of the materials was however quite low, as some chemical modification occurs upon thermal deposition of the compounds. Thus, the procedure for the fabrication of OLED devices from the methylated compounds should be optimised. It is also possible to test the performance of the materials in solution-processed devices to avoid thermal degradation of the compounds. Additionally, analysis by X-ray crystallography will be carried out in the near future to give a better understanding of the influence of the molecular structure of the materials on their photophysical properties.

Overall, this work demonstrates a variety of emissive materials that can be used in organic light-emitting diodes. It also gives an idea of the main challenges arising during the design, synthesis and application of thermally-activated delayed fluorescence materials. In all cases the emphasis was on the investigation of the properties of materials in the solid state as in each described series of materials the intermolecular interactions significantly influence the photophysical behaviour of the compounds. Helicenes in Chapter 2 demonstrate a change in PLQY depending on the packing of molecules in the crystal lattice. In Chapter 3 it is shown that intermolecular interactions can significantly affect the lifetime of luminescence as well as the rate of radiative decay. Aggregation-induced emission and mechanochromism demonstrated by quinoline-based materials presented in Chapter 4 are directly dependent on the relative position of the molecules in the solid. The main goal of this body of work was to synthesise compounds exhibiting TADF, which was achieved in most cases. The materials however have additionally demonstrated some unexpected behaviour in the solid state. This proves that it is particularly interesting in the design of optoelectronic compounds to try and predict not only the properties of the isolated molecule, but also the properties arising in the bulk material. Considering that most optoelectronic materials are used as films in semiconducting devices, a better understanding of the materials' behaviour in the solid state is required, and the future direction of this work could be a more systematic investigation of the processes occurring in the solid state for such compounds.

Chapter 6. Experimental

General experimental details

Unless stated otherwise, all reagents were purchased from Sigma Aldrich, TCI, Alfa Aesar or Fluorochem and used without further purification. Tetrakis(triphenylphosphine)palladium(0) was synthesised and stored under an inert atmosphere.

Dry solvents were obtained from a solvent purification system (SPS 400 Innovative Technologies) with alumina as a drying agent. Glassware was dried in an oven at 120 °C overnight.

Solvents were removed using a rotary evaporator with vacuum supplied by low vacuum pump, and, when necessary, a high vacuum was used to remove residual solvent.

Microwave syntheses were performed using Biotage Initiator Classic microwave heating apparatus in 10-20 mL vials. Photochemical reactions were conducted under a Black-Ray B-100AP High intensity UV Lamp with 365 nm wavelength.

Thin layer chromatography (TLC) was performed using Merck Silica gel 60 F_{254} TLC plates. Column chromatography was carried out on silica gel Zeoprep 60 Hyd (40-63 μm mesh).

Melting points were determined using a Stuart Scientific SMP1 Melting Point apparatus.

^1H and ^{13}C NMR spectra were recorded on a Bruker AVIII 400 apparatus at 400 MHz and 100 MHz, respectively, or a Bruker AV500 at 500MHz and 125MHz, respectively. NMR data are presented in the following order: chemical shifts (δ) in ppm; multiplicity as singlet (s), doublet (d), triplet (t), quartet (q), multiplet (m); coupling constants (*J)* in Hz. Multiplets are reported over the range they appeared (in ppm). Signals were sharp unless stated as broad (br). Samples were referenced to residual solvent peaks.

Z : E ratios for the products of Wittig olefination were determined after purification by column chromatography by comparing integrals for related signals in ^1H NMR spectra.

MS MALDI-TOF analyses were run on a Shimadzu Axima-CFR spectrometer (mass range 20-150000Da); GCMS were run on a Thermo Finnigan Polaris Q spectrometer using electron ionization (EI) mode (mass range 50-650Da). The high resolution mass measurements were performed on a Waters Xevo G2S instrument (ASAP-TOF-MS) or on a Finnigan MAT 95XP (EI).

Thermal analysis

Thermogravimetric analyses (TGA) were performed on a Perkin-Elmer Thermogravimetric Analyser TGA7 or on a NETZSCH TG 209 F3 - Tarsus thermogravimeter under a constant flow of Argon or Nitrogen (20 mL/min). The temperature was increased at a rate of 10 °C/min from 40 °C to 500 °C.

Differential scanning calorimetry was carried out on a TA Instruments Q1000 with a RC-90 refrigerated cooling unit attached or on a NETZSCH DSC 214 – Polyma differential scanning calorimeter. The test procedure was a standard Heat-Cool-Reheat, and the temperature range was from 20 °C to 300 °C at 10 °C min^{-1}.

X-ray crystallography

For the X-ray diffraction measurements a suitable crystal was selected and mounted on a MITIGEN holder in perfluoroether oil on a Rigaku 007HF diffractometer equipped with Varimax confocal mirrors and an AFC11 goniometer and HyPix 6000HE detector. The crystal was kept at T = 100K during data collection. Using Olex2 the structure was solved with the ShelXT structure solution program, using the Intrinsic Phasing solution method. The model was refined with version 2014/7 of ShelXL using Least Squares minimisation.

Electrochemical characterisation

Cyclic voltammetry measurements were performed using a CH Instruments 660E electrochemical workstation with iR compensation at a scan rate of 0.1 V s^{-1}. The electrochemical cell comprised of glassy carbon, platinum wire and silver wire as working, counter and reference electrodes respectively. The experiments were conducted at room temperature in degassed (Ar) 0.1 M solutions of tetrabutylammonium tetrafluoroborate in anhydrous solvent with *ca.* $5\cdot10^{-4}$ M concentrations of the studied compounds.

All measurements were referenced against the half-wave potential ($E_{1/2}$) of the Fc/Fc+ redox couple. The cathodic and anodic peaks are shown for reversible and irreversible (irr) processes. The HOMO and LUMO levels were determined according to the following equations:

LUMO = – (Eox + 4.8) (eV); HOMO = – (Ered + 4.8) (eV)

Optical properties

UV-Vis absorption spectra were recorded on a Shimadzu 2600 spectrophotometer fitted with an integrating sphere and results were normalised to λmax. Fluorescence spectroscopy measurements were conducted on a Perkin Elmer LS45 fluorescence spectrometer, an Edinburgh Instruments FLS980 fluorescence spectrometer or a Jobin Yvon FluoroMax-3 fluorescence spectrometer. Thin films for recording PL spectra were prepared by spin-coating technique utilizing a SPS-Europe Spin150 Spin processor using 2.5 mg/mL solutions of compounds in THF on pre-cleaned quartz substrates (UQG optics) or by drop casting of 1 mg/mL solutions on quartz substrates.

Photoluminescence quantum yields of degassed solutions and films in Chapter 2 were determined using an integrated sphere (Edinburgh Instruments) coupled to a FLS980 spectrometer and calibrated with two standards: quinine sulfate in 0.1M H_2SO_4 and rhodamine 6G in ethanol. Photoluminescence and photoluminescence quantum yield of crystals in Chapter 2 were recorded in an integrating sphere using a QEPro matrix spectrometer (Ocean Optics). For the materials in Chapter 3 all photoluminescence quantum yields measurements were performed in air. Photoluminescence quantum yield of powders in Chapter 3 were recorded with a Hamamatsu Quantaurus-QY Plus Absolute PL quantum yield spectrometer. Excitation was at the specified wavelengths for each measurement and was obtained from a Xe lamp that was coupled to a motorised monochromator. PLQY was calculated by the system according to the method reported by Suzuki *et al*.[283] Photoluminescence quantum yield of films and solutions in Chapter 3 were recorded using a calibrated integrating sphere[284] attached to a USB 2000 spectrometer and Gooch & Housego spectrometer. The excitation light was produced by a Quartz Tungsten Halogen lamp and the emission light was collected by an Ocean Optics USB 2000 spectrometer.

Phosphorescence (PH), prompt fluorescence (PF), and delayed fluorescence (DF) spectra and fluorescence decay curves were recorded using nanosecond gated luminescence and lifetime measurements (from 400 ps to 1 s) using either third harmonics of a high energy pulsed Nd:YAG laser emitting at 355 nm (EKSPLA) or a N2 laser emitting at 337 nm. Emission was focused onto a spectrograph and detected on a sensitive gated iCCD camera (Stanford Computer Optics) having sub-nanosecond resolution. PF/DF time resolved measurements were performed by exponentially increasing gate and integration times. Temperature-dependent experiments were conducted using a continuous flow liquid nitrogen cryostat (Janis Research) under nitrogen atmosphere, while measurements at room temperature were recorded in vacuum in the same cryostat.

Photoluminescence decay curves of materials in Chapter 3 were recorded by time-resolved single photon counting method using an Edinburgh Instruments FLS980 photoluminescence spectrometer and PicoQuant LDH-D-C-375 laser as the excitation source. The fit was convolved within the instrument response and compared to the data. Least squares fitting was used to iterate the fit parameters until the best fit was found.

The mechanochromic emission measurements for Chapter 4 were performed by exciting the samples with a UV torch of emission peak 410 nm and collecting the emission into an optical fibre attached to an Ocean Optics USB 4000 spectrometer with a 500 ms integration time. LabView software was used to interface with the spectrometer and collect the data. The measurements were performed before and after the sample was ground in a pestle and mortar. Due to the nature of the measurement emission intensities cannot be directly compared.

OLED devices fabrication and characterisation

OLEDs described in Chapter 2 were fabricated by a spin-coating / evaporation hybrid method. The hole injection layer (Heraeus Clevios HIL 1.3N), electron blocking/hole transport layer (PVKH), and emitting layer (PVK:PBD with 5% of dopant) were spin-coated, whereas the electron transport/hole blocking layer (TPBi) and cathode (LiF/Al) were evaporated. Devices of 4x2mm pixel size were fabricated. PVK – poly(9-vinylcarbazole) (MW = 90 000, Acros Organics), PVKH – poly(9-vinylcarbazole) (MW = 1 100 000, Sigma Aldrich), PBD - 2-(biphenyl-4-yl)-5-(4-*tert*-butylphenyl)-1,3,4-oxadiazole (99%, Sigma Aldrich), TPBi - 2,2',2''-(1,3,5-Benzinetriyl)-tris(1-phenyl-1-*H*-benzimidazole) (sublimed, LUMTEC), LiF (99.995%, Sigma Aldrich), and aluminium wire (99.9995%, Alfa Aesar) were purchased from the companies indicated in parentheses. OLED devices were fabricated using pre-cleaned indium-tin-oxide (ITO) coated glass substrates after ozone plasma treatment with a sheet resistance of 20 Ω cm^{-2} and ITO thickness of 100 nm. Heraeus Clevios HIL 1.3N was spin-coated and annealed on a hotplate at 200 ˚C for 3 min to give a 45 nm film. The electron blocking/hole transport layer (PVKH) was spun from chloroform:chlorobenzene (95:5 *v/v*) (3 mg/mL) and annealed at 50 ˚C for 5 min to give a 10 nm film. The emitting layer was spun from toluene solution of PVK:PBD (60:40 *w/w*) and dopant with a total concentration of host of 10 mg/mL. The solution was spun onto the

PVKH layer and then annealed at 50 ˚C for 5 min giving a 32 nm film. All solutions were filtered immediately before application using a PVDF or PTFE syringe filter with 0.45 µm pore size (excepting the PVKH solution). All other organic and cathode layers were thermally evaporated using a Kurt J. Lesker Spectros II deposition system at 10^{-6} mbar. All organic materials and aluminium were deposited at a rate of 1 Å s^{-1}. The LiF layer was deposited at 0.1-0.2 Å s^{-1}. Characterisation of OLED devices was conducted in a 10 inch integrating sphere (Labsphere) coupled with a USB spectrometer (Ocean Optics) and connected to a Source Measure Unit.

The devices fabricated in Chapter 3 were prepared using the procedure described below. Pre-patterned ITO slides (7 Ω/sq, 15 mm × 15 mm × 1.1 mm, KINTEC) were cleaned with deionised water, acetone and isopropanol in an ultrasonic bath for 5 minutes before treatment with UV–ozone for 2 minutes. This method has been shown to improve the hole injection of ITO and the performance of devices in general.[285] PEDOT:PSS (Heraeus P VP AL 4083) was spin-coated onto the pre-cleaned ITO substrates at 3000 rpm and annealed at 120 °C for 20 minutes, before cooling to room temperature. These substrates were transferred into a glove box where all the subsequent fabrication steps and measurements were performed. Solutions of compound **A1** were prepared using toluene or chloroform with varying concentrations at 1000 rpm. For compound **A1**, a solution with concentration of 20 mg/mL was found to be optimum and hence was used to continue other characterisation measurements such as annealing. The spin-coated films were annealed for 20 minutes at temperatures of 50, 100 and 150 °C. After annealing, these films were transferred into a thermal evaporator attached to the glove box for evaporation of the electrodes. An active area of 1.5 × 3.5 mm was obtained by evaporation of 40 nm of calcium and 60 nm of aluminium electrodes through a shadow mask at the base pressure of 1 × 106 mbar. JVL characteristics were measured inside the glove box with a light-tight box attached. A Keithley Semiconductor Characterisation System (SCS) 4200 was used to bias the OLEDs. Luminance measurements were performed by using a Macom L203 photometer with a calibrated silicon photodetector and a photopic filter. These calibrations can be traced back to the National Physical Laboratory, London standards. Wavelength dependent electroluminescence spectra were measured by using an Ocean Optics USB2000+ spectrometer under an ambient atmosphere and a Keithley 2450 was used to bias the OLEDs for these measurements.

The OLEDs discussed in Chapter 4 were fabricated on patterned ITO coated glass (VisionTek Systems) with a sheet resistance of 15 Ω/sq. Oxygen-plasma cleaned substrates were loaded into a Kurt J. Lesker Super Spectros deposition chamber, and both the small molecule **Q2-S1** and cathode layers thermally evaporated at pressure below 10^{-7} mbar. The materials used for the production of the devices were: N,N′-di(1-naphthyl)-N,N′-diphenyl-(1,1′-biphenyl)-4,4′- diamine (NPB) as hole injection layer (HIL), 4,4'-(diphenylsilanediyl)bis(N,N-diphenylaniline) (TSBPA) as hole transporting layer (HTL) and TPBi as electron transporting layer (ETL), lithium fluoride (LiF) as electron injection layer, and aluminium (Al) as cathode. An optional Bis[2- (diphenylphosphino)phenyl]ether oxide (DPEPO) hole blocking layer (HBL) was used in half of the devices to test the charge balance. NPB and DPEPO were purchased from Sigma Aldrich and sublimed before use. TSBPA and POT2T were purchased from Lumtec and used as received. TPBi was purchased from Lumtec and sublimed before use.

Freshly evaporated devices were encapsulated under inert atmosphere using UV-curable epoxy (DELO Katiobond) along the outer edges of the active area with a glass coverslip. Devices were then transferred into a calibrated 10-inch integrating sphere (Labsphere) and their electrical properties measured using an Agilent Source Measure Unit (6632B). Emission spectra were simultaneously measured using a calibrated fibre coupled spectrometer (Ocean Optics USB4000).

Hybrid LEDs fabrication

The light-emitting diodes used with organic colour converter in hybrid LEDs were supplied by Plessey Semiconductors Ltd, Roborough, UK. Their emission wavelength is around 445 nm, and they consist of blue-emitting GaN-on-Si LED. The forward current for the LEDs is 25 mA. Electroluminescence measurements of the LEDs were performed at room temperature with a Keithley 236 source measure unit as a current source. The LEDs were placed in an integrating sphere (Labsphere illumina®plus 600/610, diameter 25 cm) coupled to a spectrometer (CDS-610, wavelength accuracy <0.5 nm) with a 600 µm diameter single core fibre cable. The system is corrected for its response using a calibrated spectral and luminous flux standard (SCL-600). Chromaticity coordinates (CIE 1931) and correlated colour temperature (CCT) were calculated from the response-corrected spectra.

Tetrakis(triphenylphosphine) palladium (0)

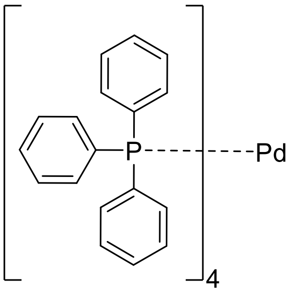

Palladium (II) chloride (1 g, 5.64 mmol, 1 eq.) and triphenylphosphine (7.4 g, 28.2 mmol, 5 eq.) were added to a two-neck flask fitted with a filter stick and connected to a second two-neck flask. Anhydrous DMSO (80 mL) was added and the mixture was heated until the solution turned orange (160 °C, ~30 min). Hydrazine monohydrate (1.1 mL, 22.56 mmol, 4 eq) was then added and the solution left to cool to room temperature with stirring. After 15 minutes of stirring a large amount of precipitate had formed. The reaction set up was inverted and DMSO removed from the second flask. The crude product was washed successively with anhydrous methanol (2×100 mL) and anhydrous diethyl ether (2×100 mL), then dried under vacuum in the filter stick. The product was obtained as a bright yellow solid (5.9 g, 91%).

Compound 2.2

(2-Chloroquinolin-3-yl)methanol

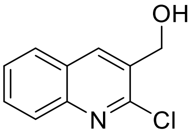

To a solution of 2-chloroquinoline-3-carboxaldehyde **2.1** (6 g, 31.3 mmol) in a mixture of MeOH (100 mL) and THF (100 mL) was added sodium borohydride (1.78 g, 47 mmol) at 0 °C, and the mixture was stirred for 30 min. The reaction mixture was quenched with water and diluted with Et_2O. The organic layer was separated, washed with brine (250 mL), dried over $MgSO_4$, and concentrated under reduced pressure giving **2.2** (5.7 g, 93%) as a white solid: mp 168-170 °C; m/z (EI-GCMS) calculated for $C_{10}H_8ClNO$ 193.03, found m/z = 193 [M^+]; ^1H NMR (400MHz, DMSO-d_6): 8.47 (s, 1H), 8.09 (d, *J* = 8.1 Hz, 1H), 7.96 (d, *J* = 8.1 Hz, 1H), 7.79 (t, *J* = 8.4 Hz, 1H), 7.65 (t, *J* = 8.1, 1H), 4.70 (d, *J* = 3.7 Hz, 2H). ^{13}C NMR (100 MHz, $CDCl_3$): δ 148.39, 146.00, 135.86, 133.89, 130.13, 127.87,127.46, 127.22, 127.16, 59.88. This was consistent with previously published data.[210]

Compound 2.3

3-(Bromomethyl)-2-chloroquinoline

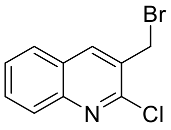

A mixture of (2-chloroquinolin-3-yl)methanol **2.2** (5.7 g, 29.4 mmol) and tetrabromomethane (14.6 g, 44.2 mmol) in dry dichloromethane (100 mL) was cooled to 0 °C, and a solution of triphenylphosphine (11.6 g, 44.2 mmol) in dry dichloromethane (50 mL) was added dropwise. The reaction mixture was stirred at room temperature for 8 h, then quenched with water. The organic layer was separated, washed with brine (250 mL), dried over $MgSO_4$, and concentrated under reduced pressure. The crude product was purified by column chromatography on silica gel, eluting with ethyl acetate : hexane (1:4) giving **2.3** as a pale-yellow solid (5.1 g, 67%): mp 120-122 °C; m/z (EI-GCMS) calculated for $C_{10}H_7BrClN$ 254.95, found m/z = 254.9 [M^+]; ^1H NMR (400MHz, $CDCl_3$): δ 8.29 (s, 1H), 8.06 – 8.04 (m, 1H), 7.88 – 7.86 (1H, m), 7.84 – 7.76 (1H, m), 7.64 – 7.59 (1H, m), 4.81 (s, 1H). ^{13}C NMR (100 MHz, $CDCl_3$): δ 149.57, 146.92, 138.83, 138.25, 130.61, 129.10, 127.87, 127.05, 126.70, 29.28. This was consistent with previously published data.[210]

Compound 2.4

((2-Chloroquinolin-3-yl)methyl)triphenylphosphonium bromide

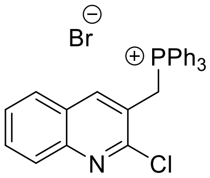

A mixture of 3-(bromomethyl)-2-chloroquinoline **2.3** (2 g, 7.8 mmol) and triphenylphosphine (6.1 g, 23.4 mmol) was dissolved in toluene (100 mL) and refluxed for 12 h, then cooled to room temperature. The solid was filtered, washed with hexane (200 mL) and dried under vacuum to give product **3** as a white powder (3.25 g, 80%): mp 254-255 °C; m/z (MALDI-TOF) calculated for $C_{28}H_{22}ClNP$ [M - Br] 438.12, found 438.20 [M^+]; ^1H NMR (400MHz, $CDCl_3$): δ 8.72 (d, *J* = 3.5 Hz, 1H), 7.93 (d, *J* = 8.3 Hz, 1H), 7.87 – 7.77 (m, 10H), 7.75 (t, *J* = 7.7 Hz, 1H), 7.71 – 7.64 (m, 6H), 7.55 (t, *J* = 7.6 Hz, 1H), 6.02 (d, *J* = 14.4 Hz, 2H). ^{13}C NMR (100 MHz, $CDCl_3$): δ 150.55, 150.50, 146.60, 142.58, 142.52, 134.88, 134.85, 133.82, 133.81, 130.90, 129.99, 129.87, 127.80, 127.56, 127.14, 126.56, 126.53, 119.71, 119.63, 117.26, 116.40, 27.97, 27.49. This was consistent with previously published data.[210]

Compound 2.5

1,2-Bis(2-chloroquinolin-3-yl)ethene

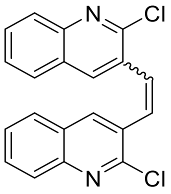

A mixture of phosphonium salt **2.4** (3 g, 5.7 mmol) and sodium hydride (608 mg, 14.5 mmol) was dissolved in dry dichloromethane (50 mL). A solution of 2-chloroquinoline-3-carbaldehyde **2.1** (923 mg, 4.8 mmol) in dry dichloromethane (20 mL) was added dropwise over 30 min. The reaction mixture was stirred at room temperature overnight, then quenched with water (150 mL), extracted with dichloromethane (2×200 mL), dried over $MgSO_4$ and concentrated under reduced pressure. The crude product was purified by column chromatography on silica gel, eluting with ethyl acetate : hexane (1:2) giving the product **2.5** as a pale yellow solid (1.5 g, 88%, Z/E ≈ 10:1): mp 218-220 °C; m/z (EI-GCMS) calculated for $C_{20}H_{12}Cl_2N_2$ 350.04, found 350.1 [M^+]; ^1H NMR (400MHz, $CDCl_3$): *cis-isomer:* δ 8.00 (dd, *J* = 7.49 Hz, 2H), 7.83 (s, 2H), 7.69 (ddd, *J* = 8.5, 6.7, 1.6 Hz, 2H), 7.53 – 7.38 (m, 4H), 7.09 (s, 2H). ^{13}C NMR (100 MHz, $CDCl_3$): δ 149.77, 146.48, 137.82, 130.22, 128.54, 128.30, 127.71, 127.07, 126.74, 126.29. This was consistent with previously published data.[210]

Compound 2.6

2,5-Dichlorodibenzo[a,k][3,8]phenanthroline

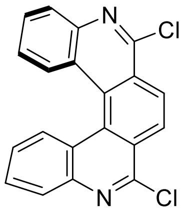

The compound **2.5** (450 mg, 1.28 mmol) was dissolved in dry toluene (300 mL) then iodine (163 mg, 1.28 mmol) added. Nitrogen was bubbled through the solution for 30 min, then propylene oxide (45 mL) added. The reaction mixture was irradiated under a UV lamp

(Black-Ray® B-100AP High intensity UV Lamp, 365 nm) for 36 h, then washed with $Na_2S_2O_3$ aqueous solution (2×100 mL), water and brine, dried over $MgSO_4$, and concentrated under reduced pressure. The crude product was purified by column chromatography on silica gel, eluting with ethyl acetate : hexane (1:6) giving the product **2.6** as a yellow solid (380 mg, 85%): mp 254-256 °C; m/z (MALDI-TOF) calculated for $C_{20}H_{10}Cl_2N_2$ 348.02, found 348.98 [M^+]; ^1H NMR (400MHz, $CDCl_3$): δ 8.61 (s, 2H), 8.46 (d, *J* = 8.4 Hz, 2H), 8.19 (dd, *J* = 8.3, 1.1 Hz, 2H), 7.76 (ddd, *J* = 8.3, 7.0, 1.3 Hz, 2H), 7.41 (ddd, *J* = 8.4, 7.0, 1.3 Hz, 2H). ^{13}C NMR (100 MHz, $CDCl_3$): δ 150.34, 143.92, 131.31, 129.82, 128.33, 127.00, 126.56, 125.98, 125.53, 123.40. This was consistent with previously published data.[210]

Compound H1-PXZ

2,5-Di(10H-phenoxazin-10-yl)dibenzo[a,k][3,8]phenanthroline

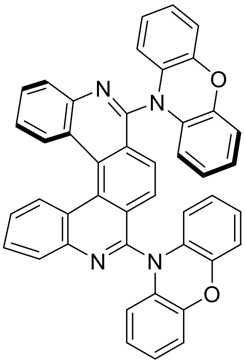

A mixture of palladium (II) acetate (37 mg, 0.16 mmol), caesium carbonate (1.24 g, 3.8 mmol), phenoxazine (159 mg, 0.87 mmol) and **2.6** (170 mg, 0.54 mmol) was dissolved in dry toluene. A 1M solution of tri-*tert*-butylphosphine in toluene (0.35 mL) was added next and the solution was bubbled with nitrogen for 30 min. The reaction mixture was heated at 100 °C in a microwave for 2 h, then filtered through celite, washed with toluene (200 mL) and concentrated under reduced pressure. The crude product was purified by column chromatography on silica gel, eluting with ethyl acetate : hexane (1:7) giving product **H1-PXZ** as a dark-red solid (115 mg, 45%): mp >360 °C; m/z (MALDI-TOF) calculated for $C_{44}H_{26}N_4O_2$ 642.21, found 642.15 [M^+]; HRMS (ASAP-TOF-MS) calculated for $C_{44}H_{26}N_4O_2+H^+$ 643.2134, found 643.2134 [$M+H^+$]; ^1H NMR (400MHz, $CDCl_3$): δ 8.80 (dd, *J* = 8.5, 0.9 Hz, 2H), 8.43 (s, 2H), 8.36 (dd, *J* = 8.3, 1.1 Hz, 2H), 7.86 (ddd, *J* = 8.3, 7.0, 1.3 Hz, 2H), 7.59 (ddd, *J* = 8.4, 7.0, 1.4 Hz, 2H), 6.83 (dd, *J* = 7.9, 1.0 Hz, 4H), 6.73 (t, *J* = 7.3 Hz, 4H), 6.55 (br s, 4H), 6.16 (br s, 2H), 6.03 (br s, 2H). ^{13}C NMR (100 MHz, $CDCl_3$):

δ 149.75, 144.93, 143.75, 133.35, 132.55, 129.46, 129.24, 127.02, 126.84, 126.11, 125.20, 124.14, 122.90, 122.09, 115.62, 113.48.

Compound 2.8

(Naphthalen-2-ylmethyl)triphenylphosphonium

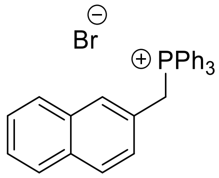

This was synthesised according to the general procedure leading to **2.4**. 2-(bromomethyl)naphthalene **2.7** (1.5 g, 6.7 mmol), triphenylphosphine (4.34 g, 20.3 mmol), and toluene (100 mL) were used. Phosphonium salt **2.8** was obtained as a white solid (3.1 g, 95%): mp 246-248 °C; m/z (MALDI-TOF) calculated for $C_{29}H_{24}P$ [M - Br] 403.16, found 403.25 [M^+]; ^1H NMR (400MHz, $CDCl_3$): δ 7.82 – 7.75 (m, 9H), 7.72 (d, *J* = 7.8 Hz, 1H), 7.65 – 7.60 (m, 6H), 7.57 (m, 3H), 7.47 – 7.39 (m, 2H), 7.20 (dt, *J* = 8.4, 1.7 Hz, 1H), 5.65 (d, *J* = 14.5 Hz, 2H). ^{13}C NMR (100 MHz, $CDCl_3$): δ 134.43, 134.40, 134.05, 133.94, 132.49, 132.21, 130.79, 130.71, 129.74, 129.71, 129.67, 129.55, 128.19, 128.15, 127.91, 127.39, 127.06, 126.05, 125.87, 124.04, 123.95, 117.90, 117.05, 30.84, 30.38. This was consistent with previously published data.[203]

Compound 2.9

2-Chloro-3-(2-(naphthalen-2-yl)vinyl)quinoline

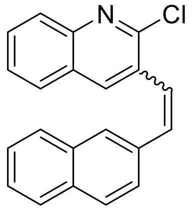

This was synthesised according to the general procedure leading to **2.5.** Phosphonium salt **2.8** (3 g, 6.2 mmol), sodium hydride (0.65 g, 15.5 mmol), 2-chloroquinoline-3-carbaldehyde **2.1** (0.99 g, 5.2 mmol), and dichloromethane (120 mL) were used. The product **2.9** was obtained as a pale yellow solid (1.31 g, 72%, Z/E ≈ 10:1): mp 112-114 °C; m/z (EI-GCMS) calculated for $C_{21}H_{14}ClN$ 315.08, found 314.9 [M^+]; HRMS (EI) calculated for $C_{21}H_{14}ClN$ 315.08, found 315.10 [M^+]; *cis-isomer:* ^1H NMR (400MHz, $CDCl_3$): δ 8.04 (dd, *J* = 8.5, 0.7 Hz, 1H), 7.79 – 7.67 (m, 4H), 7.60 (d, *J* = 8.5 Hz, 1H), 7.51 (dd, *J* = 8.1, 1.4 Hz, 1H), 7.49

– 7.43 (m, 3H), 7.26 (dd, *J* = 8.7, 1.6 Hz, 1H), 7.06 (d, *J* = 12.2 Hz, 1H), 6.86 (dd, *J* = 12.1, 0.7 Hz, 1H). ^{13}C NMR (100 MHz, $CDCl_3$): δ 150.15, 146.32, 138.01,137.98, 132.98, 132.89, 132.84, 132.25, 129.88, 129.84, 129.50, 128.13, 127.72, 127.38, 127.17, 127.05, 126.52, 126.44, 125.80, 125.78, 125.09. *trans-isomer:* ^{1}H NMR (400MHz, $CDCl_3$): δ 8.48 (s, 1H), 8.04 (d, *J* = 9.2 Hz, 1H), 7.97 (s, 1H), 7.92 – 7.83 (m, 5H), 7.73 (d, *J* = 7.0 Hz, 1H), 7.69 (d, *J* = 13.9 Hz, 1H), 7.62 – 7.58 (m, 1H), 7.54 – 7.51 (m, 2H), 7.41 (d, *J* = 16.2 Hz, 1H).

Compound 2.10

2-Chloronaphtho[2,1-k]phenanthridine

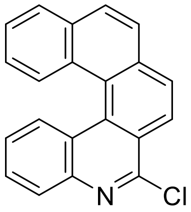

This was synthesised according to the general procedure leading to **2.6**. Compound **2.9** (500 mg, 1.58 mmol), iodine (216 mg, 1.7 mmol), propylene oxide (55 mL, 790 mmol), and toluene (600 mL) were used. Product **2.10** was obtained as a pale-yellow solid (300 mg, 60%): mp 222-224 °C; m/z (EI-GCMS) calculated for $C_{21}H_{12}ClN$ 313.07, found 313.1 [M^+]; ^{1}H NMR (400MHz, $CDCl_3$): δ 8.54 (d, *J* = 8.5 Hz, 1H), 8.47 (d, *J* = 8.5 Hz, 2H), 8.16 (dd, *J* = 8.3, 1.0 Hz, 1H), 8.06 (dd, *J* = 10.9, 8.6 Hz, 2H), 8.01 (dd, *J* = 8.0, 1.2 Hz, 1H), 7.93 (d, *J* = 8.6 Hz, 1H), 7.69 (ddd, *J* = 8.3, 7.0, 1.4 Hz, 1H), 7.61 (ddt, *J* = 8.1, 4.6, 2.3 Hz, 1H), 7.35 (qdd, *J* = 10.5, 3.6, 0.9 Hz, 2H). ^{13}C NMR (100 MHz, $CDCl_3$): δ 150.76, 143.52, 134.35, 133.19, 132.86, 132.62, 132.41, 129.97, 129.75, 128.85, 128.58, 128.21, 127.97, 127.61, 127.43, 126.74, 126.07, 125.96, 125.42, 124.73, 124.03. This was consistent with previously published data.[286]

Compound H2-PXZ

10-(Naphtho[2,1-k]phenanthridin-2-yl)-10H-phenoxazine

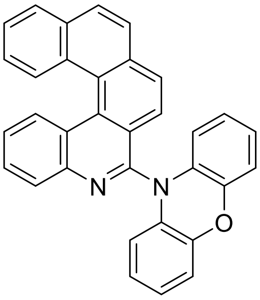

This was synthesised according to the general procedure leading to **H1-PXZ.** Palladium (II) acetate (36 mg, 0.16 mmol), caesium carbonate (1.21 g, 3.73 mmol), phenoxazine (195 mg, 1.06 mmol), **2.10** (167 mg, 0.53 mmol), 1M solution of tri-*tert*-butylphosphine in toluene (0.34 mL), and toluene (8 mL) were used. The product **H2-PXZ** was obtained as a yellow solid (120 mg, 48%): mp 336-338 °C; m/z (MALDI-TOF) calculated for $C_{33}H_{20}N_2O$ 460.16, found 460.12 [M^+]; HRMS (ASAP-TOF-MS) calculated for $C_{33}H_{20}N_2O+H^+$ 461.1653, found 461.1653 [$M+H^+$]; ^1H NMR (400MHz, $CDCl_3$): δ 8.70 (d, *J* = 8.4 Hz, 1H), 8.63 (d, *J* = 8.5 Hz, 1H), 8.38 (d, *J* = 8.4 Hz, 1H), 8.30 (dd, *J* = 8.3, 1.1 Hz, 1H), 8.08 (d, *J* = 8.5 Hz, 1H), 8.04 (dd, *J* = 8.1, 1.0 Hz, 1H), 7.92 (dd, *J* = 14.3, 8.5 Hz, 2H), 7.76 (ddd, *J* = 8.3, 7.0, 1.3 Hz, 1H), 7.64 (ddd, *J* = 8.0, 7.0, 1.1 Hz, 1H), 7.44 (dddd, *J* = 8.4, 6.9, 4.1, 1.4 Hz, 2H), 6.85 (d, *J* = 7.1 Hz, 2H), 6.73 (br s, 2H), 6.60 (br s, 1H), 6.52 (br s, 1H), 6.14 (br s, 1H), 5.99 (br s, 1H).^{13}C NMR (100 MHz, $CDCl_3$): δ 149.95, 144.64, 143.64, 134.43, 133.78, 132.81, 132.36, 129.90, 129.60, 128.90, 128.67, 128.55, 128.24, 127.68, 127.34, 126.69, 125.93, 125.59, 125.30, 125.25, 124.77, 124.72, 124.43, 123.01, 122.92, 121.66, 115.37, 113.50.

Compound 3.2

10,15-Dihydro-5H-diindeno[1,2-a:1',2'-c]fluorene

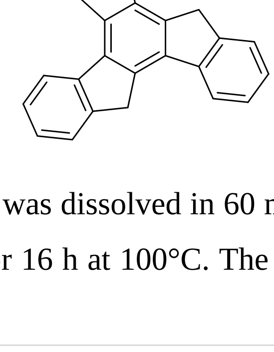

1-Indanone (13.6g, 0.1 mol, 3 eq) was dissolved in 60 mL acetic acid then 30 mL HCl was added. The solution was stirred for 16 h at 100°C. The precipitate was washed with water, acetone and dichloromethane to give the product **3.2** as a white powder (9.26 g, 0.027mol, 80%): mp >360 °C; ^{1}H NMR (400 MHz, $CDCl_3$) δ 7.97 (d, *J* = 7.5 Hz, 3H), 7.71 (d, *J* = 7.5 Hz, 3H), 7.51 (t, *J* = 7.4 Hz, 3H), 7.40 (t, *J* = 7.4 Hz, 3H), 4.30 (s, 6H). ^{13}C NMR (101 MHz, $CDCl_3$) δ 143.82, 141.74, 137.16, 135.31, 126.96, 126.34, 125.16, 121.92, 36.59. This was consistent with previously published data.[287]

Compound 3.3

5,5,10,10,15,15-Hexahexyl-10,15-dihydro-5H-diindeno[1,2-a:1',2'-c]fluorene

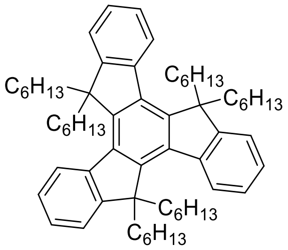

To a suspension of truxene **3.2** (4 g, 0.02 mol, 1 eq.) in THF (100 mL), n-BuLi (2.06 M solution in n-hexane, 21.4 mL, 0.044 mol, 3.8 eq.) was added over a 20 min period at 5°C. The solid dissolved, changing colour to deep red. The solution was stirred for 30 min then 1-bromohexane (6.25 mL, 0.044 mol, 3.8 eq) was added over a 10 min period at 5°C and the mixture was stirred for 4 h at room temperature. The second portion of n-BuLi (2.06 M solution in n-hexane, 21.4 mL, 0.044 mol, 3.8 eq.) was added at 5°C and after 30 min the second portion of 1-bromohexane (6.25 mL, 0.044 mol, 3.8 eq.) was added at the same temperature. After overnight stirring at room temperature, the reaction was quenched by addition of a saturated solution of NH_4Cl (200 mL) and extracted with petroleum ether (2×250 mL). The mixture was concentrated under reduced pressure and the product was purified by column chromatography on silica gel with petroleum ether as an eluent giving compound **3.3** as a pale yellow solid (9.5 g, 0.011 mol, 95%): mp 61-63 °C; MS (MALDI-TOF) calculated for $C_{63}H_{90}$ 846.70, found 846.66 [M^+]; ^{1}H NMR (400MHz, $CDCl_3$): δ 8.41 (3H d, *J* = 7.49 Hz), 7.50 (3H, d, 6.87 Hz) 7.48-7.36 (6H, m), 3.12-2.90 (6H, m), 2.20-2.02 (6H, m), 1.02-0.80 (36H, m), 0.70-0.44 (30H, m). ^{13}C NMR ($CDCl_3$): δ 153.54, 144.72, 140.26, 138.28, 126.23, 125.85, 124.54, 122.07, 55.53, 36.89, 31.41, 29.43, 23.82, 22.20, 13.89. This was consistent with previously published data.[236]

Compound 3.4

2,7,12-Tribromo-5,5,10,10,15,15-hexahexyl-10,15-dihydro-5H-diindeno[1,2-a:1',2'-c]fluorene

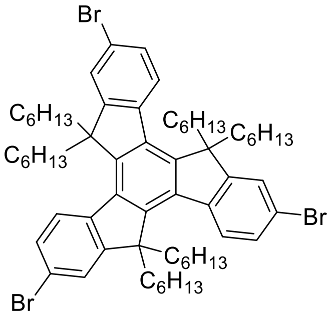

To a stirred solution of hexahexyltruxene **3.3** (4.3 g, 5 mmol, 1 eq.) in dichloromethane (40 mL) bromine (0.81 mL, 15.7 mmol, 3.1 eq.) was added over a 5 min period at 0°C under protection from light. After 14 h the reaction mixture was washed with sodium thiosulphate saturated solution (250 mL), extracted with dichloromethane (2×200 mL), washed with sodium carbonate solution (250 mL) and dried over $MgSO_4$. The solution was concentrated under reduced pressure. The residue first was recrystallized from petroleum ether and washed with cold petroleum ether and then purified by column chromatography on silica gel eluting with hexane : ethyl acetate (10:1) mixture giving product **3.4** as a white powder (5.1 g, 4.7 mmol, 76%): m.p. 224-225 °C; MS (MALDI-TOF) calculated for $C_{63}H_{87}Br_3$ 1080.44, found 1084.41 [M^+]; ^1H NMR (400MHz, $CDCl_3$): δ 8.20 (d, *J* = 8.5 Hz, 3H), 7.59 (d, *J* = 2.0 Hz, 3H), 7.54 (dd, *J* = 8.5, 1.9 Hz, 3H), 3.01 – 2.66 (m, 6H), 2.08 – 2.02 (m, 6H), 0.98 – 0.83 (m, 36 H), 0.65 (t, *J* = 7.1 Hz, 18H), 0.59 – 0.35 (m, 12H). ^{13}C NMR ($CDCl_3$): δ 155.37, 144.39, 138.35, 137.13, 128.87, 125.39, 125.02, 120.54, 55.48, 36.31, 30.93, 28.85, 23.36, 21.74, 13.34. This was consistent with previously published data.[236]

Compound 3.6

2-Bromo-5,5,10,10,15,15-hexahexyl-10,15-dihydro-5H-diindeno[1,2-a:1',2'-c]fluorene

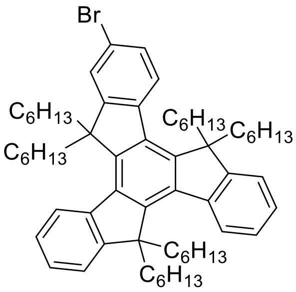

Hexahexyltruxene **3.3** (1 g, 1.2 mmol, 1 eq.) was dissolved in acetic acid (60 mL) and N-bromosuccinimide (0.18 g, 1.12 mmol, 0.95 eq.) in a solution of acetic acid (40 mL) was added dropwise over 15 minutes under protection from light. The mixture was stirred at 80 °C for 3 days, cooled to room temperature and the crude product was extracted with dichloromethane. The organic layer was washed successively with saturated solutions of Na_2CO_3 (200 mL), $NaHCO_3$ (200 mL) and water (200 mL), dried over $MgSO_4$ then concentrated under reduced pressure. The crude material was recrystallised from ethanol. Product **3.6** was isolated as a white powder (0.55 g, 57%). m.p. 128-130 °C; MS (MALDI-TOF) calculated for $C_{63}H_{89}Br$ 924.61, found 926.44 [M^+]; ^1H NMR (400 MHz, $CDCl_3$) δ 8.36 (d, *J* = 7.3 Hz, 1H), 8.32 (d, *J* = 7.0 Hz, 1H), 8.22 (d, *J* = 8.5 Hz, 1H), 7.57 (d, *J* = 2.0 Hz, 1H), 7.50 (dd, *J* = 8.5, 2.0 Hz, 1H), 7.47 – 7.42 (m, 2H), 7.41 – 7.32 (m, 4H), 3.05 – 2.89 (m, 4H), 2.89 – 2.75 (m, 2H), 2.15 – 1.92 (m, 6H), 1.05 – 0.70 (m, 36H), 0.70 – 0.54 (m, 18H), 0.55 – 0.33 (m, 12H). ^{13}C NMR (101 MHz, $CDCl_3$) δ 156.14, 153.65, 153.62, 153.45, 145.36, 144.84, 144.82, 144.35, 140.35, 140.13, 140.01, 139.42, 138.64, 138.43, 138.37, 137.30, 129.11, 126.53, 126.31, 126.07, 125.94, 125.43, 124.70, 124.63, 124.54, 122.24, 122.17, 120.59, 55.96, 55.69, 55.60, 55.57, 37.00, 36.95, 36.90, 36.82, 31.49, 31.48, 29.50, 29.49, 29.41, 23.89, 22.28, 13.88. This was consistent with previously published data.[288]

Compound A

4,7-Bis(7,12-dibromo-5,5,10,10,15,15-hexahexyl-10,15-dihydro-5H-diindeno[1,2-a:1',2'-c]fluoren-2-yl)benzo[c][1,2,5]thiadiazole

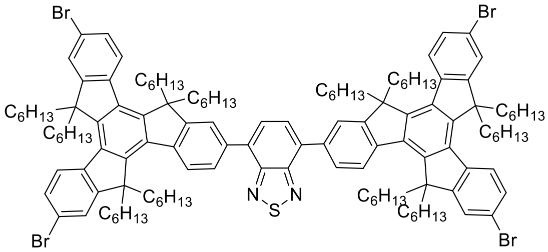

A mixture of tribromohexahexyltruxene **3.4** (13 g, 12 mmol, 7 eq.), tetrakis(triphenylphosphine)palladium (0) (0.8 g, 0.68 mmol, 0.4 eq.) and 2,1,3-benzothiadiazole-4,7-bis(boronic acid pinacol ester) **3.5** (0.665 g, 1.7 mmol, 1 eq.) was dried under reduced pressure for 30 min, then dissolved in dry degassed toluene. An aqueous degassed solution of K_2CO_3 (2M, 4.28 mL) was added and the mixture was stirred at 100°C for 3 days. The mixture was washed with water (200 mL), the toluene layer was separated and aqueous phase was extracted with dichloromethane (2×200 mL). The organic phases were combined, dried over $MgSO_4$ and concentrated under reduced pressure. The crude mixture was purified by column chromatography on silica gel. The starting material was first eluted with hexane, then the product was eluted with a hexane : toluene (5:1) mixture. Pure compound **A** was obtained as a yellow-green powder (660 mg, 0.3 mmol, 18%): mp 124-126 °C; MS (MALDI-TOF) calculated for $C_{132}H_{176}Br_4N_2S$ 2137.03, found 2141.97 [M^+]; ^{1}H NMR (400 MHz, $CDCl_3$) δ 8.53 (d, *J* = 8.9 Hz, 2H), 8.29 (d, *J* = 8.6 Hz, 2H), 8.23 (d, *J* = 8.6 Hz, 2H), 8.20 – 8.18 (m, 4H), 8.05 (s, 2H), 7.63 (dd, *J* = 7.7, 1.9 Hz, 4H), 7.57 (ddd, *J* = 8.3, 5.0, 1.9 Hz, 4H), 3.10 – 3.03 (m, 4H), 2.97 – 2.87 (m, 8H), 2.33 – 2.21 (m, 4H), 2.14 – 2.04 (m, 8H), 1.13 – 0.79 (m, 72H), 0.78 – 0.61 (m, 36H), 0.55 (dt, *J* = 20.3, 6.3 Hz, 24H). ^{13}C NMR ($CDCl_3$) δ 155.54, 155.43, 153.90, 153.48, 145.39, 144.70, 144.25, 139.60, 138.64, 138.56, 137.75, 137.21, 137.04, 135.18, 132.64, 128.83, 127.54, 126.90, 125.48, 125.39, 125.06, 125.01, 124.24, 122.62, 120.43, 55.63, 55.50, 55.37, 36.49, 36.40, 31.04, 30.97, 29.01, 28.96, 28.91, 23.50, 23.42, 21.80, 21.77, 13.40. Elemental Analysis: Found: C, 73.80, H, 8.34, N, 1.30, Expected: C, 74.00, H, 8.28, N, 1.31.

Compound A0

4,7-Bis(5,5,10,10,15,15-hexahexyl-10,15-dihydro-5H-diindeno[1,2-a:1',2'-c]fluoren-2-yl)benzo[c][1,2,5]thiadiazole

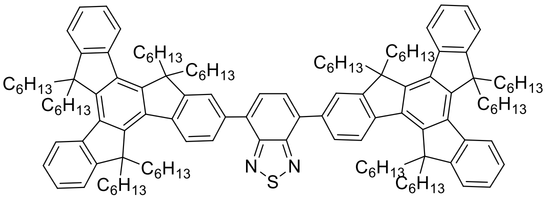

Compound **3.6** (1.43 g, 1.55 mmol, 4 eq) and tetrakis(triphenylphosphine)palladium (0) (0.09 g, 0.08 mmol, 0.2 eq.) were dissolved in degassed THF (70 mL). 2,1,3-Benzothiadiazole-4,7-bis(boronic acid pinacol ester) **3.5** (0.15 g, 0.39 mmol, 1 eq.) was dissolved in THF (30 mL) and added to the reaction mixture followed by $Ba(OH)_2{\cdot}8H_2O$ (0.37 g, 1.16 mmol, 3 eq) and degassed water (0.7 mL). The mixture was degassed and heated at 80°C overnight. THF was evaporated and the crude product was dissolved in dichloromethane (100 mL), the organic phase was washed with water (2×50 mL), dried over $MgSO_4$ and concentrated under reduced pressure. The product was purified by column chromatography on silica gel. The starting material was first eluted with hexane, then the product was eluted with a hexane : toluene (5:1) mixture. Pure compound **A0** was obtained as a bright yellow-green powder (70 mg, 10%): mp 332-334 °C; MS (MALDI-TOF) calculated for $C_{132}H_{180}N_2S$ 1825.38, found 1827.10 [M^+]. ^1H NMR (400 MHz, $CDCl_3$) δ 8.55 (d, *J* = 8.4 Hz, 2H), 8.40 (t, *J* = 7.0 Hz, 4H), 8.21 – 8.12 (m, 4H), 8.03 (s, 2H), 7.54 – 7.45 (m, 4H), 7.46 – 7.34 (m, 8H), 3.16 – 2.76 (m, 12H), 2.35 – 2.18 (m, 4H), 2.12 (ddd, *J* = 18.4, 13.1, 6.9 Hz, 8H), 1.07 – 0.73 (m, 72H), 0.75 – 0.38 (m, 60H). ^{13}C NMR (101 MHz, $CDCl_3$) δ 154.48, 154.19, 153.67, 153.62, 145.38, 145.22, 145.17, 140.67, 140.34, 140.31, 138.56, 138.51, 137.95, 135.34, 133.23, 128.02, 127.22, 126.42, 126.01, 124.76, 124.69, 123.05, 122.23, 55.84, 55.74, 55.70, 37.12, 37.01, 31.60, 31.50, 29.57, 29.52, 24.03, 23.93, 22.32, 22.30, 13.91, 13.88.

Compound A1

4,4',4'',4'''-(Benzo[c][1,2,5]thiadiazole-4,7-diylbis(5,5,10,10,15,15-hexahexyl-10,15-dihydro-5H-diindeno[1,2-a:1',2'-c]fluorene-12,2,7-triyl))tetrakis(N,N-diphenylaniline)

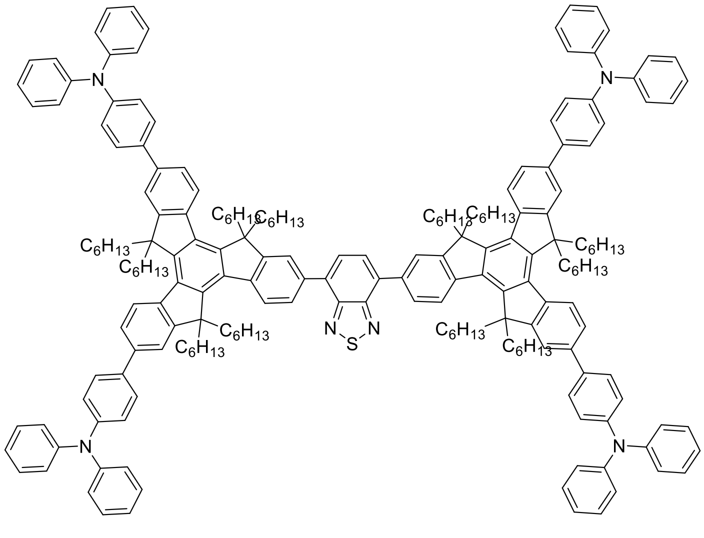

A mixture of **A** (150 mg, 0.07 mmol, 1 eq.), tetrakis(triphenylphosphine)palladium (0) (40.45 mg, 0.035 mmol, 0.5 eq.), 4-(diphenylamino)phenylboronic acid (305 mg, 1.05 mmol, 15 eq.) and $Ba(OH)_2 \cdot 8H_2O$ (552 mg, 1.75 mmol, 25 eq.) was dried under vacuum and dissolved in dry degassed THF (10 mL). Degassed (bubbled with N_2) water (1.16 mL, 2.1 mL per gram of base) was added and the mixture was heated to 85°C. After 3 days the THF was removed under reduced pressure, the crude product was diluted with toluene (100 mL) and washed with water (2×100 mL). The aqueous phase was extracted with toluene (2×100 mL), the organic phases were combined, dried over $MgSO_4$ and concentrated under reduced pressure. Product **A1** was purified by column chromatography on silica gel with hexane :

toluene (5:1) and then reprecipitated from dichloromethane with methanol giving the product **A1** as a bright yellow powder (122 mg, 61%): mp 158-160°C; MS (MALDI-TOF) calculated for $C_{204}H_{232}N_6S$ 2797.81, found 2800.32 [M^+]; ^{1}H NMR (400 MHz, $CDCl_3$) δ 8.59 (d, *J* = 8.3 Hz, 2H), 8.53 – 8.38 (m, 4H), 8.22 (d, *J* = 9.5 Hz, 4H), 8.07 (s, 2H), 7.79 – 7.61 (m, 16H), 7.37 – 7.29 (m, 16H), 7.28 – 7.17 (m, 24H), 7.08 (dt, *J* = 8.3, 1.0 Hz, 8H), 3.24 – 2.94 (m, 12H), 2.42 – 2.06 (m, 12H), 1.17 – 0.80 (m, 72H), 0.81 – 0.38 (m, 60H). ^{13}C NMR ($CDCl_3$): δ 153.97, 153.83, 153.64, 147.31, 147.25, 146.63, 144.85, 144.78, 140.17, 138.76, 137.97, 137.47, 134.86, 134.82, 132.72, 128.80, 127.54, 127.20, 124.43, 124.14, 123.92, 123.88, 123.65, 122.42, 119.52, 55.55, 55.33, 38.68, 36.69, 36.63, 36.59, 31.10, 31.01, 29.09, 29.04, 23.55, 23.44, 21.92, 21.83, 13.43. Elemental Analysis: Found: C, 87.00, H, 8.30, N, 3.00, Expected: C, 87.50, H, 8.35, N, 3.00.

Compound A2

4,7-Bis(5,5,10,10,15,15-hexahexyl-7,12-di(10H-phenoxazin-10-yl)-10,15-dihydro-5H-diindeno[1,2-a:1',2'-c]fluoren-2-yl)benzo[c][1,2,5]thiadiazole

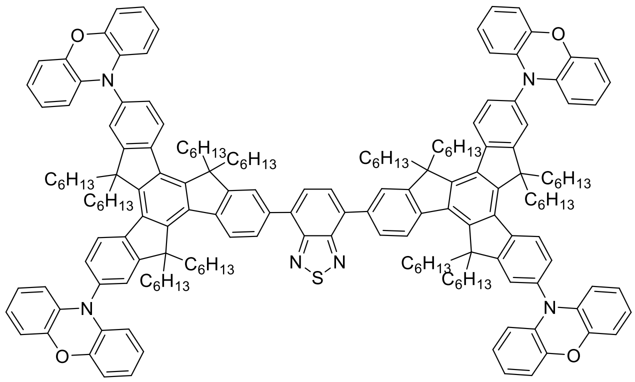

A mixture of **A** (150 mg, 0.07 mmol, 1 eq.)**,** phenoxazine (128 mg, 0.07 mmol, 1 eq.), palladium (II) acetate (16 mg, 0.07 mmol, 1 eq.), tri-*tert*-butylphosphine (45 mg, 0.22 mmol, 3.2 eq.) and potassium *tert*-butoxide (85 mg, 0.70 mmol, 10 eq.) was dissolved in dry toluene (15 mL), degassed and stirred at 110°C. After 3 days, the mixture was washed with water (100 mL), the aqueous phase extracted with toluene (2×100 mL), the organic phases were combined and then dried over $MgSO_4$. The solvent was evaporated under reduced pressure. Purification by chromatography on silica gel with a hexane : toluene (4:1, then 3:1) mixture followed by reprecipitation from dichloromethane with methanol afforded the product **A2** as orange-yellow powder (136 mg, 76%): mp > 360 °C; MS (MALDI-TOF) calculated for $C_{180}H_{208}N_6O_4S$ 2549.60, found 2551.81 [M^+]; ^{1}H NMR (400 MHz, $CDCl_3$) δ 8.66 (d, *J* = 8.5 Hz, 2H), 8.58 (dd, *J* = 8.2, 5.0 Hz, 4H), 8.27 – 8.17 (m, 4H), 8.07 (s, 2H), 7.52 (dd, *J* = 3.0, 2.2 Hz, 4H), 7.41 (ddd, *J* = 10.6, 8.4, 1.9 Hz, 4H), 6.77 (dt, *J* = 7.8, 1.5 Hz, 8H), 6.74 – 6.67 (m, 8H), 6.67 – 6.59 (m, 8H), 6.09 (ddd, *J* = 7.9, 2.3, 1.6 Hz, 8H), 3.22 – 2.96 (m, 12H), 2.43 – 2.24 (m, 4H), 2.23 – 2.04 (m, 8H), 1.15 – 0.87 (m, 72H), 0.76 – 0.61 (m, 60H). ^{13}C NMR ($CDCl_3$): δ 156.36, 156.23, 153.92, 153.49, 145.85, 145.52, 145.21, 143.59, 139.91, 139.78, 139.61, 137.92, 137.43, 137.28, 136.71, 135.27, 134.18, 132.67, 127.84, 127.58, 126.96, 126.51, 124.41, 124.02, 123.96, 122.76, 120.80, 114.99, 112.64, 55.65, 55.58, 55.50, 36.38, 36.24, 31.13, 30.95, 30.91, 29.20, 28.93, 28.82, 28.74, 23.76, 23.52, 23.42, 21.76, 18.33, 13.42. Elemental Analysis: Found: C, 84.67, H, 8.36, N, 3.22, Expected: C, 84.73, H, 8.22, N, 3.29.

Compound Q1

3,6-Di-tert-butyl-9-(quinolin-3-yl)-9H-carbazole

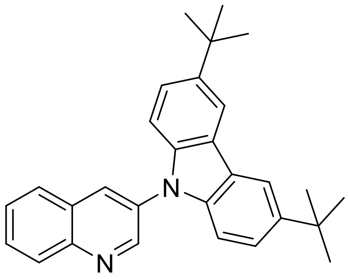

3,6-Di-*tert*-butyl-9H-carbazole **4.3** (485 mg, 1.73 mmol, 1.2 eq.) was added in a dried 3-neck flask and dissolved in 120 mL of anhydrous toluene. 3-bromoquinoline **4.1** (300 mg, 1.44 mmol, 1 eq.) was added and the mixture was bubbled with N_2 for 15 minutes while stirring. Tris(dibenzylideneacetone)dipalladium(0) ($Pd_2(dba)_3$) (66 mg, 0.075 mmol, 0.05 eq.) and 2-dicyclohexylphosphino-2′,4′,6′-triisopropylbiphenyl (XPhos) (137 mg, 0.29 mmol, 0.2 eq.) were added and the mixture was degassed for another 15 minutes. Sodium *tert*-butoxide was added (167 mg, 1.73 mmol, 1.2 eq.) followed by *tert*-butanol (4 mL) and the mixture was degassed for 15 more minutes. It was next stirred at 110 °C for 18 hours. The mixture was then cooled to room temperature, washed with water (2×100 mL), dried over $MgSO_4$ and concentrated under reduced pressure. The crude product was then purified by column chromatography with dichloromethane followed by recrystallisation from ethyl acetate giving the material **Q1** as white crystals (350 mg, 60%). mp 248 – 250 °C; HRMS (LMMS) calculated for $C_{29}H_{30}N_2$ 406.2408, found 406.2468 [M+H$^+$]; ^{1}H NMR (400 MHz, $CDCl_3$) δ 9.17 (d, *J* = 2.5 Hz, 1H), 8.33 (d, *J* = 2.3 Hz, 1H), 8.25 (d, *J* = 8.5 Hz, 1H), 8.18 (d, *J* = 1.6 Hz, 2H), 7.90 (d, *J* = 8.4 Hz, 1H), 7.82 (t, *J* = 7.7 Hz, 1H), 7.66 (t, *J* = 7.5 Hz, 1H), 7.50 (dd, *J* = 8.6, 1.9 Hz, 2H), 7.38 (d, *J* = 8.6 Hz, 2H), 1.48 (s, 18H). ^{13}C NMR (100

MHz, $CDCl_3$) δ 149.60, 146.83, 143.68, 139.21, 132.06, 131.97, 129.73, 129.60, 128.42, 127.71, 127.58, 123.98, 123.79, 116.55, 108.81, 34.82, 32.01.

Compound Q2

3,6-Di-tert-butyl-9-(quinolin-4-yl)-9H-carbazole

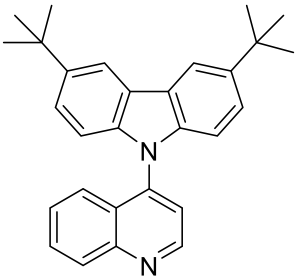

This was synthesised according to the general procedure leading to **Q1**. 3,6-di-*tert*-butyl-9H-carbazole **4.3** (2.41 g, 8.6 mmol, 1 eq.), 4-bromoquinoline **4.2** (1.5 g, 7.2 mmol, 1.2 eq.), $Pd_2(dba)_3$ (0.33 g, 0.36 mmol, 0.05 eq.), XPhos (0.69 mg, 1.44 mmol, 0.2 eq.), sodium *tert*-butoxide (0.83 mg, 8.6 mmol, 1.2 eq.) and *tert*-butanol (16.5 mL) were used. The crude product was purified by column chromatography with a hexane : ethyl acetate (10 : 1) mixture followed by recrystallisation from methanol giving the material **Q2** as a yellow powder (360 mg, 12%). mp 168 – 170 °C; HRMS (EI) calculated for $C_{29}H_{30}N_2$ 406.2408, found 406.2419 [M^+]; ^1H NMR (400 MHz, $CDCl_3$) δ 9.10 (d, *J* = 4.6 Hz, 1H), 8.29 (d, *J* = 8.4 Hz, 1H), 8.19 (d, *J* = 1.7 Hz, 2H), 7.80 (t, *J* = 7.7 Hz, 1H), 7.62 (dd, *J* = 8.4, 0.8 Hz, 1H), 7.54 (d, *J* = 4.6 Hz, 1H), 7.45 (t, *J* = 7.6 Hz, 1H), 7.41 (dd, *J* = 8.6, 1.9 Hz, 2H), 7.01 (d, *J* = 8.6 Hz, 2H), 1.48 (s, 18H). ^{13}C NMR (100 MHz, CDCl3) δ 151.01, 150.34, 143.63, 143.58, 139.74, 130.27, 130.13, 127.08, 125.61, 124.22, 123.92, 123.89, 119.91, 116.43, 109.77, 34.81, 32.00.

Compound Q1-S1

3-(3,6-Di-tert-butyl-9H-carbazol-9-yl)-1-methylquinolin-1-ium trifluoromethanesulfonate

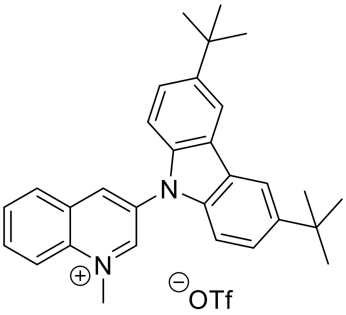

Compound **Q1** (50 mg, 0.123 mmol, 1 eq.) was dissolved in dry dichloromethane (2 mL) and cooled down to 0 °C under N_2 atmosphere. Methyl trifluoromethanesulfonate (14 µL, 0.123 mmol, 1 eq.) was added and the mixture was stirred for 20 h at room temperature. The formed precipitate was filtered off and washed with cool methanol (100 mL) to give the product **Q1-S1** as a bright yellow solid (58 mg, 82%). mp 356 – 358 °C; HRMS (LMMS) calculated for $C_{20}H_{33}N_2^+$ 421.2643, found 421.2625 [M^+]; ^{1}H NMR (400 MHz, DMSO-d_6) δ 10.15 (s, 1H), 9.73 (s, 1H), 8.67 (d, *J* = 8.9 Hz, 1H), 8.59 (d, *J* = 7.8 Hz, 1H), 8.44 (d, *J* = 1.5 Hz, 2H), 8.40 (t, *J* = 8.0 Hz, 1H), 8.19 (t, *J* = 7.6 Hz, 1H), 7.66 (d, *J* = 8.7 Hz, 2H), 7.61 (dd, *J* = 8.7, 1.8 Hz, 2H), 4.78 (s, 3H), 1.49 (s, 18H). ^{13}C NMR (100 MHz, DMSO-d_6) δ 150.00, 144.71, 142.88, 138.65, 137.62, 135.78, 132.06, 131.01, 130.86, 130.33, 124.67, 124.01, 119.65, 117.54, 109.73, 46.02, 35.14, 32.24.

Compound Q2-S1

4-(3,6-Di-tert-butyl-9H-carbazol-9-yl)-1-methylquinolin-1-ium trifluoromethanesulfonate

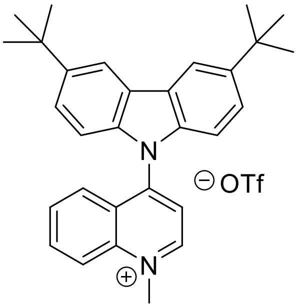

This was synthesised according to the general procedure leading to **Q1-S1**. **Q2** (50 mg, 0.123 mmol, 1 eq.), dichloromethane (2 mL) and methyl trifluoromethanesulfonate (14 µL, 0.123

mmol, 1 eq.) were used. Hexane was added to the solution of the product, then the formed precipitate was filtered off and washed with cold hexane (100 mL) giving the product **Q2-S1** as a bright yellow solid (51 mg, 72%). mp 302 – 304 °C; HRMS (LMMS) calculated for $C_{20}H_{33}N_2^+$ 421.2643, found 421618 [M^+]; ^{1}H NMR (400 MHz, $CDCl_3$) δ 9.66 (d, *J* = 6.5 Hz, 1H), 8.45 (d, *J* = 9.1 Hz, 1H), 8.30 – 8.19 (m, 2H), 8.14 (d, *J* = 1.6 Hz, 2H), 8.10 (d, *J* = 6.5 Hz, 1H), 7.84 (t, *J* = 7.7 Hz, 1H), 7.45 (dd, *J* = 8.7, 1.8 Hz, 2H), 7.20 (d, *J* = 8.7 Hz, 2H), 4.83 (s, 3H), 1.46 (s, 18H). ^{13}C NMR (101 MHz, $CDCl_3$) δ 153.16, 150.83, 146.76, 138.52, 136.43, 129.49, 127.73, 125.87, 125.32, 124.86, 119.30, 118.87, 116.96, 110.59, 45.61, 34.99, 31.80.

Compound Q1-S2

3-(3,6-Di-tert-butyl-9H-carbazol-9-yl)-1-methylquinolin-1-ium iodide

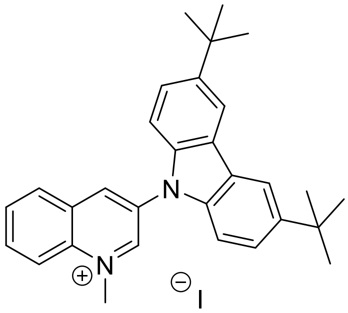

Compound **Q1** (50 mg, 0.123 mmol, 1 eq.) was dissolved in toluene (10 mL) and methyl iodide (0.38 mL, 6.15 mmol, 50 eq.) was then added. The mixture was heated to 100 °C for 2 hours in a microwave. The formed yellow precipitate was filtered off and washed with diethyl ether (100 mL) to afford the material **Q1-S2** as a bright yellow solid (40 mg, 60%). mp 242–244 °C; HRMS (LMMS) calculated for $C_{20}H_{33}N_2^+$ 421.2643, found 421.2620 [M^+]; ^{1}H NMR (400 MHz, $CDCl_3$) δ 9.57 (d, *J* = 2.0 Hz, 1H), 9.00 (d, *J* = 1.8 Hz, 1H), 8.50 (d, *J* = 9.0 Hz, 1H), 8.26 – 8.17 (m, 2H), 8.15 (d, *J* = 1.6 Hz, 2H), 7.98 (t, *J* = 7.6 Hz, 1H), 7.74 (d, *J* = 8.7 Hz, 2H), 7.56 (dd, *J* = 8.7, 1.9 Hz, 2H), 4.99 (s, 3H), 1.47 (s, 18H). ^{13}C NMR (101 MHz, $CDCl_3$) δ 147.77, 145.60, 141.62, 138.24, 137.46, 136.11, 133.50, 131.28, 130.36, 130.02, 124.92, 124.64, 119.40, 116.80, 109.18, 49.00, 34.92, 31.90.

Compound Q2-S2

4-(3,6-Di-tert-butyl-9H-carbazol-9-yl)-1-methylquinolin-1-ium iodide

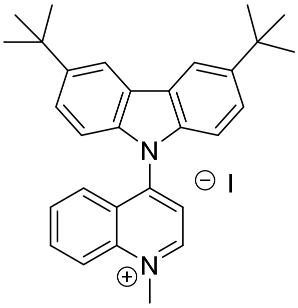

This was synthesised and purified according to the general procedure leading to **Q1-S2**. **Q2** (50 mg, 0.123 mmol, 1 eq.), toluene (10 mL) and methyl iodide (0.38 mL, 6.15 mmol, 50 eq.) were used. The material **Q2-S2** was isolated as a bright yellow solid (35 mg, 52%). mp 240–242 °C; HRMS (LMMS) calculated for $C_{20}H_{33}N_2^+$ 421.2643, found 421.2622 [M$^+$]; ^{1}H NMR (400 MHz, $CDCl_3$) δ 10.45 (d, *J* = 6.7 Hz, 1H), 8.50 (d, *J* = 8.6 Hz, 1H), 8.30 – 8.26 (m, 2H), 8.19 – 8.16 (m, 3H), 7.93 – 7.82 (m, 1H), 7.48 (dd, *J* = 8.7, 1.9 Hz, 2H), 7.26 (d, *J* = 8.7 Hz, 2H), 4.99 (s, 3H), 1.49 (s, 18H). ^{13}C NMR (101 MHz, $CDCl_3$) δ 152.95, 150.80, 146.78, 140.68, 138.49, 136.36, 129.47, 127.84, 125.88, 125.28, 124.87, 119.30, 118.98, 116.97, 110.68, 46.12, 34.99, 31.80

Compound Q1-S3

3-(3,6-Di-tert-butyl-9H-carbazol-9-yl)-1-methylquinolin-1-ium tetrafluoroborate

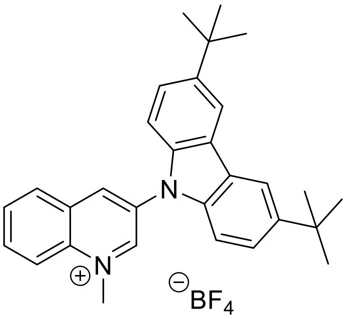

A mixture of **Q1** (250 mg, 0.6 mmol, 1 eq.) and NH_4BF_4 (80 mg, 0.77 mmol, 1.25 eq.) was dissolved in trimethyl orthoformate (10 mL). The solution was heated at 100 °C for 2 h in a microwave. The solvent was evaporated, the crude product was diluted with methanol (100 mL) and filtered through a basic aluminium oxide plug. The solution was concentrated under reduced pressure. The material was then dissolved in chloroform and reprecipitated with hexane affording the product **Q1-S3** as a bright yellow powder (170 mg, 54%). mp 296–298

°C; HRMS (LMMS) calculated for $C_{20}H_{33}N_2^+$ 421.2643, found 421.2642 [M^+]; ^{1}H NMR (400 MHz, $CDCl_3$) δ 9.20 (s, 1H), 8.89 (s, 1H), 8.37 (d, *J* = 8.9 Hz, 1H), 8.27 – 7.94 (m, 4H), 7.88 (t, *J* = 7.6 Hz, 1H), 7.53 (s, 4H), 4.76 (s, 3H), 1.46 (s, 18H). ^{13}C NMR (101 MHz, $CDCl_3$) δ 147.75, 145.53, 141.61, 138.28, 137.43, 136.03, 133.23, 131.17, 130.14, 129.82, 124.97, 124.52, 118.96, 116.73, 108.60, 47.04, 34.89, 31.88.

Compound Q2-S3

4-(3,6-Di-tert-butyl-9H-carbazol-9-yl)-1-methylquinolin-1-ium tetrafluoroborate

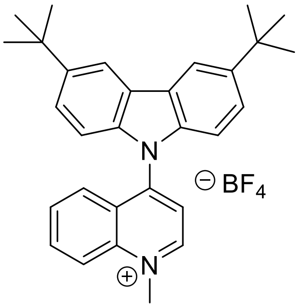

This was synthesised and purified according to the general procedure leading to **Q1-S3**. **Q2** (50 mg, 0.12 mmol, 1 eq.), NH_4BF_4 (16 mg, 0.15 mmol, 1.25 eq.) and trimethyl orthoformate (3 mL) were used. The trimethyl orthoformate was then evaporated under reduced pressure, the product was diluted with methanol (100 mL) and filtered through a basic aluminium oxide plug. The solvent was evaporated under reduced pressure, and the material was recrystallised from isopropanol giving the product **Q2-S3** as a bright-yellow solid (30 mg, 48%). mp 322–324 °C; HRMS (LMMS) calculated for $C_{20}H_{33}N_2^+$ 421.2643, found 421.2626 [M^+]; ^{1}H NMR (400 MHz, $CDCl_3$) δ 9.48 (d, *J* = 6.7 Hz, 1H), 8.49 (d, *J* = 8.9 Hz, 1H), 8.31 – 8.20 (m, 2H), 8.15 (d, *J* = 1.6 Hz, 2H), 8.11 (d, *J* = 6.5 Hz, 1H), 7.89 – 7.73 (m, 1H), 7.47 (dd, *J* = 8.7, 2.0 Hz, 2H), 7.23 (d, *J* = 8.7 Hz, 2H), 4.81 (s, 3H), 1.48 (s, 18H). ^{13}C NMR (101 MHz, $CDCl_3$) δ 153.04, 150.54, 146.62, 140.80, 138.56, 136.37, 129.44, 127.57, 125.78, 125.34, 124.86, 119.41, 118.96, 116.88, 110.64, 45.58, 34.97, 31.80.

Chapter 7. Appendix

NMR spectra

H1-PXZ

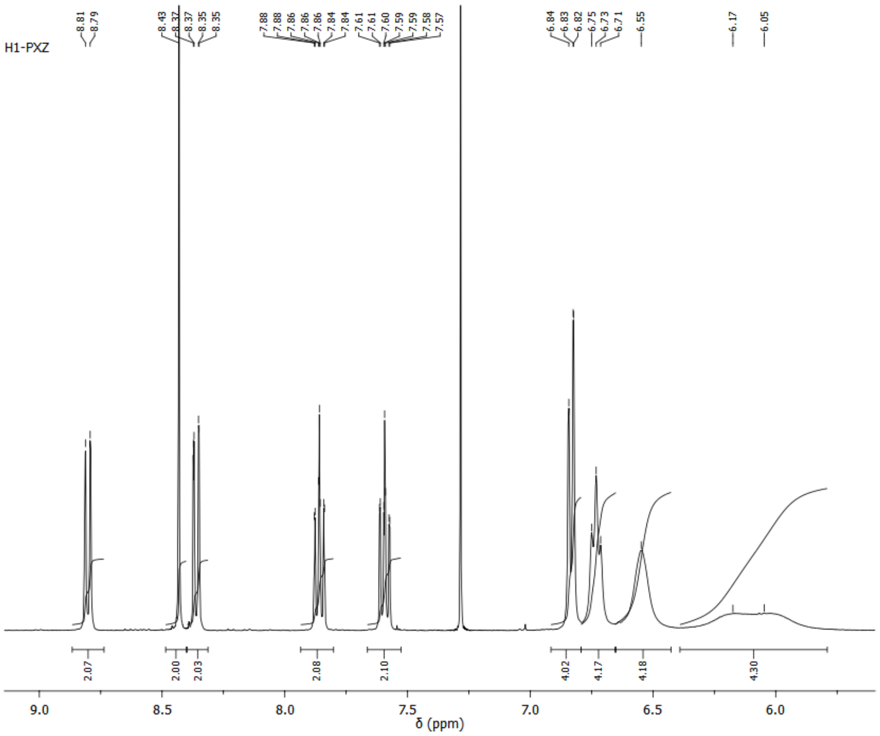

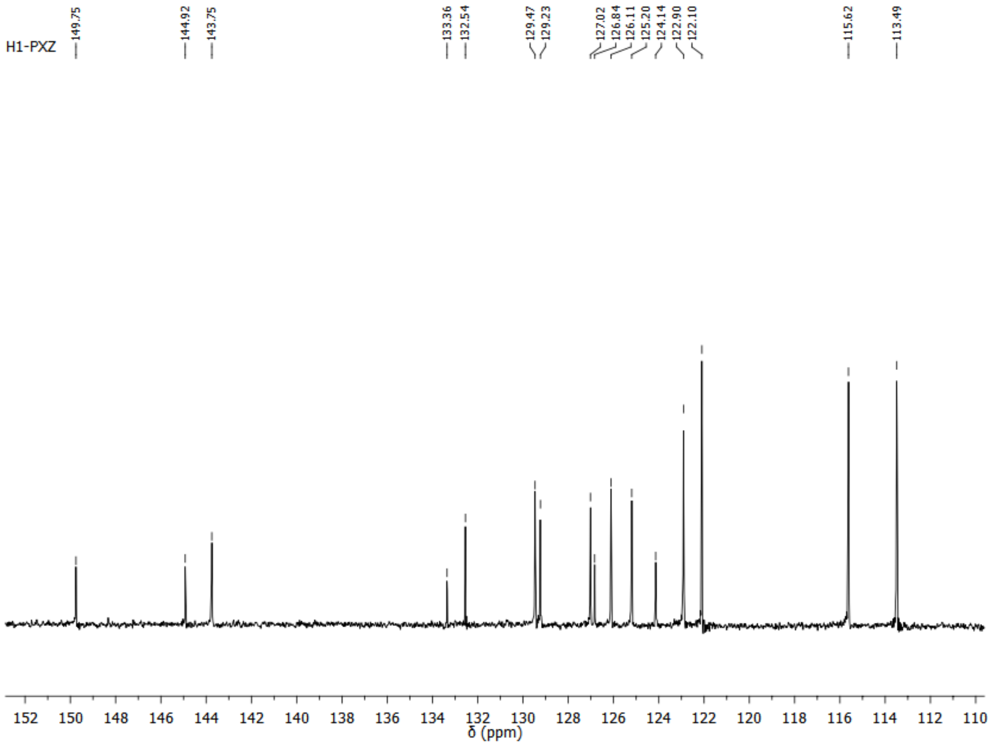

2.9

2.9

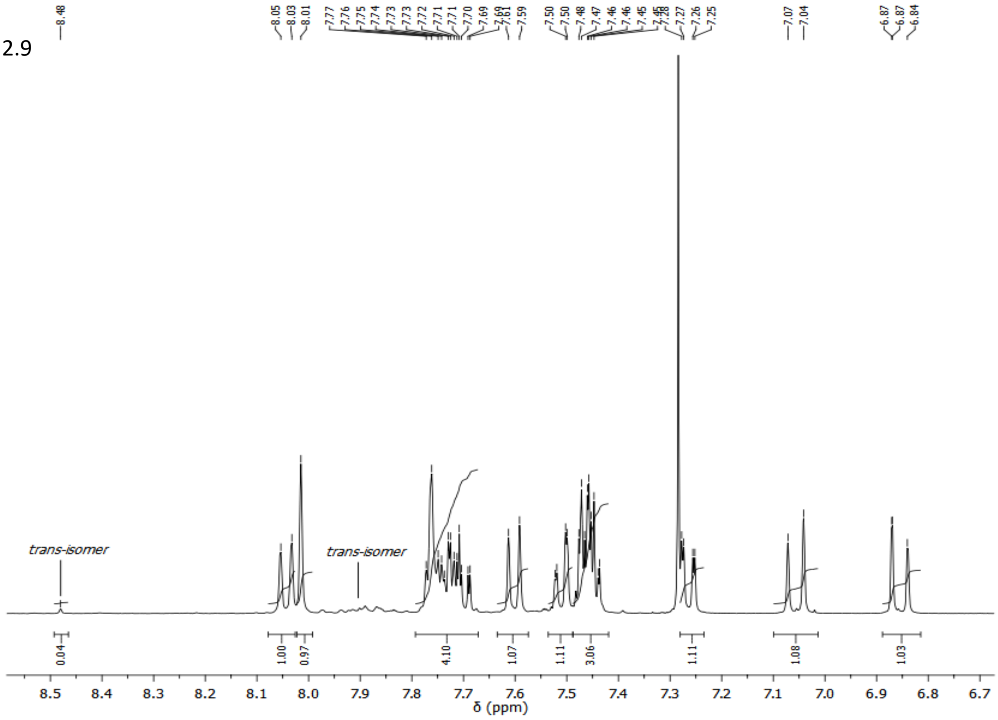
8.48
8.05
8.03
8.01
7.77
7.76
7.75
7.74
7.73
7.73
7.72
7.71
7.71
7.70
7.69
7.60
7.61
7.59
7.50
7.50
7.48
7.47
7.46
7.46
7.45
7.45
7.28
7.27
7.26
7.25
7.07
7.04
6.87
6.87
6.84
trans-isomer
trans-isomer
0.04
1.00
0.97
4.10
1.07
1.11
3.06
1.11
1.08
1.03
8.5
8.4
8.3
8.2
8.1
8.0
7.9
7.8
7.7
7.6
7.5
7.4
7.3
7.2
7.1
7.0
6.9
6.8
6.7
δ (ppm)

2.9

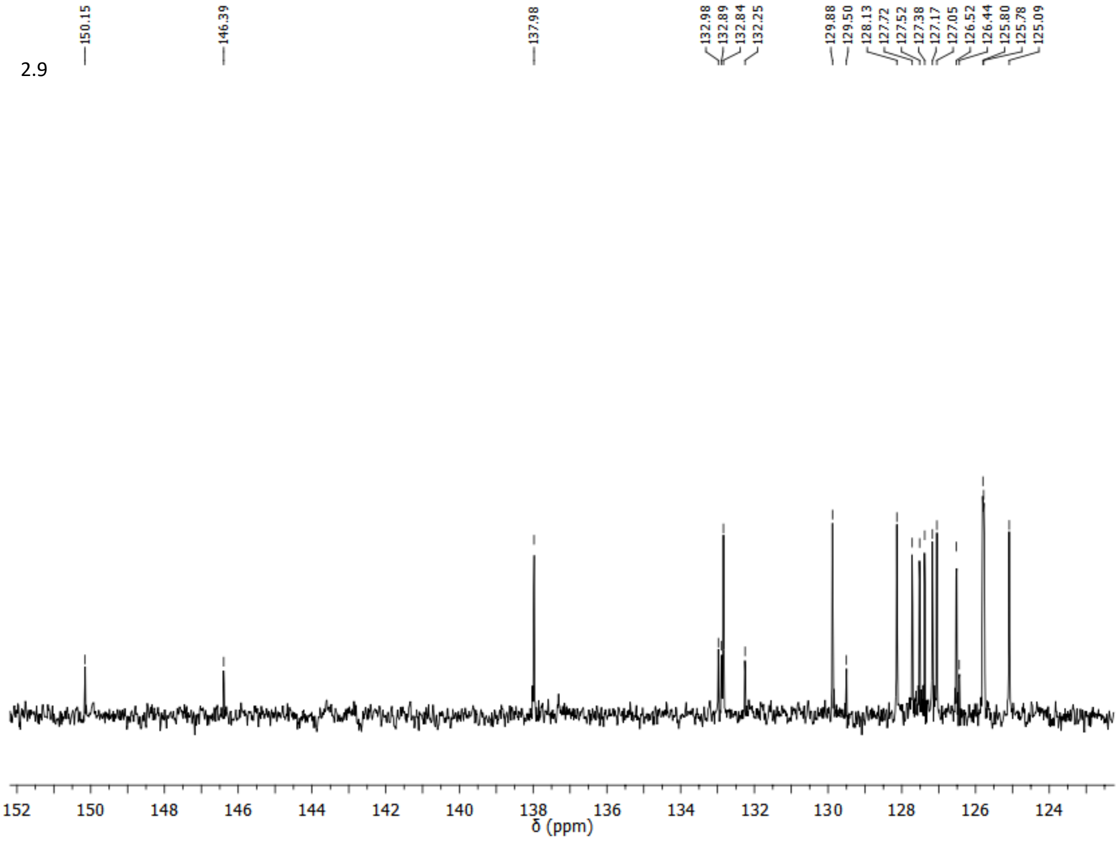
150.15
146.39
137.98
132.98
132.89
132.84
132.25
129.88
129.50
128.13
127.72
127.52
127.38
127.17
127.05
126.52
126.44
125.80
125.78
125.09
152
150
148
146
144
142
140
138
136
134
132
130
128
126
124
δ (ppm)

H2-PXZ

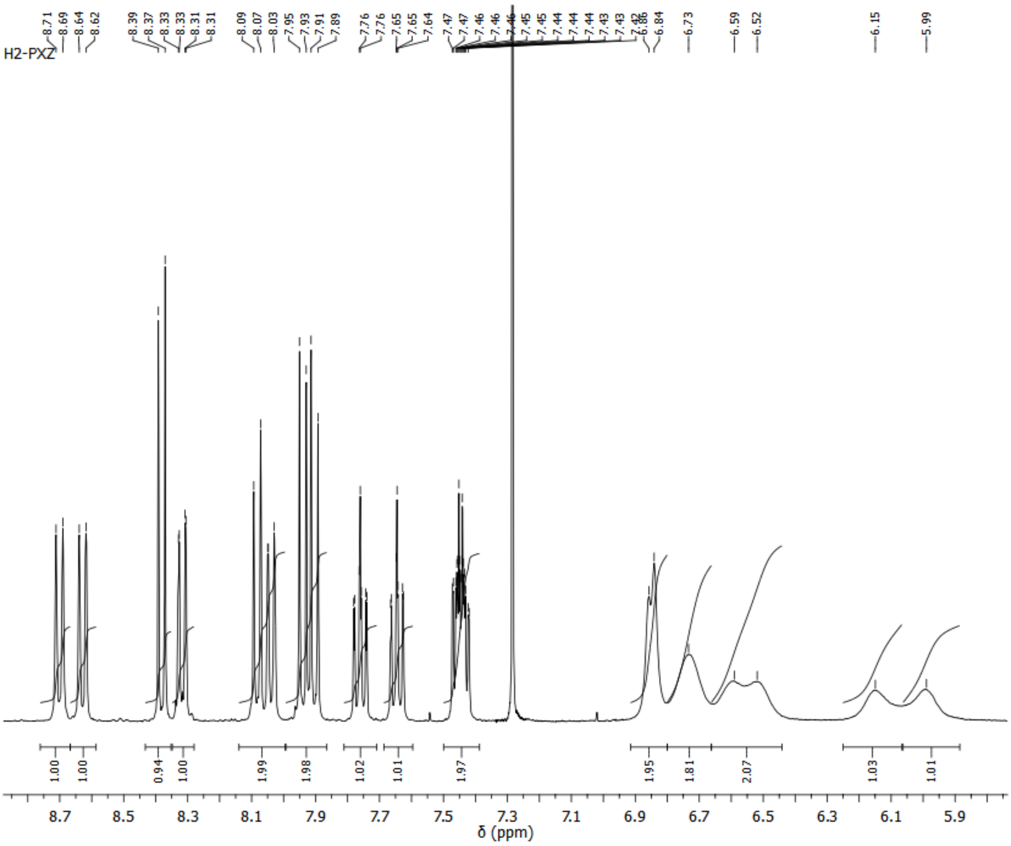
H2-PXZ
8.71
8.69
8.64
8.62
8.39
8.37
8.33
8.33
8.31
8.31
8.09
8.07
8.03
7.95
7.93
7.91
7.89
7.76
7.76
7.65
7.65
7.64
7.47
7.47
7.46
7.46
7.46
7.45
7.45
7.44
7.44
7.44
7.43
7.43
7.42
6.86
6.84
6.73
6.59
6.52
6.15
5.99
1.00
1.00
0.94
1.00
1.99
1.98
1.02
1.01
1.97
1.95
1.81
2.07
1.03
1.01
8.7
8.5
8.3
8.1
7.9
7.7
7.5
7.3
7.1
6.9
6.7
6.5
6.3
6.1
5.9
δ (ppm)

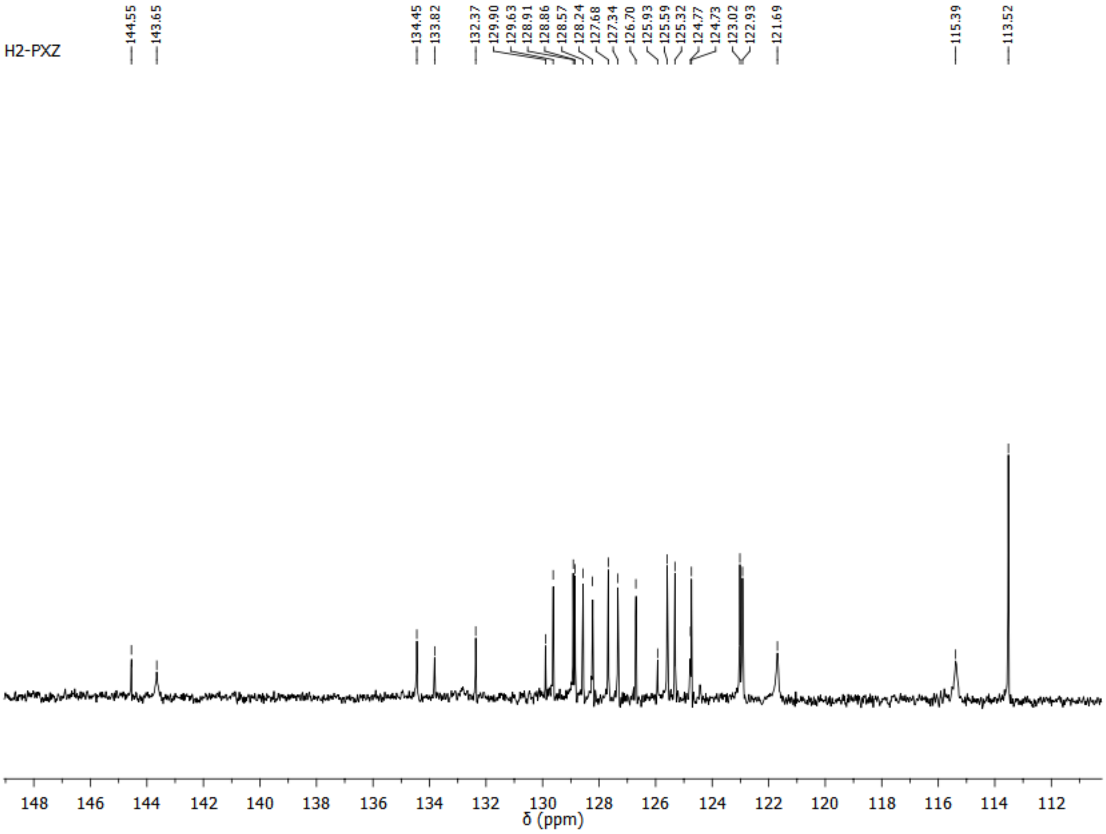
H2-PXZ
144.55
143.65
134.45
133.82
132.37
129.90
129.63
128.91
128.86
128.57
128.24
127.68
127.34
126.70
125.93
125.59
125.32
124.77
124.73
123.02
122.93
121.69
115.39
113.52
148
146
144
142
140
138
136
134
132
130
128
126
124
122
120
118
116
114
112
δ (ppm)

A0

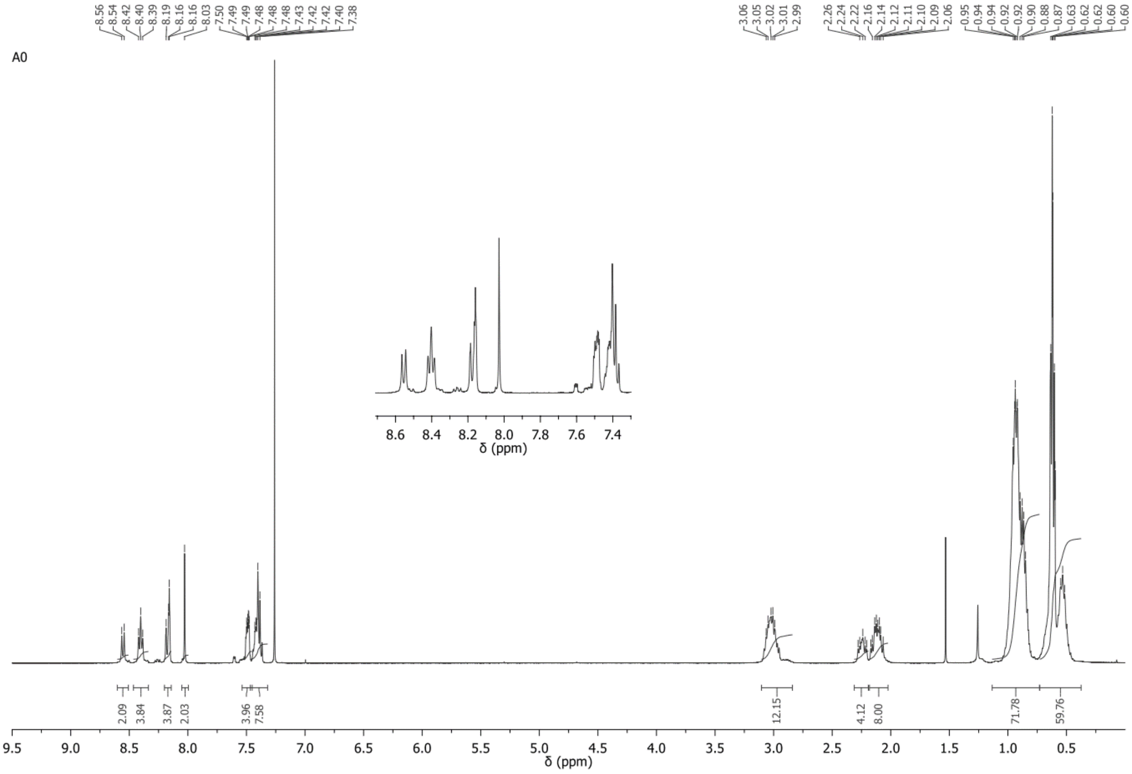
A0
8.56
8.54
8.42
8.40
8.39
8.19
8.16
8.16
8.03
7.50
7.49
7.49
7.48
7.48
7.48
7.43
7.42
7.42
7.40
7.38
3.06
3.05
3.02
3.01
2.99
2.26
2.24
2.22
2.16
2.14
2.12
2.11
2.10
2.09
2.06
0.95
0.94
0.94
0.92
0.92
0.90
0.88
0.87
0.63
0.62
0.62
0.60
0.60
2.09
3.84
3.87
2.03
3.96
7.58
12.15
4.12
8.00
71.78
59.76
8.6
8.4
8.2
8.0
7.8
7.6
7.4
δ (ppm)
9.5
9.0
8.5
8.0
7.5
7.0
6.5
6.0
5.5
5.0
4.5
4.0
3.5
3.0
2.5
2.0
1.5
1.0
0.5
δ (ppm)

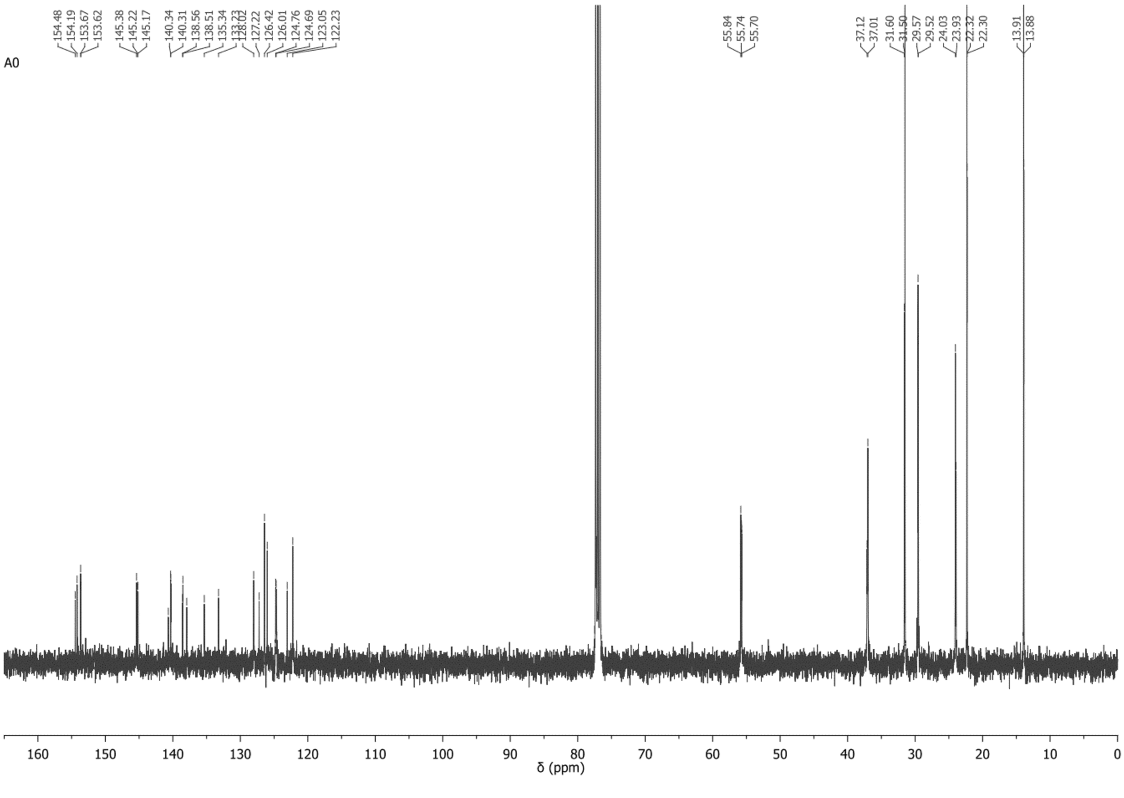
A0
154.48
154.19
153.67
153.62
145.38
145.22
145.17
140.34
140.31
138.56
138.51
135.34
133.23
128.02
127.22
126.42
126.01
124.76
124.69
123.05
122.23
55.84
55.74
55.70
37.12
37.01
31.60
31.50
29.57
29.52
24.03
23.93
22.32
22.30
13.91
13.88
160
150
140
130
120
110
100
90
80
70
60
50
40
30
20
10
0
δ (ppm)

A

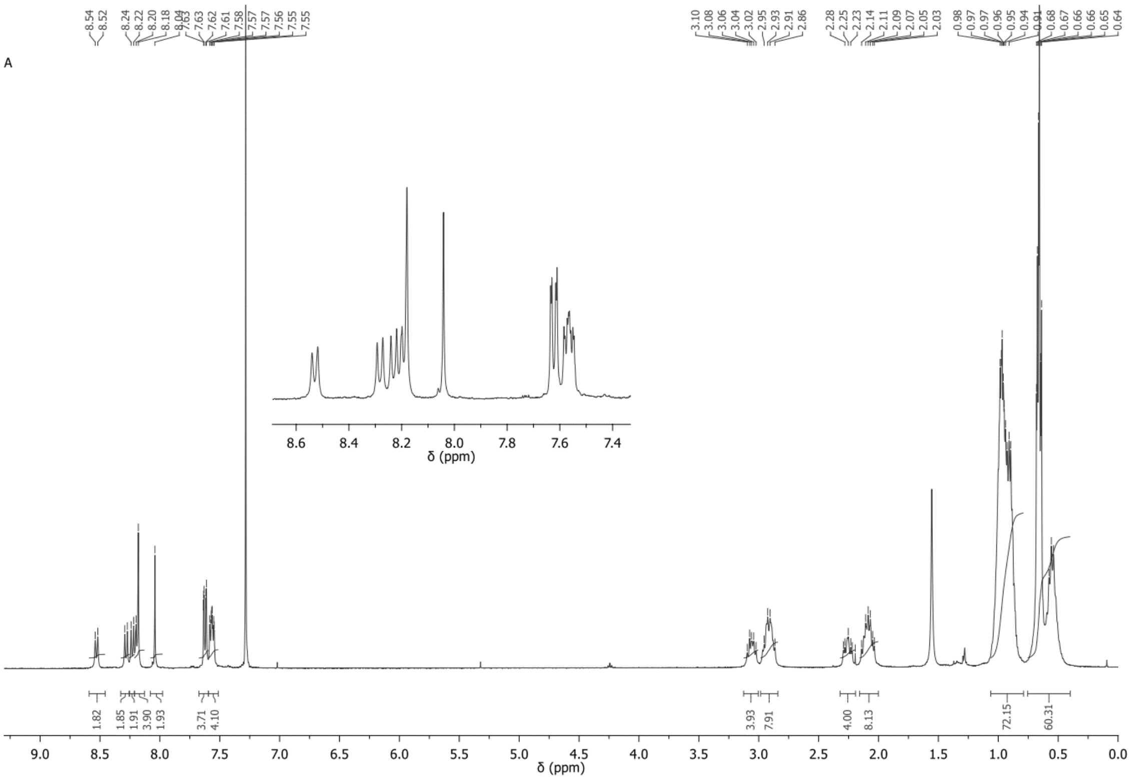
A
8.54
8.52
8.24
8.22
8.20
8.18
8.04
7.63
7.62
7.61
7.58
7.57
7.57
7.56
7.55
7.55
3.10
3.08
3.06
3.04
3.02
2.95
2.93
2.91
2.86
2.28
2.25
2.23
2.14
2.11
2.09
2.07
2.05
2.03
0.98
0.97
0.97
0.96
0.95
0.94
0.91
0.68
0.67
0.66
0.66
0.65
0.64
1.82
1.85
1.91
3.90
1.93
3.71
4.10
3.93
7.91
4.00
8.13
72.15
60.31
8.6
8.4
8.2
8.0
7.8
7.6
7.4
δ (ppm)
9.0
8.5
8.0
7.5
7.0
6.5
6.0
5.5
5.0
4.5
4.0
3.5
3.0
2.5
2.0
1.5
1.0
0.5
0.0
δ (ppm)

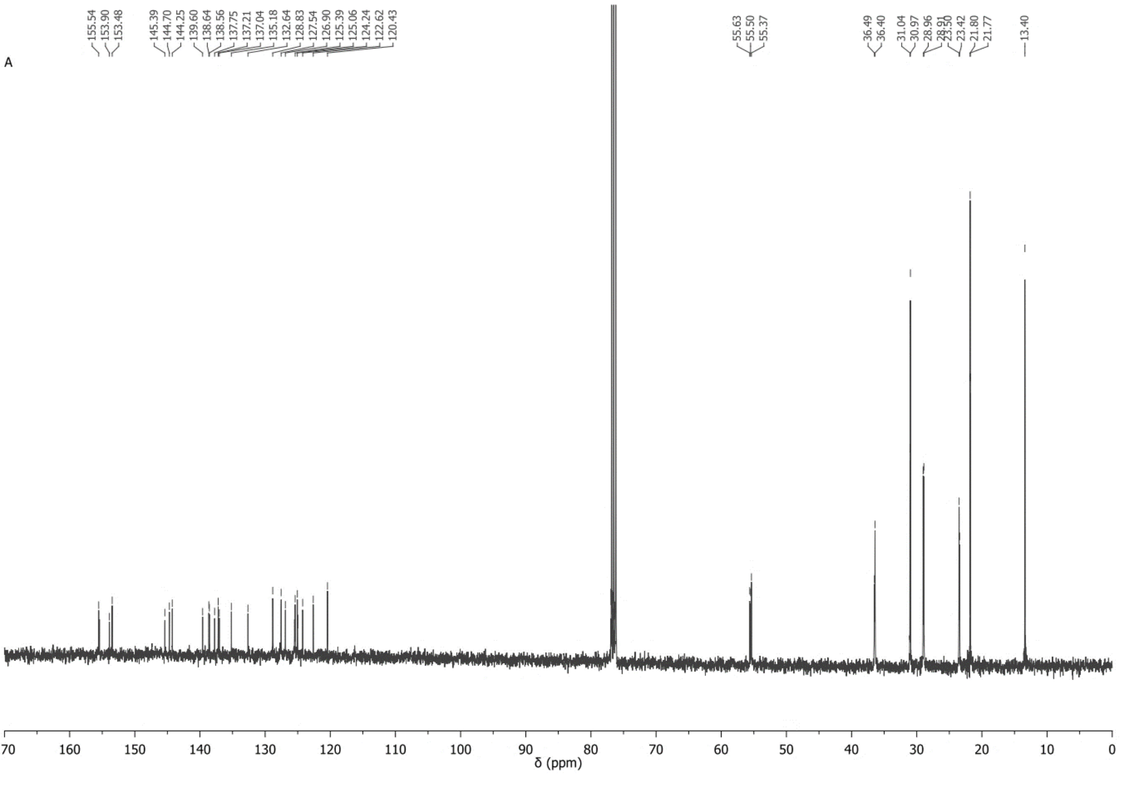
A
155.54
153.90
153.48
145.39
144.70
144.25
139.60
138.64
138.56
137.75
137.21
137.04
135.18
132.64
128.83
127.54
126.90
125.39
125.06
124.24
122.62
120.43
55.63
55.50
55.37
36.49
36.40
31.04
30.97
28.96
28.91
23.50
23.42
21.80
21.77
13.40
170
160
150
140
130
120
110
100
90
80
70
60
50
40
30
20
10
0
δ (ppm)

A1

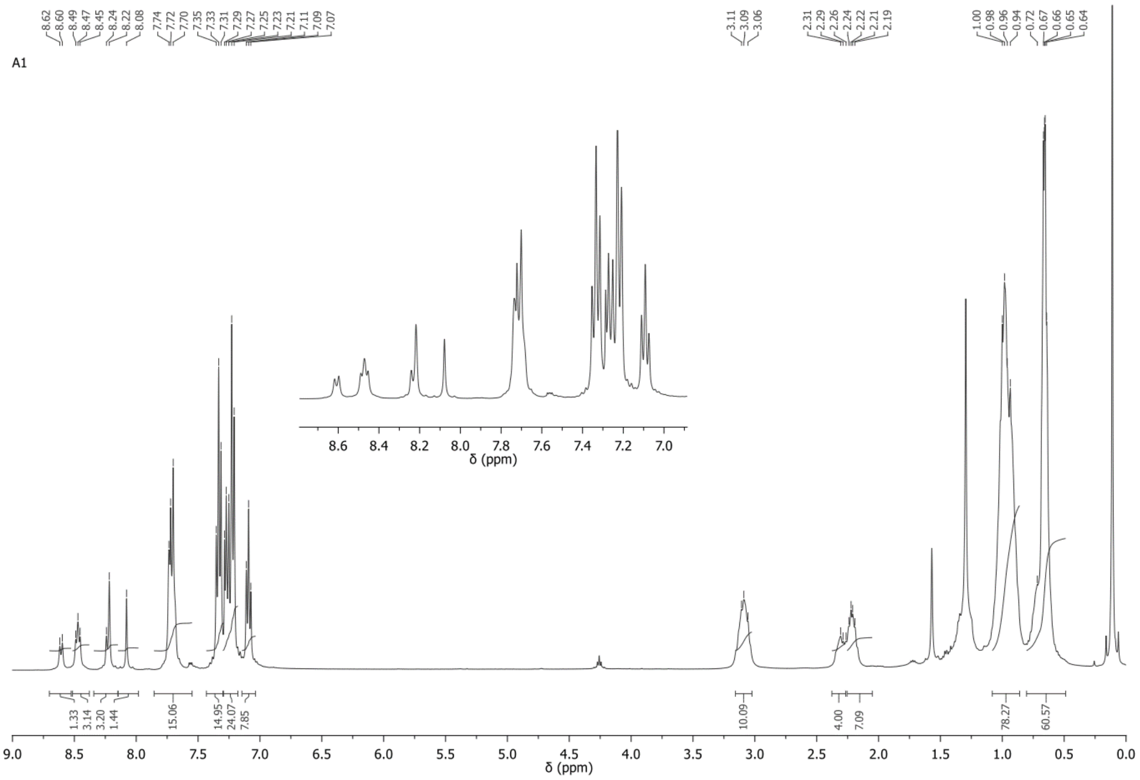
A1
8.62
8.60
8.49
8.47
8.45
8.24
8.22
8.08
7.74
7.72
7.70
7.35
7.33
7.31
7.29
7.27
7.25
7.23
7.21
7.11
7.09
7.07
3.11
3.09
3.06
2.31
2.29
2.26
2.24
2.22
2.21
2.19
1.00
0.98
0.96
0.94
0.72
0.67
0.66
0.65
0.64
1.33
3.14
3.20
1.44
15.06
14.95
24.07
7.85
10.09
4.00
7.09
78.27
60.57
8.6
8.4
8.2
8.0
7.8
7.6
7.4
7.2
7.0
δ (ppm)
9.0
8.5
8.0
7.5
7.0
6.5
6.0
5.5
5.0
4.5
4.0
3.5
3.0
2.5
2.0
1.5
1.0
0.5
0.0
δ (ppm)

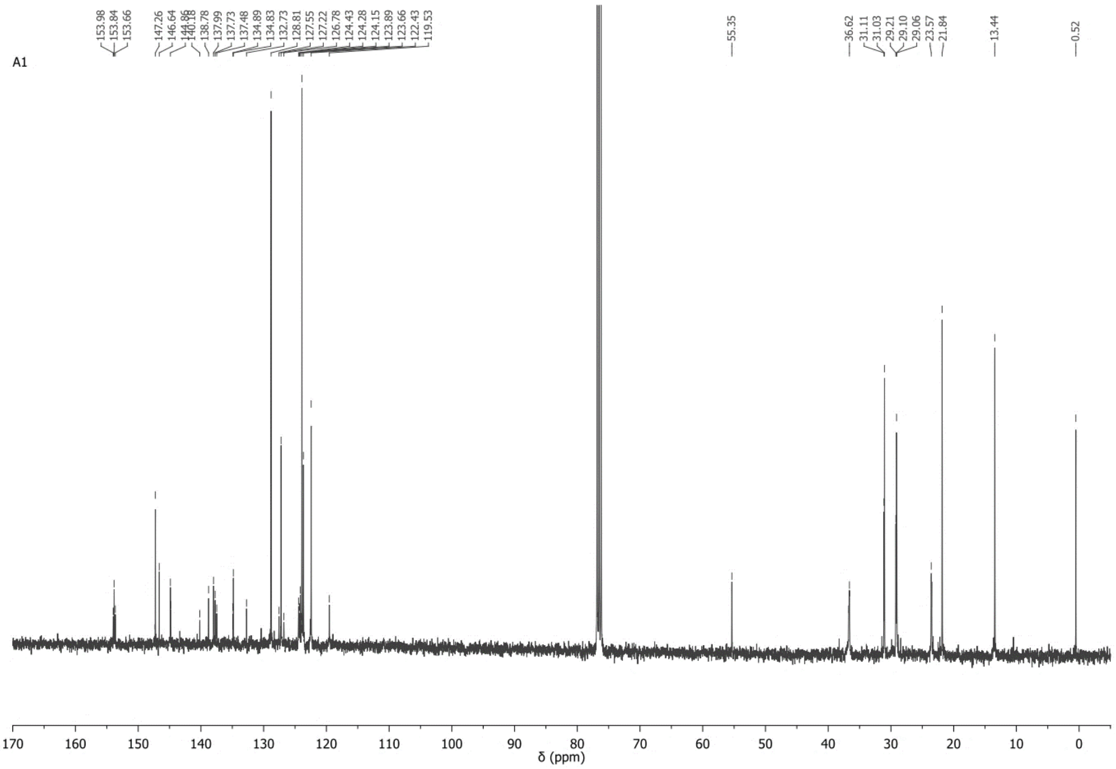
A1
153.98
153.84
153.66
147.26
146.64
144.86
140.18
138.78
137.99
137.73
137.48
134.89
134.83
132.73
128.81
127.55
127.22
126.78
124.43
124.28
124.15
123.89
123.66
122.43
119.53
55.35
36.62
31.11
31.03
29.21
29.10
29.06
23.57
21.84
13.44
0.52
170
160
150
140
130
120
110
100
90
80
70
60
50
40
30
20
10
0
δ (ppm)

A2

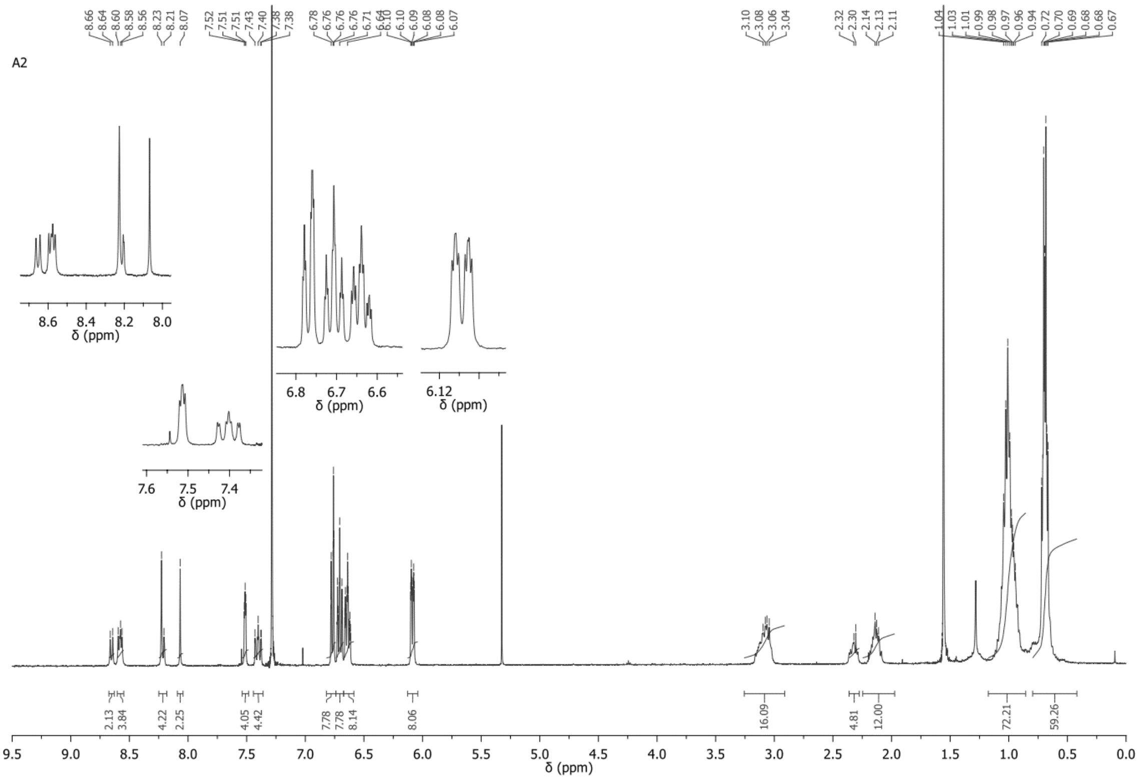
A2
8.66 8.64 8.60 8.58 8.56 8.23 8.21 8.07
7.52 7.51 7.51 7.43 7.40 7.38 7.38
6.78 6.76 6.76 6.76 6.71 6.64 6.10 6.10 6.09 6.08 6.08 6.07
3.10 3.08 3.06 3.04
2.32 2.30 2.14 2.13 2.11
1.04 1.03 1.01 0.99 0.98 0.97 0.96 0.94 0.72 0.70 0.69 0.68 0.68 0.67
8.6 8.4 8.2 8.0
δ (ppm)
7.6 7.5 7.4
δ (ppm)
6.8 6.7 6.6
δ (ppm)
6.12
δ (ppm)
2.13 3.84 4.22 2.25 4.05 4.42 7.78 7.78 8.14 8.06 16.09 4.81 12.00 72.21 59.26
9.5 9.0 8.5 8.0 7.5 7.0 6.5 6.0 5.5 5.0 4.5 4.0 3.5 3.0 2.5 2.0 1.5 1.0 0.5 0.0
δ (ppm)

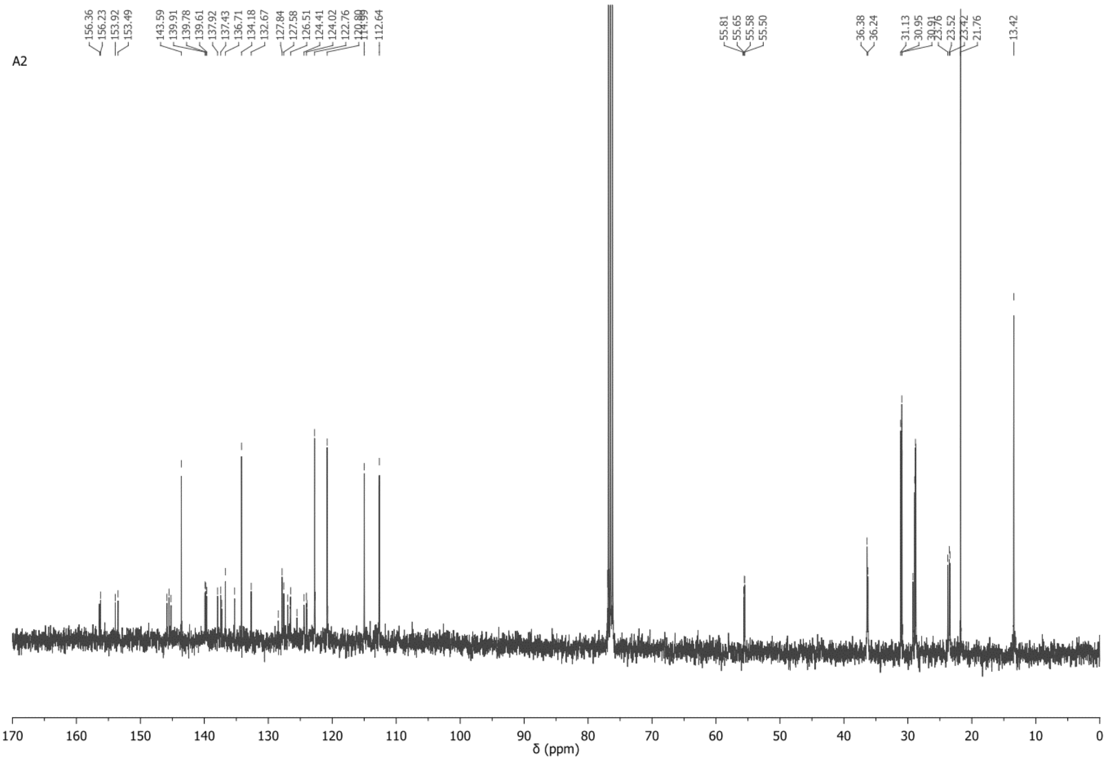
A2
156.36 156.23 153.92 153.49
143.59 139.91 139.78 139.61 137.92 137.43 136.71 134.18 132.67
127.84 127.58 126.51 124.41 124.02 122.76 120.80 114.99 112.64
55.81 55.65 55.58 55.50
36.38 36.24
31.13 30.95 30.91 29.76 23.52 23.42 21.76
13.42
170 160 150 140 130 120 110 100 90 80 70 60 50 40 30 20 10 0
δ (ppm)

Q1

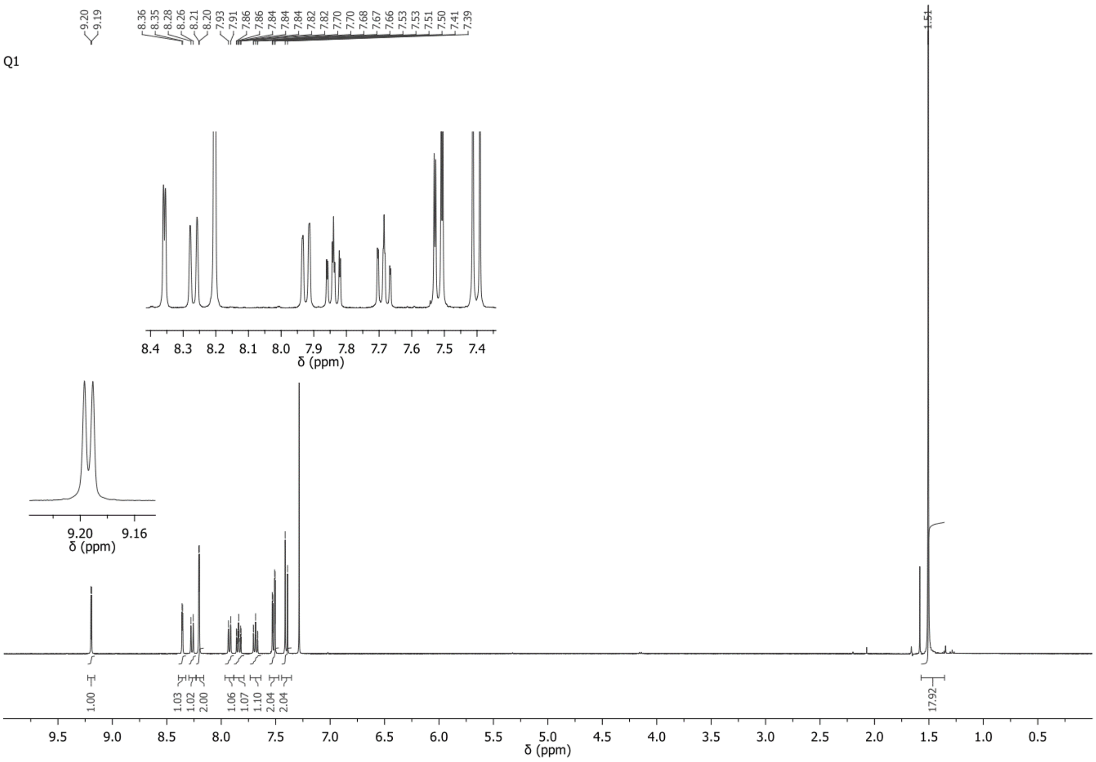
Q1
9.20
9.19
8.36
8.35
8.28
8.26
8.21
8.20
7.93
7.91
7.86
7.86
7.84
7.84
7.84
7.82
7.82
7.70
7.68
7.67
7.66
7.53
7.51
7.50
7.41
7.39
1.51
1.00
1.03
1.02
2.00
1.06
1.07
1.10
2.04
2.04
17.92
9.20
9.16
8.4
8.3
8.2
8.1
8.0
7.9
7.8
7.7
7.6
7.5
7.4
9.5
9.0
8.5
8.0
7.5
7.0
6.5
6.0
5.5
5.0
4.5
4.0
3.5
3.0
2.5
2.0
1.5
1.0
0.5
δ (ppm)

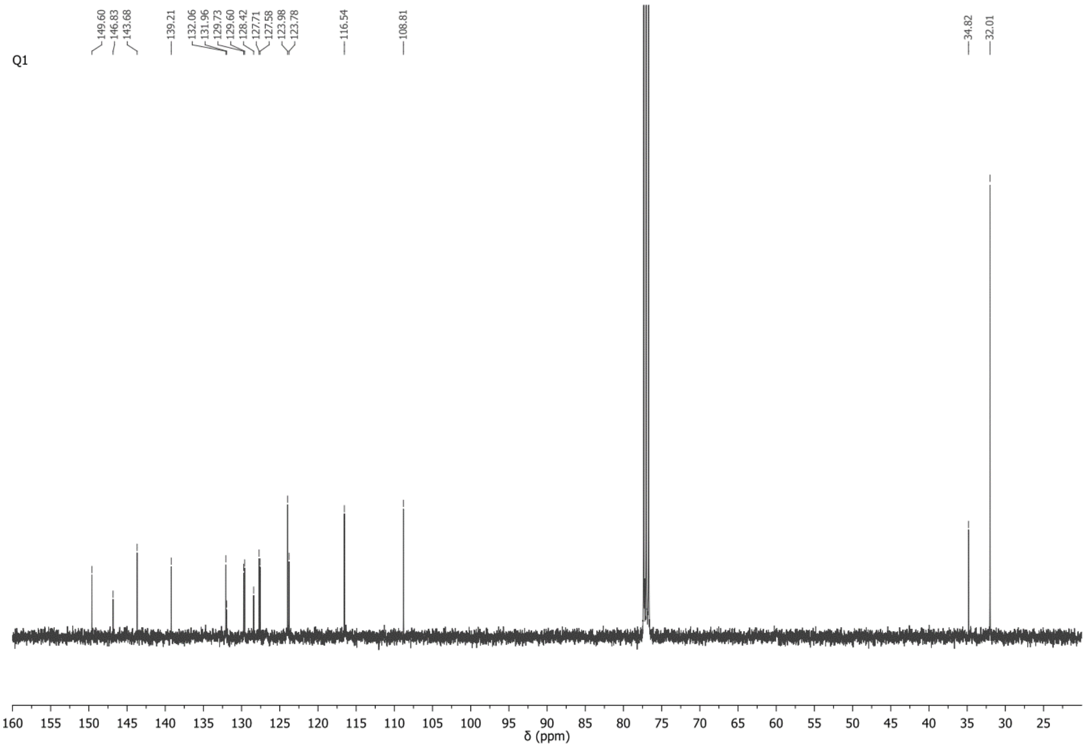
Q1
149.60
146.83
143.68
139.21
132.06
131.96
129.73
129.60
128.42
127.71
127.58
123.98
123.78
116.54
108.81
34.82
32.01
160
155
150
145
140
135
130
125
120
115
110
105
100
95
90
85
80
75
70
65
60
55
50
45
40
35
30
25
δ (ppm)

Q2

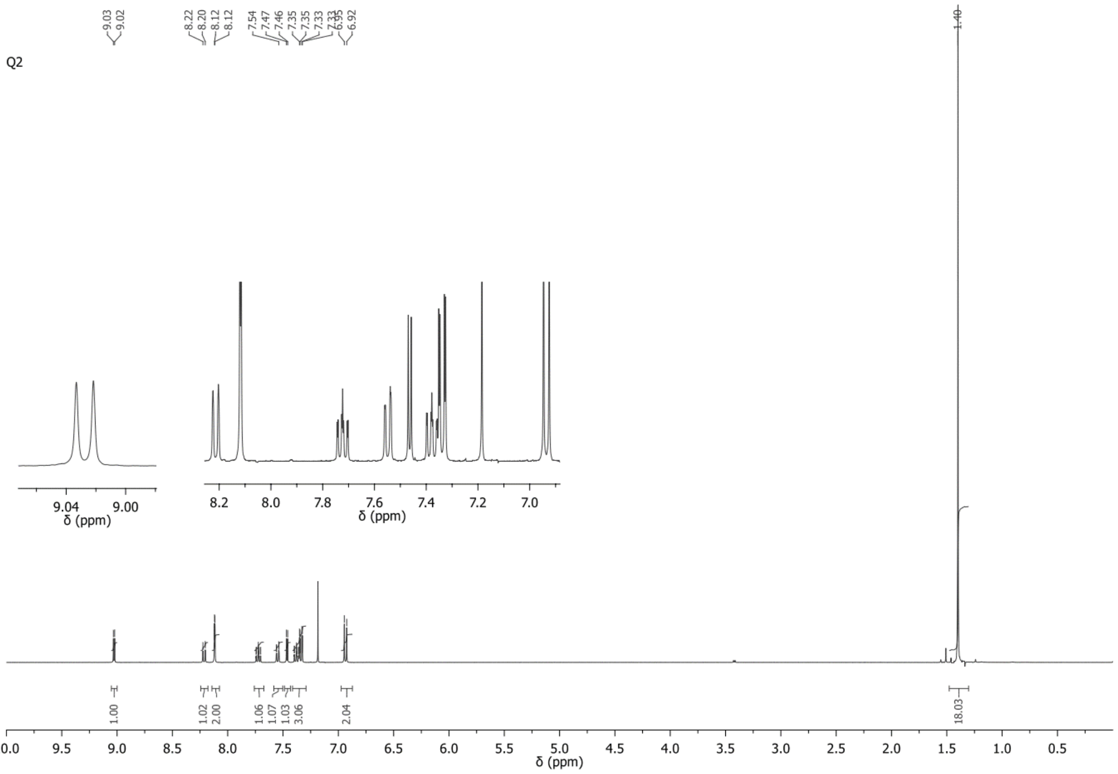
Q2
9.03
9.02
8.22
8.20
8.12
8.12
7.54
7.47
7.46
7.35
7.35
7.33
7.33
6.95
6.92
1.40
9.04
9.00
δ (ppm)
8.2
8.0
7.8
7.6
7.4
7.2
7.0
δ (ppm)
1.00
1.02
2.00
1.06
1.07
1.03
3.06
2.04
18.03
10.0
9.5
9.0
8.5
8.0
7.5
7.0
6.5
6.0
5.5
5.0
4.5
4.0
3.5
3.0
2.5
2.0
1.5
1.0
0.5
δ (ppm)

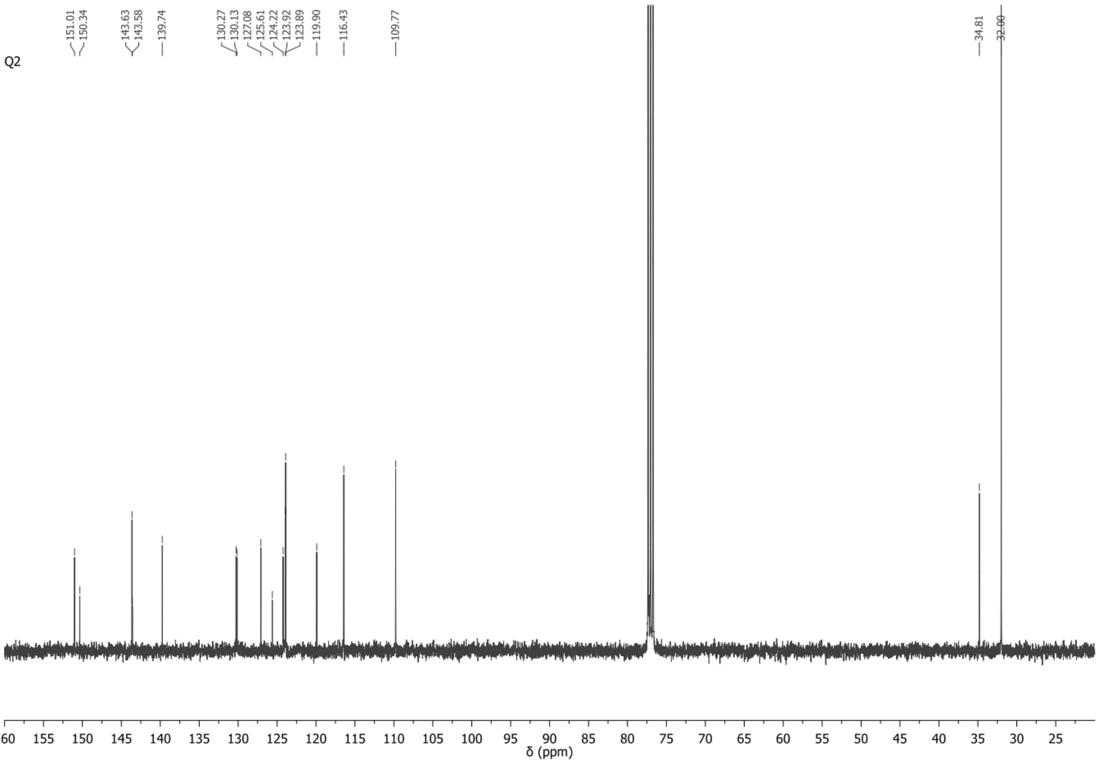
Q2
151.01
150.34
143.63
143.58
139.74
130.27
130.13
127.08
125.61
124.22
123.92
123.89
119.90
116.43
109.77
34.81
32.00
160
155
150
145
140
135
130
125
120
115
110
105
100
95
90
85
80
75
70
65
60
55
50
45
40
35
30
25
δ (ppm)

Q1-S1

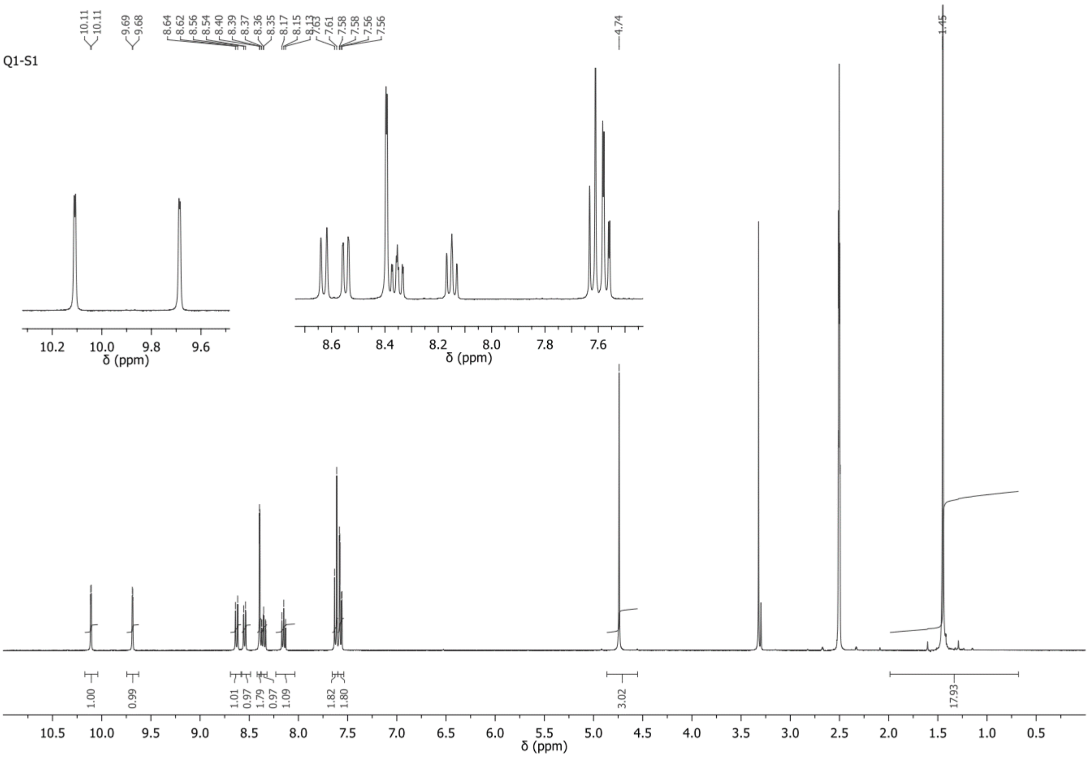
Q1-S1
10.11
10.11
9.69
9.68
8.64
8.62
8.56
8.54
8.40
8.39
8.37
8.36
8.35
8.17
8.15
8.13
7.63
7.61
7.58
7.58
7.56
7.56
4.74
1.45
1.00
0.99
1.01
0.97
1.79
0.97
1.09
1.82
1.80
3.02
17.93
δ (ppm)

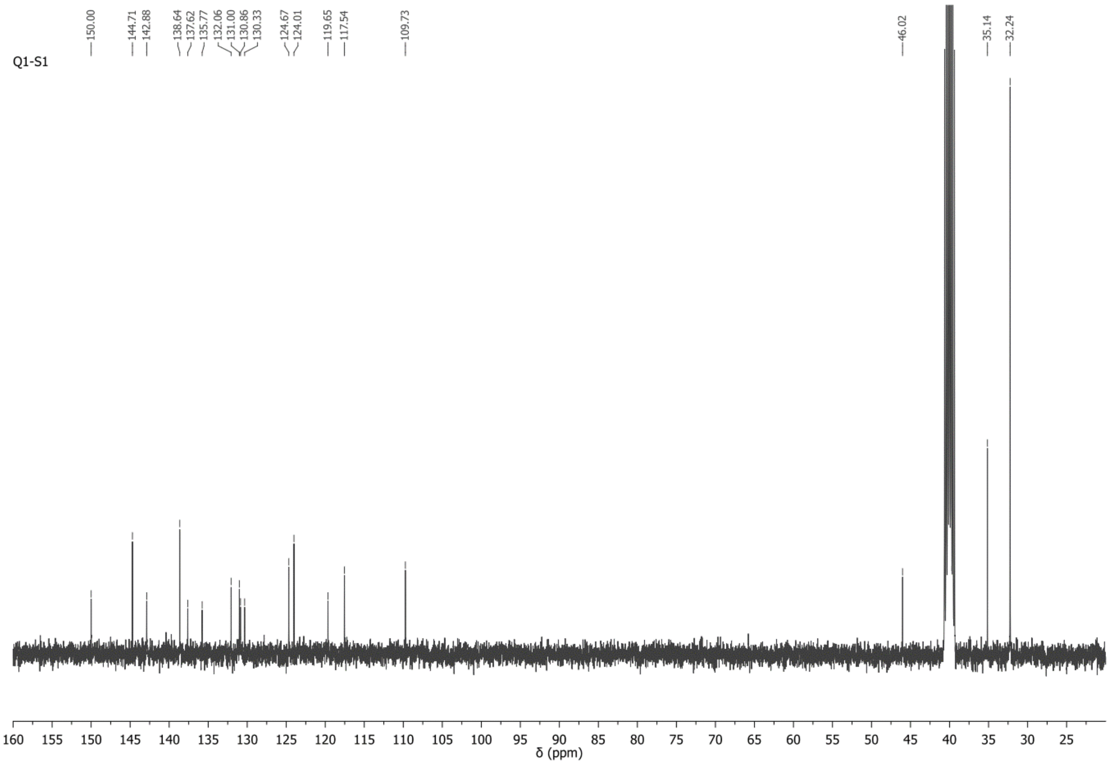
Q1-S1
150.00
144.71
142.88
138.64
137.62
135.77
132.06
131.00
130.86
130.33
124.67
124.01
119.65
117.54
109.73
46.02
35.14
32.24
δ (ppm)

Q2-S1

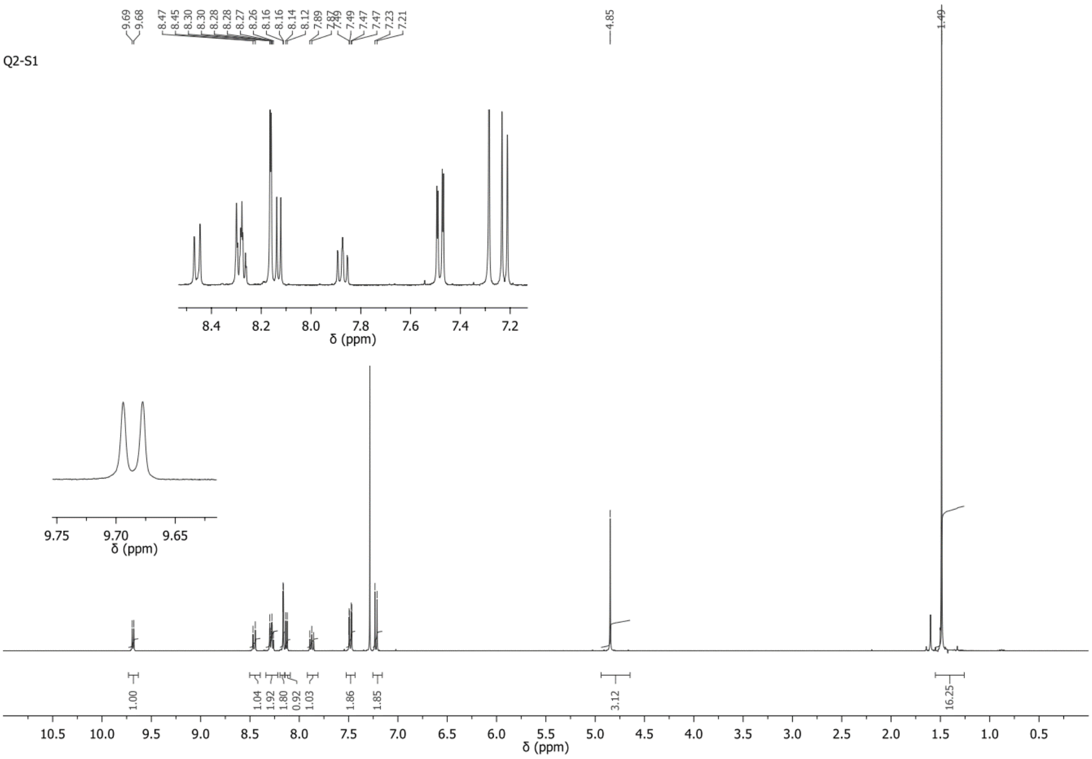
Q2-S1
9.69
9.68
8.47
8.45
8.30
8.30
8.28
8.28
8.27
8.26
8.16
8.16
8.14
8.12
7.89
7.87
7.49
7.49
7.47
7.47
7.23
7.21
4.85
1.49
8.4
8.2
8.0
7.8
7.6
7.4
7.2
δ (ppm)
9.75
9.70
9.65
δ (ppm)
1.00
1.04
1.92
1.80
0.92
1.03
1.86
1.85
3.12
16.25
10.5
10.0
9.5
9.0
8.5
8.0
7.5
7.0
6.5
6.0
5.5
5.0
4.5
4.0
3.5
3.0
2.5
2.0
1.5
1.0
0.5
δ (ppm)

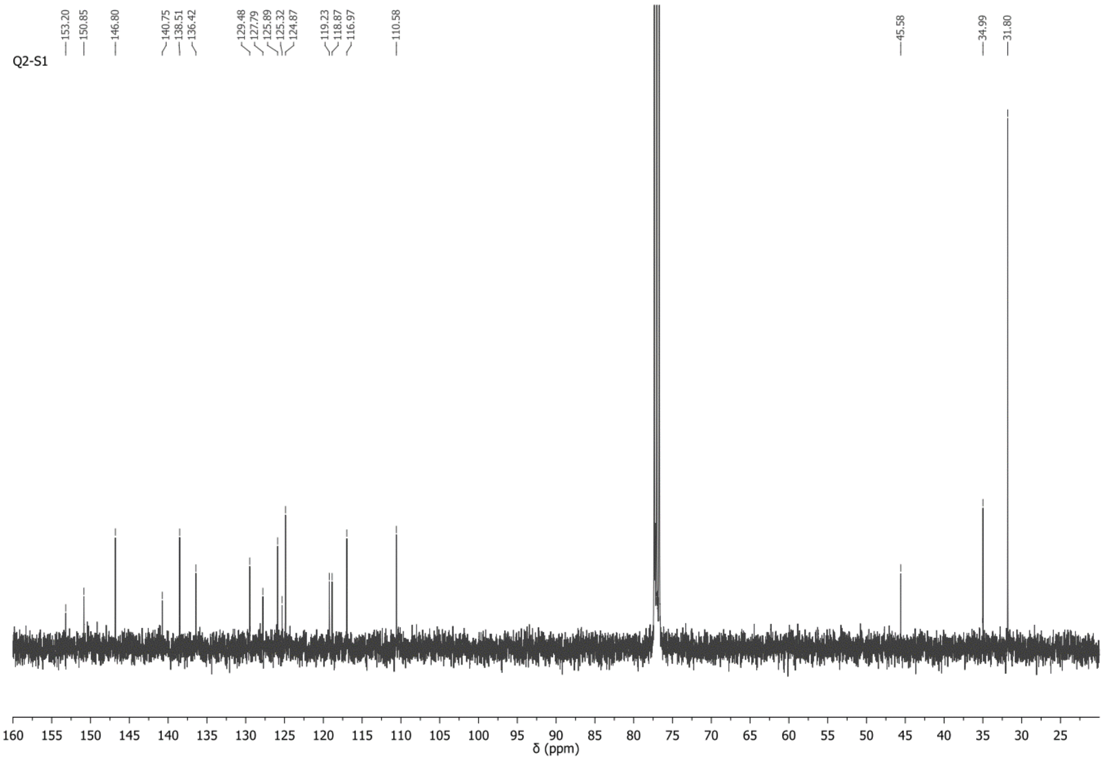
Q2-S1
153.20
150.85
146.80
140.75
138.51
136.42
129.48
127.79
125.89
125.32
124.87
119.23
118.87
116.97
110.58
45.58
34.99
31.80
160
155
150
145
140
135
130
125
120
115
110
105
100
95
90
85
80
75
70
65
60
55
50
45
40
35
30
25
δ (ppm)

Q1-S2

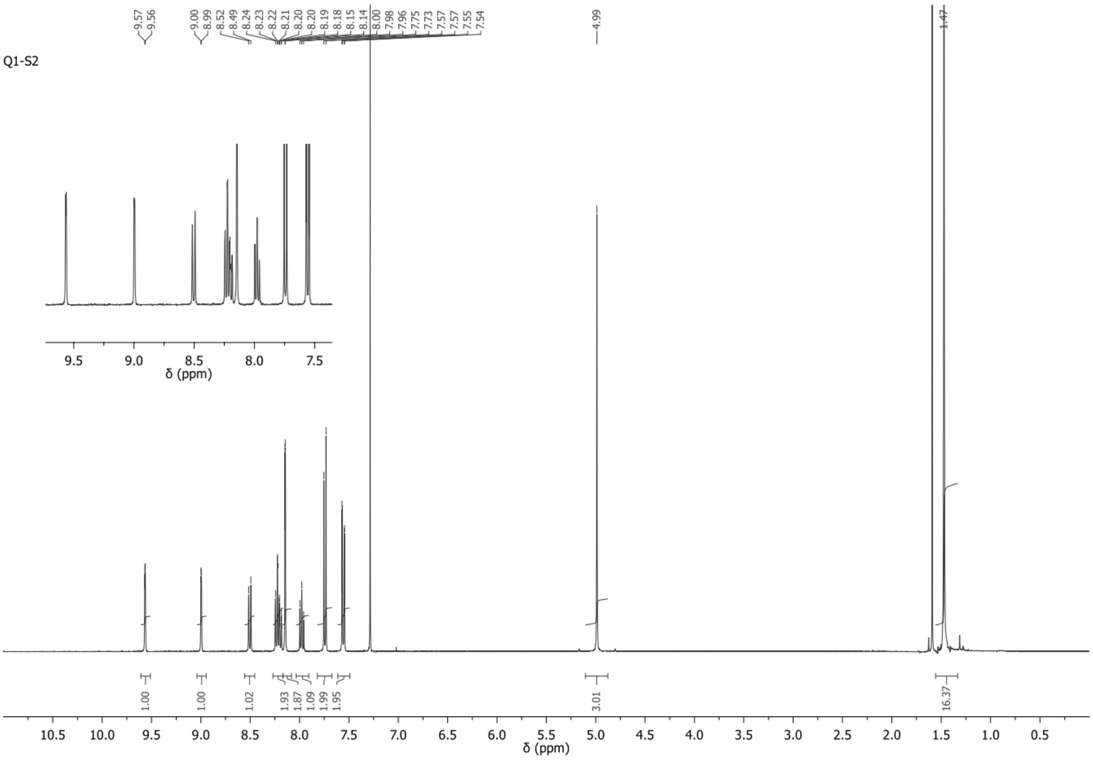
Q1-S2
9.57
9.56
9.00
8.99
8.52
8.49
8.24
8.23
8.22
8.21
8.20
8.19
8.18
8.15
8.14
8.00
7.98
7.96
7.75
7.73
7.57
7.57
7.55
7.54
4.99
1.47
9.5
9.0
8.5
8.0
7.5
δ (ppm)
1.00
1.00
1.02
1.93
1.87
1.09
1.99
1.95
3.01
16.37
10.5
10.0
9.5
9.0
8.5
8.0
7.5
7.0
6.5
6.0
5.5
5.0
4.5
4.0
3.5
3.0
2.5
2.0
1.5
1.0
0.5
δ (ppm)

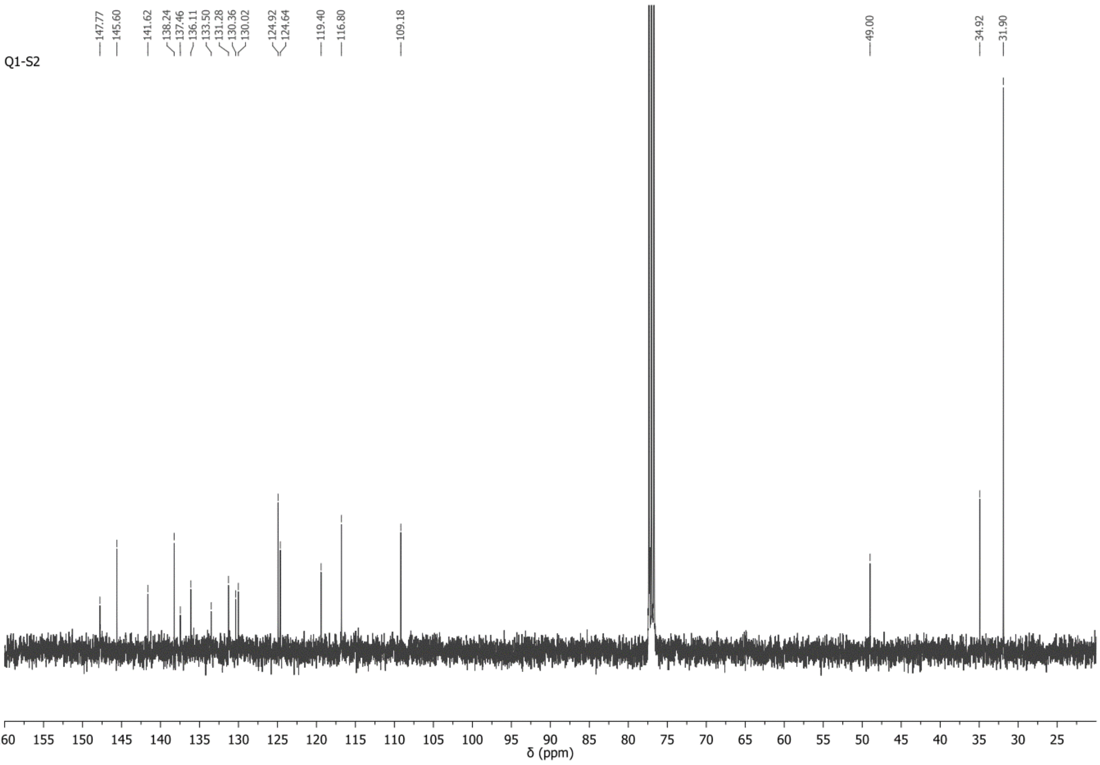
Q1-S2
147.77
145.60
141.62
138.24
137.46
136.11
133.50
131.28
130.36
130.02
124.92
124.64
119.40
116.80
109.18
49.00
34.92
31.90
160
155
150
145
140
135
130
125
120
115
110
105
100
95
90
85
80
75
70
65
60
55
50
45
40
35
30
25
δ (ppm)

Q2-S2

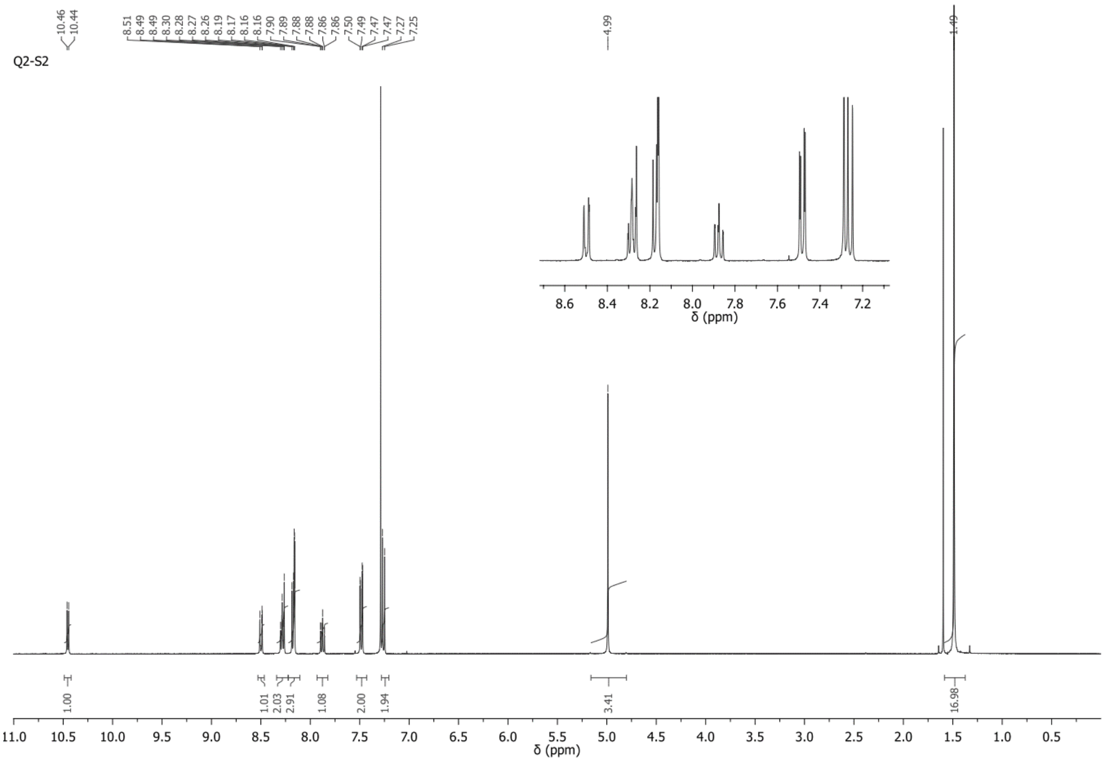
Q2-S2
10.46
10.44
8.51
8.49
8.49
8.30
8.28
8.27
8.26
8.19
8.17
8.16
8.16
7.90
7.89
7.88
7.88
7.86
7.86
7.50
7.49
7.47
7.47
7.27
7.25
4.99
1.49
1.00
1.01
2.03
2.91
1.08
2.00
1.94
3.41
16.98
δ (ppm)
8.6
8.4
8.2
8.0
7.8
7.6
7.4
7.2
11.0
10.5
10.0
9.5
9.0
8.5
8.0
7.5
7.0
6.5
6.0
5.5
5.0
4.5
4.0
3.5
3.0
2.5
2.0
1.5
1.0
0.5

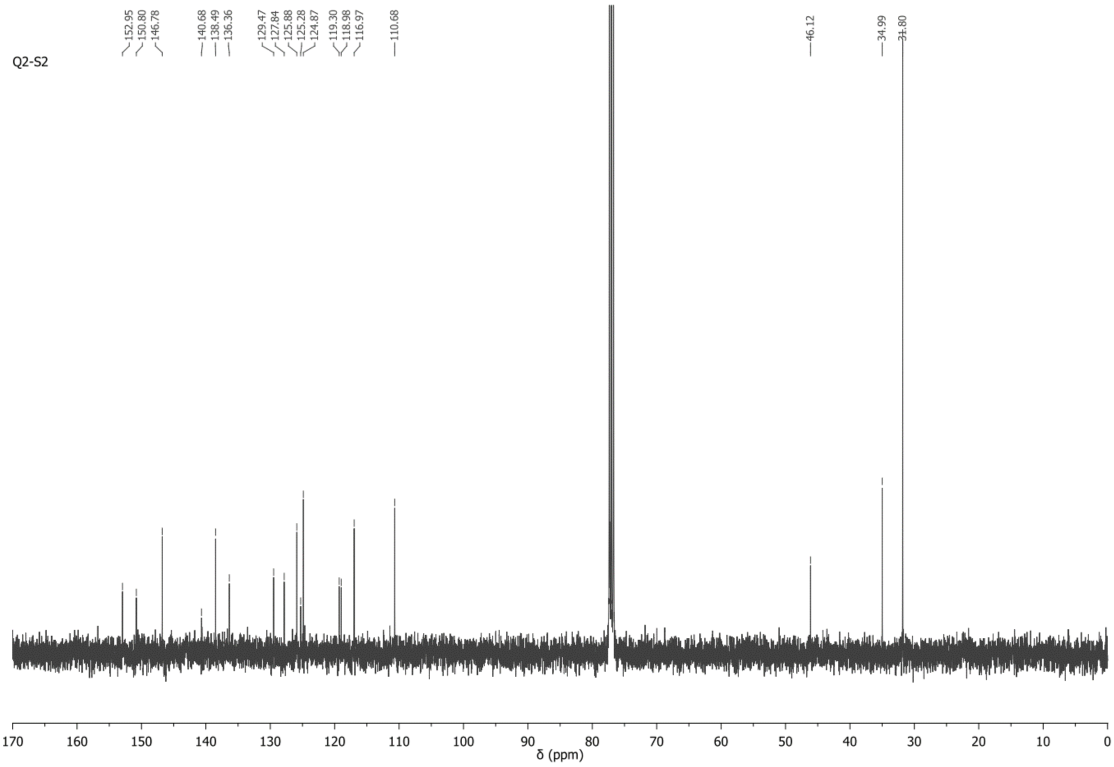
Q2-S2
152.95
150.80
146.78
140.68
138.49
136.36
129.47
127.84
125.88
125.28
124.87
119.30
118.98
116.97
110.68
46.12
34.99
31.80
δ (ppm)
170
160
150
140
130
120
110
100
90
80
70
60
50
40
30
20
10
0

Q1-S3

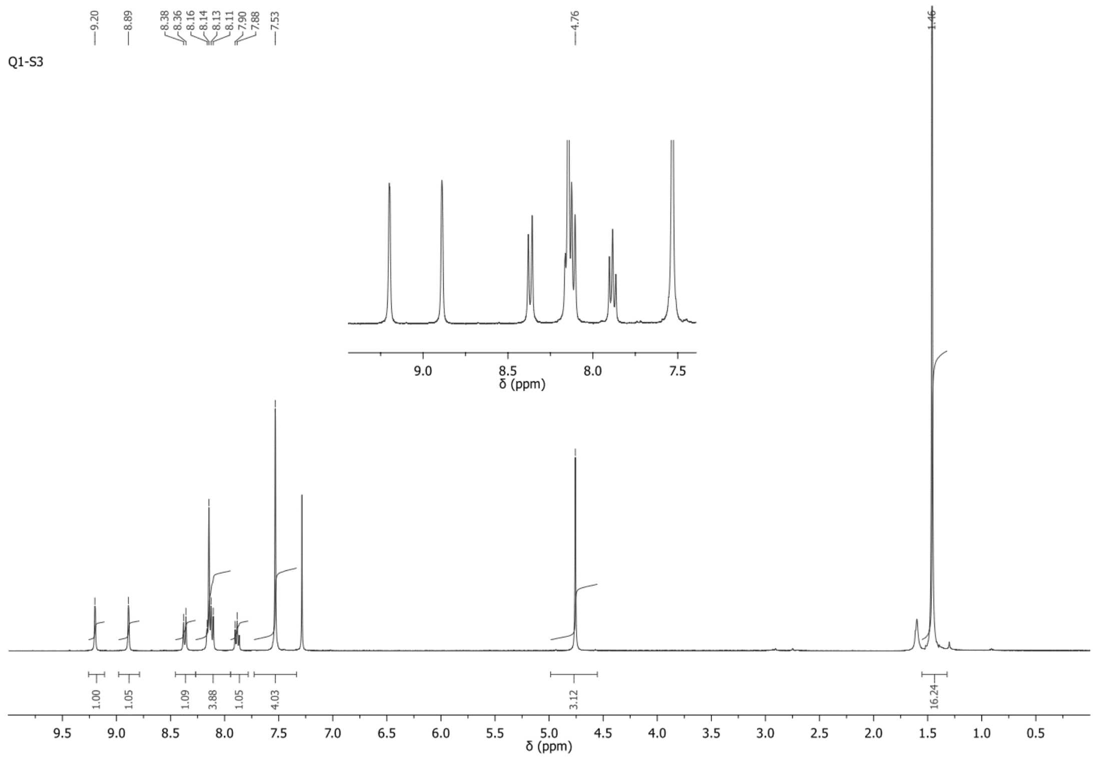
Q1-S3
9.20
8.89
8.38
8.36
8.16
8.14
8.13
8.11
7.90
7.88
7.53
4.76
1.46
9.0
8.5
8.0
7.5
δ (ppm)
1.00
1.05
1.09
3.88
1.05
4.03
3.12
16.24
9.5
9.0
8.5
8.0
7.5
7.0
6.5
6.0
5.5
5.0
4.5
4.0
3.5
3.0
2.5
2.0
1.5
1.0
0.5
δ (ppm)

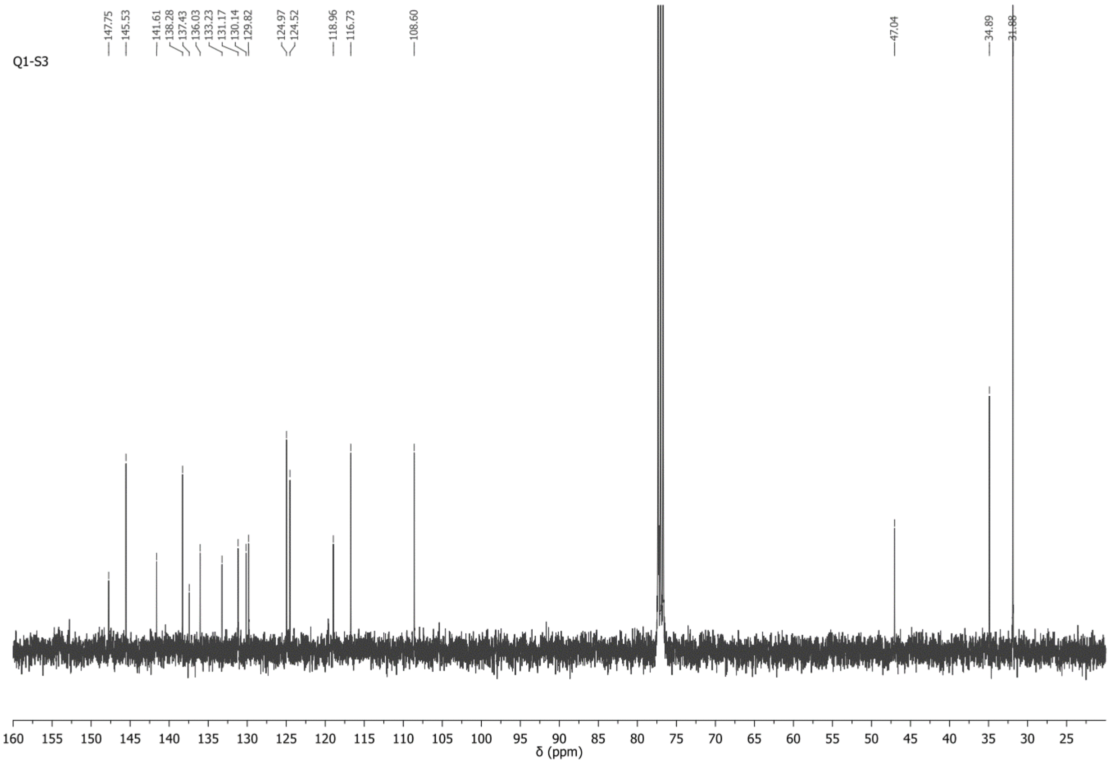
Q1-S3
147.75
145.53
141.61
138.28
137.43
136.03
133.23
131.17
130.14
129.82
124.97
124.52
118.96
116.73
108.60
47.04
34.89
31.88
160
155
150
145
140
135
130
125
120
115
110
105
100
95
90
85
80
75
70
65
60
55
50
45
40
35
30
25
δ (ppm)

Q2-S3

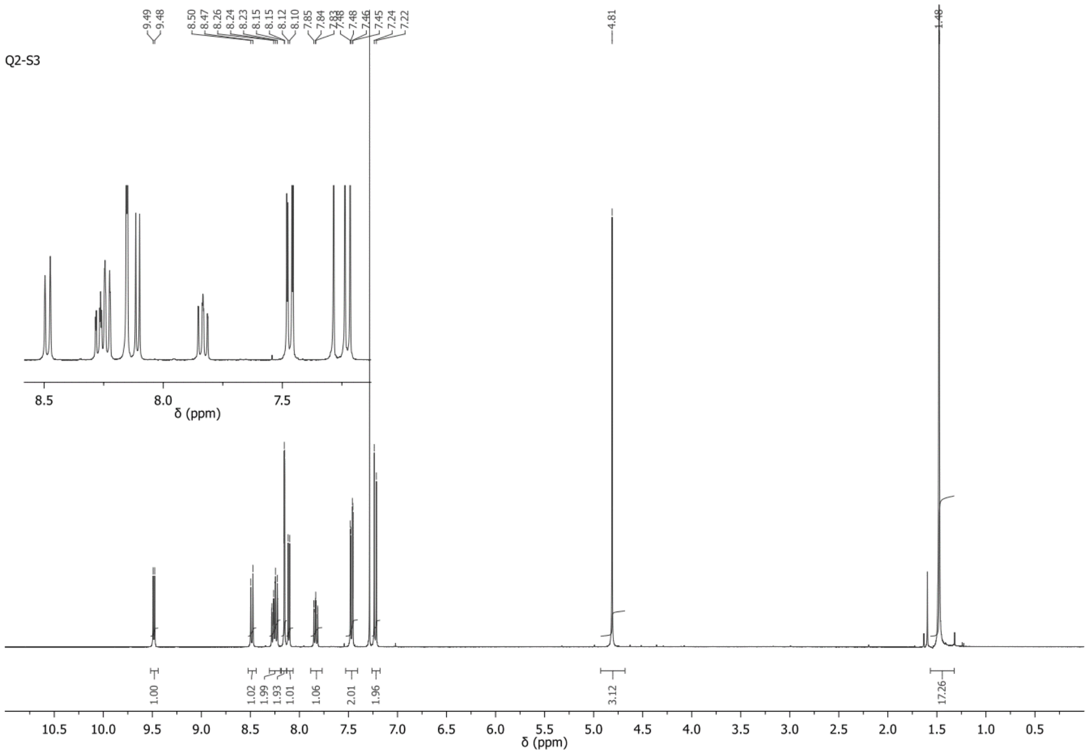
Q2-S3
9.49
9.48
8.50
8.47
8.26
8.24
8.23
8.15
8.15
8.12
8.10
7.85
7.84
7.83
7.48
7.48
7.46
7.45
7.24
7.22
4.81
1.48
1.00
1.02
1.99
1.93
1.01
1.06
2.01
1.96
3.12
17.26
8.5
8.0
7.5
δ (ppm)
10.5
10.0
9.5
9.0
8.5
8.0
7.5
7.0
6.5
6.0
5.5
5.0
4.5
4.0
3.5
3.0
2.5
2.0
1.5
1.0
0.5
δ (ppm)

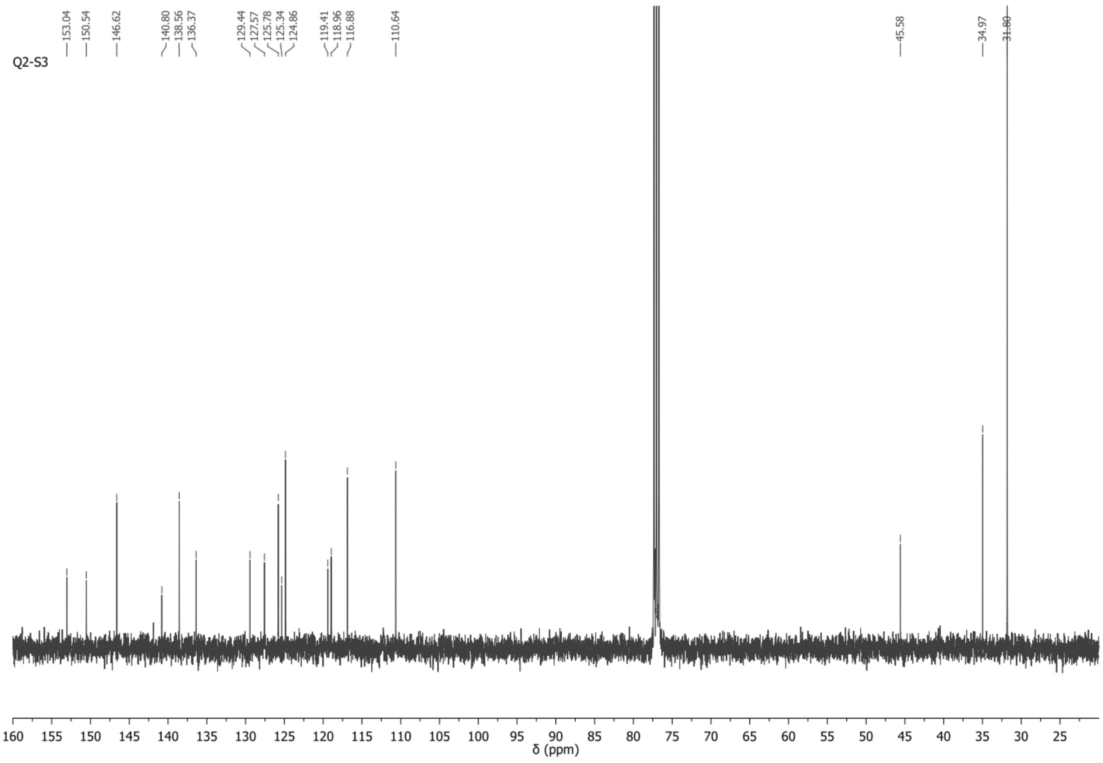
Q2-S3
153.04
150.54
146.62
140.80
138.56
136.37
129.44
127.57
125.78
125.34
124.86
119.41
118.96
116.88
110.64
45.58
34.97
31.80
160
155
150
145
140
135
130
125
120
115
110
105
100
95
90
85
80
75
70
65
60
55
50
45
40
35
30
25
δ (ppm)

Crystal data

H1-PXZ

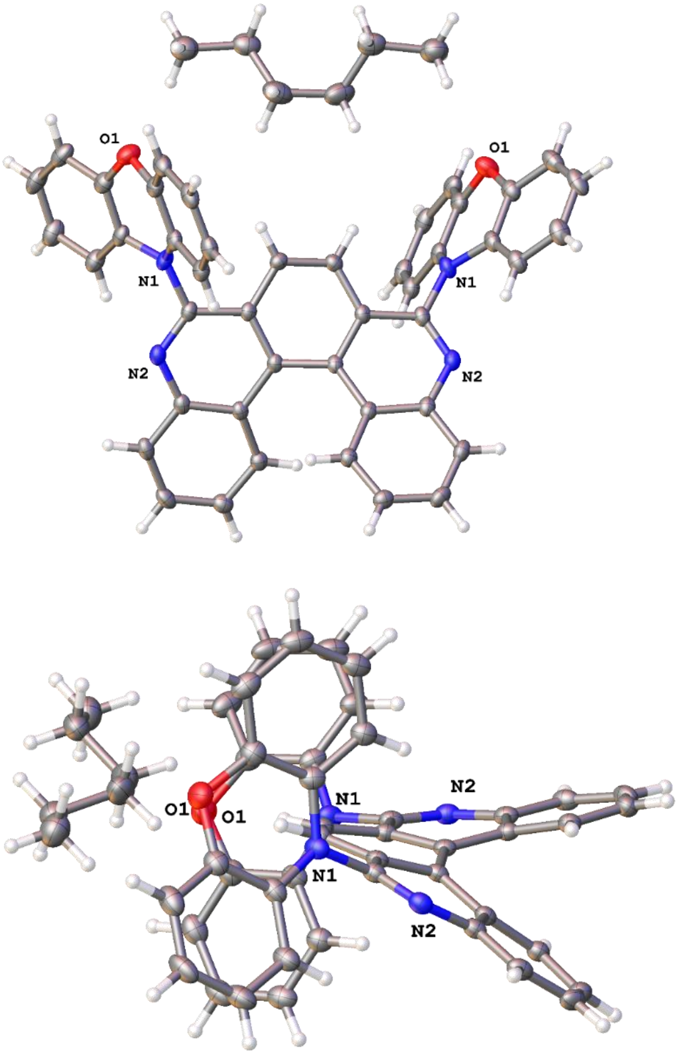

Figure 7.1. **H1-PXZ** crystal structure. Thermal ellipsoids drawn at the 50% probability level.

Table 7.1. Crystal data and structure refinement details of **H1-PXZ**.

Compound	**H1-PXZ**
Formula	$C_{50}H_{40}N_4O_2$
$D_{calc.}$/ g cm^{-3}	1.295
μ/mm^{-1}	0.623
Formula Weight	728.86
Colour	orange
Shape	block
Size/mm^3	0.200×0.150×0.100
T/K	100(2)
Crystal System	monoclinic
Space Group	C2/c
a/Å	11.28030(10)
b/Å	14.5794(2)
c/Å	22.9364(2)
α/°	90
β/°	97.5790(10)
γ/°	90
V/Å^3	3739.17(7)
Z	4
Z'	0.5
Wavelength/Å	1.54184
Radiation type	CuK$_\alpha$
Θ_{min}/°	6.376
Θ_{max}/°	68.235
Measured Refl.	31606
Independent Refl.	3349
Reflections Used	3305
R_{int}	0.0300
Parameters	254
Restraints	0
Largest Peak	0.504
Deepest Hole	-0.311
GooF	1.056
wR_2 (all data)	0.1056
wR_2	0.1053
R_1 (all data)	0.0445
R_1	0.0441

Table 7.2. Fractional atomic coordinates (×10^4) and equivalent isotropic displacement parameters (Å^2×10^3) for **H1-PXZ**. U_{eq} is defined as 1/3 of the trace of the orthogonalised U_{ij}.

Atom	x	y	z	U_{eq}
O1	6147.4(9)	6790.5(7)	5628.4(5)	33.4(3)
N2	6726.8(10)	3534.1(8)	6305.9(5)	21.6(3)
N1	6244.3(10)	5085.8(8)	6170.7(5)	22.8(3)
C20	5406.3(11)	3432.1(9)	7280.3(5)	17.9(3)
C14	6735.9(11)	2742.6(9)	6637.7(6)	20.6(3)
C19	6102.6(11)	2654.2(9)	7131.0(5)	18.7(3)
C21	5608.7(11)	4273.2(9)	7010.0(5)	18.7(3)
C13	6226.1(11)	4254.7(9)	6495.2(6)	20.3(3)
C22	5254.2(11)	5111.8(9)	7246.0(6)	20.0(3)
C12	5173.6(12)	5367.9(10)	5825.5(6)	22.8(3)
C18	6301.0(11)	1851.5(9)	7476.9(6)	21.1(3)
C1	7322.0(12)	5504.7(10)	6056.6(6)	23.5(3)
C15	7420.5(11)	2005.5(10)	6469.0(6)	24.1(3)
C11	4149.7(12)	4828.9(10)	5737.4(6)	25.0(3)
C17	7001.3(12)	1152.2(10)	7312.3(6)	24.3(3)
C7	5151.7(13)	6224.4(10)	5551.8(6)	25.8(3)
C6	7241.5(13)	6362.6(10)	5784.1(6)	26.4(3)
C2	8453.3(12)	5128.6(11)	6216.0(6)	27.6(3)
C16	7538.7(12)	1217.6(10)	6794.0(6)	26.1(3)
C8	4144.9(13)	6533.4(11)	5201.5(6)	30.1(3)
C10	3121.3(13)	5149.2(11)	5394.9(6)	28.1(3)
C5	8250.7(14)	6831.5(11)	5670.4(6)	33.1(4)
C9	3121.0(13)	5998.4(11)	5125.3(6)	30.4(3)
C3	9470.0(13)	5602.9(12)	6104.5(7)	33.3(4)
C4	9371.9(14)	6449.8(12)	5831.8(6)	34.7(4)
C24	6114.3(15)	8716.6(12)	7158.7(8)	39.3(4)
C23	6779.1(18)	8632.0(13)	6625.8(8)	47.0(4)
C25	5310.0(16)	7907.3(12)	7228.0(9)	46.9(5)

Table 7.3. Anisotropic displacement parameters (×10^4) **H1-PXZ**. The anisotropic displacement factor exponent takes the form: $-2\pi^2[h^2a^{*2} \times U_{11} + \ldots + 2hka^* \times b^* \times U_{12}]$

Atom	U_{11}	U_{22}	U_{33}	U_{23}	U_{13}	U_{12}
O1	33.8(6)	28.3(6)	38.0(6)	7.8(4)	4.2(5)	-2.7(4)
N2	18.9(5)	27.4(6)	18.8(5)	-1.2(4)	3.8(4)	-2.4(5)
N1	20.4(6)	28.4(6)	20.1(6)	5.2(5)	4.1(4)	-2.8(5)
C20	14.8(6)	22.8(7)	15.8(6)	-1.2(5)	0.7(5)	-1.8(5)
C14	16.7(6)	26.0(7)	18.9(6)	-3.2(5)	2.1(5)	-2.5(5)
C19	15.3(6)	22.1(7)	18.6(6)	-3.0(5)	1.7(5)	-1.8(5)
C21	14.4(6)	23.4(7)	17.9(6)	0.5(5)	1.4(5)	-0.9(5)
C13	16.8(6)	26.3(7)	17.6(6)	1.3(5)	1.8(5)	-3.1(5)
C22	17.4(6)	20.5(7)	21.7(6)	2.2(5)	1.4(5)	-1.0(5)
C12	23.9(7)	29.8(7)	15.2(6)	0.2(5)	5.1(5)	2.0(6)
C18	17.5(6)	23.7(7)	22.0(6)	-0.8(5)	2.3(5)	-0.9(5)
C1	25.8(7)	29.1(7)	16.0(6)	-0.5(5)	4.5(5)	-7.1(6)
C15	18.4(6)	32.0(8)	22.4(7)	-6.9(6)	4.2(5)	-0.3(5)
C11	24.9(7)	31.2(8)	19.7(6)	-0.8(6)	5.6(5)	0.3(6)
C17	19.9(6)	24.2(7)	28.0(7)	-1.2(6)	0.2(5)	1.8(5)
C7	29.4(7)	29.3(7)	19.8(6)	0.4(5)	7.2(5)	0.3(6)
C6	29.4(7)	30.3(8)	19.3(6)	1.1(6)	2.3(5)	-4.2(6)
C2	25.6(7)	34.6(8)	22.4(7)	3.5(6)	1.9(5)	-5.7(6)
C16	19.5(7)	28.6(7)	29.9(7)	-7.8(6)	1.8(5)	4.6(5)
C8	36.5(8)	34.1(8)	20.7(7)	3.6(6)	7.7(6)	9.0(6)

Atom	U_{11}	U_{22}	U_{33}	U_{23}	U_{13}	U_{12}
C10	24.1(7)	40.0(8)	20.5(7)	-6.1(6)	4.4(5)	1.7(6)
C5	40.4(9)	35.4(8)	22.7(7)	4.4(6)	1.6(6)	-14.2(7)
C9	29.0(7)	43.9(9)	18.3(7)	-1.5(6)	3.6(5)	11.3(7)
C3	25.0(7)	46.4(9)	27.6(7)	3.3(7)	0.6(6)	-8.5(7)
C4	30.8(8)	46.9(10)	25.8(7)	4.7(7)	1.3(6)	-18.1(7)
C24	35.4(9)	32.9(8)	47.3(10)	0.3(7)	-3.0(7)	3.9(7)
C23	52.7(11)	38.3(10)	49.9(11)	0.9(8)	6.4(8)	3.1(8)
C25	36.4(9)	33.5(9)	70.0(13)	-7.8(8)	3.5(8)	4.6(7)

Table 7.4. Bond Lengths in Å for **H1-PXZ**.

Atom	Atom	Length/Å
O1	C7	1.3862(18)
O1	C6	1.3869(18)
N2	C14	1.3816(18)
N2	C13	1.2946(18)
N1	C13	1.4237(17)
N1	C12	1.4151(17)
N1	C1	1.4154(17)
C20	C20[1]	1.449(2)
C20	C19	1.4462(18)
C20	C21	1.4063(18)
C14	C19	1.4215(17)
C14	C15	1.4072(19)
C19	C18	1.4150(19)
C21	C13	1.4481(18)
C21	C22	1.4158(18)
C22	C22[1]	1.365(3)
C12	C11	1.390(2)
C12	C7	1.396(2)
C18	C17	1.3729(19)
C1	C6	1.396(2)
C1	C2	1.393(2)
C15	C16	1.366(2)
C11	C10	1.393(2)
C17	C16	1.407(2)
C7	C8	1.378(2)
C6	C5	1.382(2)
C2	C3	1.391(2)
C8	C9	1.385(2)
C10	C9	1.384(2)
C5	C4	1.387(2)
C3	C4	1.382(2)
C24	C23	1.521(3)
C24	C25	1.509(2)
C25	C25[1]	1.509(4)

---

[1] 1-x,+y,3/2-z

Table 7.5. Bond Angles in ° for **H1-PXZ**.

Atom	Atom	Atom	Angle/°
C7	O1	C6	116.32(11)
C13	N2	C14	117.70(11)
C12	N1	C13	118.02(11)
C12	N1	C1	117.50(11)
C1	N1	C13	122.40(11)
C19	C20	C20[1]	125.29(8)
C21	C20	C20[1]	117.45(7)
C21	C20	C19	117.05(11)
N2	C14	C19	123.11(12)
N2	C14	C15	116.80(12)
C15	C14	C19	120.09(12)
C14	C19	C20	117.58(12)
C18	C19	C20	124.51(12)
C18	C19	C14	117.54(12)
C20	C21	C13	117.81(11)
C20	C21	C22	120.94(12)
C22	C21	C13	121.22(12)
N2	C13	N1	118.58(11)
N2	C13	C21	124.52(12)
N1	C13	C21	116.87(11)
C22[1]	C22	C21	119.86(8)
C11	C12	N1	123.28(13)
C11	C12	C7	118.37(13)
C7	C12	N1	118.33(12)
C17	C18	C19	120.94(12)
C6	C1	N1	117.56(13)
C2	C1	N1	124.15(13)
C2	C1	C6	118.26(13)
C16	C15	C14	120.64(12)
C12	C11	C10	120.46(14)
C18	C17	C16	120.64(13)
O1	C7	C12	120.63(12)
C8	C7	O1	118.10(13)
C8	C7	C12	121.27(14)
O1	C6	C1	121.44(12)
C5	C6	O1	117.13(13)
C5	C6	C1	121.41(14)
C3	C2	C1	120.34(14)
C15	C16	C17	119.74(13)
C7	C8	C9	119.92(14)
C9	C10	C11	120.20(14)
C6	C5	C4	119.75(14)
C10	C9	C8	119.75(14)
C4	C3	C2	120.56(15)
C3	C4	C5	119.67(14)
C25	C24	C23	112.84(15)
C25[1]	C25	C24	115.96(14)

---

[1] 1-x,+y,3/2-z

Table 7.6. Torsion Angles in ° for **H1-PXZ**.

Atom	Atom	Atom	Atom	Angle/°
O1	C7	C8	C9	-178.41(12)
O1	C6	C5	C4	178.16(13)
N2	C14	C19	C20	0.97(18)
N2	C14	C19	C18	-172.40(11)
N2	C14	C15	C16	175.96(12)
N1	C12	C11	C10	179.64(12)
N1	C12	C7	O1	-1.43(19)
N1	C12	C7	C8	178.85(12)
N1	C1	C6	O1	-0.20(19)
N1	C1	C6	C5	178.28(13)
N1	C1	C2	C3	-177.76(13)
C20^{1}	C20	C19	C14	172.13(14)
C20^{1}	C20	C19	C18	-15.0(2)
C20^{1}	C20	C21	C13	-168.26(13)
C20^{1}	C20	C21	C22	13.8(2)
C20	C19	C18	C17	-178.21(12)
C20	C21	C13	N2	-8.42(19)
C20	C21	C13	N1	169.67(11)
C20	C21	C22	C22^{1}	2.3(2)
C14	N2	C13	N1	177.82(11)
C14	N2	C13	C21	-4.13(19)
C14	C19	C18	C17	-5.35(18)
C14	C15	C16	C17	-1.9(2)
C19	C20	C21	C13	16.70(17)
C19	C20	C21	C22	-161.28(11)
C19	C14	C15	C16	-3.61(19)
C19	C18	C17	C16	0.0(2)
C21	C20	C19	C14	-13.26(17)
C21	C20	C19	C18	159.60(12)
C13	N2	C14	C19	7.85(18)
C13	N2	C14	C15	-171.71(12)
C13	N1	C12	C11	-7.23(19)
C13	N1	C12	C7	173.89(12)
C13	N1	C1	C6	-173.93(12)
C13	N1	C1	C2	3.9(2)
C13	C21	C22	C22^{1}	-175.62(14)
C22	C21	C13	N2	169.55(12)
C22	C21	C13	N1	-12.36(17)
C12	N1	C13	N2	105.06(14)
C12	N1	C13	C21	-73.14(15)
C12	N1	C1	C6	22.82(18)
C12	N1	C1	C2	-159.36(13)
C12	C11	C10	C9	1.8(2)
C12	C7	C8	C9	1.3(2)
C18	C17	C16	C15	3.8(2)
C1	N1	C13	N2	-58.12(17)

Atom	Atom	Atom	Atom	Angle/°
C1	N1	C13	C21	123.68(13)
C1	N1	C12	C11	156.78(13)
C1	N1	C12	C7	-22.11(18)
C1	C6	C5	C4	-0.4(2)
C1	C2	C3	C4	-0.4(2)
C15	C14	C19	C20	-179.49(11)
C15	C14	C19	C18	7.15(18)
C11	C12	C7	O1	179.63(12)
C11	C12	C7	C8	-0.1(2)
C11	C10	C9	C8	-0.6(2)
C7	O1	C6	C1	-22.94(18)
C7	O1	C6	C5	158.53(13)
C7	C12	C11	C10	-1.48(19)
C7	C8	C9	C10	-1.0(2)
C6	O1	C7	C12	23.68(18)
C6	O1	C7	C8	-156.59(13)
C6	C1	C2	C3	0.1(2)
C6	C5	C4	C3	0.1(2)
C2	C1	C6	O1	-178.16(13)
C2	C1	C6	C5	0.3(2)
C2	C3	C4	C5	0.3(2)
C23	C24	C25	C25[1]	175.62(17)

---

[1] 1-x,+y,3/2-z

Table 7.7. Hydrogen fractional atomic coordinates (×10^4) and equivalent isotropic displacement parameters (Å2×10^3) for **H1-PXZ**. U_{eq} is defined as 1/3 of the trace of the orthogonalised U_{ij}.

Atom	x	y	z	U_{eq}
H22	5370	5673	7051	24
H18	5945	1796	7828	25
H15	7804	2056	6126	29
H11	4151	4238	5912	30
H17	7124	619	7551	29
H2	8531	4545	6402	33
H16	7982	716	6671	31
H8	4153	7113	5012	36
H10	2418	4784	5346	34
H5	8177	7413	5482	40
H9	2421	6214	4889	36
H3	10238	5342	6217	40
H4	10069	6769	5755	42
H24A	6703	8774	7517	47
H24B	5626	9283	7121	47
H23A	6201	8605	6267	71
H23B	7262	8071	6659	71
H23C	7302	9165	6608	71
H25A	4692	7881	6879	56
H25B	5794	7341	7229	56

H2-PXZ

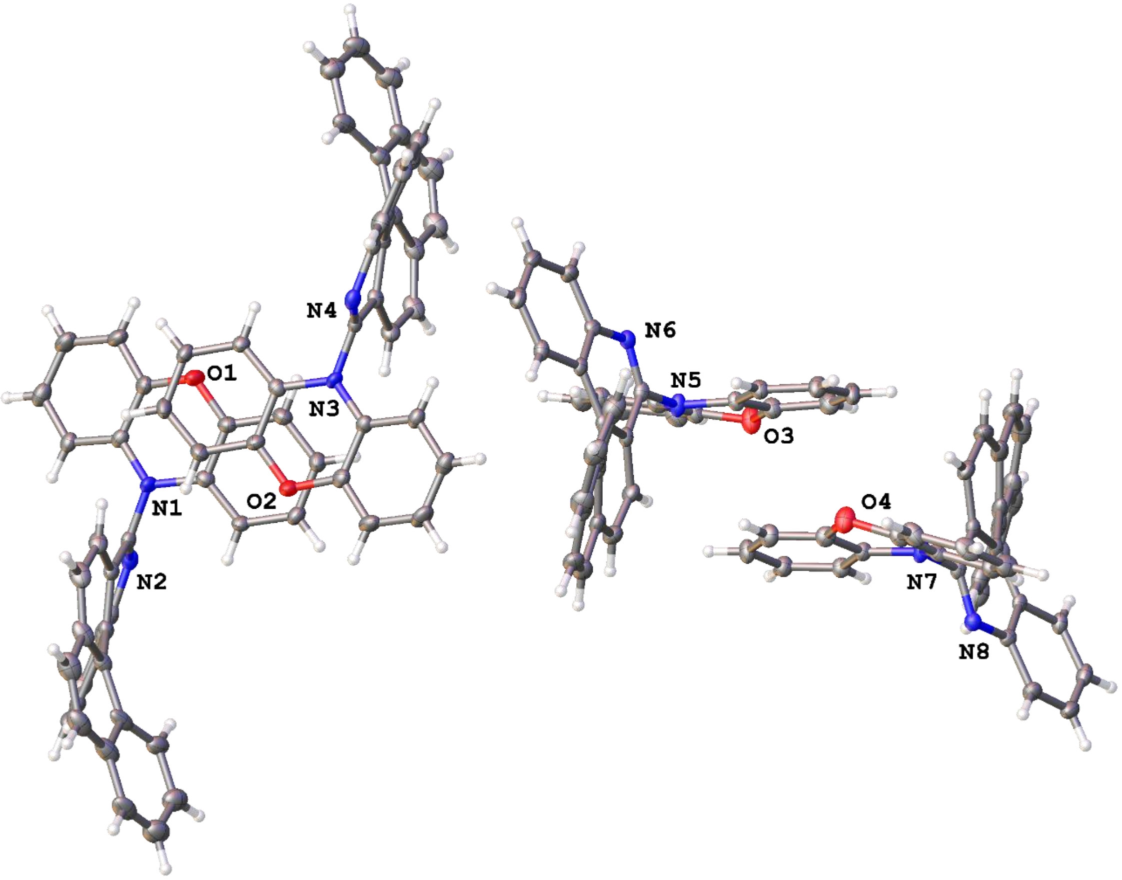

Figure 7.2. **H1-PXZ** crystal structure. Thermal ellipsoids drawn at the 50% probability level.

Table 7.8. Crystal data and structure refinement details of **H2-PXZ.**

Compound	**H2-PXZ**
Formula	$C_{33}H_{20}N_2O$
$D_{calc.}$/ g cm^{-3}	1.370
μ/mm^{-1}	0.650
Formula Weight	460.51
Colour	yellow
Shape	block
Size/mm^3	0.150×0.080×0.050
T/K	100(2)
Crystal System	triclinic
Space Group	P-1
a/Å	14.2418(2)
b/Å	14.2451(2)
c/Å	22.5117(2)
α/°	88.0520(10)
β/°	92.0040(10)
γ/°	101.8250(10)
V/Å^3	4465.74(10)
Z	8
Z'	4
Wavelength/Å	1.54184
Radiation type	CuK$_\alpha$
Θ_{min}/°	1.964
Θ_{max}/°	68.249
Measured Refl.	78986
Independent Refl.	16070
Reflections Used	15605
R_{int}	0.0352
Parameters	1298
Restraints	0
Largest Peak	0.920
Deepest Hole	-0.339
GooF	1.039
wR_2 (all data)	0.1956
wR_2	0.1941
R_1 (all data)	0.0723
R_1	0.0714

Table 7.9. Fractional Atomic Coordinates ($\times 10^4$) and Equivalent Isotropic Displacement Parameters (Å2$\times 10^3$) for **H2-PXZ**. U_{eq} is defined as 1/3 of the trace of the orthogonalised U_{ij}.

Atom	**x**	**y**	**z**	U_{eq}
O1	3159.1(16)	1622.0(13)	5853.5(8)	33.3(5)
N1	3499.3(17)	3512.1(15)	6231.7(9)	22.8(5)
N2	4608.0(16)	4813.2(16)	6596.6(8)	21.8(4)
C1	3474.9(18)	2762.5(18)	6655.6(10)	20.6(5)
C2	3583.3(18)	2900.3(19)	7263.8(10)	22.6(5)
C3	3512(2)	2123(2)	7659.8(12)	31.4(6)
C4	3341(2)	1198(2)	7455.0(12)	34.8(7)
C5	3233(2)	1046(2)	6845.8(12)	30.0(6)
C6	3294.1(19)	1819.9(19)	6450.6(11)	24.6(5)
C7	3432.9(19)	2372.8(18)	5453.3(11)	24.0(5)
C8	3516(2)	2153.5(19)	4868.3(11)	27.4(6)
C9	3778(2)	2882.7(19)	4443.2(11)	26.5(6)
C10	3964.8(19)	3823(2)	4615.7(11)	24.0(5)
C11	3884.5(19)	4040.3(18)	5204.7(10)	20.9(5)
C12	3610.9(19)	3331.0(18)	5630.2(11)	21.7(5)
C13	3744.6(18)	4489.1(18)	6403.9(9)	18.7(5)
C14	3015.2(18)	5049.0(19)	6312.4(10)	19.4(5)
C15	2025.0(19)	4597(2)	6236.1(11)	26.0(6)
C16	1363.5(19)	5174(2)	6173.4(12)	31.2(6)
C17	1641(2)	6170(2)	6084.7(12)	29.7(6)
C18	948(2)	6767(2)	5960.1(13)	38.0(7)
C19	1226(2)	7709(2)	5801.7(13)	38.8(7)
C20	2193(2)	8127(2)	5706.5(12)	35.9(7)
C21	2488(2)	9094(2)	5461.3(12)	35.9(7)
C22	3404(3)	9436(2)	5317.3(14)	43.8(8)
C23	4093(2)	8864(2)	5378.4(12)	37.9(7)
C24	3843(2)	7954.9(19)	5627.7(11)	29.7(6)
C25	2911(2)	7581(2)	5821.7(11)	30.8(7)
C26	2627.0(19)	6618.3(19)	6088.7(11)	22.9(5)
C27	3292.5(18)	6045.0(18)	6319.1(10)	18.6(5)
C28	4221.3(18)	6416.4(18)	6607.1(10)	18.1(5)
C29	4500(2)	7352.6(19)	6825.7(10)	22.7(5)
C30	5356(2)	7633.4(19)	7137.9(10)	24.9(5)
C31	5983.0(19)	6997(2)	7250.2(11)	27.2(6)
C32	5723.1(18)	6077(2)	7057.1(11)	25.7(5)
C33	4833.8(18)	5769.2(19)	6749.6(10)	20.6(5)
O2	1547.0(15)	3394.7(13)	4052.0(8)	29.1(4)
N3	1366.6(16)	1480.0(15)	3731.2(8)	20.9(4)
N4	341.1(16)	86.9(16)	3406.9(8)	21.4(4)
C34	1222.8(18)	1693.3(18)	4321.9(10)	20.2(5)
C35	1003.2(18)	997.4(18)	4767.8(10)	20.0(5)
C36	884(2)	1245(2)	5348.8(11)	25.3(5)
C37	959(2)	2205(2)	5483.1(11)	30.0(6)
C38	1168(2)	2906.2(19)	5037.8(11)	27.5(6)
C39	1309.9(19)	2658.3(18)	4465.8(11)	23.6(5)
C40	1468.3(19)	3149.8(19)	3456.6(11)	24.4(5)
C41	1514(2)	3887(2)	3041.5(12)	30.3(6)
C42	1448(2)	3693(2)	2438.9(12)	32.4(6)
C43	1329(2)	2759(2)	2264.1(12)	28.4(6)
C44	1290.1(19)	2018(2)	2685.4(11)	23.9(5)
C45	1363.4(18)	2197.0(18)	3287(1)	20.1(5)
C46	1197.2(17)	491.0(18)	3575.9(10)	17.6(5)
C47	1998.4(18)	17.9(19)	3637.8(10)	19.6(5)
C48	2955.2(19)	567.3(19)	3670.3(11)	23.6(5)
C49	3699.4(19)	100(2)	3682.3(11)	28.1(6)

Atom	x	y	z	U_{eq}
C50	3542.9(19)	-903(2)	3767.2(11)	26.7(6)
C51	4357(2)	-1348(2)	3821.1(12)	32.4(6)
C52	4237(2)	-2287(2)	3967.5(13)	34.8(6)
C53	3326(2)	-2831(2)	4122.4(12)	31.1(6)
C54	3234(2)	-3776(2)	4356.9(13)	35.3(6)
C55	2383(2)	-4263(2)	4547.5(13)	34.8(7)
C56	1564(2)	-3844(2)	4529.3(12)	35.4(6)
C57	1627(2)	-2929.0(19)	4291.6(11)	29.7(6)
C58	2490(2)	-2420.3(19)	4057.8(11)	25.7(6)
C59	2591.9(19)	-1456.6(19)	3810.5(11)	22.6(5)
C60	1814.3(18)	-982.7(18)	3628.8(10)	17.8(5)
C61	885.1(18)	-1445.2(18)	3370.2(10)	18.7(5)
C62	684.5(19)	-2383.2(19)	3154(1)	22.9(5)
C63	-180.5(19)	-2744(2)	2868.4(11)	26.0(5)
C64	-873.8(19)	-2187(2)	2777.9(11)	29.2(6)
C65	-694.6(19)	-1258(2)	2966.4(11)	26.7(6)
C66	190.2(18)	-869.1(18)	3253.9(10)	19.9(5)
O3	8414.1(13)	1505.6(15)	971.2(8)	29.5(4)
N5	6490.0(15)	1370.7(17)	1272.4(8)	21.4(4)
N6	5096.3(15)	337.7(15)	1587.4(8)	19.2(4)
C67	6713.3(17)	1219.8(18)	685.1(10)	18.8(5)
C68	6003.2(18)	991.9(19)	234.7(10)	21.9(5)
C69	6266(2)	865(2)	-342.8(11)	26.4(6)
C70	7222(2)	924(2)	-471.6(11)	27.9(6)
C71	7927.6(19)	1118.6(19)	-21.6(12)	27.5(6)
C72	7672.7(18)	1276.7(19)	542.6(11)	23.7(5)
C73	8154.5(18)	1457.8(19)	1555.9(11)	22.9(5)
C74	8886(2)	1495(2)	1979.9(12)	32.2(6)
C75	8691(2)	1474(2)	2579.1(12)	32.6(6)
C76	7754(2)	1404(2)	2751.3(12)	29.1(6)
C77	7013.9(19)	1350.2(19)	2321.8(11)	23.8(5)
C78	7211.8(17)	1385.3(17)	1721.8(10)	19.2(5)
C79	5501.4(17)	1207.9(19)	1426(1)	18.9(5)
C80	5034.4(18)	2003.0(19)	1359.9(10)	18.5(5)
C81	5567.4(19)	2951.1(19)	1331.5(11)	24.0(5)
C82	5115.2(19)	3698.0(19)	1309.6(11)	27.0(6)
C83	4108(2)	3537.7(19)	1210.0(11)	26.2(6)
C84	3659(2)	4348(2)	1145.8(11)	29.6(6)
C85	2721(2)	4231.9(19)	987.4(12)	30.1(6)
C86	2179.0(19)	3321(2)	834.3(11)	27.2(6)
C87	1238(2)	3218(2)	591.7(12)	32.4(6)
C88	736(2)	2356(2)	404.2(12)	33.1(6)
C89	1167(2)	1551(2)	425.8(12)	31.9(6)
C90	2076.6(19)	1618(2)	670.8(11)	26.8(6)
C91	2590.3(18)	2480(2)	905.6(10)	23.7(5)
C92	3561.3(18)	2596.4(19)	1164.3(10)	20.4(5)
C93	4018.1(17)	1807.7(18)	1353.6(10)	17.2(5)
C94	3563.2(17)	883.5(18)	1605.0(9)	17.7(5)
C95	2609.2(18)	666.3(19)	1808.7(10)	21.6(5)
C96	2242(2)	-196(2)	2088.9(11)	26.2(5)
C97	2801(2)	-889(2)	2177.9(11)	28.5(6)
C98	3741(2)	-697.6(19)	2000.6(11)	25.7(6)
C99	4138.9(18)	189.8(17)	1729(1)	19.0(5)
O4	6626.8(13)	3098.9(15)	-856.1(8)	30.3(4)
N7	8516.5(15)	3512.1(16)	-1239.6(8)	20.7(4)
N8	9823.4(15)	4626.9(15)	-1605.2(8)	18.8(4)
C100	8328.3(17)	3598.7(18)	-633.1(10)	18.4(5)
C101	9062.3(18)	3892.9(19)	-204.5(10)	21.2(5)

Atom	x	y	z	U_{eq}
C102	8838.5(19)	3958(2)	386.2(11)	23.6(5)
C103	7897.6(19)	3759(2)	559.3(11)	26.7(6)
C104	7164.4(18)	3469(2)	134.2(11)	27.1(6)
C105	7383.6(18)	3400.9(19)	-450.2(11)	23.5(5)
C106	6818.5(18)	3304.2(18)	-1454.4(10)	22.1(5)
C107	6036.6(19)	3257(2)	-1842.7(12)	29.2(6)
C108	6182(2)	3432(2)	-2450.2(12)	29.7(6)
C109	7112(2)	3649(2)	-2657.0(12)	30.2(6)
C110	7898(2)	3703.8(19)	-2263.9(11)	23.7(5)
C111	7752.5(17)	3521.9(17)	-1657.5(10)	19.6(5)
C112	9491.9(17)	3750.1(19)	-1413.7(10)	18.6(5)
C113	10040.4(18)	3019.3(19)	-1324.8(10)	18.9(5)
C114	9609.8(19)	2043.3(19)	-1240.1(11)	24.8(5)
C115	10175(2)	1375(2)	-1187.2(12)	31.2(6)
C116	11187(2)	1659(2)	-1112.8(11)	28.6(6)
C117	11780(2)	965(2)	-1001.4(12)	34.2(7)
C118	12736(2)	1244(3)	-850.9(12)	36.8(7)
C119	13153(2)	2204(2)	-750.0(12)	31.1(6)
C120	14118(2)	2492(2)	-509.1(12)	35.1(7)
C121	14471(2)	3401(3)	-355.8(13)	39.0(7)
C122	13889.9(19)	4085(2)	-410.3(11)	32.6(6)
C123	12979.6(19)	3848(2)	-657.6(11)	28.3(6)
C124	12594.4(19)	2916(2)	-861.9(10)	27.3(6)
C125	11621(2)	2637(2)	-1115.6(11)	24.1(5)
C126	11053.2(18)	3309.3(18)	-1336.7(10)	17.3(5)
C127	11413.6(17)	4226.7(18)	-1627.0(9)	17.0(5)
C128	12355.4(18)	4504.9(19)	-1851.1(10)	21.6(5)
C129	12632.2(19)	5357(2)	-2170.1(11)	27.1(6)
C130	11997(2)	5973.9(19)	-2271.9(11)	27.4(6)
C131	11074(2)	5721.6(19)	-2073.9(11)	25.2(5)
C132	10770.1(18)	4842.7(18)	-1765.1(10)	18.6(5)

Table 7.10. Anisotropic Displacement Parameters (×10^4) **H2-PXZ**.

The anisotropic displacement factor exponent takes the form: $-2\pi^2[h^2a^{*2} \times U_{11} + \dots + 2hka^* \times b^* \times U_{12}]$

Atom	U_{11}	U_{22}	U_{33}	U_{23}	U_{13}	U_{12}
O1	57.4(13)	17.4(9)	22.8(9)	1.3(7)	5.7(9)	1.9(8)
N1	35.2(12)	16.8(11)	16.0(9)	3.2(8)	3.1(9)	4.3(9)
N2	23.5(11)	27.5(12)	15.7(9)	2.0(8)	0.4(8)	8.3(9)
C1	19.8(12)	22.1(13)	20.6(11)	3.9(10)	3.4(9)	6.3(9)
C2	21.2(12)	26.9(13)	19.0(11)	1.8(10)	3.9(9)	2.8(10)
C3	33.6(15)	37.8(16)	23.1(12)	7.6(11)	4.9(11)	8.4(12)
C4	43.8(17)	30.1(15)	32.3(14)	11.6(12)	10.2(12)	12.4(12)
C5	37.2(15)	20.2(13)	32.8(14)	6.9(10)	12.1(11)	5.7(11)
C6	28.4(14)	22.9(13)	23.0(12)	1(1)	8.2(10)	5.3(10)
C7	28.0(14)	17.5(12)	25.6(12)	-0.3(10)	4(1)	1.7(10)
C8	34.0(15)	19.7(12)	27.9(13)	-4.4(10)	4.6(11)	2.9(10)
C9	31.7(14)	25.3(13)	21.1(12)	-3.6(10)	5(1)	1.3(11)
C10	25.8(13)	23.9(13)	20.7(12)	4.1(10)	4.1(10)	1.6(10)
C11	24.6(13)	16.5(12)	19.9(11)	-1.3(9)	-0.1(10)	-0.2(9)
C12	23.8(13)	19.1(12)	21.8(12)	-2.8(10)	-1.7(10)	3.5(9)
C13	20.5(12)	22.5(13)	12.9(10)	1.2(9)	0.6(9)	4.7(10)
C14	20.4(13)	23.0(13)	13.8(10)	-2.0(9)	-0.8(9)	2.1(10)
C15	20.6(13)	31.1(14)	23.4(12)	-7.2(10)	0.6(10)	-2.9(10)
C16	16.8(12)	42.7(17)	32.3(14)	-12.6(12)	-3.6(10)	1.1(11)
C17	24.5(14)	39.6(16)	27.6(13)	-13.5(12)	-10.3(10)	12.9(12)
C18	31.0(15)	54(2)	33.0(15)	-9.9(13)	-9.9(12)	18.4(14)
C19	48.4(19)	42.4(17)	33.1(15)	-9.1(13)	-9.3(13)	27.2(14)
C20	48.9(18)	36.7(16)	27.7(13)	-10.9(12)	-14.4(13)	22.8(14)
C21	55(2)	32.1(15)	27.2(13)	-2.0(12)	-11.4(13)	26.7(14)
C22	60(2)	34.1(17)	38.1(16)	1.9(13)	-5.2(15)	12.8(15)
C23	49.6(19)	32.3(15)	29.9(14)	2.5(12)	-6.9(13)	6.1(13)

Atom	U_{11}	U_{22}	U_{33}	U_{23}	U_{13}	U_{12}
C24	43.4(16)	22.5(13)	22.4(12)	0(1)	-6.8(11)	5.9(11)
C25	50.5(18)	26.1(14)	20.5(12)	-8.3(10)	-15.8(12)	20.6(13)
C26	25.0(13)	26.2(13)	19.1(11)	-7.2(10)	-7.2(10)	9(1)
C27	21.2(12)	21.3(12)	13.9(10)	-2.8(9)	-0.6(9)	5.9(10)
C28	18.8(12)	22.6(13)	11.6(10)	-0.4(9)	1.4(9)	1.2(9)
C29	30.7(14)	21.5(13)	14.6(10)	0.2(9)	2(1)	1.9(10)
C30	30.9(14)	21.2(12)	17.4(11)	-2.7(9)	2.9(10)	-7.2(10)
C31	19.9(13)	36.0(15)	21.1(12)	-1.1(10)	-2(1)	-4.8(11)
C32	16.5(12)	38.2(15)	22.0(12)	4.1(11)	3.1(10)	4.7(10)
C33	20.5(12)	26.9(13)	15.5(10)	0.9(10)	2.4(9)	7.4(10)
O2	43.5(12)	17.2(9)	23.9(9)	0.3(7)	6.7(8)	-0.4(8)
N3	28.3(11)	17.8(11)	17.0(9)	5.8(8)	4.9(8)	5.8(8)
N4	22.2(11)	27.7(12)	15.6(9)	3.5(8)	1.6(8)	9.1(9)
C34	18.8(12)	20.8(12)	21.0(11)	-3.9(9)	-1.0(9)	3.5(9)
C35	21.5(12)	18.2(12)	18.7(11)	-0.3(9)	0.3(9)	0.2(9)
C36	29.8(14)	24.7(13)	19.1(11)	3.4(10)	5.7(10)	0.3(10)
C37	39.1(16)	28.5(14)	19.8(12)	-5.8(10)	9.8(11)	-1.8(11)
C38	35.9(15)	20.6(12)	24.1(12)	-5.9(10)	4.1(11)	-0.1(11)
C39	29.0(14)	16.8(12)	23.2(12)	1.3(9)	3.7(10)	0.2(10)
C40	24.4(13)	24.3(13)	25.1(12)	2.2(10)	7.8(10)	5.4(10)
C41	35.8(15)	19.5(13)	36.4(14)	6.6(11)	11.0(12)	7.2(11)
C42	37.4(16)	31.0(15)	31.0(14)	15.5(11)	7.6(12)	13.6(12)
C43	28.9(14)	34.6(15)	23.0(12)	8.5(11)	4.3(10)	10.1(11)
C44	25.0(13)	27.4(14)	20.0(11)	5(1)	5.2(10)	7.4(10)
C45	20.7(12)	21.3(13)	19.2(11)	2.3(9)	2.6(9)	6.3(9)
C46	18.4(12)	21.1(12)	13.1(10)	0.3(9)	1.6(9)	3.5(9)
C47	18.8(12)	24.7(13)	15.4(10)	-3.2(9)	-2.5(9)	4.8(10)
C48	20.9(13)	23.8(13)	23.8(12)	-4.5(10)	0(1)	-1.3(10)
C49	17.7(12)	36.1(15)	30.0(13)	-11.2(11)	-6.2(10)	3.7(11)
C50	20.9(13)	35.4(15)	24.5(12)	-8.9(11)	-6.3(10)	7.4(11)
C51	20.2(13)	39.6(16)	38.2(15)	-8.8(12)	-6.8(11)	8.1(11)
C52	31.5(15)	38.4(16)	36.9(15)	-4.9(12)	-10.4(12)	13.8(12)
C53	45.6(18)	27.3(14)	24.0(12)	-4.0(11)	-6.8(12)	16.4(12)
C54	40.6(17)	29.2(14)	38.0(15)	-1.6(11)	-11.5(12)	13.7(12)
C55	47.6(18)	27.4(14)	31.2(14)	1.5(12)	-13.3(13)	14.3(13)
C56	38.7(16)	31.4(15)	32.9(14)	0.1(12)	-5.1(12)	0.8(12)
C57	46.4(17)	23.1(13)	20.8(12)	-1.5(10)	-10.2(11)	11.2(12)
C58	31.0(14)	25.3(13)	22.2(12)	-5.9(10)	-8(1)	9.6(11)
C59	25.0(13)	26.5(13)	18.8(11)	-7.2(10)	-8.7(10)	11.7(10)
C60	19.5(12)	20.6(12)	13.7(10)	-1.1(9)	-0.5(9)	5.0(9)
C61	19.2(12)	24.2(13)	11.7(10)	0.5(9)	2.4(9)	1.6(9)
C62	27.5(13)	24.3(13)	15.7(10)	0.2(9)	1.5(9)	2.4(10)
C63	26.2(13)	27.6(14)	19.7(11)	-3.8(10)	2.5(10)	-5.8(10)
C64	19.8(13)	40.2(16)	22.6(12)	-6.2(11)	-1.5(10)	-5.9(11)
C65	16.5(12)	39.3(16)	23.5(12)	2.7(11)	3.5(10)	3.7(11)
C66	19.9(12)	25.0(13)	14.8(10)	-0.3(9)	2.1(9)	4.2(10)
O3	15.7(9)	47.2(12)	25.4(9)	-7.4(8)	-2.3(7)	5.4(8)
N5	14.4(10)	35.0(12)	15.9(9)	-0.3(9)	-0.2(8)	7.8(8)
N6	18.3(10)	23.3(11)	17.0(9)	-2.0(8)	-0.2(8)	6.4(8)
C67	15.0(11)	24.3(13)	17.3(11)	-3.9(9)	-2.9(9)	4.6(9)
C68	18.9(12)	23.9(13)	21.6(12)	-3.8(10)	0.2(10)	1.3(9)
C69	24.6(13)	30.5(14)	20.7(12)	-4.1(10)	0(1)	-2.5(11)
C70	28.4(14)	30.6(14)	22.7(12)	-7.3(10)	7.1(10)	-0.9(11)
C71	20.3(12)	29.6(14)	32.0(14)	-4.5(11)	2.3(10)	2.5(10)
C72	17.7(12)	27.6(13)	24.9(12)	-4.3(10)	-2.6(10)	2.8(10)
C73	17.7(12)	28.6(13)	22.7(12)	-6.6(10)	-3.4(9)	5.5(10)
C74	20.8(13)	43.2(17)	35.0(14)	-9.8(12)	-6.9(11)	11.6(12)
C75	29.7(15)	36.7(15)	31.9(14)	-9.6(12)	-18.3(11)	9.8(12)
C76	32.3(15)	32.1(15)	23.0(12)	-4.5(11)	-8.8(11)	7.6(11)
C77	22.1(13)	27.9(13)	21.3(11)	-2.1(10)	-4.6(10)	5.2(10)
C78	18.9(12)	16.8(11)	22.5(11)	-3.1(9)	-5.5(9)	5.7(9)
C79	14.8(12)	27.4(13)	13.8(10)	-1.5(9)	-1.5(9)	3.3(10)
C80	16.7(12)	25.0(13)	13.9(10)	-2.3(9)	0.8(9)	4.2(9)
C81	22.4(13)	24.9(13)	23.1(12)	1.9(10)	5.8(10)	1.1(10)
C82	29.3(14)	23.6(13)	26.7(13)	3.1(10)	4.5(11)	2.5(10)
C83	33.0(15)	28.0(14)	18.4(11)	4.1(10)	6.6(10)	8.3(11)
C84	35.3(15)	27.8(14)	27.4(13)	2.5(11)	3.4(11)	10.9(11)
C85	39.5(16)	24.0(13)	27.9(13)	6.4(10)	3.9(11)	9.8(11)
C86	23.9(13)	40.2(16)	20.4(11)	6.2(11)	4.4(10)	13.8(11)
C87	27.1(14)	39.0(16)	34.5(14)	7.6(12)	-0.4(11)	16.5(12)
C88	23.9(14)	43.3(17)	32.8(14)	10.9(12)	-0.1(11)	10.9(12)
C89	24.2(13)	38.5(16)	29.8(13)	4.6(11)	-3.3(10)	0.8(11)

Atom	U_{11}	U_{22}	U_{33}	U_{23}	U_{13}	U_{12}
C90	24.2(13)	38.1(16)	19.0(11)	8.0(11)	3.5(10)	9.2(11)
C91	20.3(12)	34.4(15)	17.9(11)	5.7(10)	2.0(9)	9.6(10)
C92	18.3(12)	29.7(14)	15.4(10)	2.9(9)	4.8(9)	10.1(10)
C93	17.8(12)	21.1(12)	13.5(10)	-0.3(9)	-0.5(9)	6.2(9)
C94	18.2(12)	22.5(12)	11.8(10)	-1.3(9)	-0.2(9)	2.7(9)
C95	18.8(12)	28.8(13)	16.8(10)	-2.3(9)	1.7(9)	3.5(10)
C96	24.3(13)	30.4(14)	20.9(11)	-3.1(10)	5.1(10)	-2.6(10)
C97	40.0(16)	21.6(13)	19.9(11)	-1.8(10)	5.8(11)	-4.1(11)
C98	36.4(15)	20.9(13)	20.1(11)	2.4(10)	3.8(11)	6.6(11)
C99	21.5(12)	18.6(12)	15.8(10)	-2.7(9)	-1.7(9)	1.5(9)
O4	16.8(9)	45.2(12)	26.1(9)	-2.5(8)	-1.9(7)	0.5(8)
N7	13.3(10)	33.0(12)	16.6(9)	2.8(8)	0.4(8)	6.8(8)
N8	16.4(10)	21.9(11)	18.3(9)	-0.8(8)	-0.2(8)	4.6(8)
C100	15.6(11)	22.9(12)	16.1(11)	-0.4(9)	-2.4(9)	3.2(9)
C101	15.7(12)	26.0(13)	21.5(12)	-1.9(10)	-1.3(10)	3.1(9)
C102	21.4(13)	27.9(13)	20.6(12)	-1.9(10)	-0.2(10)	2.5(10)
C103	21.7(12)	36.8(15)	21.3(12)	-5.2(11)	3.6(10)	3.9(11)
C104	19.1(12)	34.0(15)	28.7(13)	-1.4(11)	1.9(10)	6.4(11)
C105	18.7(12)	27.7(13)	24.0(12)	-0.4(10)	-3.8(9)	5.1(10)
C106	19.0(12)	26.2(13)	22.2(11)	-6.1(10)	-4.9(9)	7.2(10)
C107	18.8(12)	36.1(15)	34.4(14)	-12.6(11)	-6.2(11)	8.9(11)
C108	22.7(13)	33.8(15)	32.7(14)	-12.0(11)	-15.8(11)	7.3(11)
C109	32.9(15)	31.4(15)	25.0(13)	-5.4(11)	-11.0(11)	5.1(11)
C110	23.3(13)	25.1(13)	22.5(11)	-4.1(10)	-4.5(10)	4.8(10)
C111	17.6(12)	19.5(12)	21.9(11)	-6.3(9)	-6.9(9)	4.7(9)
C112	14.6(12)	27.4(13)	13.4(10)	-0.8(9)	-2.5(9)	4(1)
C113	20.4(13)	24.2(13)	13(1)	-0.4(9)	0.6(9)	6.6(10)
C114	23.9(13)	26.4(14)	21.1(12)	1.6(10)	4.7(10)	-2(1)
C115	46.0(17)	20.9(13)	27.1(13)	3.2(10)	7.7(12)	7.0(12)
C116	36.8(16)	30.8(15)	21.8(12)	5.6(11)	7.0(11)	14.8(12)
C117	50.4(18)	25.6(14)	28.5(14)	6.5(11)	9.4(12)	12.0(13)
C118	35.8(16)	54(2)	28.7(13)	6.4(13)	4.1(12)	28.9(14)
C119	29.8(14)	43.4(16)	25.4(13)	5.8(12)	3.7(11)	20.3(12)
C120	29.8(15)	52.7(19)	30.0(14)	16.2(13)	6.8(12)	27.5(14)
C121	22.8(14)	60(2)	35.0(15)	4.3(14)	-6.1(11)	11.4(13)
C122	22.6(13)	48.9(18)	25.8(13)	1.6(12)	-1.4(10)	6.7(12)
C123	22.8(13)	44.0(16)	18.3(11)	2.5(11)	0.4(10)	8.4(11)
C124	23.0(13)	46.6(17)	17.5(11)	9.0(11)	6(1)	20.1(12)
C125	27.8(13)	30.2(14)	18.5(11)	5.5(10)	7.2(10)	15.7(11)
C126	18.3(12)	22.1(12)	12.4(10)	0.0(9)	0.5(9)	6.6(9)
C127	16.0(11)	23.2(12)	11.5(10)	-0.9(9)	-1.9(9)	3.6(9)
C128	16.9(12)	30.4(14)	16.8(11)	-2.4(10)	0.8(9)	3(1)
C129	23.8(13)	35.1(15)	18.6(11)	-1.8(10)	4.4(10)	-3.9(11)
C130	35.6(15)	21.5(13)	22.0(12)	0.4(10)	3.9(11)	-1.8(11)
C131	30.7(14)	22.9(13)	22.0(12)	2.7(10)	1.7(10)	5.4(10)
C132	19.2(12)	20.2(12)	15(1)	-1.1(9)	-2.7(9)	1.2(9)

Table 7.11. Bond Lengths in Å for **H2-PXZ**.

Atom	Atom	Length/Å
O1	C6	1.382(3)
O1	C7	1.377(3)
N1	C1	1.404(3)
N1	C12	1.407(3)
N1	C13	1.427(3)
N2	C13	1.287(3)
N2	C33	1.386(3)
C1	C2	1.388(3)
C1	C6	1.405(4)
C2	C3	1.387(4)
C3	C4	1.382(4)
C4	C5	1.394(4)
C5	C6	1.383(4)
C7	C8	1.378(3)
C7	C12	1.405(4)
C8	C9	1.390(4)

Atom	Atom	Length/Å
C9	C10	1.378(4)
C10	C11	1.385(3)
C11	C12	1.375(3)
C13	C14	1.439(3)
C14	C15	1.432(4)
C14	C27	1.393(4)
C15	C16	1.372(4)
C16	C17	1.402(4)
C17	C18	1.444(4)
C17	C26	1.419(4)
C18	C19	1.357(5)
C19	C20	1.405(5)
C20	C21	1.450(4)
C20	C25	1.419(4)
C21	C22	1.344(5)
C22	C23	1.398(4)
C23	C24	1.377(4)
C24	C25	1.404(4)
C25	C26	1.462(4)
C26	C27	1.445(3)
C27	C28	1.458(3)
C28	C29	1.411(4)
C28	C33	1.415(3)
C29	C30	1.379(4)
C30	C31	1.409(4)
C31	C32	1.368(4)
C32	C33	1.417(4)
O2	C39	1.376(3)
O2	C40	1.391(3)
N3	C34	1.405(3)
N3	C45	1.405(3)
N3	C46	1.433(3)
N4	C46	1.287(3)
N4	C66	1.388(3)
C34	C35	1.384(3)
C34	C39	1.403(3)
C35	C36	1.391(3)
C36	C37	1.392(4)
C37	C38	1.387(4)
C38	C39	1.379(3)
C40	C41	1.375(4)
C40	C45	1.400(4)
C41	C42	1.390(4)
C42	C43	1.375(4)
C43	C44	1.389(4)
C44	C45	1.383(3)
C46	C47	1.440(3)
C47	C48	1.426(4)
C47	C60	1.396(4)
C48	C49	1.362(4)
C49	C50	1.407(4)
C50	C51	1.430(4)
C50	C59	1.426(4)
C51	C52	1.345(4)
C52	C53	1.417(4)
C53	C54	1.411(4)
C53	C58	1.431(4)
C54	C55	1.344(5)

Atom	Atom	Length/Å
C55	C56	1.414(4)
C56	C57	1.379(4)
C57	C58	1.402(4)
C58	C59	1.445(4)
C59	C60	1.451(3)
C60	C61	1.463(3)
C61	C62	1.408(4)
C61	C66	1.422(3)
C62	C63	1.379(4)
C63	C64	1.393(4)
C64	C65	1.375(4)
C65	C66	1.412(4)
O3	C72	1.400(3)
O3	C73	1.375(3)
N5	C67	1.404(3)
N5	C78	1.414(3)
N5	C79	1.432(3)
N6	C79	1.301(3)
N6	C99	1.383(3)
C67	C68	1.404(3)
C67	C72	1.400(3)
C68	C69	1.393(3)
C69	C70	1.387(4)
C70	C71	1.396(4)
C71	C72	1.371(3)
C73	C74	1.382(3)
C73	C78	1.389(3)
C74	C75	1.385(4)
C75	C76	1.386(4)
C76	C77	1.397(3)
C77	C78	1.387(3)
C79	C80	1.428(3)
C80	C81	1.408(4)
C80	C93	1.416(3)
C81	C82	1.351(4)
C82	C83	1.417(4)
C83	C84	1.430(4)
C83	C92	1.411(4)
C84	C85	1.349(4)
C85	C86	1.415(4)
C86	C87	1.410(4)
C86	C91	1.439(4)
C87	C88	1.360(5)
C88	C89	1.406(4)
C89	C90	1.377(4)
C90	C91	1.404(4)
C91	C92	1.461(3)
C92	C93	1.454(3)
C93	C94	1.449(3)
C94	C95	1.419(3)
C94	C99	1.423(3)
C95	C96	1.374(4)
C96	C97	1.396(4)
C97	C98	1.381(4)
C98	C99	1.404(4)
O4	C105	1.396(3)
O4	C106	1.393(3)
N7	C100	1.415(3)

Atom	Atom	Length/Å
N7	C111	1.415(3)
N7	C112	1.426(3)
N8	C112	1.306(3)
N8	C132	1.378(3)
C100	C101	1.406(3)
C100	C105	1.391(3)
C101	C102	1.389(3)
C102	C103	1.379(4)
C103	C104	1.399(4)
C104	C105	1.374(3)
C106	C107	1.383(3)
C106	C111	1.392(4)
C107	C108	1.397(4)
C108	C109	1.390(4)
C109	C110	1.394(4)
C110	C111	1.396(3)
C112	C113	1.429(3)
C113	C114	1.409(4)
C113	C126	1.418(3)
C114	C115	1.367(4)
C115	C116	1.420(4)
C116	C117	1.437(4)
C116	C125	1.403(4)
C117	C118	1.371(5)
C118	C119	1.397(5)
C119	C120	1.443(4)
C119	C124	1.423(3)
C120	C121	1.342(5)
C121	C122	1.402(4)
C122	C123	1.374(4)
C123	C124	1.414(4)
C124	C125	1.463(4)
C125	C126	1.441(3)
C126	C127	1.445(3)
C127	C128	1.424(3)
C127	C132	1.413(3)
C128	C129	1.381(4)
C129	C130	1.394(4)
C130	C131	1.374(4)
C131	C132	1.406(4)

Table 7.12. Bond Angles in ° for **H2-PXZ**.

Atom	Atom	Atom	Angle/°
C7	O1	C6	117.3(2)
C1	N1	C12	118.9(2)
C1	N1	C13	120.68(19)
C12	N1	C13	116.9(2)
C13	N2	C33	116.9(2)
N1	C1	C6	117.7(2)
C2	C1	N1	123.6(2)
C2	C1	C6	118.6(2)
C3	C2	C1	120.6(3)
C4	C3	C2	120.5(2)
C3	C4	C5	119.7(3)
C6	C5	C4	119.9(3)
O1	C6	C1	122.1(2)
O1	C6	C5	117.2(2)

Atom	Atom	Atom	Angle/˚
C5	C6	C1	120.7(2)
O1	C7	C8	117.7(2)
O1	C7	C12	121.5(2)
C8	C7	C12	120.9(2)
C7	C8	C9	120.2(2)
C10	C9	C8	119.2(2)
C9	C10	C11	120.4(2)
C12	C11	C10	121.3(2)
C7	C12	N1	118.3(2)
C11	C12	N1	123.6(2)
C11	C12	C7	118.0(2)
N1	C13	C14	116.7(2)
N2	C13	N1	118.0(2)
N2	C13	C14	125.2(2)
C15	C14	C13	121.1(2)
C27	C14	C13	118.3(2)
C27	C14	C15	120.6(2)
C16	C15	C14	118.0(3)
C15	C16	C17	121.7(3)
C16	C17	C18	121.9(3)
C16	C17	C26	120.4(2)
C26	C17	C18	117.7(3)
C19	C18	C17	121.5(3)
C18	C19	C20	121.5(3)
C19	C20	C21	122.2(3)
C19	C20	C25	119.8(3)
C25	C20	C21	118.0(3)
C22	C21	C20	120.6(3)
C21	C22	C23	121.2(3)
C24	C23	C22	119.4(3)
C23	C24	C25	121.8(3)
C20	C25	C26	118.4(3)
C24	C25	C20	118.4(3)
C24	C25	C26	122.9(2)
C17	C26	C25	119.1(2)
C17	C26	C27	116.4(2)
C27	C26	C25	124.4(2)
C14	C27	C26	118.8(2)
C14	C27	C28	115.6(2)
C26	C27	C28	125.5(2)
C29	C28	C27	124.0(2)
C29	C28	C33	117.1(2)
C33	C28	C27	118.4(2)
C30	C29	C28	121.1(2)
C29	C30	C31	121.2(2)
C32	C31	C30	119.1(2)
C31	C32	C33	120.3(2)
N2	C33	C28	122.6(2)
N2	C33	C32	116.4(2)
C28	C33	C32	121.0(2)
C39	O2	C40	117.0(2)
C34	N3	C45	118.6(2)
C34	N3	C46	118.03(19)
C45	N3	C46	120.16(19)
C46	N4	C66	117.3(2)
C35	C34	N3	123.1(2)
C35	C34	C39	118.6(2)
C39	C34	N3	118.3(2)

Atom	Atom	Atom	Angle/°
C34	C35	C36	121.0(2)
C35	C36	C37	119.8(2)
C38	C37	C36	119.6(2)
C39	C38	C37	120.4(2)
O2	C39	C34	122.2(2)
O2	C39	C38	117.1(2)
C38	C39	C34	120.6(2)
O2	C40	C45	121.5(2)
C41	C40	O2	117.1(2)
C41	C40	C45	121.4(2)
C40	C41	C42	120.0(3)
C43	C42	C41	119.4(2)
C42	C43	C44	120.3(2)
C45	C44	C43	121.2(3)
C40	C45	N3	118.8(2)
C44	C45	N3	123.5(2)
C44	C45	C40	117.7(2)
N3	C46	C47	117.0(2)
N4	C46	N3	117.9(2)
N4	C46	C47	125.0(2)
C48	C47	C46	120.3(2)
C60	C47	C46	118.2(2)
C60	C47	C48	121.4(2)
C49	C48	C47	118.8(2)
C48	C49	C50	121.0(3)
C49	C50	C51	118.6(3)
C49	C50	C59	120.4(2)
C59	C50	C51	121.0(3)
C52	C51	C50	120.0(3)
C51	C52	C53	121.0(3)
C52	C53	C58	120.4(3)
C54	C53	C52	120.5(3)
C54	C53	C58	119.1(3)
C55	C54	C53	120.3(3)
C54	C55	C56	121.4(3)
C57	C56	C55	119.5(3)
C56	C57	C58	120.6(3)
C53	C58	C59	118.6(3)
C57	C58	C53	118.6(2)
C57	C58	C59	122.5(2)
C50	C59	C58	117.1(2)
C50	C59	C60	116.8(2)
C58	C59	C60	126.0(2)
C47	C60	C59	117.5(2)
C47	C60	C61	116.1(2)
C59	C60	C61	126.0(2)
C62	C61	C60	123.9(2)
C62	C61	C66	117.7(2)
C66	C61	C60	117.7(2)
C63	C62	C61	120.8(2)
C62	C63	C64	121.1(3)
C65	C64	C63	120.0(2)
C64	C65	C66	120.0(2)
N4	C66	C61	122.7(2)
N4	C66	C65	116.9(2)
C65	C66	C61	120.4(2)
C73	O3	C72	116.95(19)
C67	N5	C78	118.35(19)

Atom	Atom	Atom	Angle/˚
C67	N5	C79	118.61(19)
C78	N5	C79	120.17(19)
C79	N6	C99	116.4(2)
C68	C67	N5	122.2(2)
C72	C67	N5	119.3(2)
C72	C67	C68	118.5(2)
C69	C68	C67	119.8(2)
C70	C69	C68	120.5(2)
C69	C70	C71	119.9(2)
C72	C71	C70	119.6(2)
C67	C72	O3	121.2(2)
C71	C72	O3	117.2(2)
C71	C72	C67	121.6(2)
O3	C73	C74	116.6(2)
O3	C73	C78	122.6(2)
C74	C73	C78	120.8(2)
C73	C74	C75	120.3(3)
C74	C75	C76	119.5(2)
C75	C76	C77	120.0(2)
C78	C77	C76	120.5(2)
C73	C78	N5	118.8(2)
C77	C78	N5	122.3(2)
C77	C78	C73	118.9(2)
N6	C79	N5	117.1(2)
N6	C79	C80	125.7(2)
C80	C79	N5	117.1(2)
C81	C80	C79	121.0(2)
C81	C80	C93	121.2(2)
C93	C80	C79	117.7(2)
C82	C81	C80	120.3(2)
C81	C82	C83	120.1(3)
C82	C83	C84	118.8(3)
C92	C83	C82	120.5(2)
C92	C83	C84	120.7(3)
C85	C84	C83	120.6(3)
C84	C85	C86	120.9(2)
C85	C86	C91	120.4(2)
C87	C86	C85	121.0(3)
C87	C86	C91	118.5(3)
C88	C87	C86	121.5(3)
C87	C88	C89	120.1(3)
C90	C89	C88	120.0(3)
C89	C90	C91	121.3(3)
C86	C91	C92	117.9(2)
C90	C91	C86	118.2(2)
C90	C91	C92	123.6(2)
C83	C92	C91	117.7(2)
C83	C92	C93	117.7(2)
C93	C92	C91	124.5(2)
C80	C93	C92	116.3(2)
C80	C93	C94	115.8(2)
C94	C93	C92	127.5(2)
C95	C94	C93	124.0(2)
C95	C94	C99	117.2(2)
C99	C94	C93	118.3(2)
C96	C95	C94	121.5(2)
C95	C96	C97	120.5(2)
C98	C97	C96	120.0(2)

Atom	Atom	Atom	Angle/°
C97	C98	C99	120.4(2)
N6	C99	C94	122.9(2)
N6	C99	C98	116.7(2)
C98	C99	C94	120.3(2)
C106	O4	C105	116.50(19)
C100	N7	C111	117.45(19)
C100	N7	C112	117.70(19)
C111	N7	C112	121.23(19)
C112	N8	C132	116.7(2)
C101	C100	N7	122.5(2)
C105	C100	N7	119.3(2)
C105	C100	C101	118.2(2)
C102	C101	C100	120.1(2)
C103	C102	C101	120.8(2)
C102	C103	C104	119.3(2)
C105	C104	C103	120.1(2)
C100	C105	O4	120.6(2)
C104	C105	O4	117.8(2)
C104	C105	C100	121.5(2)
C107	C106	O4	117.0(2)
C107	C106	C111	121.2(2)
C111	C106	O4	121.8(2)
C106	C107	C108	119.7(3)
C109	C108	C107	119.5(2)
C108	C109	C110	120.7(2)
C109	C110	C111	119.8(3)
C106	C111	N7	118.2(2)
C106	C111	C110	119.1(2)
C110	C111	N7	122.6(2)
N7	C112	C113	116.6(2)
N8	C112	N7	117.7(2)
N8	C112	C113	125.5(2)
C114	C113	C112	122.5(2)
C114	C113	C126	120.3(2)
C126	C113	C112	117.2(2)
C115	C114	C113	119.5(2)
C114	C115	C116	120.9(3)
C115	C116	C117	121.4(3)
C125	C116	C115	119.9(2)
C125	C116	C117	118.6(3)
C118	C117	C116	121.1(3)
C117	C118	C119	121.5(2)
C118	C119	C120	122.1(2)
C118	C119	C124	119.0(3)
C124	C119	C120	118.8(3)
C121	C120	C119	121.3(2)
C120	C121	C122	120.0(3)
C123	C122	C121	120.4(3)
C122	C123	C124	121.8(3)
C119	C124	C125	119.4(3)
C123	C124	C119	117.2(3)
C123	C124	C125	123.0(2)
C116	C125	C124	118.4(2)
C116	C125	C126	117.5(2)
C126	C125	C124	124.0(2)
C113	C126	C125	117.9(2)
C113	C126	C127	115.8(2)
C125	C126	C127	126.0(2)

Atom	Atom	Atom	Angle/˚
C128	C127	C126	123.8(2)
C132	C127	C126	118.8(2)
C132	C127	C128	117.0(2)
C129	C128	C127	121.1(2)
C128	C129	C130	120.5(2)
C131	C130	C129	120.1(2)
C130	C131	C132	120.2(2)
N8	C132	C127	122.6(2)
N8	C132	C131	116.4(2)
C131	C132	C127	121.0(2)

Table 7.13. Torsion Angles in ˚ for **H2-PXZ**.

Atom	Atom	Atom	Atom	Angle/˚
O1	C7	C8	C9	179.2(2)
O1	C7	C12	N1	-0.2(4)
O1	C7	C12	C11	179.8(2)
N1	C1	C2	C3	177.3(2)
N1	C1	C6	O1	1.1(4)
N1	C1	C6	C5	-178.1(2)
N1	C13	C14	C15	19.2(3)
N1	C13	C14	C27	-162.9(2)
N2	C13	C14	C15	-164.8(2)
N2	C13	C14	C27	13.2(3)
C1	N1	C12	C7	17.1(4)
C1	N1	C12	C11	-162.9(2)
C1	N1	C13	N2	66.8(3)
C1	N1	C13	C14	-116.9(2)
C1	C2	C3	C4	0.6(4)
C2	C1	C6	O1	178.7(2)
C2	C1	C6	C5	-0.5(4)
C2	C3	C4	C5	-0.3(4)
C3	C4	C5	C6	-0.3(4)
C4	C5	C6	O1	-178.5(3)
C4	C5	C6	C1	0.7(4)
C6	O1	C7	C8	165.0(2)
C6	O1	C7	C12	-15.7(4)
C6	C1	C2	C3	-0.1(4)
C7	O1	C6	C1	15.4(4)
C7	O1	C6	C5	-165.4(2)
C7	C8	C9	C10	0.8(4)
C8	C7	C12	N1	179.0(2)
C8	C7	C12	C11	-1.0(4)
C8	C9	C10	C11	-0.5(4)
C9	C10	C11	C12	-0.5(4)
C10	C11	C12	N1	-178.7(2)
C10	C11	C12	C7	1.3(4)
C12	N1	C1	C2	165.1(2)
C12	N1	C1	C6	-17.4(3)
C12	N1	C13	N2	-91.9(3)
C12	N1	C13	C14	84.4(3)
C12	C7	C8	C9	-0.1(4)
C13	N1	C1	C2	6.9(4)
C13	N1	C1	C6	-175.6(2)
C13	N1	C12	C7	176.1(2)

Atom	Atom	Atom	Atom	Angle/˚
C13	N1	C12	C11	-3.9(4)
C13	N2	C33	C28	-11.1(3)
C13	N2	C33	C32	169.3(2)
C13	C14	C15	C16	177.6(2)
C13	C14	C27	C26	165.2(2)
C13	C14	C27	C28	-19.5(3)
C14	C15	C16	C17	10.7(4)
C14	C27	C28	C29	-159.3(2)
C14	C27	C28	C33	11.8(3)
C15	C14	C27	C26	-16.9(3)
C15	C14	C27	C28	158.5(2)
C15	C16	C17	C18	173.8(2)
C15	C16	C17	C26	-3.4(4)
C16	C17	C18	C19	-171.6(3)
C16	C17	C26	C25	161.5(2)
C16	C17	C26	C27	-13.7(4)
C17	C18	C19	C20	5.0(4)
C17	C26	C27	C14	23.5(3)
C17	C26	C27	C28	-151.4(2)
C18	C17	C26	C25	-15.8(4)
C18	C17	C26	C27	169.1(2)
C18	C19	C20	C21	171.6(3)
C18	C19	C20	C25	-5.0(4)
C19	C20	C21	C22	-172.9(3)
C19	C20	C25	C24	169.1(2)
C19	C20	C25	C26	-5.4(4)
C20	C21	C22	C23	2.3(5)
C20	C25	C26	C17	15.9(3)
C20	C25	C26	C27	-169.4(2)
C21	C20	C25	C24	-7.6(4)
C21	C20	C25	C26	177.8(2)
C21	C22	C23	C24	-4.4(4)
C22	C23	C24	C25	0.2(4)
C23	C24	C25	C20	5.8(4)
C23	C24	C25	C26	-179.9(2)
C24	C25	C26	C17	-158.5(2)
C24	C25	C26	C27	16.3(4)
C25	C20	C21	C22	3.7(4)
C25	C26	C27	C14	-151.4(2)
C25	C26	C27	C28	33.8(4)
C26	C17	C18	C19	5.6(4)
C26	C27	C28	C29	15.7(4)
C26	C27	C28	C33	-173.2(2)
C27	C14	C15	C16	-0.3(4)
C27	C28	C29	C30	174.5(2)
C27	C28	C33	N2	3.7(3)
C27	C28	C33	C32	-176.7(2)
C28	C29	C30	C31	0.0(4)
C29	C28	C33	N2	175.5(2)
C29	C28	C33	C32	-4.9(3)
C29	C30	C31	C32	-1.5(4)
C30	C31	C32	C33	-0.2(4)
C31	C32	C33	N2	-176.9(2)
C31	C32	C33	C28	3.5(4)
C33	N2	C13	N1	178.74(19)
C33	N2	C13	C14	2.8(3)
C33	C28	C29	C30	3.2(3)
O2	C40	C41	C42	179.5(2)

Atom	Atom	Atom	Atom	Angle/˚
O2	C40	C45	N3	-1.9(4)
O2	C40	C45	C44	180.0(2)
N3	C34	C35	C36	178.8(2)
N3	C34	C39	O2	-1.2(4)
N3	C34	C39	C38	179.5(2)
N3	C46	C47	C48	-18.8(3)
N3	C46	C47	C60	165.0(2)
N4	C46	C47	C48	163.1(2)
N4	C46	C47	C60	-13.2(3)
C34	N3	C45	C40	16.4(4)
C34	N3	C45	C44	-165.6(2)
C34	N3	C46	N4	88.3(3)
C34	N3	C46	C47	-90.0(3)
C34	C35	C36	C37	1.9(4)
C35	C34	C39	O2	178.5(2)
C35	C34	C39	C38	-0.8(4)
C35	C36	C37	C38	-1.1(4)
C36	C37	C38	C39	-0.6(4)
C37	C38	C39	O2	-177.8(2)
C37	C38	C39	C34	1.5(4)
C39	O2	C40	C41	167.2(2)
C39	O2	C40	C45	-13.8(4)
C39	C34	C35	C36	-0.9(4)
C40	O2	C39	C34	15.4(4)
C40	O2	C39	C38	-165.2(2)
C40	C41	C42	C43	0.5(4)
C41	C40	C45	N3	177.0(2)
C41	C40	C45	C44	-1.1(4)
C41	C42	C43	C44	-1.0(4)
C42	C43	C44	C45	0.4(4)
C43	C44	C45	N3	-177.4(2)
C43	C44	C45	C40	0.6(4)
C45	N3	C34	C35	165.3(2)
C45	N3	C34	C39	-14.9(3)
C45	N3	C46	N4	-71.3(3)
C45	N3	C46	C47	110.4(3)
C45	C40	C41	C42	0.5(4)
C46	N3	C34	C35	5.4(3)
C46	N3	C34	C39	-174.8(2)
C46	N3	C45	C40	175.9(2)
C46	N3	C45	C44	-6.1(4)
C46	N4	C66	C61	10.8(3)
C46	N4	C66	C65	-168.6(2)
C46	C47	C48	C49	-175.0(2)
C46	C47	C60	C59	-167.8(2)
C46	C47	C60	C61	19.1(3)
C47	C48	C49	C50	-11.2(4)
C47	C60	C61	C62	159.5(2)
C47	C60	C61	C66	-11.3(3)
C48	C47	C60	C59	16.0(3)
C48	C47	C60	C61	-157.1(2)
C48	C49	C50	C51	-175.3(2)
C48	C49	C50	C59	3.4(4)
C49	C50	C51	C52	172.7(3)
C49	C50	C59	C58	-163.3(2)
C49	C50	C59	C60	13.8(3)
C50	C51	C52	C53	-5.7(4)
C50	C59	C60	C47	-23.0(3)

Atom	Atom	Atom	Atom	Angle/˚
C50	C59	C60	C61	149.4(2)
C51	C50	C59	C58	15.4(4)
C51	C50	C59	C60	-167.5(2)
C51	C52	C53	C54	-170.8(3)
C51	C52	C53	C58	7.5(4)
C52	C53	C54	C55	174.7(3)
C52	C53	C58	C57	-171.2(2)
C52	C53	C58	C59	2.4(4)
C53	C54	C55	C56	-1.1(4)
C53	C58	C59	C50	-13.3(3)
C53	C58	C59	C60	169.9(2)
C54	C53	C58	C57	7.1(4)
C54	C53	C58	C59	-179.3(2)
C54	C55	C56	C57	2.4(4)
C55	C56	C57	C58	1.3(4)
C56	C57	C58	C53	-6.0(4)
C56	C57	C58	C59	-179.3(2)
C57	C58	C59	C50	160.0(2)
C57	C58	C59	C60	-16.7(4)
C58	C53	C54	C55	-3.7(4)
C58	C59	C60	C47	153.8(2)
C58	C59	C60	C61	-33.8(4)
C59	C50	C51	C52	-6.0(4)
C59	C60	C61	C62	-13.0(4)
C59	C60	C61	C66	176.2(2)
C60	C47	C48	C49	1.1(4)
C60	C61	C62	C63	-174.3(2)
C60	C61	C66	N4	-3.8(3)
C60	C61	C66	C65	175.5(2)
C61	C62	C63	C64	0.9(4)
C62	C61	C66	N4	-175.1(2)
C62	C61	C66	C65	4.2(3)
C62	C63	C64	C65	1.0(4)
C63	C64	C65	C66	-0.3(4)
C64	C65	C66	N4	177.0(2)
C64	C65	C66	C61	-2.4(4)
C66	N4	C46	N3	179.55(18)
C66	N4	C46	C47	-2.3(3)
C66	C61	C62	C63	-3.5(3)
O3	C73	C74	C75	178.5(3)
O3	C73	C78	N5	-0.7(4)
O3	C73	C78	C77	-179.4(2)
N5	C67	C68	C69	179.0(2)
N5	C67	C72	O3	-1.7(4)
N5	C67	C72	C71	178.8(2)
N5	C79	C80	C81	-19.6(3)
N5	C79	C80	C93	163.5(2)
N6	C79	C80	C81	163.8(2)
N6	C79	C80	C93	-13.2(3)
C67	N5	C78	C73	13.7(3)
C67	N5	C78	C77	-167.7(2)
C67	N5	C79	N6	86.9(3)
C67	N5	C79	C80	-90.1(3)
C67	C68	C69	C70	2.6(4)
C68	C67	C72	O3	179.7(2)
C68	C67	C72	C71	0.2(4)
C68	C69	C70	C71	-0.5(4)
C69	C70	C71	C72	-1.8(4)

Atom	Atom	Atom	Atom	Angle/˚
C70	C71	C72	O3	-177.6(2)
C70	C71	C72	C67	1.9(4)
C72	O3	C73	C74	167.5(2)
C72	O3	C73	C78	-13.1(4)
C72	C67	C68	C69	-2.4(4)
C73	O3	C72	C67	14.3(3)
C73	O3	C72	C71	-166.2(2)
C73	C74	C75	C76	0.7(5)
C74	C73	C78	N5	178.6(2)
C74	C73	C78	C77	0.0(4)
C74	C75	C76	C77	0.4(4)
C75	C76	C77	C78	-1.3(4)
C76	C77	C78	N5	-177.5(2)
C76	C77	C78	C73	1.1(4)
C78	N5	C67	C68	166.2(2)
C78	N5	C67	C72	-12.4(4)
C78	N5	C79	N6	-73.7(3)
C78	N5	C79	C80	109.4(2)
C78	C73	C74	C75	-0.9(4)
C79	N5	C67	C68	5.3(4)
C79	N5	C67	C72	-173.3(2)
C79	N5	C78	C73	174.2(2)
C79	N5	C78	C77	-7.2(4)
C79	N6	C99	C94	11.5(3)
C79	N6	C99	C98	-169.3(2)
C79	C80	C81	C82	-175.5(2)
C79	C80	C93	C92	-167.7(2)
C79	C80	C93	C94	19.5(3)
C80	C81	C82	C83	-11.1(4)
C80	C93	C94	C95	159.6(2)
C80	C93	C94	C99	-11.7(3)
C81	C80	C93	C92	15.4(3)
C81	C80	C93	C94	-157.4(2)
C81	C82	C83	C84	-175.5(2)
C81	C82	C83	C92	3.4(4)
C82	C83	C84	C85	172.8(2)
C82	C83	C92	C91	-163.7(2)
C82	C83	C92	C93	13.6(3)
C83	C84	C85	C86	-5.2(4)
C83	C92	C93	C80	-22.3(3)
C83	C92	C93	C94	149.5(2)
C84	C83	C92	C91	15.1(3)
C84	C83	C92	C93	-167.6(2)
C84	C85	C86	C87	-171.3(2)
C84	C85	C86	C91	6.7(4)
C85	C86	C87	C88	175.3(3)
C85	C86	C91	C90	-171.2(2)
C85	C86	C91	C92	2.7(3)
C86	C87	C88	C89	-2.7(4)
C86	C91	C92	C83	-13.2(3)
C86	C91	C92	C93	169.6(2)
C87	C86	C91	C90	6.9(3)
C87	C86	C91	C92	-179.3(2)
C87	C88	C89	C90	4.0(4)
C88	C89	C90	C91	0.3(4)
C89	C90	C91	C86	-5.7(4)
C89	C90	C91	C92	-179.2(2)
C90	C91	C92	C83	160.3(2)

Atom	Atom	Atom	Atom	Angle/˚
C90	C91	C92	C93	-16.8(4)
C91	C86	C87	C88	-2.7(4)
C91	C92	C93	C80	154.8(2)
C91	C92	C93	C94	-33.4(4)
C92	C83	C84	C85	-6.0(4)
C92	C93	C94	C95	-12.2(4)
C92	C93	C94	C99	176.4(2)
C93	C80	C81	C82	1.3(4)
C93	C94	C95	C96	-174.4(2)
C93	C94	C99	N6	-4.0(3)
C93	C94	C99	C98	176.7(2)
C94	C95	C96	C97	-0.4(4)
C95	C94	C99	N6	-175.9(2)
C95	C94	C99	C98	4.8(3)
C95	C96	C97	C98	2.1(4)
C96	C97	C98	C99	-0.2(4)
C97	C98	C99	N6	177.4(2)
C97	C98	C99	C94	-3.3(4)
C99	N6	C79	N5	-179.41(18)
C99	N6	C79	C80	-2.8(3)
C99	C94	C95	C96	-3.0(3)
O4	C106	C107	C108	-178.4(2)
O4	C106	C111	N7	1.2(4)
O4	C106	C111	C110	178.8(2)
N7	C100	C101	C102	-179.4(2)
N7	C100	C105	O4	1.4(4)
N7	C100	C105	C104	179.6(2)
N7	C112	C113	C114	18.3(3)
N7	C112	C113	C126	-163.0(2)
N8	C112	C113	C114	-166.2(2)
N8	C112	C113	C126	12.6(3)
C100	N7	C111	C106	-20.4(3)
C100	N7	C111	C110	162.1(2)
C100	N7	C112	N8	-93.0(3)
C100	N7	C112	C113	82.9(3)
C100	C101	C102	C103	-1.5(4)
C101	C100	C105	O4	-179.5(2)
C101	C100	C105	C104	-1.3(4)
C101	C102	C103	C104	1.3(4)
C102	C103	C104	C105	-1.1(4)
C103	C104	C105	O4	179.3(2)
C103	C104	C105	C100	1.1(4)
C105	O4	C106	C107	-162.6(2)
C105	O4	C106	C111	19.1(3)
C105	C100	C101	C102	1.5(4)
C106	O4	C105	C100	-20.4(3)
C106	O4	C105	C104	161.4(2)
C106	C107	C108	C109	0.2(4)
C107	C106	C111	N7	-176.9(2)
C107	C106	C111	C110	0.6(4)
C107	C108	C109	C110	-0.6(4)
C108	C109	C110	C111	1.1(4)
C109	C110	C111	N7	176.4(2)
C109	C110	C111	C106	-1.1(4)
C111	N7	C100	C101	-159.8(2)
C111	N7	C100	C105	19.2(3)
C111	N7	C112	N8	65.0(3)

Atom	Atom	Atom	Atom	Angle/˚
C111	N7	C112	C113	-119.0(2)
C111	C106	C107	C108	-0.2(4)
C112	N7	C100	C101	-1.0(3)
C112	N7	C100	C105	178.1(2)
C112	N7	C111	C106	-178.5(2)
C112	N7	C111	C110	4.0(4)
C112	N8	C132	C127	-12.0(3)
C112	N8	C132	C131	168.4(2)
C112	C113	C114	C115	176.7(2)
C112	C113	C126	C125	166.0(2)
C112	C113	C126	C127	-19.9(3)
C113	C114	C115	C116	11.0(4)
C113	C126	C127	C128	-159.2(2)
C113	C126	C127	C132	12.6(3)
C114	C113	C126	C125	-15.2(3)
C114	C113	C126	C127	158.9(2)
C114	C115	C116	C117	174.1(2)
C114	C115	C116	C125	-2.4(4)
C115	C116	C117	C118	-171.1(3)
C115	C116	C125	C124	161.5(2)
C115	C116	C125	C126	-14.8(3)
C116	C117	C118	C119	5.5(4)
C116	C125	C126	C113	23.3(3)
C116	C125	C126	C127	-150.2(2)
C117	C116	C125	C124	-15.2(3)
C117	C116	C125	C126	168.6(2)
C117	C118	C119	C120	170.9(3)
C117	C118	C119	C124	-6.1(4)
C118	C119	C120	C121	-172.8(3)
C118	C119	C124	C123	169.2(2)
C118	C119	C124	C125	-4.0(4)
C119	C120	C121	C122	2.1(4)
C119	C124	C125	C116	14.6(3)
C119	C124	C125	C126	-169.4(2)
C120	C119	C124	C123	-7.9(3)
C120	C119	C124	C125	179.0(2)
C120	C121	C122	C123	-4.4(4)
C121	C122	C123	C124	0.3(4)
C122	C123	C124	C119	5.8(4)
C122	C123	C124	C125	178.7(2)
C123	C124	C125	C116	-158.1(2)
C123	C124	C125	C126	17.9(4)
C124	C119	C120	C121	4.2(4)
C124	C125	C126	C113	-152.8(2)
C124	C125	C126	C127	33.8(4)
C125	C116	C117	C118	5.5(4)
C125	C126	C127	C128	14.3(4)
C125	C126	C127	C132	-173.8(2)
C126	C113	C114	C115	-1.9(4)
C126	C127	C128	C129	174.3(2)
C126	C127	C132	N8	3.6(3)
C126	C127	C132	C131	-176.8(2)
C127	C128	C129	C130	1.1(4)
C128	C127	C132	N8	176.0(2)
C128	C127	C132	C131	-4.4(3)
C128	C129	C130	C131	-2.4(4)
C129	C130	C131	C132	0.4(4)
C130	C131	C132	N8	-177.3(2)

Atom	Atom	Atom	Atom	Angle/°
C130	C131	C132	C127	3.2(4)
C132	N8	C112	N7	179.36(19)
C132	N8	C112	C113	3.8(3)
C132	C127	C128	C129	2.3(3)

Table 7.14. Hydrogen fractional atomic coordinates ($\times 10^4$) and equivalent isotropic displacement parameters (Å2×103) for **H2-PXZ**. U_{eq} is defined as 1/3 of the trace of the orthogonalised U_{ij}.

Atom	x	y	z	U_{eq}
H2	3707	3533	7410	27
H3	3582	2228	8075	38
H4	3296	669	7728	42
H5	3118	412	6702	36
H8	3394	1502	4755	33
H9	3828	2734	4039	32
H10	4150	4326	4329	29
H11	4021	4692	5317	25
H15	1832	3919	6229	31
H16	700	4891	6191	37
H18	284	6496	5990	46
H19	755	8094	5754	47
H21	2028	9489	5402	43
H22	3588	10079	5171	53
H23	4727	9101	5249	45
H24	4314	7570	5669	36
H29	4090	7797	6757	27
H30	5527	8268	7280	30
H31	6578	7203	7457	33
H32	6141	5642	7130	31
H35	933	340	4676	24
H36	752	762	5653	30
H37	868	2378	5878	36
H38	1214	3561	5127	33
H41	1591	4529	3167	36
H42	1485	4201	2150	39
H43	1273	2620	1853	34
H44	1212	1377	2558	29
H48	3071	1247	3683	28
H49	4334	456	3632	34
H51	4981	-980	3754	39
H52	4772	-2591	3967	42
H54	3777	-4069	4380	42
H55	2331	-4902	4698	42
H56	974	-4191	4680	43
H57	1082	-2641	4286	36
H62	1150	-2773	3205	27
H63	-305	-3382	2731	31
H64	-1470	-2449	2586	35
H65	-1166	-877	2903	32
H68	5345	925	324	26
H69	5787	737	-650	32
H70	7396	832	-866	33
H71	8581	1142	-106	33
H74	9526	1535	1860	39
H75	9195	1506	2870	39

Atom	**x**	**y**	**z**	***U***
H76	7614	1393	3161	35
H77	6371	1289	2442	29
H81	6248	3066	1328	29
H82	5473	4332	1361	32
H84	4025	4973	1215	35
H85	2421	4769	979	36
H87	949	3762	559	39
H88	94	2299	258	40
H89	830	960	271	38
H90	2362	1071	681	32
H95	2216	1128	1750	26
H96	1602	-321	2223	31
H97	2536	-1491	2360	34
H98	4122	-1170	2063	31
H101	9713	4047	-319	25
H102	9340	4142	675	28
H103	7749	3818	963	32
H104	6514	3320	250	32
H107	5404	3106	-1697	35
H108	5649	3402	-2720	36
H109	7213	3762	-3070	36
H110	8532	3864	-2408	28
H114	8932	1851	-1220	30
H115	9888	712	-1200	37
H117	11506	302	-1033	41
H118	13123	774	-814	44
H120	14511	2029	-458	42
H121	15115	3581	-210	47
H122	14127	4716	-275	39
H123	12598	4323	-692	34
H128	12801	4098	-1780	26
H129	13261	5523	-2321	33
H130	12201	6570	-2478	33
H131	10642	6142	-2146	30

DSC transitions

A1

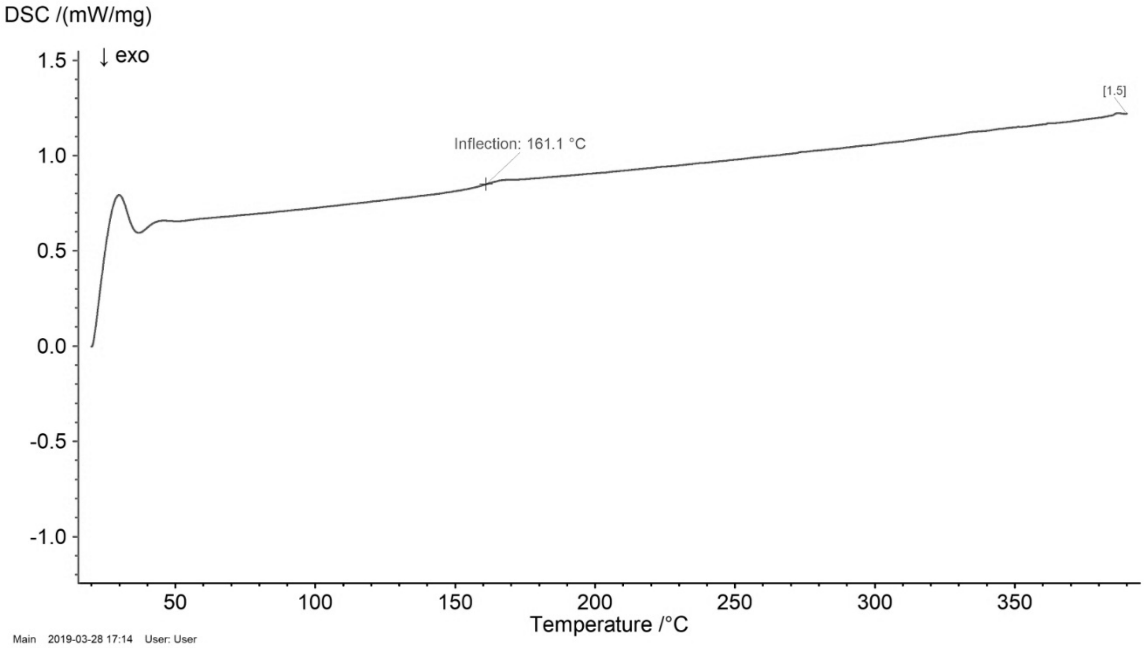

Q2

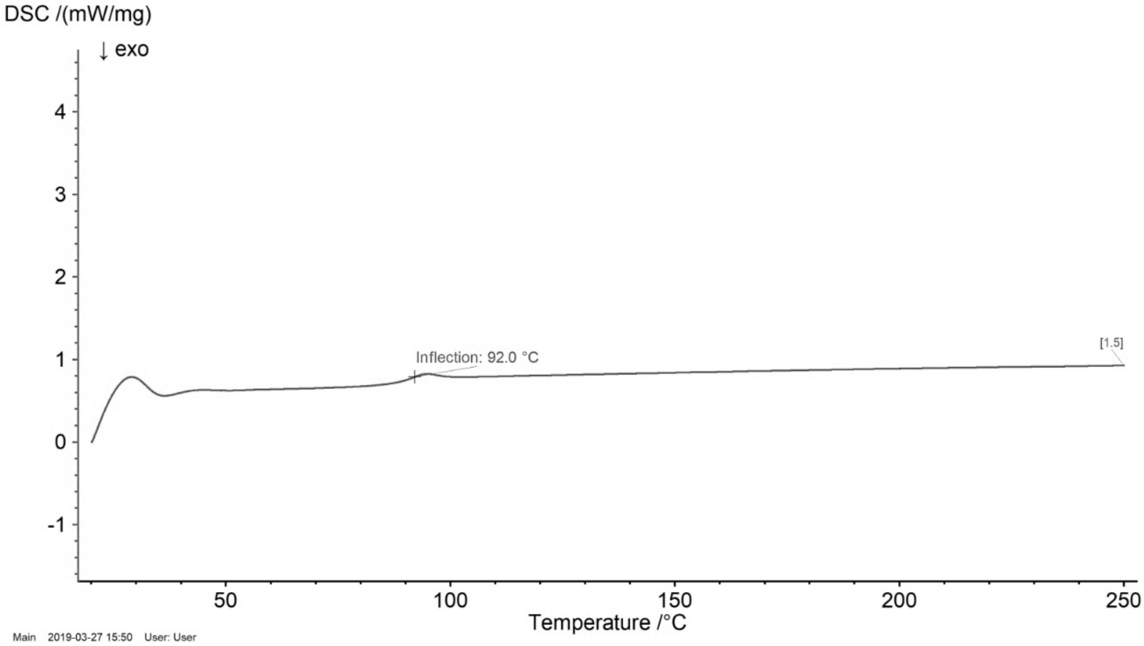

Q1-S1

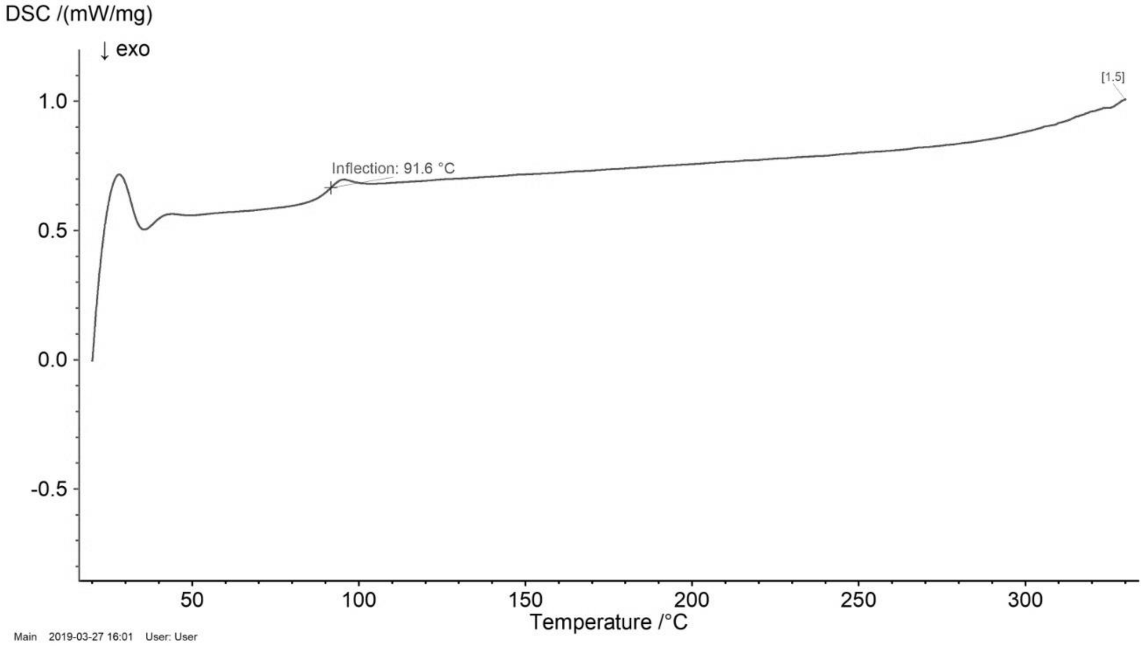
DSC /(mW/mg)
↓ exo
1.0
0.5
0.0
-0.5
Inflection: 91.6 °C
[1.5]
50
100
150
200
250
300
Temperature /°C
Main 2019-03-27 16:01 User: User

Q2-S1

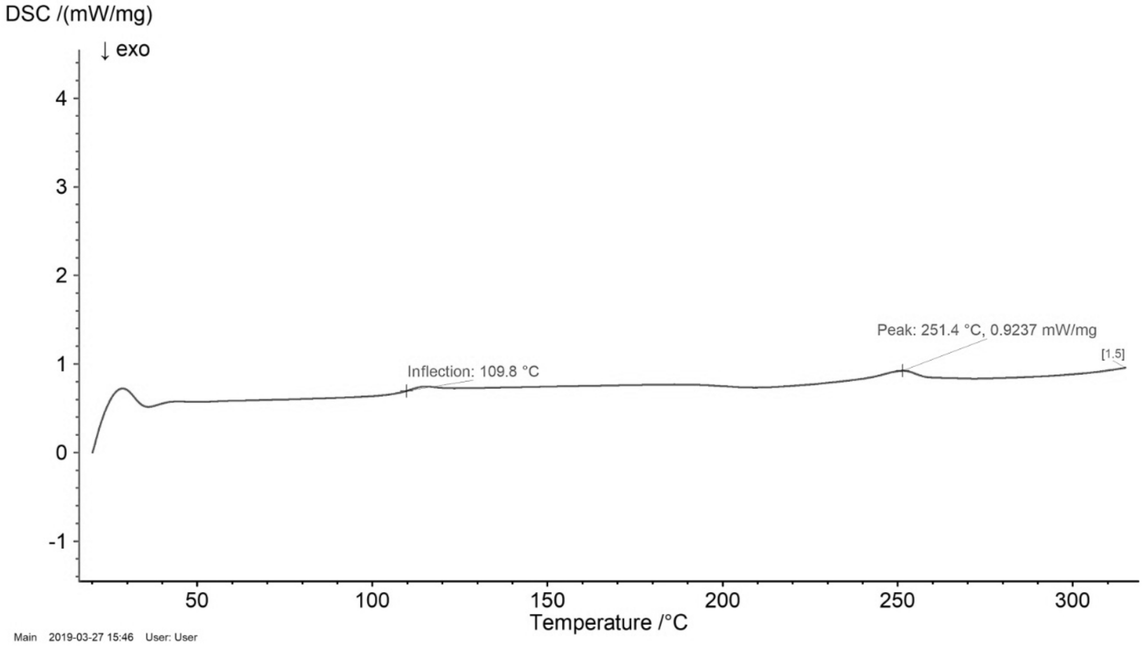
DSC /(mW/mg)
↓ exo
4
3
2
1
0
-1
Inflection: 109.8 °C
Peak: 251.4 °C, 0.9237 mW/mg
[1.5]
50
100
150
200
250
300
Temperature /°C
Main 2019-03-27 15:46 User: User

Q2-S2

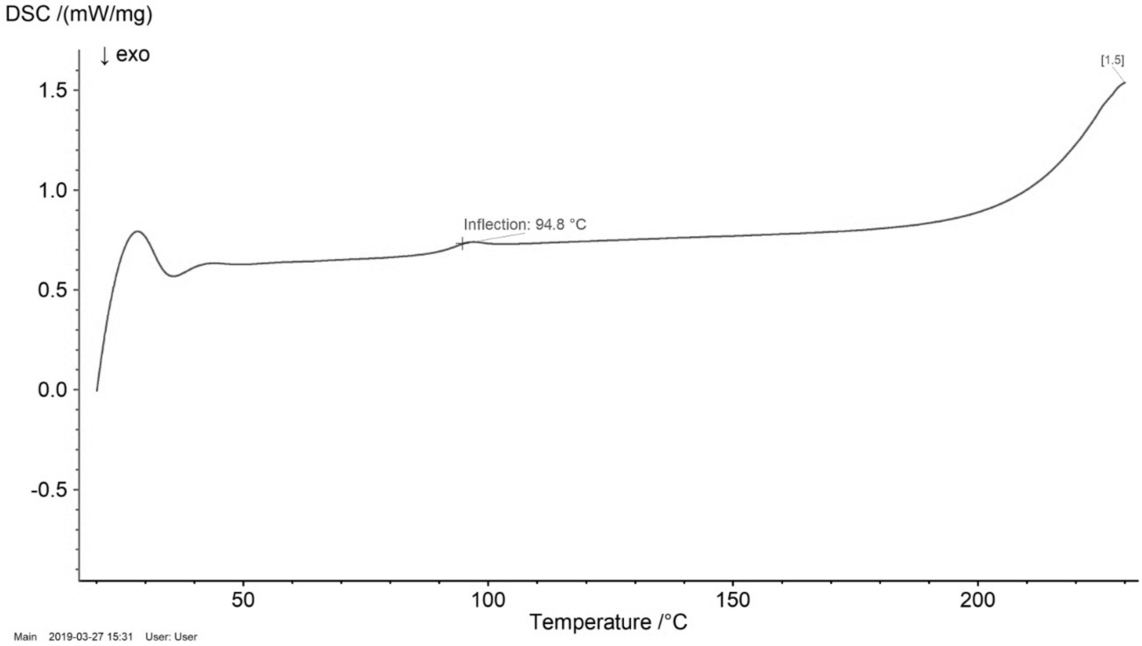
DSC /(mW/mg)
↓ exo
[1.5]
1.5
1.0
0.5
0.0
-0.5
Inflection: 94.8 °C
50
100
150
200
Temperature /°C
Main 2019-03-27 15:31 User: User

Q1-S3

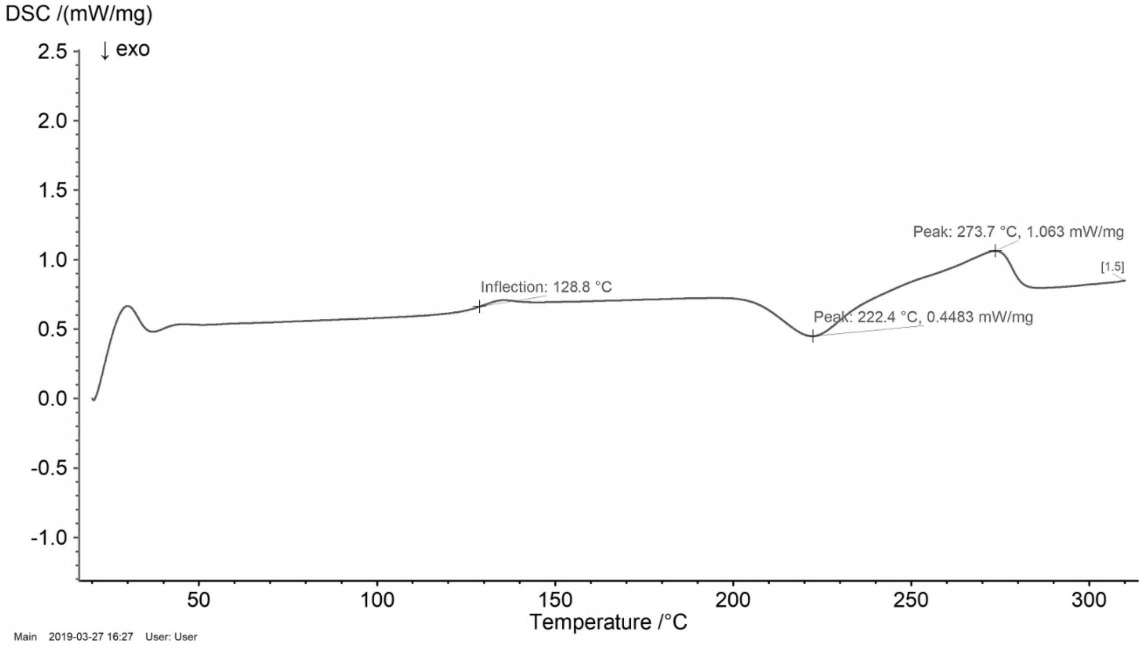
DSC /(mW/mg)
↓ exo
2.5
2.0
1.5
1.0
0.5
0.0
-0.5
-1.0
Peak: 273.7 °C, 1.063 mW/mg
[1.5]
Inflection: 128.8 °C
Peak: 222.4 °C, 0.4483 mW/mg
50
100
150
200
250
300
Temperature /°C
Main 2019-03-27 16:27 User: User

Chapter 8. Bibliography

(1) Information About Sea Turtles: Threats from Artificial Lighting – Sea Turtle Conservancy https://conserveturtles.org/information-sea-turtles-threats-artificial-lighting/ (accessed Aug 6, 2018).

(2) Irwin, A. The dark side of light: how artificial lighting is harming the natural world http://www.nature.com/articles/d41586-018-00665-7 (accessed Jun 14, 2018). https://doi.org/10.1038/d41586-018-00665-7.

(3) Potter, G. D. M.; Skene, D. J.; Arendt, J.; Cade, J. E.; Grant, P. J.; Hardie, L. J. Circadian Rhythm and Sleep Disruption: Causes, Metabolic Consequences, and Countermeasures. *Endocr. Rev.* **2016**, *37* (6), 584–608. https://doi.org/10.1210/er.2016-1083.

(4) Geoghegan, M.; Hadziioannou, G. *Polymer Electronics*; Oxford University Press, 2013.

(5) OECD/IEA. Energy Access Outlook 2017. IEA Publishing 2017.

(6) Karlicek, R.; Sun, C.-C.; Zissis, G.; Ma, R. *Handbook of Advanced Lighting Technology*; Springer International Publishing: Cham, 2017. https://doi.org/10.1007/978-3-319-00176-0.

(7) Schubert, E. F. *Light-Emitting Diodes*; Cambridge University Press, 2006. https://doi.org/10.1017/CBO9780511790546.

(8) Lehovec, K.; Accardo, C. A.; Jamgochian, E. Injected Light Emission of Silicon Carbide Crystals. *Phys. Rev.* **1951**, *83* (3), 603–607. https://doi.org/10.1103/PhysRev.83.603.

(9) Bardeen, J.; Brattain, W. H. The Transistor, A Semi-Conductor Triode. *Phys. Rev.* **1948**, *74* (2), 230–231. https://doi.org/10.1103/PhysRev.74.230.

(10) Holonyak, N.; Bevacqua, S. F. COHERENT (VISIBLE) LIGHT EMISSION FROM Ga(As1−xPx) JUNCTIONS. *Appl. Phys. Lett.* **1962**, *1* (4), 82–83. https://doi.org/10.1063/1.1753706.

(11) Nakamura, S.; Senoh, M.; Mukai, T. P-GaN/N-InGaN/N-GaN Double-Heterostructure Blue-Light-Emitting Diodes. *Jpn. J. Appl. Phys.* **1993**, *32* (1A), L8. https://doi.org/10.1143/JJAP.32.L8.

(12) The Nobel Prize in Physics 2014 https://www.nobelprize.org/prizes/physics/2014/press-release/ (accessed Feb 24, 2019).

(13) Benight, S. J.; Wang, C.; Tok, J. B. H.; Bao, Z. Stretchable and Self-Healing Polymers and Devices for Electronic Skin. *Prog. Polym. Sci.* **2013**, *38* (12), 1961–1977. https://doi.org/10.1016/j.progpolymsci.2013.08.001.

(14) Yin, D.; Feng, J.; Ma, R.; Liu, Y.-F.; Zhang, Y.-L.; Zhang, X.-L.; Bi, Y.-G.; Chen, Q.-D.; Sun, H.-B. Efficient and Mechanically Robust Stretchable Organic Light-Emitting Devices by a Laser-Programmable Buckling Process. *Nat. Commun.* **2016**, *7*, 11573. https://doi.org/10.1038/ncomms11573.

(15) Irimia-Vladu, M.; Troshin, P. A.; Reisinger, M.; Shmygleva, L.; Kanbur, Y.; Schwabegger, G.; Bodea, M.; Schwödiauer, R.; Mumyatov, A.; Fergus, J. W.; et al. Biocompatible and Biodegradable Materials for Organic Field-Effect Transistors. *Adv. Funct. Mater.* **2010**, *20* (23), 4069–4076. https://doi.org/10.1002/adfm.201001031.

(16) Gomez, E. F.; Venkatraman, V.; Grote, J. G.; Steckl, A. J. DNA Bases Thymine and Adenine in Bio-Organic Light Emitting Diodes. *Sci. Rep.* **2014**, *4*, 7105. https://doi.org/10.1038/srep07105.

(17) Lunt, R. R.; Bulovic, V. Transparent, near-Infrared Organic Photovoltaic Solar Cells for Window and Energy-Scavenging Applications. *Appl. Phys. Lett.* **2011**, *98* (11), 113305. https://doi.org/10.1063/1.3567516.

(18) Park, C. I.; Seong, M.; Kim, M. A.; Kim, D.; Jung, H.; Cho, M.; Lee, S. H.; Lee, H.; Min, S.; Kim, J.; et al. World's First Large Size 77-Inch Transparent Flexible OLED Display. *J. Soc. Inf. Disp.* *0* (0). https://doi.org/10.1002/jsid.663.

(19) Volz, D.; Wallesch, M.; Fléchon, C.; Danz, M.; Verma, A.; Navarro, J. M.; Zink, D. M.; Bräse, S.; Baumann, T. From Iridium and Platinum to Copper and Carbon: New Avenues for More Sustainability in Organic Light-Emitting Diodes. *Green Chem.* **2015**, *17* (4), 1988–2011. https://doi.org/10.1039/C4GC02195A.

(20) Wallace, P. R. The Band Theory of Graphite. *Phys. Rev.* **1947**, *71* (9), 622–634. https://doi.org/10.1103/PhysRev.71.622.

(21) Novoselov, K. S.; Geim, A. K.; Morozov, S. V.; Jiang, D.; Zhang, Y.; Dubonos, S. V.; Grigorieva, I. V.; Firsov, A. A. Electric Field Effect in Atomically Thin Carbon Films. *Science* **2004**, *306* (5696), 666–669. https://doi.org/10.1126/science.1102896.

(22) Akamatu, H.; Inokuchi, H. On the Electrical Conductivity of Violanthrone, Iso-Violanthrone, and Pyranthrone. *J. Chem. Phys.* **1950**, *18* (6), 810–811. https://doi.org/10.1063/1.1747780.

(23) Akamatu, H.; Inokuchi, H.; Matsunaga, Y. Electrical Conductivity of the Perylene–Bromine Complex. *Nature* **1954**, *173* (4395), 168–169. https://doi.org/10.1038/173168a0.

(24) Little, W. A. Possibility of Synthesizing an Organic Superconductor. *Phys. Rev.* **1964**, *134* (6A), A1416–A1424. https://doi.org/10.1103/PhysRev.134.A1416.

(25) Walatka, V. V.; Labes, M. M.; Perlstein, J. H. Polysulfur Nitride---a One-Dimensional Chain with a Metallic Ground State. *Phys. Rev. Lett.* **1973**, *31* (18), 1139–1142. https://doi.org/10.1103/PhysRevLett.31.1139.

(26) Cohen, M. J.; Garito, A. F.; Heeger, A. J.; MacDiarmid, A. G.; Mikulski, C. M.; Saran, M. S.; Kleppinger, J. Solid State Polymerization of Sulfur Nitride (S2N2) to (SN)x. *J. Am. Chem. Soc.* **1976**, *98* (13), 3844–3848. https://doi.org/10.1021/ja00429a018.

(27) Shirakawa, H.; Louis, E. J.; MacDiarmid, A. G.; Chiang, C. K.; Heeger, A. J. Synthesis of Electrically Conducting Organic Polymers: Halogen Derivatives of Polyacetylene, (CH)x. *J. Chem. Soc. Chem. Commun.* **1977**, *0* (16), 578–580. https://doi.org/10.1039/C39770000578.

(28) Chiang, C. K.; Druy, M. A.; Gau, S. C.; Heeger, A. J.; Louis, E. J.; MacDiarmid, A. G.; Park, Y. W.; Shirakawa, H. Synthesis of Highly Conducting Films of Derivatives of Polyacetylene, (CH)x. *J. Am. Chem. Soc.* **1978**, *100* (3), 1013–1015. https://doi.org/10.1021/ja00471a081.

(29) Heeger, A. J. Semiconducting and Metallic Polymers: The Fourth Generation of Polymeric Materials. *J. Phys. Chem. B* **2001**, *105* (36), 8475–8491. https://doi.org/10.1021/jp011611w.

(30) Kearns, D.; Calvin, M. Photovoltaic Effect and Photoconductivity in Laminated Organic Systems. *J. Chem. Phys.* **1958**, *29* (4), 950–951. https://doi.org/10.1063/1.1744619.

(31) Chamberlain, G. A. Organic Solar Cells: A Review. *Sol. Cells* **1983**, *8* (1), 47–83. https://doi.org/10.1016/0379-6787(83)90039-X.

(32) Che, X.; Li, Y.; Qu, Y.; Forrest, S. R. High Fabrication Yield Organic Tandem Photovoltaics Combining Vacuum- and Solution-Processed Subcells with 15% Efficiency. *Nat. Energy* **2018**, *3* (5), 422–427. https://doi.org/10.1038/s41560-018-0134-z.

(33) Meng, L.; Zhang, Y.; Wan, X.; Li, C.; Zhang, X.; Wang, Y.; Ke, X.; Xiao, Z.; Ding, L.; Xia, R.; et al. Organic and Solution-Processed Tandem Solar Cells with 17.3% Efficiency. *Science* **2018**, *361* (6407), 1094–1098. https://doi.org/10.1126/science.aat2612.

(34) Zaki, T. Introduction to Organic Electronics; Springer International Publishing: Cham, 2015; pp 5–31. https://doi.org/10.1007/978-3-319-18896-6_2.

(35) Sano, M.; Pope, M.; Kallmann, H. Electroluminescence and Band Gap in Anthracene. *J. Chem. Phys.* **1965**, *43* (8), 2920–2921. https://doi.org/10.1063/1.1697243.

(36) Tang, C. W.; VanSlyke, S. A. Organic Electroluminescent Diodes. *Appl. Phys. Lett.* **1987**, *51* (12), 913–915. https://doi.org/10.1063/1.98799.

(37) Burroughes, J. H.; Bradley, D. D. C.; Brown, A. R.; Marks, R. N.; Mackay, K.; Friend, R. H.; Burns, P. L.; Holmes, A. B. Light-Emitting Diodes Based on Conjugated Polymers. *Nature* **1990**, *347* (6293), 539–541. https://doi.org/10.1038/347539a0.

(38) Koezuka, H.; Tsumura, A.; Ando, T. Field-Effect Transistor with Polythiophene Thin Film. *Synth. Met.* **1987**, *18* (1), 699–704. https://doi.org/10.1016/0379-6779(87)90964-7.

(39) Samuel, I. D. W.; Turnbull, G. A. Organic Semiconductor Lasers. *Chem. Rev.* **2007**, *107* (4), 1272–1295. https://doi.org/10.1021/cr050152i.

(40) Vuuren, R. D. J.; Armin, A.; Pandey, A. K.; Burn, P. L.; Meredith, P. Organic Photodiodes: The Future of Full Color Detection and Image Sensing. *Adv. Mater.* **2016**, *28* (24), 4766–4802. https://doi.org/10.1002/adma.201505405.

(41) Drury, C. J.; Mutsaers, C. M. J.; Hart, C. M.; Matters, M.; de Leeuw, D. M. Low-Cost All-Polymer Integrated Circuits. *Appl. Phys. Lett.* **1998**, *73* (1), 108–110. https://doi.org/10.1063/1.121783.

(42) Borsenberger, P. M. *Organic Photoreceptors for Xerography*; CRC Press, 1998.

(43) Sony XEL-1 OLED TV | OLED-Info https://www.oled-info.com/sony-xel-1 (accessed Apr 23, 2019).

(44) Samsung Display maintains 70%, share of market of AMOLED panel for smartphones by 2020. – Ubiresearch http://www.ubiresearch.com/2017/02/17/samsung-display-maintains-70-share-of-market-of-amoled-panel-for-smartphones-by-2020/ (accessed Sep 14, 2018).

(45) DisplayMate: Samsung yet again improved its AMOLED displays, the Note 9 has the best mobile display ever | OLED-Info https://www.oled-info.com/displaymate-samsung-yet-again-improved-their-amoled-displays-note-9-has-best-mobile-display-ever (accessed Sep 14, 2018).

(46) CES 2019: Rollable TV gives OLED new life https://www.lg.com/uk/lg-magazine/tech-story/rollable-tv-ces-2019 (accessed Jan 13, 2019).

(47) Schmitz, K. S. Chapter 6 - Solid State. In *Physical Chemistry*; Elsevier: Boston, 2017; pp 261–290. https://doi.org/10.1016/B978-0-12-800514-9.00006-7.

(48) Holgate, S. A. *Understanding Solid State Physics*; CRC Press, 2009.

(49) Chakraborty, D.; Lagowski, J. B. Configuration Interaction Study of Singlet Excited State of Thiophene and Its Cyano Derivative Oligomers. *J. Chem. Phys.* **2001**, *115* (1), 184–194. https://doi.org/10.1063/1.1377876.

(50) Valeur, B. *Molecular Fluorescence: Principles and Applications*; Wiley-VCH Verlag GmbH, 2001.

(51) Köhler, A.; Bässler, H. Triplet States in Organic Semiconductors. *Mater. Sci. Eng. R Rep.* **2009**, *66* (4–6), 71–109. https://doi.org/10.1016/j.mser.2009.09.001.

(52) Lakowicz, J. R. *Principles of Fluorescence Spectroscopy*, 3rd ed.; Springer: New York, 2006.

(53) Liu, Y.; Zhan, G.; Liu, Z.-W.; Bian, Z.-Q.; Huang, C.-H. Room-Temperature Phosphorescence from Purely Organic Materials. *Chin. Chem. Lett.* **2016**, *27* (8), 1231–1240. https://doi.org/10.1016/j.cclet.2016.06.029.

(54) Ogawa, S. *Organic Electronics Materials and Devices*; Springer Japan: Tokyo, 2015. https://doi.org/10.1007/978-4-431-55654-1.

(55) Kim, W. H.; Mäkinen, A. J.; Nikolov, N.; Shashidhar, R.; Kim, H.; Kafafi, Z. H. Molecular Organic Light-Emitting Diodes Using Highly Conducting Polymers as Anodes. *Appl. Phys. Lett.* **2002**, *80* (20), 3844–3846. https://doi.org/10.1063/1.1480100.

(56) Li, Y. *Organic Optoelectronic Materials*; Lecture Notes in Chemistry; Springer International Publishing: Cham, 2015; Vol. 91. https://doi.org/10.1007/978-3-319-16862-3.

(57) Kuwabara, Y.; Ogawa, H.; Inada, H.; Noma, N.; Shirota, Y. Thermally Stable Multilared Organic Electroluminescent Devices Using Novel Starburst Molecules, 4,4′,4″-Tri(N-Carbazolyl)Triphenylamine (TCTA) and 4,4′,4″-Tris(3-Methylphenylphenylamino)Triphenylamine (m-MTDATA), as Hole-Transport Materials. *Adv. Mater.* **1994**, *6* (9), 677–679. https://doi.org/10.1002/adma.19940060913.

(58) Adamovich, V. I.; Cordero, S. R.; Djurovich, P. I.; Tamayo, A.; Thompson, M. E.; D'Andrade, B. W.; Forrest, S. R. New Charge-Carrier Blocking Materials for High Efficiency OLEDs. *Org. Electron.* **2003**, *4* (2), 77–87. https://doi.org/10.1016/j.orgel.2003.08.003.

(59) Adachi, C.; Tsutsui, T.; Saito, S. Organic Electroluminescent Device Having a Hole Conductor as an Emitting Layer. *Appl. Phys. Lett.* **1989**, *55* (15), 1489–1491. https://doi.org/10.1063/1.101586.

(60) Su, S.-J.; Chiba, T.; Takeda, T.; Kido, J. Pyridine-Containing Triphenylbenzene Derivatives with High Electron Mobility for Highly Efficient Phosphorescent OLEDs. *Adv. Mater.* **2008**, *20* (11), 2125–2130. https://doi.org/10.1002/adma.200701730.

(61) Wakimoto, T.; Fukuda, Y.; Nagayama, K.; Yokoi, A.; Nakada, H.; Tsuchida, M. Organic EL Cells Using Alkaline Metal Compounds as Electron Injection Materials. *IEEE Trans. Electron Devices* **1997**, *44* (8), 1245–1248. https://doi.org/10.1109/16.605462.

(62) Kim, Y. Power-Law-Type Electron Injection through Lithium Fluoride Nanolayers in Phosphorescence Organic Light-Emitting Devices. *Nanotechnology* **2008**, *19* (35), 355207. https://doi.org/10.1088/0957-4484/19/35/355207.

(63) Kido, J.; Matsumoto, T. Bright Organic Electroluminescent Devices Having a Metal-Doped Electron-Injecting Layer. *Appl. Phys. Lett.* **1998**, *73* (20), 2866–2868. https://doi.org/10.1063/1.122612.

(64) Schmitz, C.; Schmidt, H.-W.; Thelakkat, M. Lithium−Quinolate Complexes as Emitter and Interface Materials in Organic Light-Emitting Diodes. *Chem. Mater.* **2000**, *12* (10), 3012–3019. https://doi.org/10.1021/cm0010248.

(65) Segal, M.; Baldo, M. A.; Holmes, R. J.; Forrest, S. R.; Soos, Z. G. Excitonic Singlet-Triplet Ratios in Molecular and Polymeric Organic Materials. *Phys. Rev. B* **2003**, *68* (7), 075211. https://doi.org/10.1103/PhysRevB.68.075211.

(66) Kim, J.-S.; Ho, P. K. H.; Greenham, N. C.; Friend, R. H. Electroluminescence Emission Pattern of Organic Light-Emitting Diodes: Implications for Device Efficiency Calculations. *J. Appl. Phys.* **2000**, *88* (2), 1073–1081. https://doi.org/10.1063/1.373779.

(67) Salehi, A.; Ho, S.; Chen, Y.; Peng, C.; Yersin, H.; So, F. Highly Efficient Organic Light-Emitting Diode Using A Low Refractive Index Electron Transport Layer. *Adv. Opt. Mater.* **2017**, *5* (11), 1700197. https://doi.org/10.1002/adom.201700197.

(68) Choi, Y. H.; Jeon, Y. P.; Choo, D. C.; Kim, T. W. Enhancement of Out-Coupling Efficiency Due to an Organic Scattering Layer in Organic Light-Emitting Devices. *Org. Electron.* **2015**, *22* (Supplement C), 197–201. https://doi.org/10.1016/j.orgel.2015.03.044.

(69) Qu, Y.; Kim, J.; Coburn, C.; Forrest, S. R. Efficient, Nonintrusive Outcoupling in Organic Light Emitting Devices Using Embedded Microlens Arrays. *ACS Photonics* **2018**. https://doi.org/10.1021/acsphotonics.8b00255.

(70) Taylor, E.; Edwards, P. R.; Martin, R. W. Colorimetry and Efficiency of White LEDs: Spectral Width Dependence. *Phys. Status Solidi A* **2012**, *209* (3), 461–464. https://doi.org/10.1002/pssa.201100449.

(71) Pereira, D. D. S.; Monkman, A. P. Methods of Analysis of Organic Light Emitting Diodes. *Disp. Imaging* **2017**, *2*, 323–337.

(72) OLED Testing Guide https://www.ossila.com/pages/oled-testing-guide (accessed Feb 10, 2019).

(73) Ohno, Y. Color Rendering and Luminous Efficacy of White LED Spectra. In *Fourth International Conference on Solid State Lighting*; International Society for Optics and Photonics, 2004; Vol. 5530, pp 88–99. https://doi.org/10.1117/12.565757.

(74) en:User:PAR. *CIE Xy 1931 Chromaticity Diagram Including the Planckian Locus.*; 2005.

(75) Baldo, M. A.; O'Brien, D. F.; You, Y.; Shoustikov, A.; Sibley, S.; Thompson, M. E.; Forrest, S. R. Highly Efficient Phosphorescent Emission from Organic Electroluminescent Devices. *Nature* **1998**, *395* (6698), 151–154. https://doi.org/10.1038/25954.

(76) Schmidbauer, S.; Hohenleutner, A.; König, B. Chemical Degradation in Organic Light-Emitting Devices: Mechanisms and Implications for the Design of New Materials. *Adv. Mater.* **2013**, *25* (15), 2114–2129. https://doi.org/10.1002/adma.201205022.

(77) Kondakov, D. Y.; Pawlik, T. D.; Hatwar, T. K.; Spindler, J. P. Triplet Annihilation Exceeding Spin Statistical Limit in Highly Efficient Fluorescent Organic Light-Emitting Diodes. *J. Appl. Phys.* **2009**, *106* (12), 124510. https://doi.org/10.1063/1.3273407.

(78) Chiang, C.-J.; Kimyonok, A.; Etherington, M. K.; Griffiths, G. C.; Jankus, V.; Turksoy, F.; Monkman, A. P. Ultrahigh Efficiency Fluorescent Single and Bi-Layer Organic Light Emitting Diodes: The Key Role of Triplet Fusion. *Adv. Funct. Mater.* **2013**, *23* (6), 739–746. https://doi.org/10.1002/adfm.201201750.

(79) Li, W.; Liu, D.; Shen, F.; Ma, D.; Wang, Z.; Feng, T.; Xu, Y.; Yang, B.; Ma, Y. A Twisting Donor-Acceptor Molecule with an Intercrossed Excited State for Highly Efficient, Deep-Blue Electroluminescence. *Adv. Funct. Mater.* **2012**, *22* (13), 2797–2803. https://doi.org/10.1002/adfm.201200116.

(80) Pan, Y.; Li, W.; Zhang, S.; Yao, L.; Gu, C.; Xu, H.; Yang, B.; Ma, Y. High Yields of Singlet Excitons in Organic Electroluminescence through Two Paths of Cold and Hot Excitons. *Adv. Opt. Mater.* **2014**, *2* (6), 510–515. https://doi.org/10.1002/adom.201300467.

(81) Hu, D.; Yao, L.; Yang, B.; Ma, Y. Reverse Intersystem Crossing from Upper Triplet Levels to Excited Singlet: A 'Hot Excition' Path for Organic Light-Emitting Diodes. *Phil Trans R Soc A* **2015**, *373* (2044), 20140318. https://doi.org/10.1098/rsta.2014.0318.

(82) Parker, C. A.; Hatchard, C. G. Triplet-Singlet Emission in Fluid Solutions. Phosphorescence of Eosin. *Trans. Faraday Soc.* **1961**, *57* (0), 1894–1904. https://doi.org/10.1039/TF9615701894.

(83) Berberan-Santos, M. N.; Garcia, J. M. M. Unusually Strong Delayed Fluorescence of C70. *J. Am. Chem. Soc.* **1996**, *118* (39), 9391–9394. https://doi.org/10.1021/ja961782s.

(84) Baleizão, C.; Berberan-Santos, M. N. Thermally Activated Delayed Fluorescence in Fullerenes. *Ann. N. Y. Acad. Sci.* **2008**, *1130* (1), 224–234. https://doi.org/10.1196/annals.1430.044.

(85) Endo, A.; Ogasawara, M.; Takahashi, A.; Yokoyama, D.; Kato, Y.; Adachi, C. Thermally Activated Delayed Fluorescence from Sn4+-Porphyrin Complexes and Their Application to Organic Light Emitting Diodes - A Novel Mechanism for Electroluminescence. *Adv. Mater.* **2009**, *21* (47), 4802–4806. https://doi.org/10.1002/adma.200900983.

(86) Zeng, W.; Lai, H.-Y.; Lee, W.-K.; Jiao, M.; Shiu, Y.-J.; Zhong, C.; Gong, S.; Zhou, T.; Xie, G.; Sarma, M.; et al. Achieving Nearly 30% External Quantum Efficiency for Orange–Red Organic Light Emitting Diodes by Employing Thermally Activated Delayed Fluorescence Emitters Composed of 1,8-Naphthalimide-Acridine Hybrids. *Adv. Mater.* **2018**, *30* (5), 1704961. https://doi.org/10.1002/adma.201704961.

(87) Dias, F. B.; Penfold, T. J.; Monkman, A. P. Photophysics of Thermally Activated Delayed Fluorescence Molecules. *Methods Appl. Fluoresc.* **2017**, *5* (1), 012001. https://doi.org/10.1088/2050-6120/aa537e.

(88) Turro, N. J.; Ramamurthy, V.; Scaiano, J. C. *Modern Molecular Photochemistry of Organic Molecules*; University Science Books, 2010.

(89) Tao, Y.; Yuan, K.; Chen, T.; Xu, P.; Li, H.; Chen, R.; Zheng, C.; Zhang, L.; Huang, W. Thermally Activated Delayed Fluorescence Materials Towards the Breakthrough of Organoelectronics. *Adv. Mater.* **2014**, *26* (47), 7931–7958. https://doi.org/10.1002/adma.201402532.

(90) Uoyama, H.; Goushi, K.; Shizu, K.; Nomura, H.; Adachi, C. Highly Efficient Organic Light-Emitting Diodes from Delayed Fluorescence. *Nature* **2012**, *492* (7428), 234–238. https://doi.org/10.1038/nature11687.

(91) Nakagawa, T.; Ku, S.-Y.; Wong, K.-T.; Adachi, C. Electroluminescence Based on Thermally Activated Delayed Fluorescence Generated by a Spirobifluorene Donor–Acceptor Structure. *Chem. Commun.* **2012**, *48* (77), 9580. https://doi.org/10.1039/c2cc31468a.

(92) Kawasumi, K.; Wu, T.; Zhu, T.; Chae, H. S.; Van Voorhis, T.; Baldo, M. A.; Swager, T. M. Thermally Activated Delayed Fluorescence Materials Based on Homoconjugation Effect of Donor–Acceptor Triptycenes. *J. Am. Chem. Soc.* **2015**, *137* (37), 11908–11911. https://doi.org/10.1021/jacs.5b07932.

(93) Lee, S. Y.; Yasuda, T.; Park, I. S.; Adachi, C. X-Shaped Benzoylbenzophenone Derivatives with Crossed Donors and Acceptors for Highly Efficient Thermally Activated Delayed Fluorescence. *Dalton Trans.* **2015**, *44* (18), 8356–8359. https://doi.org/10.1039/C4DT03608E.

(94) Ward, J. S.; Nobuyasu, R. S.; Batsanov, A. S.; Data, P.; Monkman, A. P.; Dias, F. B.; Bryce, M. R. The Interplay of Thermally Activated Delayed Fluorescence (TADF) and Room Temperature Organic Phosphorescence in Sterically-Constrained Donor–Acceptor Charge-Transfer Molecules. *Chem Commun* **2016**, *52* (12), 2612–2615. https://doi.org/10.1039/C5CC09645F.

(95) Etherington, M. K.; Franchello, F.; Gibson, J.; Northey, T.; Santos, J.; Ward, J. S.; Higginbotham, H. F.; Data, P.; Kurowska, A.; Santos, P. L. D.; et al. Regio- and Conformational Isomerization Critical to Design of Efficient Thermally-Activated Delayed Fluorescence Emitters. *Nat. Commun.* **2017**, *8*, 14987. https://doi.org/10.1038/ncomms14987.

(96) Rajamalli, P.; Senthilkumar, N.; Gandeepan, P.; Huang, P.-Y.; Huang, M.-J.; Ren-Wu, C.-Z.; Yang, C.-Y.; Chiu, M.-J.; Chu, L.-K.; Lin, H.-W.; et al. A New Molecular Design Based on Thermally Activated Delayed Fluorescence for Highly Efficient Organic Light Emitting Diodes. *J. Am. Chem. Soc.* **2016**, *138* (2), 628–634. https://doi.org/10.1021/jacs.5b10950.

(97) Marian, C. M. Spin–Orbit Coupling and Intersystem Crossing in Molecules. *Wiley Interdiscip. Rev. Comput. Mol. Sci.* **2012**, *2* (2), 187–203. https://doi.org/10.1002/wcms.83.

(98) Leitl, M. J.; Zink, D. M.; Schinabeck, A.; Baumann, T.; Volz, D.; Yersin, H. Copper(I) Complexes for Thermally Activated Delayed Fluorescence: From Photophysical to Device Properties. In *Photoluminescent Materials and Electroluminescent Devices*; Armaroli, N., Bolink, H. J., Eds.; Topics in Current Chemistry Collections; Springer International Publishing: Cham, 2017; pp 141–174. https://doi.org/10.1007/978-3-319-59304-3_5.

(99) Xiang, Y.; Zhao, Y.; Xu, N.; Gong, S.; Ni, F.; Wu, K.; Luo, J.; Xie, G.; Lu, Z.-H.; Yang, C. Halogen-Induced Internal Heavy-Atom Effect Shortening the Emissive Lifetime and Improving the Fluorescence Efficiency of Thermally Activated Delayed Fluorescence Emitters. *J. Mater. Chem. C* **2017**, *5* (46), 12204–12210. https://doi.org/10.1039/C7TC04181K.

(100) Zhang, W.; Jin, J.; Huang, Z.; Zhuang, S.; Wang, L. A New Way towards High-Efficiency Thermally Activated Delayed Fluorescence Devices via External Heavy-Atom Effect. *Sci. Rep.* **2016**, *6*, 30178. https://doi.org/10.1038/srep30178.

(101) Samanta, P. K.; Kim, D.; Coropceanu, V.; Brédas, J.-L. Up-Conversion Intersystem Crossing Rates in Organic Emitters for Thermally Activated Delayed Fluorescence: Impact of the Nature of Singlet vs Triplet Excited States. *J. Am. Chem. Soc.* **2017**, *139* (11), 4042–4051. https://doi.org/10.1021/jacs.6b12124.

(102) Lim, B. T.; Okajima, S.; Chandra, A. K.; Lim, E. C. Radiationless Transitions in Electron Donor-Acceptor Complexes: Selection Rules for S1 → T Intersystem Crossing and Efficiency of S1 → S0 Internal Conversion. *Chem. Phys. Lett.* **1981**, *79* (1), 22–27. https://doi.org/10.1016/0009-2614(81)85280-3.

(103) Dias, F. B.; Santos, J.; Graves, D. R.; Data, P.; Nobuyasu, R. S.; Fox, M. A.; Batsanov, A. S.; Palmeira, T.; Berberan-Santos, M. N.; Bryce, M. R.; et al. The Role of Local Triplet Excited States and D-A Relative Orientation in Thermally Activated Delayed Fluorescence: Photophysics and Devices. *Adv. Sci.* **2016**, *3* (12), 1600080. https://doi.org/10.1002/advs.201600080.

(104) Huang, R.; Avó, J.; Northey, T.; Chaning-Pearce, E.; Santos, P. L. dos; Ward, J. S.; Data, P.; Etherington, M. K.; Fox, M. A.; Penfold, T. J.; et al. The Contributions of Molecular Vibrations and Higher Triplet Levels to the Intersystem Crossing Mechanism in Metal-Free Organic Emitters. *J. Mater. Chem. C* **2017**, *5* (25), 6269–6280. https://doi.org/10.1039/C7TC01958K.

(105) Lee, K.; Kim, D. Local-Excitation versus Charge-Transfer Characters in the Triplet State: Theoretical Insight into the Singlet–Triplet Energy Differences of Carbazolyl-Phthalonitrile-Based Thermally Activated Delayed Fluorescence Materials. *J. Phys. Chem. C* **2016**, *120* (49), 28330–28336. https://doi.org/10.1021/acs.jpcc.6b10161.

(106) Marian, C. M. Mechanism of the Triplet-to-Singlet Upconversion in the Assistant Dopant ACRXTN. *J. Phys. Chem. C* **2016**, *120* (7), 3715–3721. https://doi.org/10.1021/acs.jpcc.6b00060.

(107) Chen, X.-K.; Zhang, S.-F.; Fan, J.-X.; Ren, A.-M. Nature of Highly Efficient Thermally Activated Delayed Fluorescence in Organic Light-Emitting Diode Emitters: Nonadiabatic Effect between Excited States. *J. Phys. Chem. C* **2015**, *119* (18), 9728–9733. https://doi.org/10.1021/acs.jpcc.5b00276.

(108) Gibson, J.; Monkman, A. P.; Penfold, T. J. The Importance of Vibronic Coupling for Efficient Reverse Intersystem Crossing in Thermally Activated Delayed Fluorescence Molecules. *Chemphyschem* **2016**, *17* (19), 2956–2961. https://doi.org/10.1002/cphc.201600662.

(109) Zhang, Q.; Li, J.; Shizu, K.; Huang, S.; Hirata, S.; Miyazaki, H.; Adachi, C. Design of Efficient Thermally Activated Delayed Fluorescence Materials for Pure Blue Organic Light Emitting Diodes. *J. Am. Chem. Soc.* **2012**, *134* (36), 14706–14709. https://doi.org/10.1021/ja306538w.

(110) Etherington, M. K.; Gibson, J.; Higginbotham, H. F.; Penfold, T. J.; Monkman, A. P. Revealing the Spin–Vibronic Coupling Mechanism of Thermally Activated Delayed Fluorescence. *Nat. Commun.* **2016**, *7*, 13680. https://doi.org/10.1038/ncomms13680.

(111) Gibson, J.; Penfold, T. J. Nonadiabatic Coupling Reduces the Activation Energy in Thermally Activated Delayed Fluorescence. *Phys. Chem. Chem. Phys.* **2017**, *19* (12), 8428–8434. https://doi.org/10.1039/C7CP00719A.

(112) Penfold, T. J.; Gindensperger, E.; Daniel, C.; Marian, C. M. Spin-Vibronic Mechanism for Intersystem Crossing. *Chem. Rev.* **2018**, *118* (15), 6975–7025. https://doi.org/10.1021/acs.chemrev.7b00617.

(113) Santos, P. L.; Ward, J. S.; Data, P.; Batsanov, A. S.; Bryce, M. R.; Dias, F. B.; Monkman, A. P. Engineering the Singlet–Triplet Energy Splitting in a TADF Molecule. *J. Mater. Chem. C* **2016**, *4* (17), 3815–3824. https://doi.org/10.1039/C5TC03849A.

(114) Im, Y.; Kim, M.; Cho, Y. J.; Seo, J.-A.; Yook, K. S.; Lee, J. Y. Molecular Design Strategy of Organic Thermally Activated Delayed Fluorescence Emitters. *Chem. Mater.* **2017**, *29* (5), 1946–1963. https://doi.org/10.1021/acs.chemmater.6b05324.

(115) Shizu, K.; Noda, H.; Tanaka, H.; Taneda, M.; Uejima, M.; Sato, T.; Tanaka, K.; Kaji, H.; Adachi, C. Highly Efficient Blue Electroluminescence Using Delayed-Fluorescence Emitters with Large Overlap Density between Luminescent and Ground States. *J. Phys. Chem. C* **2015**, *119* (47), 26283–26289. https://doi.org/10.1021/acs.jpcc.5b07798.

(116) Hirata, S.; Sakai, Y.; Masui, K.; Tanaka, H.; Lee, S. Y.; Nomura, H.; Nakamura, N.; Yasumatsu, M.; Nakanotani, H.; Zhang, Q.; et al. Highly Efficient Blue Electroluminescence Based on Thermally Activated Delayed Fluorescence. *Nat. Mater.* **2015**, *14* (3), 330–336. https://doi.org/10.1038/nmat4154.

(117) Lee, D. R.; Kim, M.; Jeon, S. K.; Hwang, S.-H.; Lee, C. W.; Lee, J. Y. Design Strategy for 25% External Quantum Efficiency in Green and Blue Thermally Activated Delayed Fluorescent Devices. *Adv. Mater.* **2015**, *27* (39), 5861–5867. https://doi.org/10.1002/adma.201502053.

(118) Chen, X.-K.; Tsuchiya, Y.; Ishikawa, Y.; Zhong, C.; Adachi, C.; Brédas, J.-L. A New Design Strategy for Efficient Thermally Activated Delayed Fluorescence Organic Emitters: From Twisted to Planar Structures. *Adv. Mater.* **2017**, *29* (46), 1702767. https://doi.org/10.1002/adma.201702767.

(119) Dias, F. B.; Pollock, S.; Hedley, G.; Pålsson, L.-O.; Monkman, A.; Perepichka, I. I.; Perepichka, I. F.; Tavasli, M.; Bryce, M. R. Intramolecular Charge Transfer Assisted by Conformational Changes in the Excited State of Fluorene-Dibenzothiophene-S,S-Dioxide Co-Oligomers. *J. Phys. Chem. B* **2006**, *110* (39), 19329–19339. https://doi.org/10.1021/jp0643653.

(120) Hatakeyama, T.; Shiren, K.; Nakajima, K.; Nomura, S.; Nakatsuka, S.; Kinoshita, K.; Ni, J.; Ono, Y.; Ikuta, T. Ultrapure Blue Thermally Activated Delayed Fluorescence Molecules: Efficient HOMO–LUMO Separation by the Multiple Resonance Effect. *Adv. Mater.* **2016**, *28* (14), 2777–2781. https://doi.org/10.1002/adma.201505491.

(121) Liu, A.; Khanna, A.; Dutta, P. S.; Shur, M. Red-Blue-Green Solid State Light Sources Using a Narrow Line-Width Green Phosphor. *Opt. Express* **2015**, *23* (7), A309–A315. https://doi.org/10.1364/OE.23.00A309.

(122) Li, J.; Zhang, Q.; Nomura, H.; Miyazaki, H.; Adachi, C. Thermally Activated Delayed Fluorescence from 3nπ* to 1nπ* Up-Conversion and Its Application to Organic Light-Emitting Diodes. *Appl. Phys. Lett.* **2014**, *105* (1), 013301. https://doi.org/10.1063/1.4887346.

(123) Northey, T.; Penfold, T. J. The Intersystem Crossing Mechanism of an Ultrapure Blue Organoboron Emitter. *Org. Electron.* **2018**, *59*, 45–48. https://doi.org/10.1016/j.orgel.2018.04.038.

(124) Mamada, M.; Inada, K.; Komino, T.; Potscavage, W. J.; Nakanotani, H.; Adachi, C. Highly Efficient Thermally Activated Delayed Fluorescence from an Excited-State Intramolecular Proton Transfer System. *ACS Cent. Sci.* **2017**. https://doi.org/10.1021/acscentsci.7b00183.

(125) Kwon, J. E.; Park, S. Y. Advanced Organic Optoelectronic Materials: Harnessing Excited-State Intramolecular Proton Transfer (ESIPT) Process. *Adv. Mater.* **2011**, *23* (32), 3615–3642. https://doi.org/10.1002/adma.201102046.

(126) Park, S.; Kwon, O.-H.; Lee, Y.-S.; Jang, D.-J.; Park, S. Y. Imidazole-Based Excited-State Intramolecular Proton-Transfer (ESIPT) Materials: Observation of Thermally Activated Delayed Fluorescence (TDF). *J. Phys. Chem. A* **2007**, *111* (39), 9649–9653. https://doi.org/10.1021/jp072212p.

(127) Pander, P. H.; Motyka, R.; Zassowski, P.; Etherington, M. K.; Varsano, D.; da Silva, T. J.; Caldas, M. J.; Data, P.; Monkman, A. P. Thermally-Activated Delayed Fluorescence Mediated Through the Upper Triplet State Manifold in Non-Charge Transfer Star-Shaped Triphenylamine-Carbazole Molecules. *J. Phys. Chem. C* **2018**, *122* (42), 23934–23942. https://doi.org/10.1021/acs.jpcc.8b07610.

(128) Englman, R.; Jortner, J. The Energy Gap Law for Radiationless Transitions in Large Molecules. *Mol. Phys.* **1970**, *18* (2), 145–164. https://doi.org/10.1080/00268977000100171.

(129) Bui, T.-T.; Goubard, F.; Ibrahim-Ouali, M.; Gigmes, D.; Dumur, F. Recent Advances on Organic Blue Thermally Activated Delayed Fluorescence (TADF) Emitters for Organic Light-Emitting

Diodes (OLEDs). *Beilstein J. Org. Chem.* **2018**, *14* (1), 282–308. https://doi.org/10.3762/bjoc.14.18.

(130) dos Santos, P. L.; Ward, J. S.; Bryce, M. R.; Monkman, A. P. Using Guest–Host Interactions To Optimize the Efficiency of TADF OLEDs. *J. Phys. Chem. Lett.* **2016**, *7* (17), 3341–3346. https://doi.org/10.1021/acs.jpclett.6b01542.

(131) Im, Y.; Lee, J. Y. Recent Progress of Green Thermally Activated Delayed Fluorescent Emitters. *J. Inf. Disp.* **2017**, *18* (3), 101–117. https://doi.org/10.1080/15980316.2017.1333046.

(132) Sun, J. W.; Lee, J.-H.; Moon, C.-K.; Kim, K.-H.; Shin, H.; Kim, J.-J. A Fluorescent Organic Light-Emitting Diode with 30% External Quantum Efficiency. *Adv. Mater.* **2014**, *26* (32), 5684–5688. https://doi.org/10.1002/adma.201401407.

(133) Park, I. S.; Lee, S. Y.; Adachi, C.; Yasuda, T. Full-Color Delayed Fluorescence Materials Based on Wedge-Shaped Phthalonitriles and Dicyanopyrazines: Systematic Design, Tunable Photophysical Properties, and OLED Performance. *Adv. Funct. Mater.* **2016**, *26* (11), 1813–1821. https://doi.org/10.1002/adfm.201505106.

(134) Kim, J. H.; Yun, J. H.; Lee, J. Y. Recent Progress of Highly Efficient Red and Near-Infrared Thermally Activated Delayed Fluorescent Emitters. *Adv. Opt. Mater.* **2018**, 1800255. https://doi.org/10.1002/adom.201800255.

(135) Data, P.; Pander, P.; Okazaki, M.; Takeda, Y.; Minakata, S.; Monkman, A. P. Dibenzo[a,j]Phenazine-Cored Donor-Acceptor-Donor Compounds as Green-to-Red/NIR Thermally Activated Delayed Fluorescence Organic Light Emitters. *Angew. Chem. Int. Ed.* **2016**, *55* (19), 5739–5744. https://doi.org/10.1002/anie.201600113.

(136) Furue, R.; Matsuo, K.; Ashikari, Y.; Ooka, H.; Amanokura, N.; Yasuda, T. Highly Efficient Red–Orange Delayed Fluorescence Emitters Based on Strong Π-Accepting Dibenzophenazine and Dibenzoquinoxaline Cores: Toward a Rational Pure-Red OLED Design. *Adv. Opt. Mater.* **2018**, *6* (5). https://doi.org/10.1002/adom.201701147.

(137) Méhes, G.; Goushi, K.; Potscavage Jr., W. J.; Adachi, C. Influence of Host Matrix on Thermally-Activated Delayed Fluorescence: Effects on Emission Lifetime, Photoluminescence Quantum Yield, and Device Performance. *Org. Electron.* **2014**, *15* (9), 2027–2037. https://doi.org/10.1016/j.orgel.2014.05.027.

(138) Tsai, W.-L.; Huang, M.-H.; Lee, W.-K.; Hsu, Y.-J.; Pan, K.-C.; Huang, Y.-H.; Ting, H.-C.; Sarma, M.; Ho, Y.-Y.; Hu, H.-C.; et al. A Versatile Thermally Activated Delayed Fluorescence Emitter for Both Highly Efficient Doped and Non-Doped Organic Light Emitting Devices. *Chem. Commun.* **2015**, *51* (71), 13662–13665. https://doi.org/10.1039/C5CC05022G.

(139) Tao, Y.; Yang, C.; Qin, J. Organic Host Materials for Phosphorescent Organic Light-Emitting Diodes. *Chem. Soc. Rev.* **2011**, *40* (5), 2943–2970. https://doi.org/10.1039/C0CS00160K.

(140) Youn Lee, S.; Yasuda, T.; Nomura, H.; Adachi, C. High-Efficiency Organic Light-Emitting Diodes Utilizing Thermally Activated Delayed Fluorescence from Triazine-Based Donor–Acceptor Hybrid Molecules. *Appl. Phys. Lett.* **2012**, *101* (9), 093306. https://doi.org/10.1063/1.4749285.

(141) Cho, Y. J.; Yook, K. S.; Lee, J. Y. A Universal Host Material for High External Quantum Efficiency Close to 25% and Long Lifetime in Green Fluorescent and Phosphorescent OLEDs. *Adv. Mater.* **2014**, *26* (24), 4050–4055. https://doi.org/10.1002/adma.201400347.

(142) Gaj, M. P.; Fuentes-Hernandez, C.; Zhang, Y.; Marder, S. R.; Kippelen, B. Highly Efficient Organic Light-Emitting Diodes from Thermally Activated Delayed Fluorescence Using a Sulfone–Carbazole Host Material. *Org. Electron.* **2015**, *16*, 109–112. https://doi.org/10.1016/j.orgel.2014.10.049.

(143) Cui, L.-S.; Xie, Y.-M.; Wang, Y.-K.; Zhong, C.; Deng, Y.-L.; Liu, X.-Y.; Jiang, Z.-Q.; Liao, L.-S. Pure Hydrocarbon Hosts for ≈100% Exciton Harvesting in Both Phosphorescent and Fluorescent Light-Emitting Devices. *Adv. Mater.* **2015**, *27* (28), 4213–4217. https://doi.org/10.1002/adma.201501376.

(144) Lee, C. W.; Lee, J. Y. Systematic Control of Photophysical Properties of Host Materials for High Quantum Efficiency above 25% in Green Thermally Activated Delayed Fluorescent Devices. *ACS Appl. Mater. Interfaces* **2015**, *7* (4), 2899–2904. https://doi.org/10.1021/am508259u.

(145) Kim, B. S.; Lee, J. Y. Engineering of Mixed Host for High External Quantum Efficiency above 25% in Green Thermally Activated Delayed Fluorescence Device. *Adv. Funct. Mater.* **2014**, *24* (25), 3970–3977. https://doi.org/10.1002/adfm.201303730.

(146) Wong, M. Y.; Zysman-Colman, E. Purely Organic Thermally Activated Delayed Fluorescence Materials for Organic Light-Emitting Diodes. *Adv. Mater.* **2017**, *29* (22), 1605444. https://doi.org/10.1002/adma.201605444.

(147) Jenekhe, S. A.; Osaheni, J. A. Excimers and Exciplexes of Conjugated Polymers. *Science* **1994**, *265* (5173), 765–768. https://doi.org/10.1126/science.265.5173.765.

(148) Huang, T.; Jiang, W.; Duan, L. Recent Progress in Solution Processable TADF Materials for Organic Light-Emitting Diodes. *J. Mater. Chem. C* **2018**. https://doi.org/10.1039/C8TC01139G.

(149) Kanibolotsky, A. L.; Perepichka, I. F.; Skabara, P. J. Star-Shaped π-Conjugated Oligomers and Their Applications in Organic Electronics and Photonics. *Chem. Soc. Rev.* **2010**, *39* (7), 2695–2728. https://doi.org/10.1039/b918154g.

(150) Albrecht, K.; Matsuoka, K.; Fujita, K.; Yamamoto, K. Carbazole Dendrimers as Solution-Processable Thermally Activated Delayed-Fluorescence Materials. *Angew. Chem. Int. Ed.* **2015**, *54* (19), 5677–5682. https://doi.org/10.1002/anie.201500203.

(151) Albrecht, K.; Matsuoka, K.; Yokoyama, D.; Sakai, Y.; Nakayama, A.; Fujita, K.; Yamamoto, K. Thermally Activated Delayed Fluorescence OLEDs with Fully Solution Processed Organic Layers Exhibiting Nearly 10% External Quantum Efficiency. *Chem. Commun.* **2017**, *53* (16), 2439–2442. https://doi.org/10.1039/C6CC09275F.

(152) Luo, J.; Gong, S.; Gu, Y.; Chen, T.; Li, Y.; Zhong, C.; Xie, G.; Yang, C. Multi-Carbazole Encapsulation as a Simple Strategy for the Construction of Solution-Processed, Non-Doped Thermally Activated Delayed Fluorescence Emitters. *J. Mater. Chem. C* **2016**, *4* (13), 2442–2446. https://doi.org/10.1039/C6TC00418K.

(153) Matsuoka, K.; Albrecht, K.; Nakayama, A.; Yamamoto, K.; Fujita, K. Highly Efficient Thermally Activated Delayed Fluorescence Organic Light-Emitting Diodes with Fully Solution-Processed Organic Multilayered Architecture: Impact of Terminal-Substitution on Carbazole-Benzophenone Dendrimer and Interfacial Engineering. *ACS Appl. Mater. Interfaces* **2018**, *10* (39), 33343−33352. https://doi.org/10.1021/acsami.8b09451.

(154) Liu, Y.; Li, C.; Ren, Z.; Yan, S.; Bryce, M. R. All-Organic Thermally Activated Delayed Fluorescence Materials for Organic Light-Emitting Diodes. *Nat. Rev. Mater.* **2018**, *3* (4), 18020. https://doi.org/10.1038/natrevmats.2018.20.

(155) Ban, X.; Jiang, W.; Lu, T.; Jing, X.; Tang, Q.; Huang, S.; Sun, K.; Huang, B.; Lin, B.; Sun, Y. Self-Host Thermally Activated Delayed Fluorescent Dendrimers with Flexible Chains: An Effective Strategy for Non-Doped Electroluminescent Devices Based on Solution Processing. *J. Mater. Chem. C* **2016**, *4* (37), 8810–8816. https://doi.org/10.1039/C6TC03063G.

(156) Ban, X.; Lin, B.; Jiang, W.; Sun, Y. Constructing a Novel Dendron for a Self-Host Blue Emitter with Thermally Activated Delayed Fluorescence: Solution-Processed Nondoped Organic Light-Emitting Diodes with Bipolar Charge Transfer and Stable Color Purity. *Chem. – Asian J.* **2017**, *12* (2), 216–223. https://doi.org/10.1002/asia.201601384.

(157) Ban, X.; Jiang, W.; Sun, K.; Lin, B.; Sun, Y. Self-Host Blue Dendrimer Comprised of Thermally Activated Delayed Fluorescence Core and Bipolar Dendrons for Efficient Solution-Processable Nondoped Electroluminescence. *ACS Appl. Mater. Interfaces* **2017**, *9* (8), 7339–7346. https://doi.org/10.1021/acsami.6b14922.

(158) Zhu, Y.; Zhang, Y.; Yao, B.; Wang, Y.; Zhang, Z.; Zhan, H.; Zhang, B.; Xie, Z.; Wang, Y.; Cheng, Y. Synthesis and Electroluminescence of a Conjugated Polymer with Thermally Activated Delayed Fluorescence. *Macromolecules* **2016**, *49* (11), 4373–4377. https://doi.org/10.1021/acs.macromol.6b00430.

(159) Xie, G.; Luo, J.; Huang, M.; Chen, T.; Wu, K.; Gong, S.; Yang, C. Inheriting the Characteristics of TADF Small Molecule by Side-Chain Engineering Strategy to Enable Bluish-Green Polymers with High PLQYs up to 74% and External Quantum Efficiency over 16% in Light-Emitting Diodes. *Adv. Mater.* **2017**, *29* (11), 1604223. https://doi.org/10.1002/adma.201604223.

(160) Wang, Y.; Zhu, Y.; Xie, G.; Zhan, H.; Yang, C.; Cheng, Y. Bright White Electroluminescence from a Single Polymer Containing a Thermally Activated Delayed Fluorescence Unit and a Solution-

Processed Orange OLED Approaching 20% External Quantum Efficiency. *J. Mater. Chem. C* **2017**, *5* (41), 10715–10720. https://doi.org/10.1039/C7TC03769D.

(161) Ren, Z.; Nobuyasu, R. S.; Dias, F. B.; Monkman, A. P.; Yan, S.; Bryce, M. R. Pendant Homopolymer and Copolymers as Solution-Processable Thermally Activated Delayed Fluorescence Materials for Organic Light-Emitting Diodes. *Macromolecules* **2016**, *49* (15), 5452–5460. https://doi.org/10.1021/acs.macromol.6b01216.

(162) Shao, S.; Hu, J.; Wang, X.; Wang, L.; Jing, X.; Wang, F. Blue Thermally Activated Delayed Fluorescence Polymers with Nonconjugated Backbone and Through-Space Charge Transfer Effect. *J. Am. Chem. Soc.* **2017**, *139* (49), 17739–17742. https://doi.org/10.1021/jacs.7b10257.

(163) Wei, Q.; Kleine, P.; Karpov, Y.; Qiu, X.; Komber, H.; Sahre, K.; Kiriy, A.; Lygaitis, R.; Lenk, S.; Reineke, S.; et al. Conjugation-Induced Thermally Activated Delayed Fluorescence (TADF): From Conventional Non-TADF Units to TADF-Active Polymers. *Adv. Funct. Mater.* **2017**, *27* (7), 1605051. https://doi.org/10.1002/adfm.201605051.

(164) dos Santos, P. L.; Dias, F. B.; Monkman, A. P. Investigation of the Mechanisms Giving Rise to TADF in Exciplex States. *J. Phys. Chem. C* **2016**, *120* (32), 18259–18267. https://doi.org/10.1021/acs.jpcc.6b05198.

(165) Kavarnos, G. J.; Turro, N. J. Photosensitization by Reversible Electron Transfer: Theories, Experimental Evidence, and Examples. *Chem. Rev.* **1986**, *86* (2), 401–449. https://doi.org/10.1021/cr00072a005.

(166) Kim, H.-B.; Kim, D.; Kim, J.-J. Exciplex: Its Nature and Application to OLEDs. In *Highly Efficient OLEDs*; Wiley-Blackwell, 2018; pp 331–376. https://doi.org/10.1002/9783527691722.ch10.

(167) Itano, K.; Ogawa, H.; Shirota, Y. Exciplex Formation at the Organic Solid-State Interface: Yellow Emission in Organic Light-Emitting Diodes Using Green-Fluorescent Tris(8-Quinolinolato)Aluminum and Hole-Transporting Molecular Materials with Low Ionization Potentials. *Appl. Phys. Lett.* **1998**, *72* (6), 636–638. https://doi.org/10.1063/1.120826.

(168) Goushi, K.; Yoshida, K.; Sato, K.; Adachi, C. Organic Light-Emitting Diodes Employing Efficient Reverse Intersystem Crossing for Triplet-to-Singlet State Conversion. *Nat. Photonics* **2012**, *6* (4), 253–258. https://doi.org/10.1038/nphoton.2012.31.

(169) Hung, W.-Y.; Fang, G.-C.; Lin, S.-W.; Cheng, S.-H.; Wong, K.-T.; Kuo, T.-Y.; Chou, P.-T. The First Tandem, All-Exciplex-Based WOLED. *Sci. Rep.* **2015**, *4* (1). https://doi.org/10.1038/srep05161.

(170) Nakanotani, H.; Higuchi, T.; Furukawa, T.; Masui, K.; Morimoto, K.; Numata, M.; Tanaka, H.; Sagara, Y.; Yasuda, T.; Adachi, C. High-Efficiency Organic Light-Emitting Diodes with Fluorescent Emitters. *Nat. Commun.* **2014**, *5*. https://doi.org/10.1038/ncomms5016.

(171) Yamanaka, T.; Nakanotani, H.; Hara, S.; Hirohata, T.; Adachi, C. Near-Infrared Organic Light-Emitting Diodes for Biosensing with High Operating Stability. *Appl. Phys. Express* **2017**, *10* (7), 074101. https://doi.org/10.7567/APEX.10.074101.

(172) Arjona-Esteban, A.; Volz, D. Status and Next Steps of TADF Technology: An Industrial Perspective. In *Highly Efficient OLEDs*; Wiley-Blackwell, 2018; pp 543–572. https://doi.org/10.1002/9783527691722.ch15.

(173) Zhang, D.; Duan, L.; Li, C.; Li, Y.; Li, H.; Zhang, D.; Qiu, Y. High-Efficiency Fluorescent Organic Light-Emitting Devices Using Sensitizing Hosts with a Small Singlet–Triplet Exchange Energy. *Adv. Mater.* **2014**, *26* (29), 5050–5055. https://doi.org/10.1002/adma.201401476.

(174) Li, Y.; Zhang, D.; Zhang, Y.; Cai, M.; Duan, L. Red Phosphorescent Organic Light-Emitting Diodes Based on a Novel Host Material with Thermally Activated Delayed Fluorescent Properties. *Sci. China Chem.* **2016**, *59* (6), 684–691. https://doi.org/10.1007/s11426-015-0506-2.

(175) Li, T.; Yang, D.; Zhai, L.; Wang, S.; Zhao, B.; Fu, N.; Wang, L.; Tao, Y.; Huang, W. Thermally Activated Delayed Fluorescence Organic Dots (TADF Odots) for Time-Resolved and Confocal Fluorescence Imaging in Living Cells and In Vivo. *Adv. Sci.* **2017**, *4* (4), 1600166. https://doi.org/10.1002/advs.201600166.

(176) Report: All iPhones will ditch LCDs for OLEDs by 2020 - Android Authority https://www.androidauthority.com/apple-iphone-oled-lcd-945408/ (accessed Feb 16, 2019).

(177) Ngo, A. Every OLED laptop announced at CES 2019 https://www.notebookcheck.net/Every-OLED-laptop-announced-at-CES-2019.395041.0.html (accessed Feb 16, 2019).

(178) Cynora extends its cooperation with LGD for deep-blue TADF emitters, samples green TADF emitters | OLED-Info https://www.oled-info.com/cynora-extends-its-cooperation-lgd-deep-blue-tadf-emitters-samples-green-tadf-emitters (accessed Feb 16, 2019).

(179) Okazaki, M.; Takeda, Y.; Data, P.; Pander, P.; Higginbotham, H.; Monkman, A. P.; Minakata, S. Thermally Activated Delayed Fluorescent Phenothiazine–Dibenzo[a,j]Phenazine–Phenothiazine Triads Exhibiting Tricolor-Changing Mechanochromic Luminescence. *Chem. Sci.* **2017**, *8* (4), 2677–2686. https://doi.org/10.1039/C6SC04863C.

(180) Pashazadeh, R.; Pander, P.; Lazauskas, A.; Dias, F. B.; Grazulevicius, J. V. Multicolor Luminescence Switching and Controllable Thermally Activated Delayed Fluorescence Turn on/Turn off in Carbazole–Quinoxaline–Carbazole Triads. *J. Phys. Chem. Lett.* **2018**, 1172–1177. https://doi.org/10.1021/acs.jpclett.8b00136.

(181) Cotts, B. L.; McCarthy, D. G.; Noriega, R.; Penwell, S. B.; Delor, M.; Devore, D. D.; Mukhopadhyay, S.; De Vries, T. S.; Ginsberg, N. S. Tuning Thermally Activated Delayed Fluorescence Emitter Photophysics through Solvation in the Solid State. *ACS Energy Lett.* **2017**, *2* (7), 1526–1533. https://doi.org/10.1021/acsenergylett.7b00268.

(182) Northey, T.; Stacey, J.; Penfold, T. J. The Role of Solid State Solvation on the Charge Transfer State of a Thermally Activated Delayed Fluorescence Emitter. *J. Mater. Chem. C* **2017**, *5* (42), 11001–11009. https://doi.org/10.1039/C7TC04099G.

(183) Guo, J.; Li, X.-L.; Nie, H.; Luo, W.; Gan, S.; Hu, S.; Hu, R.; Qin, A.; Zhao, Z.; Su, S.-J.; et al. Achieving High-Performance Nondoped OLEDs with Extremely Small Efficiency Roll-Off by Combining Aggregation-Induced Emission and Thermally Activated Delayed Fluorescence. *Adv. Funct. Mater.* **2017**, *27* (13), 1606458. https://doi.org/10.1002/adfm.201606458.

(184) Song, L.; Hu, Y.; Liu, Z.; Lv, Y.; Guo, X.; Liu, X. Harvesting Triplet Excitons with Exciplex Thermally Activated Delayed Fluorescence Emitters toward High Performance Heterostructured Organic Light-Emitting Field Effect Transistors. *ACS Appl. Mater. Interfaces* **2017**, *9* (3), 2711–2719. https://doi.org/10.1021/acsami.6b13405.

(185) Liu, J.; Zhang, H.; Dong, H.; Meng, L.; Jiang, L.; Jiang, L.; Wang, Y.; Yu, J.; Sun, Y.; Hu, W.; et al. High Mobility Emissive Organic Semiconductor. *Nat. Commun.* **2015**, *6*, 10032. https://doi.org/10.1038/ncomms10032.

(186) Helicene. *Wikipedia*; 2018.

(187) Kuroda, R. Crystal and Molecular Structure of [5]Helicene: Crystal Packing Modes. *J. Chem. Soc. Perkin Trans. 2* **1982**, *0* (7), 789–794. https://doi.org/10.1039/P29820000789.

(188) Schulman, J. M.; Disch, R. L. Aromatic Character of [n]Helicenes and [n]Phenacenes. *J. Phys. Chem. A* **1999**, *103* (33), 6669–6672. https://doi.org/10.1021/jp9910587.

(189) Martin, R. H.; Marchant, M. J. Resolution and Optical Properties ([α]Max, Ord and Cd) of Hepta-, Octa- and Nonahelicene. *Tetrahedron* **1974**, *30* (2), 343–345. https://doi.org/10.1016/S0040-4020(01)91468-1.

(190) Katz, T. J.; Liu, L.; Willmore, N. D.; Fox, J. M.; Rheingold, A. L.; Shi, S.; Nuckolls, C.; Rickman, B. H. An Efficient Synthesis of Functionalized Helicenes. *J. Am. Chem. Soc.* **1997**, *119* (42), 10054–10063. https://doi.org/10.1021/ja9721327.

(191) Kawasaki, T.; Suzuki, K.; Licandro, E.; Bossi, A.; Maiorana, S.; Soai, K. Enantioselective Synthesis Induced by Tetrathia-[7]-Helicenes in Conjunction with Asymmetric Autocatalysis. *Tetrahedron Asymmetry* **2006**, *17* (14), 2050–2053. https://doi.org/10.1016/j.tetasy.2006.07.015.

(192) Yavari, K.; Aillard, P.; Zhang, Y.; Nuter, F.; Retailleau, P.; Voituriez, A.; Marinetti, A. Helicenes with Embedded Phosphole Units in Enantioselective Gold Catalysis. *Angew. Chem. Int. Ed.* **2014**, *53* (3), 861–865. https://doi.org/10.1002/anie.201308377.

(193) Weix, D. J.; Dreher, S. D.; Katz, T. J. [5]HELOL Phosphite: A Helically Grooved Sensor of Remote Chirality. *J. Am. Chem. Soc.* **2000**, *122* (41), 10027–10032. https://doi.org/10.1021/ja001904n.

(194) Wang, D. Z.; Katz, T. J. A [5]HELOL Analogue That Senses Remote Chirality in Alcohols, Phenols, Amines, and Carboxylic Acids. *J. Org. Chem.* **2005**, *70* (21), 8497–8502. https://doi.org/10.1021/jo0512913.

(195) Reetz, M. T.; Sostmann, S. 2,15-Dihydroxy-Hexahelicene (HELIXOL): Synthesis and Use as an Enantioselective Fluorescent Sensor. *Tetrahedron* **2001**, *57* (13), 2515–2520. https://doi.org/10.1016/S0040-4020(01)00077-1.

(196) Verbiest, T.; Elshocht, S. V.; Kauranen, M.; Hellemans, L.; Snauwaert, J.; Nuckolls, C.; Katz, T. J.; Persoons, A. Strong Enhancement of Nonlinear Optical Properties Through Supramolecular Chirality. *Science* **1998**, *282* (5390), 913–915. https://doi.org/10.1126/science.282.5390.913.

(197) Coe, B. J.; Rusanova, D.; Joshi, V. D.; Sánchez, S.; Vávra, J.; Khobragade, D.; Severa, L.; Císařová, I.; Šaman, D.; Pohl, R.; et al. Helquat Dyes: Helicene-like Push–Pull Systems with Large Second-Order Nonlinear Optical Responses. *J. Org. Chem.* **2016**, *81* (5), 1912–1920. https://doi.org/10.1021/acs.joc.5b02692.

(198) Field, J. E.; Muller, G.; Riehl, J. P.; Venkataraman, D. Circularly Polarized Luminescence from Bridged Triarylamine Helicenes. *J. Am. Chem. Soc.* **2003**, *125* (39), 11808–11809. https://doi.org/10.1021/ja035626e.

(199) Nakamura, K.; Furumi, S.; Takeuchi, M.; Shibuya, T.; Tanaka, K. Enantioselective Synthesis and Enhanced Circularly Polarized Luminescence of S-Shaped Double Azahelicenes. *J. Am. Chem. Soc.* **2014**, *136* (15), 5555–5558. https://doi.org/10.1021/ja500841f.

(200) Birks, J. B.; Birch, D. J. S.; Cordemans, E.; Vander Donckt, E. Fluorescence of the Higher Helicenes. *Chem. Phys. Lett.* **1976**, *43* (1), 33–36. https://doi.org/10.1016/0009-2614(76)80750-6.

(201) Sahasithiwat, S.; Mophuang, T.; Menbangpung, L.; Kamtonwong, S.; Sooksimuang, T. 3,12-Dimethoxy-7,8-Dicyano-[5]Helicene as a Novel Emissive Material for Organic Light-Emitting Diode. *Synth. Met.* **2010**, *160* (11–12), 1148–1152. https://doi.org/10.1016/j.synthmet.2010.02.039.

(202) Kubo, H.; Hirose, T.; Matsuda, K. Control over the Emission Properties of [5]Helicenes Based on the Symmetry and Energy Levels of Their Molecular Orbitals. *Org. Lett.* **2017**, *19* (7), 1776–1779. https://doi.org/10.1021/acs.orglett.7b00548.

(203) Hua, W.; Liu, Z.; Duan, L.; Dong, G.; Qiu, Y.; Zhang, B.; Cui, D.; Tao, X.; Cheng, N.; Liu, Y. Deep-Blue Electroluminescence from Nondoped and Doped Organic Light-Emitting Diodes (OLEDs) Based on a New Monoaza[6]Helicene. *RSC Adv.* **2015**, *5* (1), 75–84. https://doi.org/10.1039/C4RA13486A.

(204) Chen, T.; Zhang, B.; Liu, Z.; Duan, L.; Dong, G.; Feng, Y.; Luo, X.; Cui, D. Synthesis and Properties of a Thiophene-Substituted Diaza[7]Helicene for Application as a Blue Emitter in Organic Light-Emitting Diodes. *Tetrahedron Lett.* **2017**, *58* (6), 531–535. https://doi.org/10.1016/j.tetlet.2016.12.069.

(205) Sahasithiwat, S.; Sooksimuang, T.; Kangkaew, L.; Panchan, W. 3,12-Dimethoxy-5,6,9,10-Tetrahydro-7,8-Dicyano-[5]Helicene as a New Emitter for Blue and White Organic Light-Emitting Diodes. *Dyes Pigments* **2017**, *136*, 754–760. https://doi.org/10.1016/j.dyepig.2016.09.042.

(206) Schmidt, K.; Brovelli, S.; Coropceanu, V.; Brédas, J.-L.; Bazzini, C.; Caronna, T.; Tubino, R.; Meinardi, F. Excited-State Properties and Emission Spectra of Nonplanar Heterocyclic Helicenes. *J. Phys. Chem. A* **2006**, *110* (38), 11018–11024. https://doi.org/10.1021/jp0616258.

(207) Schmidt, K.; Brovelli, S.; Coropceanu, V.; Beljonne, D.; Cornil, J.; Bazzini, C.; Caronna, T.; Tubino, R.; Meinardi, F.; Shuai, Z.; et al. Intersystem Crossing Processes in Nonplanar Aromatic Heterocyclic Molecules. *J. Phys. Chem. A* **2007**, *111* (42), 10490–10499. https://doi.org/10.1021/jp075248q.

(208) Yang, Y.; Rice, B.; Shi, X.; Brandt, J. R.; Correa da Costa, R.; Hedley, G. J.; Smilgies, D.-M.; Frost, J. M.; Samuel, Ifor. D. W.; Otero-de-la-Roza, A.; et al. Emergent Properties of an Organic Semiconductor Driven by Its Molecular Chirality. *ACS Nano* **2017**, *11* (8), 8329–8338. https://doi.org/10.1021/acsnano.7b03540.

(209) Borowicz, P.; Herbich, J.; Kapturkiewicz, A.; Opallo, M.; Nowacki, J. Radiative and Nonradiative Electron Transfer in Donor–Acceptor Phenoxazine and Phenothiazine Derivatives. *Chem. Phys.* **1999**, *249* (1), 49–62. https://doi.org/10.1016/S0301-0104(99)00265-7.

(210) Waghray, D.; Zhang, J.; Jacobs, J.; Nulens, W.; Basarić, N.; Meervelt, L. V.; Dehaen, W. Synthesis and Structural Elucidation of Diversely Functionalized 5,10-Diaza[5]Helicenes. *J. Org. Chem.* **2012**, *77* (22), 10176–10183. https://doi.org/10.1021/jo301814m.

(211) Dias, F. B.; Bourdakos, K. N.; Jankus, V.; Moss, K. C.; Kamtekar, K. T.; Bhalla, V.; Santos, J.; Bryce, M. R.; Monkman, A. P. Triplet Harvesting with 100% Efficiency by Way of Thermally Activated Delayed Fluorescence in Charge Transfer OLED Emitters. *Adv. Mater.* **2013**, *25* (27), 3707–3714. https://doi.org/10.1002/adma.201300753.

(212) Pander, P.; Dias, F. Photophysical Characterisation of Thermally Activated Delayed Fluorescence (TADF) Materials. *Disp. Imaging* **2016**, *2*, 249–263.

(213) Dias, F. B. Kinetics of Thermal-Assisted Delayed Fluorescence in Blue Organic Emitters with Large Singlet–Triplet Energy Gap. *Philos. Trans. R. Soc. Lond. Math. Phys. Eng. Sci.* **2015**, *373* (2044), 20140447. https://doi.org/10.1098/rsta.2014.0447.

(214) Mei Ju; Hong Yuning; Lam Jacky W. Y.; Qin Anjun; Tang Youhong; Tang Ben Zhong. Aggregation-Induced Emission: The Whole Is More Brilliant than the Parts. *Adv. Mater.* **2014**, *26* (31), 5429–5479. https://doi.org/10.1002/adma.201401356.

(215) Dias, F. B.; Santos, J.; Graves, D. R.; Data, P.; Nobuyasu, R. S.; Fox, M. A.; Batsanov, A. S.; Palmeira, T.; Berberan-Santos, M. N.; Bryce, M. R.; et al. The Role of Local Triplet Excited States and D-A Relative Orientation in Thermally Activated Delayed Fluorescence: Photophysics and Devices. *Adv. Sci.* **2016**, *3* (12), 1600080. https://doi.org/10.1002/advs.201600080.

(216) Peach, M. J. G.; Benfield, P.; Helgaker, T.; Tozer, D. J. Excitation Energies in Density Functional Theory: An Evaluation and a Diagnostic Test. *J. Chem. Phys.* **2008**, *128* (4), 044118. https://doi.org/10.1063/1.2831900.

(217) Yanai, T.; Tew, D. P.; Handy, N. C. A New Hybrid Exchange–Correlation Functional Using the Coulomb-Attenuating Method (CAM-B3LYP). *Chem. Phys. Lett.* **2004**, *393* (1), 51–57. https://doi.org/10.1016/j.cplett.2004.06.011.

(218) Yang, Y.; da Costa, R. C.; Smilgies, D.-M.; Campbell, A. J.; Fuchter, M. J. Induction of Circularly Polarized Electroluminescence from an Achiral Light-Emitting Polymer via a Chiral Small-Molecule Dopant. *Adv. Mater.* **2013**, *25* (18), 2624–2628. https://doi.org/10.1002/adma.201204961.

(219) Fallon, K. J.; Wijeyasinghe, N.; Manley, E. F.; Dimitrov, S. D.; Yousaf, S. A.; Ashraf, R. S.; Duffy, W.; Guilbert, A. A. Y.; Freeman, D. M. E.; Al-Hashimi, M.; et al. Indolo-Naphthyridine-6,13-Dione Thiophene Building Block for Conjugated Polymer Electronics: Molecular Origin of Ultrahigh n-Type Mobility. *Chem. Mater.* **2016**, *28* (22), 8366–8378. https://doi.org/10.1021/acs.chemmater.6b03671.

(220) Wu, C. C.; Sturm, J. C.; Register, R. A.; Thompson, M. E. Integrated Three-color Organic Light-emitting Devices. *Appl. Phys. Lett.* **1996**, *69* (21), 3117–3119. https://doi.org/10.1063/1.116800.

(221) Søndergaard, R.; Hösel, M.; Angmo, D.; Larsen-Olsen, T. T.; Krebs, F. C. Roll-to-Roll Fabrication of Polymer Solar Cells. *Mater. Today* **2012**, *15* (1), 36–49. https://doi.org/10.1016/S1369-7021(12)70019-6.

(222) Joswick, M. D.; Campbell, I. H.; Barashkov, N. N.; Ferraris, J. P. Systematic Investigation of the Effects of Organic Film Structure on Light Emitting Diode Performance. *J. Appl. Phys.* **1996**, *80* (5), 2883–2890. https://doi.org/10.1063/1.363140.

(223) Roncali, J.; Leriche, P.; Cravino, A. From One- to Three-Dimensional Organic Semiconductors: In Search of the Organic Silicon? *Adv. Mater.* **2007**, *19* (16), 2045–2060. https://doi.org/10.1002/adma.200700135.

(224) Brunel, J.; Mongin, O.; Jutand, A.; Ledoux, I.; Zyss, J.; Blanchard-Desce, M. Propeller-Shaped Octupolar Molecules Derived from Triphenylbenzene for Nonlinear Optics: Synthesis and Optical Studies. *Chem. Mater.* **2003**, *15* (21), 4139–4148. https://doi.org/10.1021/cm030392j.

(225) Shirota, Y. Organic Materials for Electronic and Optoelectronic Devices. *J. Mater. Chem.* **2000**, *10* (1), 1–25. https://doi.org/10.1039/A908130E.

(226) Wang, S.; Oldham, W. J.; Hudack, R. A.; Bazan, G. C. Synthesis, Morphology, and Optical Properties of Tetrahedral Oligo(Phenylenevinylene) Materials. *J. Am. Chem. Soc.* **2000**, *122* (24), 5695–5709. https://doi.org/10.1021/ja992924w.

(227) Liu, F.; Lai, W.-Y.; Tang, C.; Wu, H.-B.; Chen, Q.-Q.; Peng, B.; Wei, W.; Huang, W.; Cao, Y. Synthesis and Characterization of Pyrene-Centered Starburst Oligofluorenes. *Macromol. Rapid Commun.* **2008**, *29* (8), 659–664. https://doi.org/10.1002/marc.200700847.

(228) Cao, X.-Y.; Zi, H.; Zhang, W.; Lu, H.; Pei, J. Star-Shaped and Linear Nanosized Molecules Functionalized with Hexa-Peri-Hexabenzocoronene: Synthesis and Optical Properties. *J. Org. Chem.* **2005**, *70* (9), 3645–3653. https://doi.org/10.1021/jo0480139.

(229) Jiang, Y.; Lu, Y.-X.; Cui, Y.-X.; Zhou, Q.-F.; Ma, Y.; Pei, J. Synthesis of Giant Rigid π-Conjugated Dendrimers. *Org. Lett.* **2007**, *9* (22), 4539–4542. https://doi.org/10.1021/ol702063e.

(230) Pei, J.; Wang, J.-L.; Cao, X.-Y.; Zhou, X.-H.; Zhang, W.-B. Star-Shaped Polycyclic Aromatics Based on Oligothiophene-Functionalized Truxene: Synthesis, Properties, and Facile Emissive Wavelength Tuning. *J. Am. Chem. Soc.* **2003**, *125* (33), 9944–9945. https://doi.org/10.1021/ja0361650.

(231) Sun, Y. M.; Xiao, K.; Liu, Y. Q.; Wang, J. L.; Pei, J.; Yu, G.; Zhu, D. B. Oligothiophene-Functionalized Truxene: Star-Shaped Compounds for Organic Field-Effect Transistors. *Adv. Funct. Mater.* **2005**, *15* (5), 818–822. https://doi.org/10.1002/adfm.200400380.

(232) Wang, J.-L.; Duan, X.-F.; Jiang, B.; Gan, L.-B.; Pei, J.; He, C.; Li, Y.-F. Nanosized Rigid π-Conjugated Molecular Heterojunctions with Multi[60]Fullerenes: Facile Synthesis and Photophysical Properties. *J. Org. Chem.* **2006**, *71* (12), 4400–4410. https://doi.org/10.1021/jo060097t.

(233) Tang, Z.-M.; Lei, T.; Wang, J.-L.; Ma, Y.; Pei, J. Star-Shaped Donor-π-Acceptor Conjugated Molecules: Synthesis, Properties, and Modification of Their Absorptions Features. *J. Org. Chem.* **2010**, *75* (11), 3644–3655. https://doi.org/10.1021/jo100388c.

(234) Wu, W.; Zhang, G.; Xu, X.; Wang, S.; Li, Y.; Peng, Q. Wide Bandgap Molecular Acceptors with a Truxene Core for Efficient Nonfullerene Polymer Solar Cells: Linkage Position on Molecular Configuration and Photovoltaic Properties. *Adv. Funct. Mater.* **2018**, *28* (18), 1707493. https://doi.org/10.1002/adfm.201707493.

(235) Sharma, R.; Volyniuk, D.; Popli, C.; Bezvikonnyi, O.; Grazulevicius, J. V.; Misra, R. Strategy Toward Tuning Emission of Star-Shaped Tetraphenylethene-Substituted Truxenes for Sky-Blue and Greenish-White Organic Light-Emitting Diodes. *J. Phys. Chem. C* **2018**, *122* (27), 15614–15624. https://doi.org/10.1021/acs.jpcc.8b00777.

(236) Kanibolotsky, A. L.; Berridge, R.; Skabara, P. J.; Perepichka, I. F.; Bradley, D. D. C.; Koeberg, M. Synthesis and Properties of Monodisperse Oligofluorene-Functionalized Truxenes: Highly Fluorescent Star-Shaped Architectures. *J. Am. Chem. Soc.* **2004**, *126* (42), 13695–13702. https://doi.org/10.1021/ja039228n.

(237) Guzelturk, B.; Kanibolotsky, A. L.; Orofino-Pena, C.; Laurand, N.; Dawson, M. D.; Skabara, P. J.; Demir, H. V. Ultralow-Threshold up-Converted Lasing in Oligofluorenes with Tailored Strong Nonlinear Absorption. *J Mater Chem C* **2015**, *3* (46), 12018–12025. https://doi.org/10.1039/C5TC02247A.

(238) Belton, C. R.; Kanibolotsky, A. L.; Kirkpatrick, J.; Orofino, C.; Elmasly, S. E.; Stavrinou, P. N.; Skabara, P. J.; Bradley, D. D. Location, Location, Location-Strategic Positioning of 2, 1, 3-Benzothiadiazole Units within Trigonal Quaterfluorene-Truxene Star-Shaped Structures. *Adv. Funct. Mater.* **2013**, *23* (22), 2792–2804.

(239) Neto, B. A. D.; Lapis, A. A. M.; da Silva Júnior, E. N.; Dupont, J. 2,1,3-Benzothiadiazole and Derivatives: Synthesis, Properties, Reactions, and Applications in Light Technology of Small Molecules. *Eur. J. Org. Chem.* **2013**, *2013* (2), 228–255. https://doi.org/10.1002/ejoc.201201161.

(240) Dennany, L.; Mohsan, Z.; Kanibolotsky, A. L.; Skabara, P. J. Novel Electrochemiluminescent Materials for Sensor Applications. *Faraday Discuss* **2014**, *174*, 357–367. https://doi.org/10.1039/C4FD00090K.

(241) Mohsan, Z.; Kanibolotsky, A. L.; Stewart, A. J.; Inigo, A. R.; Dennany, L.; Skabara, P. J. Highly Efficient Electrogenerated Chemiluminescence of an Oligofluorene-Truxene Star-Shaped

Compound Incorporating 2,1,3-Benzothiadiazole Units. *J Mater Chem C* **2015**, *3* (6), 1166–1171. https://doi.org/10.1039/C4TC02638A.

(242) Lai, W.-Y.; Xia, R.; He, Q.-Y.; Levermore, P. A.; Huang, W.; Bradley, D. D. C. Enhanced Solid-State Luminescence and Low-Threshold Lasing from Starburst Macromolecular Materials. *Adv. Mater.* **2009**, *21* (3), 355–360. https://doi.org/10.1002/adma.200800748.

(243) Zhang, H.; Liu, X.; Lu, T.-T.; Lv, P.; Lai, W.-Y. Monodisperse Six-Armed Starbursts Based on Truxene-Cored Multibranched Oligofluorenes: Design, Synthesis, and Stabilized Lasing Characteristics. *Chem. – Eur. J.* **2019**. https://doi.org/10.1002/chem.201805813.

(244) Wang, J.-L.; Tang, Z.-M.; Xiao, Q.; Ma, Y.; Pei, J. Energy Transfer in New D-π-A Conjugated Dendrimers: Their Synthesis and Photophysical Properties. *Org. Lett.* **2008**, *10* (19), 4271–4274. https://doi.org/10.1021/ol801671w.

(245) Shi, K.; Wang, J.-Y.; Pei, J. π-Conjugated Aromatics Based on Truxene: Synthesis, Self-Assembly, and Applications. *Chem. Rec.* **2015**, *15* (1), 52–72. https://doi.org/10.1002/tcr.201402071.

(246) Wang, J.-L.; Zhou, Y.; Li, Y.; Pei, J. Solution-Processable Gradient Red-Emitting π-Conjugated Dendrimers Based on Benzothiadiazole as Core: Synthesis, Characterization, and Device Performances. *J. Org. Chem.* **2009**, *74* (19), 7449–7456. https://doi.org/10.1021/jo901539a.

(247) Muthu, S.; Schuurmans, F. J. P.; Pashley, M. D. Red, Green, and Blue LEDs for White Light Illumination. *IEEE J. Sel. Top. Quantum Electron.* **2002**, *8* (2), 333–338. https://doi.org/10.1109/2944.999188.

(248) Sheu, J. K.; Chang, S. J.; Kuo, C. H.; Su, Y. K.; Wu, L. W.; Lin, Y. C.; Lai, W. C.; Tsai, J. M.; Chi, G. C.; Wu, R. K. White-Light Emission from near UV InGaN-GaN LED Chip Precoated with Blue/Green/Red Phosphors. *IEEE Photonics Technol. Lett.* **2003**, *15* (1), 18–20. https://doi.org/10.1109/LPT.2002.805852.

(249) Bando, K.; Sakano, K.; Noguchi, Y.; Shimizu, Y. Development of High-Bright and Pure-White LED Lamps. *J. Light Vis. Environ.* **1998**, *22* (1), 12–15. https://doi.org/10.2150/jlve.22.1_2.

(250) Smet, P. F.; Parmentier, A. B.; Poelman, D. Selecting Conversion Phosphors for White Light-Emitting Diodes. *J. Electrochem. Soc.* **2011**, *158* (6), R37–R54. https://doi.org/10.1149/1.3568524.

(251) Heliotis, G.; Gu, E.; Griffin, C.; Jeon, C. W.; Stavrinou, P. N.; Dawson, M. D.; Bradley, D. D. C. Wavelength-Tunable and White-Light Emission from Polymer-Converted Micropixellated InGaN Ultraviolet Light-Emitting Diodes. *J. Opt. Pure Appl. Opt.* **2006**, *8* (7), S445–S449. https://doi.org/10.1088/1464-4258/8/7/S20.

(252) Chun, H.; Manousiadis, P.; Rajbhandari, S.; Vithanage, D. A.; Faulkner, G.; Tsonev, D.; McKendry, J. J. D.; Videv, S.; Xie, E.; Gu, E.; et al. Visible Light Communication Using a Blue GaN Micro-LED and Fluorescent Polymer Color Converter. *IEEE Photonics Technol. Lett.* **2014**, *26* (20), 2035–2038. https://doi.org/10.1109/LPT.2014.2345256.

(253) Hide, F.; Kozodoy, P.; DenBaars, S. P.; Heeger, A. J. White Light from InGaN/Conjugated Polymer Hybrid Light-Emitting Diodes. *Appl. Phys. Lett.* **1997**, *70* (20), 2664–2666. https://doi.org/10.1063/1.118989.

(254) Findlay, N. J.; Bruckbauer, J.; Inigo, A. R.; Breig, B.; Arumugam, S.; Wallis, D. J.; Martin, R. W.; Skabara, P. J. An Organic Down-Converting Material for White-Light Emission from Hybrid LEDs. *Adv. Mater.* **2014**, *26* (43), 7290–7294. https://doi.org/10.1002/adma.201402661.

(255) Bruckbauer, J.; Brasser, C.; Findlay, N. J.; Edwards, P. R.; Wallis, D. J.; Skabara, P. J.; Martin, R. W. Colour Tuning in White Hybrid Inorganic/Organic Light-Emitting Diodes. *J. Phys. Appl. Phys.* **2016**, *49* (40), 405103. https://doi.org/10.1088/0022-3727/49/40/405103.

(256) Taylor-Shaw, E.; Angioni, E.; Findlay, N. J.; Breig, B.; Inigo, A. R.; Bruckbauer, J.; Wallis, D. J.; Skabara, P. J.; Martin, R. W. Cool to Warm White Light Emission from Hybrid Inorganic/Organic Light-Emitting Diodes. *J. Mater. Chem. C* **2016**, *4* (48), 11499–11507. https://doi.org/10.1039/C6TC03585J.

(257) Sivakamasundari, S.; Ganesan, R. Kinetics and Mechanism of the Bromination of Aromatic Compounds by N-Bromosuccinimide in Solution. *Int. J. Chem. Kinet.* **1980**, *12* (11), 837–850. https://doi.org/10.1002/kin.550121103.

(258) Sworakowski, J. How Accurate Are Energies of HOMO and LUMO Levels in Small-Molecule Organic Semiconductors Determined from Cyclic Voltammetry or Optical Spectroscopy? *Synth. Met.* **2018**, *235*, 125–130. https://doi.org/10.1016/j.synthmet.2017.11.013.

(259) Bredas, J.-L. Mind the Gap! *Mater. Horiz.* **2013**, *1* (1), 17–19. https://doi.org/10.1039/C3MH00098B.

(260) Knupfer, M. Exciton Binding Energies in Organic Semiconductors. *Appl. Phys. A* **2003**, *77* (5), 623–626. https://doi.org/10.1007/s00339-003-2182-9.

(261) Okamoto, S.; Tanaka, K.; Izumi, Y.; Adachi, H.; Yamaji, T.; Suzuki, T. Simple Measurement of Quantum Efficiency in Organic Electroluminescent Devices. *Jpn. J. Appl. Phys.* **2001**, *40* (7B), L783. https://doi.org/10.1143/JJAP.40.L783.

(262) Norrman, K.; Ghanbari-Siahkali, A.; Larsen, N. B. 6 Studies of Spin-Coated Polymer Films. *Annu. Rep. Sect. C Phys. Chem.* **2005**, *101* (0), 174–201. https://doi.org/10.1039/B408857N.

(263) Rezvani, M. H.; Farajollahi, F.; Nikfarjam, A.; Bakhtiarpour, P.; Saydanzad, E. Effect of Solvents, Their Mixture and Thermal Annealing on the Performance of Solution Processed Polymer Light-Emitting Diodes. *Materials* **2013**, *6* (5), 1994–2006. https://doi.org/10.3390/ma6051994.

(264) Matsuoka, K.; Albrecht, K.; Yamamoto, K.; Fujita, K. Mulifunctional Dendritic Emitter: Aggregation-Induced Emission Enhanced, Thermally Activated Delayed Fluorescent Material for Solution-Processed Multilayered Organic Light-Emitting Diodes. *Sci. Rep.* **2017**, *7*. https://doi.org/10.1038/srep41780.

(265) Bera, D.; Qian, L.; Tseng, T.-K.; Holloway, P. H. Quantum Dots and Their Multimodal Applications: A Review. *Materials* **2010**, *3* (4), 2260–2345. https://doi.org/10.3390/ma3042260.

(266) dos Santos, P. L.; Ward, J. S.; Congrave, D. G.; Batsanov, A. S.; Eng, J.; Stacey, J. E.; Penfold, T. J.; Monkman, A. P.; Bryce, M. R. Triazatruxene: A Rigid Central Donor Unit for a D–A3 Thermally Activated Delayed Fluorescence Material Exhibiting Sub-Microsecond Reverse Intersystem Crossing and Unity Quantum Yield via Multiple Singlet–Triplet State Pairs. *Adv. Sci.* **2018**, *5* (6). https://doi.org/10.1002/advs.201700989.

(267) Wang, F.; Li, X.-C.; Lai, W.-Y.; Chen, Y.; Huang, W.; Wudl, F. Synthesis and Characterization of Symmetric Cyclooctatetraindoles: Exploring the Potential as Electron-Rich Skeletons with Extended π-Systems. *Org. Lett.* **2014**, *16* (11), 2942–2945. https://doi.org/10.1021/ol501083d.

(268) White, N. J. The Treatment of Malaria. *N. Engl. J. Med.* **1996**, *335* (11), 800–806. https://doi.org/10.1056/NEJM199609123351107.

(269) Herschel, J. F. W. IV. ʼΑμόρφωϒa, No. I.— on a Case of Superficial Colour Presented by a Homogeneous Liquid Internally Colourless. *Philos. Trans. R. Soc. Lond.* **1845**, *135*, 143–145. https://doi.org/10.1098/rstl.1845.0004.

(270) Stokes, G. *On the Change of Refrangibility of Light*; Royal Society of London, 1852.

(271) Fletcher, A. N. Quinine Sulfate as a Fluorescence Quantum Yield Standard. *Photochem. Photobiol.* **1969**, *9* (5), 439–444. https://doi.org/10.1111/j.1751-1097.1969.tb07311.x.

(272) Melhuish, W. H. A Standard Fluorescence Spectrum for Calibrating Spectrofluorophotometers. *J. Phys. Chem.* **1960**, *64* (6), 762–764. https://doi.org/10.1021/j100835a014.

(273) Bhattacharjee, I.; Acharya, N.; Ray, D. Thermally Activated Delayed Fluorescence and Room-Temperature Phosphorescence in Naphthyl Appended Carbazole–Quinoline Conjugates, and Their Mechanical Regulation. *Chem. Commun.* **2019**, *55* (13), 1899–1902. https://doi.org/10.1039/C8CC09220F.

(274) Hancock, J. M.; Jenekhe, S. A. Unusual Protonation-Induced Continuous Tunability of Optical Properties and Electroluminescence of a π-Conjugated Heterocyclic Oligomer. *Macromolecules* **2008**, *41* (19), 6864–6867. https://doi.org/10.1021/ma8016037.

(275) Kim, S.-I.; Kang, B. J.; Jeong, C.-U.; Shin, M.-H.; Kim, W. T.; Jazbinsek, M.; Yoon, W.; Yun, H.; Kim, D.; Rotermund, F.; et al. Fluorinated Organic Electro-Optic Quinolinium Crystals for THz Wave Generation. *Adv. Opt. Mater.* **2019**, *7* (4), 1801495. https://doi.org/10.1002/adom.201801495.

(276) Tanabe, K.; Kodama, D.; Hasegawa, M.; Kato, T. Aggregation-Induced Emission of a Liquid-Crystalline Quinolinium Salt Molecule in Aqueous Solution. *Chem. Lett.* **2013**, *43* (2), 184–186. https://doi.org/10.1246/cl.130893.

(277) Yuan, C.-X.; Tao, X.-T.; Ren, Y.; Li, Y.; Yang, J.-X.; Yu, W.-T.; Wang, L.; Jiang, M.-H. Synthesis, Structure, and Aggregation-Induced Emission of a Novel Lambda (Λ)-Shaped Pyridinium Salt Based on Tröger's Base. *J. Phys. Chem. C* **2007**, *111* (34), 12811–12816. https://doi.org/10.1021/jp0711601.

(278) Zhao, N.; Li, P.; Zhuang, J.; Liu, Y.; Xiao, Y.; Qin, R.; Li, N. Aggregation-Induced Emission Luminogens with the Capability of Wide Color Tuning, Mitochondrial and Bacterial Imaging, and Photodynamic Anticancer and Antibacterial Therapy. *ACS Appl. Mater. Interfaces* **2019**. https://doi.org/10.1021/acsami.9b01655.

(279) Xu, S.; Liu, T.; Mu, Y.; Wang, Y.-F.; Chi, Z.; Lo, C.-C.; Liu, S.; Zhang, Y.; Lien, A.; Xu, J. An Organic Molecule with Asymmetric Structure Exhibiting Aggregation-Induced Emission, Delayed Fluorescence, and Mechanoluminescence. *Angew. Chem. Int. Ed.* **2015**, *54* (3), 874–878. https://doi.org/10.1002/anie.201409767.

(280) Wu, C.-K.; Yang, D.-Y. Visible-Light-Mediated Reaction: Synthesis of Quinazolinones from 1,2-Dihydroquinazoline 3-Oxides. *RSC Adv.* **2016**, *6* (70), 65988–65994. https://doi.org/10.1039/C6RA13972H.

(281) Kim, D. J.; Oh, K. H.; Park, J. K. A General and Direct Synthesis of Imidazolium Ionic Liquids Using Orthoesters. *Green Chem.* **2014**, *16* (9), 4098–4101. https://doi.org/10.1039/C4GC00684D.

(282) Serevičius, T.; Komskis, R.; Adomėnas, P.; Adomėnienė, O.; Kreiza, G.; Jankauskas, V.; Kazlauskas, K.; Miasojedovas, A.; Jankus, V.; Monkman, A.; et al. Triplet–Triplet Annihilation in 9,10-Diphenylanthracene Derivatives: The Role of Intersystem Crossing and Exciton Diffusion. *J. Phys. Chem. C* **2017**, *121* (15), 8515–8524. https://doi.org/10.1021/acs.jpcc.7b01336.

(283) Suzuki, K.; Kobayashi, A.; Kaneko, S.; Takehira, K.; Yoshihara, T.; Ishida, H.; Shiina, Y.; Oishi, S.; Tobita, S. Reevaluation of Absolute Luminescence Quantum Yields of Standard Solutions Using a Spectrometer with an Integrating Sphere and a Back-Thinned CCD Detector. *Phys. Chem. Chem. Phys.* **2009**, *11* (42), 9850–9860. https://doi.org/10.1039/B912178A.

(284) de Mello, J. C.; Wittmann, H. F.; Friend, R. H. An Improved Experimental Determination of External Photoluminescence Quantum Efficiency. *Adv. Mater.* **1997**, *9* (3), 230–232. https://doi.org/10.1002/adma.19970090308.

(285) Wu, C. C.; Wu, C. I.; Sturm, J. C.; Kahn, A. Surface Modification of Indium Tin Oxide by Plasma Treatment: An Effective Method to Improve the Efficiency, Brightness, and Reliability of Organic Light Emitting Devices. *Appl. Phys. Lett.* **1997**, *70* (11), 1348–1350. https://doi.org/10.1063/1.118575.

(286) Harrowven, D. C.; Guy, I. L.; Nanson, L. Efficient Phenanthrene, Helicene, and Azahelicene Syntheses. *Angew. Chem. Int. Ed.* **2006**, *45* (14), 2242–2245. https://doi.org/10.1002/anie.200504287.

(287) Dehmlow, E. V.; Kelle, T. Synthesis of New Truxene Derivatives: Possible Precursors of Fullerene Partial Structures? *Synth. Commun.* **1997**, *27* (11), 2021–2031. https://doi.org/10.1080/00397919708006804.

(288) Jiang, Y.; Wang, L.; Zhou, Y.; Cui, Y.-X.; Wang, J.; Cao, Y.; Pei, J. π-Conjugated Dendrimers as Stable Pure-Blue Emissive Materials: Photophysical, Electrochemical, and Electroluminescent Properties. *Chem. – Asian J.* **2009**, *4* (4), 548–553. https://doi.org/10.1002/asia.200800329.

List of molecular structures

2.1

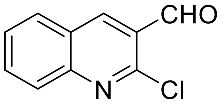

2.10

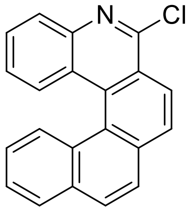

2.2

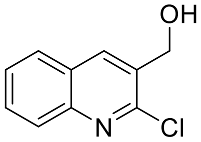

2.3

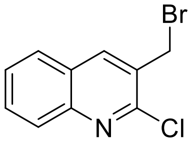

2.4

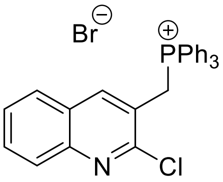

2.5

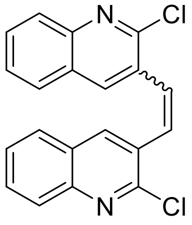

2.6

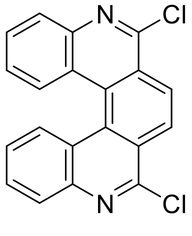

2.7

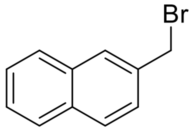

2.8

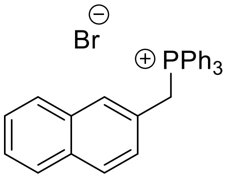

2.9

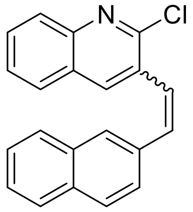

3.1

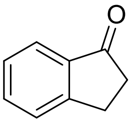

3.10

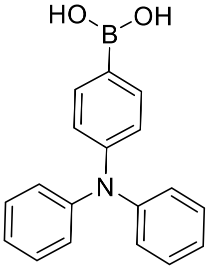

3.2

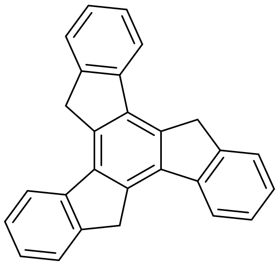

3.3

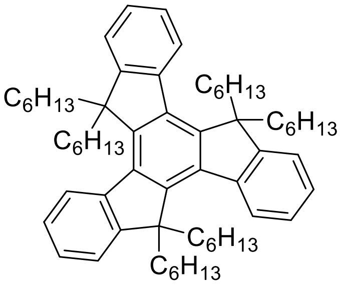

3.4

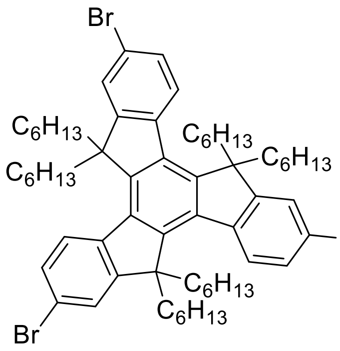

3.5

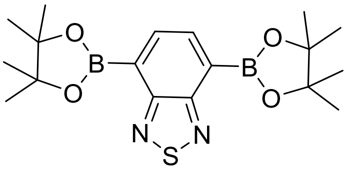

3.7

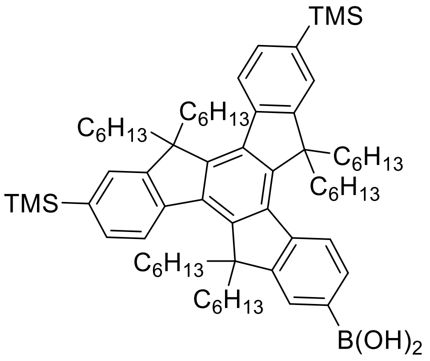

3.8

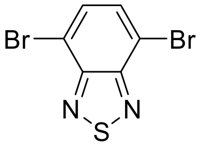

3.9

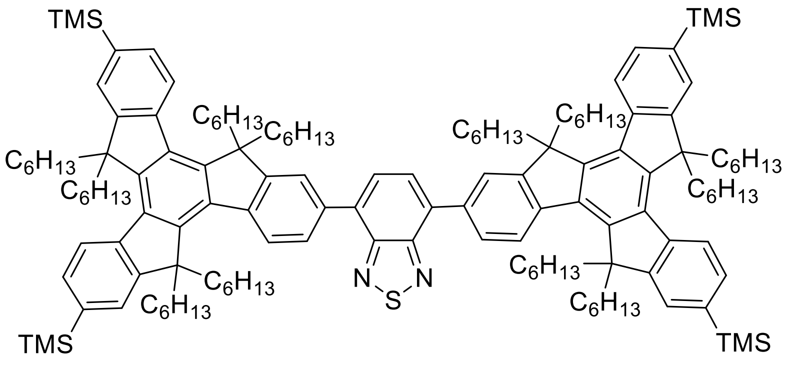

4.1

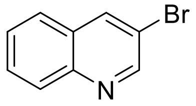

4.2

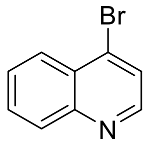

4CzIPN

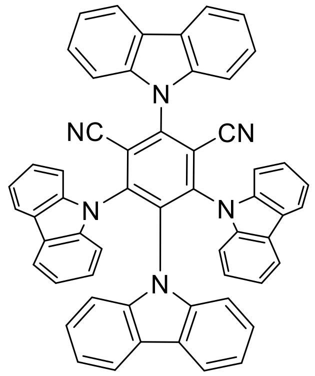

A

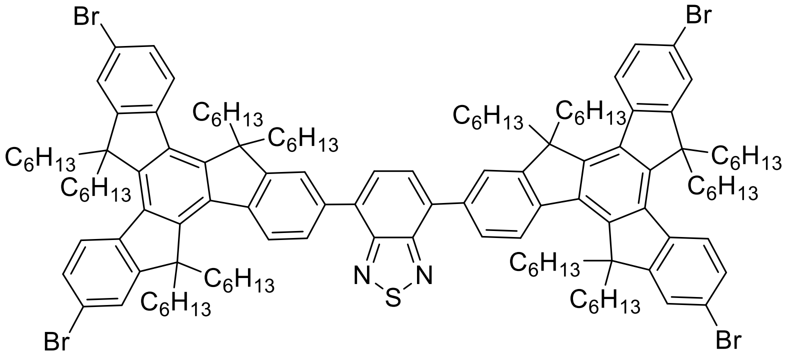

A0

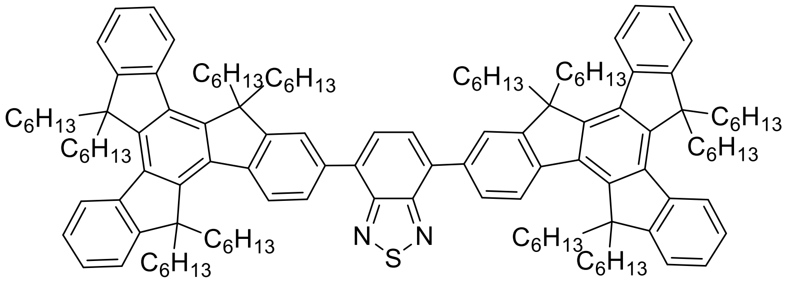

A1

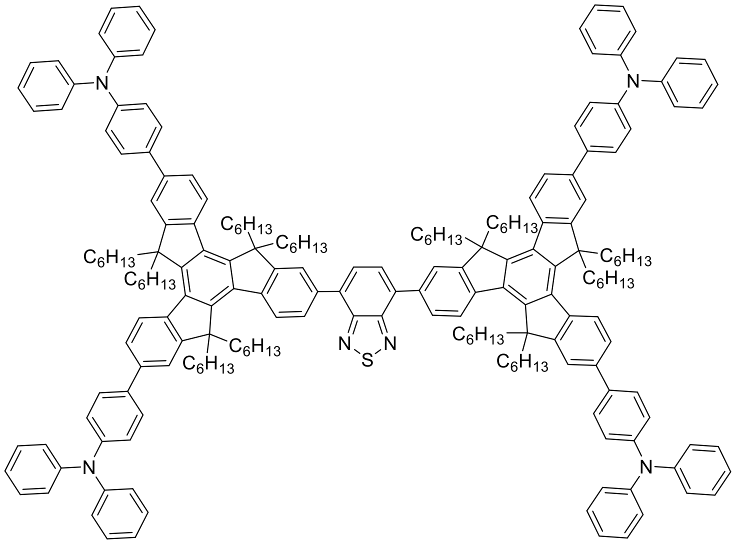

A2

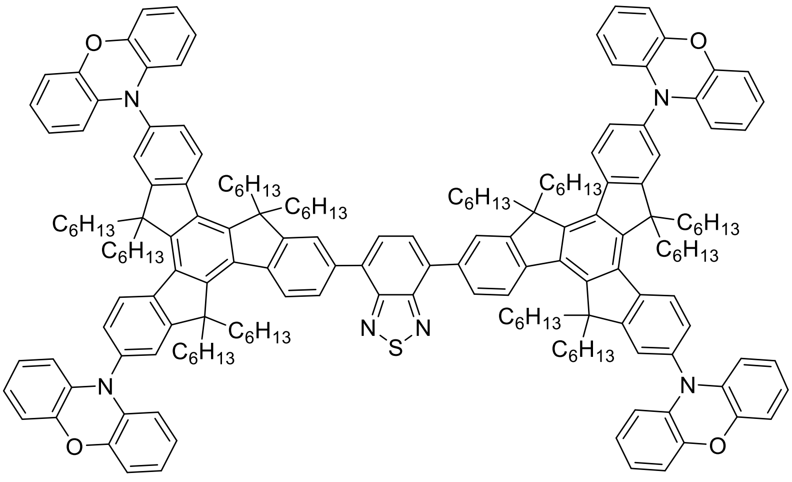

BCP

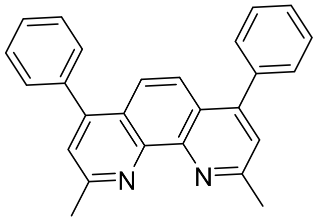

BPhen

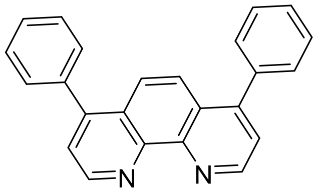

CBZ

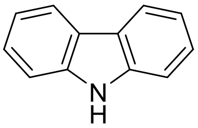

DMAC

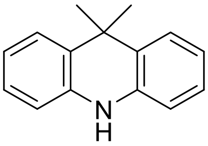

DPEPO

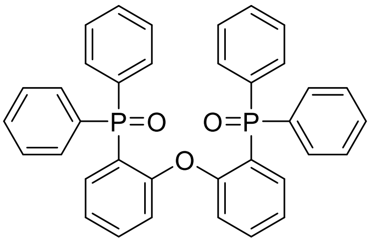

H1-PXZ

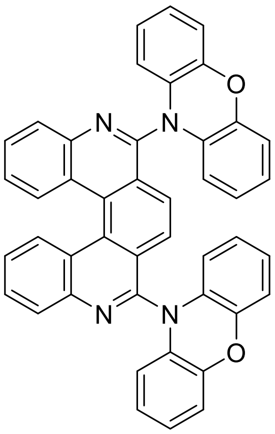

H2-PXZ

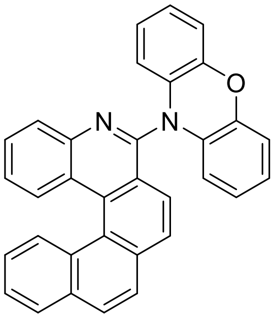

mCP

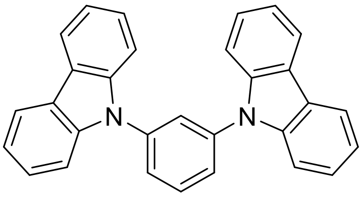

NPB

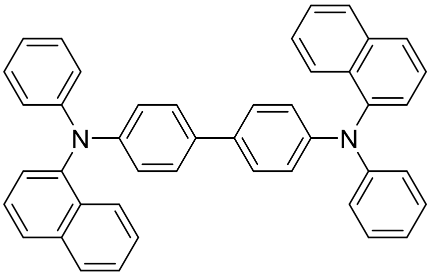

PEDOT:PSS

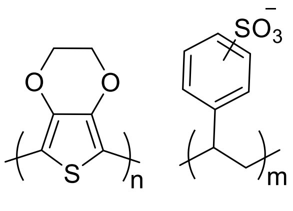

PXZ

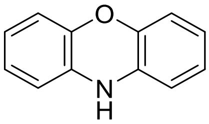

Q1

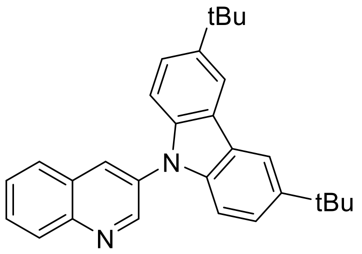

Q1-S1

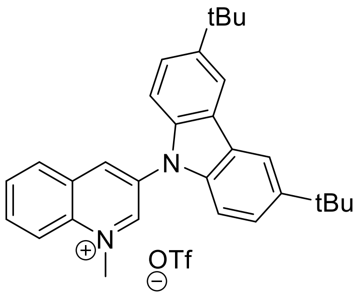

Q1-S2

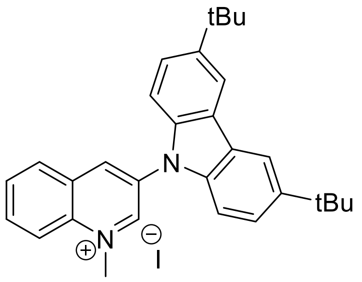

Q1-S3

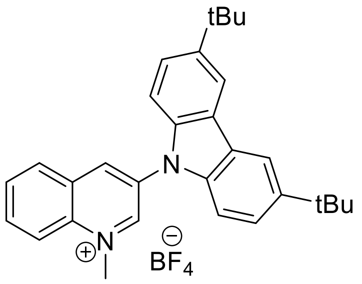

Q2

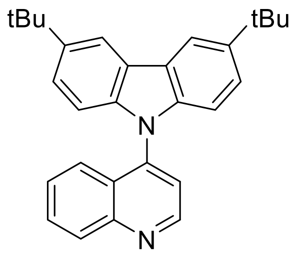

Q2-S1

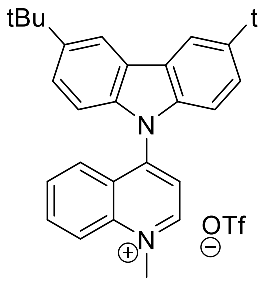

Q2-S2

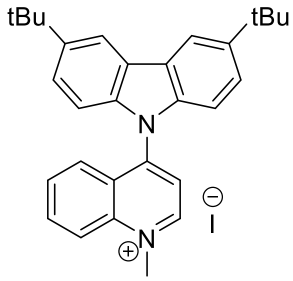

Q2-S3

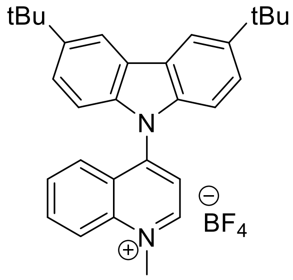

tBu-CBZ

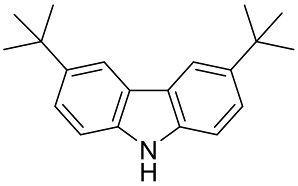

TCTA

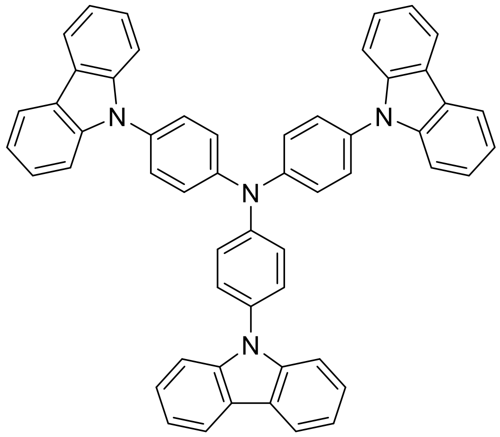

TPBi

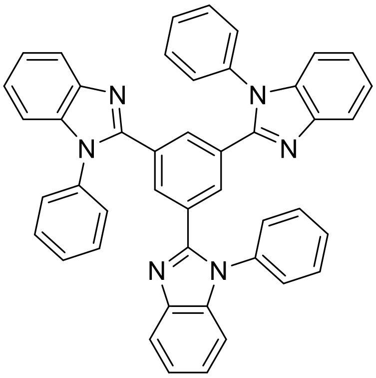

TSBPA